Peptide-Directed Metal Complex Luminophores: Candidates for Photodynamic Therapeutics

A thesis submitted to Dublin City University for the award of PhD

By

Christopher S. Burke, B.Sc. (Hons)

Under the supervision of Prof. Tia E. Keyes.

School of Chemical Sciences,

Dublin City University, Glasnevin, Dublin 9.

January 2018

Declaration

I hereby certify that this material, which I now submit for assessment on the programme of study leading to the award of PhD. is entirely my own work, that I have exercised reasonable care to ensure that the work is original, and does not to the best of my knowledge breach any law of copyright, and has not been taken from the work of others save and to the extent that such work has been cited and acknowledged within the text of my work.

Signed: _____

ID No.: _13212714_____

Date: _____

Acknowledgements

Firstly, a huge thank you to my supervisor Prof. Tia Keyes. Thank you for taking me on in the first place and then guiding my development as a researcher with your endless encouragement and knowledge. Here's to a successful PhD and hopefully the postdoc will hit the same heights!

Next, Dr. A! Aisling, thank you for being a brilliant scientist and great friend. You've had to put up with my work/chemistry rants and being handed scraps of dye (and still working your magic to produce amazing images). This thesis wouldn't be half of what it is without your hard work! Plus, when it started to get stressful towards the end, you were always there to help and I'll never forget that.

I owe a debt of gratitude to two great mentors that I had the pleasure of learning from over the last four years – Dr. Aaron Martin and Dr. Ciaran Dolan. I learned an awful lot from you both and those skills will continue to be put to good use! I was lucky enough to get some help from some fantastic students along the way. My thanks in particular to Markus, Pia, Catherine and Tasha. Thanks also to Kerileng for contributing some electrochemistry data and cheers to the rest of our research group, past and present! Perfect time to wish good luck to the next peptide-conjugators, Karmel and David – you guys can do it too!

Thank you to our brilliant technicians who keep this place ticking, particularly John, Ambrose, Veronica, Vinny, Damien, Mary and Josephine who have at some stage been there when I really needed them. I'd also like to extend my thanks in general to the staff of the Dept. of Chemical Sciences who have always been friendly and welcoming.

A PhD is more than just the piece of paper at the end and I am extremely grateful for the opportunity I've had to meet some amazing people who have become great friends over the past few years! Of course, we've had our share of 'going for a few quiet ones' (Powers!), but what really makes it is the absolute great craic you can have day-in day-out in the lab (and at coffee…for a few hours). I can't mention everyone but there's a few of you I just can't leave out. Liamy Dealz – great for a 9pm coffee, just after he puts on a bulk electrolysis. Colm Sahn Montgomery: loves cans and Sunday evenings in the lab. Aurelien, the mature one I can talk to about Amaretto and 'sayings in France'. Suzanne – I'm still living off results from jolly January! Dr. A – who will take me to gin palace someday. Darragh; the Sultan in-waiting and secret nerd - loves chemistry and rants about chemistry. Laura, always upbeat - last seen in the Ivy House. Eadaoin hon – fellow South-East legend. The new-comers, Pintman Steve and Guinny Guil - it's been a good year for random drinks! Sammy D, Ivan, Jack (partial to a Powers), and everyone else who I just don't have the space to mention – thank you! A few of the lads from Wexico deserve a mention here too who were a much-needed outlet from the PhD. Conor, it'll be your turn soon but I promise you we're not going to the Globe! Toby and Brian, don't think we'll ever forget the Euros! Plus - can't forget Sziget! (here he goes again…).

In getting to this point, I cannot forget those who have influenced my career in such a significantly positive manner. I haven't had the platform to say thanks properly before now but to Theresa Cole (Bridgetown) and Dr. Helen Hughes (WIT) – a massive thank you for your early encouragement and inspiration.

I've left the last few words for those closest to me. To my family; Mam, Dad, Saoirse and Rebecca. I know I'll have your support. Thanks for keeping my feet on the ground and for being there for me without question. I hope I can repay it someday.

To Aoife, I love you. You are the most amazing person I know. Especially after putting up with so much over the last few years! I promise to give back that time and patience you deserve as you get close to the end of your study too. I also love your randomness – that sword will look great on our mantelpiece!

Table of Contents

Chapter 2: Materials and methods

Chapter 3: Development of efficient synthetic routes to bio-conjugated Ru(II) luminophores

Chapter 4: Ru-dppz peptide conjugates; targeting nuclear and mitochondrial DNA in live cells with a molecular light switch.

Chapter 5: Nuclear-targeted Ru(II) 1,4,5,8-tetraazaphenanthrene (tap) peptide conjugates for photoinduced DNA damage in live cells

Chapter 7: Conclusions and future work

Appendices

Abbreviations

Amino Acid List:

A	Ala	Alanine	P	Pro	Proline
F	Phe	Phenylalanine	Q	Gln	Glutamine
I	Ile	Isoleucine	r	d-Arg	d-Arginine
K	Lys	Lysine	R	Arg	Arginine
L	Leu	Leucine	V	Val	Valine
M	Met	Methionine	W	Trp	Tryptophan
N	Asn	Asparagine	Y	Tyr	Tyrosine

Peptide Sequences:

Shorthand	*Target*	*Sequence (Net Charge at pH 7.4)*
Amy	Amyloid-β	NH_2-Ahx-KLVFWAK-$CONH_2$ (+2)
ER	Endoplasmic Reticulum	NH_2-Ahx-RQIKIWFQNRRMKWKK-$CONH_2$(+7)
MPP	Mitochondria	NH_2-Ahx-FrFKFrFK(Ac)-$CONH_2$ (+3)
NLS	Nucleus	NH_2-Ahx-VQRKRQKLMP-$CONH_2$ (+4)
R8	Non-specific Uptake	NH_2-Ahx-RRRRRRRR-$CONH_2$ (+8)

Other Abbreviations:

5CNU	5-cyanouracil
AcOH	Acetic acid
AFM	Atomic Force Microscopy
AMP	Adenosine monophosphate
aphen	5-amino-1,10-phenathroline
ATP	Adenosine triphosphate
ATR-IR	Attenuated Total Reflectance Infrared Spectroscopy
Aβ	Amyloid beta peptide
biq	2,2'-biquinoline
BODIPY	Boron-dipyrromethene
bpp	bis(2-pyridyl)pyrazine

bpy	2,2’-bipyridine
bpz	2,2'-bipyrazine
bqdppz	Benzo[j]quinoxalino[2,3-h]dipyrido[3,2-a:2′,3′-c]phenazine
BSA	Bovine serum albumin
Bz	Benzene
CD	Circular dichroism
chrysi	5,6-chrysenequinone diimine
CIS	Coordination induced shifts
COSY	Correlation spectroscopy (H-H COSY)
CPP	Cell penetrating peptide
ctDNA	DNA from calf thymus
DCC	N,N'-dicyclohexyl-carbodiimide
DFT	Density functional theory
DIPEA	N,N-Diisopropylethylamine
dmbpy	6,6’-dimethyl-2,2’bipyridine
dmdppz	1,12-dimethyldipyrido[3,2-a:2',3'-c]phenazine
dmdpq	7,10-dimethyl-pyrazino[2,3-f]-1,10-phenanthroline
DMF	Dimethylformamide
dmphen	2,9-Dimethyl-1,10-phenanthroline
DMSO	Dimethylsulfoxide
dmsp	(E)-4-(3,4-dimethoxystyryl)-pyridine
dop	Dioxinophenanthroline
dpa	Dipyridylamine
dppf	1,1'-Bis(diphenylphosphino)-ferrocene
dppm2	Dipyrido[3,2-a:2',3'-c]methylphenazine
dppn	Benzo[i]-dipyrido[3,2-a:20,30-c]phenazine
dppx	Dipyrido[3,2-a:2',3'-c]dimethylphenazine
dppz	Dipyrido[3,2-a:2′,3′-c]phenazine
dppz-idzo	Dipyrido-[3,2-a:2',3'-c] phenazine-imidazolone
dpq	Dipyrido[3,2-f:2′,3′-h]-quinoxaline

dpqp	Pyrazino[20,30:5,6]pyrazino-[2,3-f][1,10]phenanthroline
EB	Ethidium bromide
ECL	Electrochemiluminescence
EDC	1-Ethyl-3-(3-dimethylaminopropyl)carbodiimide
EDTA	Ethylenediaminetetraacetic acid
FLIM/LLIM	Fluorescence (luminescence) lifetime imaging
FRET	Förster resonance energy transfer
FWHM	Full width at half maximum
G4	G-quadruplex
GMP	Guanosine monophosphate
HSA	human serum albumin
hat	1,4,5,8,9,12-hexaazatriphenylene
HATU	1-[Bis(dimethylamino)methylene]-1H-1,2,3-triazolo[4,5-b]pyridinium 3-oxid hexafluorophosphate
Hbpt	1H-3-(2-pyridyl)-5-(3-pyridyl)-1,2,4-triazole
HBTU	N,N,N′,N′-Tetramethyl-O-(1H-benzotriazol-1-yl)uronium hexafluorophosphate
HPLC	High performance liquid chromatography
HRMS	High resolution mass spectrometry
IC	Internal conversion
ICD	Induced circular dichroism
ICP-MS	Inductively coupled plasma mass spectrometry
IPA	2-propanol
IR	Infrared
ISC	Intersystem crossing
K_b	Binding constant
LC	Ligand centred state
MALDI	Matrix assisted laser desorption ionisation
MC	Metal centred state
MLCT	Metal to ligand charge transfer
MMR	Mismatch repair

MPP	Mitochondrial penetrating peptide
mtDNA	Mitochondrial DNA
n	Binding site size
NHS (HOSu)	N-hydroxysuccinimide
NLS	Nuclear localising signal
NMR	Nuclear magnetic resonance
NOESY	Nuclear Overhauser spectroscopy
ODN	Oligonucleotides
ox	Oxalate
PACT	Photoactivated chemotherapeutics
PBS	Phosphate buffered saline (herein taken as Dulbecco's PBS without modifiers)
PCET	Proton coupled electron transfer
PCP	Pentachlorophenol
PDT	Photodynamic therapy
PEG	Polyethyleneglycol
PET	Photoinduced electron transfer
phehat	1,10-phenanthrolino[5,6-b]1,4,5,8,9,12-hexaazatriphenylene
phen	1,10-phenanthroline
phendione	1,10-phenanthroline-5,6-dione
phzi	Benzo[a]-phenazin-5,6-quinone diimine
PI	Phototoxicity index
pic-R	Phenylimidazo[4,5-f][1,10]phenanthroline
ppy	2-phenylpyridine
Py	Pyridine
PyBOP	Benzotriazol-1-yl-oxytripyrrolidinophosphonium hexafluorophosphate
pydppn	3-(pyrid-2′-yl)-4,5,9,16-tetraaza-dibenzo[a,c]-naphthacene
qTOF	Quadrupole time of flight (MS)
r	DNA-dye ratio; [DNA]bp/[Ru]
ROS	Reactive oxygen species
rRaman	Resonance Raman

stDNA	DNA from salmon testes
STED	Stimulated emission depletion (microscopy)
tactp	4,5,9,18-tetraazachryseno[9,10-b]triphenylene
tap	1,4,5,8-tetraazaphenanthrene
TBAC	Tetrabutylammonium chloride
TCSPC	Time correlated single photon counting
TFA	Trifluoroacetic acid
TFAM	Mitochondrial transcription factor A
THF	Tetrahydrofuran
TLC	Thin layer chromatography
TMNO	Trimethylamine-N-oxide
tpm	Tris(pyrazolyl)methane
tpphz	Tetrapyrido[3,2-a: 2′,3′-c: 3″,2″-h: 2″,3‴-j]phenazine
tpy	2,2′:6′,2″-Terpyridine
TRIR	Time resolved IR (spectroscopy)
TsOH	Tosic acid
VR	Vibrational relaxation
α	Fractional amplitude of lifetime component
ε	Molar extinction coefficient
λ	Wavelength
τ	Luminescence lifetime
φ	Quantum yield
χ^2	Goodness of fit

Abstract

Peptide-Directed Metal Complex Luminophores: Candidates for Photodynamic Therapeutics

Christopher S. Burke

Despite their potential to overcome critical limitations of conventional organic dyes, metal complex luminophores have yet to be truly accepted as probes for cellular imaging and phototherapy. Long-lived and reactive luminophore excited states grant a sensitivity not currently achievable by organic probes and offer the ability to efficiently photosensitise cellular toxicity. A barrier to their exploitation to date has been their relatively poor uptake and unpredictable localisation, especially to important theranostic targets like DNA. However, signal peptides are a powerful strategy towards achieving precision-targeting of key organelles and were previously successfully implemented to deliver metal complexes to the nucleus and mitochondria - two locales where cellular DNA resides. The overarching aim of this thesis was therefore: to explore the candidacy of peptide targeted Ru(II) luminophores for imaging and photo-destruction of DNA in live cells.

Two prominent Ru(II) complexes were established as candidate complexes to derivatise under the scope of this work. The first was $[Ru(bpy)_2(dppz)]^{2+}$ - a molecular light switch for DNA that is non-luminescent in water but switches on upon intercalating DNA. The second was $[Ru(tap)_2(bpy)]^{2+}$ - a complex which possesses an excited state reduction potential sufficiently positive to photo-oxidise and damage DNA. Chapter 3 explored efficient synthesis routes to conjugatable derivatives of Ru(II) luminophores with a highlight being the development of a novel protocol to prepare tris-heteroleptic Ru(II) complexes in unprecedented yield. Chapter 4 investigated the interaction of Ru-dppz conjugates with DNA in vitro and in live cells, where remarkably, both nuclear and mitochondrial DNA were successfully targeted permitting high resolution imaging of structure and cellular phase. Phototoxicity was induced at higher irradiation intensities leading to cellular apoptosis. Chapter 5 investigated the photo-reactivity of a nuclear-targeted Ru-tap conjugate in live cells where singlet oxygen independent photo-oxidation of DNA led to photosensitised destruction of HeLa cells with spatiotemporal control. Finally, Chapter 6 explored additional imaging and biophysical applications of Ru(II) luminophores.

Chapter 1

Introduction

1.1 Precision-targeted metal complex luminophores: candidates for DNA imaging and phototherapy in live cells

Metal complex luminophores are increasingly demonstrating their potential as viable alternatives to traditional organic probes for live cellular imaging and sensing.[1–3] In parallel, related complexes have been shown to be excellent reagents for photoinduced therapy, by exploiting photoreactive excited states or through the sensitisation of reactive oxygen species.[4–6] DNA is a critical cellular target for imaging and therapy, but despite the extensive study of its interaction with luminescent metal complexes *ex-cellulo*, there have been few successful reports of targeting these luminophores to genetic material in live cells. A barrier to achieving DNA interactions in cells is the relatively poor uptake of metal complexes and their unpredictable localisation that can lead to broad dark cytotoxicity.[7] There are several strategies to circumvent these issues, for example; our group and others have exploited signal peptides to precision target metal complexes to select organelles.[8–10] Herein, a key objective was to develop peptide-directed metal complexes to image cellular DNA, and once localised, to investigate their potential to photo-induce damage to the detriment of the cell. This chapter reviews key examples of the interaction of metal complexes with DNA and their successful use in imaging and photosensitised cellular toxicity. Two candidate complexes were established to develop further under the scope of this thesis towards DNA-targeted imaging and photodamage in live cells, and pertinent strategies to achieve their cellular uptake and localisation are examined.

1.2 Metal complex luminophores for cellular imaging and sensing

Fluorescence microscopy is by far the most widely used technique by biologists to study cellular structure and dynamics. Over the past 20 years, microscopy has moved beyond classical diffraction limited confocal imaging and towards high resolution techniques such as stimulated emission depletion (STED), stochastic optical reconstruction (STORM) and photoactivated localisation (PALM).[11] The rise of this new technology has precipitated the need for novel probes suited to the challenging photophysical demands of these microscopies. Commercial offerings are based exclusively on organic probes which suffer from some important limitations as discussed below. Metal complex luminophores exhibit

photophysical characteristics that can potentially overcome these issues but they have not been explored as super-resolution imaging probes to any significant degree to date. Furthermore, metal based probes can optically respond to dynamic cellular environments and thus, incorporate not only an imaging function but also environmental sensitivity that cannot currently be achieved using conventional organic probes. In this section, the application of metal complex luminophores for cellular imaging and sensing is explored including important aspects of their photophysics.

1.2.1 Introduction to molecular photophysics

The Jablonski diagram as shown in Figure 1.1 is a convenient means of summarising the photophysical processes of a molecule. Typically, a chromophore absorbs incident light promoting an electron from its singlet ground state (S_0) to a singlet excited state (S_n). De-excitation from higher electronic states proceeds via several different mechanisms. According to Kasha's rule, with few exceptions in condensed media, luminescence occurs from the first electronic excited state, S_1 (or T_1) such that deactivation to this energy level is largely non-radiative.[12] A corollary of Kasha's rule is Vavilov's rule which states that the quantum yield of emission is independent of the excitation wavelength, which with some exceptions is generally true.[13] Vibrational relaxation (VR) can occur from hot vibrational states, and in solution, energy can be lost by collisions with the solvent. Internal conversion (IC) occurs between states of the same multiplicity and is the iso-energetic crossover, for example, from a S_n state to a hot vibrational state of the S_{n-1} level. Non-radiative VR then yields the lowest vibrational S_{n-1} state.

From the S_1 state, an excited species may return to its ground state through the kinetically competing processes of fluorescence and non-radiative deactivation (a combination of IC and VR). A measure of the relative rates of deactivation is given by the fluorescence quantum yield, φ_{fl}, which can be simply expressed as the ratio of the number of absorbed photons to those emitted. Since the energy gap is smaller for luminescence than absorption, emission always occurs at longer wavelength than the associated excitation process. The measure of this energy difference is termed the Stokes shift.

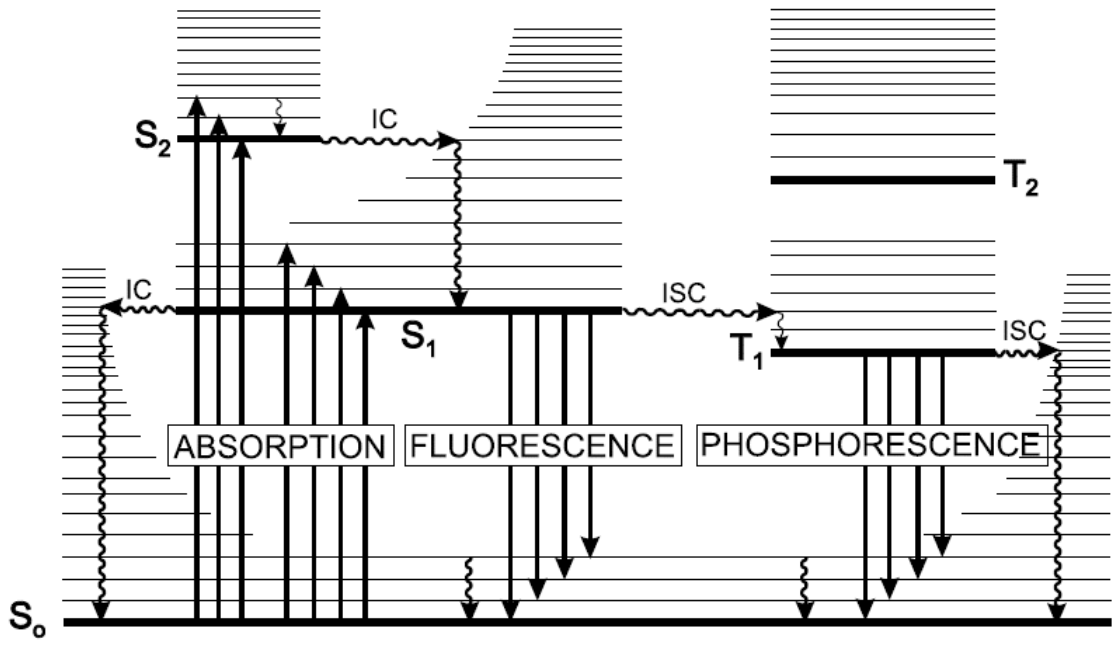

Figure 1.1: General Jablonski diagram to illustrate key photophysical mechanisms. IC = internal conversion, ISC = intersystem crossing. Reproduced from Valeur.[13]

Intersystem crossing (ISC) is an iso-energetic spin forbidden process that yields a spin-change crossover between singlet and triplet states. ISC, being a forbidden process, occurs with low quantum yield in organic species but can be enhanced by spin-orbit coupling, a mixing of the spin and angular momenta. This permits ISC with greater quantum efficiency in systems bearing heavier elements such as metal complexes and compounds containing lower-row elements like heavy halogen derivatised organics. Emission from triplet states occurs by phosphorescence and is characterised by reduced luminescence quantum yield and large Stokes shifts due to stabilisation by spin pairing that causes the lowest triplet state to sit at lower energies relative to the lowest singlet state. To return to the ground singlet state, phosphorescence requires a spin change which extends the lifetime of the excited state.

Although absorption is rapid, a species may exist in an excited state for a comparably long time before returning to its ground state with the possible accompaniment of photon emission. Absorption typically operates on the femto-second timescale (10^{-15} s), fluorescence closer to the nano-second scale (10^{-11} – 10^{-9} s) and phosphorescence occurs from the sub micro-second (10^{-6} s) range up to the order of full seconds. The luminescence lifetime, τ, can

be considered as the average time an excited species spends in the excited state before photon emission. More specifically, the decay from the excited state is exponential, typically following first order kinetics, and hence, τ is the time taken to reduce an e^{th} of the excited state population. The luminescence lifetime can be expressed in terms of the radiative rate constant (k_r) and the non-radiative rate constant (k_{nr}) as indicated in Equation 1.1.

$$\tau = \frac{1}{k_r + k_{nr}}$$

… Equation 1.1

The luminescence quantum yield (ϕ_{lum}) is related to lifetime, and since the rate constants are proportional to the absorbed and emitted photons, ϕ_{lum} can be expressed in terms of τ, k_r and k_{nr} as indicated in Equation 1.2.

$$\phi_{lum} = \frac{k_r}{k_r + k_{nr}} = \tau . k_r$$

… Equation 1.2

1.2.2 Candidacy of metal complexes for cellular imaging and sensing

Currently, commercially available imaging probes are organic dyes that suffer from some important limitations. Emission from organic probes tends to originate from short-lived fluorescent states ($\tau \approx 1 - 10$ ns) that are weakly Stokes-shifted ($\Delta\lambda < 50$ nm). This can be problematic, leading to issues with self-quenching or distortion of the emission band, especially where dye molecules accumulate in regions of high local concentration within cells. A narrow Stokes shift can also diminish imaging efficiency when used under certain super resolution microscopies. For example, in STED imaging, the closer the stimulating laser is to the λ_{max} of emission the more efficient the stimulated emission, but exciting into the tail of an absorbance can increase the prospect of bleaching or excitation to a dark state.[10] The short lived excited state of many organic fluorophores precludes environmental sensitivity, that is, a spectroscopic response to an interaction with an analyte, since deactivation to the ground state occurs typically on a time scale much faster than molecular diffusion. Although quantum yields are generally excellent, organic dyes can be quite

photochemically unstable which limits their use for longer studies of dynamic cellular processes. Finally, organic fluorophores tend to exhibit poor aqueous solubility which restricts their use in cell imaging, often requiring administration as a solution of organic solvent which can damage the cellular membrane.

Metal complex luminophores can potentially overcome the limitations of organic probes, typically bearing long-lived excited states and strongly Stokes-shifted emission. Specifically, spin-orbit coupling is mediated efficiently by the heavy atom effect which blurs formal assignment of the spin state but generally luminescence occurs from a state largely indicative of triplet character. Although quantum yields are comparably much lower than organic dyes, the strong Stokes-shift and extended luminescence lifetime of metal complexes permits time-gating that reduces background effects such as autofluorescence and enhances sensitivity.[10,14] The longer-lived nature of the excited state also imparts environmental sensitivity to diffusing analytes like oxygen, which can quench the emission and provide a semi-quantitative measure of the local concentration.[15] The modularity of metal complexes allows the exchange of ligands to tune the photophysical properties of the luminophore, for example; phenazine derived ligands can confer aqueous sensitivity and have been exploited in emissive metal complexes of Ru(II), Os(II), Re(I) and Ir(III).[16–19] This versatility is useful in other ways; ligand functionalisation can also impact uptake and localisation properties, often without disrupting the photophysical profile of a luminophore. Furthermore, the three-dimensionality of metal complexes is anchored at the coordinated metal centre and enables the incorporation of steric controls based on molecular size and shape that can induce specificity for certain biomolecules like binding cavities of proteins, or preference for DNA sequence and structure. These aspects are explored in greater detail in later sections of this chapter. Finally, metal complex luminophores tend to be cationic and aqueous solubility can be altered as desired by judicious choice of the anionic counterion.

Complexes of the platinum group metals are prominent candidates for use in cellular imaging due to their kinetic and photo-stability relative to other luminophores such as those of the first-row metals. Of this class, the various metal systems have their respective advantages and disadvantages. Ir(III) probes are prominent across the literature, particularly *bis*-cyclometallated complexes, and are known for their high quantum yields and long-lived

luminescence.[20] The excited state is mixed, comprising both triplet metal-to-ligand charge transfer (^{3}MLCT) and ligand-centred (^{3}LC) states, which enables enhanced tunability.[21] However, Ir(III) complexes tend to suffer from poor visible absorption and higher cytotoxicities, generally attributed to their lipophilicity.[22] Rh(III) complexes have been employed as important probes for DNA mismatches [23–25] but generally they are less commonly used in cellular imaging, perhaps because their emission diminishes at temperatures lower than other luminophores, thus limiting their use as imaging agents under physiological conditions (i.e. 37 °C).[26] Complexes of Re(I) are usually based on a $[Re(CO)_3(L)(N\hat{}N)]^+$ core where N^N is a polypyridyl ligand and L is a halogen or pyridyl ligand. Re(I) luminophores can be limited by their blue absorption but have demonstrated promising cellular application, for example as CO releasing agents.[27–29] Pt(II) luminescence has also been used for bioimaging,[30] although the square planar geometry of Pt(II) complexes may limit their potential for specific biointeractions. An important alternative class of metal complex for imaging is the lanthanide series, complexes of which are often utilised as magnetic contrast reagents.[31,32] However, these probes require sensitisation to access their excited states and are not considered further herein.

The photophysical properties of Ru(II) polypyridyl complexes and their Os(II) analogues are particularly attractive for imaging, typically arising from ^{3}MLCT states which are sensitised by visible absorption.[21,26] Ru(II) polypyridyl complexes bear long-lived excited states that permit environmental sensitivity to important cellular viability factors such as pH, O_2 and reactive oxygen species (ROS). The well-developed chemistry of Ru(II) polypyridyl complexes grants synthetic access to a range of derivatives which can be designed to fulfil various criteria to impact uptake, localisation, sensitivity and biomolecular interactions. In the broader literature, Ru(II) complexes have often been criticised for their lack of tunability (e.g. compared to Ir(III) complexes), usually requiring blue sensitisation and emitting in the orange-red region of the spectrum. However, although the area is comparably understudied, the absorption and emission of Ru(II) complexes can be red-shifted using extended ligand systems such as 2,2'-biquinoline, in some cases even leading to black-absorption.[33,34] Due to their attractive properties, our group has widely utilised Ru(II) complexes for cellular imaging and sensing, and herein, they are further exploited in the work of this thesis.

1.2.3 Ru(II) polypyridyl complexes for cellular imaging and sensing

Ru(II) polypyridyl complexes comprise a d^6 metal ion and polypyridine ligands that contain σ-donor orbitals on their N-atoms and π- donor and acceptor orbitals delocalised on the aromatic rings. The general photophysics of Ru(II) polypyridyl complexes can be studied using $[Ru(bpy)_3]^{2+}$ as an example (bpy = 2,2'-bipyridine).[26] In this complex, the absorbance spectrum (Figure 1.2) exhibits an intense ligand-centred (LC, π→π*) absorption in the UV region, a distinctive broad metal-to-ligand charge transfer transition (MLCT, d→π*) in the visible region centred at *ca.* 450 nm, and a higher energy MLCT at about 240 nm. Excitation into singlet MLCT states yields a triplet MLCT state, where ISC occurs with unit efficiency due to the heavy atom effect. The Stokes shift is substantial with emission centred at *ca.* 610 nm for $[Ru(bpy)_3]^{2+}$. The excited state of the ^{3}MLCT is long-lived at room temperature, for example, for $[Ru(bpy)_3]^{2+}$ in acetonitrile and water, $\tau \approx 900$ and 650 ns respectively under air. Luminescence quantum yields in the range 2 - 5 % in aerated solutions at room temperature are common for Ru(II) systems of this type.

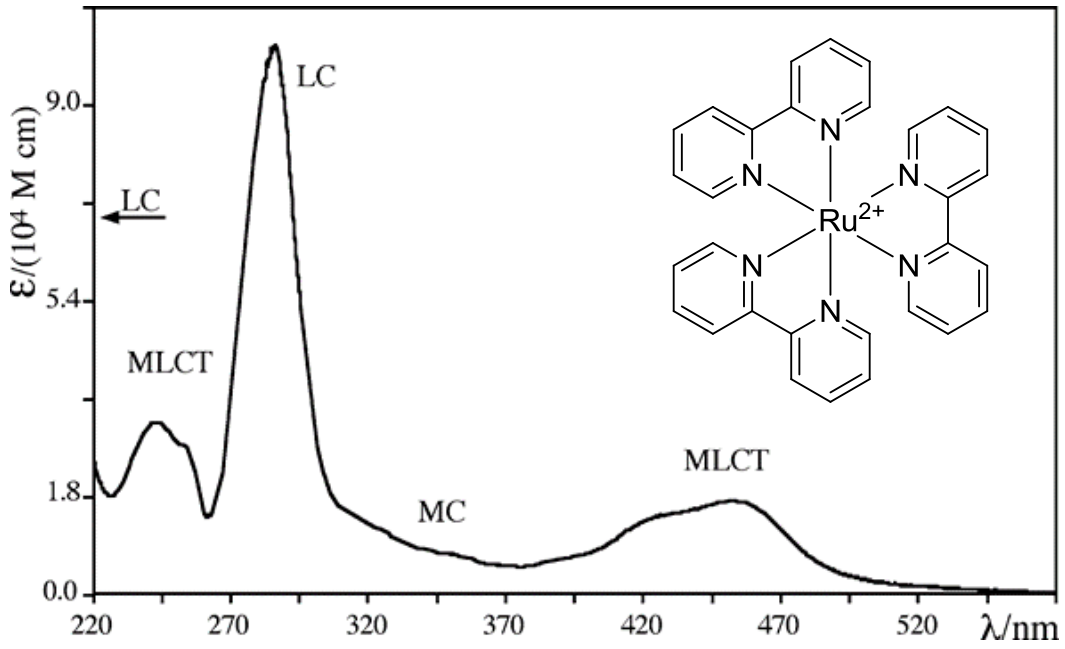

Figure 1.2: Absorbance spectrum of $[Ru(bpy)_3]^{2+}$ in alcoholic solution. Inset: structure of $[Ru(bpy)_3]^{2+}$. Image adapted from Balzani and Campagna.[26]

Excited stated decay of polypyridyl Ru(II) systems can occur via non-radiative processes such as IC and VR to the ground state or by luminescence (which is formally a phosphorescence in Ru(II) complexes). Another avenue for deactivation also exists involving population of the ^{3}MC metal-centred state, the extent of which is governed by the relative energies of the MLCT and MC states. In contrast to LC and MLCT states, the ^{3}MC state in Ru(II) polypyridyl complexes is strongly displaced relative to the ground state and its population can lead to efficient non-radiative deactivation and ligand dissociation (Figure 1.3). In $[Ru(bpy)_3]^{2+}$, the ^{3}MC state exists at higher energy than the lowest ^{3}MLCT state but can be thermally populated. The relative energies are even closer together in sterically strained complexes, such as those of 2,2'-biquinoline or 2,9-dimethyl-1,10-phenathroline, and ligand dissociations become increasingly problematic with regards to imaging. However, there are benefits to this reactivity, photorelease of ligand from strained complexes was an early strategy to synthesise *tris*-heteroleptic complexes of Ru(II)[35,36] and generation of

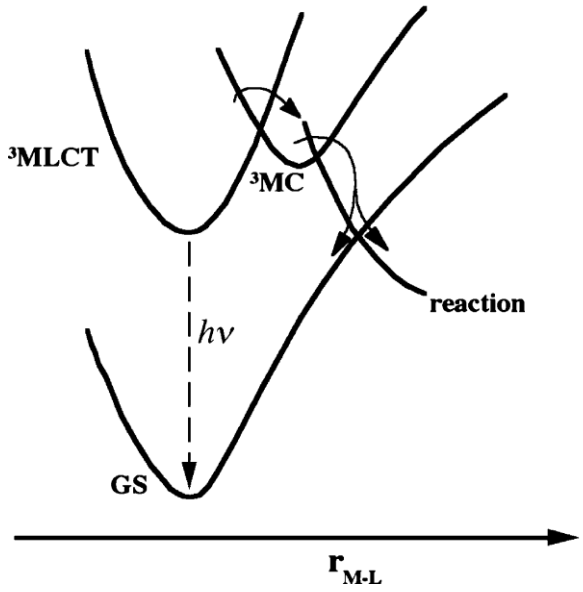

Figure 1.3: Typical deactivations of the ^{3}MLCT excited state of $[Ru(bpy)_3]^{2+}$ type systems. Luminescence or non-radiative relaxation may occur from the ^{3}MLCT state. Thermal activation to the displaced ^{3}MC state may also occur which decays by non-radiative relaxation to the ground state or photochemical reaction (ligand dechelation). Adapted from Balzani and Campagna.[26]

coordinatively unsaturated complexes can be therapeutically important, for example to target DNA (see section 1.3). In the case of $[Ru(bpy)_3]^{2+}$ and related complexes, ligand dissociation from ^3MC states can lead to ligand substitution and this is more efficient in the presence of coordinating ions like Cl^- in less polar organic solvents (e.g. CH_2Cl_2). In more polar environments and/or an absence of coordinating species, the complex can be stabilised by chelate effects. Importantly, Ru(II) polypyridyl complexes are kinetically stable as solutions in the dark.

The versatility of Ru(II) polypyridyl systems has inspired the compilation of a now burgeoning library of structures, many of which are suited to cellular imaging. While the continued development of novel Ru(II) imaging probes is important, the potential of existing Ru(II) probes to act as *sensitive* probes for the cellular environment remains relatively untapped. Significant examples include the use of ligands that impart a sensitivity to important biomolecular structures like DNA and membranes, and cellular viability factors such as O_2, ROS, pH and biorelevant ions (Figure 1.4). Indeed, complexes based on a classical $[Ru(bpy/phen)_3]^{2+}$ core (phen = 1,10-phenanthroline) are already sufficiently long-lived in their excited state to respond dynamically to O_2 and ROS.[9,37–39] The use of phenazine based ligands like dppz (dipyridophenazine) have been studied for their aqueous sensitivity

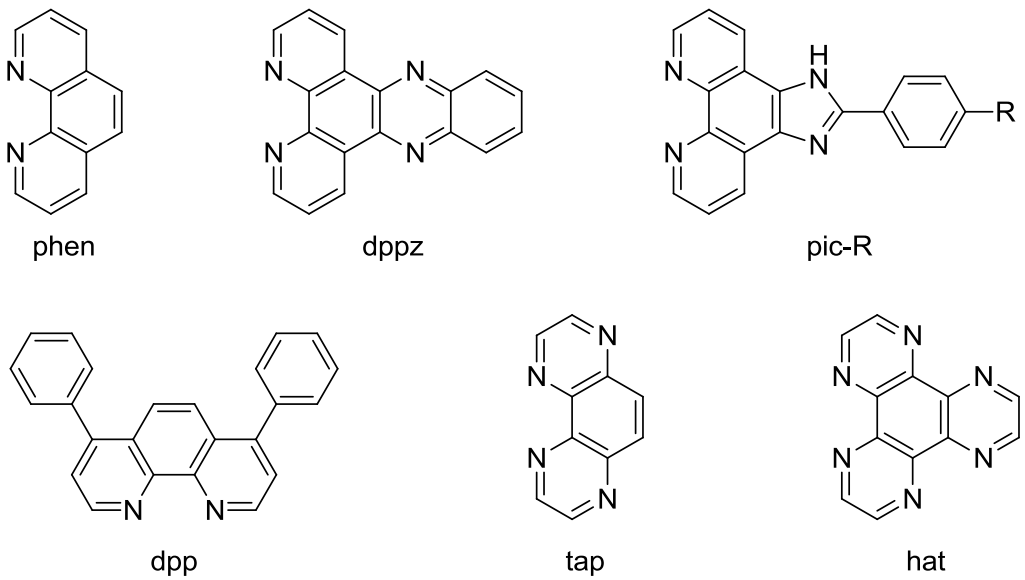

Figure 1.4: Structures of ligands of Ru(II) complexes employed in cellular imaging and sensing.

that renders them molecular light switches for DNA (section 1.3),[1,16] but also as lipophilic moieties that drive their complexes into lipid membranes with concomitant switching on of luminescence.[40] Similarly, the highly lipophilic character of diphenylphenathroline (dpp) facilitates cellular uptake, increases targeting of lipid regions and also enhances the oxygen sensitivity of the Ru(II) complex.[7,41–43] Ru(II) complexes containing polyazaaromatic ligands like tetraazapheanthrene (tap) and hexaazatriphenylene (hat) possess an excited state reduction potential sufficiently positive to abstract electrons from biomolecules that are easily oxidised like guanine, tryptophan and tyrosine.[44–46] Increasingly popular are ligands derived from phenyl-imidazophenanthroline (pip-R in broader literature, pic-R in publications from our group) due to their facile synthesis and spectroscopic response to pH, generally as ON-OFF type switches.[47–51] Similar switching has been demonstrated for ligands that respond upon binding to biorelevant ions like Cu^{2+}, Fe^{2+}, $H_2PO_4^{2-}$, Zn^{+2}, OAc^-, F^-, I^- and SO_4^{2-}.[52–62] To date, despite the potential of Ru(II) complexes for sensing, examples of cellular applications are scarce.

1.3 DNA: a critical theranostic target

1.3.1 General structural and biological aspects of DNA

Deoxyribonucleic acid, DNA, is one of the essential biomacromolecules required for life. Its helical structure hosts a library of evolving genetic information coded for biosynthesis. DNA is composed of two intertwining polynucleotides which are held together by hydrogen-bonding between complimentary base pairs.[63] The purines; Adenine (A) and Guanine (G), pair with their complimentary partner pyrimidines; Thymine (T) and Cytosine (C) as depicted in Figure 1.5. The individual strands of the right-handed double helix comprise an external polyanionic sugar-phosphate backbone which is composed of deoxyribose units bound via phosphodiester linkages to intermittent phosphate groups.

Under physiological conditions, DNA is most commonly found in the right-handed B-form, although other major conformers exist, most notably, Z-DNA and A-DNA. A-DNA was first seen in dehydrated fibres of isolated DNA and is a right-handed helix like the B form, but the A-helix is wider and shorter.[64] The Z-form is unusual in that it adopts a left-handed helical coil with the phosphates oriented in a zig-zagging chain.[65] Z-DNA forms in sequences of

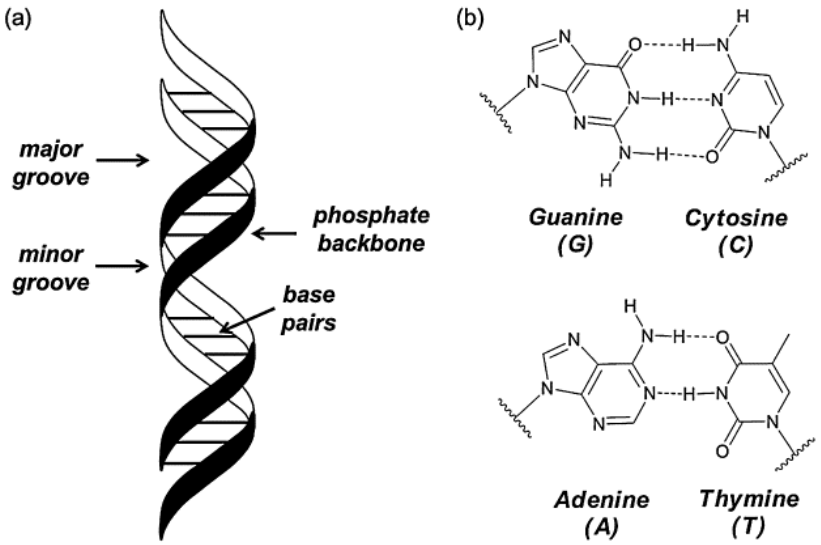

Figure 1.5: (a) A simple representation of a B-DNA helix, and (b), an illustration of the DNA bases and their complimentary bonding as G-C and A-T base pairs. Reproduced from Knoll *et al*.[4]

---

alternating pyrimidines and purines and its existence illustrates the elastic and dynamic character of DNA. In its most common cellular form as B-DNA, the turns of the double helix form minor and major grooves and allow specific interaction with substrates such as enzymes, proteins or therapeutic agents. In combination with the hydrogen-bond mediated base-pairing within the duplex, the extremely stable structure of DNA is further enhanced by the π-stacking of the nitrogenous bases within the DNA core. DNA may also adopt a variety of local conformations, for example, G-quadruplexes are found in guanine rich regions of DNA, such as at the telomeres, and are characterised by the stacking of planar tetrads comprised of four guanine units arranged under Hoogsteen type bonding (Figure 1.6).[66] Other deviations from the standard structure include branching, hairpins, i-motifs, multiplexes and junctions.[67] The bio-relevance of the tendency of DNA to adopt various structures is linked to critical cellular function. Accordingly, such constructs are pertinent targets in imaging and therapy.

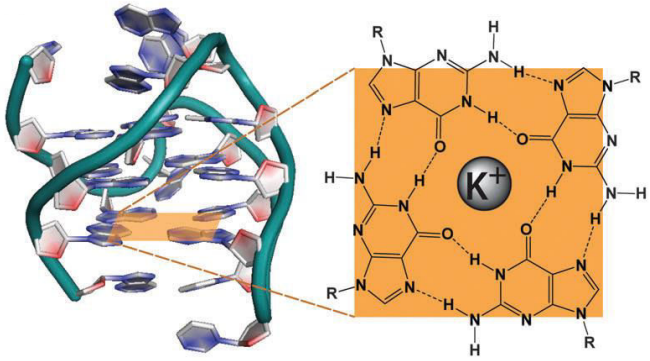

Figure 1.6: Arrangement of guanine into four-membered G-tetrads for stacking into G-quadruplexes.[67]

In human cells, DNA is stored in the nucleus and mitochondria. Typically, nuclear DNA is packaged into chromosomes with the aid of chromatin proteins such as histones which compact and organise the DNA. The full set of chromosomes in a cell make up its genome and in humans, this comprises approximately 3 billion base pairs divided into 46 linear chromosomes. The role of DNA is to store the genetic information necessary to sustain cellular processing. Its replication is crucial in cellular division, a mechanism which is essential for life. The sequence of base pairs within DNA directly codes the manufacture of proteins through the processes of transcription and translation. Clearly, the ability to target DNA using theranostic platforms is vitally important in monitoring and treating disease and this will likely form the focus of the new age of personalised medicine.[68]

1.3.2 Interaction of Ru(II) luminophores with DNA

1.3.2.1 Binding mechanisms

The interaction of coordination compounds with DNA can occur via several mechanisms governed by molecular size, shape, charge and hydrophobicity (Figure 1.7). These parameters can be exploited for selective recognition of DNA sequence and structure which is desired for targeted imaging and therapy. Groove binding is the association of a complex in the major or minor grooves, similar to the commercial DNA stain DAPI which binds at the minor groove.[69] Intercalation requires the incorporation of a rigid planar ligand between

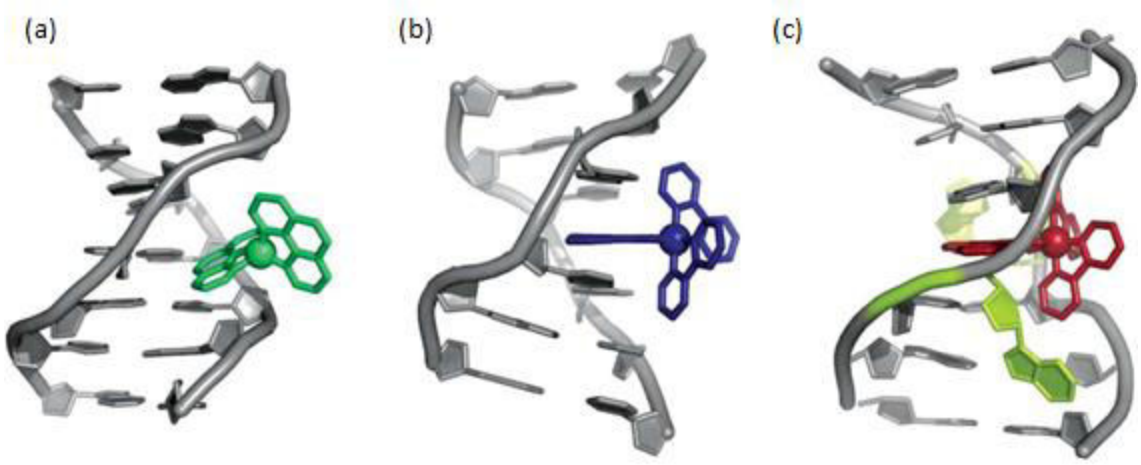

Figure 1.7: Different modes of DNA binding by metal complexes, (a) groove binding, (b) intercalation and (c) metalloinsertion with ejection of the bases marked in yellow.[72]

---

contiguous base pairs and is stabilised by π-stacking with the DNA core.[70] This mode was first proposed by Lerman who observed that binding by planar aromatic dyes led to lengthening and unwinding of the DNA helix.[70,71] Metalloinsertion, a mode particularly relevant for wide and bulky Rh(III) complexes, causes the ejection of bases at the binding site which is then accommodated by an intercalative ligand.[72] The phosphate backbone of DNA may also be targeted, for example, using cationic polyamine-platinum complexes.[73–75] Direct metalation of the bases can also occur and is important for therapeutic action.[76,77] Covalent binding may also be photosensitised and presents another avenue to interrogate the local luminophore environment or to apply therapy.[78,79]

The modularity of octahedral Ru(II) polypyridine complexes permits modification of the ligand systems to impart various functionalities that impact DNA binding selectivity (Figure 1.8). However, it is important to consider that DNA is an elastic dynamic structure which under normal cellular conditions is constantly changing; being packaged/unfolded, zipped/unzipped and so forth, and this brings extra complexity to probe design. In the following section, a focus is placed on key luminescent Ru(II) complexes which can directly report on DNA structure and function, with a view towards establishing candidate complexes for targeted live cellular imaging and photo-induced destruction of DNA.

1.3.2.2 Key literature examples of DNA binding Ru(II) luminophores

Historical developments: Towards probes for DNA handedness

The earliest studies on Ru(II) complexes and their biological interaction was pioneered by Dwyer who investigated the bacteriostatic action of *tris*-chelate complexes such as those bearing phenanthroline; $[M(phen)_n]^{2+}$.[80,81] The exact biological target in this instance was never elucidated but it was generally believed to be DNA.[72] Later, non-covalent DNA binding was explored by Sigman using cupric complexes like $[Cu(phen)_2]^{+}$.[82] The use of copper artificial nucleases is still a vibrant research topic today, although generally work has been focussed on Cu(II) dark reactivity with few examples of the exploitation of luminescent Cu(I) species.[83,84] Another key development was reported by Lippard and coworkers who presented the first example of a coordinatively-stable metal complex intercalator; $[Pt(tpy)(S\text{-}R)]^{+}$ (Figure 1.8).[85,86] However, the square planar geometry of these complexes renders the probe non-specific for DNA structure and there has been a strong focus instead placed on octahedral complexes of Ru(II), Ir(III), Rh(III) and Re(I).[20,72,87–89] In particular, Ru(II) polypyridyl complexes bear the synthetic modularity, required physical properties (e.g. water solubility, kinetic inertness, cationic charge) and the rich photophysics to spectroscopically probe DNA in the live cell. Most of the research effort to date has focussed on complexes of this type.

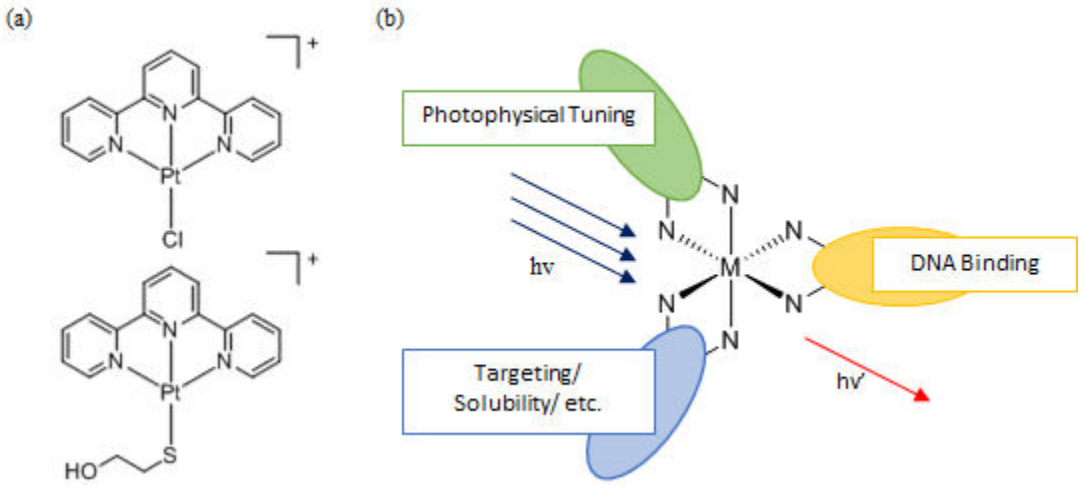

Figure 1.8: (a) Lippard's platinum intercalators. (b) Functionality that can be incorporated into modular octahedral metal complex luminophores such as Ru(II) polypyridyl complexes.

A useful feature of octahedral *tris*-chelated complexes is that they are chiral, existing as a racemate of Δ and Λ isomers. DNA is also inherently chiral, conforming to a right-handed helix in its most common B-form. DNA can also adopt a left-handed structure as Z-DNA which raised the question in the late 1970's – can the chirality of DNA be probed by enantiospecific binding of *tris*-chelates so that such complexes can be applied as reliable reporters of DNA conformation? Indeed, an initial study by Nordén *et al*. in 1976 on $[Fe(bpy)_3]^{2+}$ suggested that ctDNA showed preference for the Δ-isomer,[90] and later, the Barton group demonstrated that the phenomenon extended to $[Zn(phen)_3]^{2+}$.[91] Unfortunately chelate complexes based on these first-row metals were prone to the Pfeiffer effect; an isomer inversion that is induced upon binding to a chiral substrate.[92–94] In this manner, solutions of the pure isomers were found to racemise after only a few hours in the presence of DNA and consequently, these metal complexes were deemed too unstable to be reliable reporters of conformation.

A breakthrough was made by Yamagishi who studied the enantioselective binding of $[Ru(phen)_3]^{2+}$ with nucleic acids.[95,96] This ruthenium complex is kinetically inert and its respective isomers were found to bind in different orientations relative to the DNA central axis. The exact binding of $[Ru(phen)_3]^{2+}$ needed to be elucidated to understand the reliability of its isomers to act as enantioselective probes of nucleic acid structure. This instigated one of the more controversial debates in the field when various groups presented evidence that Δ/Λ-$[Ru(phen)_3]^{2+}$ does or does not bind DNA by groove binding, electrostatic interaction and/or (semi-) intercalation of one of the phen ligands. Reports on the use of NMR, plasmid unwinding, optical spectroscopy, molecular modelling and salt dependant binding studies to determine the binding mode (or modes) provided contradictory evidence.[97–106] The exact binding mode is still debated but can be considered less relevant given that neither isomer indicated selectivity for DNA handedness and for any one DNA conformation there was minor binding enantioselectivity.[107,108] Nonetheless, the studies on $[Ru(phen)_3]^{2+}$ were important in driving the field towards key advancements in the years that followed.

The first of these was reported by Barton, who used diphenylphenanthroline (dpp) ligands to enhance the steric bulk in the complex; $[Ru(dpp)_3]^{2+}$.[109,110] Indeed, this led to enantiospecificity with B-DNA; only the Δ-isomer binds the right-handed helix as judged

from MLCT hypochromism and ferrocyanide quenching experiments. These photophysical changes were not observed for Λ-$[Ru(dpp)_3]^{2+}$ in the presence of B-DNA. Conversely, no enantioselectivity was observed in the left-handed helix of Z-DNA, probably because Z-DNA is not an exact left-handed homologue of B-DNA, conforming instead to a zig-zagging structure and thus requiring a different set of steric parameters to introduce specificity. However, information on the handedness of DNA can be inferred from the relative proportions of binding of both enantiomers, and in cases where the probes do not bind, the DNA may be inaccessible or unstacked.

Light-switches for DNA

A limitation of the *tris*-chelates studied at that time was their relatively low binding affinities. For example, a common DNA intercalator like ethidium binds DNA with affinity at least two orders of magnitude greater than $[Ru(phen)_3]^{2+}$ ($K_b \approx 10^3$-10^4 vs 10^6-10^7).[111,112] This provoked the design of metal complexes that fully intercalate with DNA because such rigid anchoring could potentially improve sequence or structure selectivity. Barton and collaborators reported what is now considered the DNA binding metal complex archetype; $[Ru(bpy)_2(dppz)]^{2+}$ - a molecular light switch for DNA.[16] This complex exhibits virtually zero luminescence in aqueous solvent but switches on upon incorporation into organic environments, such as intercalation between base pairs of the DNA core. The photophysical mechanism of this switching arises from two low lying ^{3}MLCT states localised on either the phen or phenazine moieties of the dppz ligand, the accessibility of which is strongly influenced by the polarity and hydrogen bonding capability of the solvent (this is examined in greater detail in Chapter 4).[113–117] This complex displays only minor selectivity for DNA sequence, structure and handedness, but the light-switch effect is unparalleled as a detection tool for DNA (luminescence enhancement $>10^4$).[16,118,119] Furthermore, binding leads to luminescence with biexponential decay that may be used as an additional tool to interrogate different biological environments.[16,119,120] Critically, the intercalative binding also raises the binding affinity to the order of $K_b \approx 10^6$.[16,121–123] Despite some initial controversy, spectroscopic data[118,124–127] supported by crystal structures confirms that that intercalation occurs via the minor groove, in two primary orientations; a perpendicular (head-on) mode and a canted (angled) mode.[128–132] This is discussed in greater detail in Chapter 4.

Given the success of the dppz complex, others have attempted to alter the photophysics and binding characteristics by changing the structure of the intercalating ligand (Figure 1.9). Hartshorn and Barton demonstrated that the light-switch effect extended to $[Ru(phen)_2(dppz)]^{2+}$, however changes to the dppz ligand structure of this complex dramatically altered the luminescence properties.[120] For example, complexes containing the phendione and dppn ligands were weakly luminescent in water and exhibited poor enhancement upon binding DNA (enhancement less than two-fold; phendione = 1,10-phenanthroline-5,6-dione, dppn = benzo[i]-dipyrido[3,2-a:20,30-c]phenazine). Complexes of dpqp as studied by Turro *et al*. behaved similarly to phendione (dpqp = pyrazino[20,30:5,6]pyrazino-[2,3-f][1,10]phenanthroline).[133] Shortening of dppz by one fused ring yields the dpq ligand (dpq = dipyridoquinoxaline) which renders its complexes luminescent in water with moderate enhancement in DNA but with lower binding affinity ($K_b \approx 10^4$).[134,135] Ligands such as dppm2 and dppx exhibited better light-switch performance (in terms of emission enhancement in DNA; x300 and x20 respectively) but none of the derivatives studied were considered true molecular light switches like Ru-dppz (dppm2 = dipyrido[3,2-a:2',3'-c]methylphenazine and dppx = dipyrido[3,2-a:2',3'-c]dimethylphenazine).[120,136]

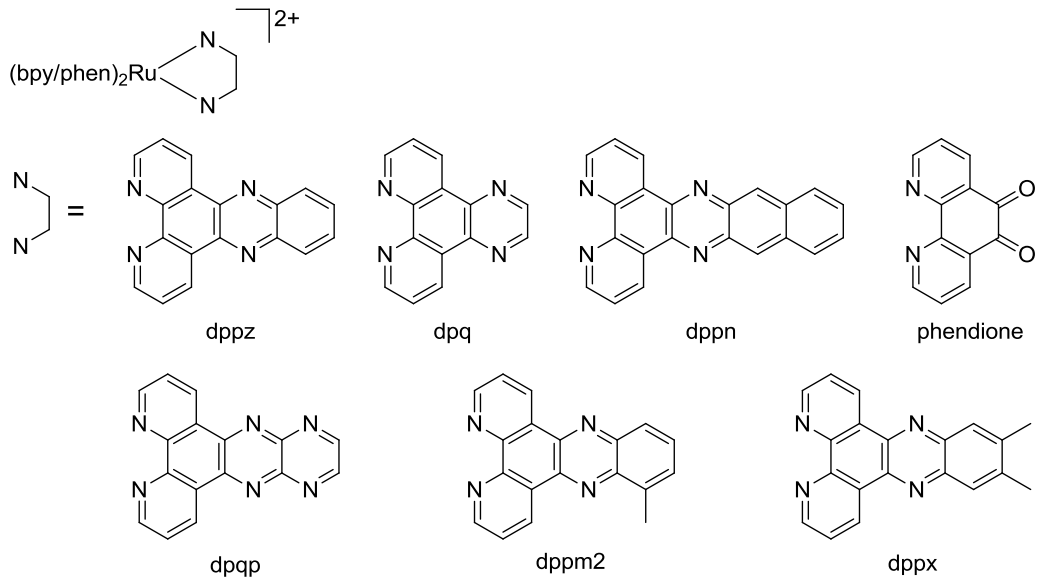

Figure 1.9: Structures of the intercalative ligands used to vary the photophysics and binding characteristics of their Ru(II) complexes.

Variation of the ancillary ligands is also an effective strategy to alter the binding properties of Ru-dppz complexes. Shade *et al*. studied a series of alkyl -ester and -carboxylic acid derivatives of $[Ru(bpy)_2(dppz)]^{2+}$ functionalised at the bpy ligands.[137] Greater selectivity for dsDNA over ssDNA in terms emission enhancement on binding was observed for complexes of greater steric bulk and less net cationic charge. The greatest selectivity for dsDNA was observed for a charge neutral complex and notably, a net anionic complex did not appear to bind DNA, probably due to electrostatic repulsion with the sugar-phosphate backbone. In support of this, Gao *et al*. have studied $[Ru(bpy)_2(dppz)]^{2+}$ complexes bearing pendant quaternary amines on the bpy ligands which improves the binding association with DNA, requiring much higher temperatures for denaturation than the parent complex.[138] Interestingly, the use of dpp ligands to provide $[Ru(dpp)_2(dppz)]^{2+}$ yields a complex that induces efficient B to Z-DNA transitions at low salt concentrations.[139]

Thomas and coworkers have developed Ru-dppz complexes based on tpm (tris (pyrazolyl)methane) that exhibit temperature dependant DNA binding; $[Ru(tpm)(Py\text{-}R)(dppz)]^{2+}$ (where Py-R is pyridine or 4-aminopyridine, see Figure 1.10).[140,141] The pyridine complex behaves as a classical Ru-dppz light switch intercalator whereas the aminopyridine complex demonstrates diminished binding affinity and does not switch on in the presence of DNA at room temperature. The amino group impacts binding modes at different temperatures; at 10 °C luminescence was switched on due to probable dppz intercalation, but at 25 and 35 °C, there was no emission which was attributed to binding in the groove. $[Ru(tpm)(Py\text{-}R)(dppz)]^{2+}$ has recently been derivatised to yield $[Ru(tpm)(dmsp)(dppz)]^{2+}$ (where dmsp = (E)-4-(3,4-dimethoxystyryl)pyridine) which exhibits dual emission and permits the ratiometric sensing of DNA.[142]

Dinuclear Ru(II) complexes to study DNA

Bolger *et al*. prepared a complex containing the tpphz ligand, an extended derivative of dppz; $[Ru(bpy)_2(tpphz)]^{2+}$ (tpphz = tetrapyrido[3,2-a:2',3'-c:3'',2''-h:2'',3'''-j]phenazine).[143,144] This complex is weakly emissive in water but emission is enhanced upon intercalation into DNA with an enhancement factor of at least 80 times. The tpphz ligand contains two bpy-type moieties at the ends of a phenazine system permitting bridging across two metal centres. The homo dinuclear complex, $[(Ru(bpy)_2)_2(tpphz)]^{4+}$, also exhibits enhanced emission in the

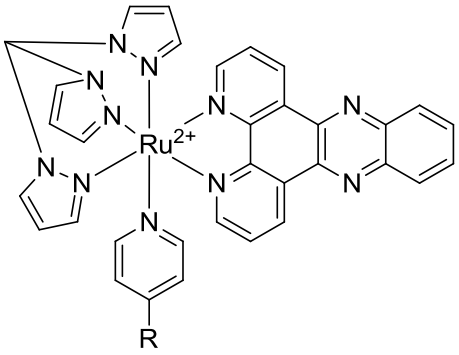

Figure 1.10: Structure of $[Ru(tpm)(Py\text{-}R)(dppz)]^{2+}$ where R = H or NH_2 as reported by Thomas *et al*.[140]

---

presence of DNA but does not intercalate with it, instead binding via a surface mode where high binding affinity is maintained due to the increase in formal charge.[136,145,146] The phen derivative of this complex gained closer attention when Thomas and coworkers demonstrated that the dinuclear complex is taken into the nucleus and lights up DNA in live cells (see Section 1.5 and Figure 1.11).[147–149] Turro *et al*. have shown that a Ru-tpphz DNA-threaded dinuclear complex can be photochemically generated from DNA-intercalated $[Ru(bpy)_2(tpphz)]^{2+}$ monomer and free $[Ru(bpy)_2(CH_3CN)_2]^{2+}$ under photolysis ($h\nu > 395$ nm).[145] Furthermore, when the monomer is DNA-intercalated, the luminescence can be switched off by coordinating metal ions like Cu^{2+} and Zn^{2+} which bind at the free second coordination site of tpphz. The emission can also be cycled on and off by successive treatments with Co^{2+} and EDTA.[150,151] Recently, heterodinuclear tpphz complexes such as $[(bpy)_2Ru(tpphz)Ir(ppy)_2]^{+3}$ have been studied as DNA cellular stains.[152,153]

Nordén, Lincoln and coworkers have been active in the field since early studies on homo *tris*-chelate complexes. Uniquely, their research has investigated the DNA binding of threaded dinuclear complexes based on two $[Ru(bpy/phen)_2(dppz)]^{2+}$ units linked directly or by alkyl bridges by substitutions to the dppz ligands (e.g. Figure 1.11).[154–156] This prevents classical Ru-dppz intercalation initially because the DNA must rearrange to accommodate dppz ligands at the core of the DNA while the bulky $Ru(bpy/phen)_2$ moieties are hosted in the groove and this process occurs by much slower intercalation kinetics than $[Ru(bpy/phen)_2(dppz)]^{2+}$.[157]

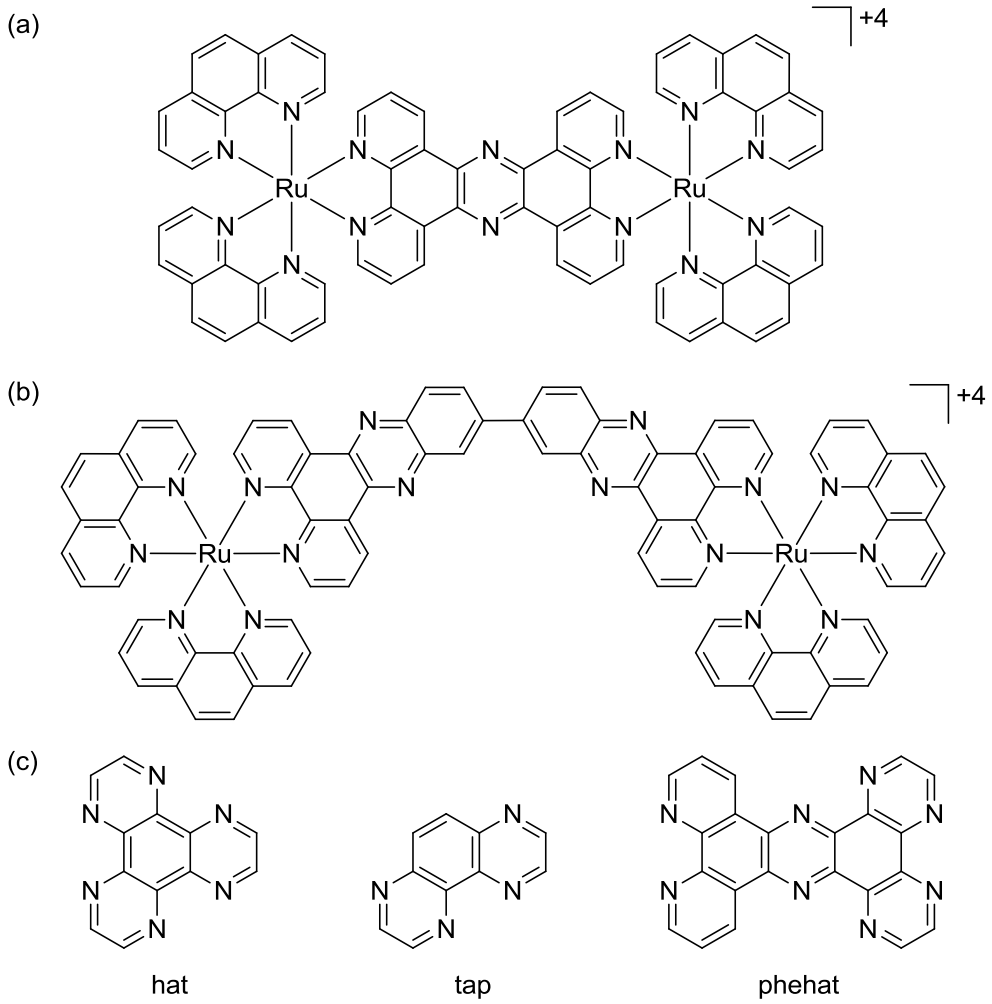

Figure 1.11: (a) Structure of $[(Ru(phen)_2)_2tpphz]^{4+}$, a live cell DNA stain. (b) An example of one of the dinuclear threading complexes based on $[Ru(phen)_2(dppz)]^{2+}$ as studied by Nordén *et al*.[155] (c) Structures of the polyazaaromatic series as studied by Kirsch-De Mesmaeker; hat, tap and phehat as indicated.

Pioneered by the Kirsch-De Mesmaeker group and collaborators, complexes bearing at least two polyazaaromatic ligands such as tap or hat render the excited states of their Ru(II) complexes sufficiently positive to photo-oxidise DNA (see Figure 1.11 for structures).[5,45] In *bis*-tap/hat complexes, guanine may be photo-oxidised by a proton coupled electron transfer (PCET) mechanism leading to quenching of the Ru(II) emission which is otherwise luminescent in aqueous solution.[158,159] In the *tris*-tap/hat complexes, adenine is capable of photo-oxidation as well as guanine.[158] In certain instances, photo-oxidation has been shown

to produce a photo-adduct; a new permanent covalent bound from the exocyclic amine of guanine to a hat or tap ligand of the Ru(II) complex.[79,160] Interestingly, $[Ru(tap)_2(dppz)]^{2+}$, the tap analogue of $[Ru(phen)_2(dppz)]^{2+}$, does not exhibit the light-switch effect, remaining luminescent in aqueous solutions and is quenched upon interaction with DNA due to guanine PCET processes.[159,161] This has been observed in crystals of this complex intercalated into DNA and persists due to the lowest MLCT state localising on a tap ligand.[162] Complexes containing the intercalative phehat ligand have also been prominent. Phehat is analogous to tpphz, capable of binding two metal centres, but possessing photooxidative properties like hat/tap complexes when bound to Ru(II) via the hat moiety and light-switch behaviour with DNA when bound via the phen moiety.[163–166]

Dinuclear bridging using flexible linkers has been demonstrated as an attractive strategy to enhance binding affinity relative to the free monomer and to permit linkage of two different DNA-interacting subunits. Increasing the size of the binding site is also important towards approximating DNA-binding protein motifs.[167] Aldrich-Wright *et al*. reported on mercapto-ethyl ether bridged complex based on $[Ru(phen\text{-}R)(dpq)_2]^{2+}$ centres that increases binding affinity 1000-fold relative to monomer ($K_b = 10^7$ vs 10^4) and leads to apparent binding site sizes that span several base pairs (up to n = 17).[135] Later, this work was expanded towards a study on the enantiopure compounds.[168] Del Guerzo and Kirsch-De Mesmaeker explored the use of a quinoline moiety conjugated to $[Ru(tap)_2(phen)]^{2+}$ as a sequence dependant light-switch.[169] In the absence of DNA, the luminescence of Ru-tap is strongly quenched by electron transfer from the tethered organic moiety (97 % quenched). However, in DNA it switches back on to an extent dependant on the guanine content of the binding site since Ru-*bis*-tap emission has been shown to be quenched by guanine and not adenine (e.g. luminescence in $[poly(dG\text{-}dC)]_2$ was ten times less than in $[poly(dA\text{-}dT)]_2$).

Bimetallic constructs may adopt special conformations such as molecular helicates which can promote unique structural recognitions with DNA. Hannon and coworkers have been prominent in this field, early work investigated the DNA interactions of Fe(II) cylinders that bind DNA in the major groove leading to bending and coiling of the polynucleotide.[170,171] Specific recognition of three-way DNA junctions was demonstrated using a triple stranded Fe(II) supramolecular helicate and represents an important example of achieving recognition

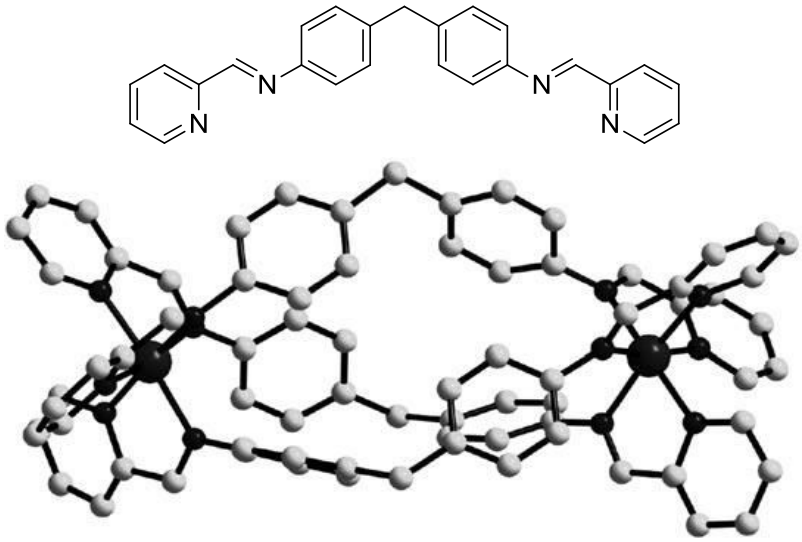

Figure 1.12: Structure of the ligand its luminescent triple stranded Ru(II) helicate as reported by the Hannon group.[181]

---

by expanding the molecular size of the probe to match specific DNA topologies.[172–178] The group also developed unsaturated Ru(II) complexes bound across two tetradentate azopyridine type ligands that yielded isomeric dinuclear cylinders which displayed cytotoxicities greater than cisplatin.[179] Interestingly, in this study, the *trans/trans* isomer exhibited superior cytotoxicity than the *trans/cis* double helicate which correlates with a later report by Glazer *et al*. suggesting that a *trans*-geometry in Ru(II) complexes is more effective towards DNA metalation.[180] Hannon *et al*. also prepared luminescent triple-stranded Ru(II) helicates (Figure 1.12) that bend and coil DNA analogous to Fe(II) helicates, but binding can be monitored in the Ru(II) case by a doubling and blue-shifting of the emission intensity at DNA saturation.[181] Unlike the coordinatively unsaturated Ru(II) helicates, cytotoxicity was reduced relative to cisplatin because of the kinetically inert nature of the saturated Ru(II) subunits. However, the cylinder was still biologically active, and later demonstrated polymerase inhibition due to non-covalent association of the triple stranded Ru(II) helicate and DNA.[182]

1.3.2.3 Probing special DNA structures with luminescent Ru(II) complexes: some important examples

G-quadruplexes

Exploring the capability of Ru(II) complexes to bind selectively to unusual DNA forms is an increasingly active area of the field, most notably in the design of probes for various forms of the G-quadruplex (G4).[183] G-quadruplexes generally require an alkali cation like K^+ or Na^+ to stabilise their structure. The formation of stabilised G4 assemblies can inhibit telomerase activity, which is not usually active in normal cells but is upregulated in 85 – 90 % of cancer cells, and its inhibition prevents telomere elongation and immortalisation of afflicted cells.[66] Accordingly, metal complexes are being explored both as diagnostic probes of quadruplex structure and as potential therapeutics.

Given its prominence in studies on duplex DNA, $[Ru(phen/bpy)_2(dppz)]^{2+}$ was explored as a probe for quadruplex DNA. Indeed, the light-switch effect is operative in G4 structures and Shi *et al*. demonstrated that this complex exhibits a preference for G-quadruplexes over i-motifs (a secondary structure that forms in C-rich DNA).[184] However, this complex exhibits little selectivity for G4 over duplex DNA and does not induce G4 stabilisation. Subtle modification of the archetype complex by Glazer and coworkers provided $[Ru(bpy)_2(dppz\text{-}Br)]^{2+}$, which was shown to be 14 times more luminescent in intermolecular G-quadruplex compared to duplex DNA (ctDNA).[185] Better stabilisation effects were achieved by Yao *et al*. who modified dppz to provide the dppz-idzo ligand and rendered the respective Ru(II) complex, $[Ru(bpy)_2(dppz\text{-}idzo)]^{2+}$, much more luminescent in duplex DNA than the archetype complex and exhibited further enhancement in certain G-quadruplexes.[186,187] Remarkably, this complex could also induce and stabilise antiparallel G4 structure without alkali cations (dppz-idzo = dipyrido-[3,2-a:2′,3′-c]phenazine-imidazolone). Chao *et al*. used a wider ligand in $[Ru(bpy)_2(bqdppz)]^{2+}$ that inhibited duplex binding, but favoured association with hybrid G-quadruplex DNA to yield a naked-eye switch-on probe (bqdppz = benzo[j]quinoxalino[2,3-h]dipyrido[3,2-a:20,30-c]-phenazine).[188] The use of higher order pendant-amines has also been successful towards G4 selectivity and stabilisation leading to telomerase activity inhibition as determined by the TRAP assay.[189,190] Polynuclear structures have also been studied, for example, light-switching in $[(Ru(bpy/phen)_2)_2tpphz]^{4+}$ is also

operative in G4 and is characterised by a blue-shift of about 30 nm.[191,192] This has been exploited in live cell studies of chromosomal DNA.[147] Studies on pic-type ligand bridged dinuclear complexes by Chao and others have also demonstrated promising selectivity and stabilisation effects.[193–195] The structures of some of the key ligands studied are provided in Figure 1.13.

Mismatches

Under normal cellular metabolism there is a chance that DNA synthesis can erroneously incorporate mismatched DNA bases. Left unrepaired, genomic integrity can become compromised, but a correction mechanism exists in healthy cells that induces DNA mismatch repair (MMR).[196] Deactivation of MMR has been shown to be more prevalent in certain cancers and hence, the development of methods to detect and eliminate DNA mismatches is an important research effort.[197]

Studies on metal complex interactions with mismatch DNA has been largely led by the Barton group.[72] The major breakthroughs have been made using Rh(III) octahedral metal complexes bearing ligands like chrysi (5,6-chysene) or phzi (benzo[a]-phenazin-5,6-quinone diimine) which are too wide to intercalate well matched DNA but bind avidly at mismatch sites (Figure 1.14).[23,25,198,199] The mechanism of binding of Rh(III) dyes is insertion leading to ejection of the bases at the mismatch site.[200] Rh-chrysi/phzi complexes demonstrate excellent affinity, are selective for mismatch sites and are enantioselective; only the Δ-isomer

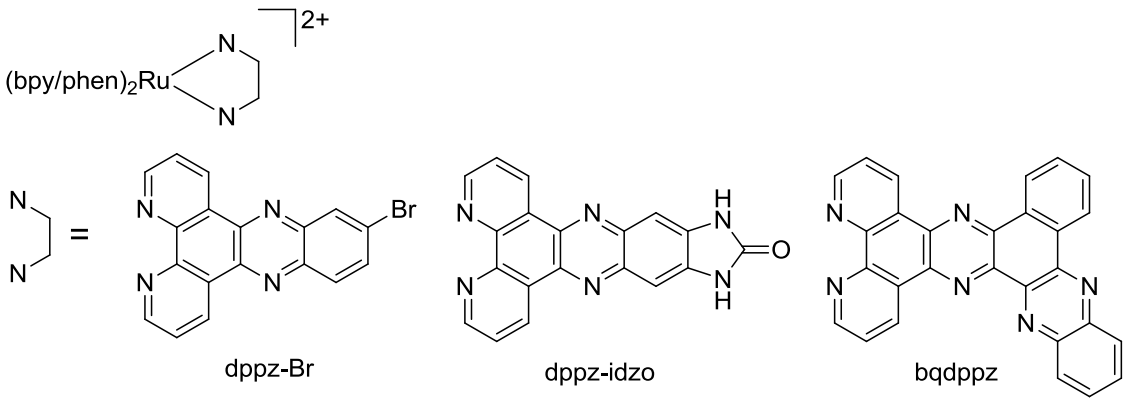

Figure 1.13: Structures of the ligands used to target G-quadruplex DNA with Ru(II) complexes.

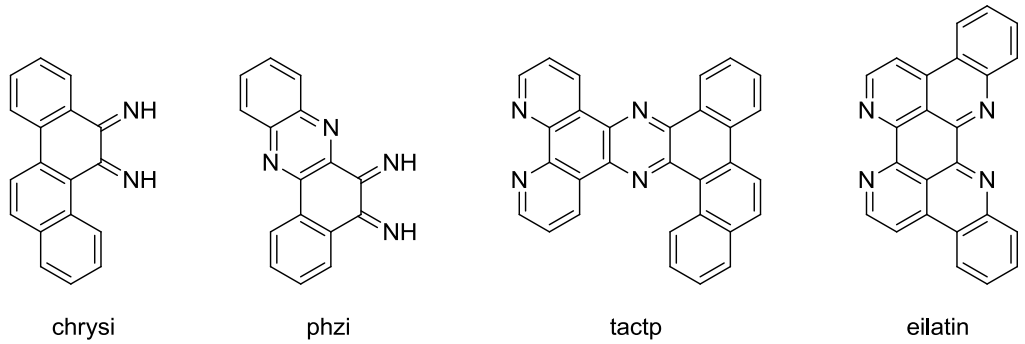

Figure 1.14: Ligands used as part of Rh(III) and Ru(II) complexes towards mismatch targeting.

---

is active.[72] These complexes are also capable of sensitising efficient strand scission upon photo-irradiation. However, a drawback of these Rh(III) complexes is that they are not luminescent which limits their diagnostic potential. Originally, Barton and coworkers attempted to design a light-switch Ru(II) analogue of the Rh-chrysi/phzi complexes using the tactp ligand; $[Ru(bpy)_2(tactp)]^{2+}$ (tactp = 4,5,9,18-tetraazachryseno[9,10-b]triphenylene), however, this complex was prone to non-specific luminescence via ligand-stacking dimerization.[201] Similarly, little progress was made using a Ru(II) complex containing a dppz-chrysi hybrid ligand.[202] Attempts to introduce specificity for mismatches were also explored using eilatin in $[Ru(bpy)_2(eilatin)]^{2+}$ but no distinction was observed.[203] Oregon Green, an anionic organic fluorophore, was tethered to Rh(III) mismatch probes and exhibits quenched luminescence off-target and a three-fold enhancement when bound at mismatch sites.[204] However, the intensity of this probe was still significantly quenched relative to the free fluorophore at the same concentration.

$[Ru(bpy)_2(dppz)]^{2+}$ demonstrates light-switch behaviour in well matched and defect DNA, such as sequences containing mismatches and abasic sites. The binding is not selective over well-matched DNA, but luminescence was shown by Lim *et al*. to be moderately enhanced in the presence of defects, particularly the Λ-isomer, which showed three-fold selective enhancement in the presence of abasic sites over mismatch or well matched DNA.[205] The luminescence difference was further enhanced using NaI selective quenching of well-matched Ru-dppz. The mechanism of binding at mismatch sites by $[Ru(bpy)_2(dppz)]^{2+}$ was postulated to be insertion from the minor groove, analogous to Rh(III) insertion complexes.[72]

This is surprising considering the width and length of the dppz ligand but was later confirmed by high resolution crystal structures.[132] A similar study revealed that $[Ru(bpy)_2(dppz)]^{2+}$ exhibits enhanced luminescence when bound to double stranded RNA at mismatches and this can be amplified using the FRET acceptor STYO 61 (importantly, the probe does not appear to bind RNA elsewhere).[206]

Modification of the ancillary ligands of the archetype complex leads to two probes that are light-switches for DNA mismatches; $[Ru(Me_4phen)_2(dppz)]^{2+}$ and $[Ru(5',5\text{-}Me_2bpy)_2(dppz)]^{2+}$ (Me_4phen = 3,4,7,8-tetramethyl-1,10-phenanthroline and 5,5'-Me_2bpy = 5,5'-dimethyl-2,2'-bipyridine).[207] In this case, the bulky ancillary ligands led to a 26-fold greater affinity of the probes for mismatches relative to well matched DNA which manifests as a greater than 7-fold relative luminescence enhancement. This difference is also reflected in the luminescence lifetime which is bi-exponential only in mismatches and much longer lived on average. Recently, Deraedt *et al*. have also explored mismatch light-switch binding using photooxidative bipyrazine ligands in Ru(II) complexes bearing 'elbow shaped' dppz-like ligands.[208]

Single Stranded DNA and Triplexes

The luminescence of $[Ru(bpy/phen)_2(dppz)]^{2+}$ has been shown to be longer-lived and enhanced in triple helices relative to duplex DNA. Jenkins *et al*. attributed this to enhanced protection of the phenazine moiety from aqueous quenching.[209] Indeed, the magnitude of the shorter component of the luminescence lifetime was greatly increased in triplex DNA compared to the duplex and the fractional amplitude of the long component was also increased.[125,210] Choi *et al*. later demonstrated that the dppz ligand offers greater stabilisation of the triplex than phen (a shorter ligand) and dppn (a longer ligand), and that intercalation in triplex DNA occurs from the Watson-Crick minor groove.[211] Recently, Peng *et al*. showed that the Δ-isomer stabilises triplex RNA significantly more than the Λ-isomer.[212]

Coates *et al*. discovered that the light-switch effect for $[Ru(phen)_2(dppz)]^{2+}$ is also operative in single stranded DNA by studying binding to oligonucleotides.[213] Later, Moon *et al*. demonstrated that single stranded DNA binding was characterised by a triexponential luminescence lifetime with two components similar to that observed in duplex DNA

(indicative of binding at a hydrophobic pocket formed by base pairs), and a third, very short component (1 – 2 ns), that was attributed to a binding mode outside this cavity.[214]

Sequence Selectivity

The modularity of metal complexes has been exploited effectively to study a diverse range of DNA structures but specific recognition of sequence is more difficult along conventional Watson-Crick polynucleotides. An effective strategy has been to conjugate an oligonucleotide (ODN) to the probe which demonstrates specific antisense recognition of the target sequence. Indeed, this has been an effective strategy in electrochemical DNA detections.[215] In relation to Ru(II) luminophores that may have cellular application, an important example was reported by Jenkins and Barton who explored $[Ru(phen)_2(dppz)]^{2+}$ tethered to the end of an ODN.[216] The luminescence was found to switch on upon binding of the conjugated ODN to its complimentary strand by intramolecular intercalation of the Ru-dppz probe and luminescence was greatly diminished in the absence of the target sequence. Kirsch-De Mesmaeker and coworkers have been particularly active in sequence targeting, using Ru-tap complexes tethered to ODNs. Since Ru-tap complexes can form photoadducts with guanine residues of DNA, the Ru-tap-ODN probe can use the G-content of its conjugated ODN to enhance selectivity for the target binding domain. For example, Le Gac *et al*. demonstrated that irradiation of the ODN conjugate in the absence of its complimentary sequence leads to a self ('seppuku') adduct and is then prohibited from off-target effect.[217] Where the ODN sequence finds its compliment, adducts are formed at the target site and thus this selectivity and photoactivated effect lends itself to theranostic therapies such as gene silencing.[218–220]

1.4 Photo-therapy: exploiting photoexcited reactive states of metal complexes

1.4.1 General aspects of photodynamic therapy

Photodynamic therapy (PDT) requires the use of otherwise non-toxic components that exert a therapeutic response upon light activation.[221] Photoactivation grants spatial and temporal control of therapy – only irradiated areas are subjected to treatment. Accordingly, PDT is well-suited to superficial lesions or tumour treatments which can be targeted selectively over surrounding healthy tissues.[222,223] PDT activity requires a photosensitiser that absorbs light and generates a toxic species by one of three mechanisms; type I, type II and type III (Figure 1.15).[224] A type I mechanism involves electron (and/or proton) transfer with non-specific cellular components leading to the formation of toxic oxidation or reduction products like hydroxyl radical ($^{\bullet}OH$), superoxide anion ($^{-\bullet}O_2$) and peroxides (i.e. collectively; ROS). A type II pathway sensitises singlet oxygen ($^1O_2$), via energy transfer from a photosensitiser in a triplet excited state to ground state oxygen ($^3O_2$), with the concomitant return of the sensitiser to the ground state. Type III reactions are ascribed to direct reaction of the

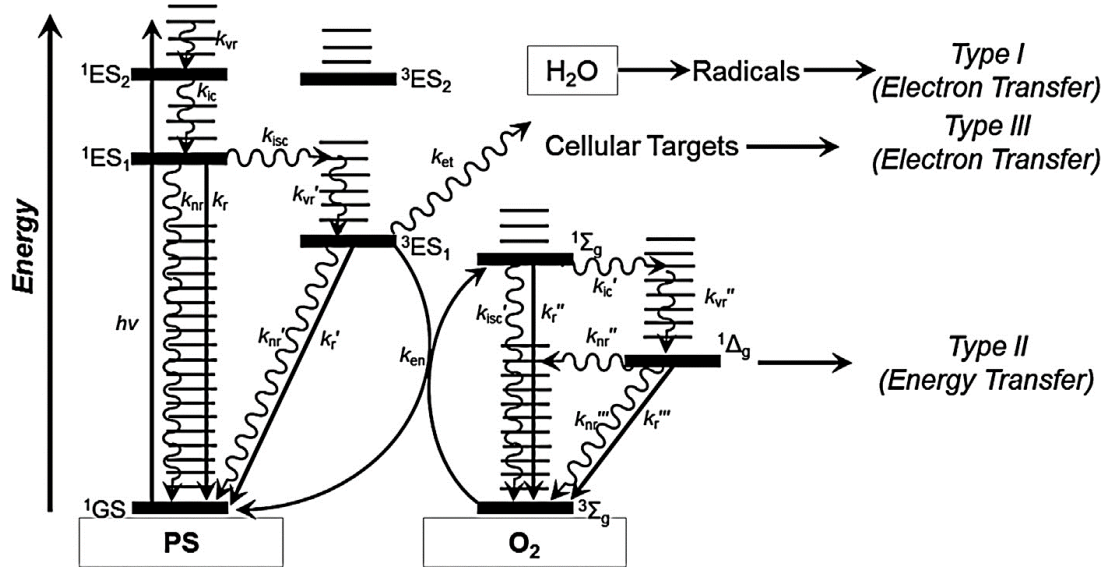

Figure 1.15: Jablonski diagram to illustrate photosensitisation of Type I, II and III PDT mechanisms. Reproduced from Knoll *et al*.[4]

photosensitiser in the excited-state with a cellular target (e.g. DNA). In the broader literature, type III is often considered as type I, but the separate treatment of type III is relevant for metal complexes.[4]

Regardless of mechanism, the objective of PDT is to sensitise cellular destruction resulting from the acute stress induced by the bioactivity of ROS. Typically, this involves irreversible damage to vital subcellular components like the plasma membrane, mitochondrial and lysosomal membranes, and the endoplasmic reticulum.[225] Discrete localisation of the photo-sensitiser is important since singlet oxygen (the most common PDT toxic species) under physiological conditions exhibits a lifetime of about 3 μs and influence radius of about 260 nm.[226] PDT drugs are less often effective at targeting nuclear contents such as DNA, but the cascade events from disruption of normal cellular function can have catastrophic effects across the cell.[227] Generally, PDT indicators are apparent, such as changes in intracellular $[Ca^{+2}]$, lipid metabolism, transcription activity and cell adhesion properties. A cell will either exhibit a net adaptive response to PDT or be destroyed, usually by apoptotic or necrotic mechanisms.[221,223–225,227]

Most PDT drugs operate by a Type II mechanism and hence, treatment efficacy depends on local concentration of both the photosensitiser and molecular oxygen, as well as the triplet crossover quantum yield (ϕ_{ISC}) and singlet oxygen quantum yield (ϕ_{Δ}). Furthermore, a good PDT will absorb in the low energy visible or NIR region (PDT window) to enhance tissue penetration.[228,229] Early generation PDT agents were organic molecules based on porphyrin, chlorin, phthalocyanine and related derivatives (e.g. Photofrin – the first clinically approved PDT agent).[230] Later, metallo-derivatives of these organic photosensitisers were developed using Zn, Ni, Fe, Al and Mn.[231] Notable other examples include Puryltin, based on a $SnCl_2$ core, and Lu-tex, a lutetium complex.[232] Most of these photosensitisers suffer from poor aqueous solubility and high aggregation rates under physiological conditions, but the high triplet state quantum yield of metal complexes remains attractive for PDT. For example, poor sensitisation of the triplet excited state is one limitation of Photofrin which exhibits ϕ_{ISC} = 0.83 thus limiting ϕ_{Δ} to 0.65.

As detailed in previous sections, polypyridyl metal complexes are characterised by their long-lived triplet excited states which, in complexes like Ru(II), are photosensitised in unit

quantum efficiency. This is ideal for type II interaction with oxygen or type I/III interaction with cellular substrates. Ligand modification can extend their light absorbance into the photodynamic window or alternatively, two photon techniques are being increasingly exploited.[149,233–235] Localisation and clearance is also important in PDT, since full body distribution and slow excretion renders the patient photosensitive and prone to off-target activation of the photosensitiser until full systemic clearance.[236] Cellular uptake and localisation is an area of intense research interest and is explored in greater detail in later sections of this chapter. Tumour targeting is more complex, but is becoming better understood, and there are strategies to direct specific tumour uptake for example, using supramolecular approaches like biodegradable nanomaterial encapsulation.[222,237,238]

A barrier to type II PDT efficiency is its dependence on high local concentrations of O_2 which can be a significant drawback for use in cancerous tissue which is often associated with hypoxia.[239–241] There is a desire to transition to oxygen independent photodrugs that operate by type I/III mechanisms. The photoreactive excited states of some non-porphyrin metal complexes hold great promise, being capable of direct electron transfer with biomolecules like guanine, tryptophan and others, which can induce cellular stress that ultimately causes destruction. The coordination chemistry of metal complexes also permits direct metalation of biomolecules bearing appropriate donor groups and currently, there is a focussed research effort to achieve photoactivated chemotherapeutics (PACT) that exhibit coordination induced toxicity upon activation (*vide infra*). This versatility underscores the candidacy of metal complex luminophores for phototherapy, and considering their ability to interrogate cellular dynamics as sensitive imaging probes, there is an opportunity to evolve further towards theranosis.

1.4.2 Ru(II) luminophore photosensitised toxicity

Undoubtedly, the most significant metal based drug to be discovered thus far is cisplatin (*cis*-$[Pt(NH_3)_2Cl_2]$). Since it's serendipitous discovery by Rosenberg and colleagues in the 1960's,[242,243] cisplatin has developed to become an important clinical chemotherapeutic, demonstrating antitumour activity against head, neck, and genitourinary tumours.[244] The activity of cisplatin is believed to operate by intracellular chloride ligand cleavage to generate aquated complexes that induce toxicity by direct metal coordination of DNA bases, usually

at guanine residues, that impedes the replication apparatus.[245] It is important to cite the activity of cisplatin as it often used as the benchmark for toxic activity of metallodrugs. Its clinical impact has inspired a continued research effort across the wider community towards novel dark-reacting metallotherapeutics. However, despite the proven performance of cisplatin, there is an opportunity to expand the scope of therapy beyond the capabilities of platinum drugs and to overcome some of their drawbacks such as; lack of specificity, extracellular deactivation and acquired tumour resistance.[244,246] Kinetically inert photoactivated metal complexes such as those of Ru(II) are capable of exerting temporal and spatial control of therapy and are driving this evolution.

Interestingly, perhaps driven by the mechanism of metallodrugs like cisplatin, the efficiency of a PDT treatment is often measured not only in $^1O_2$ quantum yield but also in the ability to induce DNA damage. This is despite PDT efficiency often being high in cases where DNA is not actually the cellular therapeutic target. Plasmid DNA is a useful template to study PDT activity by observing the rate and occurrence of uncoiling, single strand breaks and/or DNA scission in the absence and presence of illumination at different intensities or time periods. Gel electrophoresis or AFM are typically used to monitor the extent of plasmid DNA damage. Additionally, PDT efficacies can be compared by the phototoxicity index (PI) which is the ratio of phototoxicity to dark toxicity (usually in terms of IC_{50} – the concentration required to reduce the cell population by half). Cisplatin has a PI value of 1 since it is equally effective in the light or dark, while some of the better metal based PDT agents have been reported with PI values that are 100 or more.

1.4.2.1 Photoinduced damage by classical PDT mechanisms

Type II PDT can be sensitised by Ru(II) complexes by exploiting the triplet character of the lowest-lying MLCT excited state which can interact with ground state oxygen to generate singlet oxygen. The photosensitised cleavage of DNA has been well-studied for $[Ru(bpy)_3]^{2+}$ and $[Ru(phen)_3]^{2+}$. Early work by Barton and colleagues indicated that the photoinduced plasmid cleavage by the two homoleptic complexes was enhanced in D_2O indicating a singlet oxygen mechanism.[247] This behaviour was also independently observed by Kelly and coworkers.[100,248] For $[Ru(bpy)_3]^{2+}$, ϕ_Δ was determined at 0.87 (CH_3OH), 0.77 (CH_3CN), and 0.41 (H_2O, pH = 7), and the complex is often used as a standard for comparisons with related

Ru(II) complexes.[249] For example, $[Ru(bpy)_2(dppz)]^{2+}$ is a relatively poor singlet oxygen sensitiser with ϕ_Δ determined at 0.16 (CH_3CN).[250] This was reflected in the relative inefficiency of the light-switch complex to induce strand cleavage in plasmid DNA.[251] Additionally, the DNA binding mechanism may impact activity, $[Ru(bpy)_2(dppz)]^{2+}$ is intercalated and protected from oxygen which contributes to decreased efficiency.[252]

A method to enhance the PDT activity may be to use complexes in which both Ru(II) ^{3}MLCT* states and low-lying longer-lived $^3\pi\pi^*$ states contribute to therapy. Well-studied examples in this regard are complexes bearing the dppn ligand or related derivatives. Turro *et al*. prepared $[Ru(bpy)_2(dppn)]^{2+}$ and determined $\phi_\Delta = 0.88$ (CH_3OH), much greater than $[Ru(bpy)_2(dppz)]^{2+}$ at $\phi_\Delta = 0.16$ (CH_3OH).[253] Irradiation ($\lambda > 455$ nm) led to rapid complete cleavage of supercoiled plasmid DNA in the case of the dppn complex, whereas the dppz derivative was inactive. The enhanced efficiency was attributed to superior ϕ_Δ and direct guanine oxidation. Ru-dppn complexes have demonstrated excellent PDT activity under irradiation in the photodynamic window with potencies up to five times that of Photofrin.[254] Further research by the Turro group and collaborators led to the development of $[Ru(tpy)(pydppn)]^{2+}$; a complex which yields singlet oxygen with unit quantum efficiency under irradiation due to the lowest energy excited state being a $^3\pi\pi^*$ state with a lifetime of about 13 μs in DNA/buffer (pydppn = 3-(pyrid-2′-yl)-4,5,9,16-tetraaza-dibenzo[a,c]naphthacene, Figure 1.16).[250] Efficient singlet oxygen mediated plasmid cleavage was observed under visible irradiation and was prohibited in the dark.

Recently, Thomas and coworkers designed a dinuclear Ru(dppn)/Ru(dppz) complex which retains the DNA light-switch effect due to the dppz ligand and also exhibits PDT activity due to an equilibration between the short-lived Ru-dppz ^{3}MLCT* state and the longer-lived dppn based $^3\pi\pi^*$ state.[255] The presence of Ru-dppz in Ru(dppn)/Ru(dppz) lowers ϕ_Δ to 15 % (CH_3CN) and limits PDT activity relative to Ru(dppn)/Ru(dppn), where ϕ_Δ was efficient at 67 % (CH_3CN). However, the dppz complex renders the compound luminescent and permits tracking of cellular uptake and localisation of the dinuclear complex which was distributed across the cytoplasm of a resistant human ovarian cancer line (A2780cis). Thus, this represents an excellent example of progress towards optical theranosis.

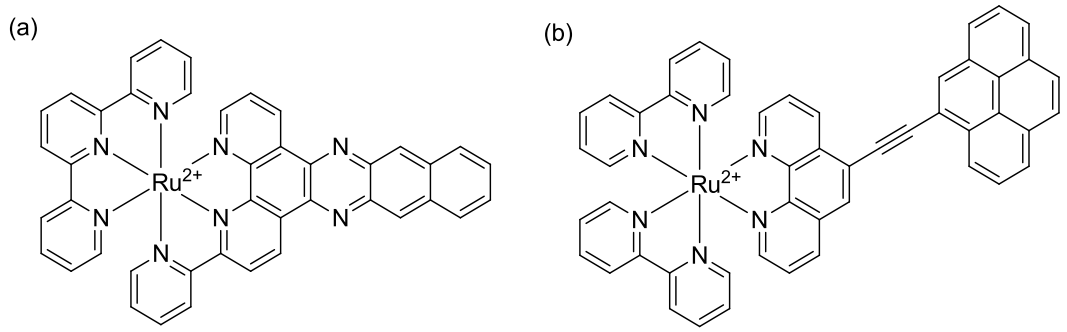

Figure 1.16: (a) Structure of $[Ru(tpy)(pydppn)]^{2+}$ as studied by Turro and coworkers and (b) Ru-pyrene dyads studied by McFarland *et al*.

Similar to work on Ru-dppn complexes, McFarland and coworkers synthesised a series of pyrene-ethynyl-Ru(II) dyads that possessed excited state lifetimes in fluid solution up to 270 μs, ϕ_Δ values in the range 0.65 – 0.87 (CH_3CN), and PI values up to 1750 (Figure 1.16).[256,257] The remarkable PDT activity of these dyads was shown to remain effective against a pigmented and hypoxic metastatic melanoma cell line. The same research group also investigated Ru-oligothiophene dyads for PDT and found that ϕ_Δ reached unity when Ru(II) was appended with three or more thiophene units. Dual reactivity was also evident in the thiophene dyads; under hypoxic conditions PDT activity persisted leading to DNA damage as observed by plasmid strand cleavage.[258]

1.4.2.2 Photoactivated chemotherapeutics

The photochemistry of metal complexes may be exploited to trigger the release of a therapeutic compound from an otherwise inactive species. This strategy has been studied using Ru(II) complexes by exploiting the thermally accessible and dissociative ^{3}MC excited state.[259,260] Ru(II) photochemistry not only opens the possibility of releasing an active ligand, but also generating a toxic coordinatively unsaturated Ru(II) species (e.g. $[Ru(N\hat{}N)_2(OH_2)_2]^{2+}$) which can coordinate potential ligands present in certain biomolecules like proteins and nucleic acids. The mechanism of action of these photoactivated chemotherapeutics (PACT) is oxygen independent and further expands their application scope to hypoxic cells against which conventional (type II) PDT treatments are less effective.

Etchenique and coworkers were active in early investigations into Ru(II) mediated photorelease of therapeutics. Complexes based on $[Ru(bpy)_2(L)(X)]^{2+}$ (where L = monodentate drug ligand and X = L or PPh_3) have been studied to deliver neurotransmitters such as 4-aminopyridine (4AP), serotonin, dopamine nicotine and GABA (γ-aminobutyric acid) by photocleavage under visible irradiation into the MLCT band.[261–266] Importantly, these complexes are stable in aqueous solutions at pH 7 in the dark, but exhibit selective release of the drug molecule under irradiation to a quantum yield of about 1-4 % with progressive extinguishing of the luminescence.[264] The group has also explored the release of glutamate from similar Ru(II) complexes using two photon IR sensitisation.[265] Concurrently, the Turro group and collaborators have been active in the field, reporting on the use of Ru(II) complexes to cage nitriles that are released upon irradiation.[267–269]

Dual reactive complexes involving DNA interactions were also reported by Turro *et al*. which exploit both photoactivated release and photosynthesis of toxic species like $[Ru(bpy)_2(OH_2)_2]^{2+}$. For example, 5CNU complexes were synthesised (5CNU = 5-cyanouracil) which under irradiation release therapeutically active 5CNU and also generate an aquated Ru(II) species which binds DNA by direct metalation of the bases.[270,271] Another study focussed on $[Ru(bpy)(dppn)(MeCN)_2]^{2+}$ which undergoes acetonitrile ligand loss under visible irradiation and also sensitises singlet oxygen formation to a high efficiency (ϕ_Δ = 0.88, CH_3OH).[272] Strikingly, although the ligand release efficiency was low (about 1 %), the PI was determined at 1110 – five times higher than the parent Ru-dppn species, $[Ru(bpy)_2(dppn)]^{2+}$, thus highlighting the therapeutic impact of generating a coordinatively unsaturated species. The group of Bonnet among others have also made important contributions to monodentate PACT release, particularly concerning release of sulfur donor ligands.[273–276]

Bidentate ligand release from Ru(II) complexes has also been investigated, primarily by the Glazer group, and typically requires strained coordination geometries to enhance dissociation via ^{3}MC population. This may be achieved using ligands which induce steric effects at the metal centre, such as methyl substitutions ortho to the pyridine nitrogen of the N^N ligand (e.g. 6,6'-dimethyl-2,2'-bipyridine, dmbpy, see Figure 1.17 for structures). Indeed, an early report compared the phototoxicity of $[Ru(bpy)_2(phen)]^{2+}$ with $[Ru(bpy)_2(dmbpy)]^{2+}$ and

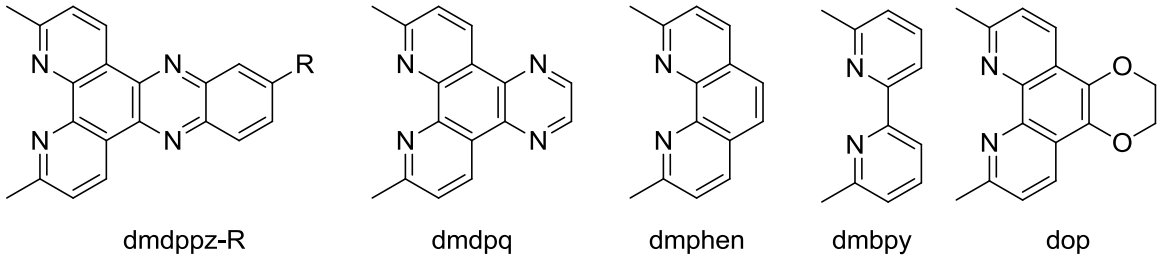

Figure 1.17: Ligands used by Glazer and coworkers towards photoinduced ligand release from Ru(II) complexes.

$[Ru(bpy)_2(dmdpq)]^{2+}$ (dmdpq is the dimethyl analogue of dpq) and found that the latter complexes exhibited PI values > 100 whereas the former complex displayed a poor PI ≈ 6.[277] This was attributed to the efficient photorelease kinetics of the strained complexes which led to detrimental biological interactions. $[Ru(bpy)_2(dmdppz)]^{2+}$, the strained analogue of $[Ru(bpy)_2(dppz)]^{2+}$, is a photochemical light-switch for DNA that is stable under irradiation in aqueous solvent but releases its dmdppz ligand upon intercalating DNA to generate $[Ru(bpy)_2(OH_2)_2]^{2+}$ which is free to metallate DNA bases. Bromination to yield $[Ru(bpy)_2(dmdppz\text{-}Br)]^{2+}$ imparts selectivity for G-quadruplex DNA while maintaining its PACT effect.[185,278] An extremely high PI of 1880 was achieved using $[Ru(dmphen)_2(dop)]^{2+}$ (where dmphen = 2,9-dimethylphenanthroline and dop = 2,3-dihydro-1,4-dioxino[2,3-f]-1,10-phenanthroline) and this complex was shown to be 19 times more potent than cisplatin under irradiation.[279] Complexes of 2,2'-biquinoline (biq) have also been investigated due to their tendency to form strained geometries. Both $[Ru(biq)_2(phen)]^{2+}$ and $[Ru(biq)(phen)_2]^{2+}$ demonstrate moderate PI in the range 20 – 40, but importantly and unlike many Ru(II) complexes, their absorbance extends well into the photodynamic window.[233] Wu *et al*. have also exploited the PACT activity of Ru-biq complexes in combination with block copolymer nanoparticle vehicles to effect tumour uptake and induce dual reactivity under irradiation by singlet oxygen generation and photorelease of Ru-aquo species.[280,281]

Cellular examples of PACT in action typically rely on indirect measurements of efficacy such as cellular viability assays post-treatment. There are few examples of the use of luminescent probes which can directly report on the photorelease of their cargo in real time. Karaoun and Renfrew reported a Ru(II) econazole complex that was stable and luminescent

in the dark (i.e. under imaging conditions) but upon irradiation releases an econazole ligand with concomitant luminescence quenching.[282] Econozole is an imidazole based drug and its use as a Ru(II) PACT in this case led to PI values of about 34. Frasconi *et al*. developed PACT-active mesoporous silica nanoparticles that were decorated with [Ru(dppz)(tpy)(NC-R)]$^{2+}$ complexes (NC-R = cyano terminated ligand that anchors Ru onto silica).[283] Surprisingly, the Ru-dppz nanoparticles were luminescent in aqueous solutions, attributed to close packing at the silica surface which prevented quenching by water molecules, and permitted cellular imaging of uptake of the particles which were observed distributed across the cytoplasm. Under illumination, photorelease of [Ru(dppz)(tpy)(OH_2)]$^{2+}$ was observed with a quenching of the emission that was recoverable upon binding of the Ru-aquo complex to DNA bases. Additionally, the photo-releasable Ru(II) complex acts as an encapping agent on the surface of the mesoporous silica which can be used to trigger release of another toxic agent that is preloaded into the particles such as the chemotherapy drug paclitaxel.

1.4.3 Candidate complexes for targeted imaging and photo-destruction of DNA in live cells

In review of the above literature examples, two candidate complexes are apparent for further development towards DNA-targeted imaging and phototoxicity in live cells. Firstly, [$Ru(bpy)_2(dppz)$]$^{2+}$; a complex that exhibits a long-lived light-switch luminescence in DNA which is excellent for high contrast imaging in the live cell. This complex is also a poor singlet oxygen sensitiser which is ideal for probing DNA structure under normal imaging conditions for long periods. However, if [$Ru(bpy)_2(dppz)$]$^{2+}$ can be precision targeted to genetic material within the cell, spatiotemporal control over imaging and phototoxicity may be possible, using an irradiation intensity that induces photosensitised DNA damage in the presence of Ru(II) but does not otherwise damage the cell in its absence.

The second candidate complex is [$Ru(tap)_2(bpy)$]$^{2+}$; a complex characterised by its photoreactive excited state which, upon PCET with guanine residues of DNA, can lead to direct oxidative DNA damage. Conversely to [$Ru(bpy)_2(dppz)$]$^{2+}$, this complex is luminescent in aqueous environment and switches off upon binding DNA, thus permitting the monitoring of its uptake and localisation. Critically, [$Ru(tap)_2(bpy)$]$^{2+}$ is also a poor

singlet oxygen sensitiser which prevents off-target cellular toxicity under imaging conditions. To date, there has been no reports of the successful application of this probe for DNA-targeted photodamage in the live cell.

1.5 Strategies for cellular uptake and localisation of metal complexes

Cellular uptake and precision localisation of the Ru-tap and Ru-dppz candidate complexes to nuclear or mitochondrial genetic material in the live cell is a pre-requisite to their successful application for DNA-targeted imaging and phototoxicity. In this section, mechanisms of uptake and strategies to achieve subcellular localisation using metal complexes are examined with reference to key literature examples.

1.5.1 Mechanisms of cellular uptake

A metal complex must translocate the lipid bilayer of the cellular membrane to enter the cell and this can be accomplished by several mechanisms that may be specific for a certain complex type (Figure 1.18).[284] In general, entry can be energy dependent or independent, and this can be deduced by monitoring uptake at 4 °C where metabolic pathways are typically switched off. Passive diffusion is an energy independent mechanism driven by a concentration gradient across the membrane. This method is useful because it is non-selective and has broad application across different cell types. Facilitated diffusion requires the

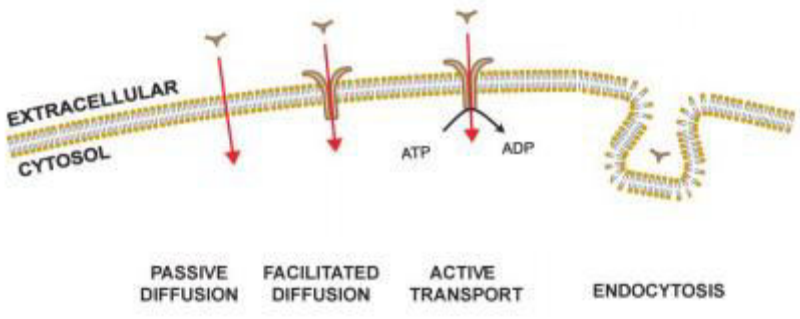

Figure 1.18: Mechanisms of cellular uptake as indicated. Image adapted from the literature.[284,285]

participation of a membrane bound protein that allows membrane transport via a channel or pore. Active transport utilises membrane ATPases to overcome the uptake barrier by spending intracellular ATP. Endocytosis is a process that wraps the incoming molecule within a vesicle compartment to ferry it across the lipid bilayer. Post-transport endocytic vesicle escape may be facilitated by endosomes and lysosomes. A final consideration is cellular expulsion, often mediated by efflux transporters, which can impact cellular application.

Once a complex arrives into the cell, it ideally localises specifically to a target site. However, such precision targeting is difficult and often non-specific distribution is observed. Entry into subcellular organelles requires the probe to overcome additional membrane barriers, for example the double mitochondrial membrane and its electrical potential gradient. To date, cellular application of luminescent metal complexes is limited by their relatively poor uptake by any of the above mechanisms. This may be circumvented using organic solvents like DMSO, detergents or electroporation to permeabilise the cell membrane but this damages the cell and limits biological application of the probes. Instead, uptake and targeting have been achieved by altering the properties of the metal complex by ligand functionalisation, conjugations or probe capture on larger delivery vehicles. Below, some of these key successful strategies are briefly described.

1.5.2 Exploiting lipophilicity and charge

In pharmacology, lipophilicity is critically important for achieving the desired absorption, distribution, metabolism and excretion (ADME) properties of a therapeutic. Log P values are a useful tool to predict the ADME characteristics of a drug, where log P is the relative partitioning of a molecule between lipid and aqueous phases, often approximated by an octanol and water partition.[286] On a cellular level, a similar analysis is useful for predicting uptake and subcellular localisation and, in general, greater lipophilicity aids uptake across the plasma membrane. Charge is also important; the net intracellular charge is negative and a cell typically exhibits a membrane potential between -30 mV and -70 mV which means that cationic molecules can aid uptake.[287] In principle, polypyridyl Ru(II) complexes are suited to cellular application being lipophilic cations, however it is the balance of lipophilicity and charge that is important, and many Ru(II) complexes do not achieve uptake. In cases where

they do, the lipophilicity-charge balance is delicate and slight modification can lead to unpredictable localisation.

Puckett and Barton explored the effect of varying the ancillary ligands in $[Ru(N^N)_2(dppz)]^{2+}$ and found that bpy and phen complexes exhibited negative log P values, and thus, did not efficiently permeate the cellular membrane.[7] In contrast, the much more lipophilic diphenylphenanthroline (dpp) complex (log P = +1.30) was taken into the cell by passive diffusion and was distributed throughout the cytoplasm.[288] Glazer and coworkers investigated another dpp complex, $[Ru(dpp)_3]^{2+}$, that localised in the mitochondria.[42] Modification with sulfonyl groups lead to a net -4 charged complex and resulted in mitochondrial exclusion. Similarly, $[Ru(bpy)_3]^{2+}$ is cell impermeable but Chao *et al.* demonstrated that augmentation with quaternary amines to provide a series of +8 charged complexes enables uptake by endocytosis and localisation to the lysosomes.[289]

Dinuclear complexes have been successful in achieving uptake; the outstanding example of which was reported by Thomas and coworkers who demonstrated nuclear uptake and DNA imaging in live cells using $[(Ru(phen)_2)_2tpphz]^{4+}$ (Figure 1.20).[147,149] However, relatively

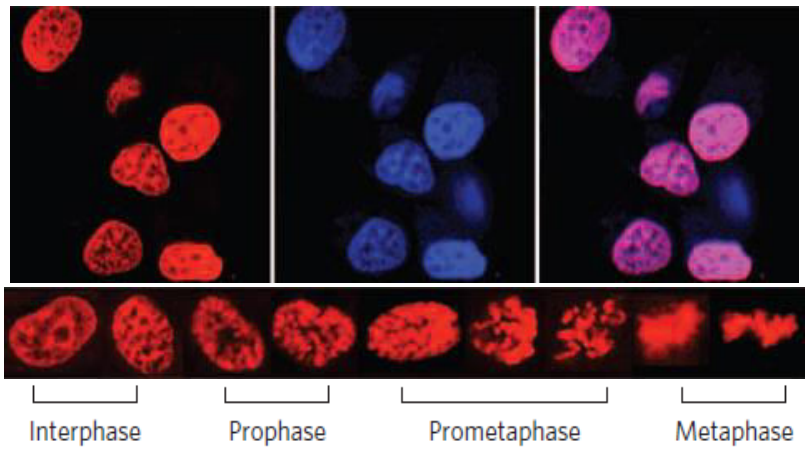

Figure 1.20: Nuclear staining of live MCF-7 cells using $[(Ru(phen)_2)_2tpphz]^{4+}$ (red stain, 500 μM, 1 h) which permits imaging of the different stages of mitosis as indicated. Co-localisation (purple) of Ru(II) (red) and commercial stain DAPI (blue) confirmed nuclear uptake. Adapted from Thomas *et al.*[147]

high concentrations of complex were required to achieve uptake (500 μM, MCF-7 cells) and slight modification to the ligand system in changing from a phen to a bpy derivative, $[(Ru(bpy)_2)_2tpphz]^{4+}$, inhibited live cell uptake. Utilisation of a more lipophilic derivative, $[(Ru(dpp)_2)_2tpphz]^{4+}$, recovered live cell uptake of the complex but with nuclear exclusion and instead, localisation at the endoplasmic reticulum with high dark toxicity.[290] It is apparent from these examples that uptake and selective localisation can be achieved by careful choice of the ligand systems and net charge. However, structural modification can lead to unpredictable uptake effects and can impact cytotoxicity which is an important consideration with respect to imaging and phototherapy.

Chao and coworkers have also investigated cyclometallation as a strategy to enhance uptake, substituting 2-phenylpyridine (ppy) for bpy in $[Ru(bpy)_2(dppz)]^{2+}$ to provide $[Ru(bpy)(ppy)(dppz)]^{+}$.[122] The reduced formal charge and increased lipophilicity of the ppy analogue led to rapid nuclear uptake in HeLa cells (> 90 % in 2 h, ICP-MS), whereas in contrast, the light-switch complex did not cross the cellular membrane under the same conditions. Additionally, $[Ru(bpy)(ppy)(N^N)]^{+}$ (where (N^N) = pic, dpq and dppn) exhibited similar rapid uptake for the cyclometallated derivatives relative to the N_6-polypyridyl complexes.[291] However, a clear drawback of these complexes is that they are weakly emissive and exhibit high dark cytotoxicity that exceeds the performance of cisplatin by up to an order of magnitude. The mode of cytotoxicity was attributed in these cases to nucleic acid binding and transcription disruption leading to anti-proliferation. Hence, cyclometallation appears to be an excellent strategy for rapid dark therapy but one which is incompatible with imaging and phototherapy.

An alternative strategy for uptake was recently uncovered by Zhu *et al*. who demonstrated the delivery of the separate enantiomers of $[Ru(bpy/phen)_2(dppz)]^{2+}$ to the nucleus using an organic ion-pairing method (Figure 1.20).[292] Pentachlorophenolate (PCP) was shown to ion-pair with the light-switch complexes to enable cellular uptake by passive diffusion and nuclear targeting whereupon the complex was found to bind DNA and switch-on for imaging. The authors briefly referred to similar uptake success for $[Ru(bpy/phen)_3]^{2+}$ that was not possible in the absence of an organic ion-pairing agent, matching that demonstrated in an early work by Dobrucki.[39] It will be interesting to discover if this approach can be generalised

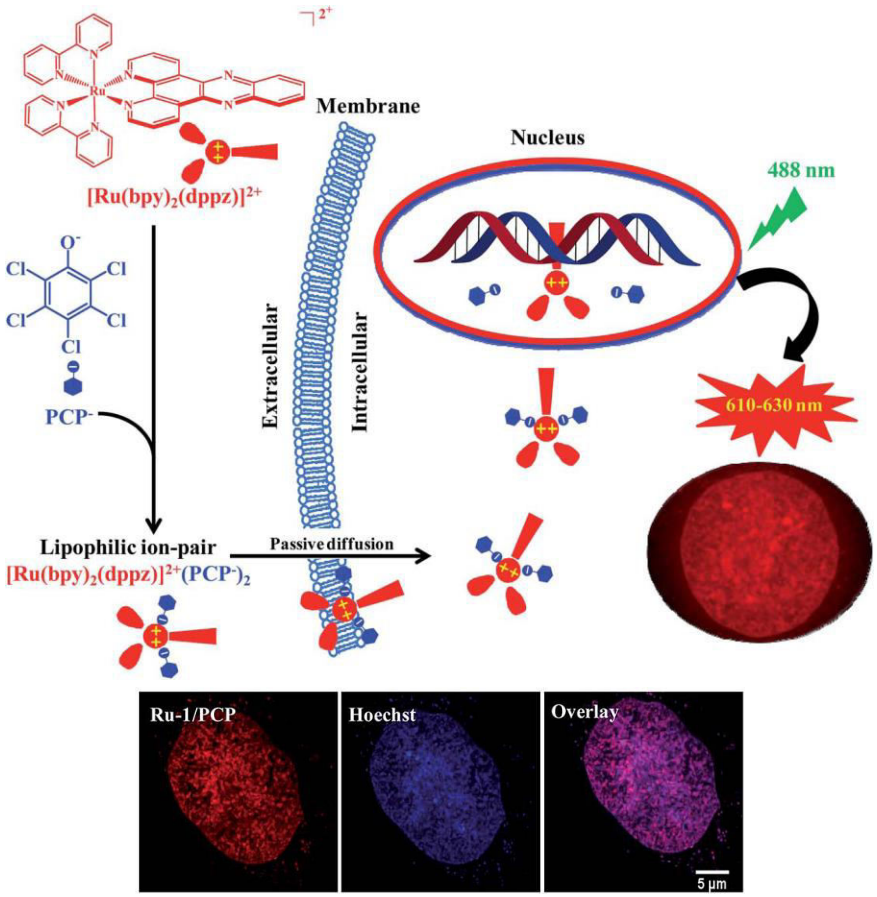

Figure 1.20: Schematic illustrating the ion-pairing strategy devised by Zhu *et al*.[292] to enable nuclear uptake of Δ/Λ-$[Ru(bpy)_2(dppz)]^{2+}$ (100 μM) in QSG-7701 cells after 3 h in the presence of PCP (300 μM). Nuclear uptake was confirmed by co-staining against Hoechst 33342 commercial DNA stain.

---

for Ru(II) luminophores. The requirement of anion mediated uptake is important since it offers a strategy to overcome the lipophilic cell membrane to improve uptake of cations. This has been demonstrated for more complex cations also, for example, in mediating the transport of polycationic oligoarginines across lipid bilayers.[293]

1.5.3 Polymers, bioconjugations and higher order assemblies

To overcome the cell impermeability of metal complexes, researchers have investigated the use of conjugates of cell penetrating agents. A simple but effective strategy has been to augment a complex with pendant polyethyleneglycol (PEG) chains to enhance amphiphilicity and uptake. Lo and coworkers have exploited this approach with cyclometallated Ir(III)

complexes which exhibit poor solubility and high toxicity in the free complex but excellent solubility and minimal dark toxicity when PEGylated.[294,295] Combined with a photoactivatable linker between the complex and PEG chain, toxicity may be triggered with temporal control.[296] Alkylations have been used to enhance lipophilicity, for example, Svensson *et al*. modified $[Ru(phen)_2(dppz)]^{2+}$ with ether alkyl chains to enable photoactivated uptake.[297,298]

Folate conjugation has been used to drive cancer cell selectivity due to a propensity to overexpress the folate receptor.[299] Additionally, sugars, estradiol and biotin conjugates have all been exploited for enhanced cellular uptake of Ru(II) complexes.[300–302] Supramolecular approaches have been successful; liposomal encapsulation of $[Ru(phen)_2(dppz)]^{2+}$ enables membrane translocation of the complex, followed by selective nuclear localisation and DNA destruction.[303] Particle based strategies have also been effective, for example; using silica or polymer substrates.[37,283]

Peptides

Conjugation of metal complexes to cell penetrating peptides (CPPs) is a particularly effective and versatile strategy to achieve uptake.[3,8] CPPs improve solubility and can also impart cell selectivity, for example, by exploiting the recognition of RGD and NGR sequences for $\alpha_V\beta_3$ and $\alpha_V\beta_5$ cell surface integrins.[43,304,305] Early research efforts unveiled the cell permeability of the Tat peptide, a natural sequence derived from the HIV Tat transactivator protein.[306,307] Derossi *et al*. reported that Penetratin was capable of cell penetration, i.e. the 16 amino acids long sequence, RQIKIWFQNRRMKWKK, corresponding to third helix of the homeodomain of Antennapedia.[308] These natural membrane translocators have inspired modern research towards 'designed' CPPs incorporating natural and synthetic amino acids for improved uptake and subcellular targeting.[309,310]

A common feature of CPPs is that they are polycationic, usually due to the presence of multiple arginine amino acids in the sequence. Wender *et al*. systematically decreased the arginine (guanidinium) content of a CPP by substitution with alanine and discovered a gradual decrease in uptake efficiency.[311] Indeed, CPPs comprised solely of polyarginines have been investigated, and it was shown by our group that while R_5 was ineffective, R_8 was

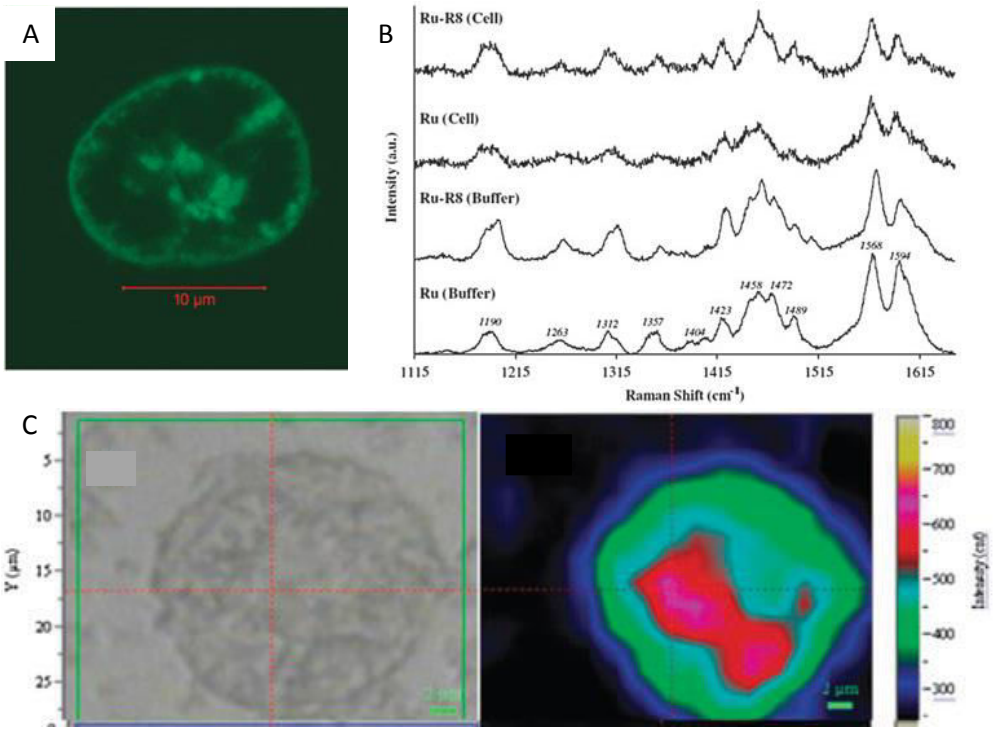

Figure 1.21: Cellular imaging of $[Ru(dppz)_2(pic\text{-}R8)]^{10+}$ in live SP2 myeloma cells. (a) Confocal luminescence imaging indicates membrane structures in live cells. (b) Resonance Raman imaging of the probe in solution and in cells confirms uptake. (c) rRaman mapping of the live cellular distribution of the Ru-peptide probe.

---

able to effect uptake of a Ru(II) polypyridyl complex; $[Ru(bpy)_2(pic\text{-}R8)]^{10+}$.[312] Importantly, octaarginine (R8) was also capable of cytoplasmic delivery of two other different Ru(II) complexes; $[Ru(bpy)_2(phen\text{-}R8)]^{10+}$ and $[Ru(dppz)_2(pic\text{-}R8)]^{10+}$.[9,40] In the latter case, the Ru-dppz complex exhibited light-switch properties permitting selective visualisation of membrane structures by confocal microscopy. Furthermore, multimodal imaging was demonstrated by resonance Raman mapping of Ru-dppz distribution (Figure 1.21). The versatility of R8 conjugation also permitted cellular uptake of Os(II) and Ir(III) complexes and thus R8 may be considered as a general non-specific uptake vector for similar metal complexes.[22,313]

Others have also explored the use of R8 mediated uptake. Brunner and Barton observed rapid uptake and some nuclear staining of D-octaarginine conjugated to $[Rh(phen)(bpy)(chrysi)]^{3+}$ at one end and to fluorescein at the other.[314] Puckett and Barton reported on the ability of

fluorescein to redirect R8 conjugated $[Ru(phen)(bpy)(dppz)]^{2+}$ to the nucleus.[315] Importantly, in the absence of fluorescein complete nuclear exclusion was apparent, and instead the complex was observed as a general punctate staining of the cell cytosol. Gamba *et al*. synthesised dinuclear Ru(II) bpy-based complexes conjugated to R8 and also observed punctate staining with poor nuclear penetration.[316]

Cellular uptake of CPPs is largely assumed to be via endocytosis, although the complete picture is likely more complex.[309,317] Entry by multiple pathways has been proposed, and the nature of the cargo and the propensity of the CPP to form secondary structures is also important.

1.5.4 Signal peptides for precision targeting

Targeted delivery of imaging probes and therapeutics to specific subcellular organelles is a challenging but valuable pursuit. Protein manufacture within cells usually occurs in the cytoplasm but their ultimate function may require uptake into specific organelles. For this purpose, localisation signal sequences are tagged onto the protein to direct cellular transport.[318,319] This mechanism has been exploited for targeted delivery of therapeutics and there is now a growing library of signal peptides that have been developed to facilitate precision targeting of key organelles. Our group has been at the forefront of exploiting signal peptides for uptake and localisation of metal complex luminophores for dynamic imaging and sensing.[2,3]

1.5.4.1 Peptides suited to precision targeting of cellular DNA

Nuclear uptake using a Nuclear Localisation Signal (NLS) peptide: VQRKRQKLMP

Nuclear uptake of small molecules occurs through nuclear pores present on the nuclear membrane but larger molecules require receptor mediated uptake such as the recognition of an NLS peptide.[318] Many NLS sequences have been derived from transcription factors such as NF-κB, TCF1-α, TFIIC-β, Oct-6 and SV40, with selective nuclear penetration achieved by the NF-κB and SV40 sequences.[320–324] Ragin *et al*. studied fluorescently labelled derivatives of the NF-κB and SV40 NLS sequences and demonstrated that VQRKRQKLMP (the NF-κB derivative) showed the most promising results regarding selective nuclear

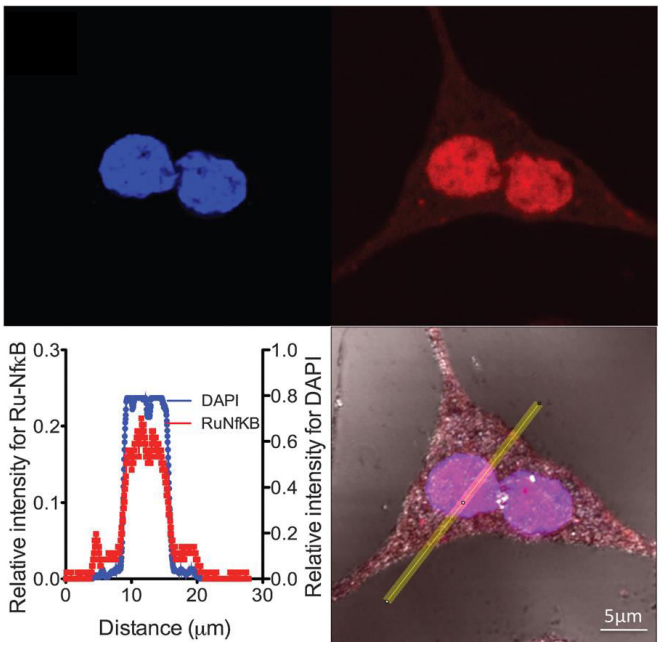

Figure 1.22: Selective nuclear localisation of $[Ru(bpy)_2(pic\text{-}NLS)]^{6+}$ in live CHO cells as indicated by co-staining with DAPI. Reproduced from Blackmore *et al*.[41]

---

uptake.[324] Similarly, work in our laboratory indicated selective nuclear uptake for Ru(II) conjugates of the NF-κB sequence (Figure 1.22) and less selective, and in some cases inhibited, nuclear uptake was observed for conjugates of the SV40 sequence.[41,323] Hence, in the present work, VQRKRQKLMP was exploited as the chosen NLS to conjugate with the candidate Ru(II) complexes (i.e. Ru-tap and Ru-dppz) in anticipation of targeting nuclear DNA for imaging and photoinduced destruction.

Mitochondrial uptake using a Mitochondria Penetrating Peptide (MPP): FrFKFrFK(Ac)

The mitochondria also contain DNA (mtDNA), and typically one or two copies are packaged into nucleoid structures in each mitochondrion.[325] Targeting the mitochondria selectively and penetrating the double membrane to access the contents of the inner mitochondrion is difficult. Previously, our group exploited the FrFKFrFK sequence developed by Kelley,[319,326] to yield a mitochondria localising peptide-bridged Ru(II) dinuclear complex.[9] In comparison to a commercial MitoTracker dye, confocal microscopy across the mitochondria revealed deeper penetration of our Ru(II) complex in comparison to the commercial dye which

suggests that access to mtDNA may be achievable. The peptide-bridged Ru(II) complex was accessed by conjugation at an aminohexyl terminus and the least-sterically hindered amine of the peptide at the terminal Lys residue. However, it was expected that acetyl blocking of this Lys amine should lead to mononuclear Ru-peptide conjugates with similar mitochondrial uptake to the dinuclear complex. Hence, in the present work, the acetyl-blocked sequence, FrFKFrFK(Ac), was conjugated to the candidate complexes in anticipation of targeting mtDNA.

Non-specific uptake using Octaarginine (R8): RRRRRRRR

The localisation ability of the NLS and MPP sequences can be compared to the R8 non-specific uptake vector which can be expected to deliver its Ru(II) cargo into the cell cytoplasm without nuclear or mitochondrial penetration.

1.6 Conclusion and project scope

Ex cellulo, Ru(II) luminophores demonstrate excellent potential as spectroscopic probes for DNA, the archetype example of which is the light-switch complex; $[Ru(bpy)_2(dppz)]^{2+}$. Ru(II) complexes can also exhibit selective photochemistry with DNA, for example, the unique photo-oxidative reactivity of complexes like $[Ru(tap)_2(bpy)]^{2+}$. These complexes were established as candidate complexes to develop under the scope of this thesis for DNA-targeted imaging and photo-destruction in live cells. A key issue in applying these complexes *in-cellulo* to date has been an inability to predictably translocate the cellular membrane and specifically localise at a target subcellular site. There is a dearth of reports that have successfully achieved nuclear uptake using metal complex luminophores for DNA-targeted imaging and therapy with low dark cytotoxicity, and to the best of our knowledge, there has been no reports which have successfully targeted mitochondrial nucleoid DNA with precision. Previously, our group has demonstrated that signal peptides are excellent vectors capable of specifically delivering their Ru(II) cargo to select organelles including the nucleus and the mitochondria, two locales where cellular DNA resides. Signal peptides appear to offer a wider scope than other uptake strategies to deliver *different* Ru(II) complexes to the *same* cellular target and it was anticipated that peptide-modification would be a successful route to targeting genetic material in the cell. The overarching aim of this thesis was therefore; to combine the precision targeting of signal peptides with the photophysical sensitivity of $[Ru(bpy)_2(dppz)]^{2+}$ or the photochemical reactivity of $[Ru(tap)_2(bpy)]^{2+}$ for live cell imaging and/or photoinduced damage of DNA.

Chapter 3 of this thesis describes the development of efficient synthetic routes to conjugatable Ru(II) luminophores and their judicious augmentation with signal peptides for precision targeted cellular application. Chapter 4 explores the use of Ru-dppz complexes tethered to NLS and MPP sequences for live cell light-switch imaging of nuclear and mitochondrial DNA, and once localised, their ability to induce targeted photodynamic toxicity. Chapter 5 describes the exploitation of the photoreactive excited state of a Ru-tap complex targeted to nuclear DNA using a conjugated NLS peptide for oxygen independent photoinduced toxicity. Finally, Chapter 6 describes efforts to employ Ru(II) probes for alternative sensing applications such as; high-resolution STED imaging of cellular structure,

electrochemiluminescence DNA detection and early progress towards potential Ru-dppz probes for amyloid fibrillisation in biological matrices.

1.7 References

(1) Li, G.; Sun, L.; Ji, L.; Chao, H. *Dalton Trans.* **2016**, *45* (34), 13261.
(2) Burke, C. S.; Byrne, A.; Keyes, T. E. In *Advances in Imaging and Sensing*; CRC Press, 2016; pp 227–254.
(3) Dolan, C.; Burke, C. S.; Byrne, A.; Keyes, T. E. In *Inorganic and Organometallic Transition Metal Complexes with Biological Molecules and Living Cells*; Lo, K. K.-W., Ed.; Academic Press, 2017; pp 55–89.
(4) Knoll, J. D.; Turro, C. *Coord. Chem. Rev.* **2015**, *282–283*, 110.
(5) Marcélis, L.; Ghesquière, J.; Garnir, K.; Kirsch-De Mesmaeker, A.; Moucheron, C. *Coord. Chem. Rev.* **2012**, *256* (15–16), 1569.
(6) Heinemann, F.; Karges, J.; Gasser, G. *Acc. Chem. Res.* **2017**.
(7) Puckett, C. A.; Barton, J. K. *J. Am. Chem. Soc.* **2007**, *129* (1), 46.
(8) Soler, M.; Feliu, L.; Planas, M.; Ribas, X.; Costas, M. *Dalton Trans.* **2016**.
(9) Martin, A.; Byrne, A.; Burke, C. S.; Forster, R. J.; Keyes, T. E. *J. Am. Chem. Soc.* **2014**, *136* (43), 15300.
(10) Byrne, A.; Burke, C. S.; Keyes, T. E. *Chem. Sci.* **2016**, *7* (10), 6551.
(11) Hell, S. W. *Science* **2007**, *316* (5828), 1153.
(12) Kasha, M. *Discuss. Faraday Soc.* **1950**, *9* (0), 14.
(13) Valeur, B. *Molecular Fluorescence: Principles and Applications*, 2nd ed.; Wiley, 2012.
(14) Suhling, K.; French, P. M. W.; Phillips, D. *Photochem. Photobiol. Sci.* **2005**, *4* (1), 13.
(15) Dmitriev, R. I.; Papkovsky, D. B. *Methods Appl. Fluoresc.* **2015**, *3* (3), 034001.
(16) Friedman, A. E.; Chambron, J. C.; Sauvage, J. P.; Turro, N. J.; Barton, J. K. *J. Am. Chem. Soc.* **1990**, *112* (12), 4960.
(17) Holmlin, R. E.; Barton, J. K. *Inorg. Chem.* **1995**, *34* (1), 7.
(18) van der Salm, H.; Fraser, M. G.; Horvath, R.; Cameron, S. A.; Barnsley, J. E.; Sun, X.-Z.; George, M. W.; Gordon, K. C. *Inorg. Chem.* **2014**, *53* (6), 3126.
(19) Stimpson, S.; Jenkinson, D. R.; Sadler, A.; Latham, M.; Wragg, D. A.; Meijer, A. J. H. M.; Thomas, J. A. *Angew. Chem. Int. Ed.* **2015**, *54* (10), 3000.
(20) Lo, K. K.-W.; Louie, M.-W.; Zhang, K. Y. *Coord. Chem. Rev.* **2010**, *254* (21–22), 2603.
(21) *Photochemistry and Photophysics of Coordination Compounds II*; Balzani, V., Campagna, S., Eds.; Topics in Current Chemistry; Springer Berlin Heidelberg: Berlin, Heidelberg, 2007; Vol. 281.
(22) Dolan, C.; Moriarty, R. D.; Lestini, E.; Devocelle, M.; Forster, R. J.; Keyes, T. E. *J. Inorg. Biochem.* **2013**, *119*, 65.
(23) Jackson, B. A.; Barton, J. K. *J. Am. Chem. Soc.* **1997**, *119* (52), 12986.
(24) Ernst, R. J.; Song, H.; Barton, J. K. *J. Am. Chem. Soc.* **2009**, *131* (6), 2359.
(25) Junicke, H.; Hart, J. R.; Kisko, J.; Glebov, O.; Kirsch, I. R.; Barton, J. K. *Proc. Natl. Acad. Sci.* **2003**, *100* (7), 3737.
(26) *Photochemistry and Photophysics of Coordination Compounds I*; Balzani, V., Campagna, S., Eds.; Topics in Current Chemistry; Springer Berlin Heidelberg: Berlin, Heidelberg, 2007; Vol. 280.
(27) Balasingham, R. G.; Coogan, M. P.; Thorp-Greenwood, F. L. *Dalton Trans.* **2011**, *40* (44), 11663.

(28) Raszeja, L. J.; Siegmund, D.; Cordes, A. L.; Güldenhaupt, J.; Gerwert, K.; Hahn, S.; Metzler-Nolte, N. *Chem. Commun.* **2017**, *53* (5), 905.
(29) Yang, J.; Zhao, J.-X.; Cao, Q.; Hao, L.; Zhou, D.; Gan, Z.; Ji, L.-N.; Mao, Z.-W. *ACS Appl. Mater. Interfaces* **2017**, *9* (16), 13900.
(30) Koo, C.-K.; Wong, K.-L.; Man, C. W.-Y.; Tam, H.-L.; Tsao, S.-W.; Cheah, K.-W.; Lam, M. H.-W. *Inorg. Chem.* **2009**, *48* (16), 7501.
(31) Faulkner, S.; Pope, S. J. A.; Burton-Pye, B. P. *Appl. Spectrosc. Rev.* **2005**, *40* (1), 1.
(32) Amoroso, A. J.; Pope, S. J. A. *Chem. Soc. Rev.* **2015**, *44* (14), 4723.
(33) Keyes, T. E.; Vos, J. G.; Kolnaar, J. A.; Haasnoot, J. G.; Reedijk, J.; Hage, R. *Inorganica Chim. Acta* **1996**, *245*, 237.
(34) Anderson, P. A.; Strouse, G. F.; Treadway, J. A.; Keene, F. R.; Meyer, T. J. *Inorg. Chem.* **1994**, *33* (18), 3863.
(35) Belser, P.; Zelewsky, A. V. *Helv. Chim. Acta* **1980**, *63* (6), 1675.
(36) von Zelewsky, A.; Gremaud, G. *Helv. Chim. Acta* **1988**, *71* (5), 1108.
(37) Byrne, A.; Jacobs, J.; Burke, C. S.; Martin, A.; Heise, A.; Keyes, T. E. *Analyst* **2017**, *142* (18), 3400.
(38) Carraway, E. R.; Demas, J. N.; DeGraff, B. A.; Bacon, J. R. *Anal. Chem.* **1991**, *63* (4), 337.
(39) Dobrucki, J. W. *J. Photochem. Photobiol. B* **2001**, *65* (2–3), 136.
(40) Cosgrave, L.; Devocelle, M.; Forster, R. J.; Keyes, T. E. *Chem. Commun.* **2010**, *46* (1), 103.
(41) Blackmore, L.; Moriarty, R.; Dolan, C.; Adamson, K.; Forster, R. J.; Devocelle, M.; Keyes, T. E. *Chem. Commun.* **2013**, *49* (26), 2658.
(42) Dickerson, M.; Sun, Y.; Howerton, B.; Glazer, E. C. *Inorg. Chem.* **2014**, *53* (19), 10370.
(43) Adamson, K.; Dolan, C.; Moran, N.; Forster, R. J.; Keyes, T. E. *Bioconjug. Chem.* **2014**, *25* (5), 928.
(44) Elias, B.; Kirsch-De Mesmaeker, A. *Coord. Chem. Rev.* **2006**, *250* (13–14), 1627.
(45) Moucheron, C.; Kirsch-De Mesmaeker, A.; Kelly, J. M. *J. Photochem. Photobiol. B* **1997**, *40* (2), 91.
(46) Pierard, F.; Kirsch-De Mesmaeker, A. *Inorg. Chem. Commun.* **2006**, *9* (1), 111.
(47) Dolan, C. The synthesis and characterisation of inorganic and organic luminophores suitable for biomolecule conjugation. PhD Thesis, Dublin City University. School of Chemical Sciences, 2012.
(48) Pellegrin, Y.; Forster, R. J.; Keyes, T. E. *Inorganica Chim. Acta* **2009**, *362* (6), 1715.
(49) Gao, F.; Chen, X.; Zhou, F.; Weng, L.-P.; Guo, L.-T.; Chen, M.; Chao, H.; Ji, L.-N. *Inorganica Chim. Acta* **2009**, *362* (14), 4960.
(50) Bai, G.-Y.; Wang, K.-Z.; Duan, Z.-M.; Gao, L.-H. *J. Inorg. Biochem.* **2004**, *98* (6), 1017.
(51) Yu, H.; Hao, Z.; Peng, H.; Rao, R.; Sun, M.; Alana W., R.; Ran, C.; Chao, H.; Yu, L. *Sens. Actuators B Chem.* **2017**, *252*, 313.
(52) Jose, D. A.; Kar, P.; Koley, D.; Ganguly, B.; Thiel, W.; Ghosh, H. N.; Das, A. *Inorg. Chem.* **2007**, *46* (14), 5576.
(53) Shang, X.-F.; Li, J.; Lin, H.; Jiang, P.; Cai, Z.-S.; Lin, H.-K. *Dalton Trans.* **2009**, *0* (12), 2096.
(54) Beer, P. D.; Timoshenko, V.; Maestri, M.; Passaniti, P.; Balzani, V. *Chem. Commun.* **1999**, *0* (17), 1755.
(55) Hao, Y.; Yang, P.; Li, S.; Huang, X.; Yang, X.-J.; Wu, B. *Dalton Trans.* **2012**, *41* (25), 7689.
(56) Langton, M. J.; Marques, I.; Robinson, S. W.; Félix, V.; Beer, P. D. *Chem. – Eur. J.* **2016**, *22* (1), 185.
(57) Barigelletti, F.; Flamigni, L.; Calogero, G.; Hammarström, L.; Sauvage, J.-P.; Collin, J.-P. *Chem. Commun.* **1998**, *0* (21), 2333.
(58) Liu, X.-W.; Xiao, Y.; Zhang, S.-B.; Lu, J.-L. *Inorg. Chem. Commun.* **2017**, *84*, 56.
(59) Zheng, Z.-B.; Duan, Z.-M.; Ma, Y.-Y.; Wang, K.-Z. *Inorg. Chem.* **2013**, *52* (5), 2306.

(60) Yang, H.-X.; Liu, Y.-J.; Zhao, L.; Wang, K.-Z. *Spectrochim. Acta. A. Mol. Biomol. Spectrosc.* **2010**, *76* (2), 146.
(61) Zhang, Y.; Liu, Z.; Yang, K.; Zhang, Y.; Xu, Y.; Li, H.; Wang, C.; Lu, A.; Sun, S. *Sci. Rep.* **2015**, *5*, srep08172.
(62) Zheng, Z.-B.; Kang, S.-Y.; Zhao, Y.; Zhang, N.; Yi, X.; Wang, K.-Z. *Sens. Actuators B Chem.* **2015**, *221*, 614.
(63) Watson, J. D.; Crick, F. H. C. *Nature* **1953**, *171* (4356), 737.
(64) Wahl, M. C.; Sundaralingam, M. *Biopolymers* **1997**, *44* (1), 45.
(65) Herbert, A.; Rich, A. *Genetica* **1999**, *106* (1–2), 37.
(66) Lipps, H. J.; Rhodes, D. *Trends Cell Biol.* **2009**, *19* (8), 414.
(67) Choi, J.; Majima, T. *Chem. Soc. Rev.* **2011**, *40* (12), 5893.
(68) Mura, S.; Couvreur, P. *Adv. Drug Deliv. Rev.* **2012**, *64* (13), 1394.
(69) Tanious, F. A.; Veal, J. M.; Buczak, H.; Ratmeyer, L. S.; Wilson, W. D. *Biochemistry (Mosc.)* **1992**, *31* (12), 3103.
(70) Liu, H.-K.; Sadler, P. J. *Acc. Chem. Res.* **2011**, *44* (5), 349.
(71) Lerman, L. S. *J. Mol. Biol.* **1961**, *3* (1), 18.
(72) Zeglis, B. M.; Pierre, V. C.; Barton, J. K. *Chem. Commun.* **2007**, No. 44, 4565.
(73) Komeda, S.; Moulaei, T.; Woods, K. K.; Chikuma, M.; Farrell, N. P.; Williams, L. D. *J. Am. Chem. Soc.* **2006**, *128* (50), 16092.
(74) Komeda, S.; Moulaei, T.; Chikuma, M.; Odani, A.; Kipping, R.; Farrell, N. P.; Williams, L. D. *Nucleic Acids Res.* **2011**, *39* (1), 325.
(75) Prisecaru, A.; Molphy, Z.; Kipping, R. G.; Peterson, E. J.; Qu, Y.; Kellett, A.; Farrell, N. P. *Nucleic Acids Res.* **2014**, *42* (22), 13474.
(76) Pizarro, A. M.; Sadler, P. J. *Biochimie* **2009**, *91* (10), 1198.
(77) Sherman, S. E.; Lippard, S. J. *Chem. Rev.* **1987**, *87* (5), 1153.
(78) Singh, T. N.; Turro, C. *Inorg. Chem.* **2004**, *43* (23), 7260.
(79) Jacquet, L.; Davies, R. J. H.; Kirsch-De Mesmaeker, A.; Kelly, J. M. *J. Am. Chem. Soc.* **1997**, *119* (49), 11763.
(80) Dwyer, F. P.; Gyarfas, E. C.; Rogers, W. P.; Koch, J. H. *Nature* **1952**, *170* (4318), 190.
(81) Brandt, W. W.; Dwyer, F. P.; Gyarfas, E. D. *Chem. Rev.* **1954**, *54* (6), 959.
(82) Sigman, D. S.; Landgraf, R.; Perrin, D. M.; Pearson, L. *Met. Ions Biol. Syst.* **1996**, *33*, 485.
(83) McGivern, T.; Afsharpour, S.; Marmion, C. J. *Inorganica Chim. Acta* **2017**.
(84) Jiang, Q.; Xiao, N.; Shi, P.; Zhu, Y.; Guo, Z. *Coord. Chem. Rev.* **2007**, *251* (15), 1951.
(85) Jennette, K. W.; Lippard, S. J.; Vassiliades, G. A.; Bauer, W. R. *Proc. Natl. Acad. Sci.* **1974**, *71* (10), 3839.
(86) Lippard, S. J.; Bond, P. J.; Wu, K. C.; Bauer, W. R. *Science* **1976**, *194* (4266), 726.
(87) Fernández-Moreira, V.; Thorp-Greenwood, F. L.; Coogan, M. P. *Chem. Commun.* **2009**, *46* (2), 186.
(88) Gill, M. R.; Thomas, J. A. *Chem. Soc. Rev.* **2012**, *41* (8), 3179.
(89) Pages, B. J.; Ang, D. L.; Wright, E. P.; Aldrich-Wright, J. R. *Dalton Trans.* **2015**, *44* (8), 3505.
(90) Nordén, B.; Tjerneld, F. *FEBS Lett.* **1976**, *67* (3), 368.
(91) Barton, J. K.; Dannenberg, J. J.; Raphael, A. L. *J. Am. Chem. Soc.* **1982**, *104* (18), 4967.
(92) Pfeiffer, P.; Quehl, K. *Berichte Dtsch. Chem. Ges. B Ser.* **1931**, *64* (10), 2667.
(93) Pfeiffer, P.; Nakatsuka, Y. *Berichte Dtsch. Chem. Ges. B Ser.* **1933**, *66* (3), 415.
(94) Kirschner, S.; Ahmad, N. *J. Am. Chem. Soc.* **1968**, *90* (7), 1910.
(95) Yamagishi, A. *J. Chem. Soc. Chem. Commun.* **1983**, No. 10, 572.
(96) Yamagishi, A. *J. Phys. Chem.* **1984**, *88* (23), 5709.
(97) Barton, J. K.; Danishefsky, A.; Goldberg, J. *J. Am. Chem. Soc.* **1984**, *106* (7), 2172.
(98) Barton, J. K.; Goldberg, J. M.; Kumar, C. V.; Turro, N. J. *J. Am. Chem. Soc.* **1986**, *108* (8), 2081.

(99) Rehmann, J. P.; Barton, J. K. *Biochemistry (Mosc.)* **1990**, *29* (7), 1701.
(100) Kelly, J. M.; Tossi, A. B.; McConnell, D. J.; OhUigin, C. *Nucleic Acids Res.* **1985**, *13* (17), 6017.
(101) Haworth, I. S.; Elcock, A. H.; Freeman, J.; Rodger, A.; Richards, W. G. *J. Biomol. Struct. Dyn.* **1991**, *9* (1), 23.
(102) Görner, H.; Tossi, A. B.; Stradowski, C.; Schulte-Frohlinde, D. *J. Photochem. Photobiol. B* **1988**, *2* (1), 67.
(103) Hiort, C.; Norden, B.; Rodger, A. *J. Am. Chem. Soc.* **1990**, *112* (5), 1971.
(104) Eriksson, M.; Leijon, M.; Hiort, C.; Norden, B.; Graeslund, A. *J. Am. Chem. Soc.* **1992**, *114* (12), 4933.
(105) Eriksson, M.; Leijon, M.; Hiort, C.; Norden, B.; Graeslund, A. *Biochemistry (Mosc.)* **1994**, *33* (17), 5031.
(106) Satyanarayana, S.; Dabrowiak, J. C.; Chaires, J. B. *Biochemistry (Mosc.)* **1992**, *31* (39), 9319.
(107) Härd, T.; Hiort, C.; Nordén, B. *J. Biomol. Struct. Dyn.* **1987**, *5* (1), 89.
(108) Satyanarayana, S.; Dabrowiak, J. C.; Chaires, J. B. *Biochemistry (Mosc.)* **1993**, *32* (10), 2573.
(109) Barton, J. K.; Basile, L. A.; Danishefsky, A.; Alexandrescu, A. *Proc. Natl. Acad. Sci. U. S. A.* **1984**, *81* (7), 1961.
(110) Barton, J. K. *Science* **1986**, *233* (4765), 727.
(111) McDonnell, U.; Hicks, M. R.; Hannon, M. J.; Rodger, A. *J. Inorg. Biochem.* **2008**, *102* (12), 2052.
(112) Prisecaru, A.; McKee, V.; Howe, O.; Rochford, G.; McCann, M.; Colleran, J.; Pour, M.; Barron, N.; Gathergood, N.; Kellett, A. *J. Med. Chem.* **2013**, *56* (21), 8599.
(113) Turro, C.; Bossmann, S. H.; Jenkins, Y.; Barton, J. K.; Turro, N. J. *J. Am. Chem. Soc.* **1995**, *117* (35), 9026.
(114) Chen, W.; Turro, C.; Friedman, L. A.; Barton, J. K.; Turro, N. J. *J. Phys. Chem. B* **1997**, *101* (35), 6995.
(115) Brennaman, M. K.; Meyer, T. J.; Papanikolas, J. M. *J. Phys. Chem. A* **2004**, *108* (45), 9938.
(116) Coates, C. G.; Olofsson, J.; Coletti, M.; McGarvey, J. J.; Önfelt, B.; Lincoln, P.; Norden, B.; Tuite, E.; Matousek, P.; Parker, A. W. *J. Phys. Chem. B* **2001**, *105* (50), 12653.
(117) Poynton, F. E.; Hall, J. P.; Keane, P. M.; Schwarz, C.; Sazanovich, I. V.; Towrie, M.; Gunnlaugsson, T.; Cardin, C. J.; Cardin, D. J.; Quinn, S. J.; Long, C.; Kelly, J. M. *Chem. Sci.* **2016**, *7* (5), 3075.
(118) Hiort, C.; Lincoln, P.; Norden, B. *J. Am. Chem. Soc.* **1993**, *115* (9), 3448.
(119) Friedman, A. E.; Kumar, C. V.; Turro, N. J.; Barton, J. K. *Nucleic Acids Res.* **1991**, *19* (10), 2595.
(120) Hartshorn, R. M.; Barton, J. K. *J. Am. Chem. Soc.* **1992**, *114* (15), 5919.
(121) Mihailovic, A.; Vladescu, I.; McCauley, M.; Ly, E.; Williams, M. C.; Spain, E. M.; Nuñez, M. E. *Langmuir* **2006**, *22* (10), 4699.
(122) Huang, H.; Zhang, P.; Yu, B.; Chen, Y.; Wang, J.; Ji, L.; Chao, H. *J. Med. Chem.* **2014**, *57* (21), 8971.
(123) Haq, I.; Lincoln, P.; Suh, D.; Norden, B.; Chowdhry, B. Z.; Chaires, J. B. *J. Am. Chem. Soc.* **1995**, *117* (17), 4788.
(124) Lincoln, P.; Broo, A.; Nordén, B. *J. Am. Chem. Soc.* **1996**, *118* (11), 2644.
(125) Tuite, E.; Lincoln, P.; Nordén, B. *J. Am. Chem. Soc.* **1997**, *119* (1), 239.
(126) McKinley, A. W.; Andersson, J.; Lincoln, P.; Tuite, E. M. *Chem. – Eur. J.* **2012**, *18* (47), 15142.
(127) Andersson, J.; Fornander, L. H.; Abrahamsson, M.; Tuite, E.; Nordell, P.; Lincoln, P. *Inorg. Chem.* **2013**, *52* (2), 1151.
(128) Niyazi, H.; Hall, J. P.; O'Sullivan, K.; Winter, G.; Sorensen, T.; Kelly, J. M.; Cardin, C. J. *Nat. Chem.* **2012**, *4* (8), 621.

(129) Hall, J. P.; Keane, P. M.; Beer, H.; Buchner, K.; Winter, G.; Sorensen, T. L.; Cardin, D. J.; Brazier, J. A.; Cardin, C. J. *Nucleic Acids Res.* **2016**, *44* (19), 9472.
(130) Hall, J. P.; Cook, D.; Morte, S. R.; McIntyre, P.; Buchner, K.; Beer, H.; Cardin, D. J.; Brazier, J. A.; Winter, G.; Kelly, J. M.; Cardin, C. J. *J. Am. Chem. Soc.* **2013**, *135* (34), 12652.
(131) Hall, J. P.; Gurung, S. P.; Henle, J.; Poidl, P.; Andersson, J.; Lincoln, P.; Winter, G.; Sorensen, T.; Cardin, D. J.; Brazier, J. A.; Cardin, C. J. *Chem. – Eur. J.* **2017**, *23* (21), 4981.
(132) Song, H.; Kaiser, J. T.; Barton, J. K. *Nat. Chem.* **2012**, *4* (8), 615.
(133) Sun, Y.; Collins, S. N.; Joyce, L. E.; Turro, C. *Inorg. Chem.* **2010**, *49* (9), 4257.
(134) Zhang, A.-G.; Zhang, Y.-Z.; Duan, Z.-M.; Wang, K.-Z.; Wei, H.-B.; Bian, Z.-Q.; Huang, C.-H. *Inorg. Chem.* **2011**, *50* (14), 6425.
(135) Aldrich-Wright, J.; Brodie, C.; Glazer, E. C.; Luedtke, N. W.; Elson-Schwab, L.; Tor, Y. *Chem. Commun.* **2004**, No. 8, 1018.
(136) Sun, Y.; Lutterman, D. A.; Turro, C. *Inorg. Chem.* **2008**, *47* (14), 6427.
(137) Shade, C. M.; Kennedy, R. D.; Rouge, J. L.; Rosen, M. S.; Wang, M. X.; Seo, S. E.; Clingerman, D. J.; Mirkin, C. A. *Chem. – Eur. J.* **2015**, *21* (31), 10983.
(138) Gao, F.; Chen, X.; Wang, J.-Q.; Chen, Y.; Chao, H.; Ji, L.-N. *Inorg. Chem.* **2009**, *48* (13), 5599.
(139) Wu, Z.; Tian, T.; Yu, J.; Weng, X.; Liu, Y.; Zhou, X. *Angew. Chem.* **2011**, *123* (50), 12168.
(140) Walker, M. G.; Gonzalez, V.; Chekmeneva, E.; Thomas, J. A. *Angew. Chem. Int. Ed.* **2012**, *51* (48), 12107.
(141) Waywell, P.; Gonzalez, V.; Gill, M. R.; Adams, H.; Meijer, A. J. H. M.; Williamson, M. P.; Thomas, J. A. *Chem. – Eur. J.* **2010**, *16* (8), 2407.
(142) Walker, M. G.; Ramu, V.; Meijer, A. J. H. M.; Das, A.; Thomas, J. A. *Dalton Trans.* **2017**, *46* (18), 6079.
(143) Bolger, J.; Gourdon, A.; Ishow, E.; Launay, J.-P. *J. Chem. Soc. Chem. Commun.* **1995**, No. 17, 1799.
(144) Bolger, J.; Gourdon, A.; Ishow, E.; Launay, J.-P. *Inorg. Chem.* **1996**, *35* (10), 2937.
(145) Lutterman, D. A.; Chouai, A.; Liu, Y.; Sun, Y.; Stewart, C. D.; Dunbar, K. R.; Turro, C. *J. Am. Chem. Soc.* **2008**, *130* (4), 1163.
(146) Burya, S. J.; Lutterman, D. A.; Turro, C. *Chem. Commun.* **2011**, *47* (6), 1848.
(147) Gill, M. R.; Garcia-Lara, J.; Foster, S. J.; Smythe, C.; Battaglia, G.; Thomas, J. A. *Nat. Chem.* **2009**, *1* (8), 662.
(148) Gill, M. R.; Derrat, H.; Smythe, C. G. W.; Battaglia, G.; Thomas, J. A. *ChemBioChem* **2011**, *12* (6), 877.
(149) Baggaley, E.; Gill, M. R.; Green, N. H.; Turton, D.; Sazanovich, I. V.; Botchway, S. W.; Smythe, C.; Haycock, J. W.; Weinstein, J. A.; Thomas, J. A. *Angew. Chem.* **2014**, *126* (13), 3435.
(150) Liu, Y.; Chouai, A.; Degtyareva, N. N.; Lutterman, D. A.; Dunbar, K. R.; Turro, C. *J. Am. Chem. Soc.* **2005**, *127* (31), 10796.
(151) Tysoe, S. A.; Kopelman, R.; Schelzig, D. *Inorg. Chem.* **1999**, *38* (23), 5196.
(152) Wragg, A.; Gill, M. R.; Turton, D.; Adams, H.; Roseveare, T. M.; Smythe, C.; Su, X.; Thomas, J. A. *Chem. – Eur. J.* **2014**, *20* (43), 14004.
(153) Wragg, A.; Gill, M. R.; McKenzie, L.; Glover, C.; Mowll, R.; Weinstein, J. A.; Su, X.; Smythe, C.; Thomas, J. A. *Chem. – Eur. J.* **2015**, *21*, 11865.
(154) Önfelt, B.; Lincoln, P.; Nordén, B. *J. Am. Chem. Soc.* **1999**, *121* (46), 10846.
(155) Önfelt, B.; Lincoln, P.; Nordén, B. *J. Am. Chem. Soc.* **2001**, *123* (16), 3630.
(156) Nordell, P.; Lincoln, P. *J. Am. Chem. Soc.* **2005**, *127* (27), 9670.
(157) Wilhelmsson, L. M.; Westerlund, F.; Lincoln, P.; Nordén, B. *J. Am. Chem. Soc.* **2002**, *124* (41), 12092.
(158) Lecomte, J.-P.; Kirsch-De Mesmaeker, A.; Feeney, M. M.; Kelly, J. M. *Inorg. Chem.* **1995**, *34* (26), 6481.

(159) Elias, B.; Creely, C.; Doorley, G. W.; Feeney, M. M.; Moucheron, C.; Kirsch-DeMesmaeker, A.; Dyer, J.; Grills, D. C.; George, M. W.; Matousek, P.; Parker, A. W.; Towrie, M.; Kelly, J. M. *Chem. – Eur. J.* **2008**, *14* (1), 369.
(160) Blasius, R.; Nierengarten, H.; Luhmer, M.; Constant, J.-F.; Defrancq, E.; Dumy, P.; van Dorsselaer, A.; Moucheron, C.; Kirsch-DeMesmaeker, A. *Chem. – Eur. J.* **2005**, *11* (5), 1507.
(161) Ortmans, I.; Elias, B.; Kelly, J. M.; Moucheron, C.; Kirsch-DeMesmaeker, A. *Dalton Trans.* **2004**, No. 4, 668.
(162) Hall, J. P.; Poynton, F. E.; Keane, P. M.; Gurung, S. P.; Brazier, J. A.; Cardin, D. J.; Winter, G.; Gunnlaugsson, T.; Sazanovich, I. V.; Towrie, M.; Cardin, C. J.; Kelly, J. M.; Quinn, S. J. *Nat. Chem.* **2015**, *7* (12), 961.
(163) Moucheron, C.; Kirsch-De Mesmaeker, A.; Choua, S. *Inorg. Chem.* **1997**, *36* (4), 584.
(164) Moucheron, C.; Kirsch-De Mesmaeker, A. *J. Phys. Org. Chem.* **1998**, *11* (8–9), 577.
(165) Boisdenghien, A.; Moucheron, C.; Kirsch-De Mesmaeker, A. *Inorg. Chem.* **2005**, *44* (21), 7678.
(166) Vanderlinden, W.; Blunt, M.; David, C. C.; Moucheron, C.; Kirsch-De Mesmaeker, A.; De Feyter, S. *J. Am. Chem. Soc.* **2012**, *134* (24), 10214.
(167) Hannon, M. J. *Chem. Soc. Rev.* **2007**, *36* (2), 280.
(168) Brodie, C. R.; Aldrich-Wright, J. R. *Eur. J. Inorg. Chem.* **2007**, *2007* (30), 4781.
(169) Del Guerzo; Kirsch-De Mesmaeker, A. *Inorg. Chem.* **2002**, *41* (4), 938.
(170) Hannon, M. J.; Moreno, V.; Prieto, M. J.; Moldrheim, E.; Sletten, E.; Meistermann, I.; Isaac, C. J.; Sanders, K. J.; Rodger, A. *Angew. Chem. Int. Ed.* **2001**, *40* (5), 879.
(171) Meistermann, I.; Moreno, V.; Prieto, M. J.; Moldrheim, E.; Sletten, E.; Khalid, S.; Rodger, P. M.; Peberdy, J. C.; Isaac, C. J.; Rodger, A.; Hannon, M. J. *Proc. Natl. Acad. Sci.* **2002**, *99* (8), 5069.
(172) Oleksy, A.; Blanco, A. G.; Boer, R.; Usón, I.; Aymamí, J.; Rodger, A.; Hannon, M. J.; Coll, M. *Angew. Chem. Int. Ed.* **2006**, *45* (8), 1227.
(173) Cerasino, L.; Hannon, M. J.; Sletten, E. *Inorg. Chem.* **2007**, *46* (16), 6245.
(174) Malina, J.; Hannon, M. J.; Brabec, V. *Chem. – Eur. J.* **2008**, *14* (33), 10408.
(175) Malina, J.; Hannon, M. J.; Brabec, V. *Nucleic Acids Res.* **2008**, *36* (11), 3630.
(176) Uerpmann, C.; Malina, J.; Pascu, M.; Clarkson, G. J.; Moreno, V.; Rodger, A.; Grandas, A.; Hannon, M. J. *Chem. – Eur. J.* **2005**, *11* (6), 1750.
(177) Phongtongpasuk, S.; Paulus, S.; Schnabl, J.; Sigel, R. K. O.; Spingler, B.; Hannon, M. J.; Freisinger, E. *Angew. Chem. Int. Ed.* **2013**, *52* (44), 11513.
(178) Cardo, L.; Sadovnikova, V.; Phongtongpasuk, S.; Hodges, N. J.; Hannon, M. J. *Chem. Commun.* **2011**, *47* (23), 6575.
(179) Hotze, A. C. G.; Kariuki, B. M.; Hannon, M. J. *Angew. Chem. Int. Ed.* **2006**, *45* (29), 4839.
(180) Wachter, E.; Zamora, A.; Heidary, D. K.; Ruiz, J.; Glazer, E. C. *Chem. Commun.* **2016**.
(181) Pascu, G. I.; Hotze, A. C. G.; Sanchez-Cano, C.; Kariuki, B. M.; Hannon, M. J. *Angew. Chem. Int. Ed.* **2007**, *46* (23), 4374.
(182) Ducani, C.; Leczkowska, A.; Hodges, N. J.; Hannon, M. J. *Angew. Chem. Int. Ed.* **2010**, *49* (47), 8942.
(183) Cao, Q.; Li, Y.; Freisinger, E.; Qin, P. Z.; Sigel, R. K. O.; Mao, Z.-W. *Inorg. Chem. Front.* **2017**, *4* (1), 10.
(184) Shi, S.; Geng, X.; Zhao, J.; Yao, T.; Wang, C.; Yang, D.; Zheng, L.; Ji, L. *Biochimie* **2010**, *92* (4), 370.
(185) Wachter, E.; Moyá, D.; Parkin, S.; Glazer, E. C. *Chem. – Eur. J.* **2016**, *22* (2), 550.
(186) Yao, J.-L.; Gao, X.; Sun, W.; Fan, X.-Z.; Shi, S.; Yao, T.-M. *Inorg. Chem.* **2012**, *51* (23), 12591.
(187) Yao, J.-L.; Gao, X.; Sun, W.; Shi, S.; Yao, T.-M. *Dalton Trans.* **2013**, *42* (16), 5661.
(188) Liao, G.-L.; Chen, X.; Ji, L.-N.; Chao, H. *Chem. Commun.* **2012**, *48* (87), 10781.

(189) Liao, G.; Chen, X.; Wu, J.; Qian, C.; Wang, H.; Ji, L.; Chao, H. *Dalton Trans.* **2014**, *43* (21), 7811.
(190) Sun, J.; An, Y.; Zhang, L.; Chen, H.-Y.; Han, Y.; Wang, Y.-J.; Mao, Z.-W.; Ji, L.-N. *J. Inorg. Biochem.* **2011**, *105* (2), 149.
(191) Rajput, C.; Rutkaite, R.; Swanson, L.; Haq, I.; Thomas, J. A. *Chem. – Eur. J.* **2006**, *12* (17), 4611.
(192) Wilson, T.; Williamson, M. P.; Thomas, J. A. *Org. Biomol. Chem.* **2010**, *8* (11), 2617.
(193) Xu, L.; Zhang, D.; Huang, J.; Deng, M.; Zhang, M.; Zhou, X. *Chem. Commun.* **2010**, *46* (5), 743.
(194) Xu, L.; Liao, G.-L.; Chen, X.; Zhao, C.-Y.; Chao, H.; Ji, L.-N. *Inorg. Chem. Commun.* **2010**, *13* (9), 1050.
(195) Xu, L.; Chen, X.; Wu, J.; Wang, J.; Ji, L.; Chao, H. *Chem. – Eur. J.* **2015**, *21* (10), 4008.
(196) Li, G.-M. *Cell Res.* **2008**, *18* (1), 85.
(197) Poulogiannis, G.; Frayling, I. M.; Arends, M. J. *Histopathology* **2010**, *56* (2), 167.
(198) Mürner, H.; Jackson, B. A.; Barton, J. K. *Inorg. Chem.* **1998**, *37* (12), 3007.
(199) Zeglis, B. M.; Barton, J. K. *Nat. Protoc.* **2007**, *2* (2), 357.
(200) Cordier, C.; Pierre, V. C.; Barton, J. K. *J. Am. Chem. Soc.* **2007**, *129* (40), 12287.
(201) Rüba, E.; Hart, J. R.; Barton, J. K. *Inorg. Chem.* **2004**, *43* (15), 4570.
(202) McConnell, A. J.; Lim, M. H.; Olmon, E. D.; Song, H.; Dervan, E. E.; Barton, J. K. *Inorg. Chem.* **2012**, *51* (22), 12511.
(203) Zeglis, B. M.; Barton, J. K. *Inorg. Chem.* **2008**, *47* (14), 6452.
(204) Zeglis, B. M.; Barton, J. K. *J. Am. Chem. Soc.* **2006**, *128* (17), 5654.
(205) Lim, M. H.; Song, H.; Olmon, E. D.; Dervan, E. E.; Barton, J. K. *Inorg. Chem.* **2009**, *48* (12), 5392.
(206) McConnell, A. J.; Song, H.; Barton, J. K. *Inorg. Chem.* **2013**, *52* (17).
(207) Boynton, A. N.; Marcélis, L.; Barton, J. K. *J. Am. Chem. Soc.* **2016**, *138* (15), 5020.
(208) Deraedt, Q.; Marcélis, L.; Loiseau, F.; Elias, B. *Inorg. Chem. Front.* **2017**, *4* (1), 91.
(209) Jenkins, Y.; Friedman, A. E.; Turro, N. J.; Barton, J. K. *Biochemistry (Mosc.)* **1992**, *31* (44), 10809.
(210) McKinley, A. W.; Lincoln, P.; Tuite, E. M. *Dalton Trans.* **2013**, *42* (11), 4081.
(211) Choi, S.-D.; Kim, M.-S.; Kim, S. K.; Lincoln, P.; Tuite, E.; Nordén, B. *Biochemistry (Mosc.)* **1997**, *36* (1), 214.
(212) Peng, M.-N.; Zhu, Z.-Y.; Tan, L.-F. *Inorg. Chem.* **2017**, *56* (13), 7312.
(213) Coates, C. G.; McGarvey, J. J.; Callaghan, P. L.; Coletti, M.; Hamilton, J. G. *J. Phys. Chem. B* **2001**, *105* (3), 730.
(214) Moon, S. J.; Kim, J. M.; Choi, J. Y.; Kim, S. K.; Lee, J. S.; Jang, H. G. *J. Inorg. Biochem.* **2005**, *99* (5), 994.
(215) Zhang, S.; Ding, Y.; Wei, H. *Molecules* **2014**, *19* (8), 11933.
(216) Jenkins, Y.; Barton, J. K. *J. Am. Chem. Soc.* **1992**, *114* (22), 8736.
(217) Le Gac, S.; Rickling, S.; Gerbaux, P.; Defrancq, E.; Moucheron, C.; Kirsch-De Mesmaeker, A. *Angew. Chem.* **2009**, *121* (6), 1142.
(218) Marcélis, L.; Surin, M.; Lartia, R.; Moucheron, C.; Defrancq, E.; Kirsch-De Mesmaeker, A. *Eur. J. Inorg. Chem.* **2014**, *2014* (19), 3016.
(219) Reschner, A.; Bontems, S.; Le Gac, S.; Lambermont, J.; Marcélis, L.; Defrancq, E.; Hubert, P.; Moucheron, C.; Kirsch-De Mesmaeker, A.; Raes, M.; Piette, J.; Delvenne, P. *Gene Ther.* **2013**, *20* (4), 435.
(220) Marcélis, L.; Van Overstraeten-Schlögel, N.; Lambermont, J.; Bontems, S.; Spinelli, N.; Defrancq, E.; Moucheron, C.; Kirsch-De Mesmaeker, A.; Raes, M. *ChemPlusChem* **2014**, *79* (11), 1597.
(221) Dougherty, T. J.; Gomer, C. J.; Henderson, B. W.; Jori, G.; Kessel, D.; Korbelik, M.; Moan, J.; Peng, Q. *JNCI J. Natl. Cancer Inst.* **1998**, *90* (12), 889.

(222) Shirasu, N.; Nam, S. O.; Kuroki, M. *Anticancer Res.* **2013**, *33* (7), 2823.
(223) Dolmans, D. E. J. G. J.; Fukumura, D.; Jain, R. K. *Nat. Rev. Cancer* **2003**, *3* (5), 380.
(224) Castano, A. P.; Demidova, T. N.; Hamblin, M. R. *Photodiagnosis Photodyn. Ther.* **2004**, *1* (4), 279.
(225) Buytaert, E.; Dewaele, M.; Agostinis, P. *Biochim. Biophys. Acta BBA - Rev. Cancer* **2007**, *1776* (1), 86.
(226) Skovsen, E.; Snyder, J. W.; Lambert, J. D. C.; Ogilby, P. R. *J. Phys. Chem. B* **2005**, *109* (18), 8570.
(227) Castano, A. P.; Demidova, T. N.; Hamblin, M. R. *Photodiagnosis Photodyn. Ther.* **2005**, *2* (1), 1.
(228) Sandell, J. L.; Zhu, T. C. *J. Biophotonics* **2011**, *4* (11–12), 773.
(229) Mallidi, S.; Anbil, S.; Bulin, A.-L.; Obaid, G.; Ichikawa, M.; Hasan, T. *Theranostics* **2016**, *6* (13), 2458.
(230) Huang, Z. *Technol. Cancer Res. Treat.* **2005**, *4* (3), 283.
(231) Josefsen, L. B.; Boyle, R. W. *Met.-Based Drugs* **2008**, *2008*.
(232) Hadjiliadis, N.; Sletten, E. *Metal Complex - DNA Interactions*; John Wiley & Sons, 2009.
(233) Wachter, E.; Heidary, D. K.; Howerton, B. S.; Parkin, S.; Glazer, E. C. *Chem. Commun.* **2012**, *48* (77), 9649.
(234) Qiu, K.; Wang, J.; Song, C.; Wang, L.; Zhu, H.; Huang, H.; Huang, J.; Wang, H.; Ji, L.; Chao, H. *ACS Appl. Mater. Interfaces* **2017**, *9* (22), 18482.
(235) McKenzie, L. K.; Sazanovich, I. V.; Baggaley, E.; Bonneau, M.; Guerchais, V.; Williams, J. A. G.; Weinstein, J. A.; Bryant, H. E. *Chem. – Eur. J.* **2017**, *23* (2), 234.
(236) Moriwaki, S.-I.; Misawa, J.; Yoshinari, Y.; Yamada, I.; Takigawa, M.; Tokura, Y. *Photodermatol. Photoimmunol. Photomed.* **2001**, *17* (5), 241.
(237) Hong, E. J.; Choi, D. G.; Shim, M. S. *Acta Pharm. Sin. B* **2016**, *6* (4), 297.
(238) Li, R.; Zheng, K.; Hu, P.; Chen, Z.; Zhou, S.; Chen, J.; Yuan, C.; Chen, S.; Zheng, W.; Ma, E.; Zhang, F.; Xue, J.; Chen, X.; Huang, M. *Theranostics* **2014**, *4* (6), 642.
(239) Bertout, J. A.; Patel, S. A.; Simon, M. C. *Nat. Rev. Cancer* **2008**, *8* (12), 967.
(240) Wilson, W. R.; Hay, M. P. *Nat. Rev. Cancer* **2011**, *11* (6), 393.
(241) Eales, K. L.; Hollinshead, K. E. R.; Tennant, D. A. *Oncogenesis* **2016**, *5* (1), e190.
(242) Rosenberg, B.; Renshaw, E.; Vancamp, L.; Hartwick, J.; Drobnik, J. *J. Bacteriol.* **1967**, *93* (2), 716.
(243) Rosenberg, B.; Van Camp, L.; Krigas, T. *Nature* **1965**, *205* (4972), 698.
(244) Kelland, L. *Nat. Rev. Cancer* **2007**, *7* (8), 573.
(245) Jamieson, E. R.; Lippard, S. J. *Chem. Rev.* **1999**, *99* (9), 2467.
(246) Galluzzi, L.; Senovilla, L.; Vitale, I.; Michels, J.; Martins, I.; Kepp, O.; Castedo, M.; Kroemer, G. *Oncogene* **2012**, *31* (15), 1869.
(247) Fleisher, M. B.; Waterman, K. C.; Turro, N. J.; Barton, J. K. *Inorg. Chem.* **1986**, *25* (20), 3549.
(248) Kelly, J. M.; McConnell, D. J.; OhUigin, C.; Tossi, A. B.; Mesmaeker, A. K.-D.; Masschelein, A.; Nasielski, J. *J. Chem. Soc. Chem. Commun.* **1987**, No. 24, 1821.
(249) Tanielian, C.; Wolff, C.; Esch, M. *J. Phys. Chem.* **1996**, *100* (16), 6555.
(250) Liu, Y.; Hammitt, R.; Lutterman, D. A.; Joyce, L. E.; Thummel, R. P.; Turro, C. *Inorg. Chem.* **2009**, *48* (1), 375.
(251) Sentagne, C.; Chambron, J.-C.; Sauvage, J.-P.; Paillous, N. *J. Photochem. Photobiol. B* **1994**, *26* (2), 165.
(252) Gicquel, E.; Souchard, J.-P.; Magnusson, F.; Chemaly, J.; Calsou, P.; Vicendo, P. *Photochem. Photobiol. Sci.* **2013**, *12* (8), 1517.
(253) Sun, Y.; Joyce, L. E.; Dickson, N. M.; Turro, C. *Chem. Commun.* **2010**, *46* (14), 2426.
(254) Yin, H.; Stephenson, M.; Gibson, J.; Sampson, E.; Shi, G.; Sainuddin, T.; Monro, S.; McFarland, S. A. *Inorg. Chem.* **2014**, *53* (9), 4548.

(255) Saeed, H. K.; Jarman, P. J.; Archer, S.; Sreedharan, S.; Saeed, I. Q.; Mckenzie, L. K.; Weinstein, J. A.; Buurma, N. J.; Smythe, C. G. W.; Thomas, J. A. *Angew. Chem. Int. Ed.* n/a.
(256) Lincoln, R.; Kohler, L.; Monro, S.; Yin, H.; Stephenson, M.; Zong, R.; Chouai, A.; Dorsey, C.; Hennigar, R.; Thummel, R. P.; McFarland, S. A. *J. Am. Chem. Soc.* **2013**, *135* (45), 17161.
(257) Monro, S.; Scott, J.; Chouai, A.; Lincoln, R.; Zong, R.; Thummel, R. P.; McFarland, S. A. *Inorg. Chem.* **2010**, *49* (6), 2889.
(258) Shi, G.; Monro, S.; Hennigar, R.; Colpitts, J.; Fong, J.; Kasimova, K.; Yin, H.; DeCoste, R.; Spencer, C.; Chamberlain, L.; Mandel, A.; Lilge, L.; McFarland, S. A. *Coord. Chem. Rev.* **2015**, *282* (Supplement C), 127.
(259) Salassa, L.; Garino, C.; Salassa, G.; Gobetto, R.; Nervi, C. *J. Am. Chem. Soc.* **2008**, *130* (29), 9590.
(260) Salassa, L.; Garino, C.; Salassa, G.; Nervi, C.; Gobetto, R.; Lamberti, C.; Gianolio, D.; Bizzarri, R.; Sadler, P. J. *Inorg. Chem.* **2009**, *48* (4), 1469.
(261) Zayat, L.; Calero, C.; Alborés, P.; Baraldo, L.; Etchenique, R. *J. Am. Chem. Soc.* **2003**, *125* (4), 882.
(262) Rial Verde, E.; Zayat, L.; Etchenique, R.; Yuste, R. *Front. Neural Circuits* **2008**, *2*.
(263) Filevich, O.; Salierno, M.; Etchenique, R. *J. Inorg. Biochem.* **2010**, *104* (12), 1248.
(264) Zayat, L.; Salierno, M.; Etchenique, R. *Inorg. Chem.* **2006**, *45* (4), 1728.
(265) Salierno, M.; Marceca, E.; Peterka, D. S.; Yuste, R.; Etchenique, R. *J. Inorg. Biochem.* **2010**, *104* (4), 418.
(266) Araya, R.; Andino-Pavlovsky, V.; Yuste, R.; Etchenique, R. *ACS Chem. Neurosci.* **2013**, *4* (8), 1163.
(267) Sharma, R.; Knoll, J. D.; Martin, P. D.; Podgorski, I.; Turro, C.; Kodanko, J. J. *Inorg. Chem.* **2014**, *53* (7), 3272.
(268) Respondek, T.; Garner, R. N.; Herroon, M. K.; Podgorski, I.; Turro, C.; Kodanko, J. J. *J. Am. Chem. Soc.* **2011**, *133* (43), 17164.
(269) Arora, K.; White, J. K.; Sharma, R.; Mazumder, S.; Martin, P. D.; Schlegel, H. B.; Turro, C.; Kodanko, J. J. *Inorg. Chem.* **2016**, *55* (14), 6968.
(270) Garner, R. N.; Gallucci, J. C.; Dunbar, K. R.; Turro, C. *Inorg. Chem.* **2011**, *50* (19), 9213.
(271) Sgambellone, M. A.; David, A.; Garner, R. N.; Dunbar, K. R.; Turro, C. *J. Am. Chem. Soc.* **2013**, *135* (30), 11274.
(272) Albani, B. A.; Peña, B.; Leed, N. A.; de Paula, N. A. B. G.; Pavani, C.; Baptista, M. S.; Dunbar, K. R.; Turro, C. *J. Am. Chem. Soc.* **2014**, *136* (49), 17095.
(273) Lameijer, L. N.; Hopkins, S. L.; Brevé, T. G.; Askes, S. H. C.; Bonnet, S. *Chem. – Eur. J.* **2016**, *22* (51), 18484.
(274) Goldbach, R. E.; Rodriguez-Garcia, I.; van Lenthe, J. H.; Siegler, M. A.; Bonnet, S. *Chem. – Eur. J.* **2011**, *17* (36), 9924.
(275) Rixel, V. H. S. van; Siewert, B.; Hopkins, S. L.; Askes, S. H. C.; Busemann, A.; Siegler, M. A.; Bonnet, S. *Chem. Sci.* **2016**, *7* (8), 4922.
(276) Askes, S. H. C.; Bahreman, A.; Bonnet, S. *Angew. Chem.* **2014**, *126* (4), 1047.
(277) Howerton, B. S.; Heidary, D. K.; Glazer, E. C. *J. Am. Chem. Soc.* **2012**, *134* (20), 8324.
(278) Wachter, E.; Howerton, B. S.; Hall, E. C.; Parkin, S.; Glazer, E. C. *Chem. Commun.* **2013**, *50* (3), 311.
(279) Hidayatullah, A. N.; Wachter, E.; Heidary, D. K.; Parkin, S.; Glazer, E. C. *Inorg. Chem.* **2014**, *53* (19), 10030.
(280) Sun, W.; Parowatkin, M.; Steffen, W.; Butt, H.-J.; Mailänder, V.; Wu, S. *Adv. Healthc. Mater.* **2016**, *5* (4), 467.
(281) Sun, W.; Li, S.; Häupler, B.; Liu, J.; Jin, S.; Steffen, W.; Schubert, U. S.; Butt, H.-J.; Liang, X.-J.; Wu, S. *Adv. Mater.* **2017**, *29* (6), n/a.
(282) Karaoun, N.; Renfrew, A. K. *Chem. Commun.* **2015**, *51* (74), 14038.

(283) Frasconi, M.; Liu, Z.; Lei, J.; Wu, Y.; Strekalova, E.; Malin, D.; Ambrogio, M. W.; Chen, X.; Botros, Y. Y.; Cryns, V. L.; Sauvage, J.-P.; Stoddart, J. F. *J. Am. Chem. Soc.* **2013**, *135* (31), 11603.
(284) Puckett, C. A.; Ernst, R. J.; Barton, J. K. *Dalton Trans.* **2010**, *39* (5), 1159.
(285) Byrne, A. The application of Ru(II) polypyridyl complexes to cellular imaging and sensing. PhD Thesis, Dublin City University, 2016.
(286) Tihanyi, K.; Vastag, M. *Solubility, Delivery and ADME Problems of Drugs and Drug-Candidates*; Bentham Science Publishers, 2011.
(287) Lodish, H.; Berk, A.; Zipursky, S. L.; Matsudaira, P.; Baltimore, D.; Darnell, J. *Molecular Cell Biology*, 4th ed.; W. H. Freeman: New York, 2000.
(288) Puckett, C. A.; Barton, J. K. *Biochemistry (Mosc.)* **2008**, *47* (45), 11711.
(289) Huang, H.; Yu, B.; Zhang, P.; Huang, J.; Chen, Y.; Gasser, G.; Ji, L.; Chao, H. *Angew. Chem. Int. Ed.* **2015**, *54* (47), 14049.
(290) Gill, M. R.; Cecchin, D.; Walker, M. G.; Mulla, R. S.; Battaglia, G.; Smythe, C.; Thomas, J. A. *Chem. Sci.* **2013**, *4* (12), 4512.
(291) Huang, H.; Zhang, P.; Chen, H.; Ji, L.; Chao, H. *Chem. – Eur. J.* **2015**, *21* (2), 715.
(292) Zhu, B.-Z.; Chao, X.-J.; Huang, C.-H.; Li, Y. *Chem. Sci.* **2016**, *7* (7), 4016.
(293) Sakai, N.; Matile, S. *J. Am. Chem. Soc.* **2003**, *125* (47), 14348.
(294) Li, S. P.-Y.; Liu, H.-W.; Zhang, K. Y.; Lo, K. K.-W. *Chem. – Eur. J.* **2010**, *16* (28), 8329.
(295) Li, S. P.-Y.; Lau, C. T.-S.; Louie, M.-W.; Lam, Y.-W.; Cheng, S. H.; Lo, K. K.-W. *Biomaterials* **2013**, *34* (30), 7519.
(296) Tso, K. K.-S.; Leung, K.-K.; Liu, H.-W.; Lo, K. K.-W. *Chem. Commun.* **2016**, *52* (24), 4557.
(297) Svensson, F. R.; Matson, M.; Li, M.; Lincoln, P. *Biophys. Chem.* **2010**, *149* (3), 102.
(298) Svensson, F. R.; Abrahamsson, M.; Strömberg, N.; Ewing, A. G.; Lincoln, P. *J. Phys. Chem. Lett.* **2011**, *2* (5), 397.
(299) Viola-Villegas, N.; Rabideau, A. E.; Cesnavicious, J.; Zubieta, J.; Doyle, R. P. *ChemMedChem* **2008**, *3* (9), 1387.
(300) Lo, K. K.-W.; Lee, T. K.-M. *Inorg. Chem.* **2004**, *43* (17), 5275.
(301) Lo, K. K.-W.; Lee, T. K.-M.; Lau, J. S.-Y.; Poon, W.-L.; Cheng, S.-H. *Inorg. Chem.* **2008**, *47* (1), 200.
(302) Gottschaldt, M.; Schubert, U. S.; Rau, S.; Yano, S.; Vos, J. G.; Kroll, T.; Clement, J.; Hilger, I. *ChemBioChem* **2010**, *11* (5), 649.
(303) Shen, J.; Kim, H.-C.; Wolfram, J.; Mu, C.; Zhang, W.; Liu, H.; Xie, Y.; Mai, J.; Zhang, H.; Li, Z.; Guevara, M.; Mao, Z.-W.; Shen, H. *Nano Lett.* **2017**, *17* (5), 2913.
(304) Mukhopadhyay, S.; Barnés, C. M.; Haskel, A.; Short, S. M.; Barnes, K. R.; Lippard, S. J. *Bioconjug. Chem.* **2008**, *19* (1), 39.
(305) Barragán, F.; López-Senín, P.; Salassa, L.; Betanzos-Lara, S.; Habtemariam, A.; Moreno, V.; Sadler, P. J.; Marchán, V. *J. Am. Chem. Soc.* **2011**, *133* (35), 14098.
(306) Vivès, E.; Brodin, P.; Lebleu, B. *J. Biol. Chem.* **1997**, *272* (25), 16010.
(307) Frankel, A. D.; Pabo, C. O. *Cell* **1988**, *55* (6), 1189.
(308) Derossi, D.; Joliot, A. H.; Chassaing, G.; Prochiantz, A. *J. Biol. Chem.* **1994**, *269* (14), 10444.
(309) Stewart, K. M.; Horton, K. L.; Kelley, S. O. *Org. Biomol. Chem.* **2008**, *6* (13), 2242.
(310) Copolovici, D. M.; Langel, K.; Eriste, E.; Langel, Ü. *ACS Nano* **2014**, *8* (3), 1972.
(311) Wender, P. A.; Mitchell, D. J.; Pattabiraman, K.; Pelkey, E. T.; Steinman, L.; Rothbard, J. B. *Proc. Natl. Acad. Sci.* **2000**, *97* (24), 13003.
(312) Neugebauer, U.; Pellegrin, Y.; Devocelle, M.; Forster, R. J.; Signac, W.; Moran, N.; Keyes, T. E. *Chem. Commun.* **2008**, No. 42, 5307.
(313) Byrne, A.; Dolan, C.; Moriarty, R. D.; Martin, A.; Neugebauer, U.; Forster, R. J.; Davies, A.; Volkov, Y.; Keyes, T. E. *Dalton Trans.* **2015**, *44* (32), 14323.
(314) Brunner, J.; Barton, J. K. *Biochemistry (Mosc.)* **2006**, *45* (40), 12295.
(315) Puckett, C. A.; Barton, J. K. *J. Am. Chem. Soc.* **2009**, *131* (25), 8738.

(316) Gamba, I.; Salvadó, I.; Rama, G.; Bertazzon, M.; Sánchez, M. I.; Sánchez-Pedregal, V. M.; Martínez-Costas, J.; Brissos, R. F.; Gamez, P.; Mascareñas, J. L.; Vázquez López, M.; Vázquez, M. E. *Chem. – Eur. J.* **2013**, *19* (40), 13369.
(317) Futaki, S.; Nakase, I. *Acc. Chem. Res.* **2017**.
(318) Freitas, N.; Cunha, C. *Curr. Genomics* **2009**, *10* (8), 550.
(319) Horton, K. L.; Stewart, K. M.; Fonseca, S. B.; Guo, Q.; Kelley, S. O. *Chem. Biol.* **2008**, *15* (4), 375.
(320) Boulikas, T. *J. Cell. Biochem.* **1994**, *55* (1), 32.
(321) Brandén, L. J.; Mohamed, A. J.; Smith, C. I. E. *Nat. Biotechnol.* **1999**, *17* (8), 784.
(322) Noor, F.; Wüstholz, A.; Kinscherf, R.; Metzler-Nolte, N. *Angew. Chem. Int. Ed.* **2005**, *44* (16), 2429.
(323) Blackmore, L. Novel luminescent peptide conjugates for assessing protein and other biomolecules location and function. PhD Thesis, Dublin City University. School of Chemical Sciences, 2013.
(324) Ragin, A. D.; Morgan, R. A.; Chmielewski, J. *Chem. Biol.* **2002**, *9* (8), 943.
(325) Kukat, C.; Wurm, C. A.; Spåhr, H.; Falkenberg, M.; Larsson, N.-G.; Jakobs, S. *Proc. Natl. Acad. Sci. U. S. A.* **2011**, *108* (33), 13534.
(326) Jean, S. R.; Ahmed, M.; Lei, E. K.; Wisnovsky, S. P.; Kelley, S. O. *Acc. Chem. Res.* **2016**.

Chapter 2

Materials and Methods

2.1 Materials

General

All materials for synthesis were procured from Sigma-Aldrich or FluoroChem and were used without further purification. Solvents were provided in-house or purchased from the same sources and used without further purification. Nitrogen was provided in-house and used as received. Analytical thin layer chromatography (TLC) was performed on Merck TLC Silica Gel 60 F_{254} foil-backed plates. Preparative TLC was performed on glass-backed 250 - 1500 μm silica or C18 plates. Column chromatography was carried out in glass columns using silica gel 60 (Sigma) as stationary phase. Filtrations were typically carried out using 0.4 μm Nylaflo membrane filters. Where light exclusion was required for synthesis, the reaction apparatus was wrapped in aluminium foil. Full synthesis procedures are provided within the relevant chapters of this thesis.

Dulbecco's phosphate buffered saline (DPBS, pH measured at 7.4 (25 °C), hereafter PBS throughout this thesis) was prepared from tablets (Sigma) or bought pre-prepared as solutions (Sigma). Peptides for synthesis were purchased from Celtek peptides (purity > 95 %) and were used as received. Discrete PEG (m-dPEG$_{15}$-NH$_2$) was purchased from Quanta Biodesign and was used as received. DNA from calf thymus (ctDNA), lyophilised or sodium salt, was purchased from Sigma-Aldrich and used without further purification. DNA quantification (as a concentration in mol base pairs) was achieved spectrophotometrically using $\varepsilon_{260} = 13{,}200\ M^{-1}\ cm^{-1}$.[1] Stocks of ctDNA were prepared at 1 – 3 mM in PBS and stored in the freezer for long term storage.

2.2 Instrumentation and data processing

Elemental analyses were performed under external contract at the Microanalytical Laboratory at University College Dublin. High Resolution Mass Spectrometry (HRMS) was performed under external contract at; the Mass Spectrometry Facility at University College Dublin, the Mass Spectrometry Unit at Trinity College Dublin, or the Mass Spectrometry Facility at NUI Maynooth. All other techniques were performed at DCU as described below.

2.2.1 NMR

NMR measurements were performed on Bruker Spectrometers at ^{1}H (^{13}C) frequencies of either 400 (100) or 600 (150) MHz. Spectra were processed using Bruker Topspin (v2.1) software and were calibrated using residual solvent peaks according to published values.[2] ^{1}H NMR multiplicities are reported as follows: s = singlet, d = doublet, t = triplet, q = quartet, qu = quintet, m = multiplet, dd = doublet of doublets, dt = doublet of triplets, etc.

2.2.2 ATR-IR

IR Spectroscopy was performed on a Varian ATR-IR system from 650 – 4000 cm^{-1}. All samples were analysed in the solid form at a screw gauge pressure of no greater than 40 units. Spectra were analysed using Perkin Elmer Spectrum Express (v1.02) software without applying an ATR correction.

2.2.3 Raman Spectroscopy

Raman spectroscopic measurements were carried out in backscattering configuration using an Olympus confocal microscope attached to a HORIBA Jobin-Yvon Labram HR 1000 spectrometer. Raman scattering was detected using a Peltier cooled (−70 ◦C) charge coupled device (CCD) camera (255×1024 pixels), excited with vertically polarised excitation lines from Ar^{+} laser (458/474/488 nm) source. The spectrometer was equipped with diffraction gratings of 600 grooves / mm and the slit allowed the spectral resolution of 2 cm^{-1}. The laser power at the sample set from 1 to 2 mW using the in-built laser power control. Data acquisition times used in the Raman experiments ranged from 8 to 60 s. Spectral calibrations were performed against a silicon wafer using the characteristic Raman active phonon mode at 520 cm^{-1} and the Rayleigh line. Generally, samples were analysed in concentrated aqueous solutions. Spectra were processed using LabSpec software.

2.2.4 UV-Vis Spectroscopy

All absorbance measurements were performed on a Jasco V670 Spectrophotometer and all data was manipulated using Jasco Spectra Manager v2 software and MS Excel. Typically, analysis was run in single beam mode and baseline correction was applied using blank

solvent. Spectra were generally recorded in the 200 - 800 nm window at a scan rate of 1000 nm/min.

2.2.5 Luminescence Spectroscopy

Emission and excitation spectra were obtained using a Varian Cary Eclipse Fluorescence Spectrophotometer (Varian Cary Eclipse Software v1.1) at a typical scan rate of 120 nm/min. Generally, slit widths were set to 10 nm. Smoothing was performed using a Savitzky-Golay function at frame of 5. Peak integrations were calculated in MS Excel using a trapezoidal summation.

2.2.6 TCSPC for luminescence lifetime determinations

Lifetime measurements were performed on a PicoQuant FluoTime 100 Compact FLS TCSPC system using a 450 nm pulsed laser source generated from a PicoQuant PDL800-B box and an external Thurlby Thandar Instruments TGP110 10 MHz pulse generator to enable acquisition of long lifetime data. A band-pass filter (< 520 nm) was used to exclude excitation light. Data was collected up to 10,000 counts and decay curves were analysed using PicoQuant Fluofit software and tail-fit statistical modelling. Chi-squared values were employed to assess the goodness-of-fit to the exponential decay and were accepted where $0.9 < \chi^2 < 1.1$.

2.2.7 HPLC

Analytical HPLC was performed on a Varian 940-LC Liquid Chromatograph and data was processed using Galaxie Chromatography software. Typically, all mobile phases and samples were degassed and filtered prior to usage.

HPLC General Method 1

Analysis was performed using an Agilent Zorbax Pursuit XRs C18 column (5 μm, 4.6 x 250 mm) fitted with a guard precolumn of the same phase. Samples were prepared in 99/1 water/acetonitrile containing 0.1 % TFA. Gradient elution at 1 mL/min flowrate was employed in the separation using a 0.1% TFA in water/acetonitrile mixture starting at 99/1 and changing linearly to 30/70 over 15 minutes and then held at 30/70 for 5 minutes. PDAD

was used for peak detection and the analysis was followed by monitoring 280 nm and 450 nm channels.

HPLC General Method 2

Analysis was performed using a Varian Pursuit Diphenyl column (5 μm, 4.6 x 250 mm). Gradient elution was performed as specified in HPLC general method 1.

2.2.8 Microwave synthesis

Microwave reactions were performed using a CEM XP-500 Plus microwave equipped with pressure vessels, temperature control and pressure control.

2.2.9 Circular dichroism

Circular dichroism experiments were carried out using Applied Photophysics Chirascan plus spectrometer. Quartz cuvettes (1 cm path length) were used for all measurements.

2.3 Photophysical and photochemical methods

De-aeration was carried out by bubbling nitrogen through the samples for 15 minutes. All photophysical measurements were performed at room temperature (293 K) unless otherwise indicated.

2.3.1 Water titrations

Water titrations were performed using 3 mL acetonitrile solutions treated with successive aliquots of water (30 μL).

2.3.2 UV/Visible and luminescence DNA titrations

Each titration was performed at least three times. Representative binding curves are included herein within the relevant chapter/appendix. In a typical experiment, aliquots of 2 - 3 mM ctDNA were titrated into solutions of 5 μM Ru(II) (PBS pH 7.4) and the absorbance and luminescence changes were measured after mixing by pipette and incubation for at least five minutes. The titration was continued until further additions of DNA did not lead to any

significant change in the luminescence of the solution. Average values for K_b and n were extracted by fitting to the binding curves according to the model described by Carter *et al*.[3] with the modifications described by Poulsen *et al*.[1] as indicated in Equations 2.1 and 2.2. Minimising the sum of square residuals in MS Excel was used to best fit the model to the data.

$$I_{app} = \frac{b - (b^2 - 4{K_b}^2 C_t\, C_{bp}/n)^{0.5}}{2K_b C_t} \,.\left(I_b - I_f\right) + I_f$$

…Equation 2.1

$$b = 1 + \, K_b C_t + K_b C_{bp}/n$$

…Equation 2.2

where; I_{app} is the apparent intensity at a given binding ratio, r = $[DNA]_{bp}/[Ru]$; I_b is the intensity at DNA saturation; I_f is the intensity of the free probe in the absence of DNA; K_b is the DNA binding constant; C_t is the total [Ru]; C_{bp} is the total $[DNA]_{bp}$, i.e. the concentration of DNA in terms of base pairs; n is the binding site size.

2.3.3 Ethidium bromide displacement assay

This procedure was adapted from a literature protocol.[4] A solution of ethidium bromide (12.6 μM) and ctDNA (10 μM) was prepared in HEPES buffer (80 mM) containing 40 mM NaCl. A series of solutions of varying concentrations were prepared from Ru(II) stock solutions to give a final solution of; ethidium bromide (6.3 μM), ctDNA (5 μM) and Ru(II) (X μM; X = 0, 0.1, 0.2…1.0, 2.0…5.0, 7.5…25.0 μM) in HEPES/NaCl buffer. At least three different series of solutions were tested and the concentration of Ru(II) required to reduce the ethidium fluorescence by half (C_{50} (μM)) was determined and used to calculate the apparent binding constant, K_{app}, from the following equation: $K_{app} = K_e$ x $6.3/C_{50}$ where K_e = ethidium binding constant, 9.5 x 10^6 M^{-1} (bp).

2.3.4 Ferrocyanide quenching studies

In a typical experiment, a series of solutions were made up from concentrated stocks (in PBS) and diluted as appropriate to give test solutions as follows; Ru(II) (10 μM), ctDNA (200 μM,

r = 20), $[Fe(CN)_6]^{4-}$ (0, 100, …, 500 μM) and buffer (X mL to yield the same net volume across the series of solutions). The luminescence spectra of these solutions were recorded and the maximum intensities plotted relative to the absence of ferrocyanide. Where the Ru(II) complex was emissive in water, the same experiment was also performed in the absence of ctDNA.

2.3.5 BSA studies

A typical procedure was carried out as follows; a series of solutions containing Ru(II) (5 μM) and BSA (X μM, X = 0, 50…250 μM) were prepared in PBS pH 7.4 buffer. The Ru emission spectra of each solution were recorded after 5 minutes incubation time in the dark at room temperature. Emission and excitation slits were set to 10 nm for all measurements.

2.3.6 Photo-irradiations

Light irradiations were performed using a fan-cooled 500 W Orwell Xenon-Arc lamp. Samples were irradiated in solution in quartz cuvettes placed 15 cm from the lamp shutter. A focussing lens was used and a λ < 355 nm cut-off filter was fitted in the path of the light to exclude low UV rays.

2.3.7 Luminescence quantum yields

Luminescence quantum yields (φ_{lum}) were determined against commercial $[Ru(bpy)_3]Cl_2$ by applying the slope method described by Equation 2.3, where x and std signify the sample and standard respectively, m is the slope of the emission intensity/absorbance plot and η is the refractive index of the solvent.

$$\phi_x = \phi_{std} \cdot \frac{m_x}{m_{std}} \cdot \frac{\eta_x}{\eta_{std}}$$

…Equation 2.3

2.4 Cell studies and electrophoresis

Cellular studies and electrophoresis was performed by Dr. Aisling Byrne, DCU. For a full set of methods see published protocols.[5] A summary is provided below.

2.4.1 Cell uptake studies

HeLa cells were seeded on a 35 mm glass bottom dish at 2 x 10^5 in 2 mL for 24 h at 37 °C at 5 % CO_2. Ru-peptide (see relevant chapters for concentrations) was added to the cells and was incubated for 1 - 3 h in the absence of light. The media was removed and the cells were washed twice with supplemented PBS ($MgCl_2$ and $CaCl_2$). Cells were imaged using a Leica DMI8 confocal system. The complex was excited using a 470 nm white light laser (0.36 μW) and the emission was collected using a band pass filter 565 – 700 nm. For nuclear co-localisation studies, DAPI (100 nM) was added to cells stained with nuclear localised Ru-peptide for 20 minutes prior to imaging, and was excited using a 405 nm laser and the emission was collected between 450-500 nm. For mitochondria co-localisation studies, MitoTracker Deep Red (100 nM) was added to cells stained with mitochondria localised Ru-peptide for 20 minutes prior to imaging, and was excited using a 633 nm laser and the emission was collected between 637 – 730 nm. To assess mode of cellular uptake, HeLa cells were prepared as described above, but the cells were incubated at 4°C for 1 h, then with the complexes at 4°C for 2 h and 24 h, then imaged.

2.4.2 Phototoxicity

To assess phototoxic effects, DRAQ 7 was added to HeLa cells stained with Ru-tap-NLS or Ru-MPP. A single cell was imaged under Ru-peptide imaging settings and DRAQ 7 settings. The cell was irradiated using the 470 nm laser (1 μW) line continuously for 5 minutes. After each 5 minute interval, an image was taken under the Ru-peptide and DRAQ 7 imaging settings. The continuous scanning intervals were carried until DRAQ 7 had entered the nucleus of the cell, indicating that the cell was dead. To image DRAQ 7, a 633 nm laser was used to excite and the emission was collected between 635 – 720 nm.

2.4.3 Cytotoxicity

HeLa cells were seeded in a 96-well plate (Sarstedt) at 1 x 10^4 in 100 μL media for 24 h at 37 °C with 5 % CO_2. Ru-peptide was added for 24 h at 37 °C and 5 % CO_2 in the absence of

light. Final concentrations were 200, 150, 100, 50, 20, 10, and 1 μM. The Alamar Blue assay was used to measure cell viability by adding 10 μL resazurin reagent and incubating for 7 h at 37 °C in the absence of light. Absorbance was measured using a Tecan 96-well plate reader at 570 nm and 600 nm (corrected for background subtraction). Cell viability is presented as a percentage (%) compared to control cells not exposed to Ru-peptide.

2.4.4 Resonance Raman in live HeLa cells

HeLa cells were seeded on a 35 mm glass bottom culture dish at 2 x 10^5 in 2 mL for 24 h at 37 °C at 5 % CO_2. Ru-peptide, (typically 150 μM, final concentration in media) was added to the cells and was incubated in the absence of light to allow nuclear uptake. Prior to Raman, the media was removed and the cells were washed twice with supplemented PBS ($MgCl_2$ and $CaCl_2$). rRaman spectra from the cytoplasmic and nuclear regions of a number of cells was then collected with a 488 nm laser (5 μW) on a Horiba Jobin-Yvon Labram HR instrument, using a 50x objective and 300 μm pinhole. An exposure time of 12 seconds per spectrum was used and 10 spectra were averaged for each location.

2.4.5 DNA cleavage Studies using pUC19 plasmid DNA

400 ng pUC19 plasmid DNA (NEB, N3041S) was exposed to Ru-tap-NLS to give a final ratio of 1:10 plasmid:Ru, with 25 mM NaCl in a total volume of 10 μL using 80 mM HEPES buffer. Samples were left to stand for 1 h at room temperature (18 °C) before irradiating. The plasmid-DNA samples were irradiated using a 458 nm argon ion laser (130 mW) for exposure times of 30 seconds to 30 minutes. Loading buffer, 6X, (NEB, B7021S) was added to the samples and they were loaded onto an agarose gel (0.75 %) stained with SYBR Safe DNA Gel Stain (Invitrogen), and electrophoresis was completed at 70 V for 70 minutes in 1x TAE buffer. Agarose gels were imaged using a Bo Rad Gel Doc EZ Imager.

2.4.6 DNA cleavage and ROS scavenger studies

400 ng pUC19 plasmid DNA was exposed to Ru-tris-bpy to give final ratio of 1:10 plasmid:Ru with 25 mM NaCl, with and without 5 % sodium azide (NaN3) scavenger, in a total volume of 10 μL using 80 mM HEPES buffer. The plasmid-DNA samples were irradiated using a 458 nm argon ion laser (280 mW) for exposure times of 30 seconds to 20 minutes. Loading buffer, 6X, (NEB, B7021S) was added to the samples and they were loaded onto an agarose gel (1.2 %) stained with SYBR Safe DNA Gel Stain (Invitrogen), and

electrophoresis was completed at 65 V for 90 minutes in 1x TAE buffer. Agarose gels were imaged using a Bo Rad Gel Doc EZ Imager.

2.5 References

(1) Poulsen, B. C.; Estalayo-Adrián, S.; Blasco, S.; Bright, S. A.; Kelly, J. M.; Williams, D. C.; Gunnlaugsson, T. *Dalton Trans.* **2016**, *45* (45), 18208.

(2) Fulmer, G. R.; Miller, A. J. M.; Sherden, N. H.; Gottlieb, H. E.; Nudelman, A.; Stoltz, B. M.; Bercaw, J. E.; Goldberg, K. I. *Organometallics* **2010**, *29* (9), 2176.

(3) Carter, M. T.; Rodriguez, M.; Bard, A. J. *J. Am. Chem. Soc.* **1989**, *111* (24), 8901.

(4) Prisecaru, A.; McKee, V.; Howe, O.; Rochford, G.; McCann, M.; Colleran, J.; Pour, M.; Barron, N.; Gathergood, N.; Kellett, A. *J. Med. Chem.* **2013**, *56* (21), 8599.

(5) Byrne, A.; Burke, C. S.; Keyes, T. E. *Chem. Sci.* **2016**, *7* (10), 6551.

Chapter 3

Development of efficient synthetic routes to bio-conjugated Ru(II) luminophores

Notes

The synthesis of the peptide and PEG conjugates described in this chapter was performed using the mixture of geometric and optical isomers of their parent complexes. As such, depending on the conjugate, the final Ru-peptide conjugates characterised in this chapter and tested in Chapter 4 are a mixture of at least four different isomers.

3.1 Introduction:

3.1.1 The development of synthetic routes towards polypyridyl complexes of Ru(II)

The rich coordination chemistry of N_6-type polypyridyl Ru(II) complexes has been exploited within many research fields ranging from catalysis to biophotonics.[1] Most Ru(II) constructs reported in the literature have their origins in photocatalysis and it was arguably this domain that first accelerated some of the most important advances in Ru(II) coordination chemistry.[2,3] This is perhaps best exemplified by prominent reviews in the 1980's that could already list physical data on over two hundred Ru(II) complexes.[4,5] The evolution of this research has seen the creation of polynuclear architectures towards dendrimer designs and novel scaffolds for catalysis providing further contributions to the growing catalogue of Ru(II) compounds.[6–8] The application of Ru(II) luminophores to cellular imaging and therapy requires a different set of parameters to tune the physical and chemical properties of the complex for uptake, sensing and toxicity. This has encouraged fresh insights into the design of Ru(II) complexes suited to the demands of cellular application and offers new perspectives towards the synthesis of these novel constructs.

Across the wealth of mononuclear Ru(II) diimine coordination complexes reported to date, the structures are broadly similar. In general, complexes are either homoleptic, or in many cases *bis*-heteroleptic, and based largely on a classical $[Ru(bpy/phen)_n]^{2+}$ core that conforms to the series; $[Ru(N^N)_2(N^N)']^{2+}$ (where N^N and N^N' are different bidentate polypyridyl ligands, bpy = 2,2'-bipyridine, phen = 1,10-phenathroline). Within this series, a robust synthesis permits the interchange of ligands to tune the physical and optical properties of the complex. However, this route is less efficient for non-classical systems which limits the diversity that can be achieved using novel synthetic strategies. Indeed, there are very few reports on *tris*-heteroleptic complexes, $[Ru(N^N)(N^N)'(N^N)'']^{2+}$; despite the added tunability and versatility that can be engendered in such compounds. For example, interesting photophysics like 'black-absorption'[9,10] can be provoked (Figure 3.1) or multiple asymmetric conjugations to a single complex achieved.[11] Below, the key historical developments towards the synthesis of Ru(II) polypyridyl complexes are reviewed in the context of introducing

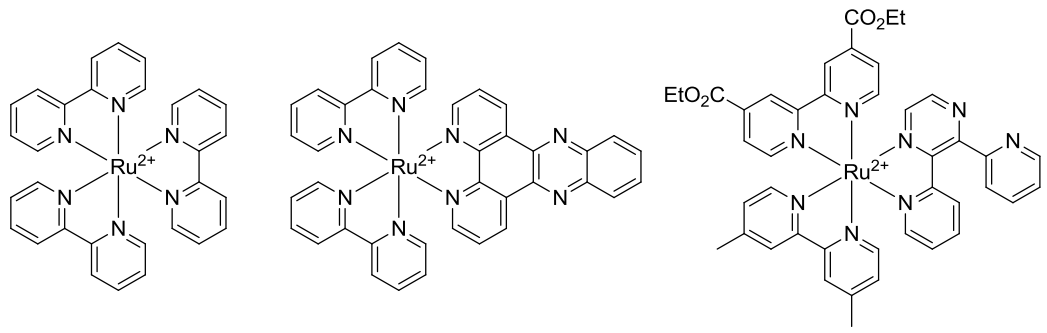

(a) (b) (c)

Figure 3.1: Examples of (a) *tris*-homoleptic, (b) *bis*-heteroleptic and (c) *tris*-heteroleptic Ru(II) complexes bearing bidentate polypyridyl ligands. (a) $[Ru(bpy)_3]^{2+}$, (b) $[Ru(bpy)_2(dppz)]^{2+}$ (dppz = dipyrido[3,3-a:2',3'-c']phenazine) and (c) A black absorber as reported by Anderson *et al.*[9,10]; $[Ru(dmbpy)((EtO_2C)_2bpy)(bpp)]^{2+}$ (dmbpy = 4,4'-dimethylbpy; (EtO_2C)bpy = 4,4'-di(ethoxycarbonyl)-2,2'-bipyridine; bpp = bis(2-pyridyl)pyrazine).

---

synthetic strategies that may be exploited in the preparation of conjugatable Ru(II) luminophores for cellular application.

Important early developments towards $[Ru(N^N)_2(N^N)']^{2+}$

The first synthesis of $[Ru(bpy)_3]^{2+}$ was reported by Burstall who used $RuCl_3.3H_2O$ as starting material under heating a neat melt in a large excess of bpy.[12] Dwyer synthesised $[Ru(phen)_3]^{2+}$ using an analogous method but found that hypophosphite reduction from polychlororuthenate salts in aqueous solutions was preferable to improve ligand economy.[13] Later, higher yields were obtained by Bailar *et al*. using aqueous solutions of sucrose or tartrate as reducers.[14] Ligand substitution in these reactions was shown to proceed via a solvate intermediate such as $[Ru(bpy/phen)_2(H_2O)_2]^{2+}$ and the Ru(III)/(II) reduction can be performed directly in aqueous alcoholic solvent.[15,16] This methodology provided a route to homochelates of Ru(II) (as shown in Scheme 3.1) but a major breakthrough was described by Dwyer and co-workers who recognised that the intermediate; $Ru(bpy/phen)_2Cl_2$, can be used as a precursor to asymmetric Ru(II) complexes.[17] Their original preparation of $Ru(bpy)_2Cl_2$ relied on heating $[Ru(bpy)_3]Cl_2$ *in vacuo* but this method did not extend to $Ru(phen)_2Cl_2$. Instead, pyrolysis of pyridinium Ru(III) salts such as [bpy-

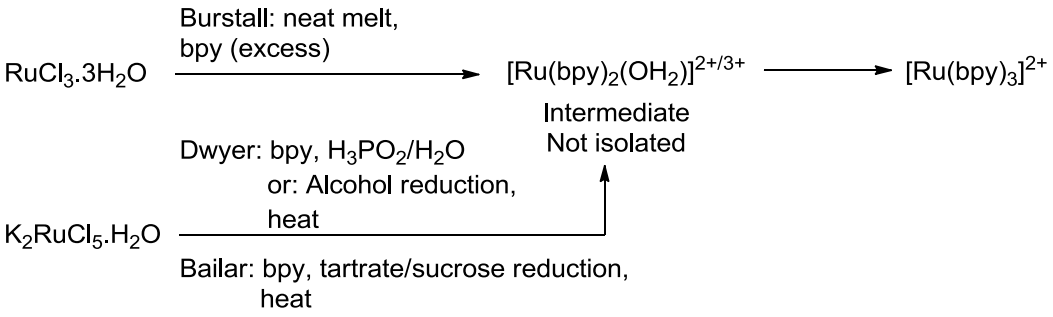

Scheme 3.1: Summary of historical routes to *tris*-homoleptic complexes of Ru(II).

H]$^{+}$[Ru(bpy/phen)Cl_4]$^{-}$ provided Ru(bpy/phen)$_2Cl_2$ which reacted with monodentate ligands by rapid cleavage of the first chloride ligand but slow aquation of the second. However, slow chloride cleavage could be circumvented using Ag^{+} precipitation in aqueous solvent to provide the reactive *bis*-aquo species.

Dwyer's methodology using Ru(III)-pyridinium salts required their preparation from materials that were not readily available such as RuO_2. Alternative routes to preparations of Ru-dihalides were desired to grant efficient generalised access to [Ru(N^N)$_2$(N^N)']$^{2+}$. Initial focus was on ruthenium blue solutions or photolysis of *tris*-homochelates such as [Ru(bpy)$_3$]I_2 in alcohol to provide a suitable Ru-halide intermediate towards bidentate polypyridyl *bis*-heteroleptic complexes.[18,19] However, a breakthrough was described by Sprintschnik *et al*., and later improved on by Sullivan *et al*., who prepared Ru(bpy)$_2Cl_2$ from $RuCl_3.3H_2O$ under reflux for several hours in DMF buffered with LiCl.[20,21] The Ru(II)-dichloride was obtained from the mother liquor as a microcrystalline product following slow precipitation from cold acetone. In their publication, Ru(bpy)$_2Cl_2$ was used to generate phosphine and arsine derivatives of Ru(II) by initial treatment with $AgClO_4$ in acetone to generate a reactive solvate, [Ru(bpy)$_2$(CH_2COCH_2)$_2$]$^{2+}$; which was then heated with ligand to provide [Ru(bpy)$_2$(L-L)]$^{2+}$. The requirement to use silver mediated cleavage of the chloride ligands supports earlier observations regarding the comparably slow substitution of the second chloride. However, the method has since become generalised and now represents the most commonly used route to prepare *bis*-heteroleptic complexes of Ru(II).[1,22] In the currently most commonly reported two-step protocol the dichloride is isolated using rapid precipitation from ether or water, and silver activation has been largely superseded by

extended higher temperature boiling in aqueous alcohol.[23,24] Scheme 3.2 provides a summary of the synthetic development towards Ru(II) *bis*-heteroleptic complexes via a Ru-dichloride intermediate.

The generalisation of the classical Sullivan method has contributed greatly to the growing number of Ru(II) complexes reported to date but it must be stressed that the original preparation was based on bpy, the simplest of the $Ru(N^N)_2Cl_2$ series, and does not always transfer directly to other ligand systems. The classical preparation also has several limitations including the need for *in situ* thermal decarbonylation of DMF to provide reducing but volatile dimethylamine to drive the Ru(III) to Ru(II) reduction.[25] This decomposition also yields CO which can coordinate directly with Ru(II) to yield $[Ru(N^N)_2(CO)Cl]^+$ as reported by Clear *et al*.[26] Until recently, this carbonyl complex was thought unreactive towards the preparation of *tris*-chelates but it was shown that it can be utilised following pre-treatment with KOH as described by Zabarska *et al,* although this requires additional synthesis via reactive solvates that should be used immediately.[27] Viala and Coudret reported that the Ru(III/II) reduction can proceed using reducing amines of heavier mass than dimethylamine, such as triethylamine, along with lower temperatures to prevent the decarbonylation of DMF.[25] They also found that glucose, sucrose and ascorbic acid can be used as non-volatile reducers to enable synthesis in ethylene glycol solvent to provide $Ru(bpy)_2Cl_2$ in good yield on the gram scale. However, the authors cite some limitations of the approach including; the high total chloride ion concentration required to prevent chloride ligand cleavage, the impracticality of the highly viscous nature of the reaction solution, the limited scope of the

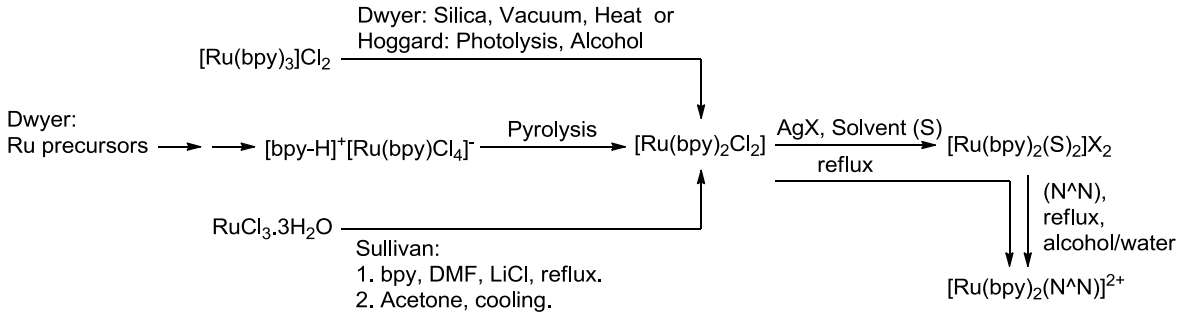

Scheme 3.2: Historical development of synthetic routes towards *bis*-heteroleptic complexes of Ru(II).

reaction as it did not extend well to more lipophilic analogues and the general instability of Ru-dichlorides which can lead to aquation, oxidation and precipitation on columns where purification was required. It becomes apparent that the issue with using Ru-dichloride intermediates is not just the reaction route to their preparation but also their inherent properties which are not always favourable towards purification and isolation in a pure and stable state. Despite these limitations, the classical route through the $[Ru(N^N)_2Cl_2]$ intermediate remains the main avenue to N_6 *bis*-heteroleptic Ru(II) complexes.

$[Ru(N^N)_2(N^N)']^{2+}$ from Ru-CO and Ru-DMSO precursors

Two other less commonly employed routes that have proven successful involve Ru-CO and Ru-DMSO precursors. $[Ru(CO)_2Cl_2]_n$ polymer can be used to generate $[Ru(N^N)_3]^{2+}$ or $[Ru(N^N)_2(N^N)']^{2+}$ by stepwise addition of bidentate ligand to the coordination sphere.[28] In both cases, cleavage of the carbonyl ligands requires photolysis or chemical treatment with trimethylamine-N-oxide (TMNO) in 2-methoxyethanol.[29,30] The DMSO route towards the synthesis of Ru(II) polypyridyl complexes uses *cis*-$[Ru(DMSO)_4Cl_2]$ as precursor which can be prepared from $RuCl_3.3H_2O$ following short reflux in DMSO as reported by Wilkinson *et al*.[31] The *tetrakis*-DMSO complex favours the *cis*-chloride configuration and for steric reasons is S-bonded through three *fac*-oriented DMSO ligands and O-bonded via the other as indicated in Scheme 3.3. The Wilkinson method can yield mixtures of the *cis*- and *trans*-isomer and requires difficult purification by recrystallisation from hot DMSO solutions.[32] While most syntheses still utilise the Wilkinson method to prepare the DMSO complex, Alston *et al*. recently described an efficient synthesis in 2-propanol which provides the *cis*-isomer selectively after boiling for an extended period.[33] *cis*-$[Ru(DMSO)_4Cl_2]$ is a valuable synthon as it is obtained in the Ru(II) state, exhibits favourable solubility in most solvents except acetone and can undergo substitution with ligands not generally suited to preparations by the Sullivan method. For example, difficult syntheses of N_6-chelates of Ru(II) have been prepared with highly substituted bpy and phen ligands,[34] polyazaaromatic ligands like 1,4,5,8-tetraazaphenanthrene (tap) and 2,2'-bipyrazine (bpz),[35–37] and bridging ligands to yield dinuclear Ru(II)-helicates.[38] Furthermore, *cis*-$[Ru(DMSO)_4Cl_2]$ reacts with a single bidentate polypyridyl ligand in ethanol or chloroform to provide

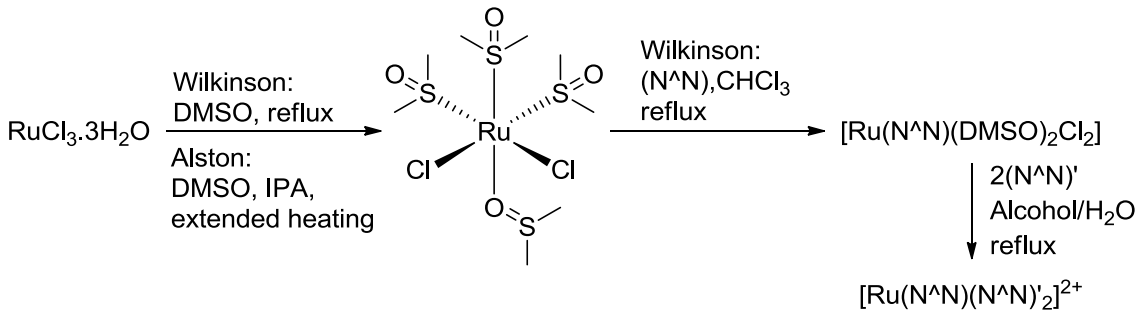

Scheme 3.3: Synthesis of Ru(II) *bis*-heteroleptic complexes via Ru-DMSO intermediates.

$[Ru(N^N)(DMSO)_2Cl_2]$.[31,39,40] This intermediate can then be reacted with two equivalents of bidentate ligand to provide *bis*-heteroleptic complexes.[41]

3.1.2 Synthesis of tris-heteroleptic complexes of Ru(II)

Ru(II) tris-heteroleptic complexes from Ru-CO precursors

Ru(II) complexes bearing three different ligands are far less prevalent in the literature than their *bis*-heteroleptic analogues which can be ascribed to their challenging synthesis. The first preparation of *tris*-heteroleptic Ru(II) complexes using purely bidentate ligands was reported by Black *et al*. utilising $[Ru(CO)_2Cl_2]_n$ polymer as precursor.[30,42] Prior to this, Krause had reported substitutions to $[Ru(bpy)(py)_4]^{2+}$ to yield complexes of the form; $[Ru(bpy)(N^N)(py)_2]^{2+}$, but the method was not extended to investigate further pyridine substitutions towards a *tris* chelate.[43] The Black route proceeds via $[Ru(phen)(CO)_2Cl_2]$ and exploits the lability of the chloride ligands relative to the carbonyls to provide $[Ru(phen)(bpy)(CO)_2]^{2+}$. Cleavage of the carbonyl ligand was achieved chemically in 70 % yield using TMNO in 2-methoxyethanol to yield a solvate which was reacted with dipyridylamine (dpa) to provide $[Ru(phen)(bpy)(dpa)]^{2+}$. This route was further generalised by Keene, Meyer and co-workers who described each step in more detail.[9,44,45] The Ru(II) yellow polymer material, $[Ru(CO)_2Cl_2]_n$, which serves as precursor for the method, was first obtained from $RuCl_3.3H_2O$ in 90 % yield following reaction with paraformaldehyde and formic acid. Single addition of a polypyridyl ligand was then achieved under alcoholic reflux to provide *trans*-$[Ru(N^N)(CO)_2Cl_2]$. The chloride ligands were substituted with more labile

triflate (trifluoromethanesulfonate, $^{-}$OTf) ligands using triflic acid which permitted displacement by a second polypyridyl ligand to yield $[Ru(N^N)(N^N')(CO)_2]^{2+}$. Finally, a threefold excess of TMNO facilitated carbonyl cleavage in 2-methoxyethanol to enable ternary ligand chelation.

The generality of the method is attractive but it suffers from poor to moderate synthetic yields and TMNO which is a strong oxidant that can react with ligands. Later, Treadway and Meyer reported that the carbonyl can be cleaved with TMNO in acetonitrile quantitatively to provide the *bis*-solvate, $[Ru(N^N)(N^N')(CH_3CN)_2]^{2+}$, which can be isolated and reacted with sensitive polypyridyl ligand in the absence of TMNO.[46] An alternative approach was described by Deacon *et al*. using photodecarbonylation of $[Ru(N^N)(CO)_2Cl_2]$ in coordinating solvent to yield a chloride-bridged dimer upon reaction with polypyridyl ligand; $[Ru(N^N)(CO)Cl_2]_2$.[47,48] This intermediate does not require triflate activation and can be converted to the *bis*-chelate; *cis*-$[Ru(N^N)(N^N)'(CO)Cl]^{+}$. However, TMNO mediated cleavage was required to enable reaction with the ternary ligand.

Mulhern *et al*. described a photodecarbonylation route in reverse order which avoids using TMNO.[29] First, $[Ru(N^N)(CO)_2Cl_2]$ was subjected to photoirradiation in acetonitrile to provide $[Ru(N^N)(CH_3CN)_2Cl_2]$, followed by prolonged heating in acetone with a second polypyridyl ligand to yield $[Ru(N^N)(N^N)'Cl_2]$. Finally, the product was converted to a *tris* heteroleptic complex under classical conditions in aqueous alcohol to provide, in this instance; $[Ru(bpy)(dmbpy)(Hbpt)]^{2+}$ (dmbpy = 4,4'-dimethyl-2,2'-bipyridine; Hbpt = 3,5-bis(pyridine-2-yl)-1,2,4-triazole). A summary of routes to *tris*-heteroleptic complexes using Ru-carbonyl intermediates is provided in Scheme 3.4.

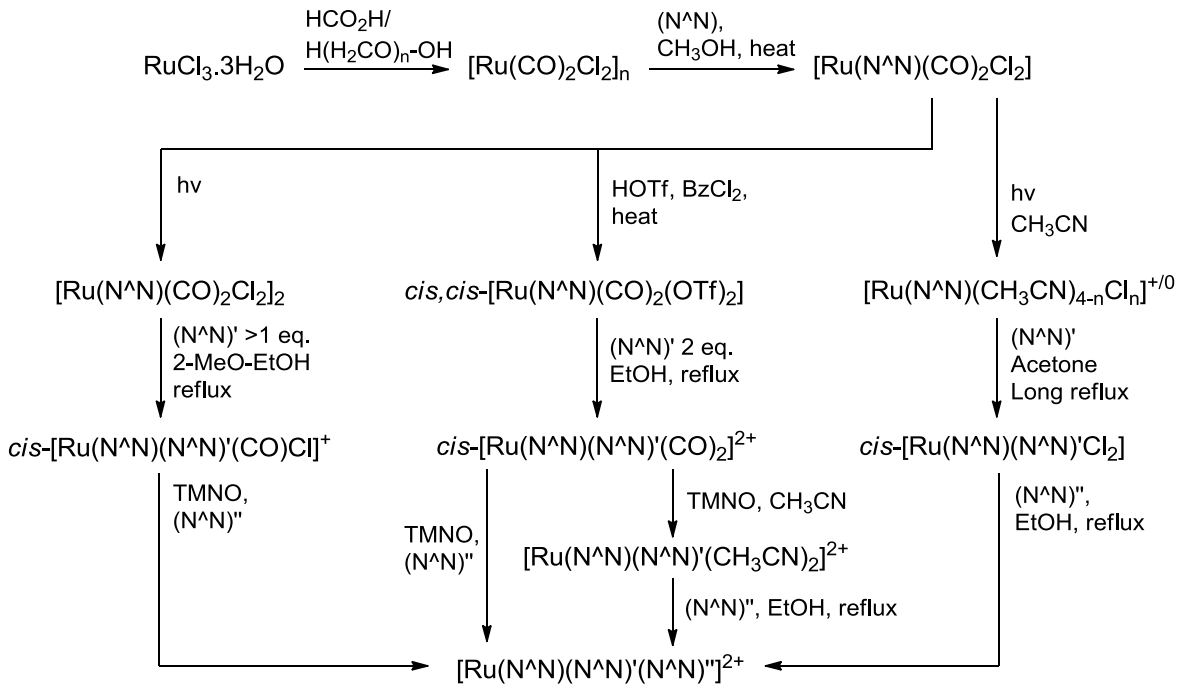

Scheme 3.4: Synthetic routes to Ru(II) *tris*-heteroleptic complexes via Ru-CO intermediates.

One pot syntheses towards [Ru(N^N)(N^N)'(N^N)'']$^{2+}$

One-pot syntheses to Ru(II) *tris*-heteroleptic complexes encompassing at least two reaction steps were also developed which proceed via the classic $[Ru(N^N)(N^N')X_2]^{n+}$ (X = solvent or Cl^-) intermediate which is generally not isolated, but instead reacted *in situ* towards Ru(II) *tris* chelates (Scheme 3.5). Thummel *et al*. prepared $[Ru(bpy)Cl_3]_n$ from $RuCl_3.nH_2O$ in HCl as originally reported by Krause[43] and subjected this precursor to stepwise substitution with rigidified, bidentate derivatives of 2,2'-biquinoline and 2,2'-binaphthyridine in refluxing ethanol to acquire the *tris* heteroleptic complex in 57 % yield following purification.[49] Hesek *et al*. described a one-pot preparation from $RuCl_3$ which uses temperature and stoichiometric control to drive single stepwise addition of each ligand to the Ru(II) coordination sphere.[50] Specifically, $RuCl_3$ was reacted in DMF at 90 °C to provide $[Ru(dmbpy)Cl_3]_n$ after 6 h which was then treated with a different 4,4'-diester modified bpy (estbpy) at 110 °C for 10 h to yield $[Ru(dmbpy)(estbpy)X_2]^{n+}$ *in situ* (X can be solvent or Cl^-). After removal of the solvent, the residue was reacted with an amide substituted bpy (ambpy) in refluxing methanol to acquire $[Ru(dmbpy)(estbpy)(ambpy)]^{2+}$ in 44 % yield post-purification.

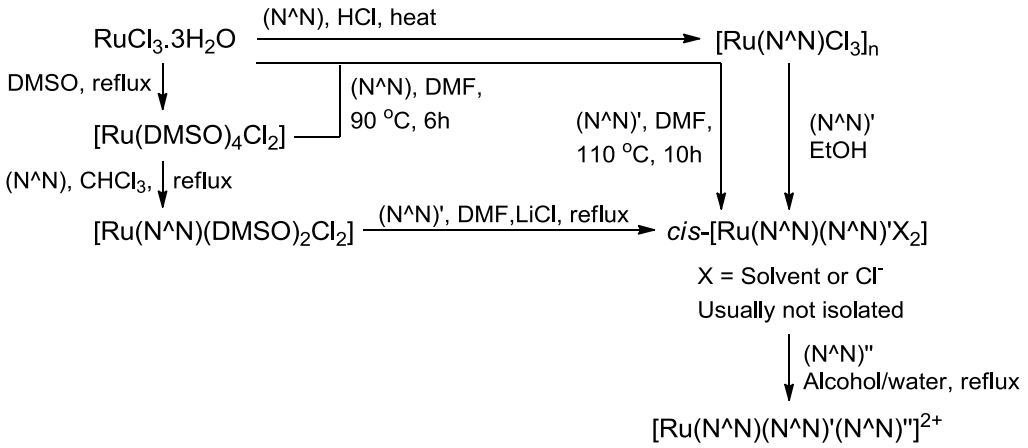

Scheme 3.5: Synthesis of Ru(II) *tris*-heteroleptic complexes via one-pot syntheses and Ru-DMSO intermediates.

Alternative one-pot syntheses have used *cis*-$[Ru(DMSO)_4Cl_2]$ as precursor instead of $RuCl_3$, for example, Maxwell *et al*. reported a one-pot preparation of a highly asymmetric chromophore-donor-acceptor assembly using a Ru(II) *tris* heteroleptic scaffold.[51] This preparation relies on order of addition, first reacting two different neutral ligands in two distinct steps in the reaction pot. The final ligand added to the reaction mixture was a dicationic methylviologen-bpy conjugate and hence, the charged nature of the complex it formed permitted its separation from scrambled products in 19 % yield using ion-exchange chromatography. A more recent synthesis of a *tris* heteroleptic complex reported by Le Gac *et al*. also used *cis*-$[Ru(DMSO)_4Cl_2]$ precursor to quantitatively generate $[Ru(tap)(DMSO)_2Cl_2]$ followed by *in situ* two-step addition of ligand under classical Sullivan-type conditions to provide $[Ru(tap)(dppz)(tap\text{-}R)]^{2+}$.[39]

A notable issue in these one-pot reactions is the inability to isolate the *bis*-chelate as an intermediate (i.e. $[Ru(N^N)(N^N')Cl_2]$) to limit the formation of scrambled products. An exception was a report by Zakeeruddin *et al*.[52] who did manage to isolate the *bis*-chelate intermediate using stepwise ligand addition to *cis*-$[Ru(DMSO)_4Cl_2]$ to generate $[Ru(dmbpy)(DMSO)_2Cl_2]$ as described originally by Wilkinson.[31] Reaction of this complex with 4,4'-dicarboxy-2,2'-bipyridine, dcbpy, under classical Sullivan-type conditions in DMF/LiCl provided $[Ru(dmbpy)(dcbpy)Cl_2]$ in good yield (75 %) which was successfully

isolated as a black powder. Finally, classical treatment of the dichloride with ternary ligand in aqueous alcohol yields the *tris* heteroleptic complex in 50 % yield start-to-finish.

Photosubstitution reactions towards [Ru(N^N)(N^N)'(N^N)'']$^{2+}$

A different approach to *tris* heteroleptic complexes was reported by von Zelewsky *et al*. employing photosubstitution from sterically crowded Ru(II) complexes bearing 2,2'-biquinoline ligands (Scheme 3.6).[53,54] In their report, the photoreactivity of $[Ru(biq)_2(bpy)]^{2+}$ in acetonitrile was exploited to generate $[Ru(biq)(bpy)(CH_3CN)_2]^{2+}$ in 85 % yield. This intermediate can then be reacted under classical conditions to provide $[Ru(biq)(bpy)(N^N)]^{2+}$. The authors noted that the complex may be further substituted upon irradiation to eject the second biq ligand but additional syntheses to non-biq complexes were not described. However, the generality of this approach was illustrated by preparation of ten different complexes. The route has not often been adopted by others but a notable exception was reported recently by Cuello-Garibo *et al*. in their preparation of photoactive L-proline complexes such as $[Ru(bpy)(dmbpy)(L\text{-}Pro)]^{+}$.[55]

Ru(II) tris-heteroleptic complexes from Ru-arene precursors

A more versatile route towards $[Ru(N^N)(N^N)'(N^N)'']^{2+}$ was reported by Mann *et al*. that operates by benzene displacement from a Ru-arene dimer, namely $[RuCl_2(Bz)]_2$ (Scheme 3.7).[56] This precursor can be prepared almost quantitatively from the more commonly used

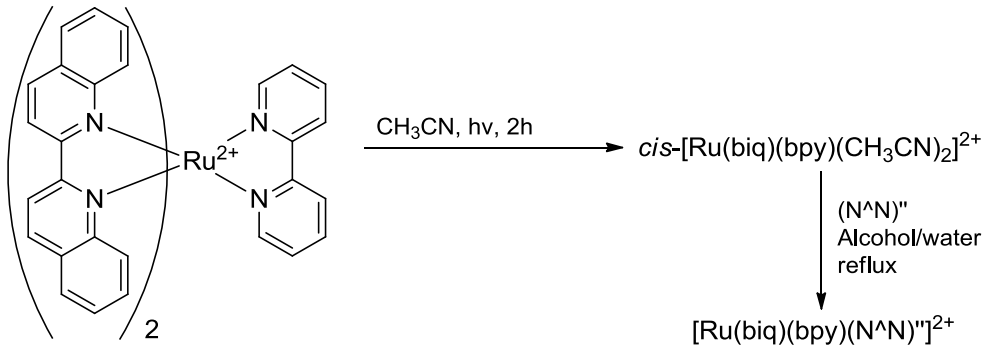

Scheme 3.6: A route to Ru(II) *tris*-heteroleptic complexes bearing sterically bulky ligands as described by von-Zelewsky *et al*.[53,54]

Ru source; $RuCl_3.nH_2O$. Refluxing the arene complex in acetonitrile in the presence of polypyridyl ligand leads to monomeric [BzRu(N^N)Cl]Cl in yields exceeding 80 %. This complex then undergoes further photosubstitution in acetonitrile to provide a mixture of $[Ru(N^N)(CH_3CN)_3Cl]Cl$ and $[Ru(N^N)(CH_3CN)_2Cl_2]$ which are prone to acetonitrile ligand substitution under heating with a second bidentate ligand in acetone to yield $[Ru(N^N)(N^N)'Cl_2]$. Finally, reaction with a ternary ligand under classical conditions yields a *tris* heteroleptic complex such as $[Ru(bpy)(dmbpy)(phen)]^{2+}$ as originally reported by Mann. Notably, Myahkostupov and Castellano used this approach to achieve the highest yield start-to-finish for a *tris* heteroleptic complex prior to this thesis at 61 % when they prepared a complex functionalised with styryl subunits; [Ru(dmbpy)(dtbbpy)(4,4'-di-R-styryl-bpy)]$^{2+}$ (dtbbpy = 4,4'-ditert-butyl-2,2'-bipyridine).[57]

The Meggers group also employed this route as part of a solid phase synthesis of *tris* heteroleptic complexes of Ru(II).[58] 5-carboxyphenathroline was immobilised on a resin and treated with $[Ru(bpy)(CH_3CN)_3Cl]Cl$/$[Ru(bpy)(CH_3CN)_2Cl_2]$. The spatial separation of the phen units was ideal to ensure formation of $[Ru(bpy)(phen\text{-}resin)Cl_2]$ and to prevent 'double-additions' of phen which can occur for the free ligand in solution phase reactions. The dichloride intermediate can be reacted with a third and different ligand to provide the final *tris* heteroleptic complex which was cleaved in TFA to produce the free compounds in net yields ranging from 34 - 56 %. Meggers has also pioneered the enantioselective synthesis of Ru(II) *tris* polypyridyl complexes using chiral auxiliaries such as salicyloxaline and

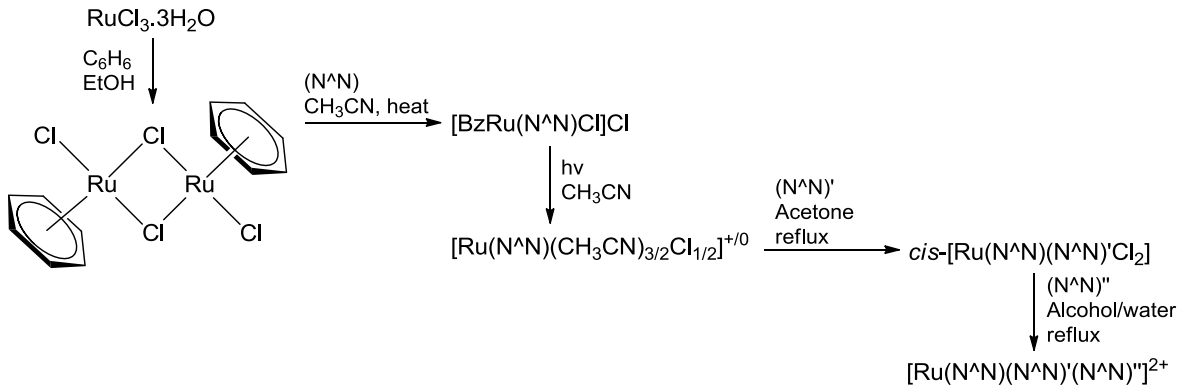

Scheme 3.7: Synthesis of Ru(II) *tris*-heteroleptic complexes using Ru-arene intermediates.

proline.[59–61] Some of these syntheses have included preparations of *tris* heteroleptic complexes using the Mann route initially to generate $[Ru(N^N)(N^N)'(Aux)]^{n+}$ followed by reaction with several equivalents of ligand in TFA to selectively form Δ- or Λ-$[Ru(N^N)(N^N)'(N^N)'']^{2+}$.[62–64]

3.1.3 Designing ligands for Ru(II) complexes suitable for peptide conjugation

A primary objective of this thesis was the application of peptide-conjugated Ru(II) complexes for DNA-targeted imaging and toxicity. As discussed in the Chapter 1, $[Ru(bpy)_2(dppz)]^{2+}$ was established as a candidate complex for this purpose but needs to be derivatised to enable peptide conjugation. Previously, our group has employed the pic ligand almost exclusively in this role in both its carboxy- and amino-functionalised forms,[23,65–70] and these ligands are easily accessible in one-step condensations with phendione.[71] However, the work of this thesis instead elected to focus on the development of carboxy-modified derivatives of the bpy and phen ligands which feature in the candidate complex. As previously demonstrated at the pic ligand, extending the separation between the Ru(II) complex and adjoined peptide is desirable to reduce steric hindrance and to limit any impact on bio-interaction of the Ru(II) complex moiety. Thus, aryl-carboxyl pendants at phen and bpy ligands were exploited as bioconjugation points. Arylation can be achieved using cross coupling reactions such as the Suzuki-Miyaura protocol which acts on boronic acids and aryl halides.[72] Accordingly, aryl-spaced carboxy modification may be attained using carboxyphenylboronic acid and an appropriate Suzuki-active bpy or phen substrate. Others have employed a similar strategy towards aryl-modified bpy and phen compounds with bromo-precursors largely employed as substrates for cross-coupling reactions.[73,74] Phen can be modified directly at the 5-position as described by Eisenberg *et al*.,[75] while bpy has most commonly been functionalised at the 4- or 5-positions, either directly by cross-coupling pyridines by Negishi reaction[76] or indirectly by substitutions to activated bpy.[77] In our lab, previous work on cross-couplings to BODIPY derivatives revealed ester derivatives to be more suited to the Suzuki reaction, probably due to solubility and consequent ease of purification. Hence, in this thesis, the aryl ester-modified bpy or phen ligands were prepared and were later hydrolysed to the free acid to provide a conjugation site.[78]

3.1.4 Peptide-coupling methodologies

There are many examples of coupling reactions that are suited to peptide conjugation[79], some of which have been used by others for metal complex decoration[80], but a full review is beyond the scope of this thesis. Instead, a focus is placed on prominent bioconjugation strategies using amine and carboxylic acid functionalised ligands that are synthetic targets of this work or have been previously developed within our group. In general, amine-ligands are less suited to conjugations to cell penetrating peptides (CPP) since the CPP itself usually bears amine residues like Lys,[81,82] and the presence of a complimentary coupling function on the peptide may lead to self-condensation. However, a notable exception was recently reported by Chakrabortty *et al.* who exploited earlier studies by Joshi *et al*. to selectively couple $[Ru(bpy)_2(pic\text{-}NH_2)]^{2+}$ to tyrosine residues of Human Serum Albumin (HSA) using a Mannich-type reaction in the presence of an aldehyde source.[83,84]

To date, our strategy in the group has been the incorporation of a carboxylic acid group in the metal complex towards amide coupling with amine-terminated peptide chains.[23,85] The amide bond is ubiquitous in nature, for example comprising the backbones of all peptides that make up proteins, and consequently its chemistry is well established. The bond is typically formed from the coupling of carboxylic acids (or derivatives) and amines in the presence of an appropriate coupling reagent.[86] The most widely used agents in this regard are probably those of the class of carbodiimides like EDC and DCC (EDC = 1-ethyl-3-(3-dimethylaminopropyl)carbodiimide; DCC = N,N'-dicyclohexylcarbodiimide). These compounds operate by forming a reactive intermediate which activates the carbonyl group of the carboxylate towards nucleophilic attack by primary amines leading to amide formation in the presence of a suitable base. The reactive intermediate is quite unstable, especially towards hydrolysis which can be problematic considering many peptide and protein modifications are performed in buffer solutions.[79] Accordingly, some protocols use large excesses of coupling reagent or instead elect to employ N-hydroxysuccinimide (HOSu) as a co-reagent to first form a dry-stable and isolatable NHS-ester derivative which may be later activated towards amide coupling.[68,85] Alternatively, greater efficiency has been achieved using more powerful coupling reagents such as HATU or PyBOP (HATU = 1-[Bis(dimethylamino)methylene]-1H-1,2,3-triazolo[4,5-b]pyridinium 3-oxid

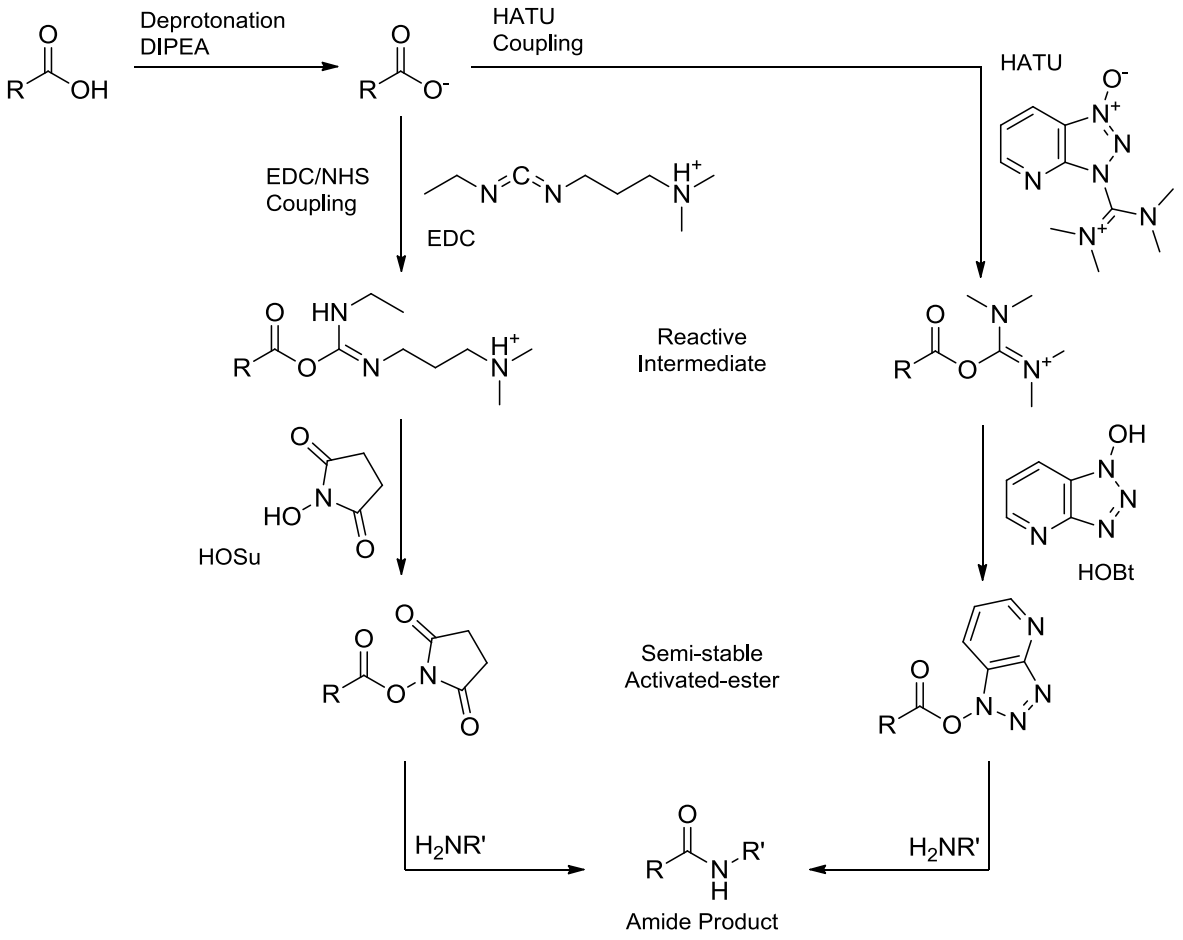

Scheme 3.8: Reaction routes of common coupling reagents towards amide bonds.

hexafluorophosphate; PyBOP = (Benzotriazol-1-yloxy)tripyrrolidinophosphonium hexafluorophosphate).[87,88] These reagents also operate by forming a reactive ester from the carboxylate which is then prone to reaction with nucleophiles. The use of EDC/NHS and HATU coupling methodologies to generate amides is illustrated in Scheme 3.8.

As described in Chapter 1, suitable peptides for precision targeting of Ru(II) luminophores in this thesis are: a non-specific vector, RRRRRRRR (R8); an NLS sequence, VQRKRQKLMP (NLS); and a MPP sequence, FrFKFrFK (MPP). Additionally, Penetratin, RQIKIWFQNRRMKWKK (ER), was exploited for endoplasmic reticulum targeting.

3.1.6 Chapter scope

This primary objective within this chapter was the synthesis of peptide-modified derivatives of $[Ru(bpy)_2(dppz)]^{2+}$. Under this aim, a route to bpy and phen ligands bearing pendant carboxylic acid groups was developed and efficient synthetic routes to conjugatable *bis*- and *tris*-heteroleptic complexes of Ru(II) was explored. Finally, the mono-conjugation and asymmetric di-conjugation of these complexes to multiple different vectors suited to cellular imaging was investigated.

3.2 Results and discussion:

3.2.1 Synthesis of the ligands

A primary aim of this chapter was to develop efficient synthetic routes to conjugatable derivatives of $[Ru(bpy)_2(dppz)]^{2+}$. The simplest component to synthesise in this context was dppz itself and has been well established in our lab.[23,85] Herein, the synthesis of dppz was adapted from the original Dickeson and Summers condensation of 1,10-phenanthroline-5,6-dione (phendione) with *ortho*-diaminobenzenes in alcohol.[89] Generally, commercial or synthesised phendione was reacted with 1.05 equivalents of *o*-phenylenediamine in refluxing methanol for three hours to yield dppz as a fluffy pale yellow solid in excellent yield (> 90 % consistently). The extended planarity of the heterocycle limits its solubility but the use of TFA-d enabled the collection of both ^{1}H and ^{13}C NMR spectra that conformed to literature reports.[23] The phendione precursor was later synthesised in-house using the method described by Paw and Eisenberg.[90]

A simple route to a conjugatable amine-modified phen ligand involves the reduction of commercially available 5-nitro-1,10-phenanthroline to 5-amino-1,10-phenanthroline (aphen) using hydrazine addition to a suspension of Pd/C catalyst in refluxing ethanol. This synthesis was attempted and provided aphen successfully as a light-brown solid in 67 % yield with the amino peak observed in the ^{1}H NMR spectrum at 6.15 ppm. This is a useful ligand for conjugation to carboxy modified cellular vectors, for example folic acid. However, as discussed in the introduction, in the case of cell penetrating peptides which tend to contain residues bearing primary amines such as Lys, it was prudent to modify the Ru(II) complexes with a carboxylic acid function to limit peptide self-condensation.

The modification of phenanthroline to yield aryl-spaced derivatives at the 5-position towards phenanthroline-BODIPY (phen-Ar-BODIPY) sensors was a major focus of the Keyes group at the beginning of this project.[91] At the same time, the translation of this synthesis to phen-Ar- -ester and -acid derivatives using an analogous protocol was under development[92] and forms the basis of the initial work towards carboxy modified bpy and phen derivatives in this thesis. The derivatisation strategy required the incorporation of a Suzuki-Miyuara active Aryl-Br function in the ligand which could then be subjected to cross-coupling reaction with

a boronic acid bearing a hydrolysable ester function that would ultimately provide a bioconjugatable terminus on the periphery of the metal complex. Accordingly, arylation of phenanthroline was achieved using the Suzuki coupling of 5-bromo-1,10-phenanthroline (Brphen) and 4-ethoxycarbonylphenylboronic acid at reflux in the presence of [$PdCl_2$(dppf)] catalyst and carbonate as base. Based on several iterations, it was found that a 3/1 dioxane/water solvent composition was optimal for the reaction, and in fact, a lower aqueous ratio (7/1) reduced the yield significantly. The reaction was also quite sensitive to scale and was less efficient either side of a starting mass of 500 mg (2.1 mmol, 267 mM) of Brphen precursor. The crude reaction mixture required purification and flash column chromatography on silica using 95/5 – 90/10 CH_2Cl_2/CH_3OH as eluent provided preliminary clean-up. Where the product still contained minor impurities, further purification was carried out by selective precipitation of dark red/black impurities from concentrated chloroform solutions using pentane, followed by trituration in the same solvents. This process provided the phenanthroline aryl ester (phen-Ar-COOEt) as an off-white solid in yields routinely ranging from 40 – 55 %. The solid could also be further purified by recrystallisation from acetonitrile/water mixtures to yield white threads but generally, the triturated material yielded acceptable purity for further synthesis and its characterisation data matched that published previously.[92]

The Brphen Suzuki precursor was obtained using a modification of Eisenberg's method[75] and utilised pressure-reactor heating of phenanthroline in the presence of oleum and elemental bromine at *ca*. 140 °C for 23 h. The crude solid isolated upon neutralisation of the reaction mixture was subjected to chloroform/pentane precipitations to provide Brphen in 53 % yield on the multi-gram scale. Characterisation by ^{1}H and ^{13}C NMR matched that reported by Eisenberg, indicating purity relative to free phen and the expected number of peaks for asymmetric mono-bromination. The entire reaction sequence towards phen-Ar-COOR is provided in Scheme 3.9.

The modification of phen translated well to bpy and enabled the synthesis of both 4-bpyArCOOEt and 5-bpyArCOOEt from their respective bromo-substituted precursors. As depicted in Scheme 3.10, 5-bromo-2,2'-bipyridine (5-Brbpy) is accessible in one step via Neigishi coupling of 2-pyridylzinc bromide and 2,5-dibromopyrdine in the presence of

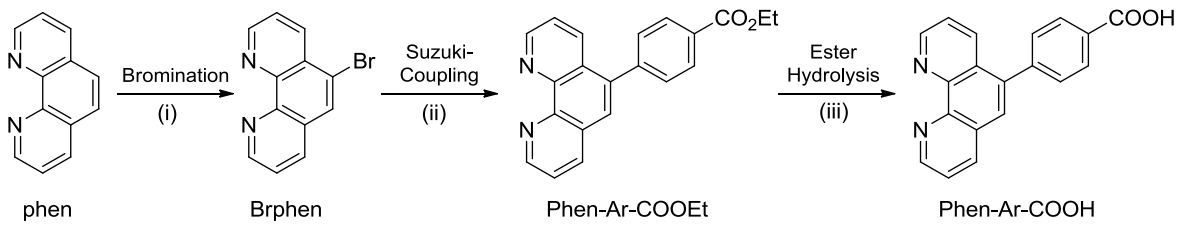

Scheme 3.9: Synthesis of phen-Ar-COOEt and phen-Ar-COOH. (i) Br_2, $H_2SO_4.SO_3$, pressure-reactor, 138 °C, 23 h, 53 %. (ii) $EtO_2CPhB(OH)_2$ (1.3 eq.), K_2CO_3 (2 eq.), dioxane/water 3/1, reflux, 6 h, 40 – 55 %. (iii) 1) CH_2Cl_2/CH_3OH 9/1, NaOH, room T, 24 h. 2) 1 M HCl (aq.) 85 – 95 %.

$Pd(Ph_3)_4$ as catalyst as reported by Fang and Hanan.[76] The yield of this reaction at just 30 % was lower than reported (73 %) possibly due to sensitivity of the Pd^0 catalyst to decomposition[93], but the ^1H NMR spectrum conformed to previous reports.[94]

The synthesis of 4-bromo-2,2'-bipyridine (4-Brbpy) was achieved following substantial modification to the procedure described by Zalas *et al*.[77], and required N-oxide activation of one of the pyridine rings of bpy to facilitate substitution at the 4-position (Scheme 3.10). This was achieved almost quantitatively as the mono-oxide as confirmed by ^1H NMR analysis which indicated asymmetry across the two rings with seven distinct signals of equal integration observed in the spectrum (Appendix A). bpy-N-oxide was then nitro-substituted under electrophilic aromatic substitution at the 4-position over the course of 48 hours in a 'nitrating-mixture' of concentrated sulfuric and nitric acids and potassium nitrate to provide 4-nitro-2,2-bipyridine (nitro-bpy-N-oxide) as a golden yellow solid. This step was by far the most yield limiting *en route* to 4-Brbpy with average yields obtained typically in the region of 35 - 46 %. However, successful mono-substitution was evident from the presence of one less peak (1 H) in the NMR spectra relative to bpy-N-oxide. Bromination was then possible by displacement of the nitro group in refluxing acetyl bromide to yield 4-bromo-2,2'-bipyridine (bromo-bpy-N-oxide) in 88 % yield. Bromination was accompanied by general upfield shifts in the ^1H NMR spectrum due to substitution with a relatively less electron withdrawing substituent. This step was followed by cleavage of the N-oxide using PBr_3 in refluxing chloroform to provide pure 4-bromo-2,2'-bipyridine (4-Brbpy) in about 30 % yield start-to-finish from bpy. The N-oxide cleavage was particularly efficient (95 %), likely driven

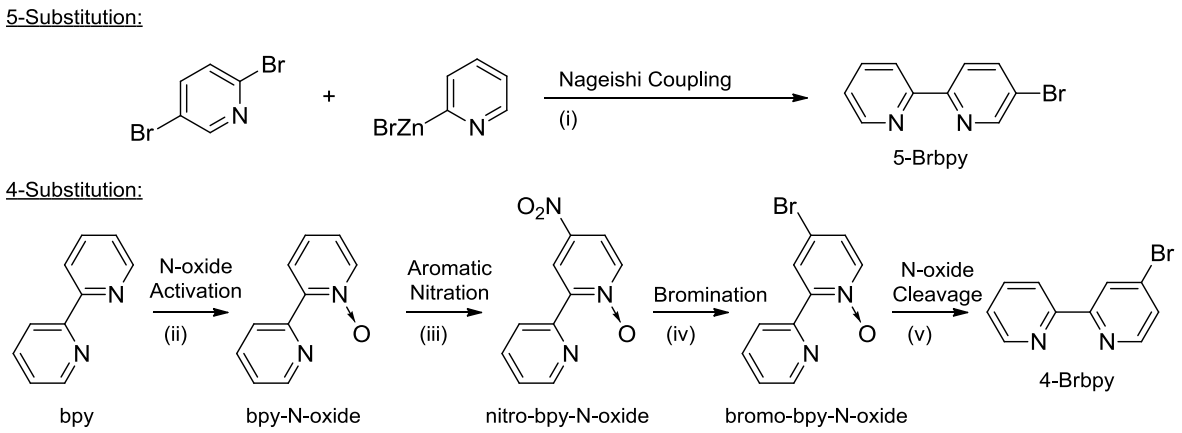

Scheme 3.10: Synthesis of 4- and 5-Brbpy. (i) $Pd(Ph_3)_4$, THF, 7 h, room T, 30 %. (ii) H_2O_2, TFA, room T, 97 %. (iii) H_2SO_4/HNO_3, KNO_3, 85 °C, 48 h, 46 %. (iv) AcBr, AcOH, reflux, 24 h, 88 %. (v) PBr_3, $CHCl_3$, reflux, 95 %.

---

by the formation of a stable phosphine oxide. 4-Brbpy was characterised by ^{1}H NMR (Appendix A) and corresponded to the data of Zalas *et al*.[77], while mass spectrometry found two peaks of almost equal intensity two mass units apart (^{78}Br and ^{80}Br) assignable to $[M+H]^+$ at 235.03 *m/z* (calculated for $C_{10}H_7N_2Br^{78}$, 234.99).

Suzuki-coupling of 4- and 5- Brbpy by an analogous protocol to phen-Ar-COOEt provided 4-bpyArCOOEt and 5-bpyArCOOEt (Figure 3.2) as white solids in moderate to good yields in the range 65 – 80 % (Scheme 3.11). These compounds were characterised by ^{1}H NMR which indicated the expected triplet (≈ 1.4 ppm, 3H, -$CH_2C\underline{H}_3$) and quartet (≈ 4.4 ppm, 2H, -$C\underline{H}_2CH_3$) peaks corresponding to the ester substituent in the aliphatic region. Additionally, the newly coupled aryl spacer was evident as a set of two new doublets relative to Brbpy (Figure 3.3). A full assignment of the peaks in the ^{1}H NMR spectra of the bpyArCOOEt ligands was facilitated using COSY NMR and is provided in Table 3.1. High resolution mass spectrometry (HRMS) (ESI(+)-TOF)) further confirmed the structures, for example for 4-bpyArCOOEt; *m/z* = 305.1282 which corresponded to that calculated for $C_{19}H_{17}N_2O_2$ $[M + H]^+$ at *m/z* = 305.1290 (Table 3.1).

The aryl-spaced phen and bpy carboxylic acids were easily obtained from their corresponding esters by the non-aqueous hydrolysis method reported by Theodorou *et al*..[95] Typically, the

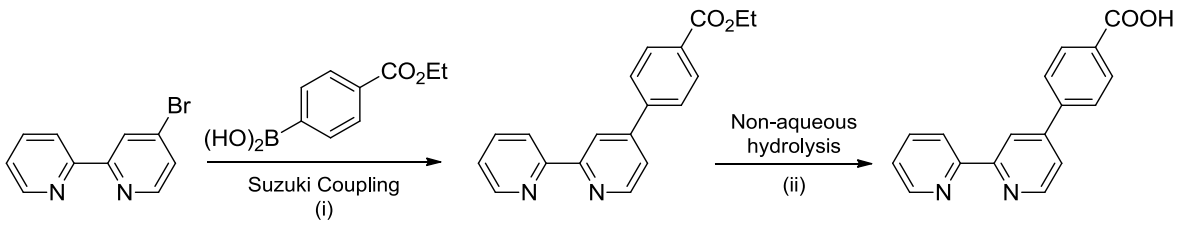

Scheme 3.11: Synthesis of 4-bpyArCOOR (R = Et, H). (i) K_2CO_3 (2 eq.), dioxane/water, reflux, 65 – 80 %. (ii) 1. NaOH, CH_2Cl_2/CH_3OH 9/1, 95 %. 2. HCl/H_2O.

---

ester derivatives were stirred overnight in hydroxide dissolved in a 1/9 methanol/dichloromethane mixture at room temperature. The reaction was then evaporated to provide the sodium carboxylate salts of the compounds which were acidified upon treatment of an aqueous solution with 1 M HCl, forming a gel which can be dehydrated in acetone and filtered to yield pure phen-Ar-COOH, 4-bpyArCOOH and 5-bpyArCOOH as white solids. The compounds were relatively insoluble but could be analysed by ^{1}H NMR in DMSO-d_6 which indicated a disappearance of the ester signals in the aliphatic region (Appendix A) and in some cases, a broad singlet was observed at *ca*. 13 ppm attributable to the carboxylic acid functional group. The ^{1}H NMR signals were assigned for the bpyArCOOH ligands as indicated in Table 3.1. High resolution mass spectrometry (HRMS) further confirmed the structures as indicated in Table 3.2, finding, for example for 4-bpyArCOOH; (ESI(+)-TOF) *m/z* = 277.0983 corresponding that calculated for $C_{17}H_{13}N_2O_2$ $[M + H]^+$ at 277.0977 (see also Appendix A).

Table 3.1 – ^{1}H NMR peak values for the substituted bipyridines.

Compound	Solvent, Frequency	^{1}H NMR Shifts δ (ppm) (multiplicity, nH) *[Structural Assignment]*
4-bpyArCOOEt	$CDCl_3$, 600 MHz	8.69 (d, 1 H) *[6]*; 8.64 (d, 1 H) *[6']*; 8.63 (s, 1 H) *[3]*; 8.39 (d, 1 H) *[3']*; 8.10 (d, 2 H) *[E,C]*; 7.77 (m, 3 H) *[4',B,F]*; 7.49 (dd, 1 H) *[5]*; 7.28 (dd, 1 H) *[5']*; 4.35 (q, 2 H) *[OEt I]*; 1.36 (t, 3 H) *[OEt II]*.
4-bpyArCOOH	DMSO-d_6, 600MHz	13.24 (s, 1 H) *[COOH]*; 8.92 (m, 2 H) *[6,3]*; 8.89 (d, 1 H) *[6']*; 8.71 (d, 1 H) *[3']*; 8.28 (t, 1 H) *[4']*; 8.17 (q, 4 H) *[B,C,E,F]*; 8.07 (d, 1 H) *[5]*; 7.76 (t, 1 H) *[5']*.
5-bpyArCOOEt	$CDCl_3$, 400 MHz	8.94 (d, 1 H) *[6]*; 8.71 (d, 1 H) *[6']*; 8.48 (dd, 2 H) *[3,3']*; 8.16 (d, 2H) *[E,C]*; 8.06 (dd, 1 H) *[4]*; 7.85 (td, 1 H) *[4']*; 7.72 (d, 2 H) *[B,F]*; 7.34 (dd, 1 H) *[5]*; 4.41 (q, 2 H) *[OEt I]*; 1.42 (t, 3 H) *[OEt II]*.
5-bpyArCOOH	DMSO-d_6, 400 MHz	13.10 (s, 1 H) *[COOH]*; 9.09 (d, 1 H) *[6]*; 8.73 (d, 1 H) *[6']*; 8.51 (d, 1 H) *[3]*; 8.45 (d, 1 H) *[3']*; 8.34 (dd, 1 H) *[4];* 8.07 (d, 2 H) *[C,E]*; 8.00 (m, 3 H) *[4',B,F]*; 7.51 (m, 1 H) *[5']*.

Table 3.2 – HR-MS data for the substituted bipyridines.

Compound	Calculated (m/z)	Found (m/z)	Assignment
4-bpyArCOOEt	305.1290	305.1282	$[M + H]^+$
4-bpyArCOOH	277.0977	277.0983	$[M + H]^+$
5-bpyArCOOEt	305.1290	305.1292	$[M + H]^+$
5-bpyArCOOH	277.0977	277.0974	$[M + H]^+$

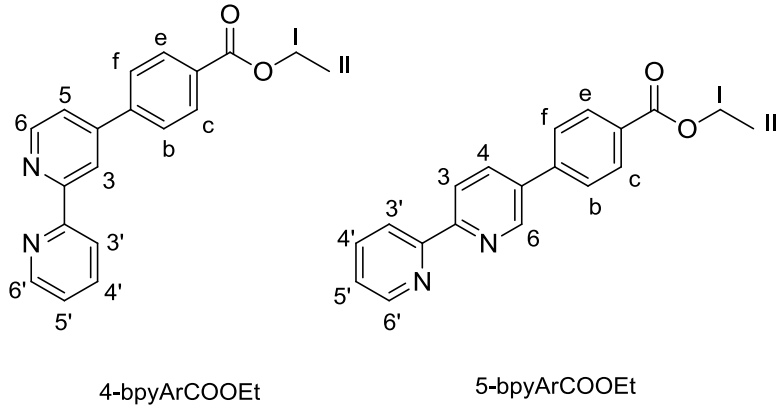

Figure 3.2: Structures of 4- and 5-substituted bpy and labelling systems for ^{1}H NMR assignments.

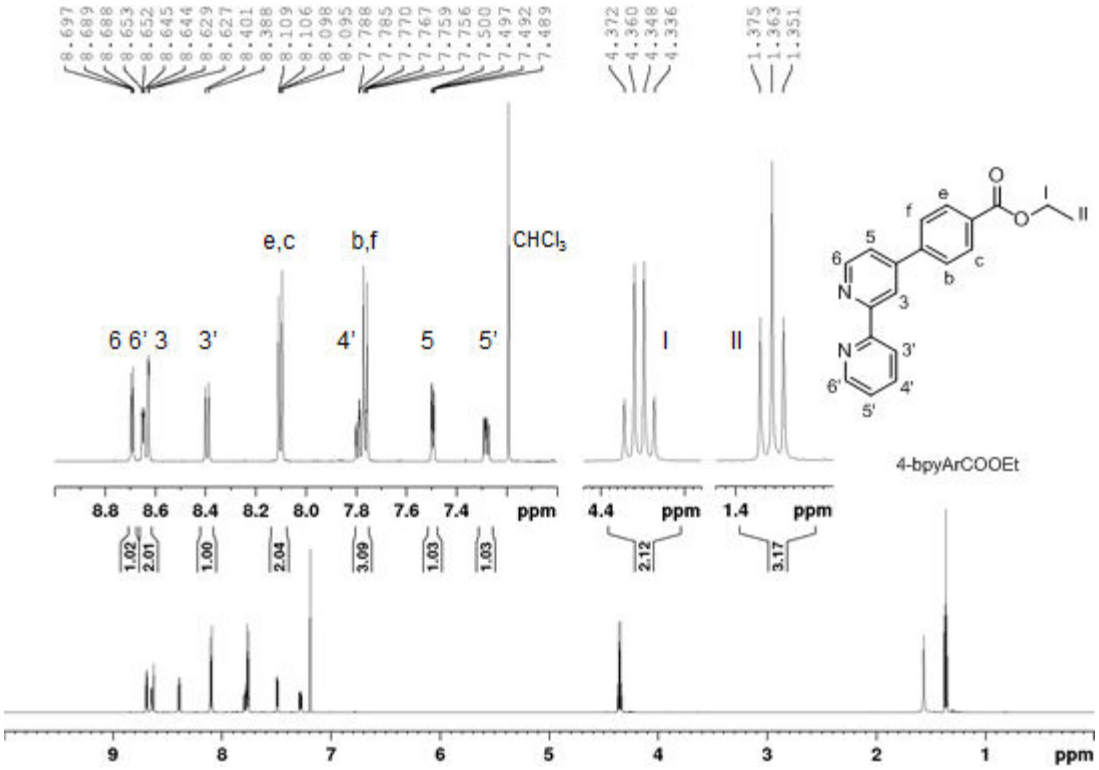

Figure 3.3: ^{1}H NMR (600 MHz, $CDCl_3$) spectrum and peak assignments for 4-bpyArCOOEt.

In the synthesis of Ru(II) complexes, phen-Ar-COOR was used as a ligand to complete other work ongoing in the group, for example $[Ru(bpy)_2(phen\text{-}Ar\text{-}COOH)]^{2+}$, and these complexes are described in brief below. The focus of this chapter shifted towards the synthesis of conjugatable derivatives of $[Ru(bpy)_2(dppz)]^{2+}$. In this regard, only the 4-substituted bpy derivatives were used in Ru(II) reactions, no further work on the 5-substituted series was attempted, and henceforth the label; bpyArCOOR, is given exclusively to correspond to 4-bpyArCOOR.

3.2.2 Synthesis of *bis*-heteroleptic Ru(II) complexes of the type: $[Ru(N^N)_2(N^N')]^{2+}$.

Traditionally, the synthesis of *bis*-heteroleptic complexes of the type, $[Ru(N^N)_2(N^N')]^{2+}$; proceeds via the neutral dichloride intermediate, $[Ru(N^N)_2Cl_2]$; where N^N and N^N' are bidentate polypyridyl ligands.[1,22] Reaction of one equivalent of the ternary ligand with the dichloride in refluxing aqueous ethanol provides the final dicationic Ru(II) *tris*-chelated complexes which can be conveniently precipitated from water as stable solids using an appropriate non-coordinating counterion such as perchlorate, ClO_4^- or hexafluorophosphate, PF_6^-.[23] This approach yielded $[Ru(bpy)_2(dppz)](ClO_4)_2$ and $[Ru(bpy)_2(phen\text{-}Ar\text{-}COOH)](ClO_4)_2$ from commercial *cis*-$[Ru(bpy)_2Cl_2]$ in yields exceeding 70 % after purification, by recrystallization from ethanol in the case of the former, or flash column chromatography to provide the latter (silica, 70/26/4/2 $CHCl_3/CH_3OH/H_2O/AcOH$) (Scheme 3.12). Characterisation data for $[Ru(bpy)_2(dppz)](ClO_4)_2$ corresponded to the original preparation by Amouyal *et al*.[96] while $[Ru(bpy)_2(phen\text{-}Ar\text{-}COOH)](ClO_4)_2$ was developed previously in our group and its structural data herein conformed to the previous report.[92]

Counterion exchange was facile and the PF_6^- salts were easily obtained either directly from the reaction solution or by dissolution of the ClO_4^- form in acetonitrile followed by addition to saturated aqueous NH_4PF_6 to precipitate the PF_6^- salt. The chloride was procured by precipitation from an acetone solution of the PF_6^- form in the presence of excess tetrabutylammonium chloride (TBAC). Successful counterion exchange was evident from an

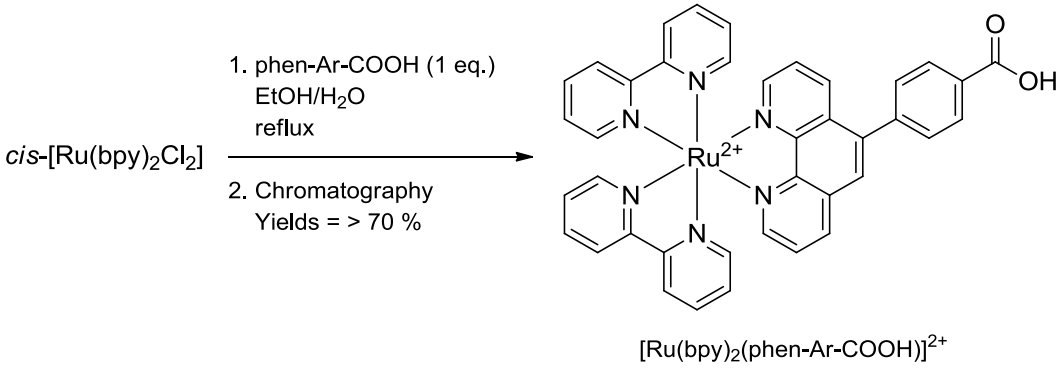

Scheme 3.12: Synthesis of $[Ru(bpy)_2(phen\text{-}Ar\text{-}COOH)]^{2+}$.

insolubility of the chloride salts in acetone but good solubility in water. Satisfyingly, this general counterion exchange protocol extends across the full range of Ru(II) complexes and conjugates presented herein. $[Ru(bpy)_2(dppz)]^{2+}$ was prepared as the model complex to provide a comparison of the photophysical responses upon DNA binding of the novel Ru(II) dppz complexes and conjugates reported in this thesis. $[Ru(bpy)_2(phen\text{-}Ar\text{-}COOH)]^{2+}$ was prepared as a cellular imaging probe that photophysically responds to dioxygen and reactive oxygen species (ROS) and its application as such has been reported elsewhere.[92,97]

Given the success of the preparation of these complexes by the classical approach via $[Ru(N\text{^}N)_2Cl_2]$, a similar strategy was initially adopted towards the synthesis of carboxy-functionalised Ru(II)-dppz complexes. Hence, our original target complex was established as $[Ru(bpyArCOOH)_2(dppz)]^{2+}$, which was accessible via $[Ru(bpyArCOOH)_2Cl_2]$. The bpyArCOOEt derivative was also desired because in comparison to the acid complex, the ester is not susceptible to acid-base chemistry and is a better model of an 'unconjugated' parent structure to compare with the peptide conjugates.

Synthesis of $[Ru(bpyArCOOR)_2(dppz)]^{2+}$ by classical routes

The synthesis of $[Ru(bpyArCOOR)_2Cl_2]$ was attempted by the classical approach described by Sullivan *et al*. employing two equivalents of ligand under reflux with $RuCl_3.3H_2O$ starting material in the presence of LiCl in DMF for several hours.[20] This reaction was found to only proceed to any discernible degree using commercial trihydrate starting material, and not $RuCl_3.nH_2O$ which is also commercially available. The protocol was quite inefficient even using the trihydrate, however, and generally provided an impure black or dark purple crude mass following post-reaction precipitation using diethyl ether, acetone or water. Purification at this stage by recrystallisation or otherwise is difficult because of insolubility in most conventional solvents and the lability of the chloride ligands that can lead to solvolysis.[17] For both the acid and ester complexes, thin layer chromatography (TLC) on silica (see Section 3.4) indicated unreacted starting material at the baseline, three purple bands corresponding to the three isomers (assuming just the *cis* configuration persists, Scheme 3.13) and a large yellow band which was assigned as a Ru-CO impurity. Correspondingly, ATR-IR analysis of crude $[Ru(bpyArCOOH)_2Cl_2]$ indicated an intense peak at *ca*. 1970 cm^{-1}. The presence of carbonylated impurities is less surprising considering this protocol has been utilised as a route

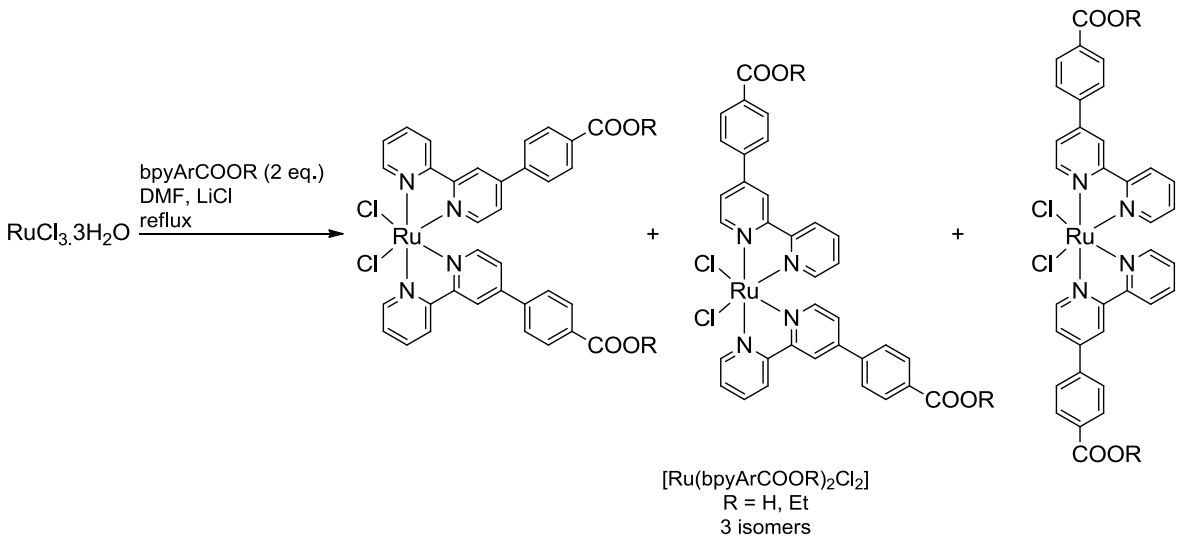

Scheme 3.13: Synthesis of $[Ru(bpyArCOOR)_2Cl_2]$.

to studies on *cis*-$[Ru(bpy)_2(CO)Cl]^+$.[26] Furthermore, NMR studies on the crude material in DMSO-d_6 indicated extensive broadening indicative of incomplete reduction of intermediate Ru(III) species. While the acid was particularly insoluble, the ester derivative $[Ru(bpyArCOOEt)_2Cl_2]$ was sufficiently soluble for purification using preparative TLC on silica with 9/1 CH_2Cl_2/CH_3OH as solvent to yield the Ru-dichloride as a burgundy solid. The expected structure was confirmed as a mixture of isomers by ^1H NMR in DMSO-d_6, however this success came at the cost of extensive yield reduction below 20 %. The best option in this scenario was to utilise the crude solids for further synthesis and perform purification at the next stage.

As discussed in the introduction (3.1.1), the classical dichloride route described by Sullivan *et al*.[20] suffers from some important limitations which may rationalise some of the difficulties encountered in the synthesis of $[Ru(bpyArCOOR)_2Cl_2]$. Herein, Viala and Coudret's method[25] was also trialled and was surprisingly even less successful than the classical approach with high yields of the by-product $[Ru(bpyArCOOR)_3]^{2+}$ frequently obtained. The limitations of these approaches appear to be magnified moving away from non-classical ligands like bpy and phen. This underlines the importance of exploring generality in synthesis and there is very little literature discussion addressing synthesis of $[Ru(N\hat{}N)_2X_2]$ intermediates that contain highly lipophilic and/or functionalised ligands. Their

corresponding complexes can be rather insoluble and difficult to purify by conventional means.

Using crude $[Ru(bpyArCOOR)_2Cl_2]$ obtained by the classical approach, ternary ligand chelation with dppz was achieved to provide $[Ru(bpyArCOOR)_2(dppz)]^{2+}$ in moderate to good yield (50 – 70 %) by traditional aqueous ethanol reflux and subsequent purification on silica using 70/26/4/X ($CHCl_3/CH_3OH/H_2O$/AcOH, X = 0 ester, X = 2 acid). Purification was difficult considering the impurities that carry over from the dichloride step and multiple columns were sometimes required which impacted the final yield. Considering the inefficiency of the net reaction from $RuCl_3.3H_2O$, alternative syntheses to the final complexes were pursued. One option explored was inspired by the work of Suzuki *et al*. on Ru-phosphinoquinoline complexes and involved ligation of the 'ternary ligand' into the coordination sphere first by addition to *cis*-$[Ru(DMSO)_4Cl_2]$, followed by efficient reaction with two equivalents of the '*bis*-ligand' to yield the final Ru(II) *tris* chelates.[41] Adapting this approach to our design required the synthesis of *cis*-$[Ru(DMSO)_4Cl_2]$ followed by conversion to $[Ru(dppz)(DMSO)_2Cl_2]$ and finally reaction with two equivalents of bpyArCOOR to yield the target complex; $[Ru(dppz)(bpyArCOOR)_2]^{2+}$. This sequence is illustrated in Scheme 3.14.

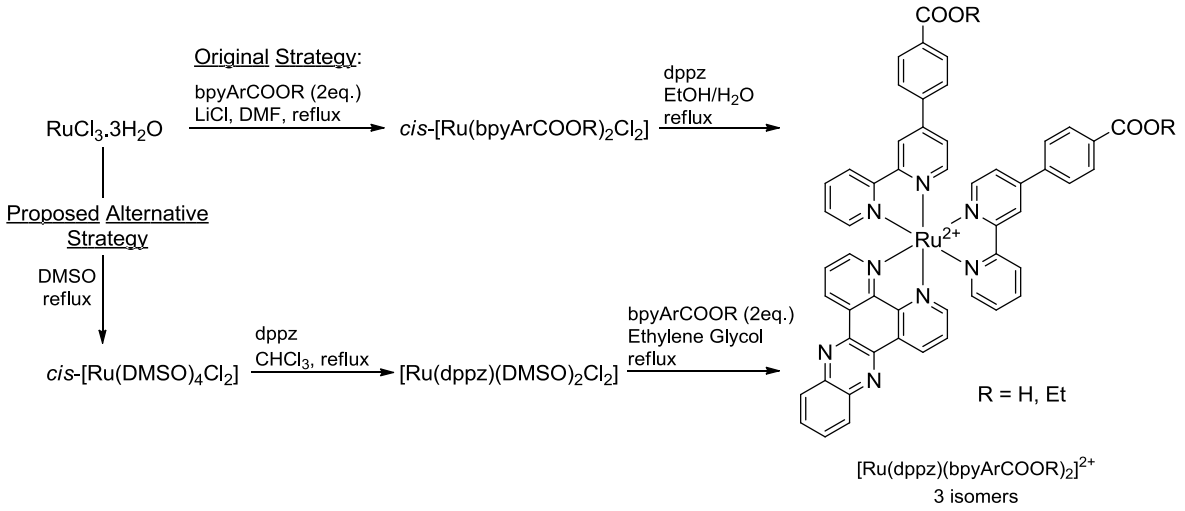

Scheme 3.14: The original strategy towards $[Ru(dppz)(bpyArCOOR)_2]^{2+}$ and the proposed modified route via Ru-DMSO intermediates.

Synthesis of [Ru(bpyArCOOR)$_2$(dppz)]$^{2+}$ via Ru-DMSO precursors

Synthesis of *cis*-[Ru(DMSO)$_4$Cl$_2$] commonly proceeds from RuCl$_3$.3H$_2$O as originally described by Wilkinson *et al*. by treating the Ru(III) species under reflux in DMSO for a few minutes with subsequent precipitation using acetone.[31] This approach was attempted and it was found that the reaction was time sensitive. Poor conversions were observed when the reflux lasted for less than two minutes but degraded green-yellow solutions were obtained if the time exceeded five minutes. The best results were achieved employing reflux of the reaction solution for precisely two minutes followed by rapid cooling on ice and treatment with cold acetone. Nonetheless, yields varied wildly ranging from 50 – 82 %. Furthermore, the material obtained contained the *trans* product and required recrystallization from hot DMSO/acetone solutions to obtain the purified complex as lemon needles as described by others.[31,32]

A modified protocol was recently published by Alston *et al*. which uses a DMSO/IPA mixture at 85 ºC for 30 hours to selectively provide the *cis*-isomer in 90 % yield.[33] As part of this thesis, the Alston protocol reproducibly provided *cis*-[Ru(DMSO)$_4$Cl$_2$] as a yellow powder in yields exceeding 95 % on the gram scale after 24 hours. A key point to ensure high yields is that the RuCl$_3$.3H$_2$O precursor must be fully dissolved (using sonication and heating) before addition of the IPA solvent. The isolated *tetrakis*-DMSO complex is soluble in chloroform and was characterised by ^{1}H NMR spectroscopy which revealed two distinct sets of peaks corresponding to the expected 3:1 ratio of S- and O- bonded ligands for the *cis*-isomer[98] (κO-DMSO (2.71 ppm, s, 1eq. H) and κS-DMSO (3.31 – 3.51 ppm, m, 3eq. H)). ATR-IR further confirmed the presence of κO- and κS- DMSO ligands with signals assignable to S=O modes at 1112 (κS), 1094 (κS) and 932 (κO) cm^{-1} that matches reports by others.[31,33]

Wilkinson *et al*. described the synthesis of [Ru(bpy/phen)(DMSO)$_2$Cl$_2$] from *cis*-[Ru(DMSO)$_4$Cl$_2$] under reflux in chloroform with the appropriate ligand and subsequent purification was achieved by extraction into acetone and selective precipitation using diethyl

ether.[31] This method was partially successful herein and yielded [Ru(dppz)(DMSO)$_2$Cl$_2$] in 49 % yield.

It was later discovered that the use of ethanol instead of chloroform was a superior approach, as described by Le Gac *et al*.[39] for [Ru(tap)(DMSO)$_2$Cl$_2$], and provided [Ru(dppz)(DMSO)$_2$Cl$_2$] as a brown solid in quantitative yield (99 %). Isolation was straightforward as the product precipitates on cooling. HRMS found a cluster that reflected the expected isotope pattern for the molecular ion at *ca*. 610 *m/z* (*m/z* calculated for $C_{22}H_{22}Cl_2N_4O_2S_2Ru$ $[M]^+$: 609.9605; found: 609.9604). Elemental analysis provided additional evidence of successful synthesis and purity. NMR indicated asymmetry in peaks attributed to dppz consistent with the *cis* configuration of the chloride and DMSO ligands. The presence of DMSO ligands was corroborated by peaks observed in the ^{1}H NMR spectrum at δ 3.26, 3.60, 3.65 and 2.70 ppm. DMSO signals were also evident as S=O modes in the ATR-IR spectra at 1120, 1094 and 919 cm^{-1} , correlating well with IR values described by Alessio.[99]

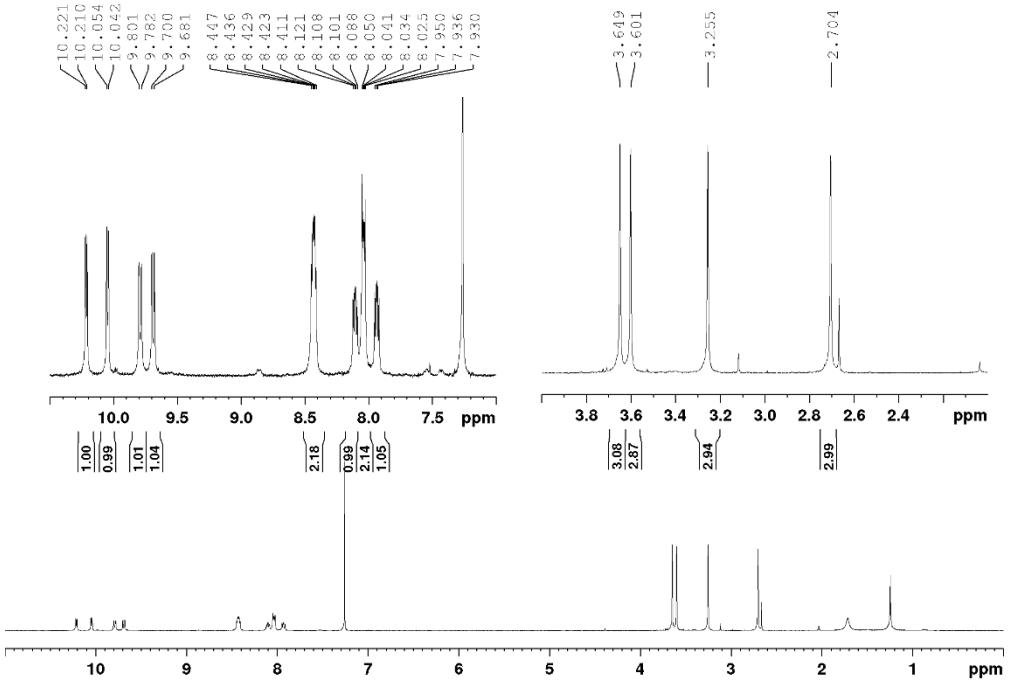

Figure 3.4: ^{1}H NMR (400 MHz, $CDCl_3$) spectrum of [Ru(dppz)(DMSO)$_2$Cl$_2$] with insets to indicate regions of interest.

Next, $[Ru(dppz)(DMSO)_2Cl_2]$ was reacted with two equivalents of bpyArCOOR in refluxing ethylene glycol to yield a solution of $[Ru(dppz)(bpyArCOOR)_2]^{2+}$ after 6 hours from which the PF_6^- salt precipitated upon addition of NH_4PF_6 (aq. satd.). The crude product was purified through celite as an acetone solution and reprecipitated using diethyl ether to yield pure $[Ru(dppz)(bpyArCOOEt)_2](PF_6)_2$ and $[Ru(dppz)(bpyArCOOH)_2](PF_6)_2$ in yields of 85 % and 98 % respectively as a mixture of geometrical isomers. On conversion to the perchlorate salt the characterisation data matched that previously obtained for the complexes prepared by the classical route via $[Ru(bpyArCOOR)_2Cl_2]$ (as discussed above). HRMS analysis (Table 3.3) returned spectra matching the expected Ru isotope pattern with values assignable to $[M]^{2+}$ (*m/z* calculated z = 2; 468.0868, found; 468.0881) for the acid complex and $[M^{2+} + ClO_4^-]^+$ for the ester (*m/z* calculated; 1091.1858, found; 1091.1901). The ^1H NMR spectrum of the chloride form of the ester complex is provided in Figure 3.5 and indicates multiple signals corresponding to the each of the geometrical isomers. Taking an isolated dppz signal at *ca*. 9.6 ppm, there appears to be a dominant isomer that has formed during the reaction. The statistical isomer (i.e. the most asymmetric configuration) is likely dominating considering the occurrence of multiple distinct bpyArCOOR signals that integrate for one proton (and are coupled under COSY analysis). Furthermore, there appears to be an inequivalence of the ester signals which suggests a lower level of symmetry in the molecule.

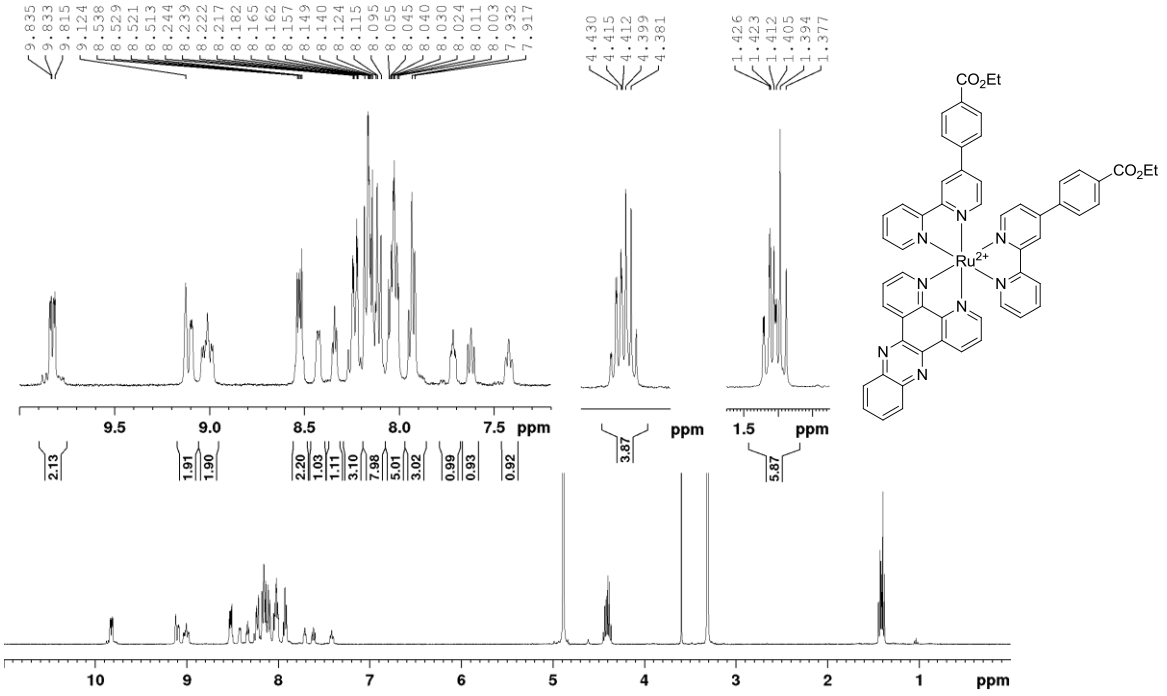

Figure 3.5: ^{1}H NMR (600 MHz, CD_3OD/D_2O) spectrum of $[Ru(dppz)(bpyArCOOEt)_2]Cl_2$ with insets to show regions of interest and chemical structure of one the isomers.

Table 3.3 – HR-MS data for $[Ru(dppz)(bpyArCOOR)_2]^{2+}$ and precursor.

Compound	Calculated (m/z)	Found (m/z)	Assignment
$[Ru(dppz)(bpyArCOOH)_2](ClO_4)_2$	468.0868	468.0881	$[M]^{2+}$
$[Ru(dppz)(bpyArCOOEt)_2](ClO_4)_2$	1091.1858	1091.1901	$[M^{2+} + ClO_4^-]^+$
$[Ru(dppz)(DMSO)_2Cl_2]$	609.9605	609.9604	$[M]^+$

3.2.3 Synthesis of *tris*-heteroleptic complexes of Ru(II) of the type: $[Ru(N^N)(N^N')(N^N'')]^{2+}$.

The successful synthesis of $[Ru(dppz)(bpyArCOOR)_2]^{2+}$ grants access to homo-diconjugated Ru-dppz derivatives and examples of peptide derivatives of this class are presented later in this chapter. In addition, we wished to develop a Ru-dppz probe which is monoconjugated to simplify potential interactions with DNA, to reduce the complexity of peptide conjugation,

and to produce a construct that more closely mimics the candidate complex; $[Ru(bpy)_2(dppz)]^{2+}$. The target complex was established as; [Ru(dppz)(bpy)(bpyArCOOR)]$^{2+}$. As detailed in the introduction to this chapter (3.1.2), there are limited literature examples towards the efficient synthesis of *tris*-heteroleptic Ru(II) complexes. Herein, the route via Ru-DMSO intermediates was selected for development towards [Ru(dppz)(bpy)(bpyArCOOR)]$^{2+}$.

Synthesis of [Ru(dppz)(bpy)(bpyArCOOR)]$^{2+}$ via [Ru(dppz)(bpy)Cl_2]

In the work towards $[Ru(bpyArCOOR)_2(dppz)]^{2+}$, a suitable Ru-DMSO derivative for further synthesis had already been prepared; $[Ru(dppz)(DMSO)_2Cl_2]$. Attempts were then made to form $[Ru(dppz)(bpy)Cl_2]$ by the classical approach in DMF/LiCl as implemented by Hesek *et al*.[50] and Zakeeruddin *et al*.[52], but this synthesis was prone to the shortcomings discussed above and often resulted in over-reaction to $[Ru(dppz)(bpy)_2]^{2+}$ even under conditions of high chloride concentration. Ideally, the conversion should limit chloride ligand dissociation and should stop further reaction to *tris*-chelates. Substitution of Ru-DMSO likely proceeds via Ru-solvate intermediates and precipitation of the Ru-dichloride as it forms should prevent over-reaction. These issues can be addressed using a non-coordinating non-polar reaction solvent spiked with minimal donor solvent. A dioxane/water system was used here and no reaction was observed upon refluxing $[Ru(dppz)(DMSO)_2Cl_2]$ and bpy in dioxane for 2 hours. However, upon adjustment of the solvent to 5 % v/v water, the reaction proceeded to completion in 2 hours with the formation of a black fine suspension in the reaction mixture. Isolation of the dichloride was straightforward since the product precipitated as it formed and could be filtered and washed with chloroform to provide $[Ru(dppz)(bpy)Cl_2]$ reproducibly in *ca*. 75 % yield as confirmed by ^{1}H NMR which indicated an absence of free ligand, Ru-DMSO and oxidation impurities. The complete reaction sequence and its modification is illustrated in Scheme 3.15.

Given the relative novelty of the dioxane/water approach, it was decided to explore the generality of this reaction. In particular, formation of $[Ru(dppz)(bpyArCOOH)Cl_2]$ (and subsequently [Ru(dppz)(bpyArCOOH)(bpyArCOOEt)]$^{2+}$) would open the possibility of exploring hetero-diconjugated Ru(II)-dppz complexes by an acid-coupling, ester-deprotection, acid-coupling approach. Unfortunately, the dioxane/water system was found to

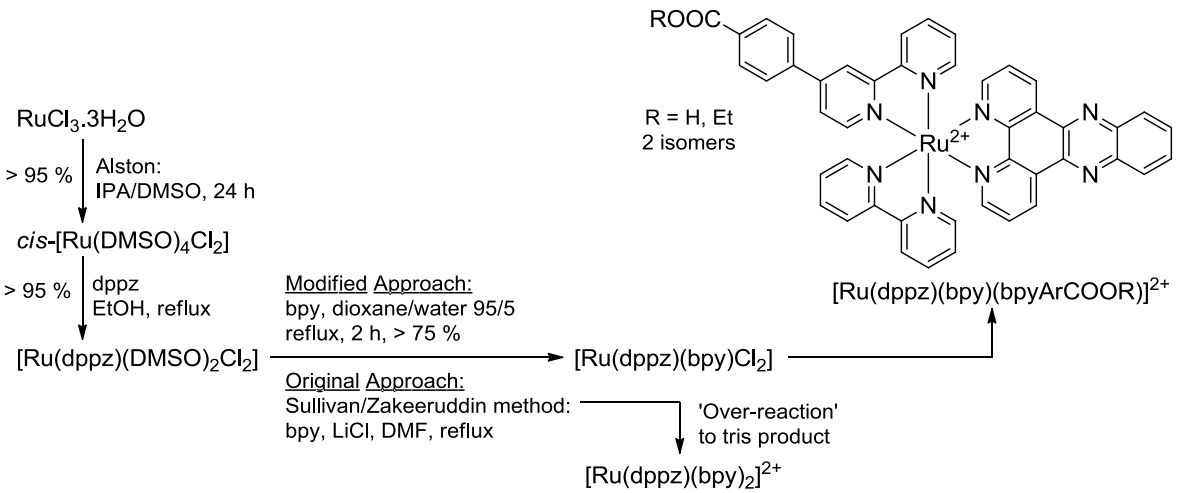

Scheme 3.15: Synthesis of the *tris*-heteroleptic complexes via [Ru(dppz)(bpy)Cl_2] and its synthesis by a modified route.

---

be limited to [Ru(dppz)(bpy)Cl_2] and over-reaction to *tris*-chelates was frequently observed where other ligand systems were implemented. The problem concerned the relative lability of the chloride ligands in most reaction environments required to initiate initial DMSO substitution in the coordination sphere of [Ru(dppz)(DMSO)$_2Cl_2$]. This prompted the development of a more robust 'protecting group' for one edge of the coordination sphere to enable specific stoichiometric addition of a single bidentate polypyridyl ligand by substituting only the DMSO ligands. The protecting group should be readily available, should maintain *cis*-configuration in the coordination sphere, should not cleave under the conditions of polypyridyl ligand addition and crucially, it must be easily removed to permit ternary ligand chelation. After limited success exploring carbonates and acetylacetonates, Ru-oxalates were revealed to be suitable for this purpose since they form stable, neutral, bidentate complexes which lock-in the *cis*-configuration and critically, can be later removed by acid hydrolysis to provide a reactive Ru-aquo species suitable for ternary ligand coordination.[100,101]

Synthesis of [Ru(dppz)(bpy-R)(bpyArCOOR)]$^{2+}$ via [Ru(dppz)(bpy-R)(ox)]

Employing the oxalate strategy, [Ru(dppz)(DMSO)$_2Cl_2$] was treated with a hot aqueous solution of sodium oxalate (1.5 eq) and subjected to reflux with the given polypyridyl ligand

in ethylene glycol for three hours. Gratifyingly, the reaction proceeded efficiently to provide the oxalates which were easily isolated by their precipitation from water, yielding [Ru(dppz)(bpy)(ox)] and [Ru(dppz)(bpyArCOOH)(ox)] as fine dark-purple/black powders in yields of 98 % and 94 % respectively. The oxalate was used in 1.5 molar excess to drive monomer formation since oxalates can also yield μ-oxo bridged dimers at low oxalate concentrations.[102] The Ru-oxalates were unambiguously characterised by elemental analysis, HRMS and ^{1}H NMR.[11] The ^{1}H NMR spectrum of [Ru(dppz)(bpy)(ox)] shown in Figure 3.6 reveals an inequivalence across both halves of the dppz and bpy ligands indicative of the expected mononuclear *cis*-configuration. The reaction sequence illustrating the novel strategy via Ru-oxalates towards *tris* heteroleptic complexes of Ru(II) is provided in Scheme 3.16.

Cleavage of the oxalate group was easily accomplished quantitatively in refluxing 1/1 CH_3CN/1M $HClO_4$ (aq.). Meyer *et al*. reported successful hydrolysis of μ-oxalate-bridged Ru(II) dimers in 1 M $HClO_4$ after 15 minutes[101] but herein, it was found that heating and a

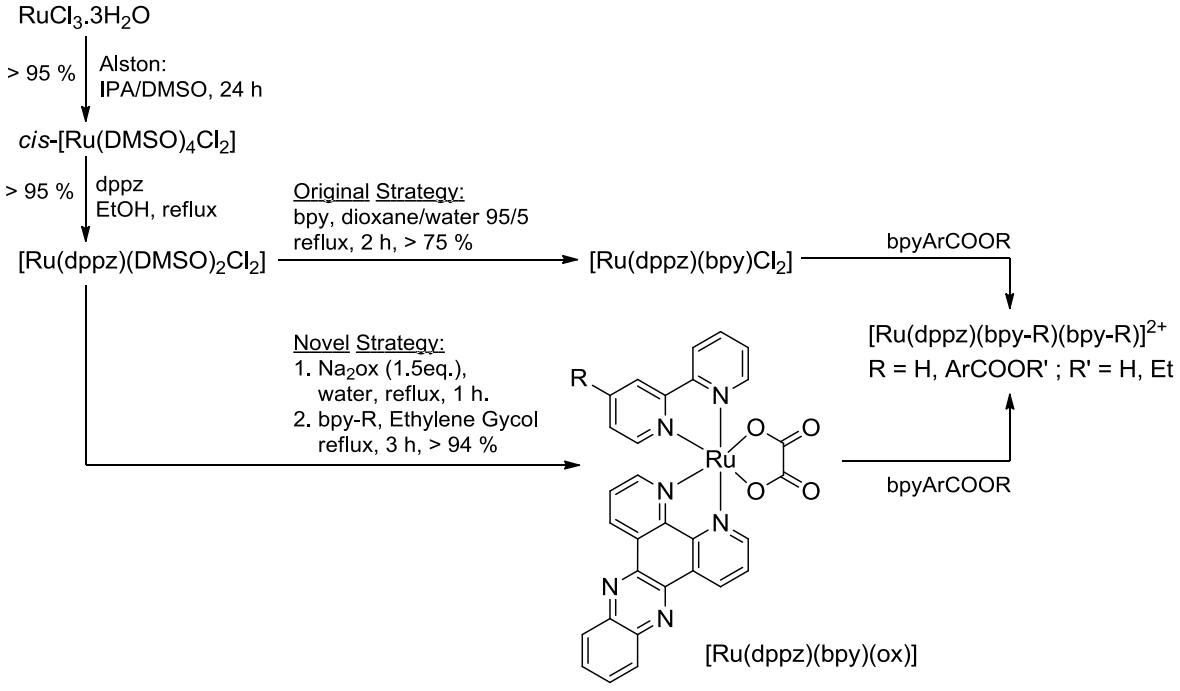

Scheme 3.16: Synthesis of tris heteroleptic complexes via Ru-oxalate intermediates.

donor and solubilising solvent such as acetonitrile was required for full cleavage of the Ru-oxalates. The perchlorate salt of the Ru-solvate product precipitated on pouring the reaction mixture into water. This intermediate was reacted immediately in ethylene glycol with bpyArCOOR to provide the crude *tris*-heteroleptic complexes which were purified on short silica columns using 90/10/1 $CH_3CN/H_2O/KNO_3$ (aq.) followed by 70/30 CH_3CN/0.1 M TsOH (aq.) as eluent. This provided the purified *tris*-heteroleptic complexes (Figure 3.7) as a mixture of geometric isomers in yields exceeding 86 %. It was also found that where the ligand was acid stable, the cleavage and chelation steps can be performed as one. Addition of $HClO_4$ (aq.) or TFA to acetonitrile/ethylene glycol reaction mixtures enabled similarly excellent conversion to the final complexes. This initially became evident during attempts to perform the cleavage and chelation in one step for bpyArCOOEt complexes, where the cleavage step hydrolysed the ester function to yield $[Ru(dppz)(bpyArCOOH)_2]^{2+}$ exclusively.

To further expand the synthetic routes to conjugatable complexes, 'on-complex' hydrolysis of $[Ru(dppz)(bpy)(bpyArCOOEt)](PF_6)_2$ to $[Ru(dppz)(bpy)(bpyArCOOH)](PF_6)_2$ was

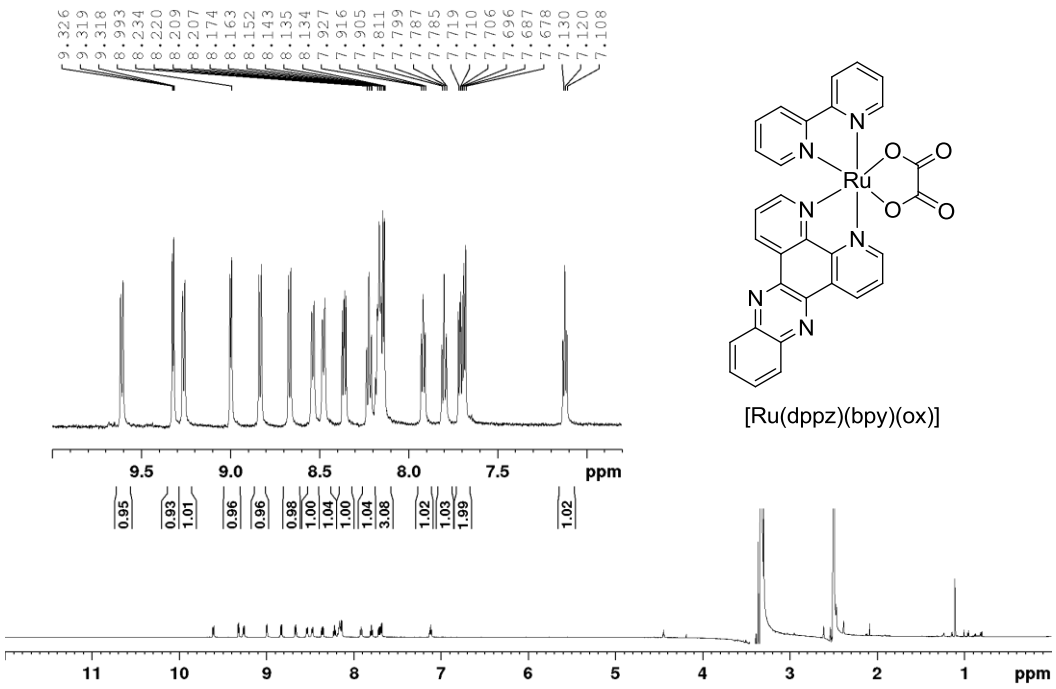

Figure 3.6: ^1H NMR (400 MHz, DMSO-d_6) of [Ru(dppz)(bpy)(ox)] with region of interest inset alongside the chemical structure.

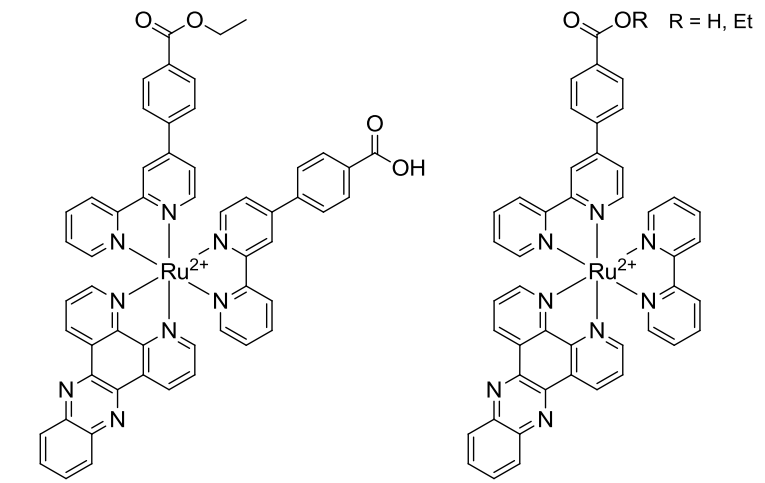

Figure 3.7: Structures of the Ru(II)-dppz tris heteroleptic complexes synthesised in high yield via the oxalate route.

---

attempted. Initially the route proved unsuccessful using the non-aqueous hydrolysis protocol implemented for the free ligand which did not transfer to the metal complex. However, applying the method described by Sattegeri *et al*.[103] provided the acid quantitatively up to the semi-gram scale using a reaction system comprising LiOH in THF/CH_3OH/H_2O 4/1/1 followed by acidic work-up and PF_6^- precipitation. Importantly, no alkaline hydrolysis of the coordination core of the metal complex was observed under these conditions. This approach eliminates the need for separate acid and ester complexation reactions and enables access to the acid complex by a more straightforward method.

The complexes; $[Ru(dppz)(bpy)(bpyArCOOH)]^{2+}$, $[Ru(dppz)(bpy)(bpyArCOOEt)]^{2+}$ and di-conjugatable $[Ru(dppz)(bpyArCOOH)(bpyArCOOEt)]^{2+}$; were structurally characterised as PF_6^- salts by ^1H NMR, ^{13}C NMR, elemental analysis and HRMS (Appendix A and elsewhere[11]). The ester function of the complexes containing the bpyArCOOEt ligand remained intact as confirmed by the signals observed in the aliphatic regions of the ^{13}C NMR spectra at *ca*. 14.5 and 62.2 ppm for the methyl and methylene carbons respectively. The ^1H NMR spectra of the bpyArCOOEt complexes also exhibited the two signals assignable to the ethyl ester at *ca*. 4.36 (2 H) and 1.37 ppm (3 H), but the presence of isomers was evident by an inequivalence in both signals which was observed as on overlay of quartets and triplets.

This is illustrated for the di-conjugatable complex in Figure 3.8. The overlaying signals integrate approximately equally suggesting an equal mixture of geometric isomers in the bulk compound. This was expected since the reaction route from the oxalate would not be likely to impart any selectivity. The *tris*-heteroleptic complexes were also analysed by HRMS which in all cases found ion clusters bearing a Ru isotope pattern at m/z values corresponding to $[M^{2+} + PF_6^-]^+$ (Table 3.4).

Table 3.4 – HR-MS data for $[Ru(dppz)(bpy\text{-}R)(bpyArCOOR)]^{2+}$ and precursors.

Compound	Calculated (m/z)	Found (m/z)	Assignment
$[Ru(dppz)(bpy)(bpyArCOOH)](PF_6)_2$	961.1183	961.1190	$[M^{2+} + PF_6^-]^+$
$[Ru(dppz)(bpy)(bpyArCOOEt)](PF_6)_2$	989.1490	989.1477	$[M^{2+} + PF_6^-]^+$
$[Ru(dppz)(bpyArCOOH)(bpyArCOOEt)](PF_6)_2$	1109.1701	1109.1757	$[M^{2+} + PF_6^-]^+$
$[Ru(dppz)(bpy)(ox)]$	651.0325	651.0358	$[M + Na]^+$

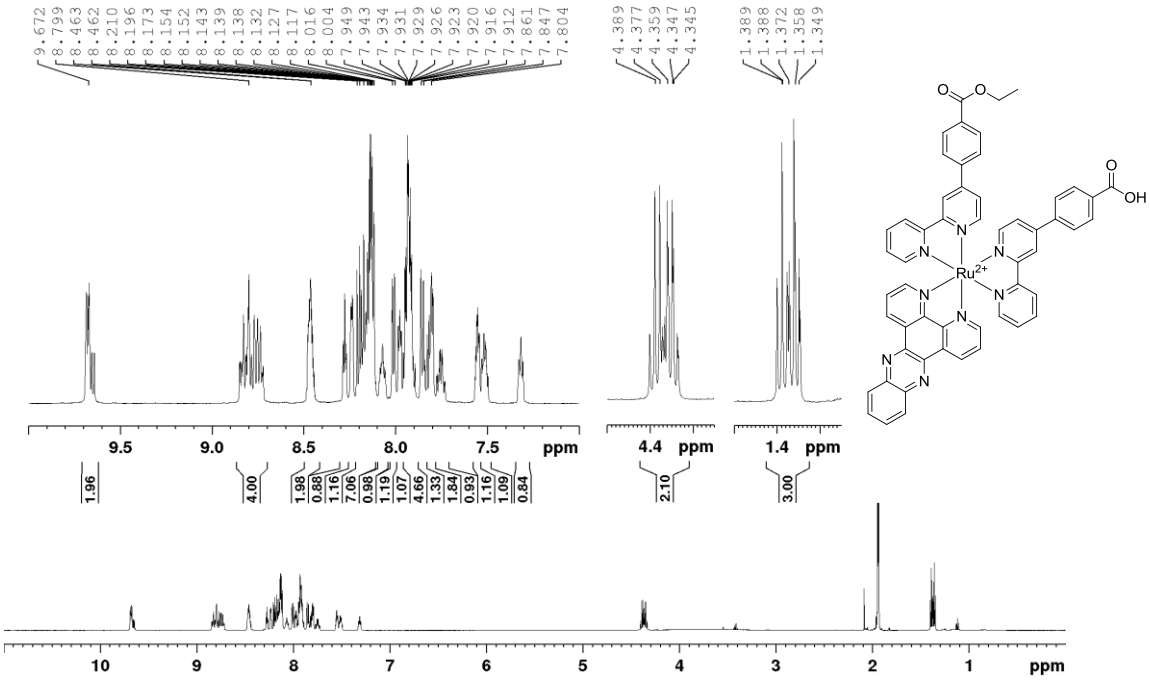

Figure 3.8: ^1H NMR (600 MHz, CD_3CN) of $[Ru(dppz)(bpyArCOOH)(bpyArCOOEt)](PF_6)_2$ with insets to show chemical structure and regions of interest.

Isolation and assignment of the geometric isomers of [Ru(dppz)(bpy)(bpyArCOOH)]$^{2+}$

[Ru(dppz)(bpy)(bpyArCOOR)]$^{2+}$ is a key complex in the context of the wider aims of this thesis. This structure exists as two geometrical isomers due to the asymmetry of the bpyArCOOR ligand (Figure 3.9). Both isomers are also racemic mixtures of their respective enantiomers but chiral resolutions were not attempted herein. Considering the geometric isomers, the orientation of the bpyArCOOH ligand in the Ru(II) complex may have significant impact on DNA binding affinity. For example, Boynton *et al*. developed [Ru(Me$_4$phen)$_2$(dppz)]$^{2+}$ (Me$_4$phen = 3,4,7,8-tetramethyl-1,10-phenanthroline) which is a light-switch complex that selectively targets mismatch DNA, operating on the basis of the steric bulk of the ancillary Me$_4$phen ligands that prohibit its binding to well-matched sequences.[104] Thus, attempts were made to resolve the isomers of the *tris*-heteroleptic Ru-bpyArCOOR complexes. The carboxylic acid functional group of [Ru(dppz)(bpy)(bpyArCOOH)]$^{2+}$ permitted the successful resolution of its two isomers under low loading (< 5 mg) on silica preparative plates (pTLC) using 70/26/4/2 $CHCl_3$/CH_3OH/H_2O/AcOH as solvent. As shown in Figure 3.10, ^{1}H NMR confirmed the resolution of the isomers with distinct spectra obtained for each isomer which when normalised are superimposable on the spectrum of the bulk mixture. In particular, the set of peaks at 8.70 – 8.85 ppm are different and easily distinguished in the spectra of each isomer.

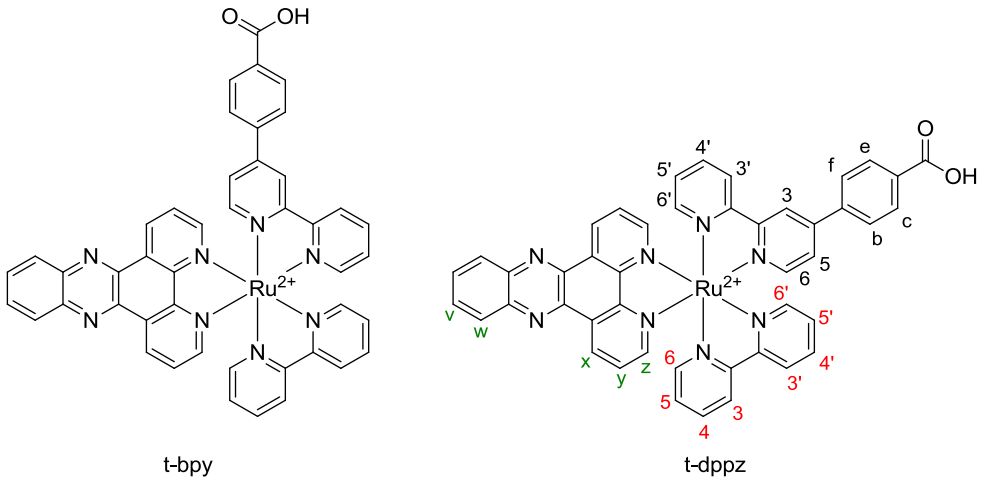

Figure 3.9: Structures of the two isomers of [Ru(dppz)(bpy)(bpyArCOOH)]$^{2+}$.

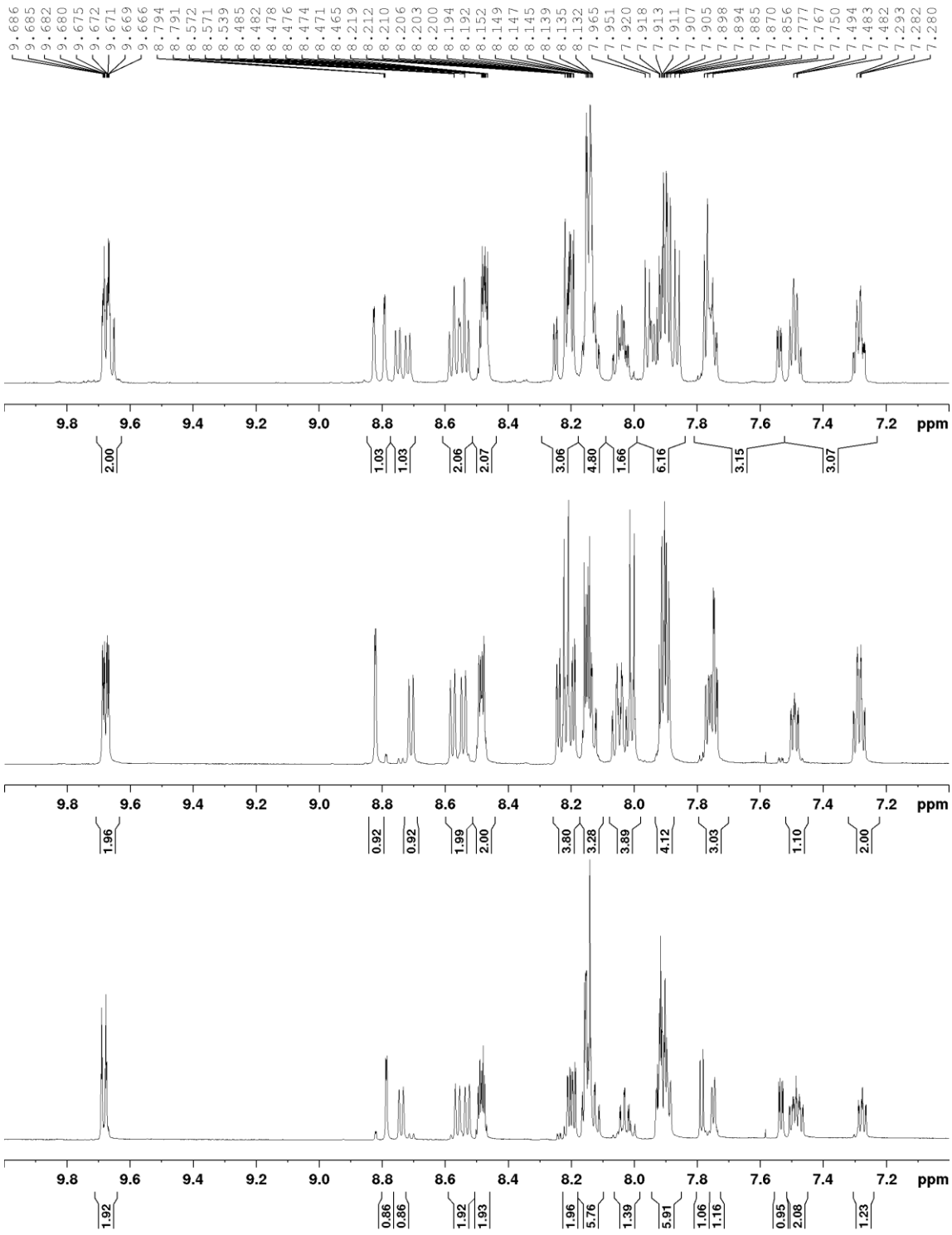

Figure 3.10: ^{1}H NMR (600 MHz, CD_3CN) spectra of $[Ru(dppz)(bpy)(bpyArCOOH)]^{2+}$. Top: the bulk mixture. Middle: the t-dppz isomer. Bottom: the t-bpy isomer.

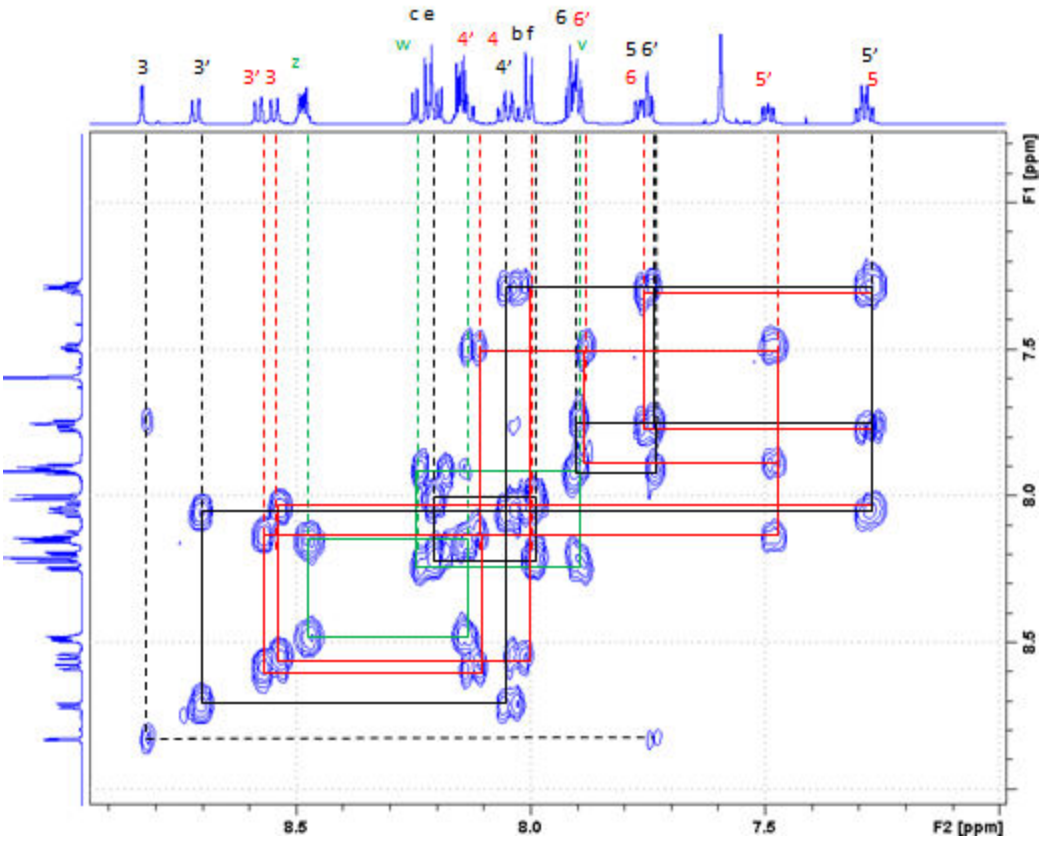

Figure 3.11: COSY spectrum of the t-dppz isomer to indicate peaks assigned to bpy (red), bpyArCOOH (black) and dppz (green).

COSY spectra of the isolated isomers enabled a tentative assignment of the peaks in the NMR spectra and hence, an indication of their configuration (Figure 3.11). Freedman *et al*. and Meggers *et al*. both used 2D NMR techniques and magnetic anisotropic effects to assign the peaks of the NMR spectra of *tris*-heteroleptic complexes.[56,105] Assignments herein were made using a similar basis and comparison to the spectra of free ligands and the model complex; $[Ru(bpy)_2(dppz)]^{2+}$.[96] The asymmetric ligand, bpyArCOOH, was easily assigned by assuming that, like $[Ru(bpy)_3]^{2+}$, the 3 and 3' peaks (see Figure 3.9) do not undergo significant coordination induced shifts (CIS).[106] Thus, the 3'/4' cross-peak was used as a reference point for the full assignment of the bpyArCOOH signals. The dppz signals were easily distinguished by their splitting pattern and resonances upon comparison to $[Ru(bpy)_2(dppz)]^{2+}$. Notably, in both cases, the H-substituents immediately adjacent to the coordinating nitrogen of the pyridine rings (z, 6, 6') underwent characteristic CIS upfield,

while the signals at the 4-positions of these rings shifted moderately downfield. Interestingly, the dppz peak positions in both isomer spectra were almost identical and comparable to that of $[Ru(bpy)_2(dppz)]^{2+}$ which indicated that bpyArCOOH does not exert any additional anisotropic effects on the dppz ligand relative to bpy. The bpy peaks were observed as a pair of 4-membered cross-correlated sets in the COSY spectrum corresponding to the asymmetric environments of the pyridine rings upon coordination, where each ring is *trans* to either dppz (n') or bpyArCOOH (n). Additionally, where measurable, J-coupling values (provided in the experimental) corroborate COSY data and peak assignments with characteristic bpy H_5/H_6 coupling determined in the range 5 – 6 Hz and H_4/H_5 or H_3/H_4 couplings typically about 8 Hz.

The configuration of the isomers was tentatively assigned using magnetic anisotropy which occurs due to the relative proximity of bpy and bpyArCOOH to the ring current of the dppz ligand. Meggers *et al*. showed using NOESY experiments that phen imparts a larger anisotropic shielding effect than dppz due to the greater electron delocalisation across the extended π-system of dppz which decreases the local ring current for anisotropic shielding.[105] However, in the present case, it is still reasonable to assume that dppz exerts a larger anisotropic effect than bpy due to its extended aromatic system. Hence, by analysis of the relative peak positions of bpyArCOOH, it was possible to assign the orientation of this ligand relative to dppz, with the arylated pyridine likely in an environment of enhanced anisotropic shielding and shifted upfield when in a *cis*-configuration to dppz. Accordingly, a study of the relative peak positions of both spectra revealed a clear difference in the shifts of both pyridyl rings of bpyArCOOH as indicated in Table 3.5. This enabled an assignment of the isomers as t-bpy and t-dppz to indicate the aryl-unit of bpyArCOOH being *trans* to either bpy or dppz respectively. In the t-bpy spectrum, the 6, 5 and 3 signals (of the substituted ring) were all shifted upfield due to anisotropic shielding from the dppz ring current. In contrast, the 6', 5', 4' and 3' signals were all shifted downfield due to the orientation of the unsubstituted ring being *trans* and away from dppz. A similar approach enabled the assignment of the bpy signals in both isomer spectra, since the pyridyl ring *cis* to dppz (n) likely experiences an anisotropic shielding effect that the ring in a *trans* orientation (n') does not.

Table 3.5 – ^{1}H NMR (600 MHz, CD_3CN) shifts of the bpyArCOOH ligand in the isolated isomers of $[Ru(dppz)(bpy)(bpyArCOOH)]^{2+}$. For clarity, the signals more relatively downfield are listed in bold.

bpyArCOOH signal	**t-dppz isomer δ (ppm)**	**t-bpy isomer δ (ppm)**
Substituted pyridyl ring:		
3	**8.83**	8.80
5	**7.76**	7.54
6	**7.91**	7.78
ce	**8.21**	8.12
bf	**8.00**	7.90
Unsubstituted pyridyl ring:		
3’	8.71	**8.74**
4’	8.04	**8.15**
5’	7.28	**7.49**
6’	7.76	**7.88**

Analysis of the fully assigned spectra revealed some observations that support the identity of the isomers in each case. In the t-bpy spectrum, the 6’, 5’ and 4’ signals of bpyArCOOH would be expected to have a similar resonance to the 6’, 5’ and 4’ signals of the bpy ligand since both systems are in a similar environment being *cis* to each other and *trans* to dppz. Indeed, these signals were separated by less than 0.05 ppm in each case, whereas the signals of the other pyridyl ring were all shifted upfield. Comparably, in the t-dppz isomer, the 6, 5 and 4 signals of bpy and the 6’, 5’ and 4’ signals of bpyArCOOH are in a similar environment being *trans* to each other and *cis* to dppz. Again, these signals were separated by less than 0.05 ppm in the NMR spectrum. Furthermore, the peaks of the pyridyl ring of bpy *cis* to dppz in each case approximated to those observed in $[Ru(bpy)_2(dppz)]^{2+}$. The impact of isomerism on the DNA-binding ability of the probes is discussed in Chapter 4 of this thesis.

3.2.4 Ru-oxalates as alternative intermediates towards *bis*-heteroleptic complexes of Ru(II).

The success of the oxalate route in *tris*-heteroleptic complex syntheses prompted a return to *bis*-heteroleptic complexes to investigate whether [Ru(N^N)$_2$(ox)] type complexes could be prepared directly from *cis*-[Ru(DMSO)$_4$Cl$_2$] as an alternative to the classical dichloride intermediate; [Ru(N^N)$_2$Cl$_2$] (Scheme 3.17). The traditional route works reasonably well for simple ligand systems such as Ru(bpy/phen)$_2$Cl$_2$ but is less reliable for expanded, more lipophilic systems that are useful across a host of domains including bio-imaging. Three prominent examples in this context are; dppz for aqueous sensitive light-switching luminescence,[67,107] 4,7-diphenyl-1,10-phenanthroline (dpp) for enhanced cellular uptake and increased sensitivity of the excited state towards quenchers such as oxygen,[108,109] and 2,2'-biquinoline (biq) for red-shifted absorbance towards the photodynamic window.[110,111] Additionally, as a comparison to the other synthetic routes described above, [Ru(bpyArCOOH)$_2$(ox)] was prepared as precursor to [Ru(bpyArCOOH)$_2$(dppz)]$^{2+}$.

Reaction of *cis*-[Ru(DMSO)$_4$Cl$_2$] with 1.5 equivalents of oxalate and two equivalents of the appropriate ligand in ethylene glycol under reflux (> 3 h) successfully provided the target [Ru(N^N)$_2$(ox)] complexes. The Ru-oxalates were easily isolated because of their precipitation from cold water. Residual starting material was easily washed free using water and an appropriate organic solvent such as acetone, methanol or dichloromethane in which the Ru-oxalate is only moderately soluble. By this simple approach, the dpp and dppz Ru-oxalates; [Ru(dppz)$_2$(ox)] and [Ru(dpp)$_2$(ox)], were obtained pure as black solids in yields greater than 90 % and their structures were confirmed by ^{1}H NMR analysis (Appendix A). The biq complex, [Ru(biq)$_2$(ox)] required further purification but its stability and solubility, in contrast to the analogous dichloride complex, permitted purification by column chromatography (silica, 70/26/4 $CHCl_3/CH_3OH/H_2O$ as eluent). After purification, [Ru(biq)$_2$(ox)] was obtained as a jade-green solid in 68 % yield. This complex exhibited the expected asymmetrical pattern in the ^{1}H NMR spectrum as depicted in Figure 3.12. [Ru(bpyArCOOH)$_2$(ox)] was obtained directly without chromatography as a purple/black powder in 78 % yield. The reduced yield in the case of the biq and bpyArCOOH complexes is likely due to the relatively poor solubility of the ligands but prolonging the reaction in

future syntheses or reducing the aqueous ratio of the solvent will likely drive quantitative conversion.

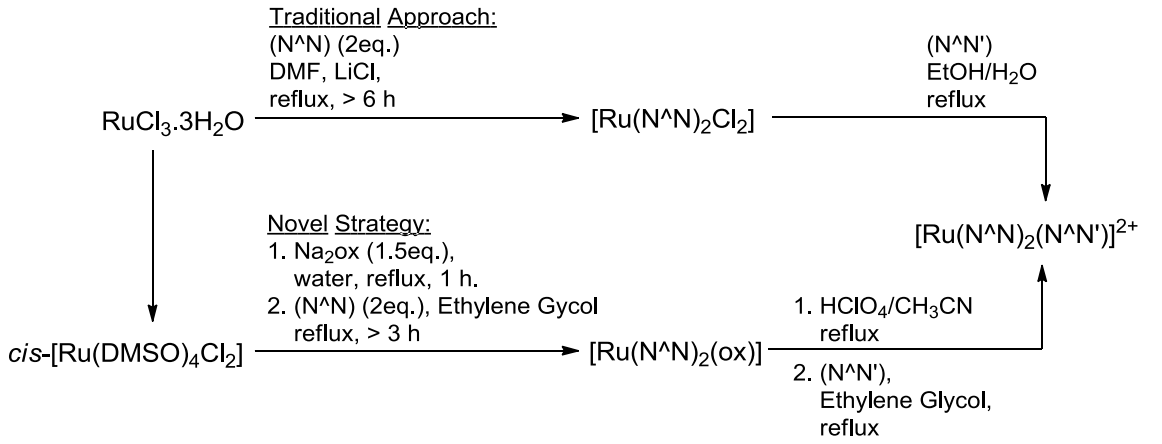

Scheme 3.17: An alternative route to *bis*-heteroleptic Ru(II) complexes via Ru-oxalate intermediates.

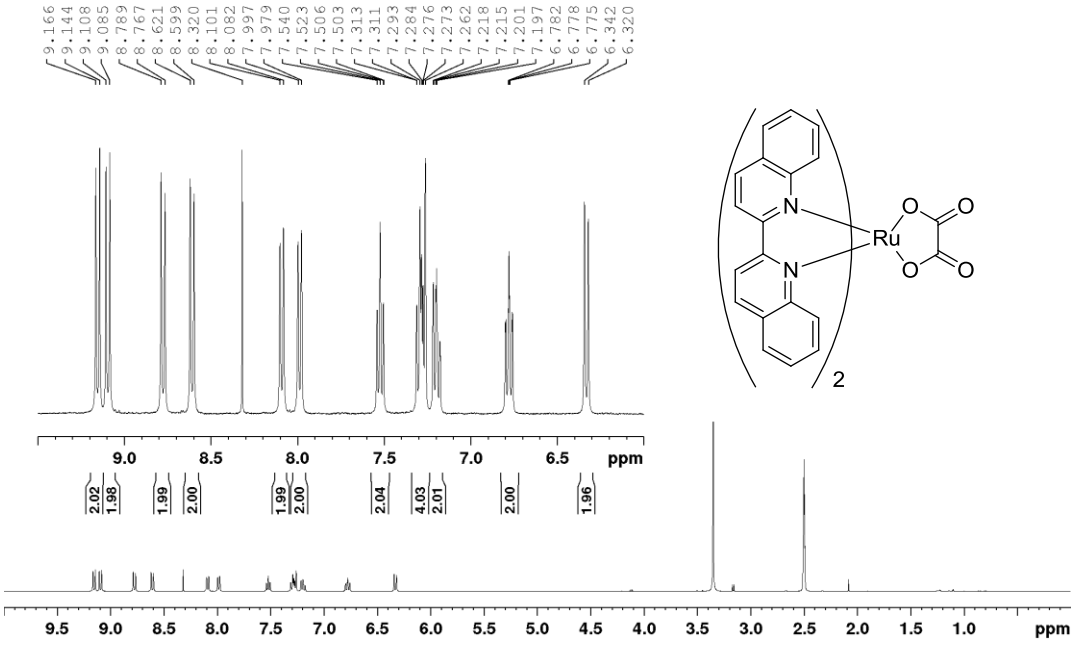

Figure 3.12: ^{1}H NMR (400 MHz, DMSO-d_6) spectrum of [Ru(biq)$_2$(ox)]. Peak at 8.32 ppm assigned to residual $CHCl_3$.

To test the applicability of the $[Ru(N^N)_2(ox)]$ complexes, the oxalates were subjected to acid cleavage and subsequent reaction with a ternary ligand. $[Ru(biq)_2(ox)]$ was converted to the purple complex, $[Ru(biq)_2(aphen)](PF_6)_2$, in 85 % yield. $[Ru(dppz)_2(ox)]$ was reacted with aphen to provide $[Ru(dppz)_2(aphen)](PF_6)_2$ as a red solid in 70 % yield following purification on silica. ^{1}H NMR analysis of both complexes confirmed their successful synthesis and expected structure. For example, the spectra in CD_3CN indicated a broad singlet integrating to 2 H at δ 5.16 and 5.60 ppm indicative of the amine functional group of Ru-bound aphen, for $[Ru(biq)_2(aphen)](PF_6)_2$ and $[Ru(dppz)_2(aphen)](PF_6)_2$ respectively (Figure 3.13).

$[Ru(dppz)_2(ox)]$ was reacted with bpyArCOOEt to provide $[Ru(dppz)_2(bpyArCOOEt)](PF_6)_2$ and the pendant ester of bpyArCOOEt was evident as quartet and triplet signals in the aliphatic region of the ^{1}H NMR spectrum at 4.36 ppm (2 H) and 1.38 (3 H) respectively. Additionally, for the ester complex, HRMS found a mass cluster at *ca*. 1115 *m/z* bearing a Ru isotope pattern and corresponding to $[M^{2+} + PF_6^-]^+$ (*m/z* calculated: 1115.1703; found: 1115.1763). 'On-complex' hydrolysis of the ester provided the corresponding acid complex quantitatively. $[Ru(dppz)_2(bpyArCOOH)](PF_6)_2$ was characterised by ^{1}H NMR which

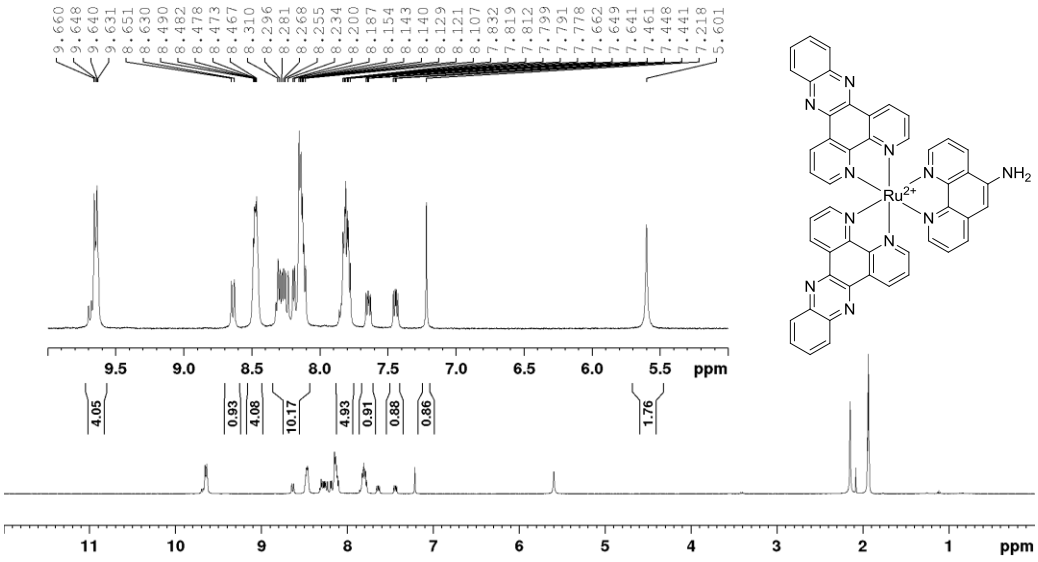

Figure 3.13: ^{1}H NMR (400 MHz, CD_3CN) spectrum of $[Ru(dppz)_2(aphen)](PF_6)_2$ with insets to indicate structure and region of interest.

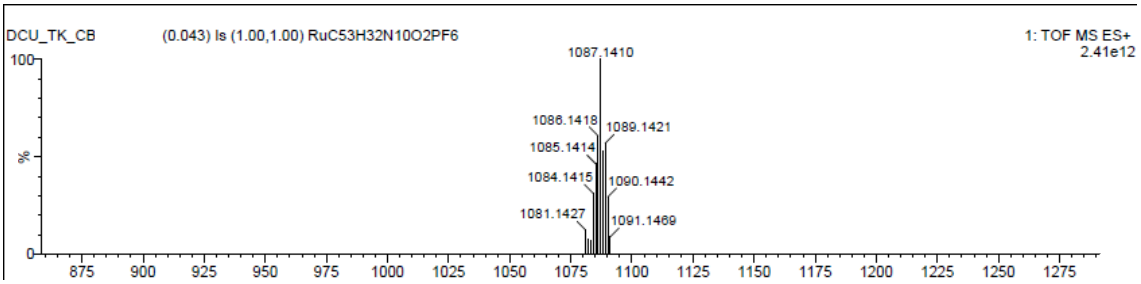

Figure 3.14: HRMS (ESI-TOF, MS+) spectrum of $[Ru(dppz)_2(bpyArCOOH)]^{2+}$ indicating a peak assignable to $[M^{2+} + PF_6^-]^+$.

---

indicated an absence of the precursor ester signals, and HRMS returned a peak cluster at *ca*. 1087 *m/z* attributable to $[M^{2+} + PF_6^-]^+$ (*m/z* calculated: 1087.1390; found: 1087.1410, see Figure 3.14).

$[Ru(bpyArCOOH)_2(dppz)]^{2+}$ was obtained from $[Ru(bpyArCOOH)_2(ox)]$. Characterisation of the perchlorate salt matched the data for the complexes synthesised by the classical method via $[Ru(bpyArCOOR)Cl_2]$ and the DMSO route via $[Ru(dppz)(DMSO)_2Cl_2]$. All complexes were obtained in over 70 % yield from the oxalate and with further development to expand generality, the oxalate route may represent a valuable avenue towards both *bis*- and *tris*-heteroleptic complexes.

3.2.5 Efficient routes to *bis* and *tris* heteroleptic complexes of Ru(II): An analysis.

In summary, this chapter describes efficient non-classical routes to asymmetric, mono- and di- conjugatable, *bis*- and *tris*- heteroleptic complexes of Ru(II) that, in some cases, also bear environmentally sensitive dppz ligands. Combined, this work clearly illustrates the benefits of Ru-DMSO chemistry as effective precursors to Ru(II) species. Arguably, the discovery of polypyridyl Ru-oxalates as versatile alternative intermediates to Ru-dichlorides is synthetically even more valuable and could yet precipitate a paradigm shift in the field, especially for highly lipophilic ligand systems. In general, Ru-oxalates are more stable, demonstrate superior solubility in common solvents, are accessible quantitatively from *cis*-$[Ru(DMSO)_4Cl_2]$, and can be easily cleaved in dilute acid.[100,101,112–114] In contrast, Ru-dichlorides are typically obtained impure by reductive thermal decarbonylation in DMF from

$RuCl_3.3H_2O$, are hydrolysis-prone and exhibit unpredictable solubility which can complicate purification, and in some cases reactivity with another ligand requires Ag^+ mediated cleavage of both chloride ligands.[22,25] The superiority of both alternate routes presented in this work was underlined in the case of *bis*-heteroleptic complexes such as $[Ru(dppz)(bpyArCOOH)_2]^{2+}$; where the reproducible net yield of the *tris*-chelate from commercial $RuCl_3.3H_2O$ via $[Ru(dppz)(DMSO)_2Cl_2]$ or $[Ru(bpyArCOOH)_2(ox)]$ intermediates, at 95 % and 66 % respectively, greatly exceeds the return from the classical method which at best afforded the final complex in 50 % yield start-to-finish following difficult purification. Acid hydrolysis prohibits the use of the oxalate route to generate $[Ru(dppz)(bpyArCOOEt)_2]^{2+}$; but this complex was efficiently obtained instead via $[Ru(dppz)(DMSO)_2Cl_2]$ in 82 % yield following straightforward purification.

The development of a protocol towards *tris*-heteroleptic complexes mediated by Ru-DMSO and Ru-oxalate intermediates is a useful advance in Ru(II) polypyridyl synthesis. The methodology offers exciting potential to generate triply functional Ru(II) architectures for application across all domains of Ru(II) research. The protocol was demonstrated to achieve complexes of the form, $[Ru(dppz)(bpy\text{-}R)(bpy\text{-}R')]^{2+}$; in unprecedented yields exceeding 82 % start-to-finish from commercial $RuCl_3.3H_2O$ (Scheme 3.18). To date, the closest net yield for a *tris*-heteroleptic complex was achieved by the 5-step procedure reported by Myahkostupov and Castellano who implemented Mann's protocol to provide a Ru(II) *tris*-heteroleptic complex from $[Ru(Bz)Cl_2]_2$ precursor in 61% yield.[56,57] The oxalate route in our method is again advantageous allowing selective stoichiometric addition of ligand to the Ru(II) sphere. It also proceeds via standard synthetic methods using commonly available materials, for example; avoiding the need for solid phases[58] or photodecarbonylation[29]. Ru-oxalates also benefit from increased stability,[101] favourable solubility and controlled reactivity of the oxalate intermediate relative to Ru-dichlorides as discussed above which facilitates purification if required by conventional methods such as recystallisations or chromatography. Undoubtedly, initial studies are promising but it is hoped further research on these non-classical routes to both *bis*- and *tris*- heteroleptic complexes by our group and others will unveil the generality of the protocols and this will be the ultimate test of their sustained utility.

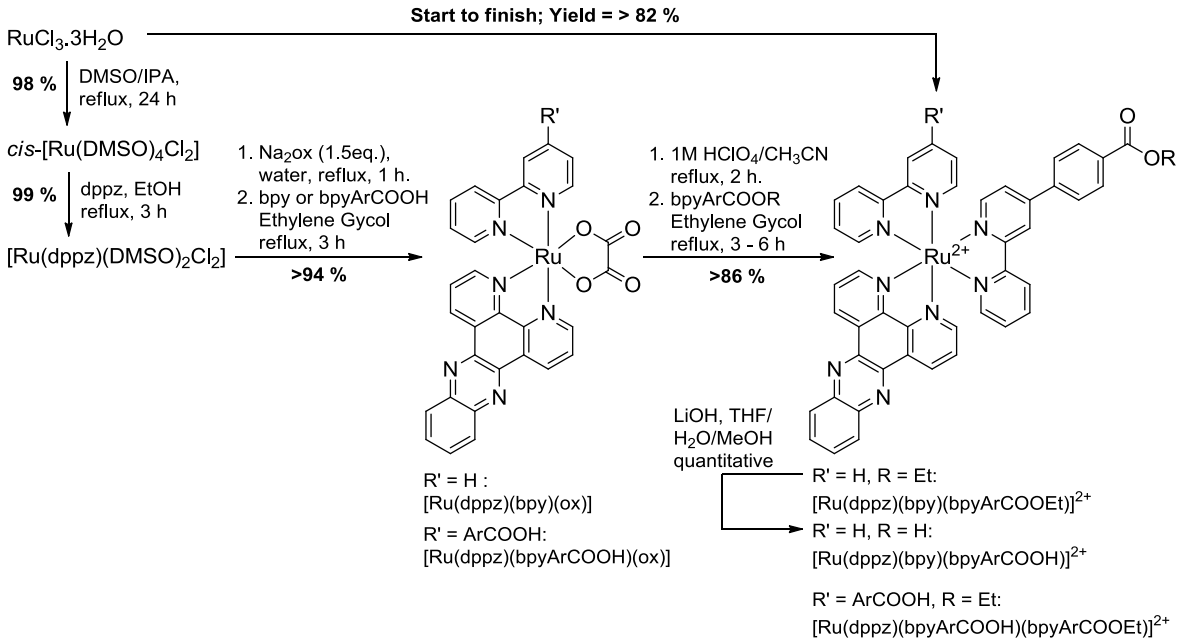

Scheme 3.18: A summary of the route to *tris*-heteroleptic Ru(II) complexes applied in this thesis.

3.2.6 Synthesis of Ru(II) conjugates using established in-house methods.

Conjugation to all Ru(II) parent complexes was achieved using amide coupling to yield a stable conjugate for bioimaging. In all cases, the Ru(II) parent complexes were functionalised with carboxy termini to facilitate coupling with amine groups on peptides or PEG chains. Previous protocols in our group utilised EDC/NHS coupling with isolation of the Ru-succinimide intermediate *en route* to the final conjugate.[85] However, this method was quite inefficient with net conjugation yields around 30 %, probably because of hydrolysis of the NHS-intermediate during chromatographic purification or in the second step on reaction with free peptide in phosphate buffer.[68] In preparation of naphthyridyl-BODIPY-PEG conjugates an alternative one-step HBTU coupling procedure in DMF in the presence of diisopropylethylamine (DIPEA) as base was effective.[78] This was later exploited for metal complexes to yield octaarginine (R8) derivatives of Os(II) and Ru(II), and a dinuclear Ru(II) conjugate bridged with a mitochondrial penetrating peptide (MPP).[65,66,70,92] Yields were still moderate at 30 – 50 % but conjugation only required a single step in comparison to the EDC/NHS method.

In this work, a similar peptide coupling strategy was initially implemented in DMF employing two equivalents of HBTU coupling agent and a slight excess of peptide (1.1 eq.) for every equivalent of Ru-COOH in the presence of DIPEA as base. This method provides the crude Ru-peptide conjugates, precipitated from the reaction solution as PF_6^- salts, generally contaminated with unreacted parent complex. Ideally, purification would have been carried out using reverse-phase chromatography on C18-silica phases with acetonitrile (or methanol)/water gradients modified with an ion-pairing reagent such as TFA or formic acid.[23,115] However, analytical column chromatography indicated that this method would be impractical for our scale. Instead, reverse-phase preparative thin layer chromatography (RP-pTLC) was used. Unreacted parent complex was easily separated from the conjugate under high organic ratio (generally 95/5) in acetonitrile/water mixtures spiked with 0.1 % TFA. The dry solid phase was cleaved from the glass-back plates and packed into a short filter column which enabled elution of the conjugate at higher aqueous ratio as a concentrated band, permitting straightforward precipitation using NH_4PF_6. Conversion to the chloride form was conveniently accomplished using TBAC/acetone precipitation, followed by methanol dissolution, filtration and evaporation to provide pure solids that are stable enough to be dried briefly in the oven at *ca*. 60 ºC. The purified conjugates were stored as solids in the freezer in the long-term to prevent degradation.

This protocol was sufficient to yield conjugates of $[Ru(bpy)_2(phenArCOOH)]^{2+}$ functionalised with an R8 non-specific uptake vector (Ru-phen-R8) and the Penetratin peptide,[116] exploited herein to target the endoplasmic reticulum, (Ru-phen-ER, see Chapter 6). Furthermore, $[Ru(dppz)(bpy)(bpyArCOOH)]^{2+}$ (as its mixture of isomers) was successfully conjugated to a nuclear localising signal peptide (NLS) to provide Ru-NLS – a light-switch probe designed to image nuclear DNA structure in the live cell. The structures of these conjugates are provided in Figure 3.16. Ru-phen-R8 was synthesised previously by our group[92] and HRMS data as part of this work confirmed its synthesis, for example, finding peaks indicative of the Ru isotope pattern at m/z = 2220.0012 corresponding to the uncharged peptide conjugate; $[M^{2+} + PF_6^-]^+$ (calculated; 2220.0054). Ru-phen-ER was characterised by HRMS and ^{1}H NMR which showed the expected signals for a 1:1 conjugate.[117] The ^{1}H NMR spectrum collected in acetone-d_6 was quite noisy due to extensive hydrogen bonding across the peptide residue and in subsequent work, conjugates were analysed in acetonitrile-d_3 (as

PF_6^- salt) or methanol-d_4 (as Cl^- salt) spiked with D_2O to reduce the complexity of the spectrum. For example, the ^1H NMR spectrum of Ru-NLS in CD_3CN/D_2O shown in Figure 3.15 is much cleaner and provides a clear indication of a 1:1 conjugate judging by the total relative integration of the Ru(II) core and peptide signals. In particular, setting the integration of the aromatic Ru(II) peaks to 29 H, the expected 10 H integration in the region 3.5 – 5 ppm, assignable to peptide alpha-H, provides strong evidence of mono-conjugation. Further characterisation by HRMS returned *m/z* = 2342.1399, indicative of the fully protonated conjugate (calculated: 2342.0035). The applications of these conjugates are described in Chapter 4 and Chapter 6 of this thesis.

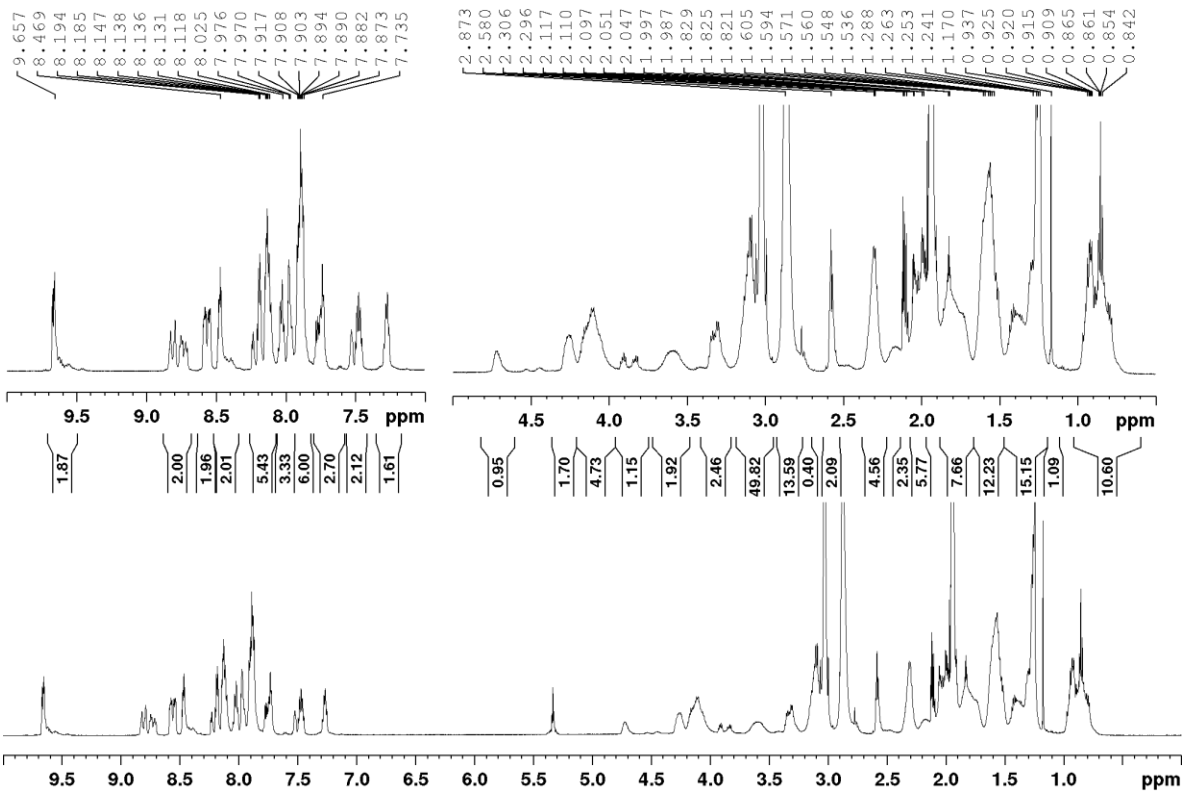

Figure 3.15: ^1H NMR (600 MHz, CD_3CN/D_2O) spectrum of Ru-NLS with insets to show regions of interest.

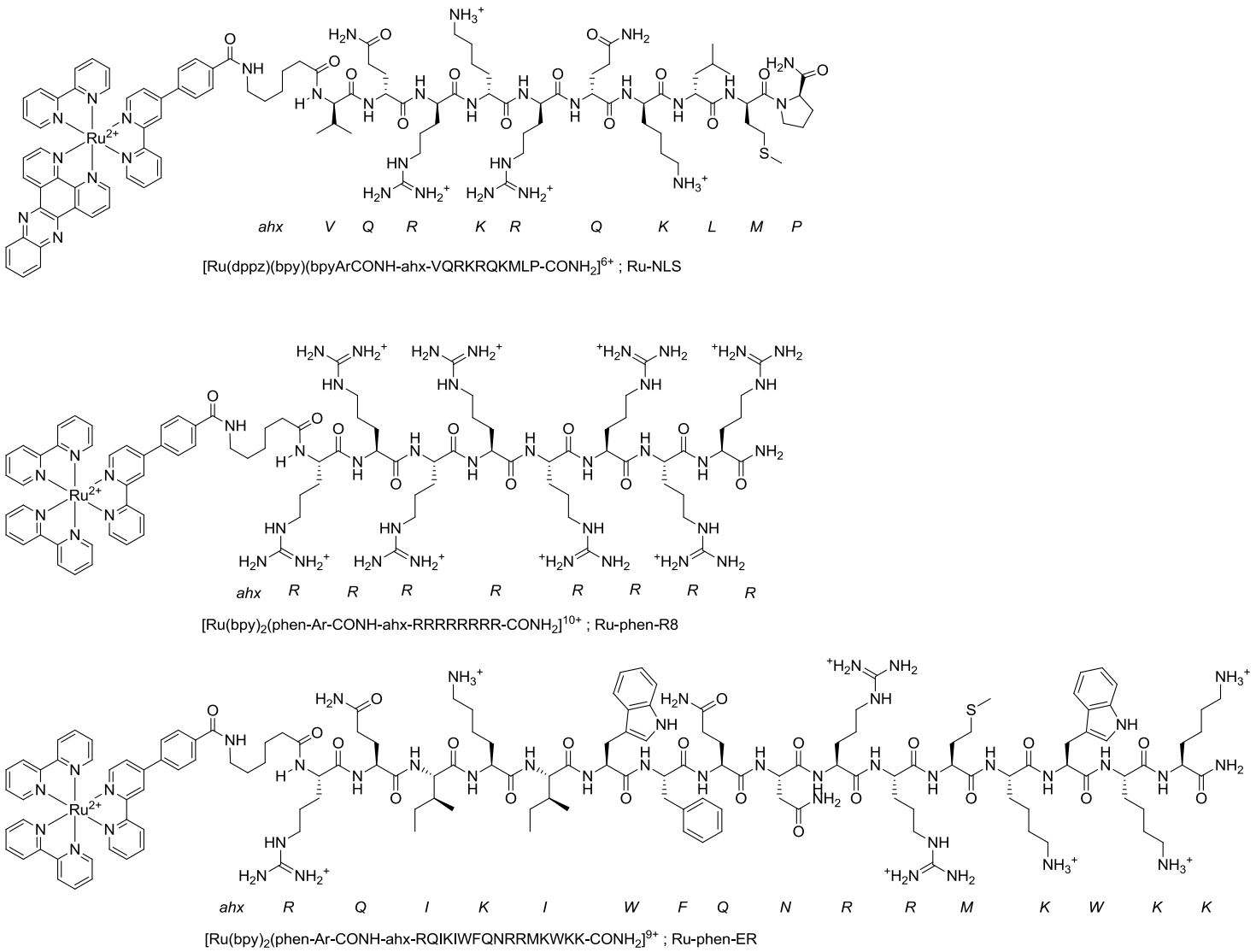

Figure 3.16: Structures of Ru-NLS, Ru-phen-R8 and Ru-phen-ER.

3.2.7 Towards quantitative mono-conjugations.

The main difficulty in synthesising conjugates by established in-house methods such as the HBTU coupling was an inefficient reaction and time-consuming purifications. Ideally, the conjugates should be obtainable by simple precipitation from the reaction mixture. Increasing the equivalents of the peptide and coupling reagent, while expensive, can dramatically improve yields. However, excess uranium/guanidinium reagents such as HBTU have been reported to guanylate free amines and should be used in stoichiometric ratio to the carboxylic acid.[87] An alternative reagent is PyBOP which demonstrates similar coupling activity to HBTU and can be used in excess.[88] Accordingly, a modified protocol was developed and employed four equivalents of PyBOP and two equivalents of peptide per mole of Ru-COOH in the presence of excess DIPEA as base in DMF. Satisfyingly, overnight stirring at room temperature yielded quantitative conversion as indicated by HPLC (RP-C18, 0.1 % TFA in CH_3CN/H_2O gradient). Isolation was facile using PF_6^- precipitation which forms an insoluble salt that was filtered and washed with water to remove free peptide residues (only the highly cationic Ru-R8 conjugates demonstrated minor solubility as the PF_6^- form and cold washing with PF_6^- (aq.) instead of neat deionised water in these cases inhibited their solubility). Residual organics were then easily separated by washing following dissolution of the crude solid in acetone and treatment with TBAC to precipitate the chloride form of the conjugate which was filtered and washed with acetone.

As a side study, this method was trialled under microwave irradiation in an attempt reduce the reaction time. Peptide formation has been reported by others in minutes using both solid and solution phase synthesis and peptides usually remain stable under irradiation even when side chains are unprotected.[86,118,119] Development work revealed that our PyBOP protocol could be modified to as low as 1.2 equivalents of peptide in some cases to provide Ru(II) conjugates quantitatively in two hours under microwave irradiation set to cycle through ramps up to 200 W and 150 ºC. ^{1}H NMR and HPLC indicated stability of the reagents under these conditions and Ru(II)-dppz conjugates could be reproducibly synthesised by the approach. This protocol is valuable when validated for a given set of substrates but more delicate systems such as Ru-tap complexes are prone to degradation under the same conditions (see Chapter 5 for conjugates of this type).

3.2.8 Expanding the range of conjugates using the optimised procedure.

Optimisation of the coupling protocol permitted rapid access to an expanded range of conjugates. $[Ru(dppz)(bpy)(bpyArCOOH)]^{2+}$ (as its mixture of isomers) was quantitatively converted to the R8 and MPP derivatives; Ru-R8 and Ru-MPP, whose structures are given in Figure 3.17. The MPP peptide was previously used to bridge two Ru(II) units by conjugation at the linker ahx-amine and the terminal lysine residue of the peptide; $[L_2Ru\text{-}phen\text{-}ahx\text{-}FrFKFrFK\text{-}phen\text{-}RuL_2]^{7+}$. Herein, the MPP sequence used was identical except for the terminal lysine which was acetyl blocked to prevent the formation of dinuclear conjugates (i.e. H_2N-Ahx-FrFKFrFK(Ac)-$CONH_2$). Mono-conjugation for both Ru-R8 and Ru-MPP was confirmed by ^1H NMR and HRMS analysis. ^1H NMR in CD_3OD/D_2O indicated the expected signals for both the peptide and the Ru(II) core and the alpha-H region (δ 4.0 - 4.6 ppm) integrated to 8 H in both cases corresponding to the eight amino acids present in each peptide. Ru-MPP also notably displayed an additional broad peak in the aromatic region assignable to the four Phe residues of the conjugated peptide (Figure 3.18). MALDI-qTOF HRMS spectrum for Ru-R8 was straightforward and exhibited peaks assignable to $[M]^+$ and $[M + PF_6^-]^+$ (for example; calculated for $[Ru\text{-}R8]^+$: 2177.0625, found: 2177.0671). Ru-MPP was analysed using a Q-Exactive system which can lead to multiply charged ions. Clusters illustrating the Ru isotope pattern were identified as $[M]^{+5}$, $[M\text{-}H]^{+4}$ and $[M\text{-}H+TFA^-]^{3+}$ at *ca*. 426, 532 and 747 *m/z* respectively. HRMS data is summarised in Table 3.6.

Table 3.6 – HR-MS data for the Ru-dppz conjugates with analysis method as indicated.

Compound *Analysis Technique*	**Calculated (m/z)**	**Found (m/z)**	**Assignment**
Ru-NLS *MALDI-qTOF*	2342.0035	2342.1399	$[Ru\text{-}NLS^{2+} + 4H\,(\text{basic residues}) + PF_6^-]^+$
Ru-R8 *MALDI-qTOF*	2177.0625 2322.0261	2177.0671 2322.1116	$[Ru\text{-}R8]^+$ $[Ru\text{-}R8^{2+} + PF_6^-]^+$
Ru-MPP *Q-Exactive*	426.1908 532.4867 747.6441	425.9915 532.2376 747.3115	$[Ru\text{-}MPP]^{5+}$ $[Ru\text{-}MPP^{5+} - H^+]^{4+}$ $[Ru\text{-}MPP^{5+} - H^+ + TFA^-]^{3+}$

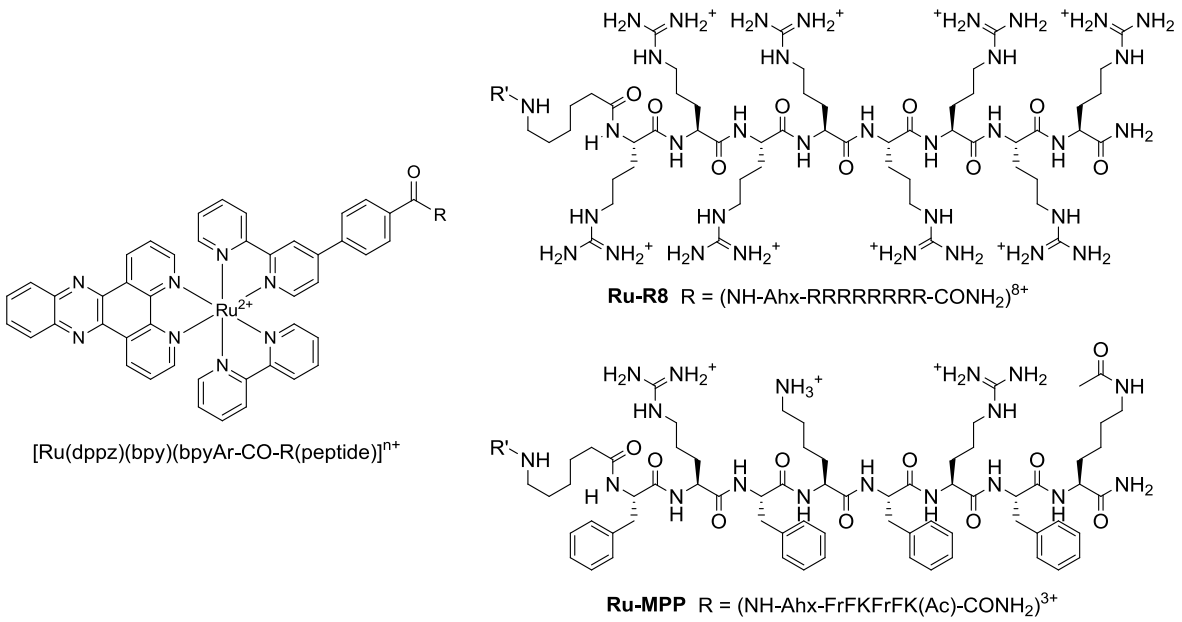

Figure 3.17: Chemical structures of Ru-R8 and Ru-MPP.

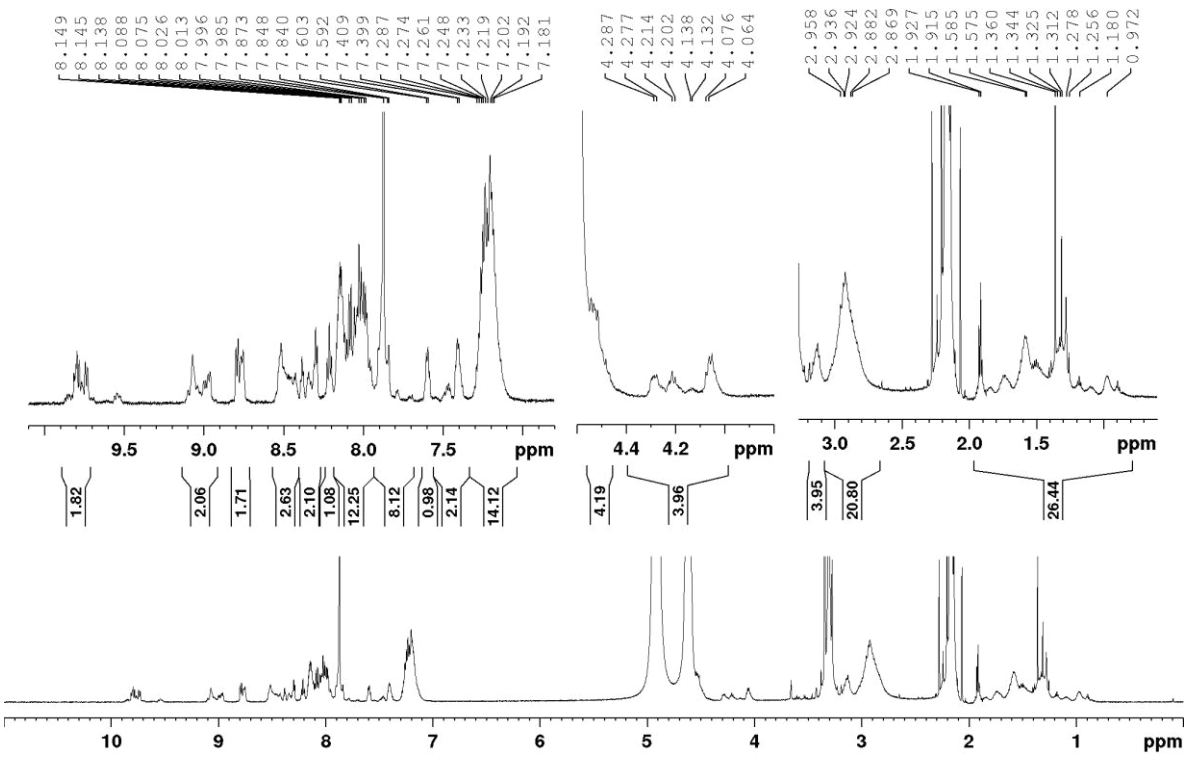

Figure 3.18: ^{1}H NMR (600 MHz, CD_3OD/D_2O) of Ru-MPP with insets to indicate regions of interest.

The purity of the conjugates relative to parent Ru(II)-COOH was confirmed by analytical RP-HPLC (diphenyl-silica, 0.1 % TFA in CH_3CN/H_2O) which indicated an absence of starting complex in all cases. The conjugates eluted slightly faster than the parent compound under ion-paired reverse phase conditions on diphenyl-silica columns, usually as broader peaks between 13.5 – 16 minutes, while the parent complex repeatedly elutes later at 17.3 minutes (Figure 3.19). In general, the conjugates elute in order of decreasing charge (i.e. retention time: R8 < NLS < MPP < parent) with a gradient moving from low to high acetonitrile ratio. Interestingly, the Ru-R8 trace exhibited two well resolved peaks at 13.3 and 14.4 minutes which likely correspond to the presence of two geometric isomers in the final conjugate due to the asymmetric nature of bpyArCOOR ligand at the Ru(II) core. The extended R8 chain in this instance seems to create enough discrimination to permit isomeric resolution in the conjugate that is not observed in the parent compound, or the other conjugates, under these chromatographic conditions.

A homo di-peptide conjugate was also synthesised using $[Ru(dppz)(bpyArCOOH)_2]^{2+}$ as precursor to achieve Ru-MPP2 – a Ru(II)-dppz di-conjugate bearing two MPP sequences. In

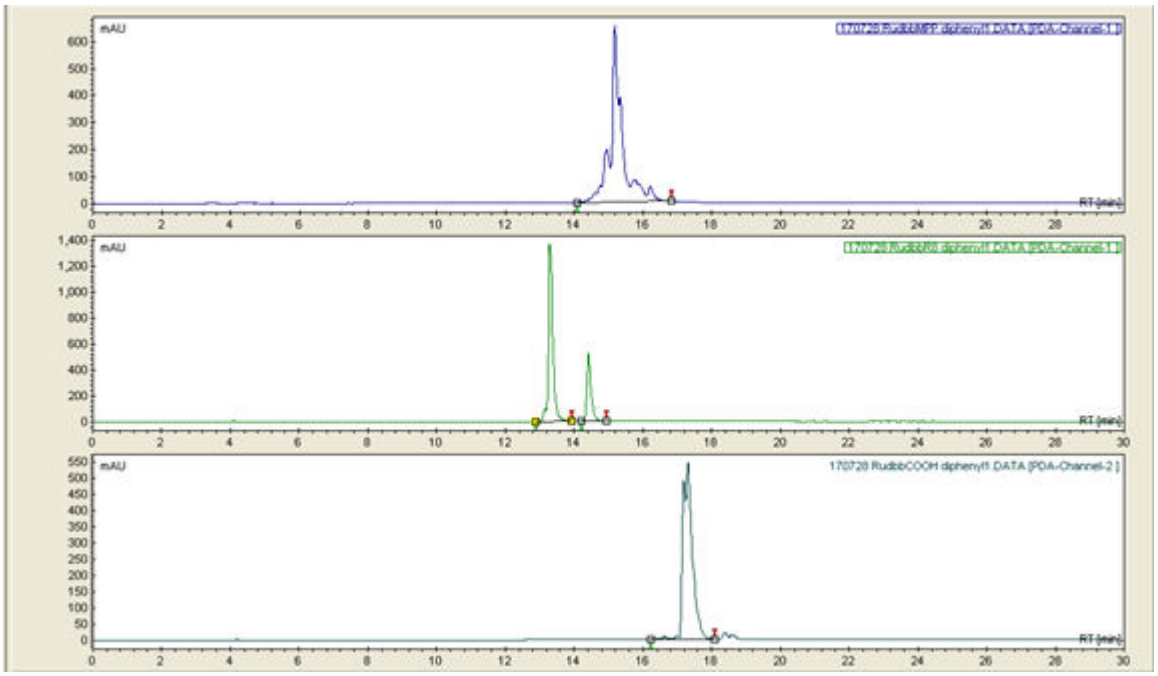

Figure 3.19: HPLC traces (450 nm, 0.1 % TFA in CH_3CN/H_2O gradient, RP-diphenyl) of Ru-MPP (top), Ru-R8 (middle) and $[Ru(dppz)(bpy)(bpyArCOOH)]^{2+}$ precursor (bottom).

this instance, the same coupling conditions as per the mono-conjugations was employed except the MPP peptide was added in 2.4 equivalents (x1.2 excess versus di-carboxy Ru-parent). ^{1}H NMR indicated a successful 2:1 conjugation with peptide regions showing identical peaks to the mono-conjugates but integrating doubly (Figure 3.20). For example, the proton spectrum of Ru-MPP2 exhibits two sets of multiplets integrating to 16 H as expected in the alpha-H region at δ 3.8 – 4.6 ppm. Additionally, relative to the parent spectrum, forty additional H was calculated on integration of the aromatic region indicative of Phe residues of two conjugated MPP chains.

The efficient synthesis of *tris*-heteroleptic Ru(II) complexes permitted access to [Ru(dppz)(bpyArCOOH)(bpyArCOOEt)]$^{2+}$, which can be coupled asymmetrically with two different vectors using an acid coupling - ester cleavage - acid coupling strategy. To demonstrate this, a discrete PEG chain (m-dPEG$_{15}$-amine) was mono-conjugated at the free

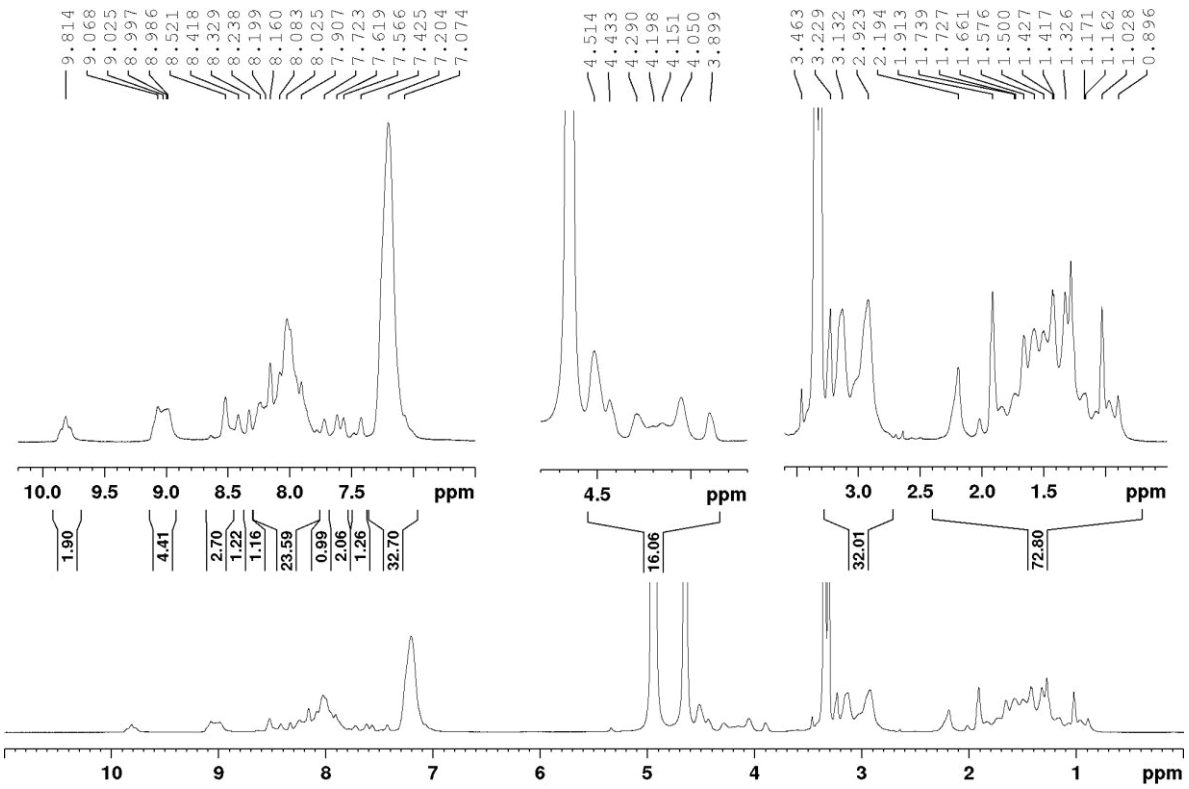

Figure 3.20: ^{1}H NMR (600 MHz, CD_3OD/D_2O) spectrum of Ru-MPP2 with insets to indicate regions of interest.

acid using HBTU coupling chemistry in dichloromethane to provide [Ru(dppz)(bpy-PEG)(bpyArCOOEt)]$^{2+}$. In contrast to peptides, the HBTU protocol works well in this instance using 1.25 equivalents of PEG, and the excellent solubility of the short polymer in dichloromethane facilitates high conversion efficiency and simple work up. The product was purified on silica using 9/1 CH_2Cl_2/CH_3OH as eluent to rapidly separate the PEGylated derivative from residual parent acid which was strongly retained near the baseline under this chromatography. Precipitation as the PF_6^- salt afforded the PEG conjugate in 71 % yield and PEGylation was confirmed by HRMS which found ions clustered at *m/z* = 1782.6034 assignable to $[M^{2+}+PF_6^-]^+$ (calculated; 1782.5950). The ^{1}H NMR spectrum, provided in Figure 3.21, displayed a large PEG-*H* chain peak at δ 3.34 – 3.72 ppm and a terminal methoxy PEG-OC*H*$_3$ signal at δ 3.25 ppm integrating for 60 H and 3 H respectively. Superimposed triplets and quartets at δ 1.37 and 4.37 ppm reflects the presence of isomers in the bulk compound and provides proof that the ester function remained intact during PEGylation.

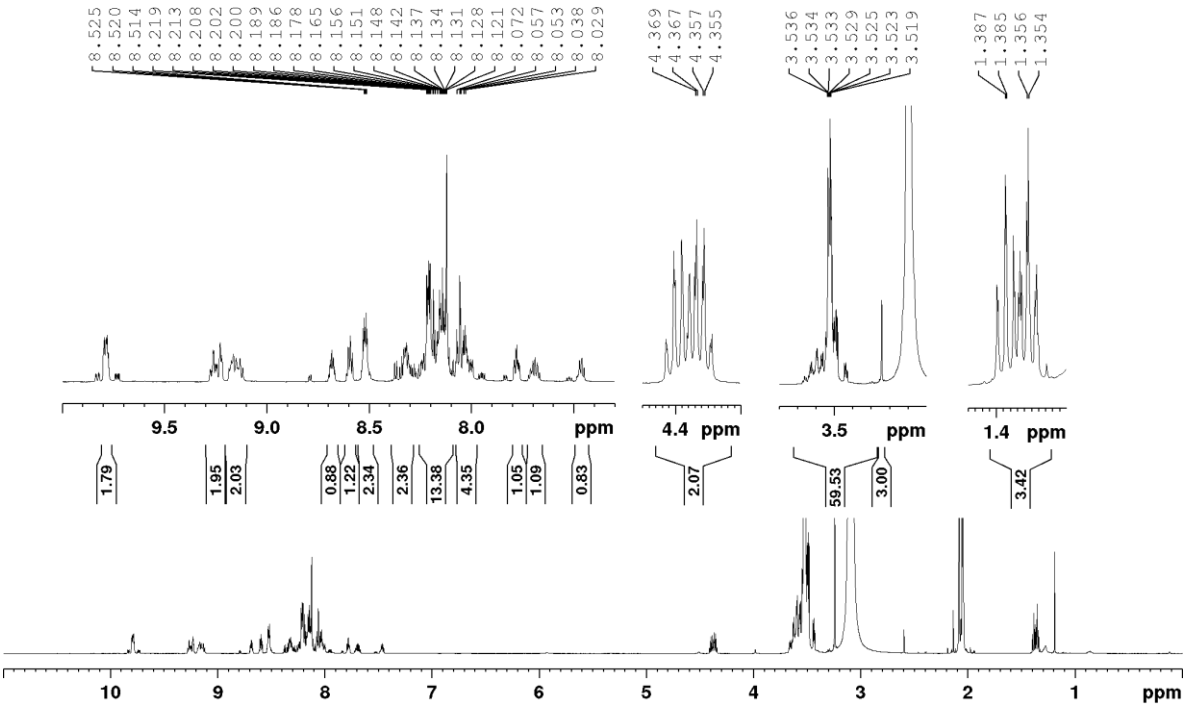

Figure 3.21: ^{1}H NMR (600 MHz, acetone-d_6) of [Ru(dppz)(bpy-PEG)(bpyArCOOEt)]$(PF_6)_2$ with insets to indicate regions of interest.

Cleavage of the ester was accomplished using base hydrolysis by the $LiOH/THF/CH_3OH/H_2O$ protocol that was successful for similar 'on-complex' ester hydrolyses for the unconjugated parent compounds. The acid was obtained quantitatively (91 % isolated yield) after 2 hours following acidification of the concentrated reaction mixture and precipitation as the PF_6^- salt. Successful hydrolysis was evident from the absence of the ester signals in the ^1H NMR spectrum relative to the precursor and HRMS further confirmed the synthesis of $[Ru(dppz)(bpy\text{-}PEG)(bpyArCOOH)](PF_6)_2$ finding *m/z* = 1754.5691 which corresponded to $[M^{2+}+PF_6^-]^+$ (calculated; 1754.5637, Figure 3.22). Importantly, the PEG group remained intact during the hydrolysis with no indication of degradation detected by HRMS or ^1H NMR (Appendix A).

Generation of the free acid enabled conjugation of different vectors to the already PEGylated complex. Using the optimised peptide coupling protocol, $[Ru(dppz)(bpy\text{-}PEG)(bpy\text{-}Peptide)]^{n+}$; was obtained quantitatively yielding two new hetero-diconjugates; Rudb-PEGb-NLS and Rudb-PEGb-MPP. Characterisation by ^1H NMR indicated the expected PEG, peptide and Ru(II) polypyridyl signals that integrate to a 1:1 conjugation in both cases. The ^1H NMR spectrum of Rudb-PEGb-MPP is provided in Figure 3.23. Purity analyses using RP-HPLC on diphenyl phase indicated a broad peak at 14 – 16 minutes for Rudb-PEGb-MPP with a maximum at 14.97 minutes and no parent $[Ru(dppz)(bpy\text{-}PEG)(bpyArCOOEt)]^{2+}$ peak at 16.33 minutes observed in the chromatogram. Under the same conditions, Rudb-PEGb-NLS exhibited a complex broad peak between 13 – 16 minutes (14.95 maximum) with a minor impurity parent peak observed at 16.35 minutes. Integration of both signals indicated an acceptable final purity of 97.3 % for Rudb-PEGb-NLS (Appendix A).

These diconjugates will be investigated further to determine the impact of asymmetric conjugation on cellular uptake and localisation as well as the impact on biomolecule interaction. The couple-cleave-couple protocol exemplified here to yield the PEG/peptide conjugates demonstrates a valuable route to highly functionalised polypyridyl constructs which may yet have exciting application not only in Ru(II) biophotonics but also across broader domains such as catalysis.

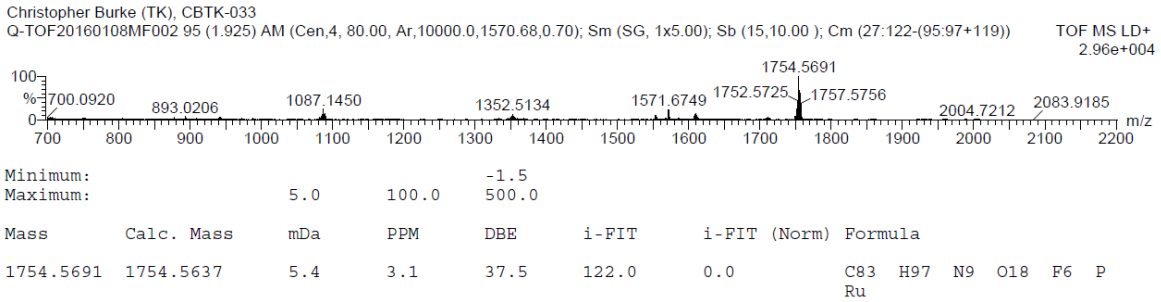

Minimum:				-1.5			
Maximum:		5.0	100.0	500.0			
Mass	Calc. Mass	mDa	PPM	DBE	i-FIT	i-FIT (Norm)	Formula
1754.5691	1754.5637	5.4	3.1	37.5	122.0	0.0	C83 H97 N9 O18 F6 P Ru

Figure 3.22: HRMS single mass analysis for [Ru(dppz)(bpy-PEG)(bpyArCOOEt)]$(PF_6)_2$.

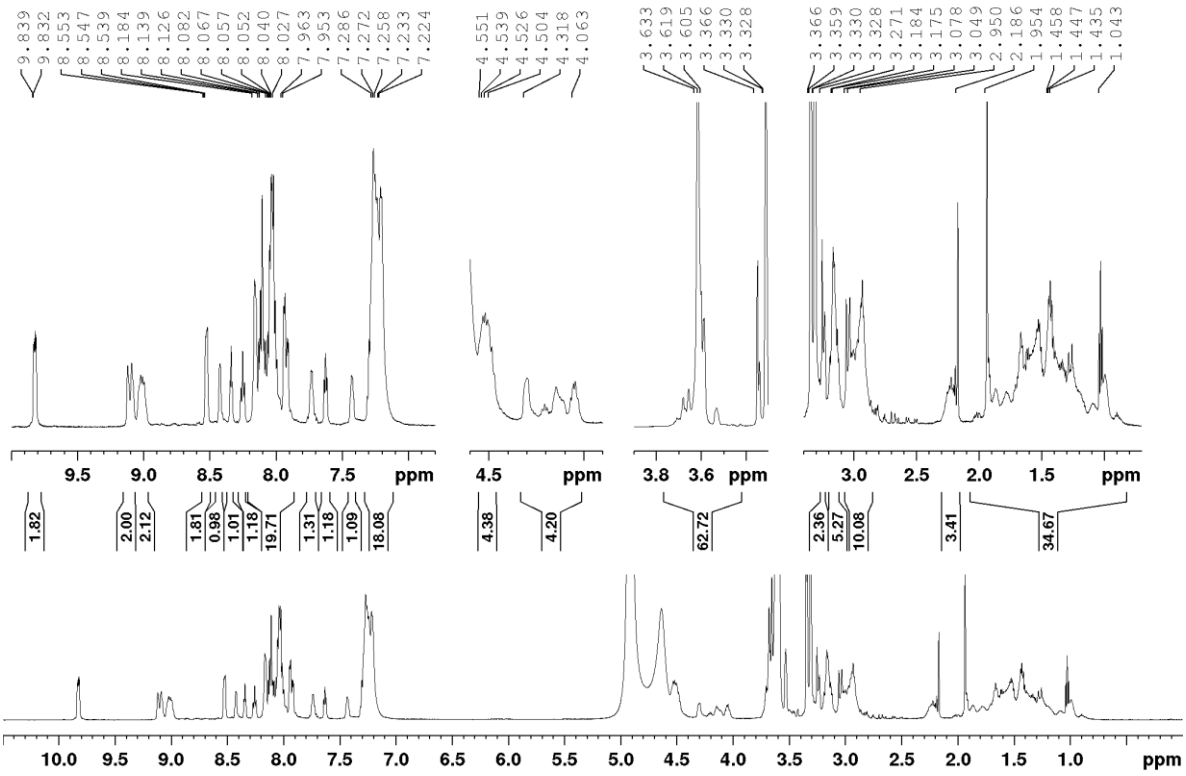

Figure 3.23: ^{1}H NMR (CH_3OD/D_2O) spectrum of Rudb-PEGb-MPP with insets to show regions of interest.

3.3 Conclusions

The development of versatile and efficient synthesis routes to peptide-modified Ru(II) luminophores was described in this chapter. The conjugatable Ru(II) parent structure was achieved by aryl-spaced carboxylic acid modification of commonly used bpy and phen ancillary ligands. These novel ligands, 4-bpyArCOOH, 5-bpyArCOOH and phen-Ar-COOH, represent a useful advancement towards new bioconjugates.

The coordination of these conjugatable ligands into *bis*- and *tris*- heteroleptic Ru(II) polypyridyl complexes was accomplished using efficient novel synthetic routes developed as part of this thesis. Ru-oxalate intermediates were revealed as valuable and synthetically easily accessible alternatives to classically used Ru-dichlorides, permitting controlled and selective addition of one or two polypyridyl ligands into the Ru(II) coordination sphere in high yield. In general, the oxalates demonstrated enhanced stability and solubility relative to their dichloride analogues, and critically, they can be cleaved quantitatively under acidic hydrolysis to yield a reactive solvate towards *tris*-chelated Ru(II) complexes. The efficiency of the route to *tris*-heteroleptic Ru(II) complexes, as exemplified by three highly asymmetric and functionalised examples, represents the highest yield achieved for this synthesis reported to date at > 82 % start-to-finish from commercial $RuCl_3.3H_2O$. Early studies indicate that this efficiency also extended to *bis*-heteroleptic complexes and further research to expand the generality of the route will determine its sustained utility.

The *tris*-heteroleptic synthesis permitted access to $[Ru(dppz)(bpy)(bpyArCOOH)]^{2+}$ - a mono-conjugatable light-switch complex and structural derivative of the DNA binding archetype; $[Ru(bpy)_2(dppz)]^{2+}$. This complex exists as two geometric isomers due to the asymmetry of the conjugatable ligand, and its acidic functionality was favourable towards successful isomer resolution on silica preparative plates. The identity of each isomer was tentatively assigned using ^1H NMR and COSY analysis, which in future studies should be supplemented by additional techniques such as 2D-NMR (e.g. NOESY) and crystallography. This isomerism may yet be useful diagnostically useful in the evolution of nucleic acid probes that are selective for DNA structure and sequence.

The development of a protocol towards quantitative peptide conjugation was also described. In general, employing a two-fold excess of peptide per Ru-COOH yielded the corresponding conjugate quantitatively under PyBOP coupling conditions. In most cases, this protocol translated to microwave synthesis, improving peptide economy and greatly reducing reaction times, while maintaining excellent coupling efficiency. Where the conjugates were not obtained pure, a reverse-phase chromatography method on C18-silica plates was developed that yielded pure Ru-dppz-peptide conjugate. The optimised protocol granted access to Ru-NLS, Ru-R8 and Ru-MPP which were characterised fully by HPLC, HRMS and ^{1}H NMR. These peptide-directed probes comprise a Ru-dppz core which will be exploited in Chapter 4 for cellular sensing of nucleic acids. Additionally, R8 and ER peptide conjugates of $[Ru(bpy)_2(phenArCOOH)]^{2+}$ were synthesised and exploited for cellular studies as described in Chapter 6. It should be noted that the optimum procedure for conjugation still represents poor efficiency in terms of the peptide equivalents required and perhaps translation to techniques such as click reactions in future work would yield a superior coupling method.

Di-conjugates were also synthesised from Ru(II)-dppz parent structures bearing two coupling functions. Ru-MPP2, a Ru-dppz derivative augmented with two MPP sequences, was efficiently obtained from $[Ru(bpyArCOOH)_2(dppz)]^{2+}$. Furthermore, two asymmetric di-conjugates, appended with dissimilar vectors, were procured from the acid and ester modified *tris*-heteroleptic complex; $[Ru(dppz)(bpyArCOOH)(bpyArCOOEt)]^{2+}$, using a stepwise PEGylation – ester hydrolysis – peptide coupling strategy to provide Rudb-PEGb-NLS and Rudb-PEGb-MPP. These di-conjugates will be studied in future work to investigate the impact of di-conjugation on cellular uptake, localisation and activity.

.

3.4 Experimental

3.4.1 General information

Materials, instrumentation and procedures used for synthesis and characterisation were as described in Chapter 2 unless otherwise indicated. Coupling constants are included for key compounds.

3.4.2 Synthesis of the ligands.

1,10-phenanthroline-5,6-dione (phendione)

Phendione was obtained commercially or using the following protocol from Paw and Eisenberg.[90] A cooled mixture of concentrated sulfuric acid (40 mL) and concentrated nitric acid (20 mL) was added dropwise to a stirring mixture of 1,10-phenanthroline hydrate (4 g, mmol) and KBr (8 g, mmol). The mixture was then heated under stirring at 130 ºC for 3 hours. After cooling to room temperature, the mixture was poured on ice and carefully neutralised to pH 6 – 8 with 25 % v/v sodium hydroxide. If the pH exceeded the range, 10 % v/v acetic acid was used to adjust. The solids that precipitate were filtered off and extracted with 3 x 50 mL dichloromethane. The filtrate was also extracted (3 x 100 mL) and the organic phases were combined, dried over magnesium sulphate, filtered and evaporated to dryness. In general, the product obtained is sufficiently pure but can purified further by recrystallization from methanol. Yield = 2.34 g (55 %). ^{1}H NMR (400 MHz, $CDCl_3$): δ (ppm) 9.09 (dd, 2 H); 8.48 (dd, 2 H); 7.58 (dd, 2 H). ^{13}C NMR (100 MHz, $CDCl_3$): δ (ppm) 178.75, 156.50, 152.97, 137.41, 128.13, 125.72.

dipyridophenazine (dppz)

The synthesis and characterisation of dppz has been described previously.[23,89] Herein, phendione (300 mg, mmol) and o-phenylenediamine (170 mg) were heated at reflux in 20 mL methanol for 3 hours. After cooling to room temperature and further on ice, the solid that precipitated was filtered, washed with cold methanol and acetone, and dried in the vacuum to give dppz as a fluffy cream coloured solid. Yield = 382 mg (95 %). ^{1}H NMR (400 MHz, d_6-DMSO): δ (ppm) 9.50 (dd, 2H); 9.20 (dd, 2H); 8.37 (m, 2H); 8.05 (m, 2H); 7.93 (dd, 2H). ^{1}H NMR (400 MHz, TFA-d): δ (ppm) 10.13 (dd, 2H, J = 1.2, 8.4 Hz); 9.37 (dd, 2H, J = 1.2, 5.2 Hz); 8.67 (dd, 2H, J = 3.2 Hz); 8.37 (2 x dd, 4 H, J = 5.2, 8.4 Hz and J = 3.2 Hz). ^{13}C NMR (100 MHz, TFA-d): δ (ppm) 152.38, 142.65, 142.15, 141.96, 139.45, 138.74, 130.54, 129.08, 128.59.

5-amino-1,10-phenathroline (aphen)

This synthesis was adapted from a literature protocol.[120] 5-nitro-1,10-phenathroline (100 mg, 0.44 mmol) and Pd/C (55 mg, 10 % wt.) were heated at reflux in ethanol (50 mL) for 30 minutes. Hydrazine hydrate (0.75 mL) was then added over the course of an hour. The reaction was heated at reflux for a further 3 hours before being filtered hot through celite. The concentrated (*ca*. 5 – 10 mL) cooled filtrate was treated with hexane to precipitate the amine as a yellow solid which was filtered, washed with hexane and dried. Yield = yellow solid, 58 mg (67 %). ^{1}H NMR (400 MHz, DMSO-d_6): δ (ppm) 9.05 (m, 1 H); 8.68 (m, 2 H); 8.04 (dd, 1 H); 7.74 (dd, 1 H); 7.50 (dd, 1 H); 6.86 (s, 1 H); 6.15 (s, 2 H, N*H*).

Synthesis of 4-bpyArCOOR

The synthesis of 4-Brbpy was adapted from the protocol described by Zalas *et al*.[77] The synthesis of 4-bpyArCOOR has also been reported previously by our group.[91]

2,2'-bipyridine-N-oxide (bpy-N-oxide)

Bipyridine (10.02 g) was dissolved in 50 mL TFA under stirring at room temperature. The reaction mixture was cooled in an ice bath and 10 mL hydrogen peroxide was added over the course of 10 minutes. The reaction was left to heat naturally to room temperature and was stirred for 3.5 hours. The mixture was then poured on ice and neutralised with 25 % w/v NaOH. The product was extracted into chloroform (5 x 70 mL) and the combined organics were dried over anhydrous magnesium sulphate, filtered and rotary evaporated down to a colourless oil. Upon drying under gentle nitrogen stream, the oil solidified to yield a white solid. Yield = 10.68 g (97 %). ^{1}H NMR (400 MHz, $CDCl_3$): δ (ppm) 8.90 (dt, 1 H); 8.74 (m, 1 H); 8.33 (m, 1 H); 8.18 (dd, 1 H); 7.85 (td, 1 H); 7.37 (m, 2 H); 7.29 (m, 1 H). ^{1}H NMR (400 MHz, Acetone-d_6) δ (ppm): 9.01 (dt, 1 H); 8.73 (qd, 1 H); 8.30 (dd, 1 H); 8.25 (dd, 1 H); 7.89 (td, 1 H); 7.43 (m, 3 H). ^{13}C NMR (100 MHz, Acetone-d_6) δ (ppm): 150.74, 150.13, 141.56, 136.80, 128.37, 126.54, 125.77, 125.18, 125.02.

4-nitro-2,2'-bipyridine-N-oxide (nitro-bpy-N-oxide)

A nitrating mixture was created by slowly adding HNO_3 (25 mL) and then KNO_3 (32 g) in small portions to a stirring solution of 85 mL oleum (20%) at room temperature. bpy-N-oxide (10.60 g) was then carefully added in portions over the course of an hour. Following this, the reaction was heated to 85 ºC and left to stir for 48 hours. After cooling to room temperature, the reaction mixture was poured over ice and neutralised with 25 % w/v NaOH. The precipitate that formed was filtered, washed with cold water, then dissolved in CH_2Cl_2 and re-filtered. The filtrate was dried over ann. $MgSO_4$, filtered and concentrated by rotary evaporation to yield a golden-brown crystalline solid.

Yield = 6.15 g (46 %). ^{1}H NMR (400 MHz, $CDCl_3$) δ (ppm): 9.14 (d, 1 H); 8.87 (dt, 1 H); 8.78 (dq, 1 H); 8.35 (dd, 1 H); 8.06 (dd, 1 H); 7.87 (td, 1 H); 7.43 (qd, 1 H). ^{13}C NMR (100 MHz, $CDCl_3$) δ (ppm): 149.93, 148.34, 147.66, 142.56, 142.06, 136.81, 125.48, 125.21, 122.72, 119.00.

4-bromo-2,2'-bipyridine-N-oxide (bromo-bpy-N-oxide)

Nitro-bpy-N-oxide (6.10 g) was suspended with stirring in glacial acetic acid (85 mL) and then carefully treated with acetyl bromide (30 mL). Then bright yellow solution that formed was heated at 85 ºC for 24 hours. The resulting white reaction mixture was poured on ice and neutralised with 25 % w/v NaOH solution. The product was extracted into CH_2Cl_2 (3 x 100 mL) and the combined organic layers washed with cold water (2 x 50 mL). The product phase was dried over $MgSO_4$, filtered, and rotary evaporated down to an off white solid. Yield = 6.15 g (88 %). ^{1}H NMR (400 MHz, $CDCl_3$) δ (ppm): 8.89 (dt, 1 H); 8.74 (dq, 1 H); 8.25 (d, 1 H); 7.86 (td, 1 H); 7.39 (m, 2 H). ^{13}C NMR (100 MHz, $CDCl_3$) δ (ppm): 149.56, 148.27, 148.03, 141.67, 136.72, 130.94, 128.54, 125.91, 125.06, 120.61.

4-bromo-2,2'bipyridine (4-Brbpy)

Bromo-Bpy-N-oxide (6.10 g) was suspended in 120 mL $CHCl_3$ and cooled in an ice-bath before phosphorus tribromide (13 mL) was added dropwise with stirring. The reaction mixture was heated at reflux for 6 hours before being poured onto ice and neutralised with 25 % w/v NaOH. The organic phase was separated and the water layer extracted with dichloromethane (3 x 100 mL). The combined organics were washed with cold water, dried over $MgSO_4$, filtered and evaporated down an off-white solid. Yield = 5.40 g (95 %). ^{1}H NMR (400 MHz, $CDCl_3$) δ (ppm): 8.68 (dq, 1 H); 8.62 (d, 1 H); 8.48 (d, 1 H); 8.38 (d, 1 H); 7.83 (td, 1 H); 7.48 (dd, 1 H); 7.34 (qd, 1 H). ^{13}C NMR (100 MHz, $CDCl_3$) δ (ppm): 157.52, 154.89, 149.98, 149.39, 137.22, 134.10, 127.03, 124.66, 124.44, 121.50. LR-MS (ESI(+)-TOF) *m/z* calculated for $C_{10}H_7N_2Br^{78}$ $[M + H]^+$: 234.99 ; found: 235.03.

4-(4-ethoxycarbonylphenyl)-2,2'-bipyridine (bpyArCOOEt)

4-Brbpy (500 mg), 4-ethoxycarbonylphenylboronic acid (540 mg) and $Pd(dppf)Cl_2$.DCM (175 mg) were suspended in 6 mL of dioxane under stirring. A solution of potassium carbonate (600 mg) in 2 mL water was then added and the reaction heated to reflux. After 6 hours, the reaction was cooled and evaporated to dryness *in vacuo*. The crude residue was purified by column chromatography on silica gel using DCM/MeOH 95/5 (R_f = 0.4). The product fractions were combined and reduced to dryness. The red-black oily residue obtained was dissolved in a minimum amount of hot chloroform and treated with cold pentane (*ca*. 5 volumes) to precipitate the coloured impurities. After concentration under vacuum, this process was repeated until a yellow solution was obtained to which further addition of pentane with cooling provides white solids. An excess of pentane was added at

this point to fully precipitate the product which was filtered and allowed to dry in the vacuum to afford an off-white solid. Where necessary, recrystallisation from 50/50 MeCN/Water gave pure ester as white threads. Typical yields: 65 – 80 %. Highest Yield: 94%. ^{1}H NMR (600 MHz, $CDCl_3$): δ (ppm) 8.69 (d, 1 H, J = 4.8 Hz); 8.64 (d, 1 H, J = 4.8 Hz); 8.63 (s, 1 H); 8.39 (d, 1 H, J = 7.8 Hz); 8.10 (d, 2 H, J = 8.4 Hz); 7.77 (m, 3 H, J = 8.4, 7.8, 1.8 Hz); 7.49 (dd, 1 H, J = 4.8, 1.8 Hz); 7.28 (dd, 1 H, J = 4.8, 1.2 Hz); 4.35 (q, 2 H, J = 7.2 Hz); 1.36 (t, 3 H, J = 7.2 Hz). ^{13}C NMR (150 MHz, $CDCl_3$): δ (ppm) 166.24, 156.88, 155.92, 149.83, 149.23, 148.28, 142.59, 137.06, 130.94, 130.27, 127.18, 123.99, 121.71, 121.35, 119.14, 61.22, 14.37. HR-MS (ESI(+)-TOF) *m/z* calculated for $C_{19}H_{17}N_2O_2$ $[M + H]^+$: 305.1290; found: 305.1282.

4-(4-carboxyphenyl)-2,2'-bipyridine (bpyArCOOH)

bpyArCOOEt (255 mg) was dissolved in 9mL CH_2Cl_2 under stirring and a solution of NaOH (230 mg; 7 eq) in 1.5 mL CH_3OH was added. The mixture was stirred for 24 hours at room temperature and was then evaporated to dryness. The sodium salt obtained was carefully washed with 10 mL DCM to remove any ester residues. Approximately 15 mL of water was then added to dissolve the salt and the pH of the resulting mixture adjusted with 1 M HCl to pH 3. The viscous mixture was stirred on ice for 20 minutes and the hydrated gel precipitate that formed was poured on acetone. The solution was then filtered, washed with acetone and allowed to dry in the vacuum to yield a white powder. Yield = 220 mg (95 %). ^{1}H NMR (600 MHz, DMSO-d_6): δ (ppm) 13.24 (bs, 1H, COO*H*); 8.92 (m, 2H, J = 4.8 Hz); 8.89 (d, 1H, J = 4.2 Hz); 8.71 (d, 1H, J = 7.8 Hz); 8.28 (t, 1H, J = 7.8 Hz); 8.17 (q, 4H, J = 8.4 Hz); 8.07 (d, 1H, J = 4.8 Hz); 7.76 (t, 1H, J = 6 Hz). ^{13}C NMR (150 MHz, DMSO-d_6): δ (ppm) 166.81, 153.10, 152.16, 149.26, 148.66, 147.96, 140.57, 139.75, 131.81, 130.16, 127.47, 125.52, 122.72, 122.09, 119.13. HR-MS (ESI(+)-TOF) *m/z* calculated for $C_{17}H_{13}N_2O_2$ $[M + H]^+$: 277.0977; found: 277.0983.

Synthesis of 5-bpyArCOOR

5-bromo-2,2'bipyridine (5-Brbpy)

The synthesis and characterisation of 5-Brbpy has been described previously.[76] 2,5-Dibromopyridine (3000 mg), 2-Pyridylzinc bromide (24 mL) and $Pd(Ph_3)_4$ (650 mg) were added to a round-bottom flask with THF (20 mL) on an ice-bath. The reaction was stirred for two hours on ice under nitrogen before being allowed to heat naturally to room temperature. After stirring for a further 5 hours, the reaction mixture was poured on a stirring solution of 8% EDTA (disodium salt) and left to stir for 12 hours. The precipitate that forms was filtered and washed with chloroform. The filtrate was extracted with 2 x 100 mL chloroform and the combined organic layers were dried over $MgSO_4$. The

chloroform was gently stripped away under nitrogen flow to provide a crude orange/brown oil. The crude material was purified by column chromatography (Silica: 1/4 EtOAc/hexane) to provide 5-bromobpy as a colourless solid. Yield = 816 mg (30 %). ^{1}H NMR (400 MHz, $CDCl_3$): δ (ppm) 8.72 (d, 1H); 8.67 (d, 1H); 8.37 (dd, 2H); 7.95 (dd, 1H); 7.83 (td, 1H); 7.35 (dd, 1H).

5-(4-ethoxycarbonylphenyl)-2,2'-bipyridine (5-BpyArCOOEt)

The 5-substituted bpy-aryl ester was synthesised by an identical procedure to bpyArCOOEt as described above. Yield = 75 %. ^{1}H NMR (400 MHz, $CDCl_3$): δ (ppm) 8.94 (d, 1H, J = 2.8 Hz); 8.71 (d, 1H, J = 4 Hz); 8.48 (dd, 2H, J = 8.4 Hz); 8.16 (d, 2H, J = 8.4 Hz); 8.06 (dd, 1H, J = 2, 8.4 Hz); 7.85 (td, 1H, J = 1.6, 8 Hz); 7.72 (d, 2H, J = 8.4 Hz); 7.34 (dd, 1H, J = 1.2, 8 Hz); 4.41 (q, 2 H, J = 7.2 Hz); 1.42 (t, 3 H, J = 7.2 Hz). HR-MS (ESI(+)-TOF) *m/z* calculated for $C_{19}H_{17}N_2O_2$ $[M + H]^+$: 305.1290; found: 305.1292.

5-(4-carboxyphenyl)-2,2'-bipyridine (5-BpyArCOOH)

The 5-substituted bpy-aryl acid was synthesised by an identical procedure to bpyArCOOH as described above. Yield = 86 %. ^{1}H NMR (400 MHz, DMSO-d_6): δ (ppm) 13.10 (broad s, 1H, COO*H*); 9.09 (d, 1H, J = 2 Hz); 8.73 (d, 1H, J = 4 Hz); 8.51 (2x d, 2H, J = 8.4 Hz); 8.34 (dd, 1H, J = 2.4, 8.4 Hz); 8.07 (d, 2H, J = 8.4 Hz); 8.00 (m, 3H, J = 2, 8 Hz); 7.51 (m, 1H, J = 8 Hz). HR-MS (ESI(+)-TOF) *m/z* calculated for $C_{17}H_{13}N_2O_2$ $[M + H]^+$: 277.0977; found: 277.0974.

Synthesis of phen-Ar-COOR

5-bromo-1,10-phenanthroline (BrPhen)

The following preparation is based on the method of Eisenberg *et al*..[75] To an ice-cooled bomb reactor was added; phenanthroline (3.606 g, mmol), Br_2 (800 uL, mmol) and oleum (20 %) (12 mL). The reactor was sealed and placed in an oven at 50 ºC. The temperature of the oven was slowly raised to 138 ºC and maintained at this temperature for 23 h. The reactor was cooled before its contents were poured onto crushed ice (*ca.* 100 g) and made alkaline with NH_4OH (pH 9 – 10). The solid that separated was filtered, washed with water and dried in the vacuum. The crude solid contains many impurities (TLC: Silica, 9/1 CH_2Cl_2/MeOH; R_f product = 0.5), but the product can be isolated by careful precipitation from a chloroform solution of the crude solid with cold pentane to yield pure BrPhen as a light brown solid. Yield = 2.77 g (53 %). ^{1}H NMR (400 MHz, $CDCl_3$): δ (ppm) 9.21 (m, 2H); 8.66 (dd, 1H); 8.18 (dd, 1H); 8.13 (s, 1H); 7.74 (dd, 1H); 7.64 (dd, 1H). ^{13}C NMR ($CDCl_3$): 151.04, 150.67, 146.38, 145.36, 136.21, 135.55, 129.76, 128.96, 128.08, 124.09, 123.89, 121.05.

The synthesis and characterisation of phen-Ar-COOR was developed in our group and has been reported previously elsewhere.[92]

5-(4-ethoxycarbonylphenyl)-1,10-phenanthroline (phen-Ar-COOEt)

phen-Ar-COOEt was synthesised by an analogous method to that described for bpyArCOOEt. Typical yields = 40 – 55 %. ^{1}H NMR (400 MHz, $CDCl_3$): δ (ppm) 9.16 (m, 2 H); 8.22 (d, 1 H); 8.16 (d, 3 H); 7.70 (s, 1 H); 7.62 (dd, 1 H); 7.54 (m, 3 H); 4.39 (q, 2 H); 1.38 (t, 3 H).

5-(4-carboxyphenyl)-1,10-phenanthroline (phen-Ar-COOH)

phen-Ar-COOH was synthesised by an analogous method to that described for bpyArCOOH. Typical yields = 85 – 95 %. ^{1}H NMR (400 MHz, DMSO-d_6): δ (ppm) 13.24 (br s, 1 H, COOH); 9.34 (s, 2 H); 9.10 (d, 1 H); 8.67 (d, 1 H); 8.38 (s, 1 H); 8.07 – 8.30 (m, 4 H); 7.77 (d, 2 H).

3.4.3 Synthesis of Ru(II) complexes.

In general, reactions involving Ru(II) were performed under nitrogen and in the absence of light. In the case of *tris* chelates, the counterion of the complex can be varied as follows: precipitation as the PF_6^- or ClO_4^- forms by treatment of a water miscible solution of the complex with NH_4PF_6 or $LiClO_4$ respectively. *Caution*! Perchlorate salts are potentially explosive. The ClO_4^- and PF_6^- salts can then be converted to the chloride form by treating an acetone solution of the complexes with minimum tetrabutylammonium chloride (TBAC) which precipitates the chloride form.

$[Ru(bpy)_2(dppz)](ClO_4)_2$

The synthesis and characterisation of this complex has been reported previously.[96] Herein, commercial $Ru(bpy)_2Cl_2$ (78 mg) and dppz (50 mg) were heated at reflux in ethanol/water (9/1, 10 mL) for 3 hours. The cooled solution was concentrated in vacuo followed by dilution with 10 mL water and cooling on ice. The solid impurities were filtered off and the crude solid was then precipitated using $LiClO_4$ (aq. sat.). *Caution*! Perchlorate salts are potentially explosive. The isolated solids were then purified by recrystallization from ethanol. Yield = red solid, 130 mg (90 %). ^{1}H NMR (400 MHz, DMSO-d_6): δ (ppm) 9.64 (d, 2 H); 8.88 (dd, 4 H); 8.53 (dd, 2 H); 8.22 (m, 6 H); 8.13 (t, 2 H); 8.03 (dd, 2 H); 7.80 (dd, 4 H); 7.61 (t, 2 H); 7.38 (t, 2 H).

$[Ru(bpy)_2(phenArCOOH)](ClO_4)_2$

This complex was prepared as described by the Keyes group in the literature.[92] Typically, reaction of stoichiometric quantities of phen-Ar-COOH ligand with $Ru(bpy)_2Cl_2$ in EtOH/H_2O 1/1 under reflux for 6 hours yielded a deep red mixture from which the crude complex precipitated upon addition of

$LiClO_4$ (aq. sat.). Purification using 70/26/4/2 $CHCl_3/CH_3OH/H_2O$/AcOH provided the purified product in yields of 70 – 80 %. *Caution*! Perchlorate salts are potentially explosive. ^{1}H NMR (400 MHz, CD_3CN): δ (ppm) 8.62 (d, 1 H); 8.54 (dd, 4 H); 8.45 (d, 1 H); 8.25 (m, 3 H); 8.10 (m, 4 H); 8.01 (t, 2 H); 7.86 (d, 2H); 7.75 (m, 3 H); 7.68 (dd, 1 H); 7.60 (t, 2 H); 7.46 (t, 2 H); 7.26 (t, 2 H).

[Ru(bpyArCOOR)$_2$Cl$_2$]

Method I: This method was adapted from the classical synthesis described by Sullivan *et al*.[20] and was found to provide variable yield and purity of the target products. In a typical preparation; $RuCl_3.3H_2O$ (≈ 50 mg, 0.192 mmol), bpyArCOOR (0.38 mmol) and LiCl (80 mg, 1.9 mmol) were dissolved in 4 mL of DMF and heated just under reflux for 8 hours. The reaction mixture was cooled and poured on stirring water to precipitate black-purple solids that were filtered and dried. Typical crude yields = 40 – 70 %.

Method II: This method was adapted from the synthesis described by Viala and Coudret[25] and was found to provide the target products in better yield and purity than the classical method. Typically, to degassed stirring ethylene glycol/water 3/1 (4 mL) at 120 ºC was added LiCl (5 eq). After 15 min, $RuCl_3.3H_2O$ (27 mg) was added and after a further 15 min, bpyArCOOH (50 mg, 1eq) was added in full. Glucose (6 mg) was added after another 15 min, and ascorbic acid (14 mg) was added 15 min later. The resulting slurry was stirred for 30 min before being cooled on ice and treated with brine solution (10 mL). The precipitates that formed were filtered off and washed extensively with water, acetone and diethyl ether. After drying, the product was obtained as a dark purple solid. Yield = 42 mg (64 %).

TLC analysis (silica, 9/1 CH_2Cl_2/CH_3OH (ester) or 70/26/4/2 $CHCl_3/CH_3OH/H_2O$/AcOH (acid)) usually indicated partially resolved isomers of the product at $R_f = 0.70$ with ligand and intense yellow impurity bands at higher R_f values, an orange band at $R_f \approx 0.30$, and a black immobile band at the baseline assignable to starting material. Generally, insolubility and product degradation prevented bulk purification at this point and the crude material was used for further synthesis. Similarly, insolubility and residual impurities precluded NMR characterisation of the acid derivative in conventional solvents. **[Ru(bpyArCOOEt)$_2$Cl$_2$]** ^{1}H NMR *Purified sample, mixture of isomers* (400 MHz, DMSO-d_6): δ (ppm) 9.95 (br d, 2 H); 9.04 (s, 1 H); 8.80 – 8.93 (m, 3 H); 8.01 – 8.34 (m, 10 H); 7.76 (br d, 2 H); 7.54 (br s, 3 H); 7.19 (br s, 1 H); 4.30 – 4.45 (2x q, 4 H); 1.28 – 1.42 (2x t, 6 H).

***cis*$_2$*fac*-[Ru(DMSO)$_4$Cl$_2$]**

Method I: Adapted from Evans *et al*.[31] – Fresh anhydrous DMSO (5 mL) was stirred at 100 ºC under nitrogen in the dark and $RuCl_3.3H_2O$ (1000 mg) was added in full. The mixture was heated to reflux

for 2 minutes before it was removed from the heat and rapidly cooled in an ice bath. The mixture was then added to 50 mL stirring acetone to precipitate the yellow complex. After stirring for 30 minutes, the solids were filtered and washed well with cold acetone to afford the complex as a bright lemon yellow powder in variable yields ranging 40 – 82 %. The complex can be recrystallized from hot DMSO/acetone solutions to yield bright yellow needles. Yield (best, crude) = 1513 mg (82 %). IR (ATR, solid) $\bar{\nu}$ (cm^{-1}): 1122 (s, S-bonded S=O), 1095 (s, S-bonded S=O), 920 (s, O-bonded S=O).

Method I: Adapted from Alston *et al*.[33] - Ruthenium(III) chloride trihydrate (1000 mg) was stirred at room temperature in DMSO (3.5 mL) until full dissolution of the complex was complete. Isopropyl alcohol (10 mL) was then added and the mixture was heated at 85 °C for 24 hours. The fine yellow solids that gradually precipitate from the orange solution during the reaction were filtered, washed with copious amounts of acetone and diethyl ether, and dried to yield the pure *cis*-isomer as a bright yellow powder. Yield = 1828 mg (98 %). ^{1}H NMR (400 MHz, $CDCl_3$): Ratio of κO-DMSO (2.71 ppm, s): κS-DMSO (3.31 – 3.51 ppm) = 1H : 3H. IR (ATR, solid) $\bar{\nu}$ (cm^{-1}): 1112 (s, S-bonded S=O), 1094 (s, S-bonded S=O), 932 (s, O-bonded S=O).

[Ru(dppz)(DMSO)$_2$Cl$_2$]

Method I: As Evans *et al*.[31]: *cis*-$Ru(DMSO)_4Cl_2$ (300 mg, 0.6 mmol) and dppz (160 mg, 0.55 mmol) were heated at reflux in chloroform (10 mL) for 2 h. The solution was filtered hot and the filtrate evaporated to leave a dark brown oil. Acetone was added to precipitate unreacted Ru(II) precursor which was filtered off. The filtrate was concentrated and added to stirring diethyl ether to precipitate the product which was filtered and dried. Yield = Brown solid, 168 mg (49 %).

Method II: cis-$Ru(DMSO)_4Cl_2$ (500 mg, 1.03 mmol) and dppz (290 mg, 1.03 mmol) were heated at reflux in ethanol (35 mL) for 3 h. The reaction was then cooled to room temperature and the solvent volume reduced to ca. 10 mL in vacuo. The precipitate that forms upon cooling was filtered, washed with minimal cold ethanol and copious amounts of hexane/diethyl ether and dried under nitrogen. In general, the product is isolated pure in this manner, otherwise extraction into acetone and re-precipitation using ether/hexane yields the pure Ru(II) DMSO-solvate. Yield: light-brown solid, 625 mg (1.02 mmol, 99 %). ^{1}H NMR (400 MHz, $CDCl_3$) δ (ppm): 10.22 (d, 1 H); 10.05 (d, 1 H); 9.79 (d, 1 H); 9.69 (d, 1 H); 8.43 (m, 2 H); 8.11 (t, 1 H); 8.05 (m, 2 H); 7.93 (t, 1 H); 3.65 (s, 3 H); 3.60 (s, 3 H); 3.26 (s, 3 H); 2.70 (s, 3 H). ^{13}C NMR (100 MHz, $CDCl_3$) δ (ppm): 157.66, 154.26, 152.02, 150.162, 142.90, 139.58, 139.49, 134.89, 133.91, 132.04, 130.36, 129.88, 129.68, 126.10, 126.03, 47.20, 46.47, 45.49, 44.39. Anal. Calculated (Found) for $C_{22}H_{22}Cl_2N_4O_2S_2Ru$: C 43.28 (43.78); H 3.63 (3.35); N 9.18 (9.26); Cl 11.61 (11.42). HR-MS (ESI(+)-TOF) *m/z*: Calculated for

$C_{22}H_{22}Cl_2N_4O_2S_2Ru$ $[M]^+$: 609.9605; Found: 609.9604. IR (ATR, solid) $\bar{\nu}$ (cm^{-1}): 1120, 1094 (S-bonded DMSO) and 919 (O-bonded DMSO).

[Ru(dppz)(bpyArCOOR)$_2$]X$_2$ (X = PF_6^-, ClO_4^-, Cl^-)

Classical method: [Ru(bpyArCOOR)$_2$Cl$_2$] (50 mg, 1 eq) and dppz (*ca*. 19 mg, 1 eq.) were heated at reflux in EtOH/H_2O 3/1 (8 mL) for 6 hours. The reaction mixture was cooled and poured on stirring $LiClO_4$ (aq.) to precipitate the crude product. Purification was performed on silica using 70/26/4/X $CHCl_3$/MeOH/H_2O/AcOH (X = 2 for Ru-acid, X = 0 for Ru-ester). The product fractions were collected, concentrated and treated with aqueous solutions of either NH_4PF_6 or $LiClO_4$ to precipitate the salt of choice which was filtered, washed with water and diethylether and dried. Typical yields = 50 - 70 %. *Caution*! Perchlorate salts are potentially explosive.

Developed method: [Ru(dppz)(DMSO)$_2$Cl$_2$] (100 mg, 0.164 mmol) and bpyArCOOR (90 mg, 0.328 mmol, 2 equiv) were added to a 9/1 ethylene glycol/water mixture (10 mL) and the resulting suspension was heated at reflux for 6 h. The resulting deep red mixture was cooled to room temperature and the PF_6^- salt precipitated by the addition of a saturated aqueous solution of ammonium hexafluorophosphate. The crude solid was isolated by filtration and washed with water. The solid was then dissolved in acetone and filtered through a narrow bed of celite. The filtrate was concentrated *in vacuo* and added dropwise to rapidly stirring diethyl ether to precipitate bright orange solids which were filtered, washed with ether and dried in the vacuum to yield the pure PF_6^- salt as a mixture of geometric isomers. Typical yields = 85 – 98 %.

The complex can also be synthesised via the oxalate as described below.

[Ru(dppz)(bpyArCOOH)$_2$](ClO$_4$)$_2$

Orange/red solid. ^{1}H NMR (600 MHz, DMSO-d_6): *Major Isomer peaks*: δ (ppm) 9.65 (d, 2H); 9.22 (m, 4 H); 8.53 (dd, 2 H); 8.39 (m, 2 H); 8.28 (m, 2 H); 8.20 (m, 3 H); 8.11 (q, 3 H); 8.05 (m, 7 H); 7.97 (m, 2 H); 7.88 (d, 1 H); 7.80 (m, 3 H); 7.64 (q, 1 H); 7.43 (q, 1 H). HR-MS (ESI(+)-TOF) *m/z*: Calculated for $C_{52}H_{34}N_8O_4Ru$ $[M^{2+}]$: 468.0868 (z = 2); Found: 468.0881.

[Ru(dppz)(bpyArCOOEt)$_2$](ClO$_4$)$_2$

Orange/red solid. ^{1}H NMR (Chloride form, 400 MHz, CD_3OD): *Isomer mixture*: δ (ppm) 9.83 (m, 2 H, J = 1.08, 3.24, 8.19 Hz); 9.11 (d, 2 H, J = 1.52, 3.84 Hz); 9.01 (m, 2 H, J = 3.80 Hz); 8.52 (m, 2 H, J = 3.52, 6.6 Hz); 8.43 (d, 1 H, J = 5.29 Hz); 8.34 (t, 1 H, J = 3.89 Hz); 8.23 (m, 3 H); 8.08 – 8.19 (m, 8 H); 8.03 (m, 5 H); 7.93 (t, 3 H, J = 6.6 Hz); 7.72 (m, 1 H); 7.62 (t, 1 H, J = 6.52 Hz); 7.42 (t, 1

H, J = 5.47 Hz); 4.41 (m, 4 H, J = 7.12 Hz, C*H*$_2$CH$_3$); 1.41 (m, 6 H, J = 7.16 Hz, CH$_2$C*H*$_3$). HR-MS (ESI(+)-TOF) *m/z*: Calculated for $C_{56}H_{42}N_8O_8ClRu$ $[M^{2+} + ClO_4^-]^+$: 1091.1858; Found: 1091.1901.

General procedure for synthesis of [Ru(dppz)(N^N)(ox)]

Ru(dppz)(DMSO)$_2$Cl$_2$ (312 mg, 0.511 mmol) and sodium oxalate (100 mg, 0.746 mmol) were heated at reflux in water (15 mL) for 1 h. The reaction was then cooled to room temperature and added to a hot solution of the polypyridyl ligand (0.511 mmol) in 15 mL ethylene glycol. The resulting mixture was heated at reflux for 3 h, cooled to room temperature and then added dropwise to 50 mL of stirring water. After 30 minutes, the precipitates were filtered through a 0.4 μm membrane. The solids were washed with copious amounts of water and minimal acetone before drying thoroughly under a nitrogen stream.

[Ru(dppz)(bpy)(ox)]

Yield: purple-black fine powder, 313 mg (0.499 mmol, 98 %). ^{1}H NMR (600 MHz, DMSO-d$_6$) δ (ppm): 9.62 (d, 1 H); 9.32 (d, 1 H); 9.26 (d, 1 H); 9.00 (d, 1 H); 8.83 (d, 1 H); 8.67 (d, 1 H); 8.53 (d, 1 H); 8.47 (d, 1 H); 8.36 (dd, 1 H); 8.22 (q, 1 H); 8.15 (m, 3 H); 7.92 (t, 1 H); 7.80 (t, 1 H); 7.70 (m, 2 H); 7.12 (t, 1 H). Anal. Calculated (Found) for $C_{30}H_{18}N_6O_4Ru.2H_2O$: C 54.70 (54.30); H 2.89 (3.34); N 12.72 (12.66). HR-MS (ESI(+)-TOF) *m/z*: Calculated for $C_{30}H_{18}N_6O_4RuNa$ $[M + Na]^+$: 651.0325; Found: 651.0358.

[Ru(dppz)(bpyArCOOH)(ox)]

Yield (from 200 mg Ru(II) starting material): black solid, 231 mg (0.308 mmol, 94 %). ^{1}H NMR (400 MHz, DMSO-d$_6$) δ (ppm): 13.16 (br s, 1 H, COOH); 9.61 (d, 1 H); 9.33 (d, 1 H); 9.26 (d, 1 H); 9.11 (d, 1 H); 9.01 (2s, 2 H); 8.51 (d, 1 H); 8.46 (d, 1 H); 8.37 (dd, 1 H); 8.26 (m, 1 H); 8.15 (m, 3 H); 8.03 (s, 4 H); 7.94 (t, 1 H); 7.76 (d, 1 H); 7.73 (dd, 1 H); 7.50 (dd, 1 H). Anal. Calculated (Found) for $C_{37}H_{22}N_6O_6Ru.H_2O$: C 58.04 (57.50); H 3.16 (2.98); N 10.98 (11.17).

General procedure for [Ru(dppz)(bpy)(bpyArCOOR)](PF$_6$)$_2$

Ru(dppz)(bpy)(ox) (100 mg, 0.159 mmol) was suspended in 2 mL acetonitrile and 2 mL of 1 M perchloric acid was added. After refluxing for 2 h, a red-brown solution of the Ru-solvate was obtained and after cooling it was poured on 10 mL stirring water. The solids that precipitated were filtered and dried yielding the crude burnt-orange *bis*-solvated Ru(II) complex. *Caution*! Perchlorate salts are potentially explosive. The intermediate was dissolved in ethylene glycol (10 mL) with the bpyArCOOR ligand (0.16 mmol) and heated at reflux for 4 – 6 h. The deep red mixture was cooled to room temperature and poured on stirring aqueous ammonium hexafluorophosphate to precipitate

the crude complex as the hexafluorophosphate salt. The solids were filtered, washed with water and dried under a nitrogen stream to afford the target complexes as a mixture of geometric isomers. Purification was performed on short silica flash columns using 90/10/1 CH_3CN/H_2O/20% w/v KNO_3 (aq) followed by 70/30 CH_3CN/0.1M TsOH aq. if necessary for full elution. The product fraction was concentrated *in vacuo*, precipitated using ammonium hexfluorophosphate and filtered. The solids were taken up in minimum acetone, filtered, concentrated and re-precipitated by slow addition to stirring diethyl ether. Filtration yielded the bright orange pure complexes as a mixture of geometric isomers.

[Ru(dppz)(bpy)(bpyArCOOEt)](PF$_6$)$_2$

Yield: orange solid, 166 mg (0.146 mmol, 92 %). ^{1}H NMR (600 MHz, CD_3CN) δ (ppm): 9.68 (m, 2 H); 8.80 (2x dd, 1 H); 8.73 (2x dd, 1 H); 8.56 (2x t, 2 H); 8.49 (m, 2 H); 8.12 – 8.25 (m, 8 H); 8.00 – 8.07 (m, 2 H); 7.91 (m, 5 H); 7.49 – 7.79 (2x m, 3 H); 7.29 – 7.48 (2x m, 3 H); 4.37 (2x q, 2 H); 1.38 (2x t, 3 H). ^{13}C NMR (150 MHz, CD_3CN) δ (ppm): 166.56, 158.78, 158.57, 158.20, 158.17, 157.97, 157.92, 154.71, 154.63, 153.33, 153.16, 153.06, 153.01, 152.96, 151.47, 151.42, 149.41, 143.77, 141.01, 140.88, 140.78, 139.03, 138.94, 138.86, 134.56, 133.54, 133.20, 133.12, 131.89, 131.16, 131.09, 128.76, 128.69, 128.61, 128.50, 128.44, 128.39, 126.10, 125.91, 125.59, 125.53, 125.34, 125.28, 123.21, 123.15, 62.20, 14.48. Anal. Calculated (Found) for $C_{47}H_{34}N_8O_2P_2F_{12}Ru$: C 49.79 (49.18); H 3.02 (2.68); N 9.88 (9.59). HR-MS (ESI(+)-TOF) *m/z*: Calculated for $C_{45}H_{30}N_8O_2PF_6Ru$ $[M - PF_6]^+$: 989.1490; Found: 989.1477.

[Ru(dppz)(bpy)(bpyArCOOH)](PF$_6$)$_2$

Yield: orange solid, 148 mg (0.134 mmol, 86 %). ^{1}H NMR (600 MHz, CD_3CN) δ (ppm): 9.68 (m, 2 H); 8.81 (2x dd, 1 H); 8.73 (2x d, 1 H); 8.56 (2x t, 2 H); 8.48 (m, 2 H); 8.22 (m, 3 H); 8.14 (m, 5 H); 8.04 (m, 2 H); 7.84 – 7.97 (m, 5 H); 7.54 – 7.76 (m, 3 H); 7.28 – 7.49 (m, 3 H). ^{13}C NMR (150 MHz, CD_3CN) δ (ppm): 168.65, 158.68, 158.47, 158.26, 158.21, 158.04, 157.99, 157.96, 154.71, 154.66, 153.21, 153.15, 153.07, 152.98, 151.49, 143.77, 141.02, 139.00, 138.93, 138.84, 134.53, 133.53, 131.88, 131.35, 131.28, 130.62, 128.71, 128.61, 128.57, 128.49, 128.44, 128.25, 128.17, 126.03, 125.85, 125.60, 125.54, 125.34, 125.27, 123.13, 123.08. Anal. Calculated (Found) for $C_{45}H_{30}N_8O_2P_2F_{12}Ru$: C 48.88 (49.41); H 2.73 (2.58); N 10.13 (10.10). HR-MS (ESI(+)-TOF) *m/z*: Calculated for $C_{45}H_{30}N_8O_2PF_6Ru$ $[M - PF_6]^+$: 961.1183; Found: 961.1190.

Isomer isolation:

The two geometric isomers of the complex were resolved on preparative TLC plates (Silica, 20 x 20 mm; 500 um layer, load: 3 – 5 mg) using 70/26/4 $CHCl_3$/MeOH/Water as solvent. The respective isomers were obtained by taking the centre of the two bands and the cleaved silica was washed with

the same solvent, followed by evaporation to dryness. The solids were taken up in minimum methanol and added dropwise to stirring tetrabutylammonium chloride/acetone to provide the chloride salts which precipitated and were filtered and washed with acetone. The isomers were named t-dppz and t-bpy, reflecting the trans orientation of the 4-substituted pyridyl ring of 4-bpyArCOOH being in a trans orientation relative to dppz (t-dppz) or bpy (t-bpy) respectively. Assignments were made using COSY analysis and is discussed further in the main text of this chapter.

t-dppz: ^{1}H NMR (600 MHz, CH_3CN): δ (ppm) 9.68 (dd, 2 H, J = 1.14, 3.36, 8.23 Hz, *[x]*); 8.83 (d, 1 H, J = 1.8 Hz, *[3]*); 8.71 (d, 1 H, J = 8.16 Hz, *[3']*); 8.56 (2x d, 2 H, J = 8.2 Hz, *[b3,b3']*); 8.48 (m, 2 H, J = 3.42, 6.24 Hz, *[z]*); 8.24 (d, 1 H, J = 0.72, 5.34 Hz, *[w]*); 8.21 (dt, 2 H, J = 8.2 Hz, *[ce]*); 8.19 (d, 1 H, J = 1.14, 5.34 Hz, *[w']*); 8.11 – 8.16 (m, 3 H, J = 1.44, 3.36, 6.60 Hz, *[y, b4']*); 8.04 (m, 2 H, J = 1.40, 8.04 Hz, *[4',b4]*); 8.00 (d, 2 H, J = 8.7 Hz, *[bf]*); 7.91 (m, 4 H, J = 4.50, 8.94 Hz, *[v, 6, b6']*); 7.76 (m, 3 H, J = 1.86, 5.95 Hz, *[b6, 6', 5]*); 7.49 (m, 1 H, J = 1.32, 6.73 Hz, *[b5']*); 7.28 (dq, 2 H, J = 1.30, 5.60, 7.74 Hz, *[b5,5']*).

t-bpy: ^{1}H NMR (600 MHz, CH_3CN): δ (ppm) 9.68 (dt, 2 H, J =1.32, 8.22 Hz, *[x]*); 8.80 (d, 1 H, J = 1.8 Hz, *[3]*); 8.74 (d, 1 H, J = 8.16 Hz, *[3']*); 8.55 (dd, 2 H, J = 8.17 Hz, *[b3,b3']*); 8.48 (dt, 2 H, J = 3.18, 6.24 Hz, *[z]*); 8.20 (dd, 2 H, J = 1.14, 5.46 Hz, *[w]*); 8.11 – 8.17 (m, 6 H, J = 1.44, 8.04 & undefined Hz, *[ce, b4', 4]*); 8.03 (td, 1 H, J = 1.44, 7.74 Hz, *[b4]*); 7.88 – 7.93 (m, 6 H, J = undefined, *[v, bf, b6', 6']*); 7.78 (d, 1 H, J = 6 Hz, *[6]*); 7.75 (d, 1 H, J = 5.58 Hz, *[b6]*); 7.54 (dd, 1 H, J = 1.92, 6.8 Hz, *[5]*); 7.49 (m, 2 H, J = undefined, *[5', b5']*); 7.27 (t, 1 H, J = 1.2, 6.7 Hz, *[5]*).

[Ru(dppz)(bpyArCOOH)(bpyArCOOEt)]$(PF_6)_2$

The crude product was obtained using an identical procedure to that described for **(4)** and **(5)**. Purification was performed on silica using 70/26/4/2 $CHCl_3$/MeOH/H_2O/AcOH. The concentrated product fraction was treated with aqueous hexafluorophosphate to precipitate the product salt which was filtered. Dissolution in minimum acetone and re-precipitation from diethyl ether yielded the final complex as a mixture of isomers. Yield: orange solid, 152 mg (0.121 mmol, 91 %). ^{1}H NMR (600 MHz, CD_3CN) δ (ppm): 9.67 (m, 2 H); 8.80 (m, 4 H); 8.46 (m, 2 H); 8.28 (t, 1 H); 8.24 (m, 1 H); 8.10 – 8.22 (m, 7 H); 8.07 (m, 1 H); 8.01 (d, 1 H); 7.98 (t, 1 H); 7.89 – 7.96 (m, 5 H); 7.86 (d, 1 H); 7.81 (m, 2 H); 7.75 (qd, 1 H); 7.55 (m, 1 H); 7.52 (m, 1 H); 7.32 (t, 1 H); 4.37 (2x q, 2 H); 1.38 (2x t, 3 H). ^{13}C NMR (150 MHz, CD_3CN) δ (ppm): 166.55, 166.51, 158.26, 154.75, 154.67, 153.30, 151.48, 149.90, 143.76, 140.99, 140.89, 138,99, 138.90, 134.58, 133.52, 131.90, 131.33, 131.27, 131.14, 131.09, 130.62, 128.71, 128.62, 128.49, 128.24, 128.17, 125.95, 125.89, 125.63, 123.23,

123.17, 123.07. Anal. Calculated (Found) for $C_{54}H_{38}N_8O_4P_2F_{12}Ru.H_2O$: C 50.99 (51.11); H 3.17 (3.05); N 8.81 (8.59). HR-MS (ESI(+)-TOF) *m/z*: Calculated for $C_{54}H_{38}N_8O_4PF_6Ru$ $[M - PF_6]^+$: 1109.1701; Found: 1109.1757.

General synthesis of $[Ru(N^N)_2(ox)]$

cis-$Ru(DMSO)_4Cl_2$ (200 mg, 1 eq.) and sodium oxalate (1.5 eq., 83 mg) were heated at reflux for 1.5 hours in water (8 mL). The solution was then cooled and ligand (2 eq.) and ethylene glycol added (8 mL). The reaction solution was heated at reflux for at least 3 hours, cooled, and poured on stirring water (*ca*. 50 mL). After 30 minutes, the solids that precipitated were filtered, washed with water and ether (20 mL of each), and dried briefly in the oven (no longer than 1 h) at *ca*. 60 ºC. Generally, the products were obtained pure but where necessary purification on silica using 70/26/4 $CHCl_3/CH_3OH/H_2O$ afforded pure Ru-oxalate.

$[Ru(dpp)_2(ox)]$

Yield: Black powder, 270 mg (77 %). ^{1}H NMR (400 MHz, $CDCl_3$): δ (ppm) 9.72 (d, 2 H); 8.14 (d, 2 H); 8.09 (d, 2 H); 8.02 (d, 2 H); 7.95 (d, 2 H); 7.56 – 7.71 (m, 10 H); 7.47 – 7.55 (m, 6 H); 7.40 – 7.45 (m, 4 H); 7.24 (d, 2 H).

$[Ru(dppz)_2(ox)]$

Yield: Black powder, 284 mg (91 %). ^{1}H NMR (400 MHz, DMSO-d_6): δ (ppm) 9.58 (d, 4 H); 9.23 (s, 4 H); 8.42 (s, 4 H); 8.08 (s, 4 H); 7.98 (s, 4 H).

$[Ru(biq)_2(ox)]$

The procedure was modified to an 80/20 glycol/water ratio to account for the poor solubility of the biq ligand. Yield: Jade-green solid, 197 mg (68 %). ^{1}H NMR (400 MHz, DMSO-d_6): δ (ppm) 9.16 (d, 2 H); 9.10 (d, 2 H); 8.78 (d, 2 H); 8.61 (d, 2 H); 8.09 (d, 2 H); 7.99 (d, 2 H); 7.53 (t, 2 H); 7.28 (m, 4 H); 7.20 (t, 2 H); 6.78 (t, 2 H); 6.33 (d, 2 H).

$[Ru(bpyArCOOH)_2(ox)]$

The procedure was modified to an 75/25 glycol/water ratio to account for the poor solubility of the ligand. Yield: Purple solid, 229 mg (78 %). ^{1}H NMR (400MHz, DMSO-d_6/D_2O/NaOD, isomer mixture): δ (ppm) 8.76 – 8.95 (m, 3 H); 8.55 – 8.76 (m, 2 H); 7.82 – 8.13 (m, 9 H); 7.66 – 7.82 (m, 4 H); 7.43 – 7.64 (m, 2 H); 7.06, 7.41 (t, d, 1 H).

General synthesis of $[Ru(N^N)_2(N^N')]^{2+}$ from $[Ru(N^N)_2(ox)]$.

The oxalate cleavage step and subsequent reaction with a stoichiometric equivalent of ternary ligand was largely carried out as described for the *tris*-heteroleptic complexes. However, in some cases, lower relative solubility of the more lipophilic Ru-oxalates required 2 - 4 hours for full cleavage to provide Ru-solvate. The isolated solvates were then reacted in ethylene glycol for 3 – 6 hours as required to provide the final complexes which were precipitated from water as perchlorate or hexafluorophosphate salts. *Caution*! Perchlorate salts are potentially explosive.

$[Ru(bpyArCOOH)_2(dppz)](ClO_4)_2$

Yield = Orange-red solid (85 %). NMR characterisation matched that obtained previously by the Ru-dichloride and Ru-DMSO routes.

$[Ru(biq)_2(aphen)](PF_6)_2$

Yield = Purple solid (85 %). ^{1}H NMR (400 MHz, CD_3CN): δ (ppm) 9.05 (t, 2 H); 8.98 (m, 2 H); 8.80 (t, 2 H); 8.39 (d, 2 H); 8.28 (d, 1 H); 8.22 (m, 1 H); 8.15 (d, 2 H); 7.85 (m, 2 H); 7.72 (m, 3 H); 7.51 (m, 3 H); 7.38 (t, 2 H); 7.26 (q, 2 H); 7.17 (d, 1 H); 7.08 (t, 3 H); 6.82 (qu, 2 H); 6.58 (s, 1 H); 5.16 (bs, 2 H, N*H*$_2$).

$[Ru(dppz)_2(aphen)](PF_6)_2$

Yield = Orange solid (70 %). ^{1}H NMR (400 MHz, CD_3CN): δ (ppm) 9.64 (d, 4 H); 8.65 (d, 1 H); 8.48 (br s, 4 H); 8.12 – 8.32 (m, 10 H); 7.81 (m, 5 H); 7.65 (dd, 1 H); 7.45 (dd, 1 H); 7.22 (s, 1 H); 5.60 (bs, 2 H, N*H*$_2$). ^{13}C NMR (100 MHz, CD_3CN): δ (ppm) 155.37, 155.27, 155.11, 155.08, 153.85, 151.79, 151.76, 149.49, 149.20, 145.51, 143.78, 143.74, 143.09, 141.05, 135.06, 134.97, 134.91, 134.79, 134.52, 134.48, 134.44, 133.91, 133.59, 133.55, 133.49, 132.73, 131.95, 131.78, 130.60, 128.33, 128.23, 128.20, 126.69, 125.62, 125.01.

$[Ru(dppz)_2(bpyArCOOEt)](PF_6)_2$

Yield = Red solid (93 %). ^{1}H NMR (400 MHz, CD_3CN): δ (ppm) 9.62 – 9.73 (m, 4 H); 8.86 (s, 1 H); 8.79 (d, 1 H); 8.48 (m, 4 H); 8.40 (s, 1 H); 8.35 (m, 1 H); 8.11 – 8.21 (m, 8 H); 7.97 (m, 6 H); 7.85 (d, 1 H); 7.78 (d, 2 H); 7.62 (d, 1 H); 7.41 (t, 1 H); 4.36 (q, 2 H); 1.38 (t, 3 H). ^{13}C NMR (100 MHz, CD_3CN): δ (ppm) 166.52, 158.83, 158.21, 155.43, 155.15, 155.08, 155.04, 154.99, 153.65, 153.48, 151.70, 151.49, 151.44, 149.61, 143.76, 141.00, 140.81, 139.08, 134.80, 134.75, 134.65, 133.54, 133.17, 131.95, 131.89, 131.27, 131.12, 130.63, 130.61, 128.67, 128.67, 128.50, 128.46, 126.00, 125.65, 123.24, 62.22, 14.51. HR-MS (ESI(+)-TOF) *m/z*: Calculated for $C_{55}H_{36}N_{10}O_2PF_6Ru$ $[M + PF_6^-]^+$: 1115.1703; Found: 1115.1763.

General protocol for 'on-complex' ester hydrolysis

In a typical preparation, Ru-ester (1eq., *ca*. 200 mg) was suspended in THF/CH_3OH 4/1 (15 mL) and a solution of LiOH (20 mg) in 3 mL H_2O was added. The mixture was stirred overnight at room temperature before being concentrated by evaporation (to about 5 mL). The solution was diluted with water (20 mL) and made acidic with 1 M HCl. Addition of PF_6^- (aq.) precipitated the product which was filtered and washed with water. Yields were generally quantitative.

[Ru(dppz)(bpy)(bpyArCOOH)]$(PF_6)_2$

This complex was obtained quantitatively from the ester and characterisation data matched that previously for compound obtained by addition of bpyArCOOH to [Ru(dppz)(bpy)(ox)].

[Ru(dppz)$_2$(bpyArCOOH)]$(PF_6)_2$

Yield = > 99 %. ^{1}H NMR (600 MHz, DMSO-d_6): δ (ppm) 9.70 (d, 1 H); 9.66 (d, 2 H); 9.61 (d, 1 H); 9.21 – 9.30 (m, 1 H); 8.70 – 8.80 (m, 1 H); 8.54 (m, 4 H); 8.45 (m, 1 H); 8.27 – 8.39 (m, 3 H); 8.22 (m, 1 H); 8.19 (m, 4 H); 8.18 (d, 1 H); 8.15 (d, 1 H); 8.10 (m, 2 H); 8.02 (d, 1 H); 7.93 – 7.99 (m, 3 H); 7.90 (m, 1 H); 7.84 (m, 1 H); 7.50 (t, 1 H). ^{13}C NMR (150 MHz, DMSO-d_6): δ (ppm) 154.38, 150.58, 150.27, 150.21, 149.33, 141.94, 140.20, 133.46, 133.35, 132.62, 130.41, 130.15, 130.06, 129.44, 127.89, 127.78, 127.67, 127.60, 127.24, 127.13, 124.47, 121.84, 120.68, 117.78. HR-MS (ESI(+)-TOF) *m/z*: Calculated for $C_{53}H_{32}N_{10}O_2RuPF_6$, $[M^{2+} + PF_6^-]^+$: 1087.1390; Found: 1087.1410. Calculated for $C_{53}H_{32}N_{10}O_2Ru$ $[M]^+$: 942.1748; Found: 942.1768.

3.4.4 Synthesis of the Ru(II) PEG conjugates

Note; in all cases, the parent complex starting material was used as its mixture of isomers.

[Ru(dppz)(bpy-PEG)(bpyArCOOEt)](PF$_6$)$_2$

A suspension of DIPEA (15 μL, 0.086 mmol), HBTU (3.5 mg, 0.009 mmol) and [Ru(dppz)(bpyArCOOH)(bpyArCOOEt)](PF$_6$)$_2$ (10 mg, 0.008 mmol) in 2 mL dichloromethane was allowed to stir for 15 minutes at room temperature. To this was added a solution of m-dPEG$_{15}$-amine (7 mg, 0.010 mmol) in dichloromethane (2 mL). The mixture was left to stir for 16 hours and was then concentrated to dryness under a nitrogen stream. The residue was purified by column chromatography on silica using 9/1 CH_2Cl_2/MeOH as eluent. The product fraction was evaporated to dryness under nitrogen and treated to acetone/diethyl ether reprecipitation to provide the final PEG conjugate as a sticky red solid. Yield: isomer mixture, red tacky solid, 11 mg (0.006 mmol, 71 %). ^{1}H NMR (600 MHz, acetone-d$_6$) δ (ppm): 9.80 (m, 2 H); 9.25 (m, 2 H); 9.15 (m, 2 H); 8.69 (m, 1 H); 8.59 (m, 1 H); 8.52 (m, 2 H); 8.32 (m, 2 H); 8.09 – 8.26 (m, 13 H); 7.98 – 8.08 (m, 4 H); 7.78 (m, 1 H); 7.69 (m, 1 H); 7.46 (m, 1 H); 4.37 (2x q, 2 H, OEt -CH_2-); 3.34 – 3.72 (m, 60 H, PEG -OCH_2-); 3.25 (s, 3 H, PEG –OCH_3); 1.37 (2x t, 3 H, OEt –CH_3). HR-MS (MALDI-QTOF) *m/z*: Calculated for $C_{85}H_{101}N_9O_{18}PF_6Ru$ [M - PF_6^-]$^+$: 1782.5950; Found: 1782.6034.

[Ru(dppz)(bpy-PEG)(bpyArCOOH)](PF$_6$)$_2$

The Ru-PEG precursor (10 mg, 0.005 mmol) was dissolved in 1.25 mL of a 4/1 THF/methanol mixture under stirring at room temperature. To this was added an aqueous solution of LiOH.H_2O (1 mg in 0.25 mL). After 2 h, the mixture was concentrated under nitrogen to *ca*. 0.5 mL and treated with 0.5 mL of 0.1 M HCl and 0.5 mL of saturated aqueous ammonium hexafluorophosphate. After diluting with 1 mL water, the product was extracted into 4 x 2 mL dichloromethane and the combined organic phase was washed with 5 mL water. The separated organic layer was dried over anhydrous magnesium sulphate, filtered and evaporated to dryness under nitrogen. Yield = red solid, 9 mg (0.005 mmol, 91 %). ^{1}H NMR (400 MHz, acetone-d$_6$) δ (ppm): 9.80 (d, 2 H); 9.25 (tm, 2 H); 9.16 (m, 2 H); 8.70 (m, 1 H); 8.62 (m, 1 H); 8.53 (m, 2 H); 8.26 – 8.41 (m, 3 H); 8.08 – 8.26 (m, 11 H); 7.96 – 8.08 (m, 4 H); 7.87 – 7.96 (m, 1 H); 7.78 (m, 1 H); 7.70 (m, 1 H); 7.46 (m, 1 H); 3.38 – 3.80 (m, 60 H, PEG –OCH_2-); 3.28 (s, 3 H, PEG –OCH_3). HR-MS (MALDI-QTOF) *m/z*: Calculated for $C_{83}H_{97}N_9O_{18}PF_6Ru$ [M - PF_6]$^+$: 1754.5637; Found: 1754.5691.

3.4.5 Synthesis of the peptide conjugates

Note; in all cases, the parent complex starting material was used as its mixture of isomers.

General procedure for synthesis of the peptide conjugates:

A generalised approach was developed as follows: Ru-COOH (1 eq), Peptide-NH_2 (2 eq), DIPEA (20 eq) and PyBOP (4 eq) were dissolved in DMF (700 uL for 10 mg Ru-COOH) in a glass vial. The resultant mixture was stirred at room temperature for at least 16 hours when reaction progress was checked by HPLC. The conjugates were precipitated by the addition of minimum sat. NH_4PF_6 aq. solution and were filtered and washed carefully with water and ether. Conversion to the chloride form was achieved using TBAC/acetone precipitation. In general, this protocol yielded pure conjugate but purification if necessary was performed using reverse phase pTLC on C18-silica 100 um plates with 0.1 % TFA in 95/5 MeCN/H_2O as mobile phase to separate free parent and peptide from the conjugate which remains near the baseline. The product band was then eluted from a packed filter column using 0.1 % TFA in 50/50 MeCN/H_2O. Evaporation of this solution provides the TFA salt but typically the PF_6^- and subsequently the Cl^- salt were obtained using NH_4PF_6/H_2O and TBAC/Acetone precipitations from a concentrated solution of the eluate.

$[Ru(dppz)(bpy)(bpyAr\text{-}CONH\text{-}Ahx\text{-}RRRRRRRR\text{-}CONH_2)]^{10+}$; Ru-R8

^1H NMR (600 MHz, 99/1 CD_3OD/D_2O); δ (ppm) 9.78 – 9.86 (m, 2 H); 9.01 – 9.13 (2x dd, 2H); 8.50 – 8.81 (m, 2x dd, 4 H); 8.43 (2x d, 1 H); 8.30 – 8.34 (2x m, 1 H); 8.21 (td, 1 H); 7.96 – 8.16 (m, 12 H); 7.80 – 7.94 (m, 3 H); 7.39 – 7.62 (m, 3 H); 4.32 (m, 8 H, Peptide Alpha-H); 3.43 (m, 2 H, Ahx-H); 3.24 (m, 16 H, Arg-H); 3.20 (m, 2 H, Ahx-H); 2.38 (t, 2 H, Ahx-H); 1.62 – 1.99 (br m, 38 H, Arg-H and Ahx-H). HR-MS (MALDI-QTOF) *m/z*: Calculated for $C_{99}H_{138}N_{42}O_{10}Ru$ $[M^+]$: 2177.0625; Found 2177.0671. Calculated for $C_{99}H_{138}N_{42}O_{10}RuPF_6$ $[M+PF_6^-]^+$: 2322.0261 ; Found 2322.1116. HPLC (Purity vs parent: RP-Diphenyl, 450 nm, 0.1 % TFA in H_2O/CH_3CN gradient): Ru-R8 peaks at 13.29 and 14.41 minutes and no parent peak observed at 17.32 minutes.

$[Ru(dppz)(bpy)(bpyAr\text{-}CONH\text{-}Ahx\text{-}VQRKRQKLMP\text{-}CONH_2)]^{6+}$; Ru-NLS

The synthesis and characterisation of this compound has been previously reported elsewhere.[117] ^1H NMR (600 MHz, D_2O drop in CD_3CN) δ (ppm) 9.66 (d, 2 H); 8.77 (m, 2 H); 8.57 (m, 2 H); 8.42 (m, 2 H); 8.08 – 8.25 (m, 5 H); 7.94 – 8.07 (m, 3 H); 7.90 (m, 6 H); 7.74 (m, 3 H); 7.50 (m, 2 H); 7.27 (m, 2 H); 5.34 (t, 1 H); 4.72 (s, 1 H); 4.26 (s, 2 H); 4.11 (s, 5 H); 3.87 (m, 1 H); 3.59 (s, 2 H); 3.31 (s, 2 H); 2.96 – 3.17 (m, 50 H); 2.87 (m, 14 H); 2.58 (m, 2 H); 2.30 (m, 5 H); 2.11 (m, 2 H); 1.97 – 2.07 (m, 6 H); 1.67 – 1.88 (m, 8 H); 1.57 (m, 12 H); 1.20 – 1.45 (m, 15 H); 1.17 (s, 1 H); 0.73 – 0.98 (m, 11 H). HR-MS (MALDI (CHCA)-QTOF) *m/z*: Calculated for $C_{106}H_{146}N_{30}O_{14}PF_6Ru$ [M + 4H (Basic

Residues) + PF_6^-]$^+$: 2342.0035; Found: 2342.1399. HPLC (Purity vs parent, RP-Diphenyl, 450 nm, 0.1 % TFA in H_2O/CH_3CN gradient): Ru-NLS broad peak at 13.5 – 16.0 minutes (maximum at 14.81 minutes) and no parent peak observed at 17.32 minutes.

[Ru(dppz)(bpy)(bpyAr-CONH-Ahx-FrFKFrFK(Ac)-$CONH_2$)]$^{5+}$; Ru-MPP

^{1}H NMR (600 MHz, 99/1 CD_3OD/D_2O); δ (ppm) 9.80 (m, 2 H); 8.96 – 9.10 (m, 2 H); 8.78 (m, 2 H); 8.41 – 8.54 (m, 3 H); 8.28 – 8.40 (m, 2 H); 8.21 (t, 1 H); 7.94 – 8.18 (m, 12 H); 7.82 – 7.92 (m, 8 H); 7.59 (m, 1 H); 7.37 – 7.51 (m, 2 H); 7.04 – 7.31 (br m, 14 H, Phe-H); 4.53 (m, 4 H, Peptide Alpha-H); 4.00 – 4.31 (3x m, 4 H, Peptide Alpha-H); 3.14 (m, 4 H, Ahx-H); 2.93 (m, 18 H, Peptide-H); 0.89 – 1.94 (m, 27 H, Ahx-H, Peptide-H). HR-MS (Q-Exactive, Ion-Trap MS$^+$, MeOH/TFA); Calculated for $C_{113}H_{131}N_{26}O_{11}Ru$: [M]$^{5+}$ 426.1908, Found 425.9915; [M-H]$^{4+}$ Calculated 532.4867, Found 532.2376; [M-H+TFA^-]$^{3+}$ Calculated 747.6441, Found 747.3115. HPLC (Purity vs parent, RP-Diphenyl, 450 nm, 0.1 % TFA in H_2O/CH_3CN gradient): Ru-MPP broad peak at 14 – 16.5 minutes (maximum at 15.17 minutes) and no parent peak observed at 17.32 minutes.

[Ru(dppz)(bpyAr-PEG)(bpyAr-CONH-Ahx-VQRKRQKLMP-$CONH_2$)]$^{6+}$;
Rudb-PEGb-NLS

^{1}H NMR (600 MHz, CD_3OD/D_2O): δ (ppm) 9.82 (s, 2 H); 9.09 (m, 2 H); 9.00 (s, 2 H); 8.53 (s, 2 H); 8.42 (s, 1 H); 8.34 (s, 1 H); 8.27 (s, 1 H); 7.99 – 8.19 (m, 15 H); 7.94 (m, 3 H); 7.74 (s, 1 H); 7.63 (s, 1 H); 7.44 (s, 1 H); 3.84 – 4.48 (m, 10 H, alpha-H); 3.47 – 3.78 (m, 63 H, PEG-H); 2.79 – 3.28 (m, 15 H); 2.67 (s, 3 H); 1.24 – 2.47 (m, 52 H); 0.79 – 1.05 (m, 14 H). HPLC (Purity vs parent: RP-Diphenyl, 450 nm, 0.1 % TFA in H_2O/CH_3CN gradient): Rudb-PEGb-NLS peak observed at 13 -16 minutes (maximum at 14.95 minutes; integration to 97.3 %) and impurity parent peak observed at 16.35 minutes (integration to 2.7 %).

[Ru(dppz)(bpyAr-PEG)(bpyAr-CONH-Ahx-FrFKFrFK-$CONH_2$)]$^{5+}$;
Rudb-PEGb-MPP

^{1}H NMR (600 MHz, CD_3OD/D_2O): δ (ppm) 9.82 (m, 2 H); 9.11 (d, 2 H); 9.02 (m, 2 H); 8.53 (s, 2 H); 8.42 (s, 1 H); 8.34 (t, 1 H); 8.26 (t, 1 H); 7.87 – 8.19 (m, 20 H); 7.74 (m, 1 H); 7.63 (t, 1 H); 7.43 (m, 1 H); 7.12 – 7.33 (m, 18 H, Phe-H); 4.52, 4.02 – 4.33 (m, 8 H, alpha-H); 3.45 – 3.75 (m, 63 H, PEG-H); 3.25 (m, 3 H); 3.17 (m, 5 H); 2.86 – 3.07 (m, 10 H); 2.23 (m, 3 H); 0.84 – 2.05 (m, 35 H). HPLC (Purity vs parent: RP-Diphenyl, 450 nm, 0.1 % TFA in H_2O/CH_3CN gradient): Rudb-PEGb-MPP peak observed at 14 -16 minutes (maximum at 14.97 minutes) and no impurity parent peak observed at 16.33 minutes.

[Ru(dppz)(bpyAr-CONH-Ahx-FrFKFrFK(Ac)-$CONH_2$)]$^{8+}$; RuMPP2

^{1}H NMR (600 MHz; MeOD/D_2O): δ (ppm) 9.82 (t, 2 H); 9.03 (m, 4 H); 7.79 – 8.68 (m, 28 H); 7.36 – 7.79 (m, 5 H); 7.21 (br s, 33 H, Phe-H); 3.83 – 4.58 (m, 16 H, alpha-H); 2.81 – 3.27 (m, 31 H); 0.80 – 2.30 (m, 72 H).

[$Ru(bpy)_2$(phen-Ar-CONH-RQIKIWFQNRRMKWKK-$CONH_2$)]$^{9+}$; Ru-phen-ER

The synthesis and characterisation of this compound has been previously reported elsewhere.[117] ^{1}H NMR (600 MHz; Acetone-d_6): δ (ppm) 9.32 (m, 2 H); 8.94 (s, 1H); 8.82 (m, 1 H); 8.64 (m, 5 H, Ru-Ar-*H*); 8.30 (d, 1 H, Ru-Ar-*H*); 8.21 (m, 5 H, Ru-Ar-*H*); 8.12 (t, 3 H, Ru-Ar-*H*); 7.97 (s, 1 H, Ru-Ar-*H*); 7.88 (dd, 1 H, Ru-Ar-*H*); 7.80 (m, 2 H, Ru-Ar-*H*); 7.69 (dd, 2 H); 7.63 (d, 1 H, Ru-Ar-*H*); 7.57 (m, 3 H, Ru-Ar-*H*); 7.40 (m, 9 H); 7.18 (m, 3 H, Ru-Ar-*H*); 7.03 (m, 1 H); 6.88 (m, 2 H); 6.55 (m, br, 3 H); 6.36 (m, 1 H); 6.30 (q, 1 H); 6.21 (m, 10 H); 5.97 (m, 10 H); 5.56 (s, 1 H); 5.46 (t, 2 H); 3.6 – 4.5 (m, 16 H, peptide backbone H); 3.62 (s, 2 H); 3.47 (m, 6 H); 3.20 (m, 16 H); 2.68 (m, 8 H); 2.49 (m, 8 H); 2.28 (s, 4 H); 2.21 (t, 3 H); 2.14 (m, 5 H); 1.97 (s, 2 H); 1.94 (p, 2 H); 1.88 (m, 5 H); 1.71 (m, 14 H); 1.57 (s, 4 H); 1.3 – 1.5 (m, 21 H); 1.29 (s, 1 H). HR-MS (MALDI (DCTB)-QTOF ES$^+$): Found (Calcd.) *m/z* ; 1001.5954 (Calcd. for $C_{148}H_{203}N_{42}O_{21}Ru$ [(M - SMe (Met residue))]$^{3+}$: 1002.1717); 751.4481 (Calcd. for $C_{148}H_{203}N_{42}O_{21}Ru$ [(M - SMe (Met residue))]$^{4+}$: 751.6288).

[$Ru(bpy)_2$(phen-Ar-CONH-RRRRRRRR-$CONH_2$)]$^{10+}$; Ru-phen-R8

^{1}H NMR matched that published previously.[92] HR-MS (MALDI (DCTB)-QTOF ES+): *m/z* calculated for $C_{93}H_{136}F_6N_{40}O_{10}PRu$ [(M + PF_6^-)]$^+$: 2220.0054, Found: 2220.0012.

3.5 References

(1) Vos, J. G.; Kelly, J. M. *Dalton Trans.* **2006**, No. 41, 4869.
(2) Kiwi, J.; Grätzel, M. *Nature* **1979**, *281* (5733), 657.
(3) Dini, D.; Pryce, M. T.; Schulz, M.; Vos, J. G. In *Functional Metallosupramolecular Materials*; 2015; pp 345–396.
(4) Juris, A.; Balzani, V.; Barigelletti, F.; Campagna, S.; Belser, P.; von Zelewsky, A. *Coord. Chem. Rev.* **1988**, No. 84, 85.
(5) Kalyanasundaram, K. *Coord. Chem. Rev.* **1982**, *46*, 159.
(6) Balzani, V.; Juris, A.; Venturi, M.; Campagna, S.; Serroni, S. *Chem. Rev.* **1996**, *96* (2), 759.
(7) Balzani, V.; Campagna, S.; Denti, G.; Juris, A.; Serroni, S.; Venturi, M. *Acc. Chem. Res.* **1998**, *31* (1), 26.
(8) Balzani, V.; Bergamini, G.; Marchioni, F.; Ceroni, P. *Coord. Chem. Rev.* **2006**, *250* (11–12), 1254.
(9) Anderson, P. A.; Strouse, G. F.; Treadway, J. A.; Keene, F. R.; Meyer, T. J. *Inorg. Chem.* **1994**, *33* (18), 3863.
(10) Anderson, P. A.; Keene, F. R.; Meyer, T. J.; Moss, J. A.; Strouse, G. F.; Treadway, J. A. *J. Chem. Soc. Dalton Trans.* **2002**, No. 20, 3820.
(11) Burke, C. S.; Keyes, T. E. *RSC Adv.* **2016**, *6* (47), 40869.
(12) Burstall, F. H. *J. Chem. Soc. Resumed* **1936**, No. 0, 173.
(13) Dwyer, F. P.; Humpoletz, J. E.; Nyholm, R. S. *J. Proc. R. Soc. NSW* **1946**, *80*, 212.
(14) Liu, C. F.; Liu, N. C.; Bailar, J. C. *Inorg. Chem.* **1964**, *3* (8), 1085.
(15) Miller, R. R.; Brandt, W. W.; Puke, M.; Puke, O. S. F. *J. Am. Chem. Soc.* **1955**, *77* (12), 3178.
(16) Brandt, W. W.; Dwyer, F. P.; Gyarfas, E. D. *Chem. Rev.* **1954**, *54* (6), 959.
(17) Dwyer, F. P.; Goodwin, H. A.; Gyarfas, E. C. *Aust. J. Chem.* **1963**, *16* (4), 544.
(18) Togano, T.; Nagao, N.; Tsuchida, M.; Kumakura, H.; Hisamatsu, K.; Howell, F. S.; Mukaida, M. *Inorganica Chim. Acta* **1992**, *195* (2), 221.
(19) Wallace, W. M.; Hoggard, P. E. *Inorg. Chem.* **1979**, *18* (10), 2934.
(20) Sullivan, B. P.; Salmon, D. J.; Meyer, T. J. *Inorg. Chem.* **1978**, *17* (12), 3334.
(21) Sprintschnik, G.; Sprintschnik, H. W.; Kirsch, P. P.; Whitten, D. G. *J. Am. Chem. Soc.* **1977**, *99* (15), 4947.
(22) Spiccia, L.; Deacon, G. B.; Kepert, C. M. *Coord. Chem. Rev.* **2004**, *248* (13–14), 1329.
(23) Dolan, C. The synthesis and characterisation of inorganic and organic luminophores suitable for biomolecule conjugation. PhD Thesis, Dublin City University. School of Chemical Sciences, 2012.
(24) Belser, P.; Zelewsky, A. V. *Helv. Chim. Acta* **1980**, *63* (6), 1675.
(25) Viala, C.; Coudret, C. *Inorganica Chim. Acta* **2006**, *359* (3), 984.
(26) Clear, J. M.; Kelly, J. M.; O'Connell, C. M.; Vos, J. G.; Cardin, C. J.; Costa, S. R.; Edwards, A. J. *J. Chem. Soc. Chem. Commun.* **1980**, No. 16, 750.
(27) Zabarska, N.; Vos, J. G.; Rau, S. *Polyhedron* **2015**, *102*, 173.
(28) Thomas, N. C.; Deacon, G. B.; Llobet, A.; Meyer, T. J. In *Inorganic Syntheses*; Allcock, H. R., Ed.; John Wiley & Sons, Inc., 1989; pp 107–110.
(29) Mulhern, D.; Brooker, S.; Görls, H.; Rau, S.; Vos, J. G. *Dalton Trans.* **2006**, No. 1, 51.
(30) Black, D. S. C.; Deacon, G. B.; Thomas, N. C. *Inorganica Chim. Acta* **1982**, *65*, L75.
(31) Evans, I. P.; Spencer, A.; Wilkinson, G. *J. Chem. Soc. Dalton Trans.* **1973**, No. 2, 204.
(32) Mulhern, D. Synthesis and characterisation of Ruthenium(II) tris(heteroleptic) complexes containing a triazole ligand. PhD Thesis, Dublin City University. School of Chemical Sciences, 2003.
(33) Alston, J. R.; Kobayashi, S.; Younts, T. J.; Poler, J. C. *Polyhedron* **2010**, *29* (13), 2696.

(34) Adeloye, A. O.; Ajibade, P. A.; Cummings, F. R.; Roux, L. J. L.; Mamphweli, S. N.; Meyer, E. L. *J. Chem. Sci.* **2013**, *125* (1), 17.
(35) Crutchley, R. J.; Lever, A. B. P. *J. Am. Chem. Soc.* **1980**, *102* (23), 7128.
(36) Crutchley, R. J.; Lever, A. B. P. *Inorg. Chem.* **1982**, *21* (6), 2276.
(37) Kirsch-De Mesmaeker, A.; Nasielski-Hinkens, R.; Maetens, D.; Pauwels, D.; Nasielski, J. *Inorg. Chem.* **1984**, *23* (3), 377.
(38) Pascu, G. I.; Hotze, A. C. G.; Sanchez-Cano, C.; Kariuki, B. M.; Hannon, M. J. *Angew. Chem. Int. Ed.* **2007**, *46* (23), 4374.
(39) Le Gac, S.; Foucart, M.; Gerbaux, P.; Defrancq, E.; Moucheron, C.; Kirsch - De Mesmaeker, A. *Dalton Trans.* **2010**, *39* (40), 9672.
(40) Zakeeruddin, S. M.; Nazeeruddin, M. K.; Humphry-Baker, R.; Péchy, P.; Quagliotto, P.; Barolo, C.; Viscardi, G.; Grätzel, M. *Langmuir* **2002**, *18* (3), 952.
(41) Suzuki, T.; Kuchiyama, T.; Kishi, S.; Kaizaki, S.; Takagi, H. D.; Kato, M. *Inorg. Chem.* **2003**, *42* (3), 785.
(42) Black, D. S. C.; Deacon, G. B.; Thomas, N. C. *Aust. J. Chem.* **1982**, *35* (12), 2445.
(43) Krause, R. A. *Inorganica Chim. Acta* **1977**, *22*, 209.
(44) Strouse, G. F.; Anderson, P. A.; Schoonover, J. R.; Meyer, T. J.; Keene, F. R. *Inorg. Chem.* **1992**, *31* (14), 3004.
(45) Anderson, P. A.; Deacon, G. B.; Haarmann, K. H.; Keene, F. R.; Meyer, T. J.; Reitsma, D. A.; Skelton, B. W.; Strouse, G. F.; Thomas, N. C. *Inorg. Chem.* **1995**, *34* (24), 6145.
(46) Treadway, J. A.; Meyer, T. J. *Inorg. Chem.* **1999**, *38* (10), 2267.
(47) Deacon, G. B.; Kepert, C. M.; Sahely, N.; Skelton, B. W.; Spiccia, L.; Thomas, N. C.; White, A. H. *J. Chem. Soc. Dalton Trans.* **1999**, *0* (3), 275.
(48) Kepert, C. M.; Bond, A. M.; Deacon, G. B.; Spiccia, L.; Skelton, B. W.; White, A. H. *Dalton Trans.* **2004**, *0* (11), 1766.
(49) Thummel, R. P.; Lefoulon, F.; Chirayil, S. *Inorg. Chem.* **1987**, *26* (18), 3072.
(50) Hesek, D.; Inoue, Y.; Everitt, S. R. L.; Ishida, H.; Kunieda, M.; Drew, M. G. B. *Inorg. Chem.* **2000**, *39* (2), 308.
(51) Maxwell, K. A.; Sykora, M.; DeSimone, J. M.; Meyer, T. J. *Inorg. Chem.* **2000**, *39* (1), 71.
(52) Zakeeruddin, S. M.; Nazeeruddin, M. K.; Humphry-Baker, R.; Grätzel, M.; Shklover, V. *Inorg. Chem.* **1998**, *37* (20), 5251.
(53) von Zelewsky, A.; Gremaud, G. *Helv. Chim. Acta* **1988**, *71* (5), 1108.
(54) Juris, A.; Campagna, S.; Balzani, V.; Gremaud, G.; Von Zelewsky, A. *Inorg. Chem.* **1988**, *27* (20), 3652.
(55) Cuello-Garibo, J.-A.; Pérez-Gallent, E.; van der Boon, L.; Siegler, M. A.; Bonnet, S. *Inorg. Chem.* **2017**, *56* (9), 4818.
(56) Freedman, D. A.; Evju, J. K.; Pomije, M. K.; Mann, K. R. *Inorg. Chem.* **2001**, *40* (22), 5711.
(57) Myahkostupov, M.; Castellano, F. N. *Inorg. Chem.* **2011**, *50* (19), 9714.
(58) Mulcahy, S. P.; Li, S.; Korn, R.; Xie, X.; Meggers, E. *Inorg. Chem.* **2008**, *47* (12), 5030.
(59) Meggers, E. *Chem. – Eur. J.* **2010**, *16* (3), 752.
(60) Gong, L.; Lin, Z.; Harms, K.; Meggers, E. *Angew. Chem. Int. Ed.* **2010**, *49* (43), 7955.
(61) Gong, L.; Wenzel, M.; Meggers, E. *Acc. Chem. Res.* **2013**, *46* (11), 2635.
(62) Fu, C.; Wenzel, M.; Treutlein, E.; Harms, K.; Meggers, E. *Inorg. Chem.* **2012**, *51* (18), 10004.
(63) Gong, L.; Mulcahy, S. P.; Devarajan, D.; Harms, K.; Frenking, G.; Meggers, E. *Inorg. Chem.* **2010**, *49* (17), 7692.
(64) Gong, L.; Mulcahy, S. P.; Harms, K.; Meggers, E. *J. Am. Chem. Soc.* **2009**, *131* (28), 9602.
(65) Neugebauer, U.; Pellegrin, Y.; Devocelle, M.; Forster, R. J.; Signac, W.; Moran, N.; Keyes, T. E. *Chem. Commun.* **2008**, No. 42, 5307.
(66) Cosgrave, L.; Devocelle, M.; Forster, R. J.; Keyes, T. E. *Chem. Commun.* **2010**, *46* (1), 103.

(67) Blackmore, L.; Moriarty, R.; Dolan, C.; Adamson, K.; Forster, R. J.; Devocelle, M.; Keyes, T. E. *Chem. Commun.* **2013**, *49* (26), 2658.
(68) Adamson, K.; Dolan, C.; Moran, N.; Forster, R. J.; Keyes, T. E. *Bioconjug. Chem.* **2014**, *25* (5), 928.
(69) Dolan, C.; Moriarty, R. D.; Lestini, E.; Devocelle, M.; Forster, R. J.; Keyes, T. E. *J. Inorg. Biochem.* **2013**, *119*, 65.
(70) Byrne, A.; Dolan, C.; Moriarty, R. D.; Martin, A.; Neugebauer, U.; Forster, R. J.; Davies, A.; Volkov, Y.; Keyes, T. E. *Dalton Trans.* **2015**, *44* (32), 14323.
(71) Steck, E. A.; Day, A. R. *J. Am. Chem. Soc.* **1943**, *65* (3), 452.
(72) Miyaura, N.; Yamada, K.; Suzuki, A. *Tetrahedron Lett.* **1979**, *20* (36), 3437.
(73) Das, N.; Bindra, G. S.; Paul, A.; Vos, J. G.; Schulz, M.; Pryce, M. T. *Chem. – Eur. J.* **2017**, *23* (22), 5330.
(74) Kowacs, T.; O'Reilly, L.; Pan, Q.; Huijser, A.; Lang, P.; Rau, S.; Browne, W. R.; Pryce, M. T.; Vos, J. G. *Inorg. Chem.* **2016**, *55* (6), 2685.
(75) Hissler, M.; Connick, W. B.; Geiger, D. K.; McGarrah, J. E.; Lipa, D.; Lachicotte, R. J.; Eisenberg, R. *Inorg. Chem.* **2000**, *39* (3), 447.
(76) Fang, Y.-Q.; Hanan, G. S. *Synlett* **2003**, *2003* (06), 0852.
(77) Zalas, M.; Gierczyk, B.; Cegłowski, M.; Schroeder, G. *Chem. Pap.* **2012**, *66* (8), 733.
(78) Martin, A.; Moriarty, R. D.; Long, C.; Forster, R. J.; Keyes, T. E. *Asian J. Org. Chem.* **2013**, *2* (9), 763.
(79) Hermanson, G. T. *Bioconjugate techniques*, 2. ed.; Elsevier Acad. Press: Amsterdam, 2008.
(80) Lo, K. K.-W.; Choi, A. W.-T.; Law, W. H.-T. *Dalton Trans.* **2012**, *41* (20), 6021.
(81) Stewart, K. M.; Horton, K. L.; Kelley, S. O. *Org. Biomol. Chem.* **2008**, *6* (13), 2242.
(82) Horton, K. L.; Stewart, K. M.; Fonseca, S. B.; Guo, Q.; Kelley, S. O. *Chem. Biol.* **2008**, *15* (4), 375.
(83) Chakrabortty, S.; Agrawalla, B. K.; Stumper, A.; Vegi, N. M.; Fischer, S.; Reichardt, C.; Kögler, M.; Dietzek, B.; Feuring-Buske, M.; Buske, C.; Rau, S.; Weil, T. *J. Am. Chem. Soc.* **2017**.
(84) Joshi, N. S.; Whitaker, L. R.; Francis, M. B. *J. Am. Chem. Soc.* **2004**, *126* (49), 15942.
(85) Adamson, K. Peptide Modified Probes and Surfaces for Protein Sensing and Platelet Capture. PhD Thesis, 2014.
(86) Montalbetti, C. A. G. N.; Falque, V. *Tetrahedron* **2005**, *61* (46), 10827.
(87) del Fresno, M.; El-Faham, A.; Carpino, L. A.; Royo, M.; Albericio, F. *Org. Lett.* **2000**, *2* (23), 3539.
(88) Coste, J.; Le-Nguyen, D.; Castro, B. *Tetrahedron Lett.* **1990**, *31* (2), 205.
(89) Dickeson, J.; Summers, L. *Aust. J. Chem.* **1970**, *23* (5), 1023.
(90) Paw, W.; Eisenberg, R. *Inorg. Chem.* **1997**, *36* (11), 2287.
(91) Martin, A.; Byrne, A.; Dolan, C.; Forster, R. J.; Keyes, T. E. *Chem. Commun.* **2015**.
(92) Martin, A.; Byrne, A.; Burke, C. S.; Forster, R. J.; Keyes, T. E. *J. Am. Chem. Soc.* **2014**, *136* (43), 15300.
(93) Paul, A. Synthesis and characterisation of polypyridyl metal complexes for new fuels. PhD Thesis, Dublin City University. School of Chemical Sciences, 2012.
(94) Romero, F. M.; Ziessel, R. *Tetrahedron Lett.* **1995**, *36* (36), 6471.
(95) Vassiliki Theodorou, K. S. *Tetrahedron Lett.* **2007**, *48* (46), 8230.
(96) Amouyal, E.; Homsi, A.; Chambron, J.-C.; Sauvage, J.-P. *J. Chem. Soc. Dalton Trans.* **1990**, No. 6, 1841.
(97) Byrne, A.; Jacobs, J.; Burke, C. S.; Martin, A.; Heise, A.; Keyes, T. E. *Analyst* **2017**, *142* (18), 3400.
(98) Mercer, A.; Trotter, J. *J. Chem. Soc. Dalton Trans.* **1975**, No. 23, 2480.
(99) Alessio, E. *Chem. Rev.* **2004**, *104* (9), 4203.

(100) Concepcion, J. J.; Jurss, J. W.; Templeton, J. L.; Meyer, T. J. *J. Am. Chem. Soc.* **2008**, *130* (49), 16462.
(101) Lebeau, E. L.; Adeyemi, S. A.; Meyer, T. J. *Inorg. Chem.* **1998**, *37* (25), 6476.
(102) Bratsos, I.; Serli, B.; Zangrando, E.; Katsaros, N.; Alessio, E. *Inorg. Chem.* **2007**, *46* (3), 975.
(103) Sattigeri, V. J.; Soni, A.; Gupta, L. K.; Ray, A.; Ahmad, S.; Gupta, J. B.; Salman, M. *Indian J. Chem.* **2006**, *45B*, 2534.
(104) Boynton, A. N.; Marcélis, L.; Barton, J. K. *J. Am. Chem. Soc.* **2016**, *138* (15), 5020.
(105) Xie, X.; Mulcahy, S. P.; Meggers, E. *Inorg. Chem.* **2009**, *48* (3), 1053.
(106) Luis, E. T.; Ball, G. E.; Gilbert, A.; Iranmanesh, H.; Newdick, C. W.; Beves, J. E. *J. Coord. Chem.* **2016**, *69* (11–13), 1686.
(107) Friedman, A. E.; Chambron, J. C.; Sauvage, J. P.; Turro, N. J.; Barton, J. K. *J. Am. Chem. Soc.* **1990**, *112* (12), 4960.
(108) Puckett, C. A.; Barton, J. K. *J. Am. Chem. Soc.* **2007**, *129* (1), 46.
(109) Carraway, E. R.; Demas, J. N.; DeGraff, B. A.; Bacon, J. R. *Anal. Chem.* **1991**, *63* (4), 337.
(110) Keyes, T. E.; Vos, J. G.; Kolnaar, J. A.; Haasnoot, J. G.; Reedijk, J.; Hage, R. *Inorganica Chim. Acta* **1996**, *245*, 237.
(111) Wachter, E.; Heidary, D. K.; Howerton, B. S.; Parkin, S.; Glazer, E. C. *Chem. Commun.* **2012**, *48* (77), 9649.
(112) Bratsos, I.; Birarda, G.; Jedner, S.; Zangrando, E.; Alessio, E. *Dalton Trans.* **2007**, No. 36, 4048.
(113) Adeyemi, S. A.; Dovletoglou, A.; Guadalupe, A. R.; Meyer, T. J. *Inorg. Chem.* **1992**, *31* (8), 1375.
(114) Dovletoglou, A.; Adeyemi, S. A.; Meyer, T. J. *Inorg. Chem.* **1996**, *35* (14), 4120.
(115) Blackmore, L. Novel luminescent peptide conjugates for assessing protein and other biomolecules location and function. PhD Thesis, Dublin City University. School of Chemical Sciences, 2013.
(116) Derossi, D.; Joliot, A. H.; Chassaing, G.; Prochiantz, A. *J. Biol. Chem.* **1994**, *269* (14), 10444.
(117) Byrne, A.; Burke, C. S.; Keyes, T. E. *Chem. Sci.* **2016**, *7* (10), 6551.
(118) Pedersen, S. L.; Tofteng, A. P.; Malik, L.; Jensen, K. J. *Chem. Soc. Rev.* **2012**, *41* (5), 1826.
(119) Mahindra, A.; Sharma, K. K.; Jain, R. *Tetrahedron Lett.* **2012**, *53* (51), 6931.
(120) Lecomte, J.-P.; Mesmaeker, A. K.-D.; Demeunynck, M.; Lhomme, J. *J. Chem. Soc. Faraday Trans.* **1993**, *89* (17), 3261.

Chapter 4

Ru-dppz peptide conjugates; targeting nuclear and mitochondrial DNA in live cells with a molecular light switch.

Notes

With the exception of the isolated geometric isomers of Ru-acid (t-bpy and t-dppz), all other complexes and Ru-peptide conjugates were analysed as their mixture of isomers (geometric and stereoisomers). All practical cell work was carried out by Dr. Aisling Byrne (DCU); for methods see Chapter 2. Cell data interpretation described herein was also carried out in collaboration with Dr. Byrne.

4.1 Introduction:

Optical probes capable of precisely targeting cellular DNA for dynamic imaging are crucially important to further our understanding of cellular function in areas such as DNA damage, repair and signalling. DNA is a vital therapeutic target, responsible for regulating cellular proliferation, and its targeting and destruction are a key approach in chemotherapy.[1–4] Capacity to both selectively destroy cell DNA and simultaneously monitor its destruction and consequences are key objectives in theranostics. Fluorescence microscopy is a key modality employed across biochemistry to study live cellular processes and function. As discussed in Chapter 1, there is a growing appreciation for metal complex luminophores as viable alternatives to commercial cellular imaging probes which are typically organic-based dyes and often limited by their relatively poor photostability, environmental insensitivity, and a short-lived and narrow Stokes-shifted fluorescence.[5–7] In contrast, coordinatively-saturated metal complexes like Ru(II) polypyridyl complexes, exhibit visible absorption, large Stokes shifts and moderate to long-lived luminescence lifetime that consequently renders the emission environmentally sensitive permitting sensing of important cellular viability indicators such as pH, O_2 and reactive oxygen species (ROS).[8–11] Importantly, judicious ligand choice may induce spectroscopic responses upon interactions with various biomolecules including DNA, and the modular nature of Ru(II) polypyridyl complexes also leads to a broad range of dark and photo-cytotoxicities.[12] In terms of theranosis, there is a clear balance needed between characteristics suited to imaging and those that facilitate therapeutic effect.

The DNA light switch complex, $[Ru(bpy)_2(dppz)]^{2+}$ (Figure 4.1) was established in Chapter 1 as a candidate complex to develop toward cellular imaging and photo-induced destruction of DNA.[13,14] This complex exhibits virtually zero aqueous luminescence but switches on in organic environments such as suitable solvent or incorporation into hydrophobic cavities of biomolecules. In the presence of DNA, which it binds avidly ($K_b > 10^6$),[14–17] the complex intercalates by insertion of the dppz ligand between base pairs. This interaction isolates the complex from water causing emission enhancement of over 10^4 (in comparison, the emission of ethidium bromide, a common DNA stain, is about twenty times enhanced in DNA relative to buffer).[14,18] Specifically, the MLCT of $[Ru(bpy/phen)_2(dppz)]^{2+}$ is considered to comprise

two distinct states; a bright state localised on the phen portion of the dppz ligand which is dominant in organic solvent or DNA, and a dark state localised on the phenazine moiety which persists in aqueous environment. Generally, the dark state is believed to lie at higher energy and is inaccessible until stabilisation by the hydrogen bonding of water molecules to the phenazine nitrogens. The theory was originally postulated by Barton and coworkers who recognised that proton transfer quenching of the luminescence was not operative.[19,20] Recently, Poynton *et al*. observed the bright and dark states directly in CD_3CN and D_2O respectively using ultrafast TRIR techniques that identified spectral marker bands that were characteristic of the two photophysical states. DFT calculations supported this analysis and confirmed that the marker bands were assignable to the dppz ligand.[21]

The exact mechanism of water quenching remains somewhat controversial, Coates *et al*. suggest that a precursor state exists higher in energy than the emitting state.[22] Brennaman *et al*. proposed a temperature dependent model in which the light-switch arises from a dynamic equilibrium between the dark and bright states which are enthalpically and entropically favoured respectively.[23] Their model was derived from the solvent dependence of the emission; the dark state requires ordering of water around the dipole and thus solvents of higher dielectric constant favour the dark state due to greater stabilisation. The current rationale for the photophysical deactivation of the excited state of $[Ru(bpy/phen)_2(dppz)]^{2+}$ are summarised in Figure 4.1.

The light-switch effect of $[Ru(bpy/phen)_2(dppz)]^{2+}$ in the presence of DNA has been the subject of intense research over the past two decades.[12] In DNA, the luminescence lifetime of either enantiomer is biexponential, and although only moderate enantioselectivity towards DNA is apparent,[17,24] the magnitude and the fractional amplitude of each lifetime component greatly varies with Ru/DNA ratio, sequence, structure, ancillary ligand and complex enantiomer. Interestingly, the luminescence lifetime of racemic complex also fits well to a biexponential decay, and this was found to arise because the intensity of the Δ-enantiomer accounts for around 85 % of the total intensity in duplex DNA.[24] Hence, the origin of the two lifetimes has been attributed to at least two different binding modes with DNA in which the phenazine moiety of dppz is better protected from water in the longer-lived orientation. Originally, this concept and the groove at which the complex binds was controversial with

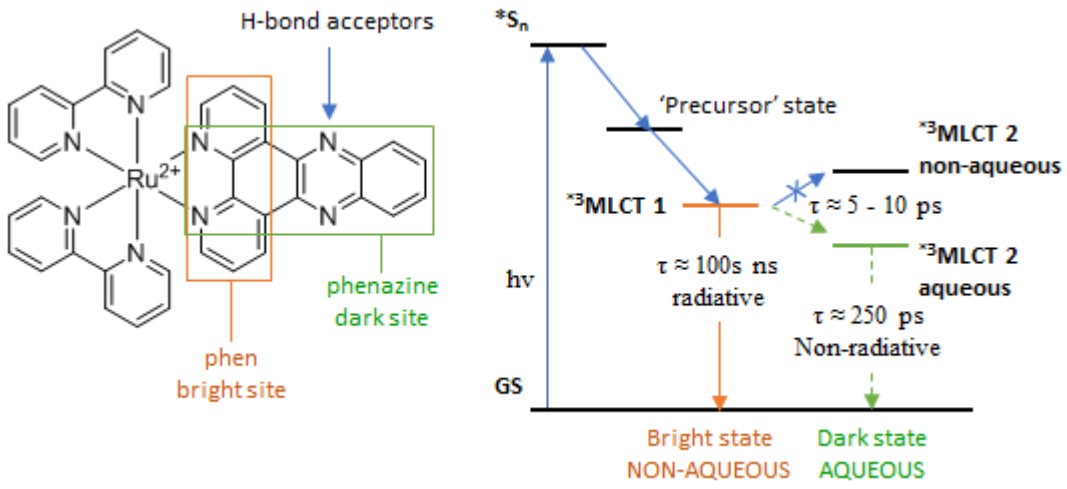

Figure 4.1: Structure of $[Ru(bpy)_2(dppz)]^{2+}$ (left) indicating the phen and phenazine fragments of the dppz ligand and a simplified Jablonski diagram (right) illustrating some possible deactivations in different solvents upon photoexcitation. Included is a depiction of the proposition of Coates' precursor state [22] and two possible positions of the phenazine based excited states (MLCT 2) which exist in aqueous or non-aqueous environment as shown. In the Brennaman model,[23] the MLCT 2 state is permanently at lower energy but not accessible in non-aqueous solvent at room temperature.

---

two different mechanisms proposed for interaction. Experimental data from Barton and coworkers supported binding at the major groove from quenching and NMR experiments, and posited that the enhanced luminescence lifetime arose from a perpendicular (i.e. head-on) intercalation.[19,25–27] Conversely, Lincoln and coworkers suggested binding at the minor groove was operative supported by dichroism and other spectroscopies, and argued that a canted (angled, non-classical) intercalation yielded better phenazine protection with consequent extended lifetime (Figure 4.2).[24,28–33]

Crystal structures, obtained by Cardin and coworkers, elucidated the binding of Λ/Δ/*rac*-$[Ru(phen)_2(dppz)]^{2+}$ bound to different DNA sequences and revealed that the complexes all bind from the minor groove (Figure 4.3).[34–37] Corroboratively, Barton and coworkers also reported that Λ-$[Ru(bpy)_2(dppz)]^{2+}$ bound mismatch DNA from the minor groove.[38] However, the origin of the extended luminescence lifetime and the relative proportions of each component of the biexponential decay is complex. Isothermal titration calorimetry and spectroscopy led Lincoln and coworkers to propose that different lifetimes occur for different

enantiomers, different ancillary ligands and the favoured geometry of a given complex upon binding DNA. For example, they showed that cooperativity exists between Δ-enantiomers of $[Ru(phen)_2(dppz)]^{2+}$ and that stacking interactions of ancillary ligands of adjacent complexes can promote canted binding geometry at the ends of contiguous sequences of complexes (Figure 4.2).[31,32]

Crystal structures also clearly indicated both perpendicular and canted geometries and, in one instance, illustrated that a canted geometry can afford less accessibility of water to one of the phenazine nitrogens, whereas both are accessible in a perpendicular orientation (Figure 4.3).[35] Also, stacking of ancillary ligands was evident between metalloinserted Λ-$[Ru(bpy)_2(dppz)]^{2+}$ and the ejected base pairs of a mismatch site.[38] However, crystal structures revealed other binding modes are possible, for example, up to five different modes are evident in Δ-$[Ru(phen)_2(dppz)]^{2+}$,[36] and surprisingly, semi-intercalation of a phen ligand of $[Ru(phen)_2(dppz)]^{2+}$ is also possible.[34] Evidently, the exact binding of the dppz complex can be difficult to interrogate from luminescence lifetime alone. However, the biexponential behaviour is an important marker of DNA interaction and can be used as general indication

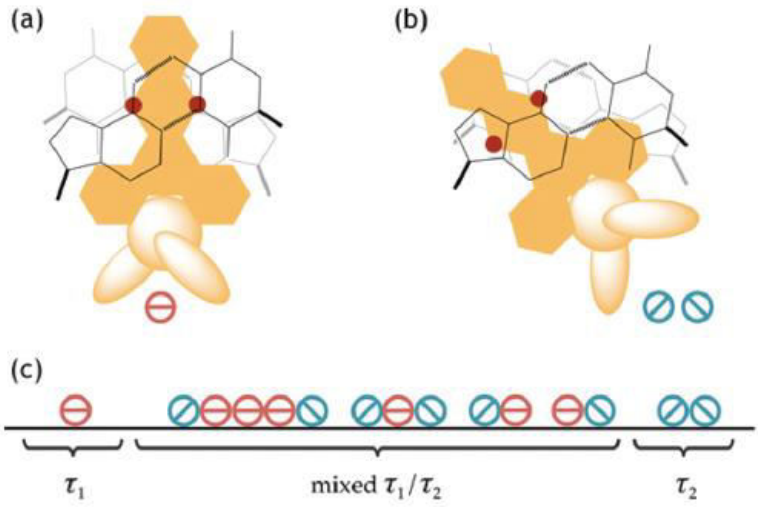

Figure 4.2: Perpendicular and canted geometries of $[Ru(bpy/phen)_2(dppz)]^{2+}$ when bound to DNA (a) and (b) respectively. (c) - the Lincoln model used to explain the distributions of luminescence lifetime where in this case, a canted geometry exists at the ends of contiguous sequences of complex. Image reproduced from McKinley *et al*.[33]

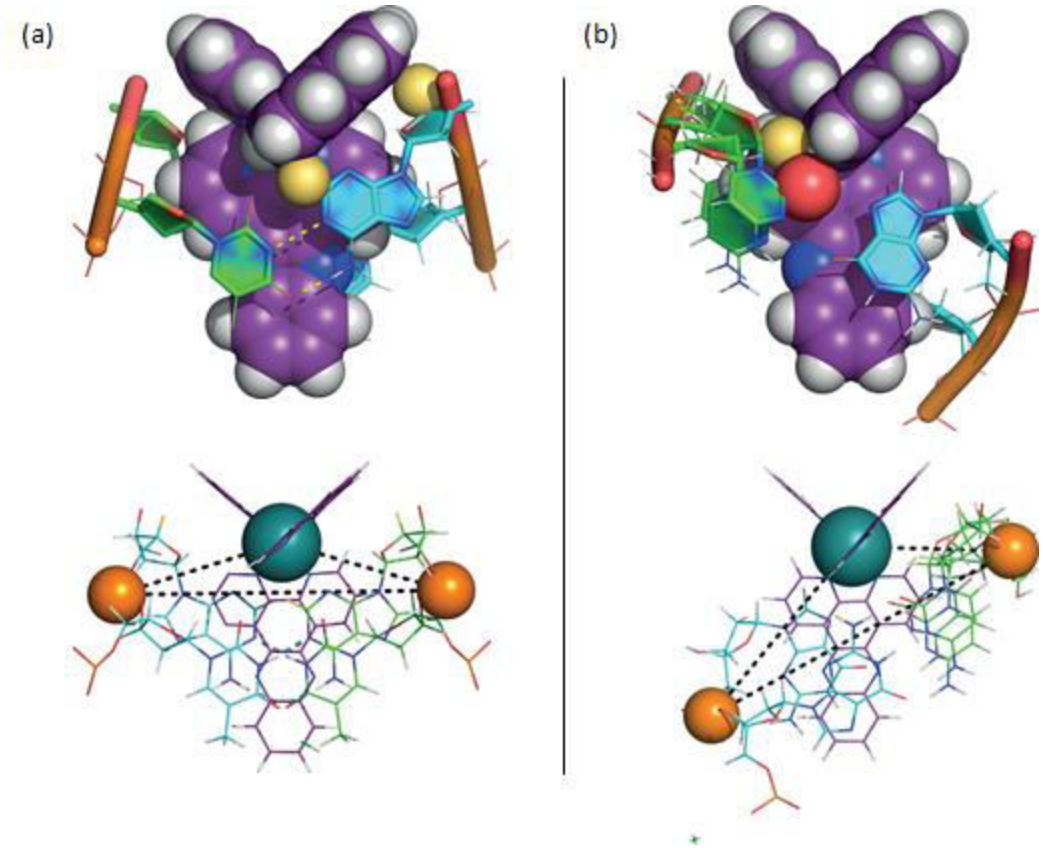

Figure 4.3: Space-filling and ball and stick models of crystal structures of Λ-$[Ru(phen)_2(dppz)]^{2+}$ intercalating oligonucleotides containing TA/TA and AT/AT base pair steps to highlight (a) perpendicular (at TA/TA step) and (b) canted (at CC/GG) geometries. Structure in purple is the Ru complex with dppz ligand intercalated from the minor groove in both cases. Orange spheres represent backbone phosphate, yellow and red spheres have been rendered to indicate interaction of the bases with the phen ligands. Reproduced from Niyazi *et al*., full details available in the original article.[34]

---

of the averaged accessibility of water molecules to intercalated Ru-dppz. This may be diagnostic of DNA macrostructure, for example, a changing luminescence lifetime in live cell imaging could be symptomatic of mesoscale changes to bulk DNA, perhaps signalling a change of cellular phase.

Thermodynamic calculations indicate that Ru-dppz intercalation is entropically driven, due to contributions from changes in hydration of Ru-dppz and DNA, disruption of DNA-bound water and hydrophobic interactions.[17] The high binding affinity due to dppz intercalation is further apparent in the 2-phenylpyridine (ppy) analogue, $[Ru(ppy)(bpy)(dppz)]^{+}$, in which

the formal charge (and the electrostatic contribution to binding) is reduced but the DNA affinity is still strong ($K_b \approx 9 \times 10^5$).[16] Structural modification has been used to generate Ru-dppz derivatives that interact selectively with certain nucleic acid structures, for example, Shade *et al*. demonstrated that charge-neutral complexes can distinguish double stranded DNA more selectively than single stranded DNA.[39] Others have exploited sterically bulky ligands to impart binding selectivity. Glazer *et al*. developed brominated dppz derivatives that exhibit a 15-fold enhancement in G-quadruplex DNA versus duplex DNA.[40] Yao *et al*. have developed imidazolone-dppz derivatives that stabilise G-quadruplex structures.[41,42] The Barton group reported the use of methylated phen ligands in $[Ru(Me_4phen)_2(dppz)]^{2+}$ to generate selectivity towards DNA mismatches.[43] Thomas *et al*. demonstrated temperature dependant intercalation using tris(pyrazolyl)methane Ru-dppz complexes.[44] Furthermore, RNA-mismatches, ssDNA, triplex DNA/RNA and i-motifs have all been targeted by exploiting isomerism and sterics.[45–50]

Despite the extensive literature on $[Ru(bpy/phen)_2(dppz)]^{2+}$, applications of Ru-dppz complexes to the live cell are scarce, and fewer still report successful cellular nuclear DNA staining. The slow translation of these complexes to cells is likely to originate from the relatively poor cellular uptake of the archetype complex.[16] Puckett and Barton reported that although $[Ru(phen)_2(dppz)]^{2+}$ is not suited to live cells, the complex exhibits enhanced uptake in dead cells and can be a marker as such.[51] Live cell imaging is more challenging, requiring not only cell membrane permeability but also efficient nuclear uptake. Structural modification of the ligands to alter the lipophilicity-charge balance has been a well-practised tactic across broader cellular imaging applications of metal complexes towards exalted uptake and has been attempted for Ru-dppz derivatives.[5] Mari *et al*. studied a series of $[Ru(bpy)_2(dppz\text{-}R)]^{2+}$ complexes and achieved some non-specific nuclear uptake when R = methoxy and amino functionalisations.[52] Diphenylphenanthroline (dpp) derivatives of Ru-dppz demonstrate enhanced cellular uptake but complete nuclear exclusion.[51,53,54] Extending the dppz ligand of Ru-dppz by one fused benzene ring provides Ru-dppn (dppn = 4,5,9,16-tetraazadibenzo[a,c]naphthacene) which greatly enhances uptake but also dark cytotoxicity.[55] Substitution of dppz for tpphz, an even more extended planar ligand; $[Ru(bpy/phen)_2(tpphz)]^{2+}$ (tpphz = tetrapyridophenazine), enables uptake and DNA staining but with high dark cytotoxicity, prohibiting its use as an imaging probe.[56] Similarly, Pierroz

et al. demonstrated high DNA binding affinity of a *bis*-dppz probe, that localised to the mitochondria in live cells, but with efficient membrane disruption.[57]

Lincoln and coworkers synthesised dimeric derivatives of $[Ru(phen)_2(dppz)]^{2+}$ which can *bis*-intercalate and thread DNA.[58–62] However, in cells, such structures were only able to achieve uptake following electroporation which renders it an unsuitable imaging probe.[63] The same group have experimented with *bis*- alkyl ether ($2 \times C_4 - C_6$) substituted derivatives of $[Ru((phen)_2(dppz\text{-}R_2)]^{2+}$ which demonstrated altered light-activated uptake and localisation depending on subtle changes in both alkyl-ether chains.[64,65] In these cases, addition of an ethylene unit to each chain radically impacts localisation and highlights that slight modification of structure can cause dramatic changes to the uptake and localisation characteristics of the probe. This is not ideal for imaging since any photophysical or structural selectivity for the target (e.g. DNA) which has been 'built-in' to the probe by judicious ligand design may not conform to the required physical properties for localisation. However, in some cases, there is a fortuitous balance struck which yields structures with the photophysical characteristics suited to imaging and the structural characteristics that facilitate uptake and localisation.

In the context of nuclear DNA imaging, the outstanding example reported to date was reported by Thomas and coworkers who used a tpphz bridged dinuclear complex; $[(phen)_2Ru(tpphz)Ru(phen)_2]^{4+}$, to image DNA structure in live cells.[66,67] While undoubtedly a major stride towards the realised potential of Ru-phenazine probes for cellular imaging, the use of this series of probes is limited by the very high concentrations required to achieve efficient nuclear uptake (500 μM). Furthermore, substitution of phen for bpy inhibits cellular uptake of the complex, while substitution of phen with the more lipophilic dpp ligand efficiently drives the complex into the ER.[66,68] The probes are excellent demonstrations of the imaging potential of Ru luminophores, but dinuclear tpphz complexes are not intercalators[69] which limits bio-structural differentiation. There is also a desire to exploit the well-studied rich chemistry of Ru-dppz derivatives for live cell diagnostics of DNA structure and function. In this regard, the recent work of Zhu *et al*. is exciting where a simple ion-pairing strategy (e.g. with pentachlorophenol, PCP) was used to achieve nuclear uptake and DNA staining in live cells of all enantiomers of $[Ru(bpy/phen)_2(dppz)]^{2+}$.[70] This strategy may

yet enable a selective study of important DNA constructs in the live cell, if the substrate scope can be generalised. Notably, the mitochondria also contains DNA (mtDNA) in the form of nucleoid structures[71] but there has yet to be a strategy reported that can achieve selective staining of mtDNA using metal complex luminophores.

Our group has been investigating the use of signal peptides bearing luminescent metal complexes as cargo to precision target cellular organelles including the nucleus and the mitochondria.[72–75] As detailed in Chapter 3 and elsewhere,[76,77] the development of conjugatable derivatives of bpy and an efficient synthesis of *tris*-heteroleptic complexes of Ru(II) permits access to peptide directed derivatives of the archetype complex; $[Ru(bpy)_2(dppz)]^{2+}$ to target both nuclear DNA and mtDNA. Previously, the Barton group have explored peptide conjugation to study Ru-dppz in the live cell.[78,79] However, nuclear uptake was only achieved when the peptide was augmented with fluorescein. Herein, it was anticipated that peptides previously shown to be highly effective in transporting metal complex across the nuclear envelope by our group can be exploited again to achieve precision targeting without further modification. For nuclear uptake; the nuclear localisation signal (NLS) peptide derived from the transcription factor NF-κB which enables nuclear penetration is exploited again; H_2N-ahx-VQRKRQKLMP-$CONH_2$ (NLS, ahx = aminohexyl linker).[74,80,81] For mitochondrial uptake; a mitochondrial penetrating peptide (MPP) can be used; H_2N-ahx-FrFKFrFK(Ac)-$CONH_2$ (MPP) - a sequence designed by Kelley *et al*. and shown by us to deliver Ru(II) complexes selectively to the mitochondria.[73,82,83] The synthesis of these Ru(II) peptide conjugates is described in Chapter 3.

A key issue in cellular imaging is achieving low cytotoxicity in the dark and under imaging conditions. Ru(II) polypyridyl complexes exhibit long-lived triplet photo-excited states that can sensitise the formation of reactive oxygen species (ROS) such as singlet oxygen $^1O_2$.[8,9,84] The efficient formation of ROS can be detrimental to the DNA integrity, for example, singlet oxygen can mediate single strand breaks in plasmid DNA.[85] Interestingly, studies on $[Ru(bpy)_2(dppz)]^{2+}$ have revealed that the model complex exhibits only modest singlet oxygen quantum yield (ϕ_Δ = 0.29 vs 0.84 for $[Ru(bpy)_3]^{2+}$ in ethanol) and although the complex strongly interacts with DNA, its induced single strand breakage efficiency (attributable to $^1O_2$) is much lower than $[Ru(bpy)_3]^{2+}$ (ϕ_{SSB} = 1 x 10^{-6} vs 8 x 10^{-6}).[86–88] This

low phototoxicity should be beneficial for imaging. Photosensitised ROS production is intensity dependent, and for $[Ru(bpy)_2(dppz)]^{2+}$ it would be interesting to investigate the threshold at which phototoxicity may be induced in DNA-stained cells. Importantly, this threshold must be below that which damages cells in the absence of Ru-dppz and if these balancing criteria are met, derivatives of $[Ru(bpy)_2(dppz)]^{2+}$ may be suited to single colour theranosis.

This chapter describes an assessment of the candidacy of two peptide-directed derivatives of $[Ru(bpy)_2(dppz)]^{2+}$ for cellular imaging of DNA, namely; Ru-NLS and Ru-MPP. A non-specific uptake conjugate, Ru-R8 was also studied (R8: H_2N-ahx-RRRRRRRR-$CONH_2$, structures given in Figure 4.4). The conjugates and their parent structures were photophysically characterised and their interaction with DNA in solution assessed using various spectroscopies as a basis on which to interpret cellular data. The interaction of the complexes with BSA was also investigated to assess their propensity for non-specific protein binding and the impact this may have on their photophysical properties. In all solution studies, the probes were compared to the model complex, $[Ru(bpy)_2(dppz)]^{2+}$, which was synthesised (Chapter 3) and subjected to the same experiments as the novel probes. The uptake and localisation of the Ru-dppz conjugates was captured using a range of microscopies including super-resolution STED microscopy, FLIM imaging and resonance Raman microscopy. Finally, the potential of the conjugates to act as DNA-targeted imaging and photodamage agents was assessed by exploring their relative dark and photo-cytotoxicites and their ability to induce strand breaks in closed circular plasmid DNA.

4.1.4 Chapter Aims

The aims of this chapter are as follows;

- The photophysical characterisation of the Ru-dppz parent complexes (Ru-acid and Ru-ester) and conjugates (Ru-MPP, Ru-R8 and Ru-NLS).
- The investigation of the spectroscopic response of the probes to DNA in solution by assessing the changes to the UV/Vis and emission spectra, the luminescence lifetime, circular dichroism spectra and resonance Raman spectra.
- The determination of the relative binding affinity of the probes towards DNA and assessment of the relative impact of isomerism and the nature of the conjugated peptide.
- The investigation of the propensity of the probes to bind BSA and the concomitant spectroscopic response if any.
- The determination of the uptake and localisation characteristics of the conjugates in live cells and their ability to precision target nucleic acids.
- The determination of the ability of the probes to report on dynamic DNA structures in live and fixed cells using a variety of imaging techniques including FLIM and STED microscopy.
- The investigation of the ability of the probes to induce strand cleavage in closed circular plasmids.
- The investigation of the cytotoxicity of the probes; both in the dark and under irradiation to establish their ability to induce DNA damage with spatiotemporal control.

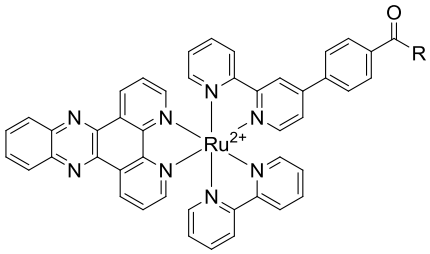

R = OH [Ru(dppz)(bpy)(bpyArCOOH)]$^{2+}$ **Ru-acid**

R = OEt [Ru(dppz)(bpy)(bpyArCOOEt)]$^{2+}$ **Ru-ester**

R = -Ahx-VQRKRQKLMP-CONH$_2$

[Ru(dppz)(bpy)(bpyAr-Ahx-NLS)]$^{6+}$

Ru-NLS

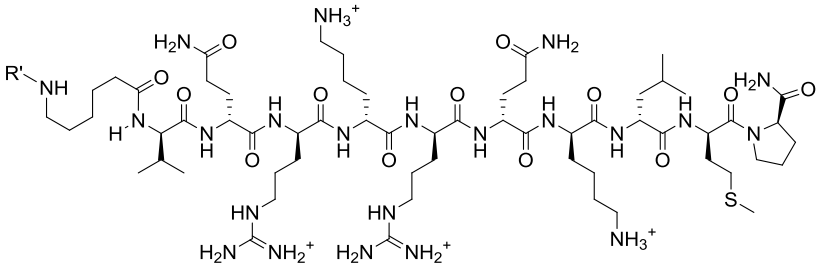

R = -Ahx-FrFKFrFK(Ac)-CONH$_2$

[Ru(dppz)(bpy)(bpyAr-Ahx-MPP)]$^{5+}$

Ru-MPP

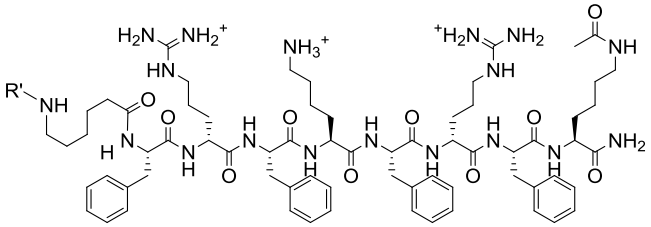

R = -Ahx-RRRRRRRR-CONH$_2$

[Ru(dppz)(bpy)(bpyAr-Ahx-NLS)]$^{10+}$

Ru-R8

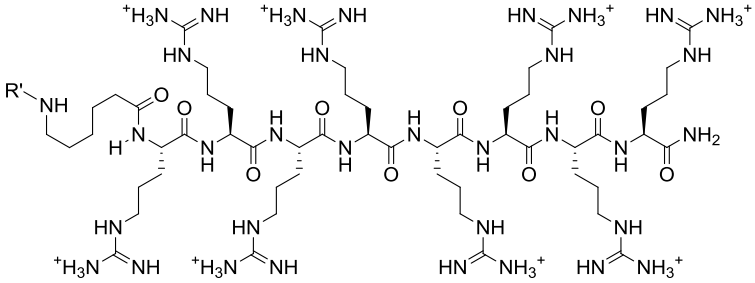

Figure 4.4: Chemical structures of the parent complexes and conjugates studied in this chapter. Note that each compound was tested herein as its mixture of four isomers.

4.2 Results and discussion

4.2.1 Photophysical characterisation

The absorbance and emission spectra of the conjugates were identical to those of the parent complexes as indicated in Table 4.1. Ligand-centred transitions in the UV region of the absorbance spectra were assigned to bpy and dppz based absorptions at 280 nm and 355 – 360 nm respectively (Figure 4.5 and Appendix B). The dppz band was bathochromic to that of bpy due to its extended planar aromaticity. A broad MLCT band characteristic of Ru(II) polypyridyl complexes was evident in the blue portion of the visible region with a maximum at 451 – 457 nm for all compounds in acetonitrile and aqueous solvent. The extinction coefficients were determined in triplicate from calibration plots and were moderately higher in acetonitrile than in aqueous solvent. The complexes and conjugates are luminescent in acetonitrile but consistent with light-switch behaviour like $[Ru(bpy)_2(dppz)]^{2+}$ are non-luminescent in aqueous solvent.[14] In acetonitrile, the luminescence was strongly Stokes-

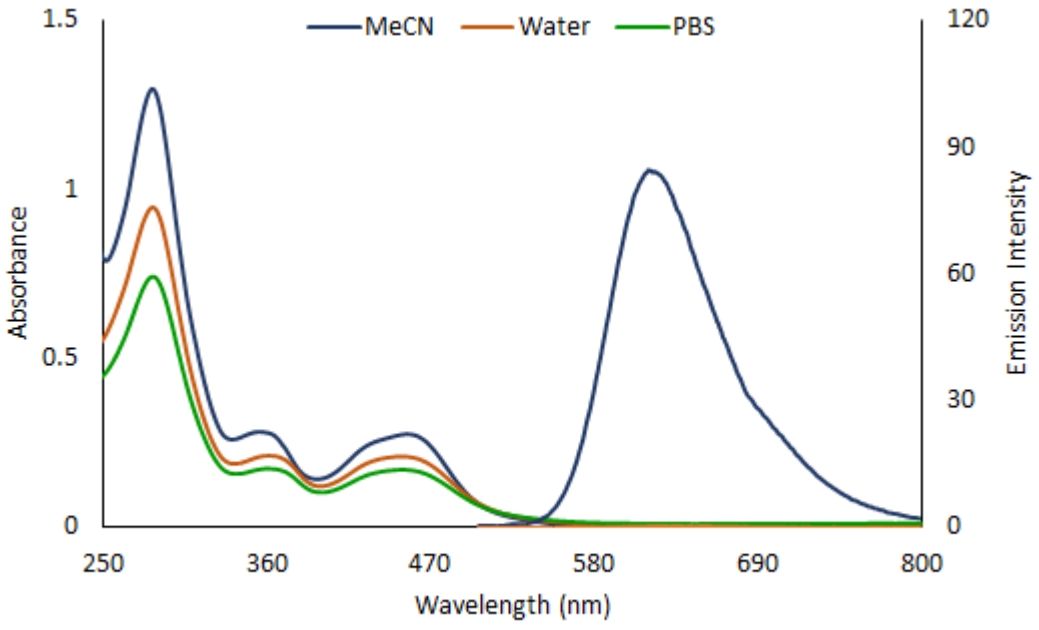

Figure 4.5: Absorbance and emission spectra of Ru-NLS measured at 10 μM in acetonitrile, water, and PBS pH 7.4 as indicated. Emission slits were set to 10 nm and excitations were performed at λ_{max} (vis).

Table 4.1: Summary of photophysical data for the Ru-dppz complexes and conjugates.

	Solvent[a]	λ_{abs} (ε)[b] nm (x10^3 M^{-1} cm^{-1})	λ_{em} nm	τ_{lum} [c] ns	
				Aerated	Deaerated
Ru-acid	MeCN	282 (94.8), 354 (24.0), 454 (23.2).	620	228 ± 1	420 ± 14
	H_2O	281 (68.8), 358 (18.3), 455 (17.1).			
	PBS	281 (58.3), 360 (13.2), 451 (12.3).			
Ru-ester	MeCN	282 (112.6), 355 (29.0), 454 (28.1).	617	239 ± 1	372 ± 17
	H_2O	281 (86.1), 359 (20.3), 452 (18.5).			
	PBS	282 (57.9), 363 (18.4), 455 (18.3).			
Ru-R8	MeCN	282 (131.7), 355 (29.2), 454 (28.1).	619	404 ± 21 (15 %) 202 ± 3 (85 %)	491 ± 19
	H_2O	282 (88.3), 359 (21.2), 451 (18.9).			
	PBS	282 (83.2), 359 (18.9), 452 (17.3).			
Ru-NLS	MeCN	282 (119.4), 354 (29.4), 454 (28.1).	617	374 ± 13 (17 %) 209 ± 3 (83 %)	408 ± 20
	H_2O	282 (90.8), 361 (20.6), 450 (18.5).			
	PBS	283 (79.6), 360 (18.8), 451 (18.5).			
Ru-MPP	MeCN	288 (95.5), 359 (29.1), 457 (27.1).	628	673 ± 6 (74 %) 212 ± 14 (26 %)	477 ± 4
	H_2O	282 (77.5), 363 (19.6), 452 (17.8).			
	PBS	284 (56.2), 361 (17.6), 456 (16.2).			

Notes: [a] PBS = Commercial Dulbecco's Phosphate Buffered Saline without modifiers, measured at pH 7.4. [b] Averaged from triplicate analyses. Relative standard deviations (not shown) were typically < 5 %. [c] 450 nm excitation, data fit to tailfit criteria; $0.9 < \chi^2 < 1.1$. De-aeration by N_2 purge for 15 minutes. Averaged data is shown ±S.D. For bi-exponential fitting, % relative amplitude values are provided in parentheses.

shifted upon excitation into the ^{3}MLCT* state with the emission maximum centred typically at about 620 nm. Luminescence quantum yields for the parent complexes were determined in aerated acetonitrile using the slope method against $[Ru(bpy)_3]^{2+}$ as a standard and were calculated at 2.8 % and 2.9 % for the acid and ester respectively.[77,89] This emission was shown to progressively switch-off with increasing aqueous ratio as demonstrated in Figure 4.6 (and Appendix B). In general, about 97 % of the emission was quenched at 15 % v/v water in acetonitrile. Importantly, the light-switch effect of the complexes was not impacted by peptide conjugation.

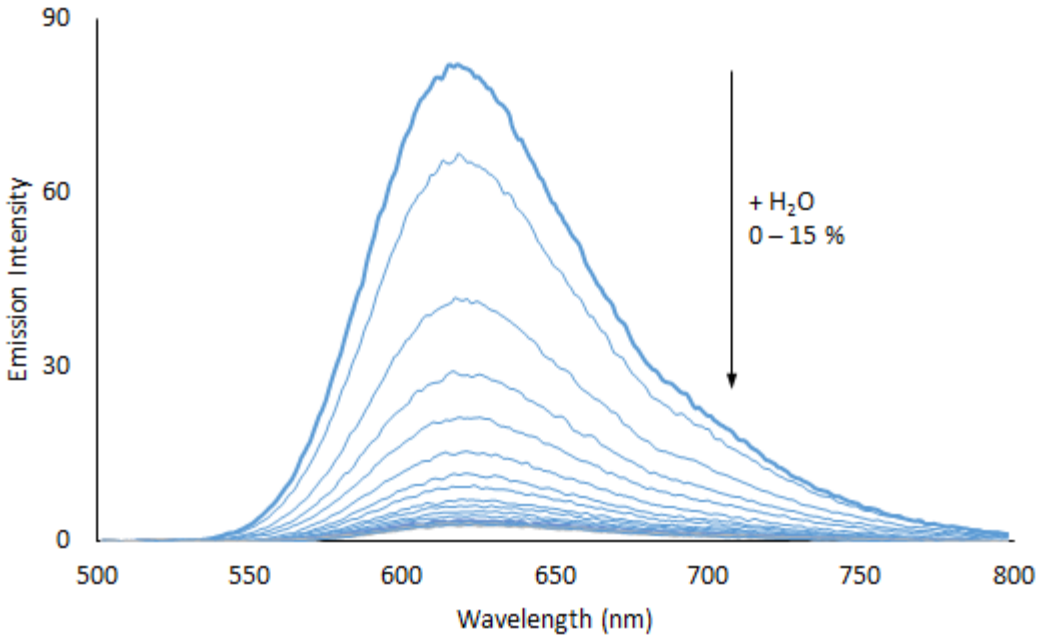

Figure 4.6: Luminescence quenching of Ru-NLS in acetonitrile on addition of water. The arrow indicates direction of intensity change with increasing aqueous ratio up to 15 % v/v..

Luminescence lifetimes of the parent complexes and conjugates were measured in acetonitrile (Table 4.1). As expected, the parent complexes exhibit monoexponential luminescent decays with the lifetime under air determined at about 230 ns and the emission was shown to be quite oxygen sensitive with doubling of the luminescence lifetime to about 400 ns upon de-aeration under N_2 purge. Interestingly, the peptide conjugates required bi-exponential fits to their luminescence decays in acetonitrile. For Ru-R8 and Ru-NLS, a short component was measured at $\tau_s \approx 205$ ns with a fractional amplitude (α_s) of about 85 %. A longer component was determined at $\tau_l \approx 385$ ns. These values correspond to the aerated and deaerated lifetimes of the parent complex and hence, considering the low α_l (*ca*. 15 %), a minor protecting effect of the conjugated peptide towards oxygen quenching is likely operative.

A more interesting behaviour was exhibited by the MPP conjugate in which the decay was also bi-exponential in aerated solution but in this case, the longer component was longer-lived and contributed a much greater fractional amplitude; $\alpha_l = 74$ %, $\tau_l = 673 \pm 6$ ns. The

short component of the Ru-MPP decay, $\tau_s = 212 \pm 14$ ns, can be attributed to aqueous exposed Ru-dppz given its similarity to the lifetime of the parent complexes. The longer component is tentatively attributed to enhanced protection from oxygen afforded the Ru-dppz moiety due to π-stacking interactions with the Phe residues of the tethered peptide (there are four of these residues in total). Indeed, the emission maximum of Ru-MPP in acetonitrile is red-shifted to 628 nm whereas the maxima of the R8 and NLS conjugates are the same as the parent complexes at about $\lambda_{em} = 620$ nm. The notion that the aromatic amino acids protect the dppz is consistent with the observation that de-aeration of the conjugate solutions rendered the luminescence decays monoexponential and comparable to the parent complexes under deaerated conditions.

4.2.2 DNA binding

Cellular chromatin and mitochondrial nucleoids are dynamic structures that are difficult to model in vitro, for example, nucleic acids are tightly packaged and are often associated with protein in cells. However, solution DNA binding studies are a useful comparison basis, especially against published data on related Ru(II) compounds which are focussed on ctDNA (DNA from calf thymus) and similar duplex DNA. The signal peptides conjugated to the Ru(II) complexes herein are charged and large, with 8 or 10 amino acids and a linker, and hence, are expected to strongly influence the way Ru-dppz complexes interact with the DNA duplex. For example, peptides containing lysine and arginine interact differently with DNA but in combination can mediate structural changes that are important for cellular function, a process that is driven by entropic displacement of DNA bound cations.[90–92] The MPP sequence also contains Phe residues which can stabilise protein-DNA assemblies by intercalation as exemplified by the TATA box binding protein.[93] Furthermore, other biologically relevant basic molecules such as linear polyamines are 'phosphate clamps' or 'arginine-forks' and remain a strategy to target the DNA polyanionic backbone.[94–96] Hence, to assess the Ru(II)-dppz interaction separately, binding studies were extended to include the unconjugated parent complexes and the behaviour of the novel complexes and conjugates was also compared to the archetype light-switch; $[Ru(bpy)_2(dppz)]^{2+}$, also tested here under identical conditions.

4.2.2.1 The impact of DNA binding on absorbance and emission

Significant changes to the absorbance and emission spectra of all the examined Ru-dppz compounds were observed upon addition of concentrated aliquots of ctDNA to solutions of the complex up to saturation (Figure 4.7 and Appendix B). The dppz and MLCT absorbance bands underwent extensive hypochromism up to about 30 % at saturation. The dppz $\pi \rightarrow \pi^*$ band was also noticeably red-shifted in all cases from about 360 nm in buffer to about 370 nm in DNA and combined, this behaviour is characteristic of dppz ligand intercalation into the DNA base stack.[24,97] This was supported by the characteristic light-switch effect which was active in all cases with a switching-on of the luminescence at 615 – 618 nm with increasing ctDNA concentration up to saturation (Figure 4.7 and Appendix B). As described in the introduction to this chapter, this mechanism has been well studied for $[Ru(bpy/phen)_2(dppz)]^{2+}$ and is associated with protection of the dppz ligand from aqueous quenching within the organic core of the minor groove of the DNA double-helix.[14,20,21]

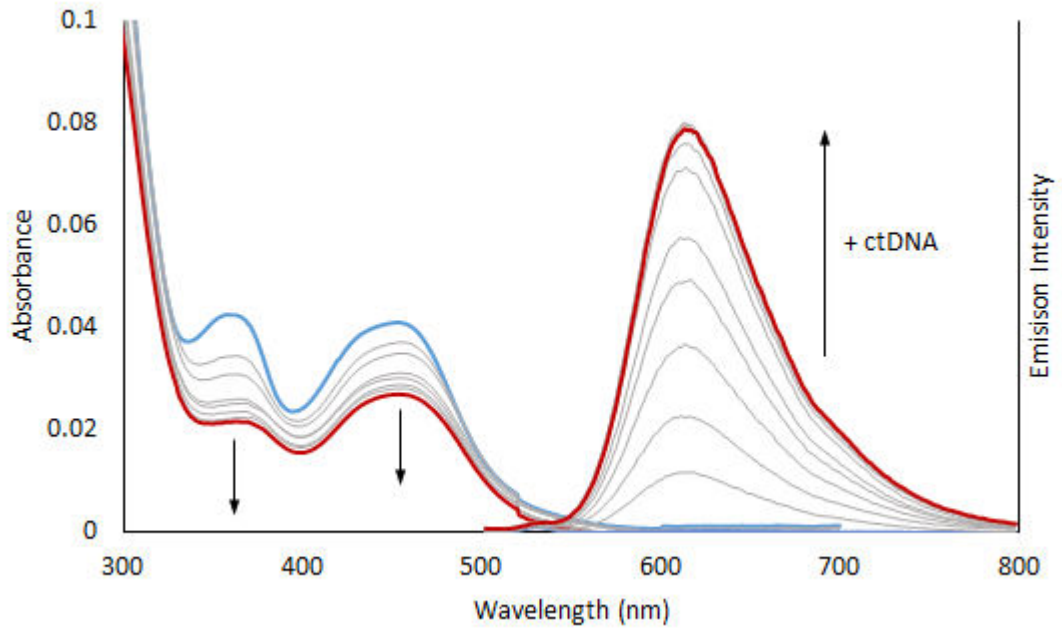

Figure 4.7: Changes to absorbance and emission spectra of Ru-NLS in PBS upon addition of ctDNA from r = 0 (blue trace) up to saturation (red trace, r = 4).

A simple experiment to investigate the binding affinity of luminescent metal complexes involves studying their quenching in the presence of DNA and increasing concentration of a quencher such as ferrocyanide, $[Fe(CN)_6]^{4-}$. In solution, ferrocyanide efficiently quenches Ru(II) polypyridyl luminescence, for example, as shown in Figure 4.8, the luminescence of $[Ru(bpy)_3]^{2+}$ was successively extinguished with increasing $[Fe(CN)_6]^{4-}$. Thus, the absence of quenching in the presence of DNA can be attributed to strong binding affinity and protection of the luminophore, since ferrocyanide being an anion, is effectively repelled from interaction with an intimately bound probe by electrostatic repulsion from the DNA polyanionic backbone.[18,98] $[Ru(bpy)_3]^{2+}$ exhibits poor DNA affinity ($K_b \approx 700\ M^{-1}$)[99] and unsurprisingly, its luminescence was quenched to the same extent in the presence of DNA (r = 20) as it was in its absence (see Figure 4.8, overlapping traces). In contrast, it was observed that addition of $[Fe(CN)_6]^{4-}$ to solutions of DNA saturated Ru-dppz did not lead to significant luminescence changes, even in the presence of up to 50 equivalents of quencher (Figure 4.8).

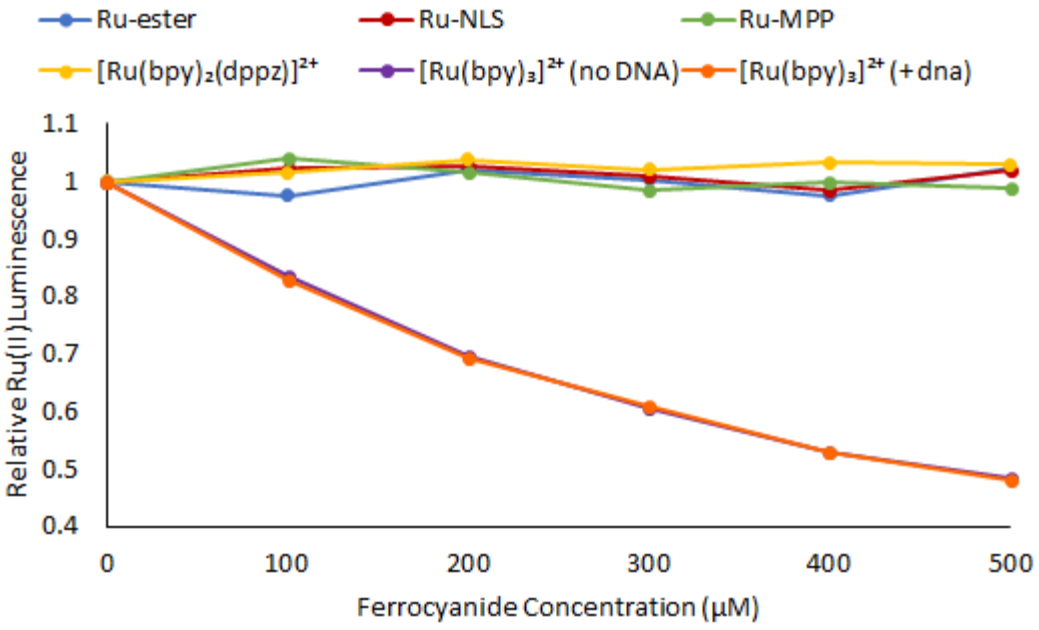

Figure 4.8: Relative Ru(II) emission intensity of the Ru-dppz complexes in PBS (10 μM) in the presence of ctDNA (r = 20) as indicated with increasing ferrocyanide concentration. The chart also shows $[Ru(bpy)_3]^{2+}$ (10 μM) in the presence and absence of ctDNA (r = 20) as overlapping traces.

The absence of quenching by $[Fe(CN)_6]^{4-}$ supports high affinity binding in which intercalation is probably occurring. There are reported instances in which intercalation is not required for light-switch behaviour or inhibition of ferrocyanide quenching, for example, in the case of the groove-binder $[(bpy)_2Ru(tpphz)Ru(bpy)_2]^{4+}$.[69,100] However, the results herein are identical to those described by Barton and coworkers on intercalating dppz complexes,[19] and hence dppz intercalation is likely operative in all cases.

The binding titration data was used to generate binding curves that were fit to the binding model described by Carter *et al*. and later modified by Poulsen *et al*. (see Chapter 2, Equations 2.1 and 2.2).[101,102] Typically at least three titrations were performed for each compound and the binding data fit to the model equation with the inclusion of the variables K_b, the binding constant, and n, the binding site size, by minimising the sum of the square residuals. It was important to include the model compound, $[Ru(bpy)_2(dppz)]^{2+}$, in these experiments to provide a comparison against the present Ru-dppz complexes and conjugates under the same conditions. Using the Poulsen protocol,[102] the binding constant of $[Ru(bpy)_2(dppz)]^{2+}$ was determined as; $K_b = 0.8 (\pm 0.2) \times 10^6$ M^{-1} ($n = 4.16 \pm 1.3$), a value on the scale of that calculated using AFM by Mihailovic *et al*.[15] but slightly lower than the widely cited $> 10^6$ value originally reported by Barton and coworkers from dialysis and absorption measurements.[14] This deviation can be attributed to differences in ionic strength due to the use of PBS buffer herein (≈ 150 mM NaCl, ≈ 10 mM phosphate) in comparison to the Tris buffer (5 mM Tris, 50 mM NaCl) used in the original report. Kalsbeck and Thorp have shown previously that binding constants are significantly higher in Tris buffer than in the presence of K^+/Na^+ probably due better solvation of the alkali cation.[103]

The agreement between the literature and the experimental data presented above for the model compound permitted the use of the Poulsen protocol to analyse the novel Ru-dppz complexes and conjugates reported herein. A summary of this analysis is presented in Table 4.2 and representative binding curves are provided in Appendix B. Ru-acid was found to have a similar binding constant to $[Ru(bpy)_2(dppz)]^{2+}$, measured at $K_b = 0.79 (\pm 0.3) \times 10^6$ M^{-1} ($n = 1.79 \pm 0.8$). However, Ru-ester recorded a much greater K_b value at $5.04 (\pm 1.6) \times 10^6$ M^{-1} ($n = 2.43 \pm 0.4$), which could be attributed to the greater lipophilicity of the pendant aryl-ester in comparison to the carboxylated and underivatized compounds. The high binding

Table 4.2: Summary of photophysical data for the parent complexes and conjugates from binding studies versus ctDNA in PBS.

	K_b / ($x10^6$ M^{-1})[a]	n [a]	λ_{em} [b]	τ / ns [c]		
			nm	τ_l	τ_s	α_l (%)
$[Ru(bpy)_2(dppz)]^{2+}$	0.80 (± 0.2)	4.16 (± 1.3)	618	365 ± 13	80 ± 2	24 ± 1
Ru-Acid	0.79 (± 0.3)	1.79 (± 0.8)	617	446 ± 26	105 ± 2	27 ± 2
Ru-Acid t-dppz	2.65 (± 1.3)	4.07 (± 0.1)	617	425 ± 8	94 ± 1	24 ± 1
Ru-Acid t-bpy	0.57 (± 1.1)	2.33 (± 1.0)	617	401 ± 9	97 ± 1	31 ± 9
Ru-Ester	5.04 (± 1.6)	2.43 (± 0.4)	615	852 ± 27	155 ± 11	41 ± 4
Ru-NLS	35.8 (± 8)	2.75 (± 0.8)	614	573 ± 54	145 ± 23	43 ± 3
vs 1M NaCl [d]	1.26 (± 0.1)	0.68 (± 0.1)				
Ru-MPP	27.8 (± 11)	1.04 (± 0.2)	615	671 ± 34	120 ± 17	49 ± 3

Notes: [a] Binding constant, K_b, and binding site size, n, averaged from calculated values from fits to triplicate binding titrations using the method described by Poulsen et al.[102] [b] Emission maximum in ctDNA at r = 10 (saturation). [c] r = 10 (saturation), τ_l and τ_s are the long and short components of the biexponential decay respectively where α_l is the fractional amplitude of τ_l. All lifetime measurements were performed in aerated PBS. α_l is the relative amplitude of the long component, τ_l. [d] 1 M NaCl in PBS buffer. Total ionic content; *ca*. 1150 mM NaCl, 10 mM phosphate.

affinity in both cases for the Ru^{+2} complexes lends further support to intercalative binding, since comparative values have not been reported for groove binders bearing the same formal charge, for example, for $[Ru(phen)_3]^{2+}$; $K_b \approx 10^3$.[99] Interestingly, the n values for Ru-acid and Ru-ester were much smaller than that of $[Ru(bpy)_2(dppz)]^{2+}$. The presence of multiple geometric isomers in Ru-acid and Ru-ester, as well as optical isomers, may lead to deviation from the binding model used to calculate n values which assumes binding homogeneity and the absence of cooperativity.[102]

To investigate this further, the resolved Ru-acid isomers, t-dppz and t-bpy (Chapter 3 and Figure 4.9), were also subjected to binding titrations. The relative configurations of the isomers were assigned using NMR analysis and estimations of relative anisotropic diamagnetic shielding effects in Chapter 3. Considering their interaction with DNA, the relative orientation of the pendant aryl-carboxylate should induce binding discrimination. The t-dppz isomer (both of its enantiomers) is configured with the substituent approximately projecting along the plane of the dppz ligand but in the opposite direction and away from the

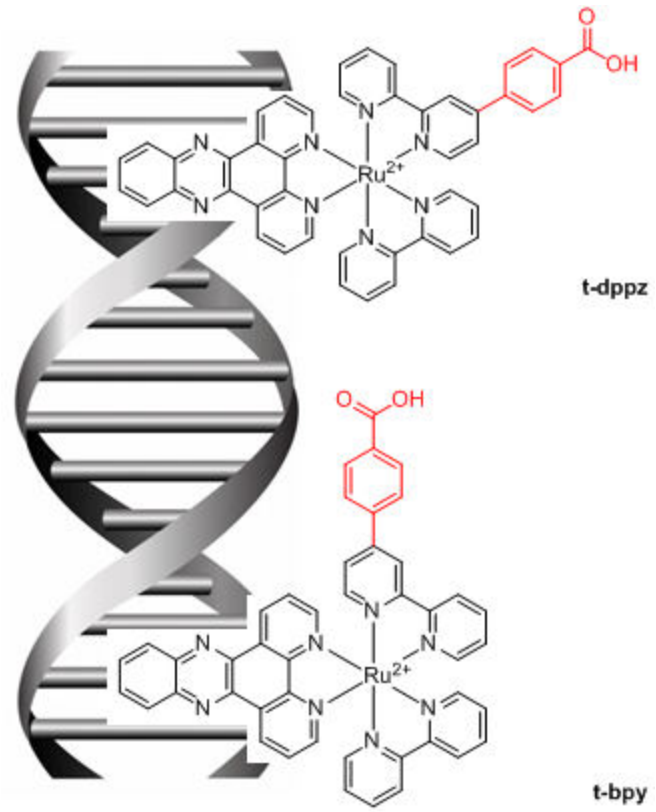

Figure 4.9: A rough illustration of the relative orientation of the aryl-COOH for the t-dppz and t-bpy isomers of Ru-acid unit upon binding DNA.

---

complex and DNA-binding motif. This should manifest as an enhanced relative binding constant and should lead to a more lipophilic derivative of $[Ru(bpy)_2(dppz)]^{2+}$.

In contrast, the t-bpy isomer (both of its enantiomers) is characterised by the substituent residing almost perpendicular to the plane of the dppz ligand, near the apex of the coordination octahedron, and critically, adjacent to the binding ligand. Hence, the substituent of the t-bpy isomer should be in intimate contact with the DNA helix, resulting in a decreased relative binding constant due to steric inhibition and phosphate-carboxylate repulsion. This distinction is illustrated in Figure 4.9 and indeed, this expected pattern was observed in the binding data and further corroborates the isomer assignments made in Chapter 3. The binding constant of the t-dppz isomer was determined at $K_b = 2.65 (\pm 1.3) \times 10^6$ ($n = 4.07 \pm 0.1$), much higher than the bulk isomer mixture (Ru-acid) and the n value is similar to that of $[Ru(bpy)_2(dppz)]^{2+}$ as expected, since the substituent in this case should not interfere at the

binding site. In contrast, t-bpy was found to exhibit $K_b = 0.57 (\pm 1.1) \times 10^6 M^{-1}$ ($n = 2.33 \pm 1.0$), slightly lower than Ru-acid, probably due to repulsion effects as described.

The differentiation in binding affinity due to isomerism is not surprising and can be useful considering the exploitation of Ru-dppz enantiomerism towards specific diagnoses of DNA structure previously studied by others.[18] However, the impact of geometrical isomerism herein was found to be completely overridden upon peptide conjugation, with calculated K_b values an order of magnitude higher for the conjugates relative to the parent complexes. Brunner and Barton have previously reported Rh-polyarginine conjugates exhibiting binding affinity on this order of magnitude ($K_b \approx 10^7$).[104] The enhancement was postulated to be electrostatically driven considering the relative binding constants of the NLS and MPP conjugates where Ru-NLS ($K_b = 35.8 (\pm 8) \times 10^6 M^{-1}$) exhibits higher affinity than Ru-MPP ($K_b = 27.8 (\pm 11) \times 10^6 M^{-1}$) as this peptide contains additional cationic residues in its polypeptide sequence. To investigate further, Ru-NLS was subjected to binding titrations at high ionic strength (1 M NaCl in PBS, total [NaCl] ≈ 1150 mM) which caused the binding constant to reduce to $K_b = 1.26 (\pm 0.1) \times 10^6 M^{-1}$ – a value on the order of the unconjugated complexes. The increased affinity of the peptide conjugates is a positive outcome for this work because high affinity will aid in the precision targeting of cellular DNA. However, it also highlights a future challenge in imaging; developing a targeting strategy that does not impact DNA interaction of the free probe to retain sequence or structure selectivity in cellular applications.

4.2.3.2 The impact of DNA binding on luminescence lifetime

Changes to the luminescence lifetime upon DNA binding was assessed for the parent complexes and conjugates (Table 4.2). As described in the introduction, Barton and coworkers explained the biexponential decay kinetics of $[Ru(bpy/phen)_2(dppz)]^{2+}$ in terms of a shorter-lived but more accessible canted intercalation and longer-lived perpendicular intercalation of the dppz ligand.[105] However, Lincoln and coworkers later rationalised the reverse hypothesis;[32] in the canted geometry, one of the phenazine nitrogens is strongly protected within the DNA core, whereas in the perpendicular orientation, both nitrogens of the phenazine moiety are more accessible, and this leads to a quenched luminescence lifetime. Enantiomerism also impacts binding due to the chirality of DNA that leads to further

lifetime distinction.[24] Lincoln and coworkers have also demonstrated that ancillary ligands impact neighbouring complex-complex interactions along sections of contiguously bound Ru-dppz complexes which dictates binding geometry and consequent luminescent lifetime magnitude and fractional amplitude.[31,32] Differences in DNA sequence and structure add additional complexity, and in the present work is complicated further considering geometrical isomerism as well as enantiomerism, and of course, the impact of peptide-DNA interactions at or near the binding site which may induce distortion. Nevertheless, broad comparisons can still be identified in the lifetime data.

The luminescence lifetime of the model compound $[Ru(bpy)_2(dppz)]^{2+}$ was measured as part of this work in the presence of ctDNA in PBS (r = 10, saturation) and was found to be biexponential with long (τ_l) and short (τ_s) components as follows; τ_l = 365 ± 13 ns (α_l = 24 %), τ_s = 80 ± 2 ns. This corresponds to previously published data for this complex; τ_l (α_l),τ_s = 340 ns (20 %), 90 ns (r = 10), the minor deviation likely arises from the use of different buffers. It is important to recognise that the amplitude distribution does not arise from an enantiomer effect since α_s and α_l are inequivalent and hence, the differentiation likely corresponds to a longer lifetime observed in a canted versus a symmetrical intercalation as reported irrespective of the isomer.[32]

In general, Ru-acid was shown to exhibit comparable behaviour to the model complex in terms of the fractional amplitude of the biexponential components (τ_l (α_l),τ_s = 446 ± 26 ns (27 %), 105 ± 2 ns (r = 10)). The average lifetime increase observed for Ru-acid relative to the model complex was comparable to the relative lifetimes of free Ru-acid and $[Ru(bpy/phen)_2(dppz)]^{2+}$ in acetonitrile ($\tau/_{MeCN}$ = 228 ns and 180 ns respectively).[19] The fractional amplitude of the long component was shown to be larger successively in the following order; t-dppz isomer (α_l = 24 %) < bulk mixture (Ru-acid) (α_l = 27 %) < t-bpy isomer (α_l = 31 %). This suggests that more t-bpy complexes are oriented in a canted geometry. According to studies by Lincoln and coworkers, binding cooperativity for the Δ-enantiomers of $[Ru(bpy)_2(dppz)]^{2+}$ and $[Ru(phen)_2(dppz)]^{2+}$ was dramatically enhanced for the more hydrophobic phen complex, leading to a preference of the phen Δ-enantiomer to bind DNA as contiguous pairs in canted geometry, with corresponding increase in fractional amplitude of the longer component.[31,32] The Λ-enantiomers were not distinguished to the

same extent because the handedness of DNA does not favour their intimate binding. While the scenario is undoubtedly more complex in this work, it is reasonable to assume that the aryl-carboxylate substituent is involved in mediating binding orientations, especially in the case of the t-bpy isomer in which the substituent protrudes parallel to the DNA axis. In this fashion, a head-on perpendicular intercalation may be less favoured due to increased steric inhibition which forces the complex to intercalate by a canted mode, thus increasing the magnitude of α_l relative to the t-dppz isomer. This effect may arise due to complex-complex interactions as per Lincoln and coworkers, or due to steric factors between isolated complexes and the DNA backbone. Notably, α_l for t-dppz was identical to that observed for $[Ru(bpy)_2(dppz)]^{2+}$ supporting the isomer assignment and the spectroscopic binding titration data where the n values were similar.

The substitution effect was more apparent for Ru-ester which exhibited the longest-lived lifetime in DNA for both decay components: τ_l (α_l),τ_s = 852 ± 27 ns (41 %), 155 ± 11 ns (r = 10). Early studies by Barton showed that the lifetime of *rac*-$[Ru(phen)_2(dppz)]^{2+}$ is markedly longer-lived than the bpy analogue in DNA (τ_s = 120 vs 90 ns; τ_l = 770 vs 340 ns).[19] The effect was originally attributed to greater hydrophobicity of the phen ligand, so that when $[Ru(phen)_2(dppz)]^{2+}$ was DNA-bound, it created a relatively more rigid and lipophilic barrier than $[Ru(bpy)_2(dppz)]^{2+}$ that reduces the accessibility of water, thus increasing the average lifetime. However, as shown in more recent studies, the impact of cooperativity and complex-complex interactions as described by Lincoln *et al*. must also play a role.[31,32] Herein, for Ru-ester, the relative lifetime increases in τ_s and τ_l versus Ru-acid were inequivalent and the fractional amplitude of the longer component increases to α_l = 41 %. This suggested a higher population of canted binding geometries occurring for Ru-ester than Ru-acid. Hence, the enhanced lipophilicity of the ester derivative versus Ru-acid and $[Ru(bpy)_2(dppz)]^{2+}$ may inhibit water access, but it is also probable that the aryl-ester substituent plays a significant steric role which leads to the differences in binding geometry and luminescence lifetime. This may occur via neighbouring complex-complex interactions like $[Ru(phen)_2(dppz)]^{2+}$, or due to steric effects of the aryl-ester substituent against the DNA backbone that favours the longer-lived canted intercalation, even in the absence of the influence of neighbouring complexes.

The conjugates were also found to exhibit bi-exponential behaviour upon DNA-binding but the average lifetime for both Ru-MPP and Ru-NLS was not as long-lived as Ru-ester. The fractional amplitude of the long component was determined to be greater in both cases; α_l = 43 % and 49 % for Ru-NLS and Ru-MPP respectively supporting a higher proportion of Ru-dppz complexes in a more protected intercalation. However, the change in the distribution of binding geometries may also be a result of the influence of peptide-DNA interactions that impacts both the structure of the binding site and how the Ru-dppz moiety is hosted. Furthermore, the presence of four isomers undoubtedly complicates matter further and one must be cautious in overinterpretation of the lifetime data on association with DNA as contributing decays may arise from differences in how isomers interact with the structure. In any case, this complexity limits a reliable comparison to the model cases of unfunctionalized pure enantiomers reported by Lincoln and coworkers.[31,32] In terms of the application of the probes towards cellular imaging, an increase in α_l is useful in terms of extending the average luminescence lifetime when DNA bound which can be beneficial for time-gating experiments.[75] Conversely, the luminescence lifetime and the relative distribution of its components can be a sensitive diagnostic of the environment of the binding site as well as neighbouring effects.[19] In the cases of the conjugates reported herein, it is apparent that peptide interaction with DNA is what ultimately defines τ_l, τ_s, α_l and α_s, which reduces the level of sensitivity that can be achieved with pure enantiomers of $[Ru(bpy)_2(dppz)]^{2+}$. However, although outside the scope of this work, the differences in the magnitude and distribution of luminescence lifetimes upon DNA binding may still be sensitive enough to differentiate DNA structure on a larger scale, for example, in reporting on DNA phase or interrogating special structures such as G-quadruplexes.

4.2.2.3 The impact of Ru-dppz complexes on the circular dichroism spectrum of ctDNA

Changes to the characteristic bisignate circular dichroism spectrum of native B-form ctDNA were observed in all cases with increasing relative concentration of Ru, measured in PBS up to $r = [DNA]_{bp}/[Ru] = 5$. The most notable change was the emergence of a strong negative induced circular dichroism (ICD) band at *ca*. 295 nm that was not evident in the spectrum of free ctDNA (Figures 4.10 – 4.13). As expected, the CD spectra of the racemic free probes do not exhibit optical activity in the experimental range 220 – 500 nm. However, CD activity in

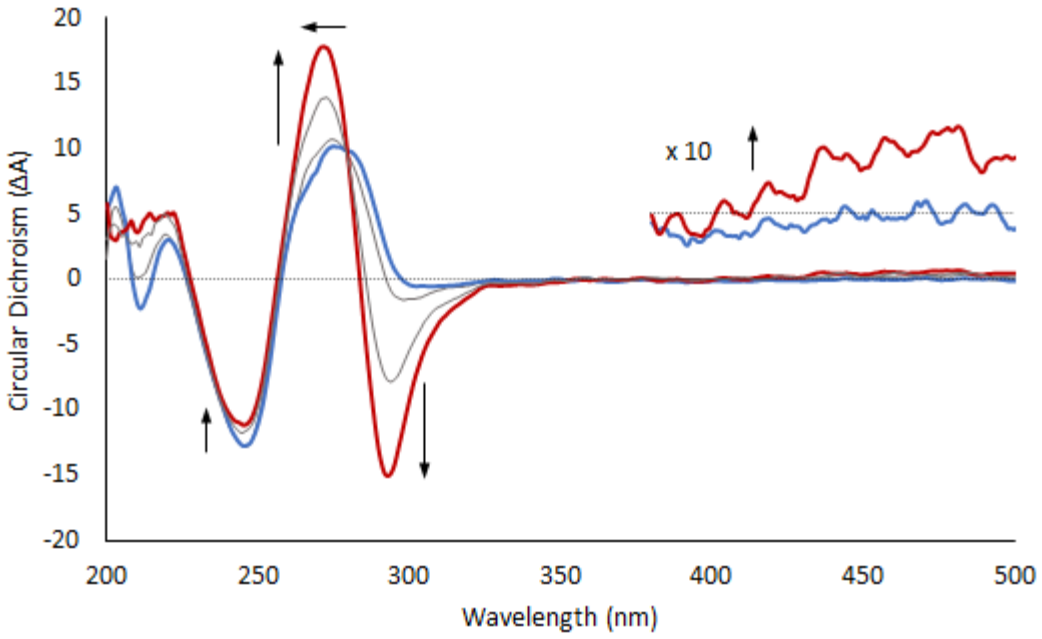

Figure 4.10: Changes to CD spectrum of ctDNA in PBS with increasing $[Ru(bpy)_2(dppz)]^{2+}$ concentration from [Ru] = 0 (blue trace) to r = $[DNA]_{bp}/[Ru]$ = 5 (red trace).

---

the complexes may be induced upon binding DNA, which is chiral by its helicity, through a coupling of the respective electronic transition moments.[106] In general, DNA groove binders tend to exhibit ICD at intensities an order of magnitude higher than intercalators.[107–109] Accordingly, the ICD band observed in the spectra herein at *ca*. 295 nm may be assigned to a bpy based transition since dppz intercalation causes bpy to bind at the groove. This assignment is supported by the position of the band below 300 nm, as the dppz absorbance occurs *ca*. 355 nm (Section 4.2.1). Much weaker ICD was observed in the visible region of the spectra at about 485 nm. At higher concentrations of Ru, this could indicate enantioselective binding, but in the present case, this band was probably due to ICD corresponding to MLCT transitions.

In all cases, the shape of the CD spectra indicated that B-form DNA largely persists in the presence of Ru, at least up to r = 5, characterised by a negative band at 246 nm and a positive band at 279 nm.[110] In both cases, the negative DNA CD band (246 nm) underwent a comparable and moderate decrease in intensity. In the case of $[Ru(bpy)_2(dppz)]^{2+}$, the

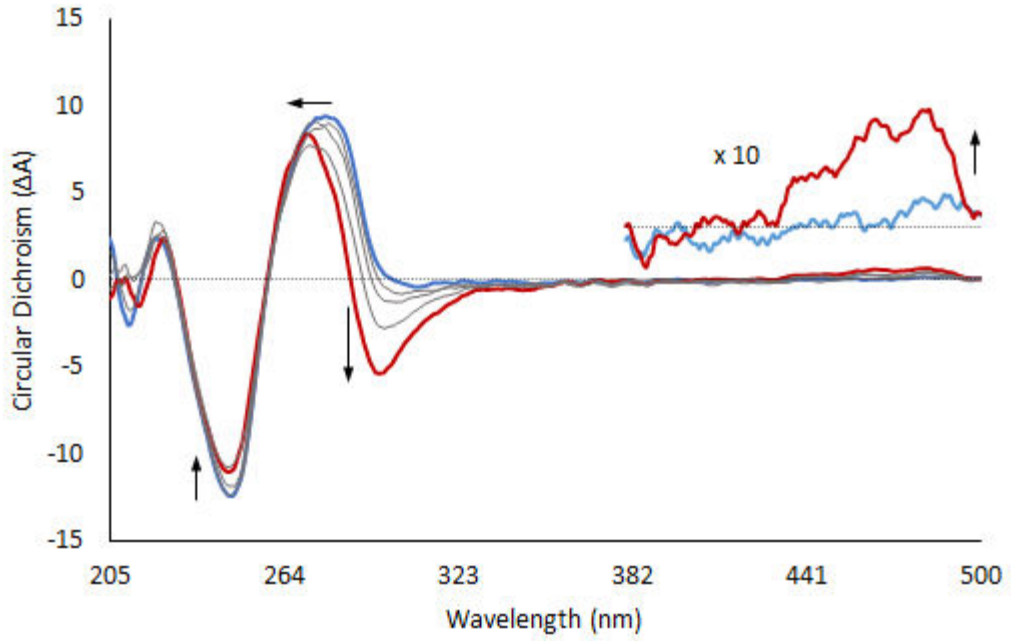

Figure 4.11: Changes to CD spectrum of ctDNA in PBS with increasing Ru-ester concentration from [Ru] = 0 (blue trace) to r = $[DNA]_{bp}/[Ru]$ = 5 (red trace).

---

positive band blue-shifted to 273 nm and became significantly more positive. A similar hypsochromic shift was observed in the positive band of Ru-ester (to 271 nm), but the magnitude of the CD intensity was only marginally impacted. An increase in the intensity of the positive band suggests structural non-denaturational distortion,[111] probably due to full dppz intercalation in the case of $[Ru(bpy)_2(dppz)]^{2+}$ which disrupts normal base stacking. Hence, full dppz intercalation may not be operative to the same degree in Ru-ester as the model complex, perhaps due to the influence of the aryl-ester substituent of Ru-ester and higher proportions of the canted geometry as indicated by the differences in luminescence lifetime data discussed above.

More pronounced changes in the intrinsic negative band were evident in the CD spectra of ctDNA in the presence of the NLS and MPP conjugates at r = 5. The largest change was observed in the case of Ru-NLS which bears the greatest net cationic charge and binding affinity, and hence the evolution of this band in the conjugates was attributed to structural distortion due to peptide-DNA interactions. Notably, comparable changes to the intrinsic

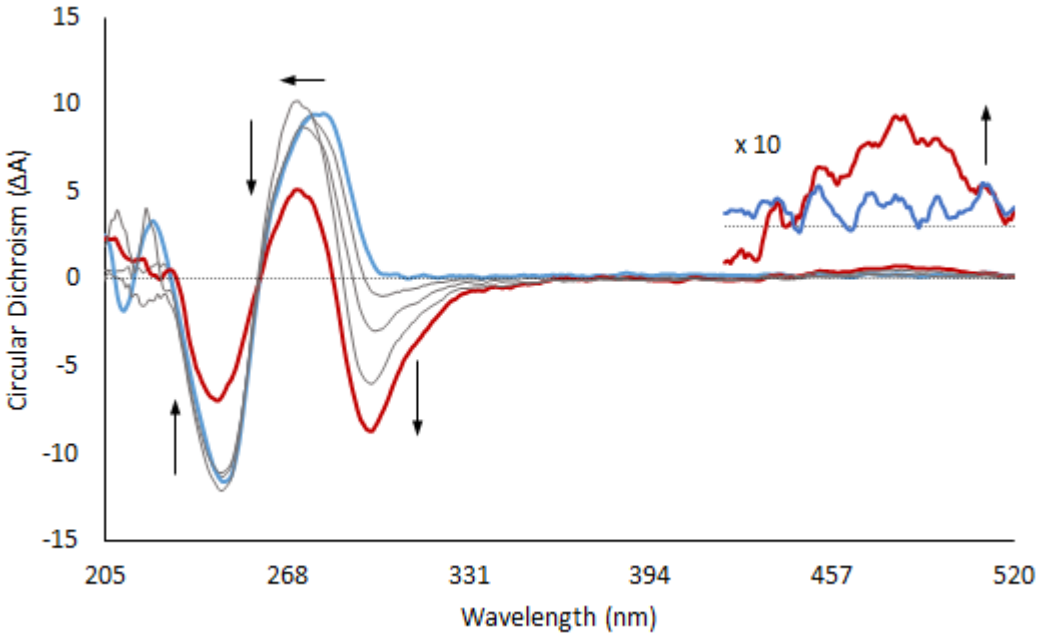

Figure 4.12: Changes to CD spectrum of ctDNA in PBS with increasing Ru-NLS concentration from [Ru] = 0 (blue trace) to r = $[DNA]_{bp}/[Ru]$ = 5 (red trace).

---

ctDNA CD bands were previously reported by Zama who studied DNA/polyarginine/polylysine/dye systems under conditions of comparable binding ratio and buffer composition to that described herein.[91] Interestingly, Ru-NLS also caused a much larger decrease in the intensity of the positive ctDNA CD band than Ru-MPP. This effect may have arisen not just because of a greater net cationic charge but also possibly due to structural stabilisation involving the binding of Phe residues present on the MPP, similar to the binding mechanism of the TATA-box binding protein.[93] The secondary structural changes induced by peptide-DNA interactions may not be ideal for imaging and highlights the future challenge in designing a targeting strategy that limits DNA distortion to provide representative DNA diagnostic information in live cells.

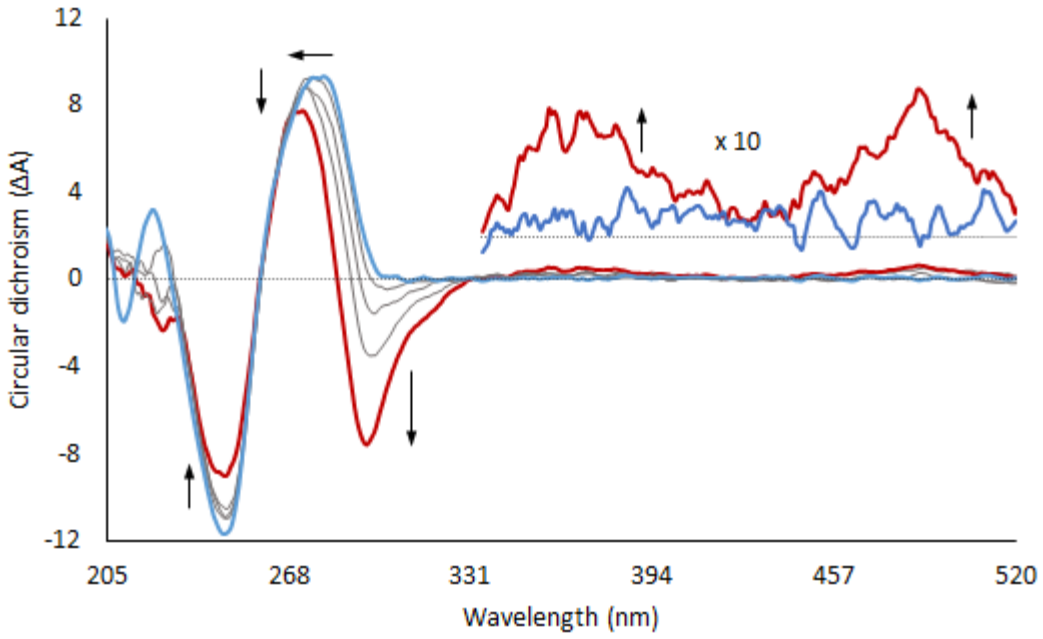

Figure 4.13: Changes to CD spectrum of ctDNA in PBS with increasing Ru-MPP concentration from [Ru] = 0 (blue trace) to r = $[DNA]_{bp}/[Ru]$ = 5 (red trace).

4.2.3 Non-specific binding: BSA as a protein model

Wragg *et al*. reported that human serum albumin can inhibit the nuclear uptake of Ru-Ir dimer complexes by binding within hydrophobic cavities such as the Sudlow Site I.[112,113] This binding was accompanied by a significant increase in the luminescence intensity of the dimer complex as it becomes protected from aqueous quenching. Charge is also important since metal complex luminophores (and conjugated peptides) are typically cationic and can electrostatically bind to proteins like albumin which exhibits a net anionic charge at physiological pH (pI BSA ≈ 4.7).[114] The interaction of Ru(II) complexes with proteins has also been studied by others and can be useful diagnostically and therapeutically by exploiting the relatively modular, three-dimensional coordination geometry to impart specific lipophilic and steric characteristics towards protein binding at hydrophobic surfaces and cavities.[115–118]

Herein, bovine serum albumin (BSA), a structural homologue of HSA,[119,120] was exploited to study the non-specific interaction of the Ru-dppz parent complexes and conjugates with

proteins to assess their binding propensities and the impact this has on their photophysics compared to DNA. This is important in the context of targeting, to determine if targeting can be impacted as described by Wragg *et al.*,[112] and also to investigate the spectroscopic response under non-specific affinity versus that observed in DNA in order to recognise off-target binding in cells.

As illustrated in Figure 4.14, solutions of $[Ru(bpy)_2(dppz)]^{2+}$, Ru-ester and Ru-NLS were found to be weakly luminescent in the presence of BSA. The luminescence was found to switch on approximately linearly with increasing relative BSA concentration up to 20 equivalents and the relative luminescence observed for increasing BSA compared to ctDNA at saturation was identical across the three compounds. The linearity suggests a non-specific binding, possibly driven by electrostatic interactions, which imparts an increasing protecting effect of the phenazine moiety of the dppz ligand from the aqueous environment, thereby switching on the luminescence. Importantly, the emission intensity even at 20 equivalents of BSA was found to be only roughly 8 % of that observed in the presence of ctDNA at saturation under the same conditions.

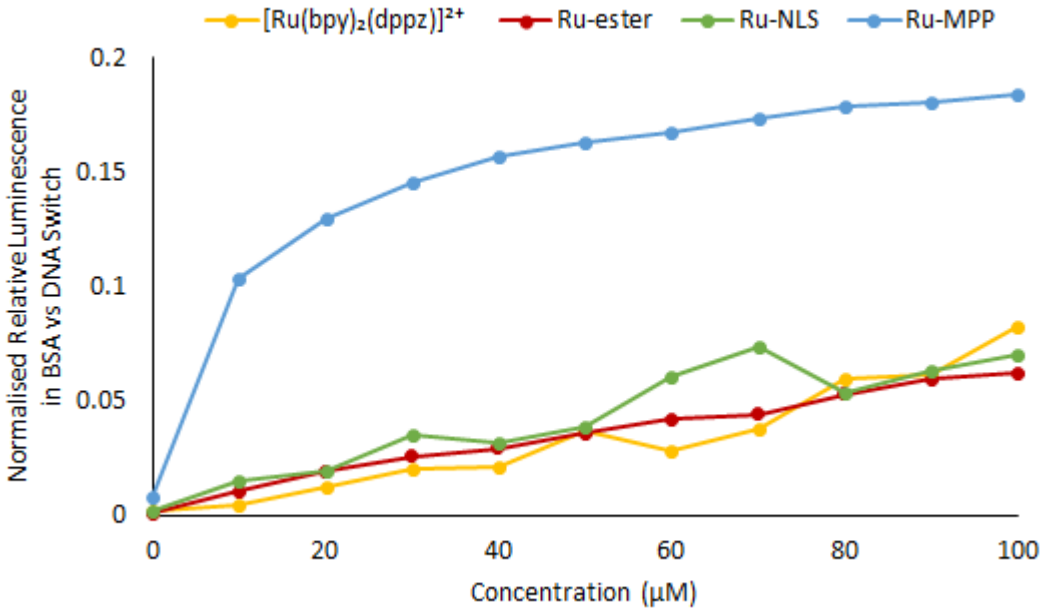

Figure 4.14: Normalised relative luminescence intensity ctDNA in the presence of BSA versus the light-switch in ctDNA for the Ru-dppz as indicated.

In contrast, Ru-MPP exhibited a greater spectroscopic response, with the luminescence about 18 % of that observed versus ctDNA at saturation (Figure 4.14). The binding curve also appears more indicative of specific binding that plateaus at a saturation of about 3 – 5 equivalents (< 25 μM BSA, Figure 4.13) but then continues to rise, probably due to an underlying non-specific binding as observed for the other complexes, judging by the comparable slopes of the respective binding curves at higher BSA concentrations. Since Ru-NLS and Ru-ester exhibit a similar response in BSA, the behaviour observed for Ru-MPP is probably linked to the presence of Phe residues on the MPP peptide. Indeed, Kumar *et al*. studied the enantioselective binding of phenylalanine conjugated to achiral moieties such as pyrene and demonstrated that stereoisomerism at the phenylalanine residue greatly impacts BSA binding by factors greater than 100.[121,122]

Using the same binding model exploited for the DNA binding studies as reported above (Equation 2.1), the binding affinity of Ru-MPP for BSA was estimated at K_b (BSA) = 5.7 x 10^5 M^{-1} (n = 1.4), which corresponds to a dissociation constant in the micromolar range; K_d ≈ 2 μM. The Ru-MPP binding constant with BSA is comparable to values reported by Mazuryk *et al*. for $[Ru(dpp)_2(bpy)]^{2+}$ and related complexes ($K_b \approx 10^5$), but is about 10 times higher than that reported by Wragg *et al*. for the Ru-Ir dimer which was inhibited from nuclear penetration due to serum binding in live cells ($K_b = 4.5 \times 10^4$).[112,123] The high binding affinity of Ru-MPP for BSA in the present case is not expected to divert the cellular transport of the probe, since the same MPP sequence was previously demonstrated by our group to successfully deliver its Ru(II) cargo to the mitochondria.[73] However, once localised, the high affinity for protein could impact specific staining of mtDNA, although it is notable that mtDNA is often packaged in nucleoid aggregates using proteins such as the mitochondrial transcription factor A (TFAM).[71] Hence, DNA staining should still be apparent and cellular application of the Ru-dppz peptide conjugates should not be significantly impacted.

4.2.4 Luminescence at 37 °C

The luminescence lifetime of Ru-ester was measured at 37 °C to determine the impact of physiological temperature on the photophysics of Ru-dppz complexes in acetonitrile and intercalated in ctDNA (Table 4.3, Figure 4.15). A marginal increase in the luminescence lifetime of Ru-ester in acetonitrile was observed at 37 °C. This behaviour is typical of Ru-

Table 4.3: Luminescence lifetime of Ru-ester at 20 °C and 37 °C in aerated acetonitrile and in the presence of ctDNA in aerated PBS (r = 20).

Temperature (°C)	**τ / free** MeCN	**τ / ctDNA** PBS
20	239 ± 1	852 ± 27 (41 %) 155 ± 11 (59 %)
37	253 ± 4	1061 ± 43 (20 %) 325 ± 33 (38 %) 77 ± 13 (42 %)

Notes: Errors included as ± SD (n = 3). Percentage relative amplitudes are given in parentheses.

dppz complexes and has been observed previously in $[Ru(bpy)_2(dppz)]^{2+}$ by Brennaman *et al.*.[23] In their study, the temperature dependence of $[Ru(bpy)_2(dppz)]^{2+}$ exhibited a rollover around 300 K in acetonitrile due to kinetic competition of the enthalpically favoured dark state and the entropically favoured bright state. Given the similarity of the photophysics of Ru-ester and $[Ru(bpy)_2(dppz)]^{2+}$, it is likely that a similar phenomenon occurs in the ester complex reported herein.

The changes in the photophysical behaviour of Ru-ester in DNA at higher temperatures are more complex. At 37 °C, the decay conformed to tri-exponential kinetics with large changes in the relative amplitudes and magnitudes of the component lifetimes relative to that observed at 20 °C (Table 4.3). McKinley *et al*. studied the effect of temperature on the luminescence lifetime of Δ/Λ-$[Ru(phen)_2(dppz)]^{2+}$ upon binding DNA and observed changes to the relative amplitudes and magnitudes in both enantiomers, which they attributed to changing populations of canted and perpendicular binding modes as DNA flexibility increases with heating.[33] Considering Ru-ester as tested here exists as a mixture of geometric and stereochemical isomers, the observed changes probably reflect a similar change in binding geometries. Haq *et al*. determined that the intercalation of $[Ru(phen)_2(dppz)]^{2+}$ is entropically driven leading to increased binding affinity with temperature.[17] This may also impact the binding modes and lifetimes observed here at 37 °C for Ru-ester.

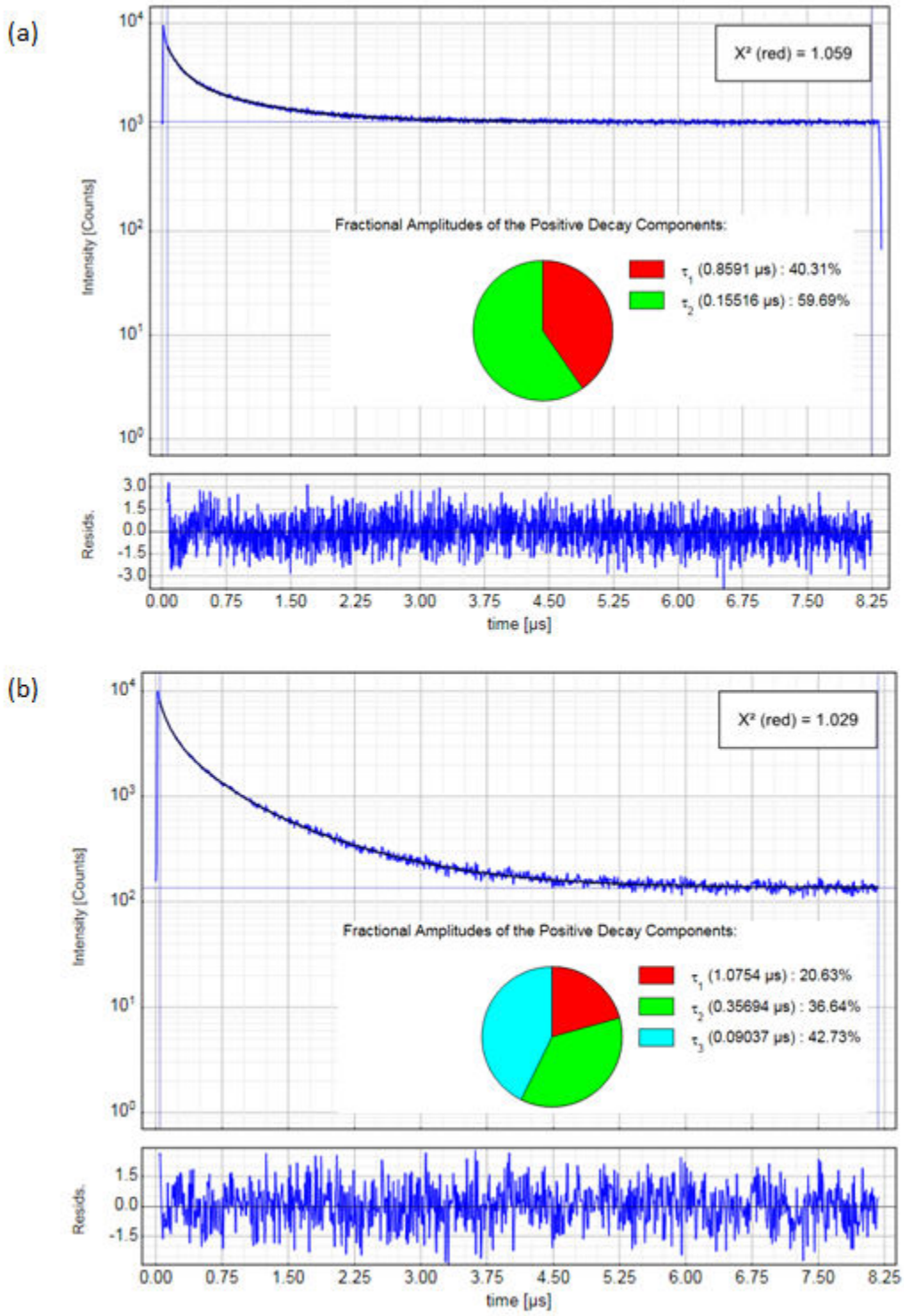

Figure 4.15: Luminescence decay curves for Ru-ester in the presence of ctDNA at (a) 20 °C and (b) 37 °C.

At 37 °C, the very short-lived component measured at $\tau = 77 \pm 13$ ns ($\alpha = 42$ %) may be tentatively ascribed to temperature activated quenching by electron transfer with guanine residues, the most easily oxidised base. Indeed, McKinley *et al*. observed consistently lower lifetimes in $[poly(dG\text{-}dC)]_2$ than $[poly(dA\text{-}dT)]_2$ which they attributed to poorer protection from groove hydration in GC steps and/or guanine quenching.[31] Further experiments using transient absorption are necessary in future studies to ascertain the impact of guanine on the luminescence at different temperatures.

4.2.5 Cell studies

4.2.5.1 Uptake, localisation and imaging of Ru-NLS

Confocal imaging of cellular uptake

Cellular uptake of Ru-NLS was assessed in live HeLa cells at 4 °C and 37 °C. Ru-NLS is non-emissive in water which made early stage uptake difficult to monitor in real time. At 37 °C, after 6 h Ru-NLS was observed staining membrane regions of the cell where luminescence switches on due to incorporation of the probe into lipid environments which inhibits aqueous quenching. We have previously observed this for conjugates of $[Ru(dppz)_2(pic\text{-}R)]^{n+}$.[124] Importantly, the parent complex is cell impermeable which demonstrates the penetrating ability of the conjugated peptide. At 4 °C, uptake was inhibited which, notwithstanding effects on membrane fluidity, suggests an energy dependent uptake mechanism was operative at 37 °C (Appendix B). After 24 h incubation in the dark at 37 °C, Ru-NLS was observed to have penetrated the nuclear envelope and was bound to chromosomal DNA (Figure 4.16, A - D) with concomitant switching-on of its luminescence. Excellent contrast imaging was achieved due to the light-switch effect which only illuminates the structures bound by luminophores and protected from water, thus effectively providing zero background.

Nuclear staining was confirmed by co-localisation with DAPI (a commercial nuclear stain), as shown in Figure 4.16E by the purple overlay of the DAPI (blue) and Ru-NLS (red) images. Additionally, the relative emission profile taken across a cell co-stained with DAPI and Ru-NLS indicates that Ru-dppz was confined to DAPI localised regions of the cell. The precision targeting of Ru-NLS to nuclear DNA in live cells underlines the success of the signal peptide

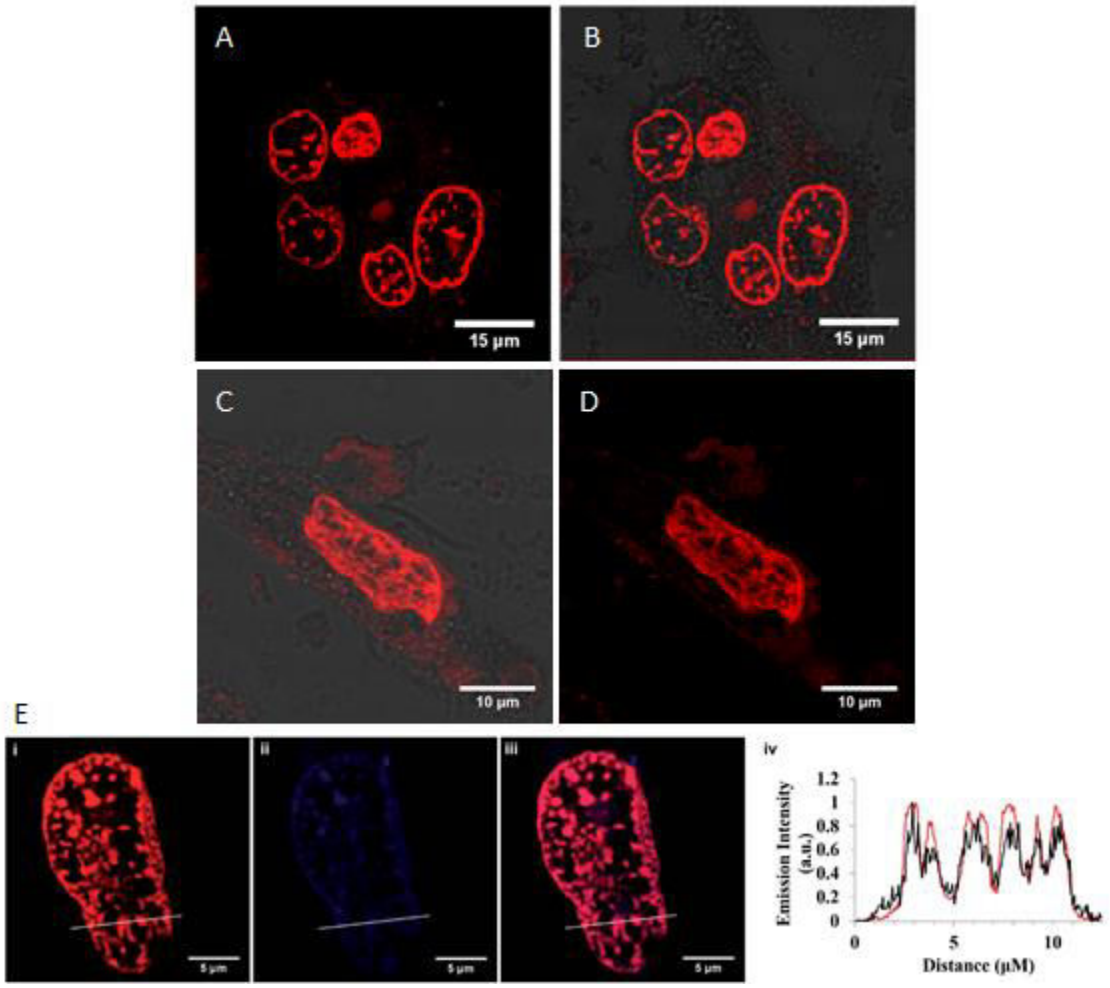

Figure 4.16: Confocal imaging of the cellular uptake of Ru-NLS (40 µM) in live HeLa cells over 24 h. A and B shows Ru-NLS distribution in a group of cells. C and D shows nuclear staining by Ru-NLS in a single cell. E shows Ru-NLS (40 µM) co-localisation with DAPI (300 nM); (i) Ru-NLS channel, (ii) DAPI channel, (iii) overlay, (iv) relative emission of Ru-NLS (red trace) and DAPI (black trace) across the plane indicated by the inserted white line in (i) – (iii). Ru-NLS was excited using a 470 nm white light laser and the emission was collected between 565 and 700 nm. DAPI was excited at 633 nm and the emission was collected between 637 and 730 nm. Data courtesy of Dr. Aisling Byrne (DCU).

---

targeting uptake strategy. Notably, this was the third example of the use of this *same* NLS to deliver *different* Ru(II) complex cargo to the nucleus. Previously our group observed nuclear uptake of NLS-directed $[Ru(dppz)_2(pic\text{-}R)]^{2+}$ and $[Ru(dpp)_2(pic\text{-}R)]^{2+}$.[74] Hence, NLS targeting is a robust strategy to achieve reproducible nuclear uptake of Ru(II) complexes.

The successful nuclear uptake and luminescence imaging of chromosomal DNA in live cells represents one of the first of its kind using metal complex luminophores. Critically, the concentration required for successful nuclear uptake of Ru-NLS at 40 μM was much lower in comparison to other key literature examples, for example, $[(Ru(phen)_2)_2(tpphz)]^{4+}$ was reported by Gill *et al*. to enter the nucleus at concentrations of 500 μM, and the ion pairing strategy of Zhu *et al*. required 100 μM of $[Ru(bpy)_2(dppz)]^{2+}$ and 300 μM of an ion-pair reagent.[66,70] However, it must be noted that the timescale of the NLS approach reported herein is much longer than reported in the literature examples (24 h versus 1 – 3 h). A similar incubation time (16 h at 37 °C) was required to achieve nuclear uptake of other Ru-dppz conjugates reported previously by our group. Future work using NLS peptide targeting could investigate methods to reduce the time taken for nuclear uptake, for example by studying the rate of endosomal escape and translocation across the nuclear membrane, or by exploring the impact on uptake using multiple peptides or conjugations to a single complex, such as the diconjugated complexes presented in Chapter 3.

Luminescence Lifetime imaging (LLIM) of Ru-NLS

Figure 4.17 shows confocal and LLIM images of nuclear localised Ru-NLS in live HeLa cells indicating chromosomal DNA observed at metaphase. DNA-bound Ru-NLS exhibited dual exponential decay kinetics with the component lifetimes determined at τ_l = 299 ns (57 %) and τ_s = 35 ns (43 %). *Ex-cellulo*, bi-exponential behaviour was ascribed to binding to ctDNA in either a perpendicular or canted geometry. In cells, the lifetime values reflect a

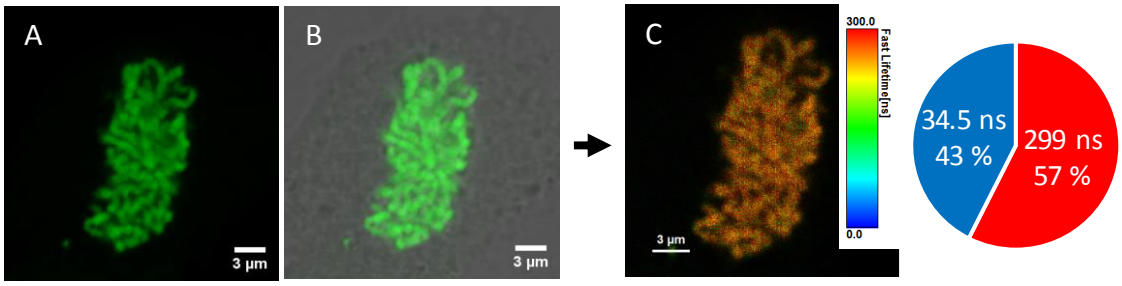

Figure 4.17: Confocal (a), false-colour (b), and LLIM images (c) of nuclear localised Ru-NLS in a live HeLa cell. The chart represents the lifetime distribution across the image with the magnitude and relative amplitudes of the bi-exponential decay as indicated. Data courtesy of Dr. Aisling Byrne.

more complex scenario. The longer lifetime could be attributed to an averaged DNA binding value considering that its magnitude at 299 ns suggests protection of the Ru-dppz moiety from aqueous quenching. However, it is notable that a much longer component attributed to binding in a canted geometry was not observed (where $\tau \approx 570$ ns), especially since this component was shown to increase at 37 °C for Ru-ester (Table 4.3). This indicates that binding *in cellulo*, unsurprisingly, is more complex than association with ctDNA and suggests that full intercalation and protection of the Ru-dppz chromophore is not occurring to the same degree upon binding nuclear DNA. In comparison to the luminescence data measured at 37 °C (Table 4.3), the shorter-lived component could arise due to guanine quenching of the luminescence or may reflect surface binding to DNA or nuclear proteins. Further experiments are necessary to determine the origin of the short-lived component, but the magnitude of the long-lived component is strong evidence for DNA binding of Ru-NLS in live cells.

Ru-NLS: A new probe for stimulated emission depletion (STED) microscopy

Ru-NLS was assessed as part of the first study on metal complex luminophores for super resolution STED microscopy reported by our group (see Chapter 6 for greater detail and elsewhere[75]). Briefly, STED operates by depleting a doughnut shaped region around the focal area which leads to sharpened resolution, exceeding that achieved by conventional diffraction-limited microscopies.[125,126] Figure 4.18a shows a comparison of images of DNA-bound Ru-NLS in HeLa cells during metaphase obtained under confocal or STED microscopy. The high contrast achieved using a light-switch luminophore permits a comparison of the resolution of both techniques. As well as staining chromosomal DNA, spherical structures were also labelled slightly out of focus at the edge of the nuclear envelope. These structures were attributed to ribosomes where Ru-NLS may be switching-on upon binding mismatch or higher-order RNA.[45,50]

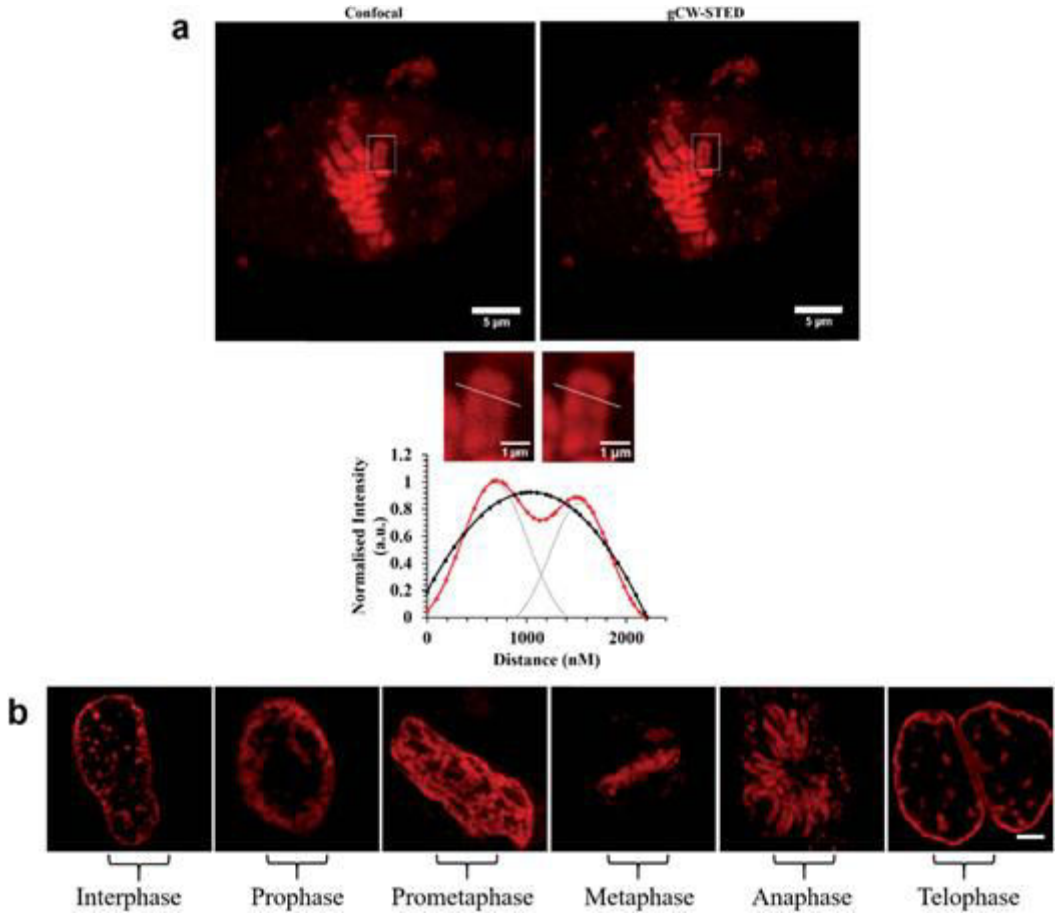

Figure 4.18: (a) Confocal and STED images of Ru-NLS bound to chromosomal DNA in the nucleus during metaphase. Bottom (a), line traces through a single chromosome (white) and the corresponding plot profile show the greatly improved resolving power of STED imaging (red) compared to confocal (black). The FWHM was obtained by fitting fluorescence-intensity to Gaussian distributions (OriginPro). Two separated Gaussian distributions are indicated by grey dashed lines for the STED profile fitting. (b) STED images of Ru-NLS bound to DNA in the nucleus in fixed HeLa cells showing the different stages of cell division. HeLa cells were incubated with 40 mM complex for 24 h in the absence of light. The samples were fixed with 3.8% paraformaldehyde for 15 minutes, and then mounted with Prolong Gold for 24 h before imaging. Ru-NLS was excited at 470 nm white light laser and the emission was collected between 565 and 700 nm. The 660 nm STED depletion laser was used to acquire the STED images. Data is raw with no post-processing performed. Data courtesy of Dr. Aisling Byrne (DCU).

Lateral resolution, as indicated in the plot profile taken across a single chromosome in Figure 4.18a, clearly reveals superior performance under STED compared to confocal. Under STED, individual chromatids were distinguishable and grooves were apparent in individual structures, possibly attributable to centromere sites. The remarkable image quality achieved using STED with high resolution and contrast permitted the imaging of different phases of cell division. Different HeLa nuclei stained with Ru-NLS were selected to observe the stages of mitosis as shown in Figure 4.18b; starting at interphase where the chromosomes replicate, through chromosomal condensation and alignment at metaphase, separation in anaphase and finally, the splitting of chromosomes into two new cells at telophase.

Precision-targeted Ru(II) luminophores are evidently well-suited to STED microscopy and may be applied in future studies to examine cellular processes at the nanoscale in super resolution. Further examples of the application of Ru(II) polypyridyl luminophores to STED microscopy are presented in Chapter 6 of this thesis.

4.2.5.2 Confirming nuclear localisation of Ru-NLS using resonance Raman in live cells.

Ru-dppz is non-luminescent in cells without the protection of the luminophore from aqueous quenching, for example through DNA intercalation or lipid membrane binding. This complicates an assessment of uptake and localisation of the probe under confocal imaging alone. Instead, resonance Raman spectroscopy (rRaman) can be employed to scan regions of the cell to determine the presence or absence of the probe. rRaman operates by selectively enhancing Raman vibrational modes associated with the chromophore involved in the resonant electronic transition. This effect makes it possible to record spectra of Ru(II) complexes under visible excitation into the MLCT band where the chromophore modes are resonant but the cellular background is not. Previously, our group exploited this technique to confirm nuclear localisation of NLS-directed $[Ru(dppz)_2(pic\text{-}R)]^{2+}$.[74]

Before investigating rRaman spectra of Ru-NLS across the cell, it was important to record the rRaman spectra of $[Ru(bpy)_2(dppz)]^{2+}$, Ru-ester and Ru-NLS in the presence and absence of DNA in PBS buffer (473 nm, [Ru] = 100 μM). Peaks were assigned as bpy or dppz modes with reference to the values reported by Coates *et al*. and Basu *et al*. for $[Ru(dppz)_3]^{2+}$ and $[Ru(bpy)_3]^{2+}$ respectively.[127,128] Additionally, a comparison of the spectra of

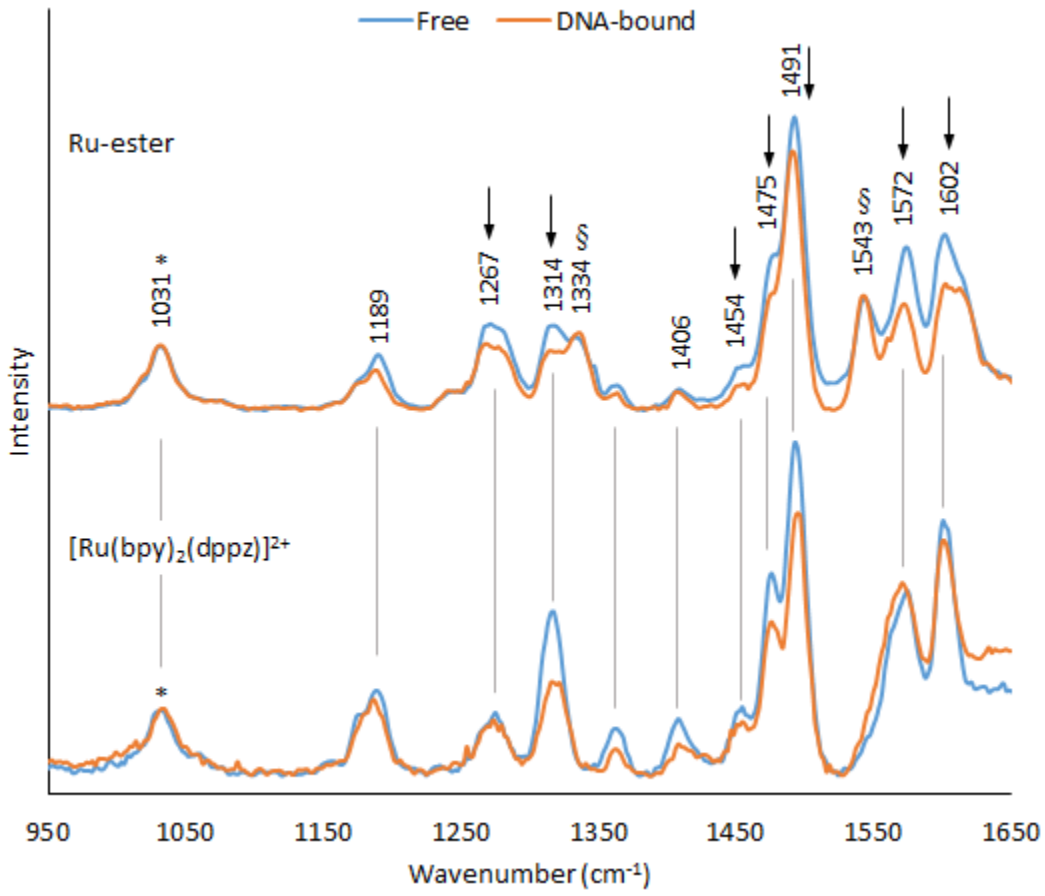

Figure 4.19: rRaman spectra (473 nm) of $[Ru(bpy)_2(dppz)]^{2+}$ and Ru-ester in the presence (orange) and absence (blue) of DNA (r = 10). Spectra were normalised to the peak at 1031 cm^{-1} (*). Peaks unique to Ru-ester are marked (§). Arrows indicate changes in relative intensity upon DNA binding.

$[Ru(bpy)_2(dppz)]^{2+}$ and Ru-ester revealed new peaks attributable to the influence of the aryl-ester pendant, most notably at 1336 cm^{-1} and 1543 cm^{-1} (see Figure 4.19 and Appendix B).

In the presence of DNA, Ru-ester and $[Ru(bpy)_2(dppz)]^{2+}$ exhibit relative intensity decreases in peaks attributable to dppz modes (Figure 4.19). An isolated bpy peak at 1031 cm^{-1} was used for spectral normalisation and notably, relative to this peak, the aryl-ester signals of Ru-ester at 1336 cm^{-1} and 1543 cm^{-1} do not exhibit changes in relative intensity in the presence of DNA. This supports binding by dppz ligand intercalation since the bpy and bpy-Ar-COOEt modes should be less perturbed upon binding DNA at the groove relative to the intercalating dppz ligand. Similar changes to the rRaman spectra of $[Ru(phen)_2(dppz)]^{2+}$ were observed

independently by Coates *et al*. and Chen *et al*. and can be rationalised in terms of the hyperchromicity of the MLCT band in the visible absorbance spectrum of Ru-dppz complexes upon DNA intercalation (e.g. Figure 4.7 herein), due to broadening and red shifting of the underlying dppz component that leads to decreased resonance at 473 nm.

The rRaman spectra of Ru-NLS was more complex; in the absence of DNA, the spectra of Ru-ester and the conjugate exhibited small but significant differences upon normalisation to the bpy mode at 1031 cm^{-1} in terms of relative intensity in the dppz and bpyArCOOEt peaks (Appendix B). These differences are not due to an effect of amide conjugation (by comparison to the spectrum of Ru-ester) and instead signify interaction of the peptide with the Ru(II) chromophore. Earlier, the luminescence lifetime of Ru-NLS in aerated acetonitrile was bi-exponential which was attributed to a protecting effect afforded to the emission centre from quenching by oxygen. Hence, the observed differences in the rRaman spectra may be due to a wrapping of the conjugated peptide around the Ru-dppz moiety which places it in a more organic environment that impacts resonance of certain modes at 473 nm.

It was difficult to assess the changes to the rRaman spectra of Ru-NLS upon DNA binding because of the influence of the peptide on the spectra in the absence of DNA. Instead, the spectrum of DNA-bound Ru-NLS may be compared to the spectrum of DNA-bound Ru-ester since the chromophore should be intercalated in DNA and in a similar environment. Indeed, as shown in Figure 4.20, the spectrum of Ru-NLS in the presence of DNA mirrored that of Ru-ester upon normalisation to the peak at 1031 cm^{-1}, with the pendant aryl signals of bpyAr-R almost coincident at 1334 cm^{-1} and 1543 cm^{-1}. Minor relative intensity decreases in peaks attributable to dppz modes were observed for Ru-NLS which suggests slightly enhanced protection of the chromophore, possibly due to the influence of the peptide at the binding site.

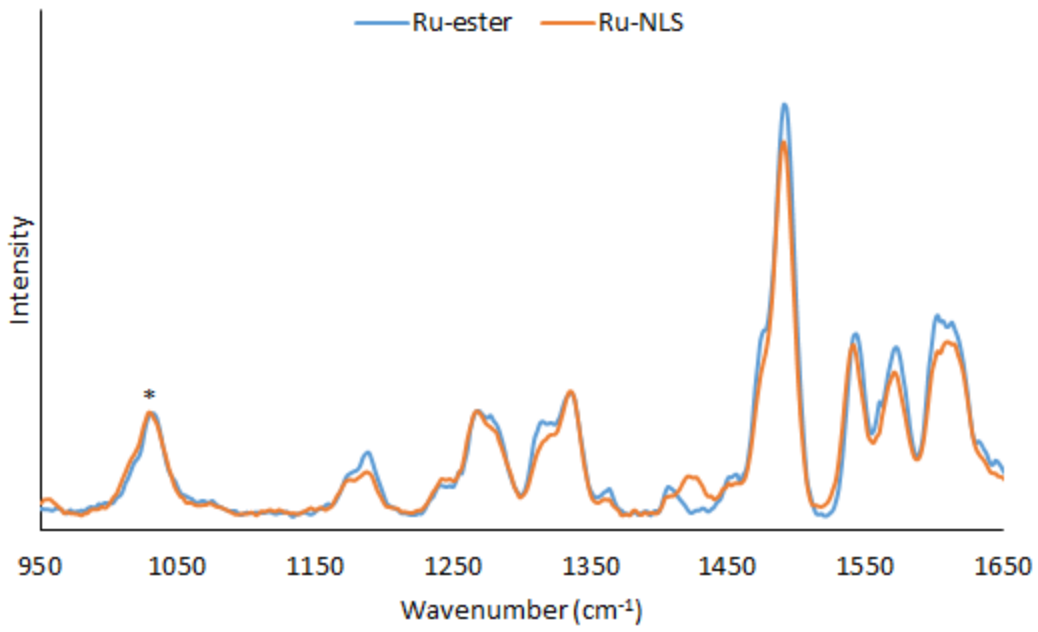

Figure 4.20: rRaman spectra (473 nm) of Ru-ester and Ru-NLS as indicated in the presence of DNA (r = 10). Spectra were normalised to the peak at 1031 cm^{-1} (*).

---

rRaman spectra were acquired in nuclear and cytoplasmic regions of HeLa cells treated with Ru-NLS. In support of luminescence co-localisation studies, the intensity of the rRaman signals were consistently much greater in the nucleus than in the cytoplasm and, as shown in Figure 4.21, comparable peaks were observed in the spectrum of the nucleus that corresponded to the rRaman spectrum of Ru-NLS recorded in PBS buffer. However, the relative intensities of the bpy and dppz peaks of the two spectra were dissimilar which prevented a clear observation of DNA binding by rRaman *in-cellulo*. This may support the FLIM data reported above, perhaps unsurprisingly indicating that dppz intercalation is not occurring in the same fashion with chromosomal DNA as observed *ex cellulo* in the presence of ctDNA. In any case, the rRaman data in live cells provides strong evidence of the successful nuclear confinement of Ru-NLS.

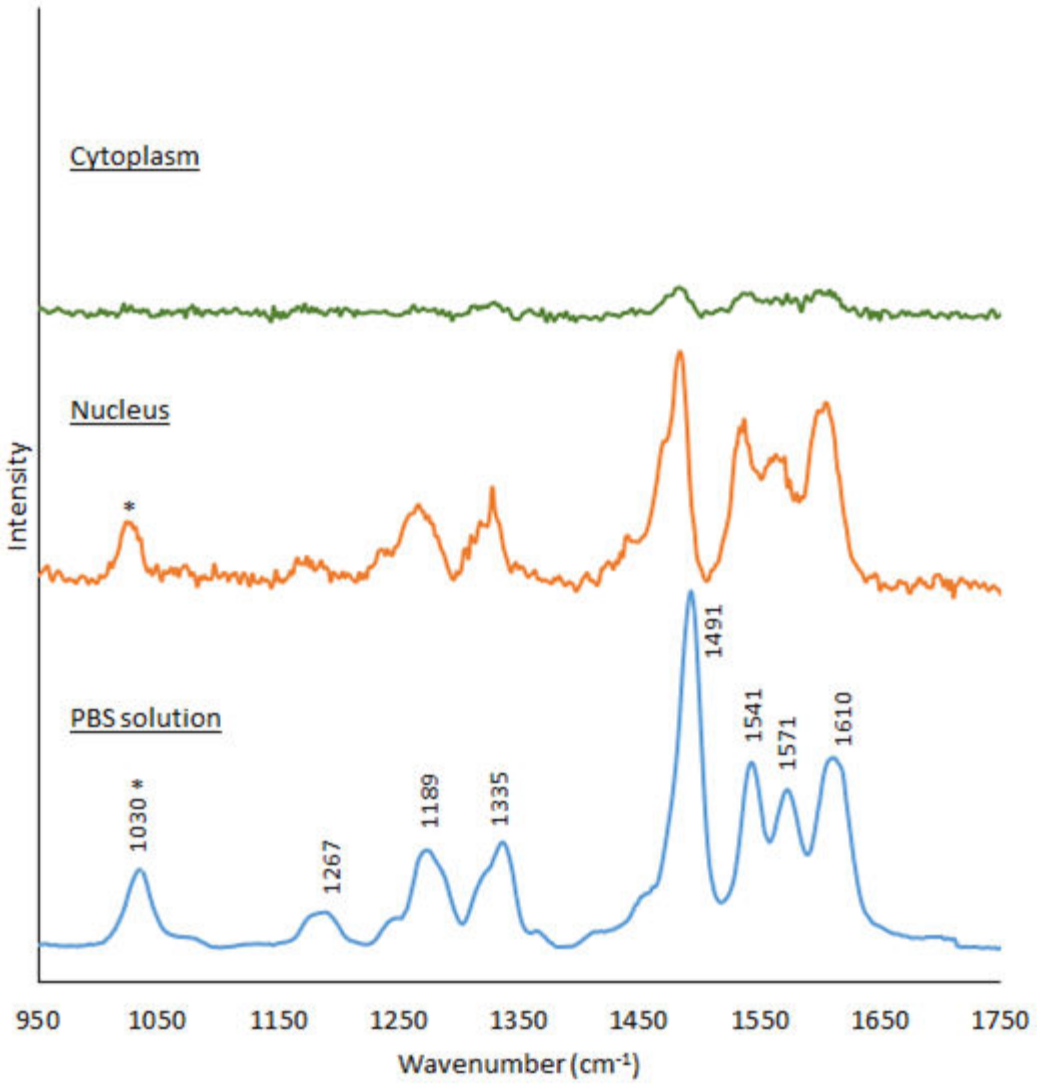

Figure 4.21: rRaman spectra (473 nm) of Ru-NLS in buffer solution (bottom, blue) and in a HeLa cell at the nucleus (middle, orange) or cytoplasm (top, green). The cellular spectra are shown as measured with background correction. The buffer spectrum was normalised to the peak at 1031 cm^{-1} (*) in the nucleus spectrum. Cellular data courtesy of Dr. Aisling Byrne (DCU).

4.2.5.3 Uptake, localisation and imaging of Ru-MPP

The cellular uptake of Ru-MPP in live HeLa cells was found to be energy dependent with no uptake observed at 4 °C and, like Ru-NLS, suggested that an activated process such as endocytosis was operative (see Appendix B). In contrast to Ru-NLS, the uptake of Ru-MPP at 37 °C in the absence of light was rapid, observed in the cytoplasm after 1 h, and apparent in mitochondrial regions of the cell as bright punctate spots after 2 h. Mitochondrial localisation was confirmed by co-staining with MitoTracker Deep Red as shown in Figure 4.22 (A – E). MitoTracker appears to stain the whole of a mitochondrion (Figure 4.22 E), and although similar staining was observed for Ru-MPP, the probe was also apparent as bright punctate spots within the mitochondrial regions (Figure 4.22 D). Overlay images further highlight this, where coincidence of MitoTracker and Ru-MPP produces an orange colour confirming co-localisation. However, in these images, one or two brighter Ru-MPP spots were evident as yellow (Figure 4.22 B,C) or green (Figure 4.22 A) patterns within the co-stained orange mitochondrial regions. mtDNA is frequently observed as one or two copies per mitochondrion which may suggest that the staining pattern exhibited by Ru-MPP herein is evidence for mitochondrial nucleoid binding. Further evidence is that this punctate pattern was also observed by Kukat *et al*. who specifically targeted mtDNA and the nucleoid bound TFAM protein for STED microscopy.[71]

To further probe the environment of Ru-MPP, luminescence lifetime imaging (LLIM) of Ru-MPP in live HeLa cells was carried out (Figure 4.22 F – H). Again, Ru-MPP was observed as punctate spots under confocal imaging and LLIM of the same cell yielded a similar pattern with 'hot-spots' of a longer-lived emission against a background of shorter-lived emission (Figure 4.22 H). The luminescence from these structures decayed under dual-exponential kinetics with a longer-lived component determined at $\tau_l = 182 \pm 5$ ns ($\alpha_l = 32$ %) and a very short-lived component measured at $\tau_s = 28 \pm 4$ ns ($\alpha_s = 68$ %). Interestingly, the short-lived component observed for Ru-MPP in the mitochondria is comparable to τ_s measured for Ru-NLS in nuclear DNA and may lend further support to guanine quenching. Alternatively, τ_s arises from unbound Ru-MPP, partially protected from complete aqueous quenching within the mitochondria, perhaps due to membrane or protein binding.

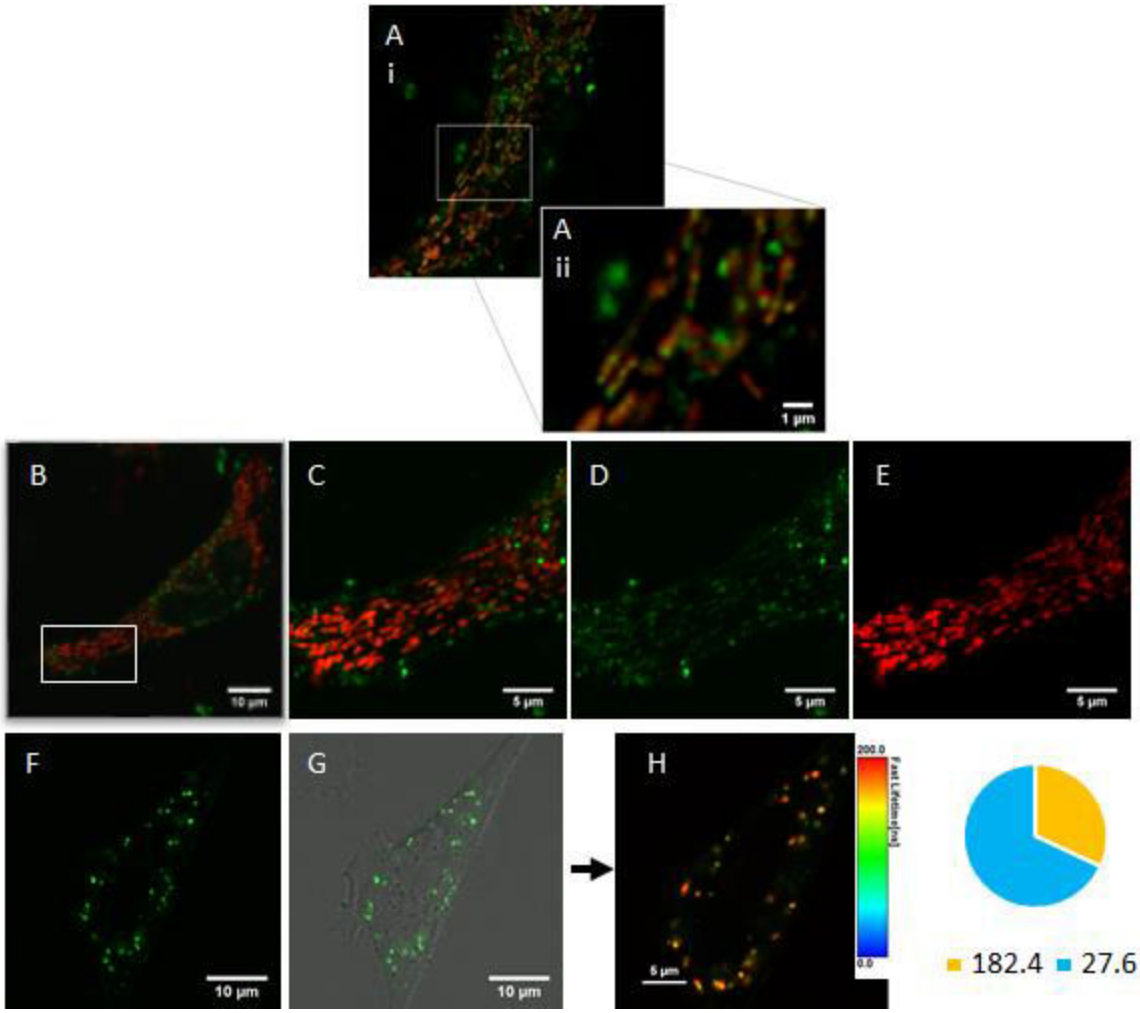

Figure 4.22: Cellular uptake and mitochondrial localisation of Ru-MPP (10 µM) in live HeLa cells. A – E: co-localisation studies of Ru-MPP (green) and Mitotracker Deep Red (100 nM). (A) shows a close-up of a selected region to indicate punctate green Ru-MPP staining within mitochondria (orange) co-stained with MitoTracker Deep Red. Similarly, B and C show an overlay of the staining of Ru-MPP (D) and MitoTracker Deep Red (E). C – E are close-ups of the region marked by a white box in (B). F and G show Ru-MPP distribution in a single HeLa cell that was imaged using LLIM (H) to provide a colour coded map of the luminescence lifetime distribution of Ru-MPP. The pie-chart represents the magnitude and relative distribution of the luminescence lifetime which was fit to dual exponential decay kinetics. Data courtesy of Dr. Aisling Byrne (DCU).

The longer-lived component of Ru-MPP likely indicates intimate binding with mtDNA which protects the luminophore from aqueous quenching. Notably, the luminescence lifetime in mtDNA was reduced compared to nuclear DNA, probably because of mtDNA typically existing in plasmid form within protein-DNA nucleoids and offers less protection to aqueous quenching than concentrated and protected nuclear DNA.

Confocal imaging and LLIM both provide strong evidence for mtDNA binding and thus, this represents the first example of precision targeted imaging of mtDNA in the live cell using metal complex luminophores. The power of using targeting peptides to deliver Ru(II) cargo was again demonstrated, in this case using an MPP sequence to translocate a Ru-dppz complex across the double mitochondrial membrane and into the core of the mitochondria for DNA binding. Previously, this MPP sequence transported a dinuclear conjugate based on $[Ru(bpy)_2(phenAr\text{-}R)]^{2+}$ to the mitochondria[73] which again indicates that signal peptides appear to be a versatile strategy in targeting select organelles with different metal complex cargo.

4.2.5.4 Cytotoxicity and photocytotoxicity

Dark cytotoxicity

The dark cytotoxicity of Ru-MPP and Ru-NLS was determined in HeLa cells using the resazurin assay.[129] As shown in Figure 4.23, Ru-MPP was relatively more cytotoxic than Ru-NLS and significant toxicities were observed at > 20 μM Ru-MPP and > 150 μM Ru-NLS. However, at the working concentrations of the probes, 10 μM for Ru-MPP and 40 μM for Ru-NLS, the cells exhibit about 80 % viability which is well suited to imaging studies.

Photo-cytotoxicity

Under imaging conditions, the Ru-dppz conjugates did not induce phototoxicity, for example for Ru-MPP, cells remained viable under imaging periods of at least 3 h. This is unsurprising considering that $[Ru(bpy)_2(dppz)]^{2+}$ is a poor singlet oxygen photosensitiser which limits the photosynthesis of toxic species under imaging. However, considering the precision localisation of the Ru-dppz conjugates to genetic material in live cells, we were interested in

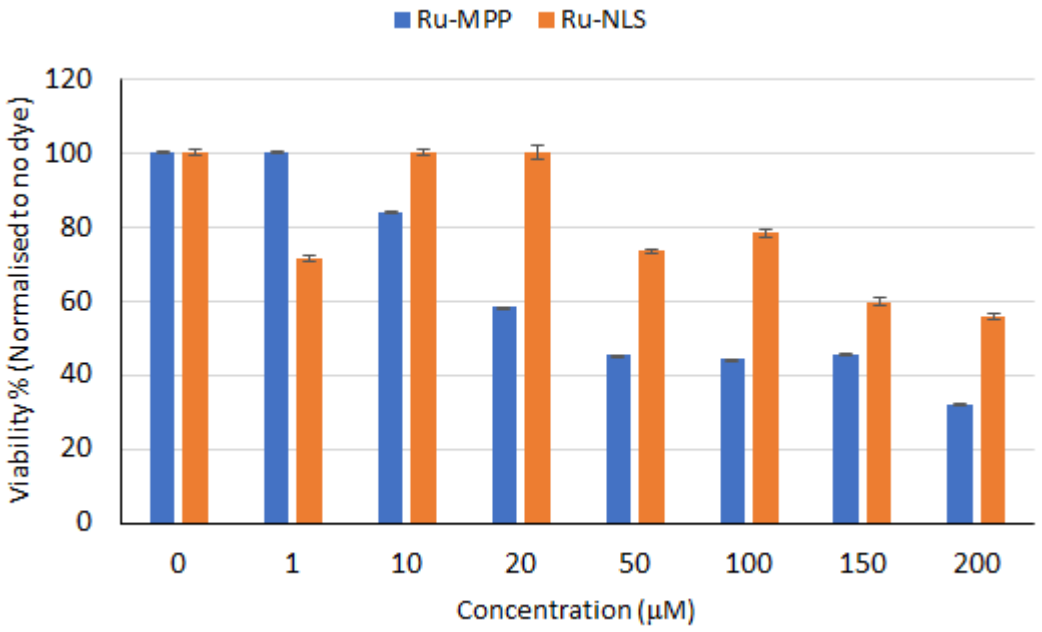

Figure 4.23: Cellular viability in the presence of various concentrations of Ru-NLS and Ru-MPP as indicated. Viability was determined using the resazurin assay and is expressed as a percentage of viable dye-treated cells relative to untreated cells. Data courtesy of Dr. Aisling Byrne (DCU).

---

investigating if photo-induced DNA damage could be sensitised at higher photo-irradiation intensities.

As a control experiment, an untreated sample live cell was scanned continuously at intensities at least 2.5-fold higher than imaging (0.78 µW, 470 nm) in 5 minute intervals and then imaged to assess indicators of cell distress. As shown in Figure 4.24, for this control cell, there was a clear absence of structural damage to the cell and no staining by DRAQ-7 (a dead cell stain) was observed. Conversely, scanning a selected cell which contained Ru-MPP probe was observed to undergo blebbing after 10 minutes of irradiation, and after 15 minutes DRAQ-7 staining was apparent from within the cell (Figure 4.24).

The damage induced by Ru-MPP likely originated from the localised production of singlet oxygen and other ROS which efficiently damaged mtDNA to trigger cellular destruction by apoptosis. Although not addressed elsewhere in the literature, the occurrence of quenching by guanine at 37 °C, as suggested by the lifetime and FLIM data, may indicate that direct

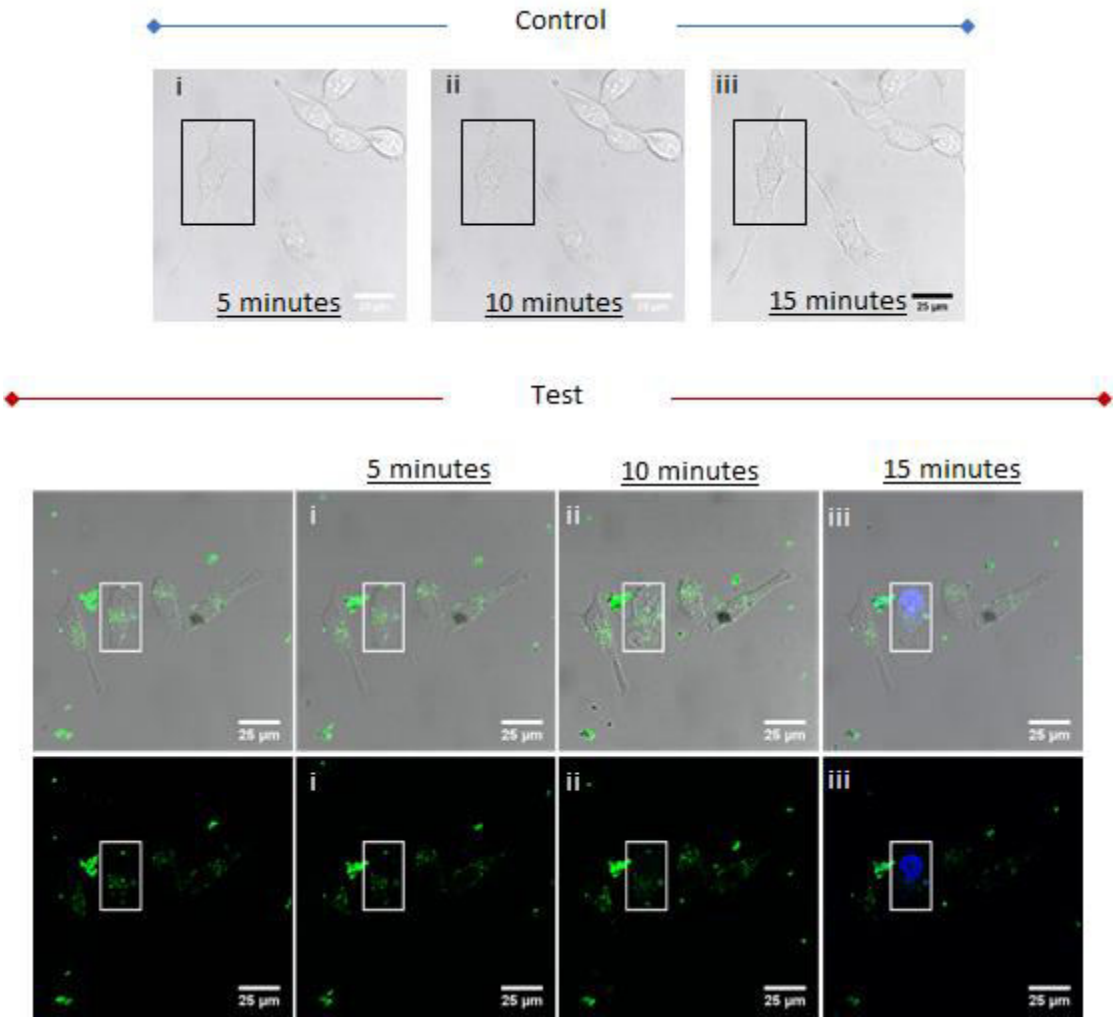

Figure 4.24: Photocytotoxicity of Ru-MPP in live HeLa cells. A cell was selected for a control or test experiment as indicated and was exposed to continuous scanning in 5 minute intervals (0.78 µW, 470 nm). Between intervals, the same cells were imaged as shown (i) – (iii), with blebbing observed in the test cell at 10 minutes and DRAQ-7 entering the test cell at 15 minutes (blue staining). Data courtesy of Dr. Aisling Byrne (DCU).

---

oxidation of guanine could also be contributing to toxicity and should be investigated further in future work. Importantly, no indicators of damage were observed to cells surrounding the test cell that also contained the same dose of Ru-MPP but were not subjected to irradiation.

Since Ru-dppz complexes are typically poor singlet oxygen generators,[87] precision-targeting evidently enhances the capability of these complexes to photo-induce cellular damage that

can be activated with spatiotemporal control. Further experiments are ongoing to explore if similar photo-damage can be induced using localised Ru-NLS.

4.3 Conclusions

This chapter demonstrates that Ru-dppz peptide conjugates can be precision targeted to the nucleus or mitochondria for light-switch imaging of DNA in live cells. The probes are non-toxic under imaging conditions but phototoxicity can be induced using higher power irradiation that leads to localised DNA damage and cellular apoptosis.

Ex-cellulo, the novel Ru-dppz parent complexes, Ru-acid and Ru-ester, exhibit light-switch luminescence like the model complex $[Ru(bpy)_2(dppz)]^{2+}$, being emissive in acetonitrile and switching off in aqueous solvent. Similarly, in the presence of DNA, absorbance hypochromicity and luminescence switch-on that was insensitive to quenching by ferrocyanide was observed; behaviour that mirrors that of $[Ru(bpy)_2(dppz)]^{2+}$ and strongly suggests DNA binding by the novel Ru-dppz probes occurs by dppz intercalation which was further supported by CD measurements. In line with studies on $[Ru(bpy)_2(dppz)]^{2+}$, the luminescence lifetime in the presence of DNA was bi-exponential and can be attributed to binding in different geometries; canted and perpendicular. The magnitudes and relative amplitudes of the short and longer-lived lifetimes suggested that peptide conjugation and the aryl-pendant of the parent complexes impacts idealised perpendicular geometry and leads to greater populations of canted geometries relative to $[Ru(bpy)_2(dppz)]^{2+}$.

The parent complexes exhibited DNA affinity on the order of $[Ru(bpy)_2(dppz)]^{2+}$ at $K_b \approx 10^6$ M^{-1} in PBS. Isomerism of Ru-acid led to binding distinction with DNA, attributable to the relative orientation of the pendant aryl carboxylate group, but this selectivity was overridden upon peptide conjugation which increases the DNA affinity by an order of magnitude relative to the parent complexes ($K_b \approx 10^7$ M^{-1}). Enhanced affinity for the cationic conjugates was shown to arise from electrostatic binding to the polyanionic backbone.

Ru-NLS and Ru-ester exhibited non-specific affinity for BSA which was studied here as a protein model. In contrast, Ru-MPP demonstrated high BSA affinity, estimated at K_b (BSA) $\approx 10^5$ M^{-1}, and ascribed to binding mediated by the Phe residues of the MPP. In studies on

related complexes, high serum albumin affinity was shown to impact cellular targeting but herein, localisation of Ru-MPP was unperturbed, and entered HeLa cells by an energy dependent mechanism at 37 °C with prompt localisation to the mitochondria. Within the mitochondrial regions, brighter Ru-MPP punctate spots were observed which exhibit dual exponential decay kinetics and is good evidence for binding of Ru-MPP to mtDNA. The ability to precision target a Ru-dppz complex to the mitochondria as demonstrated herein represents the first example of its kind for cellular imaging.

Ru-NLS selectively targets nuclear DNA in live HeLa cells, observed here by a switching on of the luminescence upon DNA binding which permitted confocal imaging with excellent contrast. The nuclear localisation of Ru-NLS was confirmed by co-localisation with DAPI and by rRaman spectroscopy which showed a spectrum characteristic of Ru-NLS in the nucleus with minimal signal observed in the cytoplasm. Under LLIM, Ru-NLS exhibited biexponential decay within the nucleus, with a longer-lived component attributed to efficient dppz ligand protection by DNA intercalation. A shorter-lived component, which was also observed for Ru-MPP, may be due to off-target binding or guanine quenching and requires further investigation in future work. Ru-NLS was also explored as part of the first study of the application of metal complex luminophores for high resolution STED imaging. Using STED, chromosomal structure was observed with remarkable clarity and permitted imaging of the different phases of cellular mitosis in high resolution using Ru-NLS.

4.4 Experimental

The instrumentation used for absorbance, emission, lifetime and circular dichroism characterisation is provided in Chapter 2. All cellular studies were carried out by Dr. Aisling Byrne (DCU).

4.5 References

(1) Hoeijmakers, J. H. J. *N. Engl. J. Med.* **2009**, *361* (15), 1475.
(2) Norbury, C. J.; Zhivotovsky, B. *Oncogene* **2004**, *23* (16), 2797.
(3) Hurley, L. H. *Nat. Rev. Cancer* **2002**, *2* (3), 188.
(4) Gavande, N. S.; VanderVere-Carozza, P. S.; Hinshaw, H. D.; Jalal, S. I.; Sears, C. R.; Pawelczak, K. S.; Turchi, J. J. *Pharmacol. Ther.* **2016**, *160*, 65.
(5) Burke, C. S.; Byrne, A.; Keyes, T. E. In *Advances in Imaging and Sensing*; CRC Press, 2016; pp 227–254.
(6) Coogan, M. P.; Fernández-Moreira, V. *Chem. Commun.* **2013**, *50* (4), 384.
(7) Lo, K. K.-W. *Inorganic and Organometallic Transition Metal Complexes with Biological Molecules and Living Cells*; Academic Press, 2016.
(8) *Photochemistry and Photophysics of Coordination Compounds II*; Balzani, V., Campagna, S., Eds.; Topics in Current Chemistry; Springer Berlin Heidelberg: Berlin, Heidelberg, 2007; Vol. 281.
(9) Knoll, J. D.; Turro, C. *Coord. Chem. Rev.* **2015**, *282–283*, 110.
(10) Dmitriev, R. I.; Papkovsky, D. B. *Cell. Mol. Life Sci.* **2012**, *69* (12), 2025.
(11) Liu, F.; Wang, K.; Bai, G.; Zhang, Y.; Gao, L. *Inorg. Chem.* **2004**, *43* (5), 1799.
(12) Li, G.; Sun, L.; Ji, L.; Chao, H. *Dalton Trans.* **2016**, *45* (34), 13261.
(13) Amouyal, E.; Homsi, A.; Chambron, J.-C.; Sauvage, J.-P. *J. Chem. Soc. Dalton Trans.* **1990**, No. 6, 1841.
(14) Friedman, A. E.; Chambron, J. C.; Sauvage, J. P.; Turro, N. J.; Barton, J. K. *J. Am. Chem. Soc.* **1990**, *112* (12), 4960.
(15) Mihailovic, A.; Vladescu, I.; McCauley, M.; Ly, E.; Williams, M. C.; Spain, E. M.; Nuñez, M. E. *Langmuir* **2006**, *22* (10), 4699.
(16) Huang, H.; Zhang, P.; Yu, B.; Chen, Y.; Wang, J.; Ji, L.; Chao, H. *J. Med. Chem.* **2014**, *57* (21), 8971.
(17) Haq, I.; Lincoln, P.; Suh, D.; Norden, B.; Chowdhry, B. Z.; Chaires, J. B. *J. Am. Chem. Soc.* **1995**, *117* (17), 4788.
(18) Friedman, A. E.; Kumar, C. V.; Turro, N. J.; Barton, J. K. *Nucleic Acids Res.* **1991**, *19* (10), 2595.
(19) Jenkins, Y.; Friedman, A. E.; Turro, N. J.; Barton, J. K. *Biochemistry (Mosc.)* **1992**, *31* (44), 10809.
(20) Turro, C.; Bossmann, S. H.; Jenkins, Y.; Barton, J. K.; Turro, N. J. *J. Am. Chem. Soc.* **1995**, *117* (35), 9026.
(21) Poynton, F. E.; Hall, J. P.; Keane, P. M.; Schwarz, C.; Sazanovich, I. V.; Towrie, M.; Gunnlaugsson, T.; Cardin, C. J.; Cardin, D. J.; Quinn, S. J.; Long, C.; Kelly, J. M. *Chem. Sci.* **2016**, *7* (5), 3075.
(22) Coates, C. G.; Olofsson, J.; Coletti, M.; McGarvey, J. J.; Önfelt, B.; Lincoln, P.; Norden, B.; Tuite, E.; Matousek, P.; Parker, A. W. *J. Phys. Chem. B* **2001**, *105* (50), 12653.
(23) Brennaman, M. K.; Meyer, T. J.; Papanikolas, J. M. *J. Phys. Chem. A* **2004**, *108* (45), 9938.
(24) Hiort, C.; Lincoln, P.; Norden, B. *J. Am. Chem. Soc.* **1993**, *115* (9), 3448.
(25) Dupureur, C. M.; Barton, J. K. *J. Am. Chem. Soc.* **1994**, *116* (22), 10286.
(26) Dupureur, C. M.; Barton, J. K. *Inorg. Chem.* **1997**, *36* (1), 33.
(27) Holmlin, R. E.; Stemp, E. D. A.; Barton, J. K. *Inorg. Chem.* **1998**, *37* (1), 29.
(28) Lincoln, P.; Broo, A.; Nordén, B. *J. Am. Chem. Soc.* **1996**, *118* (11), 2644.
(29) Tuite, E.; Lincoln, P.; Nordén, B. *J. Am. Chem. Soc.* **1997**, *119* (1), 239.
(30) McKinley, A. W.; Lincoln, P.; Tuite, E. M. *Coord. Chem. Rev.* **2011**, *255* (21–22), 2676.
(31) McKinley, A. W.; Andersson, J.; Lincoln, P.; Tuite, E. M. *Chem. – Eur. J.* **2012**, *18* (47), 15142.

(32) Andersson, J.; Fornander, L. H.; Abrahamsson, M.; Tuite, E.; Nordell, P.; Lincoln, P. *Inorg. Chem.* **2013**, *52* (2), 1151.
(33) McKinley, A. W.; Lincoln, P.; Tuite, E. M. *Dalton Trans.* **2013**, *42* (11), 4081.
(34) Niyazi, H.; Hall, J. P.; O'Sullivan, K.; Winter, G.; Sorensen, T.; Kelly, J. M.; Cardin, C. J. *Nat. Chem.* **2012**, *4* (8), 621.
(35) Hall, J. P.; Cook, D.; Morte, S. R.; McIntyre, P.; Buchner, K.; Beer, H.; Cardin, D. J.; Brazier, J. A.; Winter, G.; Kelly, J. M.; Cardin, C. J. *J. Am. Chem. Soc.* **2013**, *135* (34), 12652.
(36) Hall, J. P.; Keane, P. M.; Beer, H.; Buchner, K.; Winter, G.; Sorensen, T. L.; Cardin, D. J.; Brazier, J. A.; Cardin, C. J. *Nucleic Acids Res.* **2016**, *44* (19), 9472.
(37) Hall, J. P.; Gurung, S. P.; Henle, J.; Poidl, P.; Andersson, J.; Lincoln, P.; Winter, G.; Sorensen, T.; Cardin, D. J.; Brazier, J. A.; Cardin, C. J. *Chem. – Eur. J.* **2017**, *23* (21), 4981.
(38) Song, H.; Kaiser, J. T.; Barton, J. K. *Nat. Chem.* **2012**, *4* (8), 615.
(39) Shade, C. M.; Kennedy, R. D.; Rouge, J. L.; Rosen, M. S.; Wang, M. X.; Seo, S. E.; Clingerman, D. J.; Mirkin, C. A. *Chem. – Eur. J.* **2015**, *21* (31), 10983.
(40) Wachter, E.; Moyá, D.; Parkin, S.; Glazer, E. C. *Chem. – Eur. J.* **2016**, *22* (2), 550.
(41) Yao, J.-L.; Gao, X.; Sun, W.; Fan, X.-Z.; Shi, S.; Yao, T.-M. *Inorg. Chem.* **2012**, *51* (23), 12591.
(42) Yao, J.-L.; Gao, X.; Sun, W.; Shi, S.; Yao, T.-M. *Dalton Trans.* **2013**, *42* (16), 5661.
(43) Boynton, A. N.; Marcélis, L.; Barton, J. K. *J. Am. Chem. Soc.* **2016**, *138* (15), 5020.
(44) Walker, M. G.; Gonzalez, V.; Chekmeneva, E.; Thomas, J. A. *Angew. Chem. Int. Ed.* **2012**, *51* (48), 12107.
(45) McConnell, A. J.; Song, H.; Barton, J. K. *Inorg. Chem.* **2013**, *52* (17).
(46) Lim, M. H.; Song, H.; Olmon, E. D.; Dervan, E. E.; Barton, J. K. *Inorg. Chem.* **2009**, *48* (12), 5392.
(47) Shi, S.; Geng, X.; Zhao, J.; Yao, T.; Wang, C.; Yang, D.; Zheng, L.; Ji, L. *Biochimie* **2010**, *92* (4), 370.
(48) Moon, S. J.; Kim, J. M.; Choi, J. Y.; Kim, S. K.; Lee, J. S.; Jang, H. G. *J. Inorg. Biochem.* **2005**, *99* (5), 994.
(49) Yun, B. H.; Kim, J.-O.; Lee, B. W.; Lincoln, P.; Nordén, B.; Kim, J.-M.; Kim, S. K. *J. Phys. Chem. B* **2003**, *107* (36), 9858.
(50) Peng, M.-N.; Zhu, Z.-Y.; Tan, L.-F. *Inorg. Chem.* **2017**, *56* (13), 7312.
(51) Puckett, C. A.; Barton, J. K. *J. Am. Chem. Soc.* **2007**, *129* (1), 46.
(52) Mari, C.; Pierroz, V.; Rubbiani, R.; Patra, M.; Hess, J.; Spingler, B.; Oehninger, L.; Schur, J.; Ott, I.; Salassa, L.; Ferrari, S.; Gasser, G. *Chem. – Eur. J.* **2014**, *20* (44), 14421.
(53) Puckett, C. A.; Ernst, R. J.; Barton, J. K. *Dalton Trans.* **2010**, *39* (5), 1159.
(54) Puckett, C. A.; Barton, J. K. *Biochemistry (Mosc.)* **2008**, *47* (45), 11711.
(55) Schatzschneider, U.; Niesel, J.; Ott, I.; Gust, R.; Alborzinia, H.; Wölfl, S. *ChemMedChem* **2008**, *3* (7), 1104.
(56) Gill, M. R.; Derrat, H.; Smythe, C. G. W.; Battaglia, G.; Thomas, J. A. *ChemBioChem* **2011**, *12* (6), 877.
(57) Pierroz, V.; Joshi, T.; Leonidova, A.; Mari, C.; Schur, J.; Ott, I.; Spiccia, L.; Ferrari, S.; Gasser, G. *J. Am. Chem. Soc.* **2012**, *134* (50), 20376.
(58) Önfelt, B.; Lincoln, P.; Nordén, B. *J. Am. Chem. Soc.* **1999**, *121* (46), 10846.
(59) Önfelt, B.; Lincoln, P.; Nordén, B. *J. Am. Chem. Soc.* **2001**, *123* (16), 3630.
(60) Wilhelmsson, L. M.; Westerlund, F.; Lincoln, P.; Nordén, B. *J. Am. Chem. Soc.* **2002**, *124* (41), 12092.
(61) Nordell, P.; Lincoln, P. *J. Am. Chem. Soc.* **2005**, *127* (27), 9670.
(62) Nordell, P.; Westerlund, F.; Reymer, A.; El-Sagheer, A. H.; Brown, T.; Nordén, B.; Lincoln, P. *J. Am. Chem. Soc.* **2008**, *130* (44), 14651.
(63) Önfelt, B.; Göstring, L.; Lincoln, P.; Nordén, B.; Önfelt, A. *Mutagenesis* **2002**, *17* (4), 317.
(64) Svensson, F. R.; Matson, M.; Li, M.; Lincoln, P. *Biophys. Chem.* **2010**, *149* (3), 102.

(65) Matson, M.; Svensson, F. R.; Nordén, B.; Lincoln, P. *J. Phys. Chem. B* **2011**, *115* (7), 1706.
(66) Gill, M. R.; Garcia-Lara, J.; Foster, S. J.; Smythe, C.; Battaglia, G.; Thomas, J. A. *Nat. Chem.* **2009**, *1* (8), 662.
(67) Baggaley, E.; Gill, M. R.; Green, N. H.; Turton, D.; Sazanovich, I. V.; Botchway, S. W.; Smythe, C.; Haycock, J. W.; Weinstein, J. A.; Thomas, J. A. *Angew. Chem.* **2014**, *126* (13), 3435.
(68) Gill, M. R.; Cecchin, D.; Walker, M. G.; Mulla, R. S.; Battaglia, G.; Smythe, C.; Thomas, J. A. *Chem. Sci.* **2013**, *4* (12), 4512.
(69) Lutterman, D. A.; Chouai, A.; Liu, Y.; Sun, Y.; Stewart, C. D.; Dunbar, K. R.; Turro, C. *J. Am. Chem. Soc.* **2008**, *130* (4), 1163.
(70) Zhu, B.-Z.; Chao, X.-J.; Huang, C.-H.; Li, Y. *Chem. Sci.* **2016**, *7* (7), 4016.
(71) Kukat, C.; Wurm, C. A.; Spåhr, H.; Falkenberg, M.; Larsson, N.-G.; Jakobs, S. *Proc. Natl. Acad. Sci. U. S. A.* **2011**, *108* (33), 13534.
(72) Dolan, C.; Burke, C. S.; Byrne, A.; Keyes, T. E. In *Inorganic and Organometallic Transition Metal Complexes with Biological Molecules and Living Cells*; Lo, K. K.-W., Ed.; Academic Press, 2017; pp 55–89.
(73) Martin, A.; Byrne, A.; Burke, C. S.; Forster, R. J.; Keyes, T. E. *J. Am. Chem. Soc.* **2014**, *136* (43), 15300.
(74) Blackmore, L.; Moriarty, R.; Dolan, C.; Adamson, K.; Forster, R. J.; Devocelle, M.; Keyes, T. E. *Chem. Commun.* **2013**, *49* (26), 2658.
(75) Byrne, A.; Burke, C. S.; Keyes, T. E. *Chem. Sci.* **2016**, *7* (10), 6551.
(76) Martin, A.; Byrne, A.; Dolan, C.; Forster, R. J.; Keyes, T. E. *Chem. Commun.* **2015**.
(77) Burke, C. S.; Keyes, T. E. *RSC Adv.* **2016**, *6* (47), 40869.
(78) Puckett, C. A.; Barton, J. K. *Bioorg. Med. Chem.* **2010**, *18* (10), 3564.
(79) Puckett, C. A.; Barton, J. K. *J. Am. Chem. Soc.* **2009**, *131* (25), 8738.
(80) Boulikas, T. *J. Cell. Biochem.* **1994**, *55* (1), 32.
(81) Ragin, A. D.; Morgan, R. A.; Chmielewski, J. *Chem. Biol.* **2002**, *9* (8), 943.
(82) Jean, S. R.; Ahmed, M.; Lei, E. K.; Wisnovsky, S. P.; Kelley, S. O. *Acc. Chem. Res.* **2016**.
(83) Horton, K. L.; Stewart, K. M.; Fonseca, S. B.; Guo, Q.; Kelley, S. O. *Chem. Biol.* **2008**, *15* (4), 375.
(84) DeRosa, M. C.; Crutchley, R. J. *Coord. Chem. Rev.* **2002**, *233–234*, 351.
(85) Blazek, E. R.; Peak, J. G.; Peak, M. J. *Photochem. Photobiol.* **1989**, *49* (5), 607.
(86) Gicquel, E.; Souchard, J.-P.; Magnusson, F.; Chemaly, J.; Calsou, P.; Vicendo, P. *Photochem. Photobiol. Sci.* **2013**, *12* (8), 1517.
(87) Abreu, F. D.; Paulo, T. de F.; Gehlen, M. H.; Ando, R. A.; Lopes, L. G. F.; Gondim, A. C. S.; Vasconcelos, M. A.; Teixeira, E. H.; Sousa, E. H. S.; de Carvalho, I. M. M. *Inorg. Chem.* **2017**.
(88) Sentagne, C.; Chambron, J.-C.; Sauvage, J.-P.; Paillous, N. *J. Photochem. Photobiol. B* **1994**, *26* (2), 165.
(89) Suzuki, K.; Kobayashi, A.; Kaneko, S.; Takehira, K.; Yoshihara, T.; Ishida, H.; Shiina, Y.; Oishi, S.; Tobita, S. *Phys. Chem. Chem. Phys.* **2009**, *11* (42), 9850.
(90) Ichimura, S.; Zama, M. *Biochem. Biophys. Res. Commun.* **1972**, *49* (3), 840.
(91) Zama, M. *Biochim. Biophys. Acta BBA - Nucleic Acids Protein Synth.* **1974**, *366* (2), 124.
(92) Mann, A.; Thakur, G.; Shukla, V.; Singh, A. K.; Khanduri, R.; Naik, R.; Jiang, Y.; Kalra, N.; Dwarakanath, B. S.; Langel, U.; Ganguli, M. *Mol. Pharm.* **2011**, *8* (5), 1729.
(93) Mondal, M.; Mukherjee, S.; Bhattacharyya, D. *J. Mol. Model.* **2014**, *20* (11), 2499.
(94) Komeda, S.; Moulaei, T.; Woods, K. K.; Chikuma, M.; Farrell, N. P.; Williams, L. D. *J. Am. Chem. Soc.* **2006**, *128* (50), 16092.
(95) Komeda, S.; Moulaei, T.; Chikuma, M.; Odani, A.; Kipping, R.; Farrell, N. P.; Williams, L. D. *Nucleic Acids Res.* **2011**, *39* (1), 325.

(96) Calnan, B. J.; Tidor, B.; Biancalana, S.; Hudson, D.; Frankel, A. D. *Science* **1991**, *252* (5009), 1167.
(97) Ortmans, I.; Elias, B.; Kelly, J. M.; Moucheron, C.; Kirsch-DeMesmaeker, A. *Dalton Trans.* **2004**, No. 4, 668.
(98) Zhao, X.-L.; Li, Z.-S.; Zheng, Z.-B.; Zhang, A.-G.; Wang, K.-Z. *Dalton Trans.* **2013**, *42* (16), 5764.
(99) Pyle, A. M.; Rehmann, J. P.; Meshoyrer, R.; Kumar, C. V.; Turro, N. J.; Barton, J. K. *J. Am. Chem. Soc.* **1989**, *111* (8), 3051.
(100) Burya, S. J.; Lutterman, D. A.; Turro, C. *Chem. Commun.* **2011**, *47* (6), 1848.
(101) Carter, M. T.; Rodriguez, M.; Bard, A. J. *J. Am. Chem. Soc.* **1989**, *111* (24), 8901.
(102) Poulsen, B. C.; Estalayo-Adrián, S.; Blasco, S.; Bright, S. A.; Kelly, J. M.; Williams, D. C.; Gunnlaugsson, T. *Dalton Trans.* **2016**, *45* (45), 18208.
(103) Kalsbeck, W. A.; Thorp, H. H. *Inorg. Chem.* **1994**, *33* (15), 3427.
(104) Brunner, J.; Barton, J. K. *Biochemistry (Mosc.)* **2006**, *45* (40), 12295.
(105) Hartshorn, R. M.; Barton, J. K. *J. Am. Chem. Soc.* **1992**, *114* (15), 5919.
(106) Rodger, A. In *Encyclopedia of Analytical Chemistry*; John Wiley & Sons, Ltd, 2006.
(107) Garbett, N. C.; Ragazzon, P. A.; Chaires, J. B. *Nat. Protoc.* **2007**, *2* (12), 3166.
(108) Lyng, R.; Rodger, A.; Nordén, B. *Biopolymers* **1992**, *32* (9), 1201.
(109) Lyng, R.; Rodger, A.; Nordén, B. *Biopolymers* **1991**, *31* (14), 1709.
(110) Kypr, J.; Kejnovská, I.; Renčiuk, D.; Vorlíčková, M. *Nucleic Acids Res.* **2009**, *37* (6), 1713.
(111) Kasparkova, J.; Vrana, O.; Farrell, N.; Brabec, V. *J. Inorg. Biochem.* **2004**, *98* (10), 1560.
(112) Wragg, A.; Gill, M. R.; McKenzie, L.; Glover, C.; Mowll, R.; Weinstein, J. A.; Su, X.; Smythe, C.; Thomas, J. A. *Chem. – Eur. J.* **2015**, *21*, 11865.
(113) Sudlow, G.; Birkett, D. J.; Wade, D. N. *Mol. Pharmacol.* **1975**, *11* (6), 824.
(114) Ge, S.; Kojio, K.; Takahara, A.; Kajiyama, T. *J. Biomater. Sci. Polym. Ed.* **1998**, *9* (2), 131.
(115) Adamson, K.; Dolan, C.; Moran, N.; Forster, R. J.; Keyes, T. E. *Bioconjug. Chem.* **2014**, *25* (5), 928.
(116) Feng, L.; Geisselbrecht, Y.; Blanck, S.; Wilbuer, A.; Atilla-Gokcumen, G. E.; Filippakopoulos, P.; Kräling, K.; Celik, M. A.; Harms, K.; Maksimoska, J.; Marmorstein, R.; Frenking, G.; Knapp, S.; Essen, L.-O.; Meggers, E. *J. Am. Chem. Soc.* **2011**, *133* (15), 5976.
(117) Cook, N. P.; Torres, V.; Jain, D.; Martí, A. A. *J. Am. Chem. Soc.* **2011**, *133* (29), 11121.
(118) Gao, X.; Wang, L.; Huang, H.-L.; Wang, L.-L.; Yao, J.-L.; Shi, S.; Yao, T.-M. *Analyst* **2015**, *140* (22), 7513.
(119) He, X. M.; Carter, D. C. *Nature* **1992**, *358* (6383), 209.
(120) Majorek, K. A.; Porebski, P. J.; Dayal, A.; Zimmerman, M. D.; Jablonska, K.; Stewart, A. J.; Chruszcz, M.; Minor, W. *Mol. Immunol.* **2012**, *52* (3–4), 174.
(121) Kumar, C. V.; Buranaprapuk, A.; Sze, H. C. *Chem. Commun.* **2001**, *0* (3), 297.
(122) Kumar, C. V.; Buranaprapuk, A.; Sze, H. C.; Jockusch, S.; Turro, N. J. *Proc. Natl. Acad. Sci.* **2002**, *99* (9), 5810.
(123) Mazuryk, O.; Magiera, K.; Rys, B.; Suzenet, F.; Kieda, C.; Brindell, M. *J. Biol. Inorg. Chem.* **2014**, *19* (8), 1305.
(124) Cosgrave, L.; Devocelle, M.; Forster, R. J.; Keyes, T. E. *Chem. Commun.* **2010**, *46* (1), 103.
(125) Hell, S. W.; Wichmann, J. *Opt. Lett.* **1994**, *19* (11), 780.
(126) Hell, S. W. *Science* **2007**, *316* (5828), 1153.
(127) Coates, C. G.; Jacquet, L.; McGarvey, J. J.; Bell, S. E. J.; Al-Obaidi, A. H. R.; Kelly, J. M. *Chem. Commun.* **1996**, No. 1, 35.
(128) Basu, A.; Gafney, H. D.; Strekas, T. C. *Inorg. Chem.* **1982**, *21* (6), 2231.
(129) Byrne, A. The application of Ru(II) polypyridyl complexes to cellular imaging and sensing. PhD Thesis, Dublin City University, 2016.

Chapter 5

Nuclear-targeted Ru(II) 1,4,5,8-tetraazaphenanthrene (tap) peptide conjugates for photoinduced DNA damage in live cells

Notes

All practical cell work and electrophoresis experiments were performed by Dr. Aisling Byrne (DCU). Cell and electrophoresis data interpretation for this thesis was also carried out in collaboration with Dr. Byrne.

5.1 Introduction

5.1.1 DNA destruction by photo-activated oxygen independent mechanisms.

As outlined in Chapter 1, several transition metal complexes are effective therapeutic agents towards DNA, for example, platinum and copper based chemotherapeutics are potent 'dark-reacting' metallodrugs.[1–3] However, in these cases, poor selectivity can lead to broad cytotoxicity with detrimental side effects. Selectivity may be increased with spatial and temporal control over drug activity through photo-activation of the chemotherapeutic effect. Photoactive metal complexes of Ru(II), which typically bear long-lived and reactive ^{3}MLCT states, offer untapped potential within the phototherapy domain.

The mechanisms of DNA destruction associated with most Ru(II) photo-metallodrugs are oxygen dependant pathways such as Type II singlet oxygen sensitisation ($^1O_2$) or reactions that lead to the generation of other reactive oxygen species (ROS).[4] For example, McFarland *et al*. developed a series of intercalative pyrene-augmented Ru(II) dyads which demonstrate exceptional phototoxicity indices by sensitisation of long-lived $^3\pi\pi^*$ states that are efficient generators of singlet oxygen. These dyads were even able to induce cellular destruction of a pigmented and hypoxic metastatic melanoma line (Malme-3M) which is resistive to conventional treatments.[5–7] However, mechanisms that rely on O_2 as a reagent can be inefficient in the characteristically hypoxic environments of cancerous cells.[8–10] A pertinent oxygen-independent strategy is to induce the photo-release of DNA-toxic Ru(II)-aquo species from photoactive coordination compounds. This can be promoted using sterically strained complexes through thermal population of the dissociative ^{3}MC state following photosensitisation from the MLCT excited state.[11–18] A related approach uses photolabile ligand exchange of monodentate ligands, although $^1O_2$ production can also be sensitised by complexes of this route.[19–27] Both strategies provide potent photo-therapeutics, with fast photorelease kinetics, but such reactivity can inhibit tracking of cellular uptake and localisation, since there is a danger of off-target activation of the therapeutic.

Using a prodrug can circumvent off-target effects, for example; $[Ru(bpy)_2(dmdppz)]^{2+}$ (bpy = 2,2'-bipyridine; dmdppz = 3,6-dimethyl dipyridophenazine) only undergoes photo-release upon DNA binding and remains coordinatively stable in its absence, however other examples

of this type of control remain scarce.[12,13] It is also important to highlight that these prodrugs exhibit high photocleavage activity against plasmid DNA *in vitro*, but there are few examples of their application to live cells. Where cellular studies have been reported, it is unlikely that nuclear DNA is the therapeutic target.

An attractive oxygen independent DNA damaging reaction involves the photoactivated oxidation of guanine – the most easily oxidised DNA base.[28] Notable examples are Ru(II) complexes bearing the dppn ligand (dppn = benzo[i]-dipyrido[3,2-a:20,30-c]phenazine) which intercalate DNA and oxidise guanine under visible irradiation leading to efficient photo-cleavage of plasmid DNA.[29,30] Additionally, complexes such as $[Ru(tap)_2(bpy)]^{2+}$ that bear polyazaaromatic ligands, are excellent DNA photo-oxidisers and this particular complex was established in Chapter 1 as a candidate complex to develop towards DNA-targeted oxygen independent phototherapy. To date, this complex has not been successfully studied in the live cell and thus represents an opportunity to investigate its potential for theranosis as part of this thesis.

5.1.2 Polyazaaromatic complexes of Ru(II): unique photo-reactivity leading to covalent adducts with guanine.

Ru(II) complexes bearing at least two polyazaaromatic ligands such as tap or hat (tap = 1,4,5,8-tetraazaphenanthrene, hat = 1,4,5,8,9,12-hexaazatriphenylene, Figure 5.1) possess an excited state reduction potential sufficiently positive to oxidise DNA and yield permanent covalent photoadducts.[31–34] Complexes of the form; $[Ru(tap)_2(N\hat{}N)]^{2+}$ (N^N is tap or another polypyridyl ligand) are excellent candidates for cellular application, given the comparably easier synthesis of the tap ligand and its complexes in comparison to hat. For example, the hat ligand is synthesised via triaminotrinitrobenzene (TATB), a military grade explosive,[35,36] that is further treated under a difficult synthesis involving sodium metal reduction in liquid ammonia to provide air-sensitive hexaaminobenzene.[37] Finally, this undergoes ring-forming imine-condensation to provide a crude hat sample that requires purification by Soxhlet extraction over several days.[38] Furthermore, complexes of hat can potentially yield polynuclear assemblies which can complicate their synthesis and application.[39] In contrast,

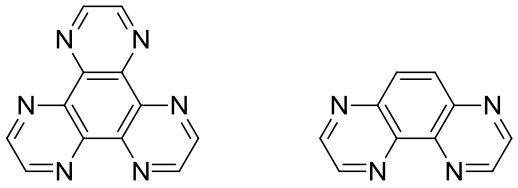

Figure 5.1: Chemical structures of hat and tap ligands.

Ru-tap complexes are mononuclear and the synthesis of tap has been reported by a few groups who have optimised its original preparation towards a more straightforward route.[40,41]

The ^{3}MLCT* states of Ru(II) tap complexes containing at least two tap ligands are powerful oxidants due to the good π-accepting character of the polyazaaromatic ligand which contains unchelated N atoms in its structure. In the homoleptic complex, $[Ru(tap)_3]^{2+}$, the excited state reduction potential is sufficiently anodic to oxidise adenine residues as well as guanine, whereas in $[Ru(tap)_2(bpy/phen)]^{2+}$ the photo-oxidation is selective for G-sites, as indicated by the emission quenching observed versus GMP and AMP for both series of compounds.[42] Extensive studies on the complexes, including pH dependence, transient absorption and isotope effect measurements, suggest that their redox chemistry with guanine involves a proton-coupled electron transfer (PCET).[42–46] The oxidation efficiency is enhanced in DNA relative to free guanine because PCET should be more exergonic in polynucleotides due to the π-stacking effect.[47] This led to the proposed guanine oxidation mechanism for $[Ru(tap)_2(bpy)]^{2+}$ as illustrated by the series of reactions in Equations 5.1 – 5.5.

The formation of photoinduced covalent adducts was indicated by gel electrophoresis (GE) using ^{32}P labelled single stranded oligonucleotides (ssODN) that were incubated with $[Ru(tap)_3]^{2+}$ and subjected to visible irradiation. A higher mobility band was observed that increased in intensity with increasing illumination time.[46] Furthermore, in the same study, dialysis experiments suggested that Ru-tap remained bound to DNA following irradiation. The photo-adduct structure was elucidated using MS and NMR following isolation of the $[Ru(tap)_2(bpy)]^{2+}$ adduct with DNA and revealed a new covalent bond formed from the 2- or 7-position of a tap ligand to the exocyclic N2-amine of guanine generating two isomers (Figure 5.2).[33] The mechanism for addition at this position was later uncovered by analysis

$$[Ru^{II}(tap)_2(bpy)]^{2+} + h\nu \rightarrow [Ru^{III}(tap^{\bullet -})(tap)(bpy)]^{2+*}$$

… Equation 5.1: Photoexcitation.

$$\{[Ru^{III}(tap^{\bullet -})(tap)(bpy)]^{2+*}\ldots G\} \rightarrow [Ru^{II}(tap^{\bullet -})(tap)(bpy)]^{+} + G^{\bullet +}$$

… Equation 5.2: PET guanine oxidation.

$$G^{\bullet +} \rightarrow G(-H)^{\bullet} + H^{+}$$

… Equation 5.3: Guanine deprotonation.

$$[Ru^{II}(tap^{\bullet -})(tap)(bpy)]^{+} + H^{+} \rightarrow [Ru^{II}(tap+H)^{\bullet}(tap)(bpy)]^{2+}$$

… Equation 5.4: PCET.

$$\{[Ru^{II}(tap+H)^{\bullet}(tap)(bpy)]^{2+}\ldots G(-H)^{\bullet}\} \rightarrow [Ru^{II}(tap\text{-}G)(tap)(bpy)]^{2+}\ (\text{photo-products})$$

… Equation 5.5: Adduct formation.

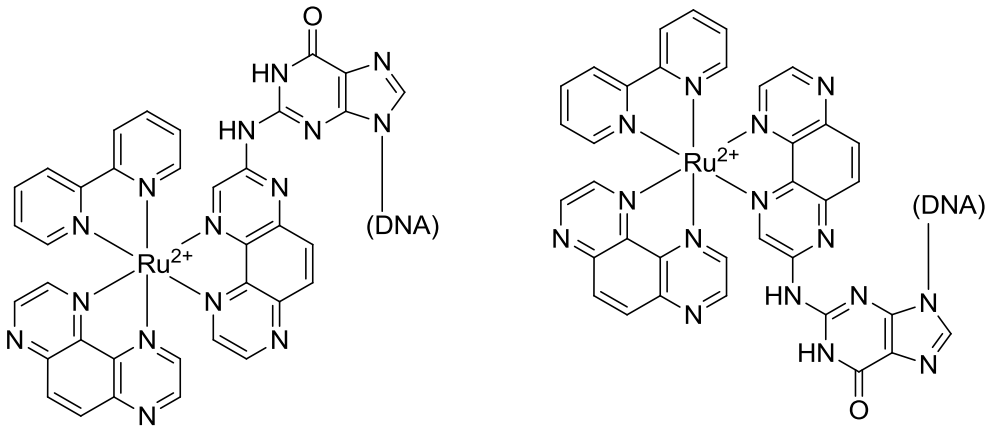

Figure 5.2: Structures of the two photoadduct isomers formed upon irradiation of $[Ru(tap)_2(bpy)]^{2+}$ with DNA leading to photoaddition across the tap C-2 or C-7 positions to the N2 of guanine residues.

of spin density data from steady-state ^1H photo-chemically induced dynamic nuclear polarization (CIDNP) experiments.[48]

$[Ru(tap)_3]^{2+}$ appears to be the most attractive candidate for cellular therapeutics within the Ru-tap series because it has the most reductive photo-excited state.[32] However, the complex exhibits some interesting photophysical behaviour that is less favourable for cellular application, for example, it has an unusually high quantum yield of dechelation in CH_3CN/Cl^-

which was found to be a result of a high rate of cross-over to the ^{3}MC state at room temperature.[49] As predicted, this does not persist in the analogue $[Os(tap)_3]^{2+}$ due to greater d-d separation, but this complex was found to be less efficient towards G-oxidation than $[Ru(tap)_2(phen)]^{2+}$.[50]

Since two coordinated tap ligands are required to render the Ru(II) complex excited state sufficiently oxidising toward guanine, the third bidentate coordination position can be utilised to incorporate an intercalative moiety to enhance DNA affinity. The binding constant for $[Ru(tap)_3]^{2+}$ is estimated to be relatively low ($K_b \approx 10^4$ M^{-1}),[42] likely due to mostly electrostatically driven interaction and only partial intercalation of the tap ligands similar to $[Ru(phen)_3]^{2+}$.[51] Accordingly, $[Ru(tap)_2(dppz)]^{2+}$ was synthesised and exhibits an affinity for DNA comparable to $[Ru(phen)_2(dppz)]^{2+}$ at $K_b \approx 10^6$ M^{-1}.[43] Unlike the latter complex, $[Ru(tap)_2(dppz)]^{2+}$ is not a molecular light-switch for DNA, consistent with the tap character of the ^{3}MLCT state that enables PET processes with guanine.[52] However, using Ru-ODN conjugates, the efficiency of formation of DNA photoadducts was shown to be decreased for the dppz complex relative to a poorly intercalating complex.[53] Similar behaviour was observed for another intercalating complex; $[Ru(tap)_2(tpac)]^{2+}$ (tpac = tetrapyridoacridine).[54] This was attributed to the notion that although PET may be efficient due to short donor-acceptor distances, back electron transfer is likely enhanced, and a complex that is not rigidly held at a binding site is free to reorganise to attain the optimum geometry to yield the covalent photoadduct.

The potential of Ru-tap complexes as cytotoxic (genome damaging) material has been widely demonstrated *in vitro*, for example, early work by Kelly *et al*. indicated enhanced plasmid cleavage efficiency of $[Ru(tap)_3]^{2+}$ relative to $[Ru(phen)_3]^{2+}$, and this was later explored using AFM and GE.[55,56] Also, $[Ru(tap)_2(phen)]^{2+}$ was found to be 2.5 times more efficient than $[Ru(bpy)_2(phen)]^{2+}$ at inhibiting the transcription activity of a bacteriophage RNA polymerase.[57] Importantly, this enhanced activity is likely due to PCET and oxidation of guanine leading to strand cleavage, since Ru-*bis/tris*-tap complexes exhibit inferior singlet oxygen quantum yields compared to their Ru-*bis/tris*-bpy/phen analogues.[58]

A major focus to date in the application of Ru-tap complexes has been their conjugation with ODNs to direct specific gene targeting of DNA through an antisense strategy.[53,59–63] Once

the ODN binds its complimentary strand, photoirradiation yields a crosslinked photo-adduct. Specificity is enhanced if the tethered ODN contains a G residue, since irradiation then leads to self-adducts (or 'seppuku' adducts) in the absence of the target, thus preventing non-specific crosslinking of Ru-tap with off-target G-residues (Figure 5.3).[60,61] The Ru-tap-ODN conjugates were developed in the context of gene therapy and have demonstrated partial success in gene silencing applications including suppression of the activity of the human papillomavirus (HPV) and cellular production of the green fluorescent protein (GFP).[64,65]

Recently, a series of $[Ru(tap)_2(N\hat{}N)]^{2+}$ complexes were reported by Poulsen *et al*. bearing extended dppz-like ligands which demonstrated cellular uptake but non-specific distribution across the cytoplasm.[66] This work built upon a previous study by Cloonan *et al*. on similar complexes and the combined work indicated photoactivatable toxicity of the Ru-tap complexes with greater phototoxicity indices in comparison to their Ru-phen analogues.[67] Elmes *et al*. used $[Ru(tap)_2(phen\text{-}R)]^{2+}$ conjugated to gold nanoparticles for cellular imaging with non-specific distribution upon uptake observed.[68] However, the Ru-tap luminescence was slightly diminished which may indicate interaction with nucleic acids, although this was not conclusively addressed.

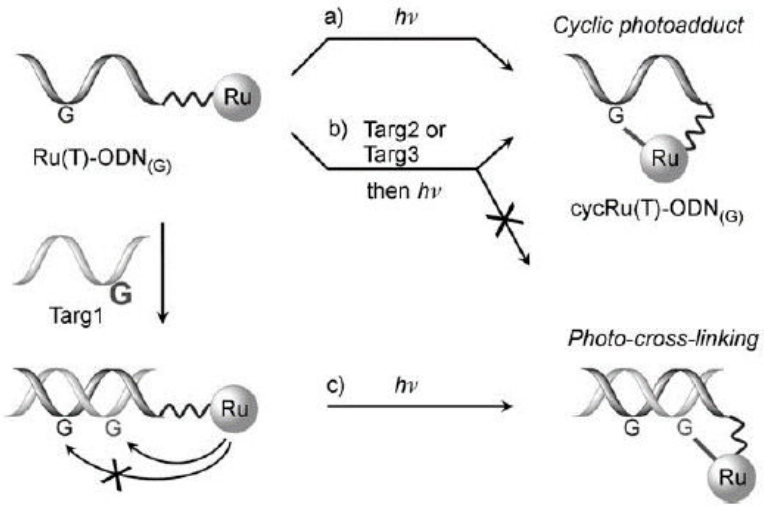

Figure 5.3: Ru-tap-ODNs containing a G residue. If the ODN is on-target, irradiation leads to a photo-crosslinked adduct (path c), but if the ODN conjugate is off-target (path a, b), a 'seppuku' self-adduct is formed. Reproduced from Le Gac *et al*.[61]

5.1.3 Exploiting the photo-reactivity of Ru-tap complexes towards peptide-directed DNA destruction in live cells.

The mechanism of photo reaction of Ru-tap complexes with DNA is unique and has not yet been successfully explored in the live cell. The oxygen independence of their DNA photoreactivity is advantageous over conventional phototherapies which rely on singlet oxygen generation as the toxic species, especially in hypoxic environments typically fostered by cancerous cells. Furthermore, the photostability of the Ru-tap complexes in the absence of reductants permits imaging of their uptake and sub-cellular localisation, thus enabling spatial and temporal control of their activation while reducing off-target activity.

This chapter is focussed on the study of Ru-tap photoreactivity in the cellular environment using precision organelle targeting signal peptide conjugates of $[Ru(tap)_2(N\hat{}N)]^{2+}$. Specifically, the nuclear localising sequence (NLS, H_2N-ahx-VQRKRQKLMP-$CONH_2$; ahx = aminohexyl linker) which was successfully exploited in Chapter 4 to drive a Ru-dppz complex to the nucleus is again utilised here. It is important to mention that a Ru-tap peptide-conjugate was reported by the Kirsch-De Mesmaeker group during this course of this work.[58] Their conjugate utilised a $[Ru(tap)_2(phen\text{-}R)]^{2+}$ core tethered via an oxime bond to (S)GRKKRRQRR – a sequence corresponding to 48 – 57 of the trans-activating transcription protein (TAT) of HIV-1. That conjugate demonstrated the characteristic photoreactivity of Ru-tap complexes, yielding photoadducts with ODNs containing guanine which highlighted that the peptide does not interfere with the action of the Ru-tap core. The conjugate was taken up efficiently into HeLa cells but, perhaps not surprisingly, was not phototoxic - due its complete exclusion from the cell nucleus. Herein, using a proven NLS peptide that can specifically deliver its Ru(II) cargo to the nucleus (as demonstrated in Chapter 4 of this thesis and elsewhere[69,70]), the ability of Ru-tap conjugates to target nuclear DNA is explored for the first time. The heteroligand in the $[Ru(tap)_2(N\hat{}N)]^{2+}$ complex can be utilised in our case for peptide conjugation, since only two coordinated tap ligands are required to achieve the desired photo-reactivity in Ru-tap complexes. Ligands suited to this purpose are; bpyArCOOR, the aryl-spaced conjugatable bpy derivative used in previous chapters of this work, and pic-COOR, a ligand continually employed by the Keyes group for its interesting pH dependant photophysics and as a conjugation site towards cellular imaging.[71–76]

5.1.4 Chapter Aims

The aims of this chapter are;

- The synthesis and structural characterisation of two series of *bis*-tap complexes; $[Ru(tap)_2(bpyArCOOR)]^{2+}$ and $[Ru(tap)_2(pic\text{-}COOR)]^{2+}$.
- Their spectroscopic and photophysical characterisation.
- Peptide-conjugation to the NLS vector and subsequent structural and photophysical characterisation of the conjugate.
- Investigation of the interaction of the conjugate and parent complexes with ctDNA, GMP and AMP to determine their propensity to selectively target and oxidise DNA at guanine residues in the dark and under illumination.
- Determination of the cleavage efficiency of the conjugates and parent structures against plasmid DNA.
- Investigation of the cellular uptake and localisation of the Ru-tap conjugates and their dark and photo- cytotoxicity.

5.2 Results and discussion

5.2.1 Synthesis and characterisation of the ligands

The synthesis of the tap ligand was accomplished using the method described originally by Nasielski-Hinkens *et al*..[41] proceeding as indicated in Scheme 5.1; from commercially available 4-nitro-orthophenylenediamine and via the intermediate 5,6-diaminoquinoxaline (diaminoquin). The synthesis of this intermediate was originally described by Case and Brennan who performed direct nitration of quinoxaline but their approach provided the diamine in poor yield and purity.[77] More recently, Elmes *et al*. adapted the Nasielski-Hinkens protocol towards a pyrazine-grafted dppz derivative (pyrazino[2,3-h]dipyrido[3,2-a:20 ,30 -c]phenazine; pdppz) and their synthesis was used as the basis of the route to tap in the present work.[40]

Specifically, 4-nitro-orthophenylenediamine was condensed with excess glyoxal in refluxing ethanol for 3 hours. The product precipitated on cooling the reaction mixture to provide 6-nitroquinoxaline (nitroquin) of acceptable purity in 75 % yield. Next, amination was accomplished at the 5-position using sodium-treated hydroxylamine hydrochloride under reflux to provide 5-amino-6-nitroquinoxaline (aminonitroquin) in 51 % yield following recrystallisation from aqueous acetic acid. ^{1}H NMR and ^{13}C NMR characterisation of nitroquin and aminoquin matched that reported by Elmes *et al*.,[40] confirming successful

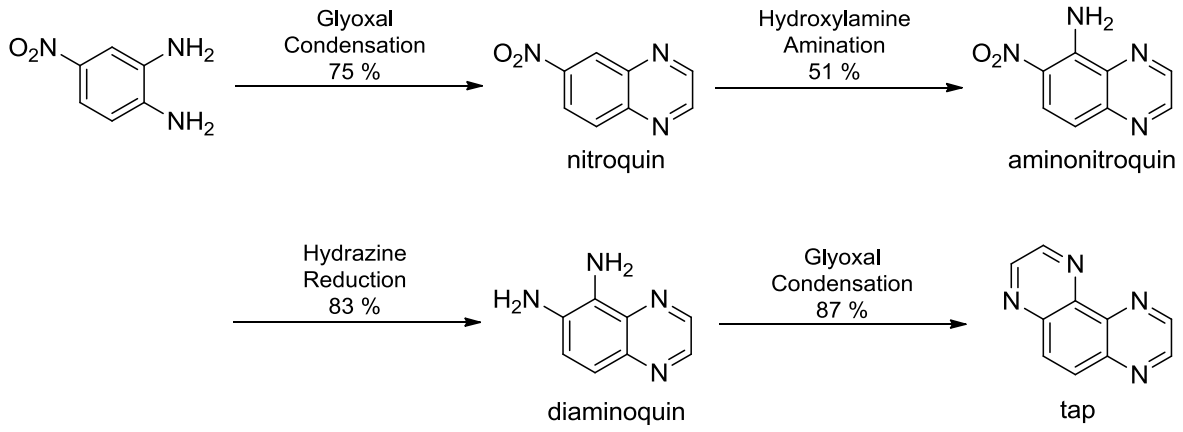

Scheme 5.1: Synthesis of tap by the route applied herein.

synthesis and purity (Appendix C). Next, reduction of the nitro substituent of aminonitroquin using hydrazine on Pd/C catalyst in refluxing ethanol afforded diaminoquin in high yield (83 %). The nitro reduction was accompanied by a decrease in the number of signals in the ^{1}H NMR spectrum due to increased symmetry of diaminoquin relative to aminonitroquin, and a broad singlet amine signal was observed at δ 5.24 ppm integrating to 4 H (Appendix C). Finally, glyoxal condensation yielded tap in 87 % yield and typically, this protocol gave tap of suitable purity but where necessary, recrystallisation from 2-propanol/hexane solutions provided the purified heterocycle as a golden solid. ^{1}H and ^{13}C NMR analysis of tap indicated; three and five signals in the aromatic region respectively, as expected for the symmetrical molecule, and COSY analysis permitted peak assignment of the proton spectrum.

The target parent Ru-tap complex in this work must include a conjugatable function to permit peptide modification. Functionalisation of a tap ligand is possible at the 9-position as described by Nasielski-Hinkens *et al*. by nitration of tosylated diaminoquin, followed by subsequent reductions or substitutions of 9-nitro-tap after the amine deprotection and condensation reactions to first afford the full tap scaffold.[78] This method was implemented by Villien *et al*. in their publication showcasing the use of oxime coupled Ru-tap-oligonucleotides,[79] but to date, there are no other notable examples of its use, probably because of the difficult multi-step synthesis.

A peptide-conjugatable terminus can instead be achieved using other ligands, since only two or more coordinated tap ligands are required in the final complex to demonstrate photo-redox activity towards DNA.[42] Indeed, $[Ru(tap)_2(N\hat{}N)]^{2+}$ (N^N is a bidentate polypyridyl ligand) complexes demonstrate enhanced photostability relative to $[Ru(tap)_3]^{2+}$, with four-fold lower quantum yields of photoactivated dechelation in degassed acetonitrile/TBAC.[49] Accordingly, the bpyArCOOH ligand used previously for the Ru-dppz series in this thesis was deemed suitable towards a photoactive Ru-tap complex; $[Ru(tap)_2(bpyArCOOH)]^{2+}$. In addition, the pic-COOH ligand was selected to develop photoactive derivatives of peptide-directed luminophores reported previously by the Keyes group.[70–74]

The pic-COOH ligand was synthesised using a protocol well-established in our lab by condensing 4-carboxybenzaldehyde with 1,10-phenathroline-5,6-dione (phendione) in a refluxing mixture of ammonium acetate and acetic acid to afford the bright yellow imidazole compound in 79 % yield. A methyl ester derivative was also synthesised using a similar methodology to provide pic-COOMe in 90 % yield, which was more straightforward and efficient than the 'on-complex' esterification previously described by Pellegrin *et al*. (Ru-pic-COOMe yield: 60 % from Ru-pic-COOH). These imidazole-forming reactions likely follow the same mechanism originally proposed by Steck and Day.[80] The pic-COOR compounds were characterised by NMR and corresponded to previous analyses within the group[81] which aided in peak assignments of the spectra, additionally corroborated by COSY NMR analysis (see Appendix C).

5.2.2 Synthesis and structural characterisation of the complexes

Complexes of the form; $[Ru(tap)_2(N\text{^}N)]^{2+}$, have generally been synthesised via the classical intermediate; $[Ru(tap)_2Cl_2]$.[82] Recently, Poulsen *et al*. reported a microwave synthesis from polymeric dichloro(1,5-cyclooctadiene)ruthenium(II) to provide the dichloride in 85 % yield.[66] However, most syntheses employ the classical Sullivan preparation from $RuCl_3.3H_2O$ in DMF/LiCl.[83] Herein, this method was attempted but unfortunately was found to be prone to the shortcomings discussed for Ru-dppz derivatives in Chapter 3 of this thesis; typically yielding impure crude material contaminated with Ru(III) and Ru-CO byproducts. Given the success in developing efficient routes towards complexes of Ru(II) via *cis*-$[Ru(DMSO)_4Cl_2]$,[84] this complex was instead installed as a viable precursor to $[Ru(tap)_2Cl_2]$.

A prominent issue encountered in the work described in Chapter 3, was 'over-reaction' to homo *tris*-chelates where the dichloride intermediate was the synthetic target. However, tap complexes appear to be a special case in this regard, with many reports indicating comparatively inefficient reactions from $[Ru(tap)_2Cl_2]$ towards $[Ru(tap)_2(N\text{^}N)]^{2+}$, even using microwave irradiation[66,68]. This stability of the dichloride was utilised herein to develop a protocol that provided $[Ru(tap)_2Cl_2]$ in > 75 % yield consistently, following simple reflux of *cis*-$[Ru(DMSO)_4Cl_2]$ and tap (2 eq.) in ethylene glycol for just 15 minutes. The product was easily isolated as a black/purple powder by pouring the cooled reaction mixture

on stirring water which permitted its facile isolation by vacuum filtration. ^{1}H NMR characterisation in DMSO-d_6 revealed a clean spectrum of 5 peaks (one of which shows coincidental equivalence) and indicates the expected *cis*-geometry of the ligands. Importantly, this analysis matches almost exactly with that reported by Poulsen *et al*.[66], thus verifying the Ru-DMSO route as an expeditious alternative to commonly used protocols. However, as is common with Ru-dichlorides, the complex was not very soluble in DMSO-d_6, leading to a low signal-to-noise ratio and broad peaks (Appendix C). Hence, ^{1}H NMR analysis was also performed in TFA-d and revealed the fully resolved set of six signals as expected with each integrating to 2 H (Appendix C).

The poor reactivity of $[Ru(tap)_2Cl_2]$ rendered it unsuited to the preparation of $[Ru(tap)_2(N\text{^}N)]^{2+}$ under classical conditions (i.e. aqueous alcoholic reflux). To circumvent this issue, others have reported the use of Ag^{+} mediated chloride cleavage to generate the substitutionally labile *bis*-aquo species; $[Ru(tap)_2(OH_2)_2]^{2+}$, which can then be reacted efficiently with a ternary polypyridyl ligand.[53,79] Herein, AgOTf (silver triflate) was exploited to yield the deep-red aquo-intermediate from $[Ru(tap)_2Cl_2]$ under simple aqueous reflux for two hours. Filtration through celite removed insoluble AgCl precipitate and residual dichloride (minimal), and subsequent rotary evaporation provided the solvate as a red sticky oil. Treatment of this residue with 1.1 equivalents of pic-COOR or bpyArCOOR in refluxing aqueous ethylene glycol yielded a solution of $[Ru(tap)_2(N\text{^}N)]^{2+}$ after 4 – 8 hours. The complexes were precipitated as their PF_6^{-} salts and filtered to provide a crude solid which could be conveniently purified by simple acetone dissolution, celite filtration and reprecipitation from diethyl ether. Where necessary, additional purification was carried out using flash chromatography on silica with $CH_3CN/H_2O/$(20 %w/v KNO_3 (aq.) or 1 M TsOH (aq.) as eluent. The final complexes were isolated as their PF_6^{-} salts in yields ranging from 76 – 86 % for the picCOOR and bpyArCOOEt complexes, while strangely, a lower yield at 57 % was obtained for $[Ru(tap)_2(bpyArCOOH)](PF_6)_2$. The water-soluble chloride form of the complexes was easily obtained from the PF_6^{-} salt using tetrabutylammonium chloride (TBAC)/acetone precipitation. The entire reaction sequence for the preparation of the four novel Ru-tap complexes is shown in Scheme 5.2.

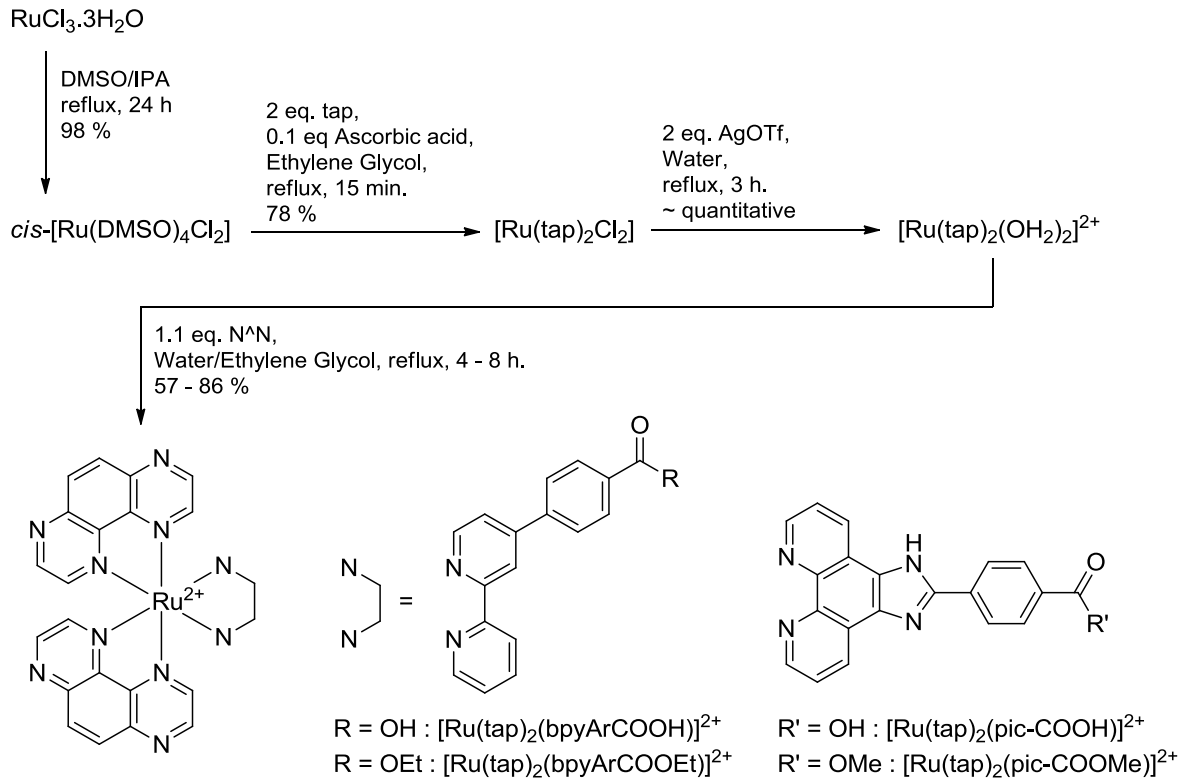

Scheme 5.2: Synthesis of the Ru-tap complexes via a Ru-DMSO precursor and silver activation of the dichloride to provide the final pic-COOR and bpyArCOOR series.

The structures of the complexes were unambiguously confirmed by NMR and HRMS. As Table 5.1 indicates, HRMS found *m/z* peaks assignable to $[M^{2+} + PF_6^-]^+$ for the bpyArCOOR complexes, whereas the pic-COOR complexes were identified as their deprotonated free complexes; $[M^{2+} - H^+]^+$ most likely due to proton loss from the imidazole moiety. Deuterium exchange also prevents detection of the imidazole-H in the pic-COOR complexes using ^1H NMR. However, a carboxylic-H was observed in the case of $[Ru(tap)_2(pic\text{-}COOH)](PF_6)_2$ at δ 12.53 ppm. Similarly, the ester complexes indicated the expected signals in the aliphatic region of the ^1H and ^{13}C NMR spectra, for example, $[Ru(tap)_2(bpyArCOOEt)](PF_6)_2$ exhibited a quartet (δ 4.38 ppm, 2 H) and triplet (δ 1.38 ppm, 3 H) in the proton spectrum and two peaks at in the carbon spectrum (δ 62.18 and 14.43 ppm) corresponding to its pendant ethyl ester.

Table 5.1 – HR-MS data for the Ru-tap complexes.

Compound	Calculated (m/z)	Found (m/z)	Assignment
$[Ru(tap)_2(bpyArCOOH)](PF_6)_2$	887.0764	887.0806	$[M^{2+} + PF_6^-]^{2+}$
$[Ru(tap)_2(bpyArCOOEt)](PF_6)_2$	915.1077	915.1121	$[M^{2+} + PF_6^-]^{2+}$
$[Ru(tap)_2(pic\text{-}COOH)](PF_6)_2$	805.1105	805.1080	$[M^{2+} - H^+]^+$
$[Ru(tap)_2(pic\text{-}COOMe)](PF_6)_2$	819.1261	819.1304	$[M^{2+} - H^+]^+$

A full assignment of the ^1H NMR spectra was possible in all cases using COSY analysis, comparison to spectra of the free ligands and published values for Ru-tap compounds[33,85]. In the case of $[Ru(tap)_2(bpyArCOOR)]^{2+}$ (see Figure 5.4 for labels), the bpyArCOOR peaks were easily assigned by finding the bpy-4' signal which exhibits cross-peaks with the bpy-3' and bpy-5' positions of the unsubstituted pyridyl ring under COSY analysis. The analogous positions on the substituted ring (bpy-3 and bpy-5) of bpyArCOOR were observed marginally downfield, probably due to delocalisation onto the aryl substituent (bf and ce). The characteristically large coordination induced shift (CIS) of the bpy-6/6' signal was also observed as it moved from being the most relatively downfield in the free ligand to being the second most relatively upfield upon coordination. Coordination renders the tap ligand inequivalent across its two halves as expected. Comparison to the data on $[Ru(tap)_2(bpy)]^{2+}$ reported by Jacquet *et al*.[33] indicates that there is a larger ring current anisotropic shielding experienced by ligand substituents *cis*-tap than *cis*-bpy, and by extension, it can be assumed that a similar effect is operative for $[Ru(tap)_2(bpyArCOOR)]^{2+}$. Accordingly, the tap positions; 2 and 3 (adjacent to bpy) were assigned to the signals less shielded and downfield relative to tap-6 and tap-7 (adjacent to tap), while tap-9 and tap-10 remain coincidentally equivalent due to their position at the periphery of the complex and outside the proximity of the effect. Interestingly, this assignment is supported further by the inequivalence of tap-3 and tap-3', which arises due to the asymmetry across bpyArCOOR. Assuming extended aromaticity on the substituted side of bpyArCOOR leads to an enhanced anisotropic shielding effect, the 3' position was assigned as the signal most relatively upfield in the 3/3' pair. Notably, this assignment leads to almost exactly to the same chemical shifts reported for

$[Ru(tap)_2(bpy)]^{2+}$ at the positions; tap-6, tap-7, tap-2 and tap-3, protons which are in a similar environment in $[Ru(tap)_2(bpyArCOOR)]^{2+}$.[33] The ^1H NMR spectrum of the acid complex mirrored that of the ester and was assigned accordingly (Figure 5.4 and Table 5.2).

A similar analysis was applied to the ^1H NMR spectra of $[Ru(tap)_2(pic\text{-}COOR)]^{2+}$ (Figure 5.5). At first glance, the spectrum is much simpler compared to the bpyArCOOR analogue, due to the greater symmetry in the pic-COOR case. The pic-COOR signals were assigned using COSY and comparison to the NMR data for similar pic-COOR complexes synthesised in our lab.[81] The spectrum exhibits the expected pic-2/9 peak upfield relative to the free ligand due to CIS. The pic-4/7 peak is furthest downfield, the pic-3/8 peak is furthest upfield and the aryl moiety of pic-COOR remains relatively unchanged in comparison to the free ligand, with the pic-b/f positions assigned downfield to pic-c/e because of imidazole deshielding. In comparison to $[Ru(tap)_2(bpyArCOOR)]^{2+}$, the pic-COOR spectra indicate

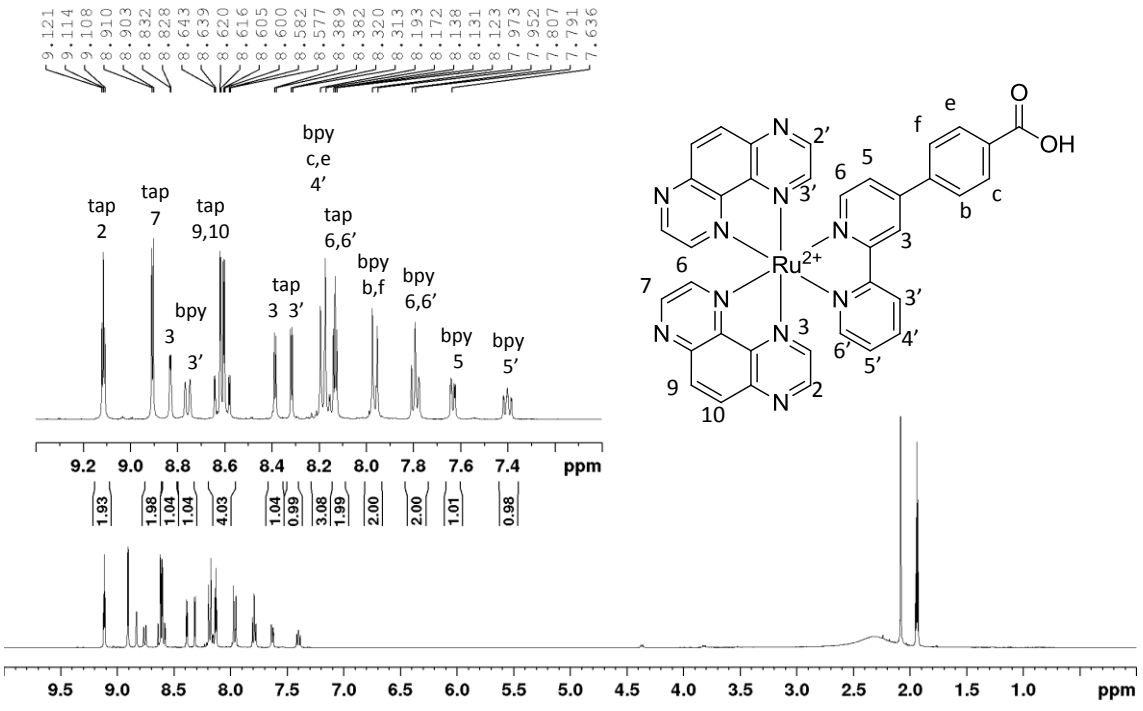

Figure 5.4: ^1H NMR (400 MHz, CD_3CN) spectrum of $[Ru(tap)_2(bpyArCOOH)](PF_6)_2$ with insets to show chemical structure and peak assignments. Peaks at 2.08 and 2.13 ppm assigned to residual acetone and water respectively.

less of an anisotropic shielding effect with decreased resolution of the tap-6/tap-3 and tap-2/tap-7 signals (< 0.1 ppm versus > 0.2 ppm in the bpyArCOOR case). To distinguish the tap-6/7 and tap-3/2 signals, it can be assumed that the ring current on tap leads to a greater shielding effect than pic-COOR where electron delocalisation is greater. A similar effect has been reported by others where phen imparts greater shielding than hat or dppz.[85,86] If this effect holds true in the pic-COOR case, a tentative assignment can be made where the tap-3/2 signals are placed more downfield than tap-6/7. The full ^{1}H NMR assignment is illustrated in Figure 5.5 (and Table 5.2).

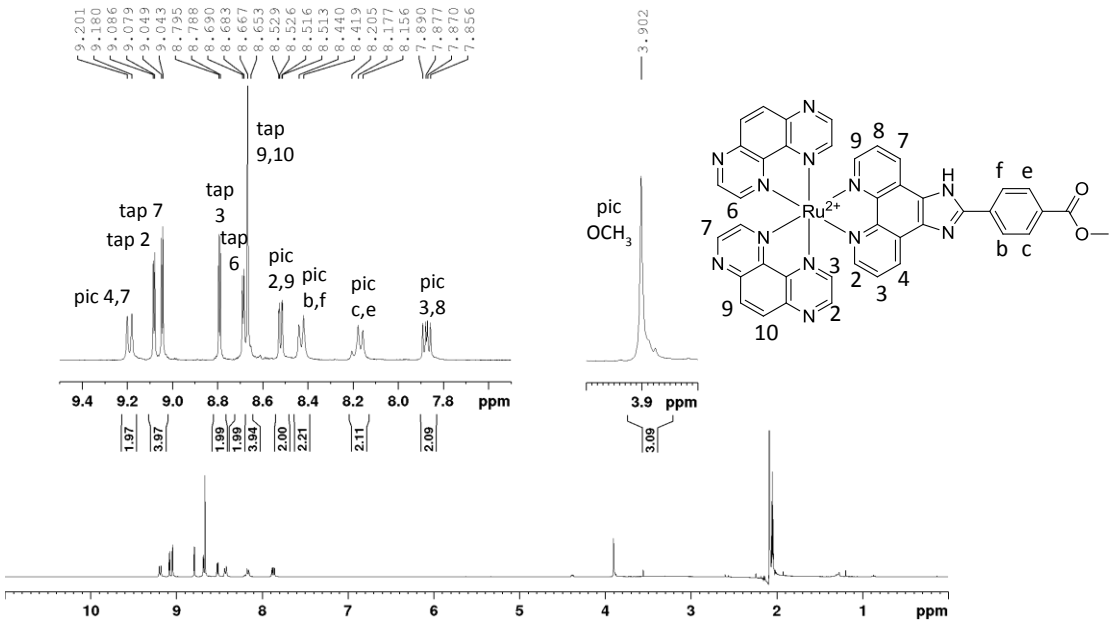

Figure 5.5: ^{1}H NMR (400 MHz, acetone-d_6) spectrum of $[Ru(tap)_2(pic\text{-}COOMe)](PF_6)_2$ with insets to show chemical structure and peak assignments.

Table 5.2 – ^{1}H NMR shifts for the Ru(tap)$_2$(L) complexes with corresponding ligand values listed for reference.

Compound	**Solvent, Field Frequency**	**^{1}H NMR Shifts δ (ppm) (multiplicity, nH) *[structural assignment]***
tap	$CDCl_3$, 400 MHz	9.14 (d, 2 H) *[3,6]*; 9.08 (d, 2 H) *[2,7]*; 8.33 (s, 2 H) *[9,10]*.
pic-COOMe	DMSO-d_6, 400 MHz	9.00 (dd, 2 H) *[2,9]*; 8.89 (dd, 2 H) *[4,7]*; 8.38 (d, 2 H) *[b,f]*; 8.09 (d, 2 H) *[c,e]*; 7.79 (dd, 2 H) *[3,8]*; 3.87 (s, 3 H) *[OCH_3]*.
pic-COOH	DMSO-d_6, 400 MHz	13.95 (s, 1 H) *[NH]*; 12.71 (s broad, 1 H) *[COOH]*; 9.04 (dd, 2 H) *[2,9]*; 8.93 (dd, 2 H) *[4,7]*; 8.39 (d, 2 H) *[b,f]*; 8.17 (d, 2 H) *[c,e];* 7.84 (d, 2 H) *[3,8]*.
bpyArCOOEt	$CDCl_3$, 600 MHz	8.69 (d, 1 H) *[6]*; 8.64 (d, 1 H) *[6']*; 8.63 (s, 1 H) *[3]*; 8.39 (d, 1 H) *[3']*; 8.10 (d, 2 H) *[e,c]*; 7.77 (m, 3 H) *[4',b,f]*; 7.49 (dd, 1 H) *[5]*; 7.28 (dd, 1 H) *[5']*; 4.35 (q, 2 H) *[OEt I]*; 1.36 (t, 3 H) *[OEt II]*.
bpyArCOOH	DMSO-d_6, 600 MHz	13.24 (s, 1 H) *[COOH]*; 8.92 (m, 2 H) *[6,3]*; 8.89 (d, 1 H) *[6']*; 8.71 (d, 1 H) *[3']*; 8.28 (t, 1 H) *[4']*; 8.17 (q, 4 H) *[b,c,e,f]*; 8.07 (d, 1 H) *[5]*; 7.76 (t, 1 H) *[5']*.
Ru(tap)$_2$(pic-COOMe)	Acetone-d_6, 400 MHz	9.19 (d, 2 H) *[H_{pic}-4,7]*; 9.06 (dd, 4 H) *[H_{tap}-7,2]*; 8.79 (d, 2 H) *[H_{tap}-3]*; 8.69 (d, 2 H) *[H_{tap}-6]*; 8.67 (s, 4 H) *[H_{tap}-9,10]*; 8.52 (dd, 2 H) *[H_{pic}-2,9]*; 8.43 (d, 2 H) *[H_{pic}-b,f]*; 8.18 (t, 2 H) *[H_{pic}-c,e]*; 7.87 (dd, 2 H) *[H_{pic}-3,8]*; 3.90 (s, 3 H) *[H_{pic}-OCH_3]*.
Ru(tap)$_2$(pic-COOH)	MeCN-d_3, 400 MHz	12.53 (s, 1 H) *[H_{pic}-COOH]*; 9.06 (d, 2 H) *[H_{pic}-4,7]*; 8.96 (dd, 4 H) *[H_{tap}-7,2]*; 8.61 (s, 4 H) *[H_{tap}-9,10]*; 8.26 (m, 4 H) *[H_{tap}-3, ; H_{pic}-b,f]*; 8.23 (d, 2 H) *[H_{tap}-6]*; 8.07 (dd, 2 H) *[H_{pic}-2,9]*; 8.02 (d, 2 H) *[H_{pic}-c,e]*; 7.75 (dd, 2 H) *[H_{pic}-3,8]*.
Ru(tap)$_2$(bpyArCOOEt)	MeCN-d_3, 400 MHz	9.11 (t, 2 H) *[H_{tap}-2]*; 8.91 (d, 2 H) *[H_{tap}-7]*; 8.82 (d, 1 H) *[H_{bpy}-3]*; 8.75 (d, 1 H) *[H_{bpy}-3']*; 8.61 (qd, 4 H) *[H_{tap}-9,10]*; 8.39 (d, 1 H) *[H_{tap}-3]*; 8.31 (d, 1 H) *[H_{tap}-3']*; 8.18 (m, 3 H) *[H_{bpy}-c,e,4']*; 8.13 (t, 2 H) *[H_{tap}-6]*; 7.97 (d, 2 H) *[H_{bpy}-b,f]*; 7.79 (t, 2 H) *[H_{bpy}-6,6']*; 7.63 (t, 2 H) *[H_{bpy}-5]*; 7.40 (t, 1 H)) *[H_{bpy}-5']*; 4.38 (q, 2 H) *[H_{bpy}-OEt I];* 1.38 (t, 3 H) *[H_{bpy}-OEt II]*.
Ru(tap)$_2$(bpyArCOOH)	MeCN-d_3, 400 MHz	9.11 (t, 2 H) *[H_{tap}-2]*; 8.91 (d, 2 H) *[H_{tap}-7]*; 8.83 (d, 1 H) *[H_{bpy}-3]*; 8.76 (d, 1 H) *[H_{bpy}-3']*; 8.61 (qd, 4 H) *[H_{tap}-9,10]*; 8.38 (d, 1 H) *[H_{tap}-3]*; 8.31 (d, 1 H) *[H_{tap}-3']*; 8.18 (m, 3 H) *[H_{bpy}-c,e,4']*; 8.13 (t, 2 H) *[H_{tap}-6,6']*; 7.96 (d, 2 H) *[H_{bpy}-b,f]*; 7.78 (t, 2 H) *[H_{bpy}-6,6']*; 7.63 (dd, 1 H) *[H_{bpy}-5]*; 7.40 (td, 1 H) *[H_{bpy}-5']*.

5.2.3 Photophysics of parent complexes

The absorbance and emission properties of the Ru-tap complexes in acetonitrile, water and PBS buffer pH 7.4 (hereafter PBS) are provided in Table 5.3 and Figures 5.6 and 5.7. The absorbance spectra exhibited the expected bpy and tap based ligand-centred (LC) transitions at $\lambda < 300$ nm. A shoulder at $\lambda \approx 315$ nm was evident in the pic-COOR spectra assignable to pic-COOR LC transitions. This band was red shifted relative to that of bpy and tap due to the extended pi-system of the planar ligand.[76] Broad visible absorptions in the blue-green region of the spectra were observed in both series and attributed to the characteristic metal-to-ligand charge transfer (MLCT) transition typical of Ru(II) polypyridyl complexes. The band displays two maxima, the most bathochromic of which is probably due to a MLCT of largely Ru→tap character given the similarity between the bpyArCOOR and pic-COOR spectra, and that of other published heteroleptic Ru-tap complexes.[87]

The emission spectra of both series were also comparable, and in all solvents, were strongly Stokes-shifted to the order of about 170 – 180 nm, consistent with emission from a tap based ^{3}MLCT* state. In acetonitrile, the emission maxima occurred at $\lambda = 623$ - 629 nm, but were red-shifted (*ca*. 10 nm) in aqueous solvent with the emission intensity reduced by at least 30 %. This behaviour is expected given the stabilisation of the CT excited state in more polar solvents. Excitation spectra in all solvents mirrored the MLCT absorbance bands. Quantum yields, measured in aerated solutions using $[Ru(bpy)_3]^{2+}$ as a standard,[88] were determined to be about 4 – 5 % in acetonitrile and 3 % in water, in line with trends observed for the emission spectra.

Luminescence lifetimes collected from TCSPC experiments fitted well to single exponential decays. Goodness of fit was confirmed by visual inspection of the residuals and tail-fit criteria of $0.9 < \chi^2 < 1.1$. In acetonitrile, aerated lifetimes are comparable across both the $[Ru(tap)_2(pic\text{-}R)]^{2+}$ and $[Ru(tap)_2(bpyArCOOR)]^{2+}$ series at $\tau \approx 730$ ns, and all complexes exhibit notable oxygen sensitivity, with a two-fold increase in lifetime upon de-aeration under N_2 purge. Consistent with emission intensity in water, the lifetimes in water are decreased in all cases relative to acetonitrile, but demonstrate more modest sensitivity towards oxygen (*ca*. 20 % increase). Generally, lifetimes in water are slightly longer-lived

for the pic-COOR series ($\tau_{av} \approx 660$ ns) in comparison to that of bpyArCOOR ($\tau_{av} \approx 590$ ns). This photophysical behaviour reflects that reported for $[Ru(tap)_2(bpy/phen)]^{2+}$.[87]

In PBS, the lifetimes exhibited some unusual behaviour in the pic-COOR case. For $[Ru(tap)_2(bpyArCOOR)]^{2+}$, the lifetime remained mono-exponential and was only marginally reduced relative to water. However, for $[Ru(tap)_2(pic\text{-}COOR)]^{2+}$, the lifetime data conformed to a dual exponential decay, with a long component of $\tau \approx 440$ ns contributing *ca*. 15 % of the luminescence (based on relative amplitude), and a shorter component recorded at $\tau \approx 200$ ns contributing the rest. This behaviour was independent of oxygen with no significant changes observed upon de-aeration under N_2 purge. Kirsch-De Mesmaeker *et al*. reported quenching of $[Ru(tap)_2(bpy)]^{2+}$ in buffers containing carboxylic acids due to hydrogen bond formation with the unchelated N-atoms of tap, but importantly, this was not observed in phosphate buffer.[82] Also, since the quenching was not observed in the bpyArCOOR series, ionisation of the pic-COOR ligand is likely responsible because of its imidazole function.

The pH dependent photophysics of a related pic complex, $[Ru(bpy)_2(pic\text{-}COOR)]^{2+}$, was reported previously by our group where pKa and pKa* were determined in the range 8 – 9 and deprotonation of the imidazole led to luminescence quenching.[76,81] Conversely, herein, a decrease in the average lifetime was observed with decreasing pH for $[Ru(tap)_2(pic\text{-}COOMe)]^{2+}$ which perhaps indicates the impact of the strong π-accepting ability of the coordinated tap ligands on the pKa of the pic-imidazole. Single exponential decay kinetics were observed at higher pH (Table 5.3, H_2O measured at pH 8.6) and the lifetime was extended compared to PBS buffer (pH 7.4). In contrast, at a decreased pH = 4.0, the luminescence lifetime of $[Ru(tap)_2(pic\text{-}COOMe)]^{2+}$ conformed to a dual exponential decay like that observed in PBS buffer (pH 7.4), but with a large increase in the relative amplitude of the short component (98 %) which was significantly shorter-lived at $\tau = 35$ ns (relative to PBS pH 7.4; 183 ± 6 (86 %)). The longer component of the decay at pH 4.0 was determined at $\tau = 316 \pm 27$ ns (2 %) which was also reduced relative to pH 7.4 (443 ± 59 (14 %)). Further experiments are necessary in future studies to elucidate the origin of this behaviour since it may have interesting applications for intracellular pH sensing within a bio-relevant pH range.

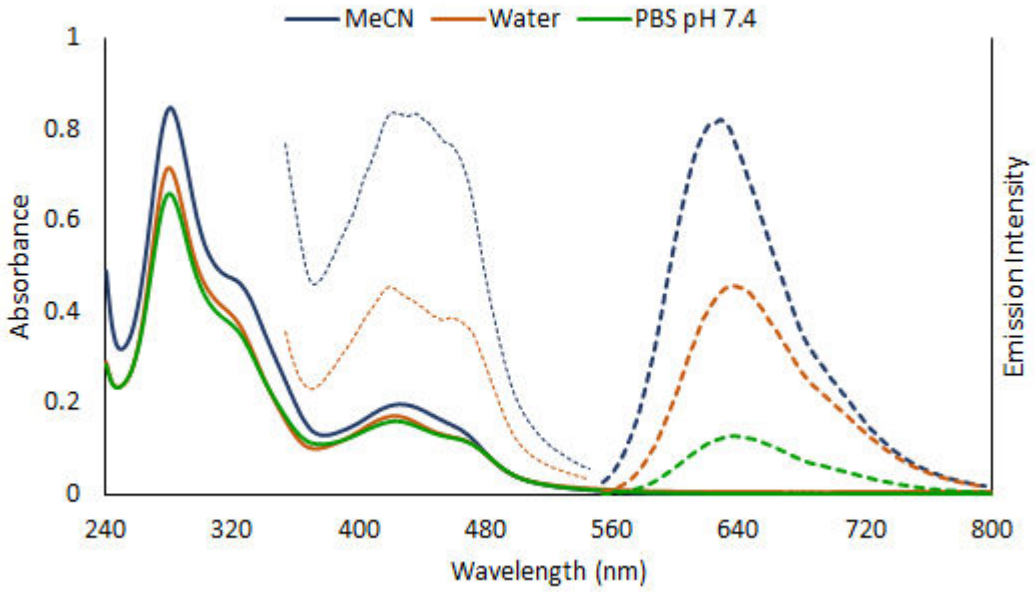

Figure 5.6: Absorbance (solid traces), emission and excitation spectra (dashed traces) of $[Ru(tap)_2(pic\text{-}COOMe)]^{2+}$ measured at 10 μM in acetonitrile, water, and PBS pH 7.4 as indicated. Emission slits were set to 10 nm and excitations were performed at λ_{max} (vis).

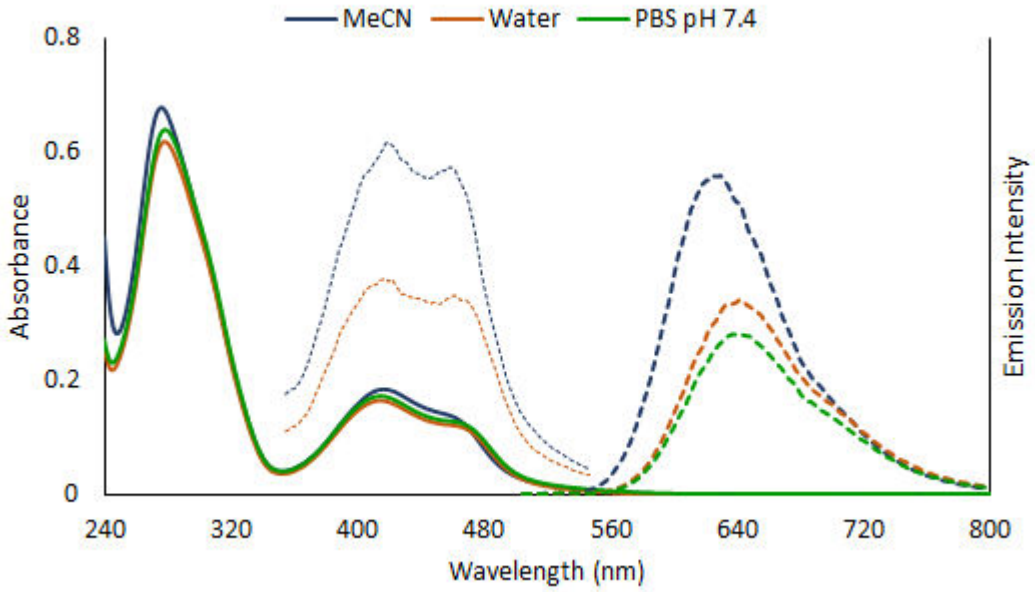

Figure 5.7: Absorbance (solid traces), emission and excitation spectra (dashed traces) of $[Ru(tap)_2(bpyArCOOEt)]^{2+}$ measured at 10 μM in acetonitrile, water, and PBS pH 7.4 as indicated. Emission slits were set to 10 nm and excitations were performed at λ_{max} (vis).

Table 5.3: Summary of photophysical data for the Ru-tap complexes.

Compound	**Solvent**[a]	**λ_{abs} (ε)**[b] nm ($x10^3$ M^{-1} cm^{-1})	**λ_{em}** nm	**τ_{lum}**[c] ns		**ϕ_{lum}**[d]
				Aerated	Deaerated	
$[Ru(tap)_2(pic\text{-}COOH)]^{2+}$	MeCN	281 (85.6), 424 (20.1), 458 (15.2).	623	760 ± 4	1533 ± 92	0.050
	H_2O	279 (76.9), 423 (18.0), 461 (13.1).	638	653 ± 2	824 ± 9	0.033
	PBS	279 (69.8), 424 (17.5), 461 (13.3).	638	201 ± 5 (81 %) 443 ± 30 (19 %)	225 ± 1 (84 %) 473 ± 21 (16 %)	
$[Ru(tap)_2(pic\text{-}COOMe)]^{2+}$	MeCN	281 (85.1), 317 (47.9), 425 (19.7), 459 (15.1).	625	720 ± 7.6	1436 ± 154	0.043
	H_2O *(pH 8.6)*	279 (71.2), 315 (39.9), 422 (17.2), 460 (12.4).	637	663 ± 3	871 ± 15	0.033
	H_2O *(pH 4.0)*			35 ± 1 (98 %) 316 ± 27 (2 %)		
	PBS *(pH 7.4)*	280 (66.1), 314 (38.8), 423 (16.1), 459 (12.0).	638	183 ± 6 (86 %) 443 ± 59 (14 %)	190 ± 3 (87 %) 440 ± 24 (13 %)	
$[Ru(tap)_2(bpyArCOOH)]^{2+}$	MeCN	277 (61.1), 417 (18.0), 455 (13.9).	627	746 ± 14	1352 ± 9	0.039
	H_2O	279 (60.4), 415 (17.2), 460 (13.0).	639	572 ± 3	705 ± 3	0.028
	PBS	280 (59.1), 415 (16.8), 460 (12.7).	639	502 ± 2	560 ± 10	
$[Ru(tap)_2(bpyArCOOEt)]^{2+}$	MeCN	276 (67.9), 416 (18.1), 456 (14.0).	629	680 ± 9	1332 ± 62	0.041
	H_2O	279 (61.9), 415 (16.7), 459 (12.5).	639	607 ± 7	753 ± 8	0.029
	PBS	278 (61.3), 414 (17.3), 459 (13.1).	639	515 ± 1	594 ± 9	

Notes: [a] PBS = commercial Dulbecco's Phosphate Buffered Saline without modifiers, measured at pH 7.4. H_2O was measured at pH 8.6. [b] ε was averaged from triplicate analyses. Relative standard deviations (not shown) were typically < 5 %. [c] 450 nm excitation, data fit to tailfit criteria; $0.9 < \chi^2 < 1.1$. De-aeration by N_2 purge for 15 minutes. Averaged data is shown ± SD (n = 3). For bi-exponential fitting, % relative amplitude values are provided in parentheses. [d] Quantum yields were averaged from triplicate measurements in aerated solutions using the slope method (see Chapter 2, estimated error ± 10 %) and $[Ru(bpy)_3]^{2+}$ as a reference standard (ϕ(air) = 0.018 (MeCN); 0.040 (H_2O)[88]).

5.2.4 Synthesis of the Ru-tap-NLS conjugate

Given the evident ionisation of pic derivatives at physiological pH, to simplify the study, it was decided to focus on the bpyArCOOR series for peptide conjugation and biostudies. It is anticipated that the pic-COOR series will be revisited in future work to investigate these aspects further, but the focus of this chapter will shift exclusively to the bpyArCOOR series.

Peptide conjugation to the nuclear localising signal sequence (NLS: H_2N-ahx-VQRKRQKLMP-$CONH_2$), exploited in early chapters of this thesis, was accomplished using the protocol described in Chapter 3. Typically, $[Ru(tap)_2(bpyArCOOH)]^{2+}$ was stirred overnight in DMF in the presence of two equivalents of peptide, PyBOP (4 equivalents) and DIPEA as base. This generally yielded pure conjugate but further purification where necessary was performed on C18-silica pTLC plates followed by precipitation of the eluate from TBAC/acetone solutions to provide Ru-tap-NLS (Figure 5.8) as the chloride salt. HRMS confirmed successful synthesis of the conjugate finding peaks corresponding to $[M]^{3+}$ and $[M]^{6+}$ at *ca. m/z* = 707 and 354 respectively as indicated in Table 5.4 and Figure 5.10. ^{1}H NMR of Ru-tap-NLS indicated mono-conjugation upon integration with the ratio of ligand signals in the aromatic region (e.g. tap, δ 9.13 – 9.21, 2 H) to the alpha-H region (δ 3.87 – 4.46 ppm, 10 H) indicating the ten amino acids expected for the NLS sequence (Figure 5.9). Furthermore, other peptide signals in the aliphatic region are comparable to the NLS conjugates synthesised as part of the work contained in Chapter 3. HPLC analysis of Ru-tap-NLS under reverse phase chromatography confirmed purity with the conjugate eluting at 11.2 minutes and no parent peak observed at its characteristic retention time of 14 minutes (Figure 5.11).

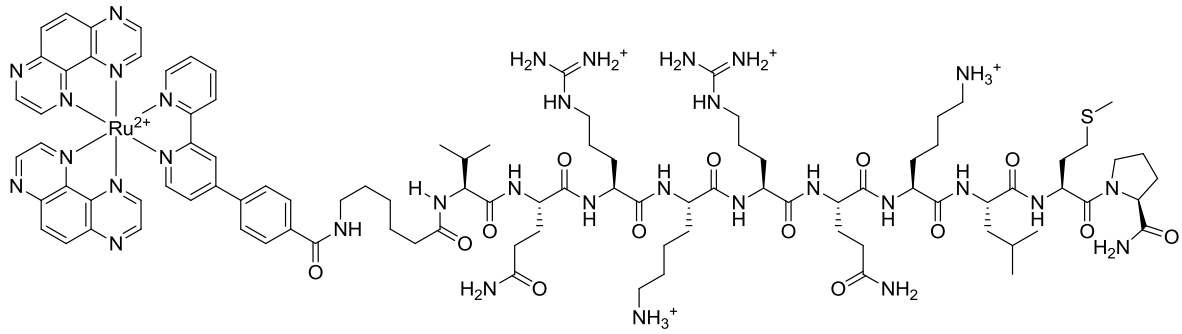

Figure 5.8: Chemical structure of Ru-tap-NLS.

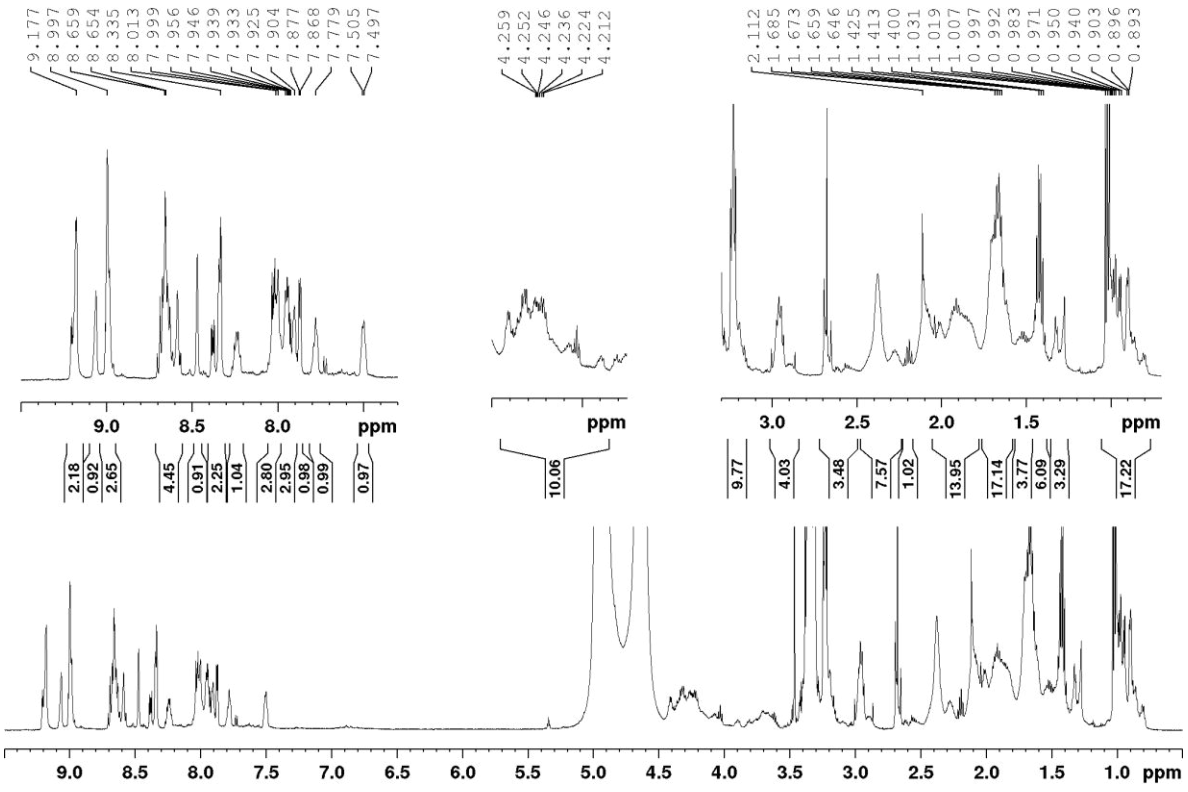

Figure 5.9: ^{1}H NMR (600 MHz, CD_3OD/D_2O) of Ru-tap-NLS with insets to show regions of interest

Table 5.4: HR-MS data for the Ru-tap-NLS.

	Calculated (m/z)	Found (m/z)	Assignment
Ru-tap-NLS	353.9999	353.7231	$[M]^{6+}$
	706.9925	706.4377	$[M]^{3+}$

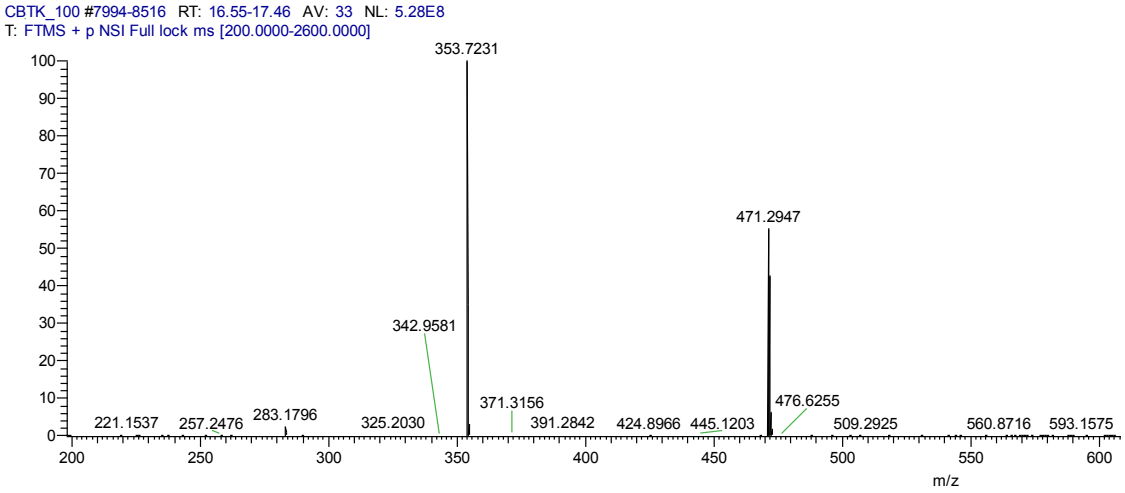

Figure 5.10: HRMS (Q-Exactive, MS+) spectrum of Ru-tap-NLS indicating $[M]^{+3}$ and $[M]^{+6}$ peaks.

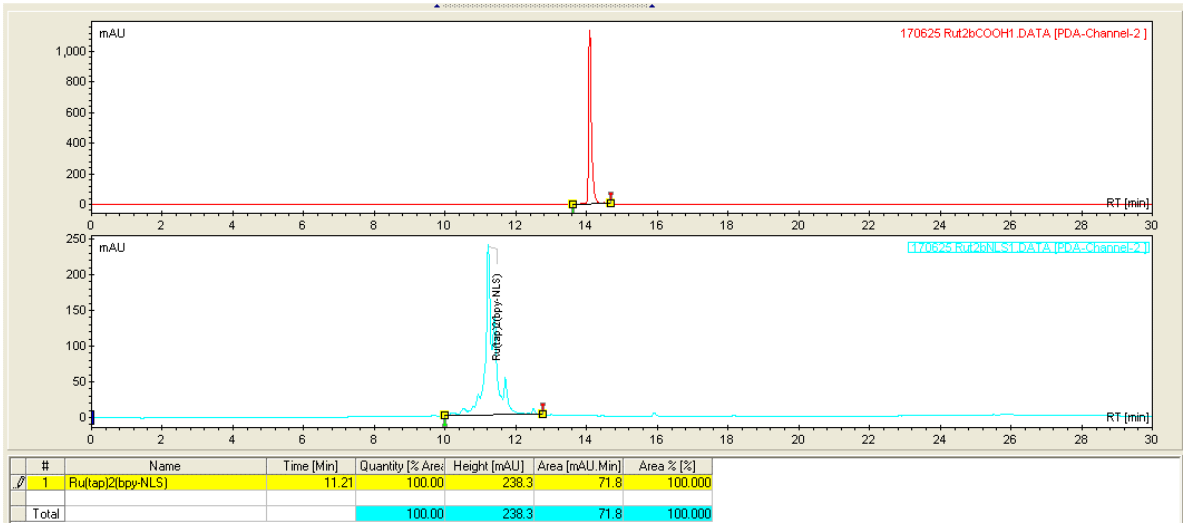

Figure 5.11: HPLC chromatograms for Ru-tap-NLS and parent reveals relative purity of the conjugate. HPLC conditions: C18-silica column, 0.1 % TFA in CH_3CN/H_2O gradient.

5.2.5 Photophysical characterisation of the Ru-tap-NLS conjugate.

The photophysical characteristics of the NLS conjugate are comparable to $[Ru(tap)_2(bpyArCOOEt)]^{2+}$ (hereafter Ru-tap-ester) as indicated in Table 5.5 and Figure 5.12. The NLS conjugate absorbance spectra in acetonitrile, water and PBS exhibited the LC and MLCT bands identical to those in Ru-tap-ester, and the emission maxima were also comparable, measured for Ru-tap-NLS at $\lambda = 631$ nm in acetonitrile and $\lambda = 640$ nm in water. The quantum yield determined at 2.8 % in water was also unchanged within error upon peptide conjugation, measured using the slope method versus $[Ru(bpy)_3]^{2+}$. In aerated aqueous solvent, the lifetime was moderately longer lived (60 – 90 ns), possibly due some protection afforded to the emission centre from O_2 quenching by the pendant peptide. A similar effect was observed by Kirsch-De Mesmaeker and co-workers; their TAT-derived peptide conjugate of $[Ru(tap)_2(phen)]^{2+}$ was longer lived than the parent compound by about 70 ns on average in aerated buffer.[58] In any case, the oxygen sensitivity of Ru-tap-NLS was moderate, with *ca*. 15 % increase in luminescence lifetime observed upon N_2 purge, comparable to deaerated values for Ru-tap-ester.

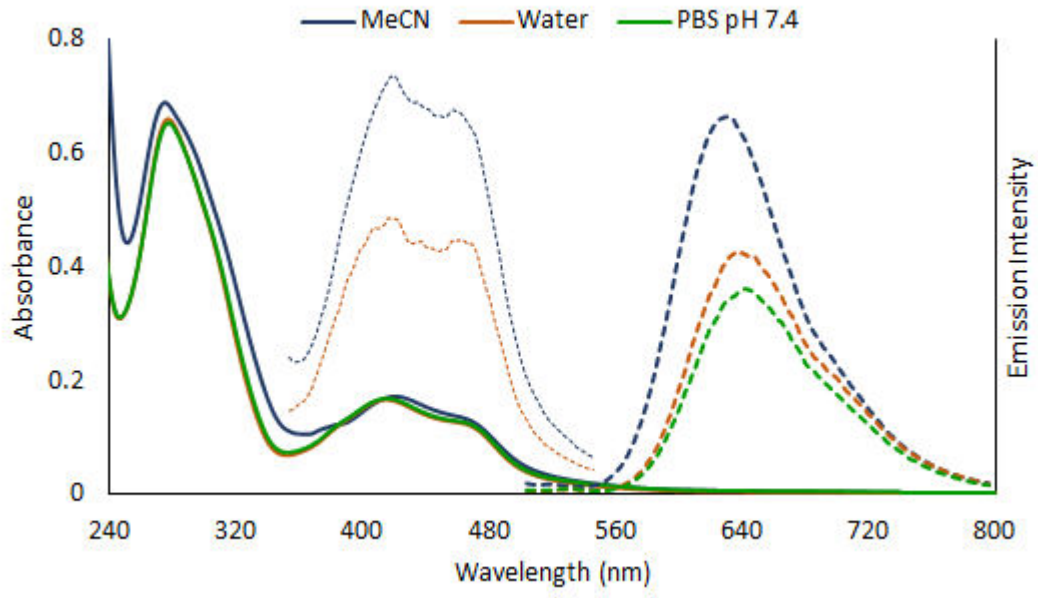

Figure 5.12: Absorbance (solid traces), emission and excitation spectra (dashed traces) of Ru-tap-NLS measured at 10 μM in acetonitrile, water, and PBS pH 7.4 as indicated. Emission slits were set to 10 nm and excitations were performed at λ_{max} (vis).

Table 5.5 – Summary of photophysical data for Ru-tap-NLS and its parent complex.

	Solvent[a]	λ_{abs} (ε)[b] nm (x10^3 M^{-1} cm^{-1})	λ_{em} nm	τ_{lum} [c] ns		ϕ_{lum} [d]
				Aer.	Deaer.	
Ru-tap-Ester	MeCN	276 (67.9), 416 (18.1), 456 (14.0).	629	680 ± 9	1332 ± 62	0.041
	H_2O	279 (61.9), 415 (16.7), 459 (12.5).	639	607 ± 7	753 ± 8	0.029
	PBS	278 (61.3), 414 (17.3), 459 (13.1).	639	515 ± 1	594 ± 9	
Ru-tap-NLS	MeCN	275 (68.8), 421 (17.2), 460 (13.7).	631	695 ± 2 (71 %)/ 74 ± 3	1015 ± 5 (68 %)/ 119 ± 15	
	H_2O	279 (65.8), 415 (16.7), 460 (12.6).	640	659 ± 1	760 ± 3	0.028
	PBS	280 (65.3), 415 (16.8), 460 (12.8).	640	605 ± 1	659 ± 4	

Notes: [a b c d] See Table 5.3.

A more interesting behaviour was observed in aerated acetonitrile where the NLS conjugate lifetime decay was found to require bi-exponential fitting. A long-lived component (τ_{long}) contributing 71 % by amplitude (A_{long}) of the total decay was measured at τ_{long} = 695 ns on average, which is comparable to the lifetime of τ = 680 ns measured on average for Ru-tap-ester which decays mono-exponentially. However, the short component indicated strong quenching, measured at τ_{short} = 74 ns. The effect persists upon de-aeration, with similar increases in lifetime of both components of the decay observed with no significant change to the relative amplitude. A similar quenching in acetonitrile was observed by Rebarz *et al*. who studied the photophysical behaviour of $[Ru(tap)_2(phen)]^{2+}$ in the presence of protonated calix[6]crypturea, where proton transfer from an amine group on the crypturea motif to the exited state of the complex resulted in quenching.[89] A similar effect may operate for Ru-tap-NLS, where depending on the relative orientation of the peptide, proton transfer from lysine or arginine of the NLS (there are four of these residues in total), may occur via H-bridge between the peptide and Ru leading to a quenched component of the luminescence decay. In any case, the effect was not observed in aqueous solvent, probably because of better ion solvation and disruption of the H-bonding promoted in aprotic media. Thus, biophysical application of Ru-tap-NLS should not be impacted.

5.2.6 Non-specific interaction with BSA.

To better understand the interaction of the complexes reported here with DNA, it was important to assess the extent of photophysical change non-specific interaction elicits with biomolecules other than nucleic acids. Indeed, understanding of interactions with protein is especially important for Ru-tap complexes since their excited state reduction potentials have been shown to be positive enough to oxidise the amino acids; Trp and Tyr, leading to luminescence quenching and possible adduct formation.[62,90–92] Similar to work reported in Chapter 4, bovine serum albumin (BSA) was again exploited as a protein model. BSA is anionic in PBS at pH 7.4 (pI ≈ 4.5) and contains hydrophobic cavities that could favour the hosting of cationic lipophilic drug molecules resulting in increases in their luminescence intensity.[93,94] It has also been reported that within one of these cavities likely resides one of the two Trp residues of BSA that can quench photo-excited Ru-tap complexes.[95,96]

In a typical experiment, solutions of varying [BSA]/[Ru] ratio (r) from 0 – 50 in PBS were prepared and changes in the luminescence of the complex were monitored. As shown in Figure 5.13, within error, increasing the [BSA]/[Ru-tap] ratio does not significantly impact the luminescence of Ru-tap-ester or Ru-tap-NLS up to a relatively high concentration of BSA at r = 50 (5 μM Ru, 250 μM BSA). Luminescence lifetime experiments (Table 5.6) similarly indicated no significant change to the ester complex photophysics in the presence of BSA (r = 15). Ru-tap-NLS lifetime was found to be marginally reduced in the presence of BSA, but still exhibited mono-exponential decay. If quenching by Tyr or Trp were occurring, the decay would be expected to be multi-exponential with one of its components quenched significantly to the order of $\tau < 100$ ns.[92] Hence, the marginal quenching observed here is probably due to

Table 5.6: Luminescence lifetimes of Ru-tap probes measured in PBS in the absence and presence of BSA (r = 15).

	τ (free) ns	**τ (BSA)** ns
Ru-tap-Ester	515 ± 1	515 ± 2
Ru-tap-NLS	605 ± 1	564 ± 4

Notes: Errors included as ± SD (n = 3).

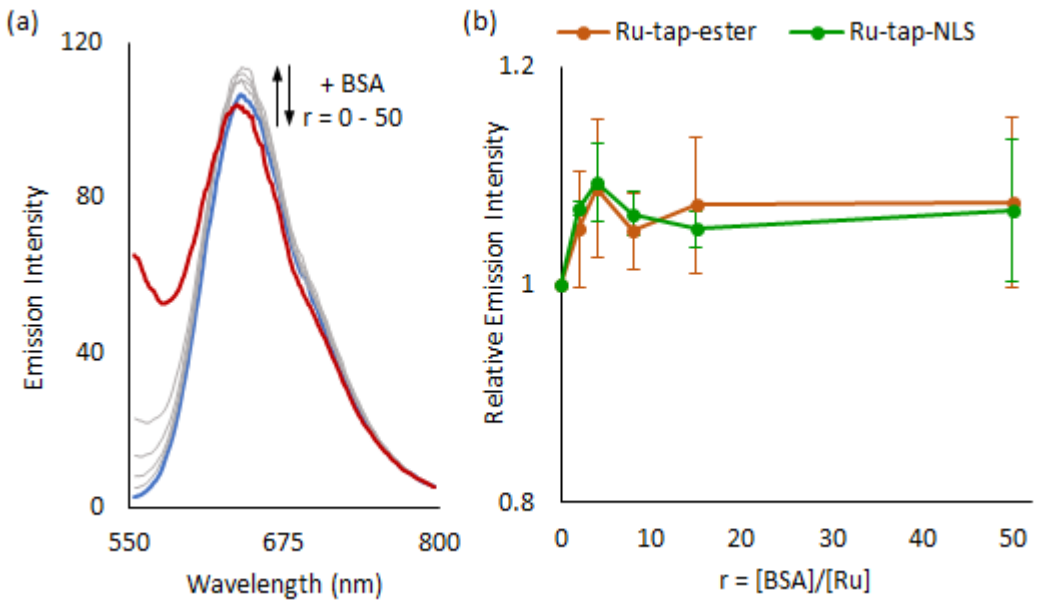

Figure 5.13: (a) Changes to emission spectrum of Ru-tap-NLS (5 μM, PBS) with increasing r = [BSA]/[Ru] up to r = 50. (b) Changes in the intensity at the emission maximum with increasing r = [BSA]/[Ru] for the ester and NLS complexes as indicated. Error bars inserted as ± SD (n = 3).

---

a slight affinity of the peptide for BSA that reduces the protecting effect at the Ru-tap moiety, perhaps driven by electrostatic binding to BSA which exhibits a net anionic charge at pH 7.4. It was interesting that the parent complex did not appear to exhibit affinity for BSA which indicates that off-target binding by Ru-tap-NLS should be limited *in cellulo*.

5.2.7 Interaction with DNA and free bases.

5.2.7.1 Spectroscopic changes upon interaction with ctDNA and free bases.

Absorbance and emission responses to ctDNA

Changes to the absorbance and emission spectra of Ru-tap-NLS and Ru-tap-ester induced by DNA were assessed by titrating aliquots of highly concentrated ctDNA (1 – 3 mM, PBS) into solutions of Ru (5 – 10 μM, PBS). Representative spectra of Ru-tap-NLS shown in Figure 5.14 indicate the expected changes as r = [DNA]bp/[Ru] (hereafter, r) increases to saturation. Moderate hypochromicity was observed in the MLCT absorbance band, in line with reports by Lecomte *et al*. on the structural analogue, $[Ru(tap)_2(bpy)]^{2+}$.[42] The luminescence

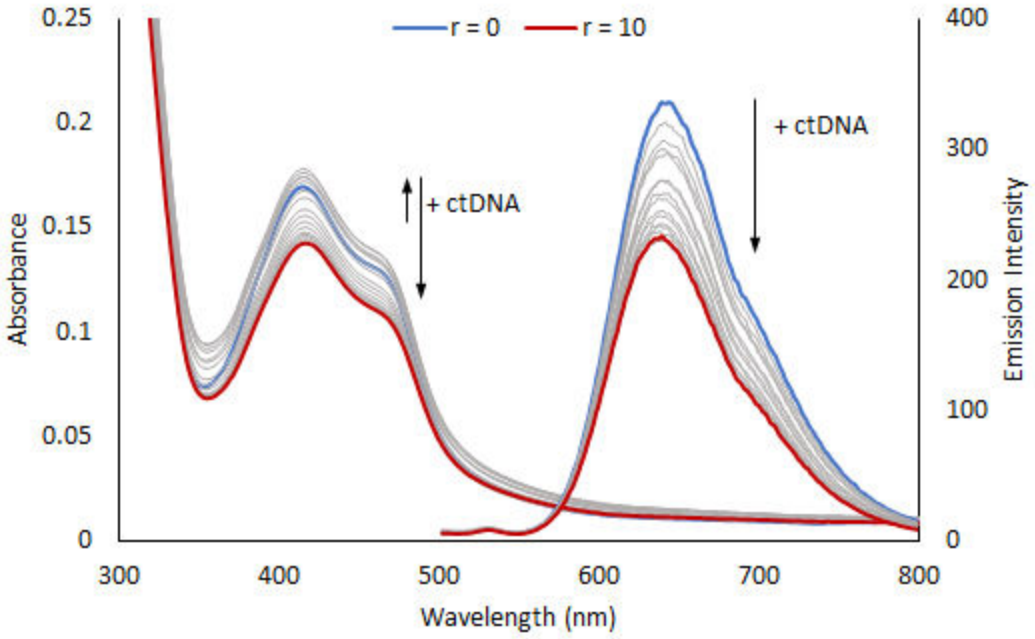

Figure 5.14: Changes to the absorbance and emission spectra of Ru-tap-NLS (blue traces, 10 μM, PBS) upon titration with ctDNA up to r = [DNA]bp/[Ru] = 10 (red traces).

---

decreased with increasing DNA ratio indicative of PET quenching by the polynucleotide and is characteristic of Ru-*bis*-tap complexes. The intensity decrease was found to be about 20 – 30 %, at saturation, significantly lower than that described for $[Ru(tap)_2(bpy)]^{2+}$ (*ca*. 60 - 70 %), which may suggest that the $[Ru(tap)_2(bpy\text{-}R)]^{2+}$ moiety of Ru-tap-NLS does not bind as intimately as unmodified $[Ru(tap)_2(bpy)]^{2+}$.

Interestingly, the spectrum of Ru-tap-ester remains insensitive to DNA up to r = 50 (Figure 5.15). This behaviour is similar to $[Ru(Me_2tap)_3]^{2+}$ which was found by dialysis experiments to be too sterically hindered to bind DNA.[42] Comparing the structure of $[Ru(tap)_2(bpyArCOOEt)]^{2+}$ which does not appear to bind DNA, to $[Ru(tap)_2(bpy)]^{2+}$ which does, it is clear but very surprising that the aryl-ester substituent is responsible for the inhibition. Hence, DNA binding by Ru-tap-NLS is predominantly an electrostatic interaction promoted by the cationic nature of the peptide (NLS^{+4}, pH 7.4). The impact of the peptide on binding is unsurprising considering the binding constants of the peptide-conjugated Ru-dppz series discussed in Chapter 4 were an order of magnitude higher than their parent complexes

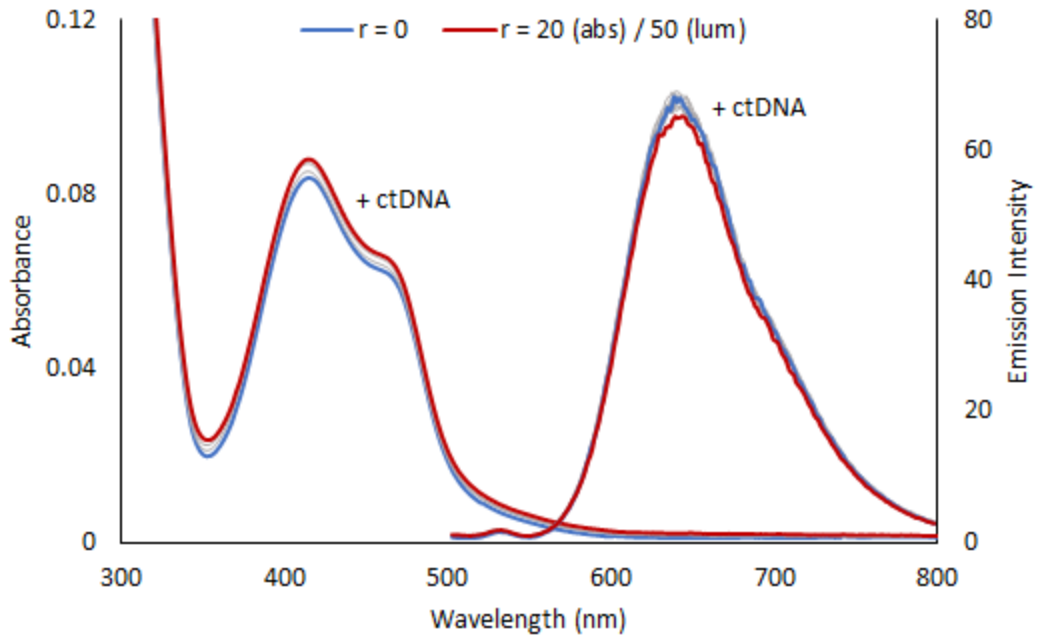

Figure 5.15: Changes to the absorbance and emission spectra of Ru-tap-ester (blue traces, 5 μM, PBS) upon titration with ctDNA up to r = [DNA]bp/[Ru] = 20 (absorbance) or 50 (luminescence) (red traces).

---

due to electrostatic association of DNA with the tethered peptide. The incapacity of $[Ru(tap)_2(bpyArCOOEt)]^{2+}$ to bind DNA could yet be useful as an extracellular selective probe of Trp or Tyr rich proteins in the presence of nucleic acids such as histone targeting.

Photophysical response to AMP and GMP

The luminescence quenching behaviour of the Ru-tap complexes was assessed in the presence of a large excess of AMP and GMP (100 equivalents, PBS, see Table 5.7, Figure 5.16). As expected, quenching was observed in the presence of GMP for Ru-tap-NLS, where the lifetime reduced from 605 ns on average to 483 ns, while no significant changes were observed in the presence of AMP. Similar quenching was observed for Ru-tap-ester in the presence of GMP and is further evidence that its lack of spectroscopic response in the presence of DNA (Figure 5.15) is due to poor binding affinity and inhibited access to guanine. The lifetime of Ru-tap-ester in GMP (402 ns) was found to be lower than that of Ru-tap-NLS, probably due to the protecting effect of the peptide. Using lifetime values in the

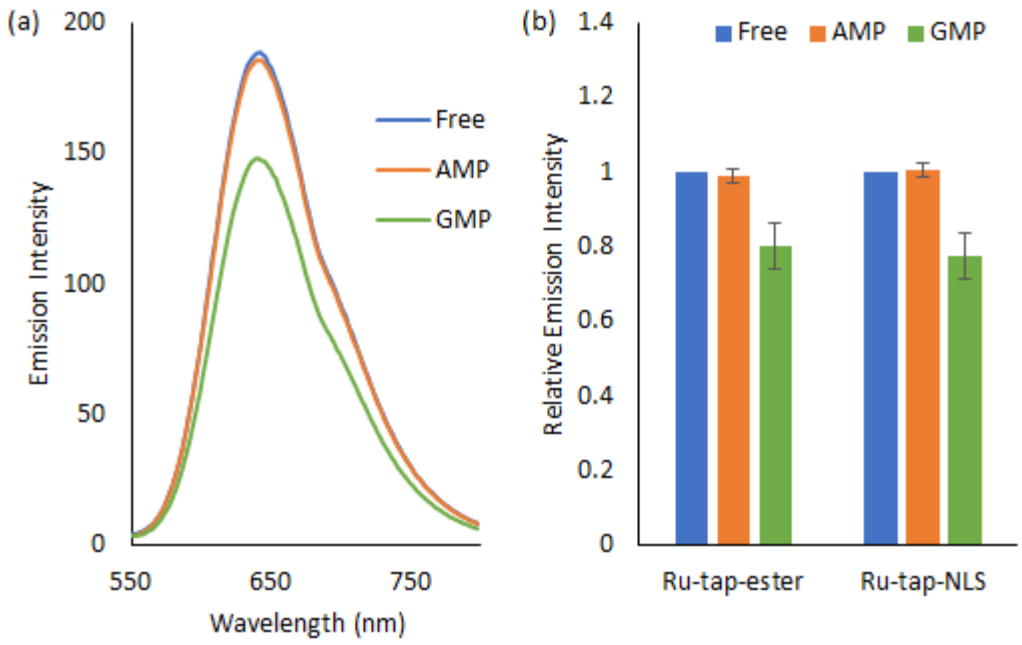

Figure 5.16: (a) Emission intensity of Ru-tap-NLS (5 μM, PBS) in the absence (blue trace) and presence of AMP and GMP (orange and green respectively, 100 mole equivalents). (b) Relative emission intensities of Ru-tap-NLS and Ru-tap-ester as indicated in the absence (blue) and presence of AMP and GMP (orange and green respectively, 100 mole equivalents). Error bars inserted as ± SD (n = 3).

---

presence and absence of GMP, an electron transfer rate between Ru-tap-ester and GMP was calculated at $K_{et} = 5.46 \times 10^5\ s^{-1}$.

Luminescence lifetime response to DNA

Luminescence lifetime data presented in Table 5.7 for the free Ru-tap complexes and DNA saturated solutions supports the above reported spectral changes. The lifetime of Ru-tap-ester increased only marginally in the presence of DNA, which may be due to a slight increase in the viscosity of the solution. In contrast, the luminescence decay kinetics of Ru-tap-NLS became complex in the presence of DNA, requiring a tri-exponential model to fit the decay. A longer-lived component was measured at $\tau_{long} = 1294 \pm 66$ ns (fractional amplitude, $A_{long} = 17$ %) and can be attributed to intimate binding at A-rich regions which restrict the mobility of the complex and enhance the luminescence lifetime of the probe.

Table 5.7: Summary of the luminescence lifetime data for Ru-tap complexes in the presence and absence of ctDNA.

Compound	τ / free	τ / ctDNA	τ / GMP	τ / AMP
Ru-tap-Ester	515 ± 1	535 ± 1	402 ± 2	536 ± 1
Ru-tap-NLS	605 ± 1	1294 ± 66 (17 %) 482 ± 19 (54 %) 51 ± 5 (29 %)	483 ± 1	559 ± 16
Ru-tap-NLS *1M NaCl/PBS*	582 ± 3 (72 %) 42 ± 11 (28 %)	574 ± 4 (67 %) 31 ± 1 (33 %)		

Notes: Errors included as ± SD (n = 3). Percentage relative amplitudes are given in parentheses. 100 mole equivalents of GMP and AMP. 20 mole base pair equivalents of ctDNA.

An intermediate component determined at τ_{mid} = 482 ± 19 ns (A_{mid} = 54 %), was likely attributed to guanine quenching since the lifetime in the presence of GMP is similar at 483 ns on average (Table 5.7). Further studies in the presence of $(poly[dA\text{-}dT])_2$ and $(poly[dG\text{-}dC])_2$ are necessary to explore whether this component persists in A-rich DNA. Alternatively, this component arises due to a binding geometry in which the Ru-tap moiety of Ru-tap-NLS is less restricted. In this scenario, the NLS is strongly electrostatically associated with DNA and no longer confers a protecting effect to the Ru-tap moiety. To support this notion, it is notable that τ_{mid} is comparable to the luminescence lifetime of Ru-tap-ester in the absence of DNA (τ = 515 ± 1 ns).

The third component of the decay of DNA-bound Ru-tap-NLS was significantly quenched at τ_{short} = 51 ± 5 ns (A_{short} = 29 %), and probably reflects PET quenching in cases where binding places the Ru-tap moiety near G-rich sequences. Notably, similar triexponential behaviour was observed by Kirsch-De Mesmaeker and co-workers who studied the photophysical behaviour of a Ru-TAT conjugate in the presence of short ODNs.[58]

Photophysical response to DNA at high ionic strength

The spectroscopic changes in the presence of ctDNA were also assessed at high ionic strength (1 M NaCl in PBS, $[Cl^-]_{total}$ = 1.14 M). Under these conditions, there was no change in the luminescence observed at r = 20 (see Appendix C). The luminescence lifetime was

biexponential at high ionic strength, with a strongly quenched component (τ = 42 ± 11 ns, A = 28 %), but the lifetime magnitude or fractional amplitude was not significantly altered in the presence of ctDNA at r = 20 (Table 5.7). This ionic dependence of the longest component of the decay indicates, as expected, that electrostatic association between the cationic peptide and the polyanionic DNA backbone drives binding affinity by Ru-tap-NLS.

Binding affinity by ethidium displacement assay

The moderate changes in the luminescence of Ru-tap-NLS upon titration with DNA made it difficult to make an accurate quantitative measurement of binding affinity. To circumvent this issue, an apparent binding constant, K_{app}, was instead calculated using an ethidium bromide (EB) displacement assay. EB is a known DNA intercalator with $K_b = 9.5 \times 10^6\ M^{-1}$ in HEPES buffer (80 mM, 40mM NaCl). EB can be used to provide K_{app} from the concentration of probe required to displace it from DNA and reduce its fluorescence by half (see Chapter 2 for methods). Figure 5.17a reveals that Ru-tap-ester is ineffective in displacing

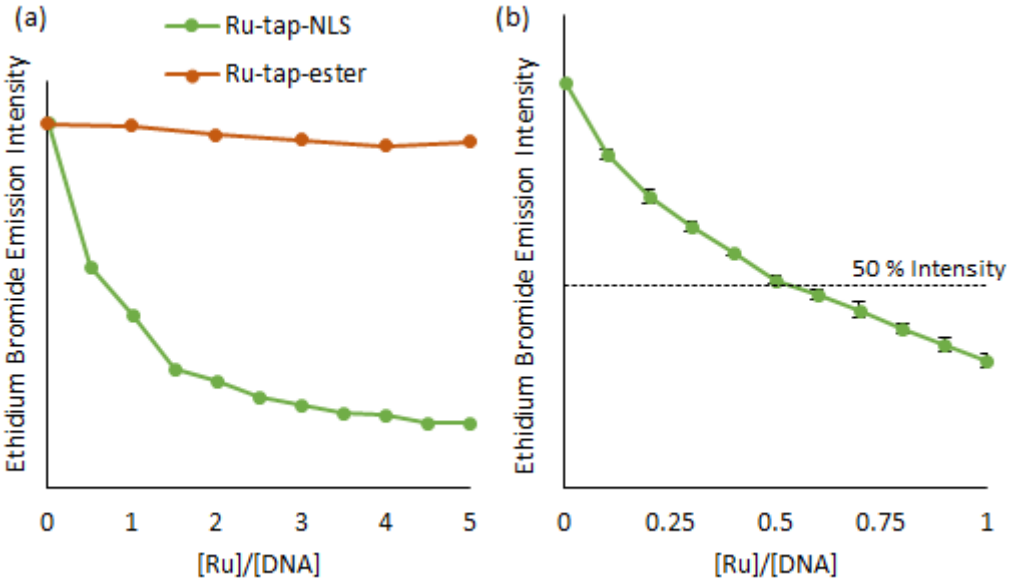

Figure 5.17: (a) Changes to the relative EB fluorescence intensity with increasing [Ru]. (b) Average competitive binding curve for Ru-tap-NLS versus EB from triplicate measurements with error bars set to ±SD.

EB with constant relative fluorescence observed up to r = [Ru]/[EB] = 5, highlighting the relatively poor binding affinity of the complex towards DNA. In contrast, Ru-tap-NLS reduces the fluorescence by 50 % at about r = 0.5 and triplicate measurements in the range r = 0 – 1 (Figure 5.17b) permitted calculation of $K_{app} = 2.26 \times 10^7\ M^{-1}$. This value is comparable to the value calculated for Ru-dppz-NLS in Chapter 4 ($K_b = 3.6 \times 10^7\ M^{-1}$), thus indicating binding of Ru-tap-NLS with DNA is driven by the conjugated NLS peptide. This observation is significant for cellular applications; the NLS is not only responsible for delivering the Ru-tap photoreactive cargo to the nucleus, but may also drive its affinity for chromosomal DNA.

Ferrocyanide Quenching

To further investigate the interaction of the Ru-tap complexes with ctDNA, a ferrocyanide quenching study was performed (Figure 5.18). Ru-tap-ester and Ru-tap-NLS are luminescent in buffer but were quenched successively with increasing $[Fe(CN)_6]^{4-}$. Upon DNA binding, a strongly associated luminophore will be protected from ferrocyanide quenching, for example, the emission spectrum of $[Ru(bpy)_2(dppz)]^{2+}$ (a known intercalator, see Chapter 4), remained insensitive to $[Fe(CN)_6]^{4-}$. Conversely, in the presence of ctDNA (r = 20), Ru-tap-ester was significantly quenched, almost to the same extent as in the absence of ctDNA, which was expected given its poor DNA binding affinity.

Driven by the cationic nature of the peptide, Ru-tap-NLS exhibits a very high binding constant with DNA ($K_{app} = 2.26 \times 10^7\ M^{-1}$). However, for such affinity, the probe strangely exhibits relatively minor spectroscopic change in the presence of ctDNA (Figure 5.15) which suggests that although the NLS of Ru-tap-NLS is strongly associated with DNA, its Ru-tap cargo may not be as intimately bound. Correspondingly, as shown in Figure 5.18, the luminescence of Ru-tap-NLS in the presence of DNA was observed to be quenched by $[Fe(CN)_6]^{4-}$ indicating that the Ru-tap moiety is accessible to the quencher. Given that the quenching was less efficient in the presence of DNA than its absence, the Ru-tap moiety was protected by DNA to some extent, perhaps by binding via a surface mode. This rationalises the data reported earlier in that the luminophore of Ru-tap-NLS must be close enough to DNA to undergo PET with guanine. Weaker affinity of Ru-tap complexes may have beneficial ramifications for cellular applications, for example, studies have indicated that

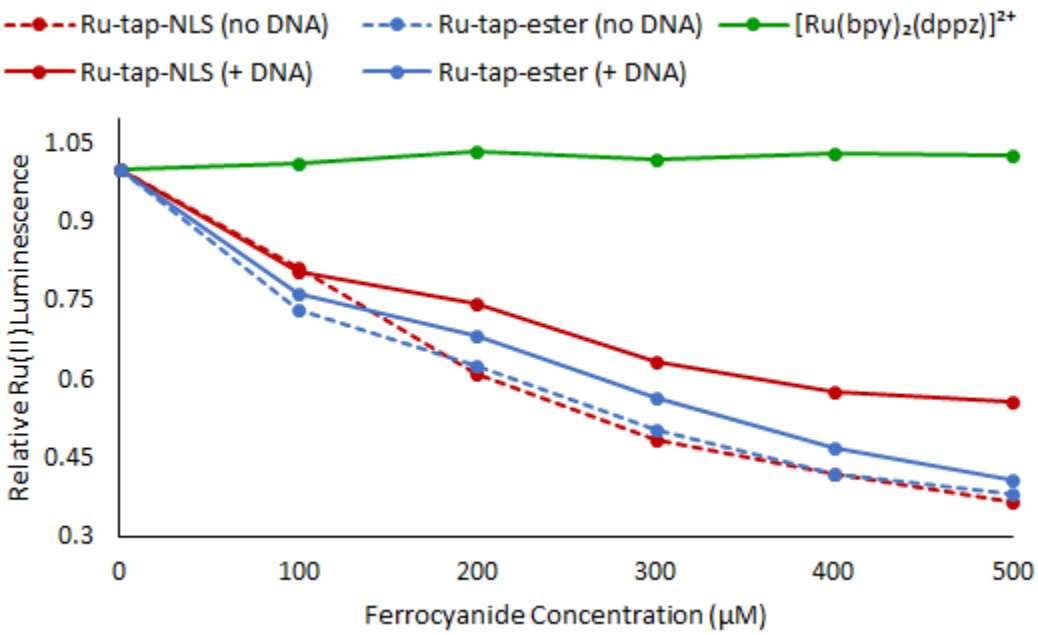

Figure 5.18: Relative Ru(II) luminescence (10 μM, PBS) in the presence and absence of ctDNA (r = 20) as indicated with increasing ferrocyanide concentration.

---

rigidly DNA-bound Ru-tap complexes are less effective at producing photoadducts because their photochemistry may require molecular reorientation to achieve a geometry better suited to the formation of a new covalent bond with guanine.[53,54]

5.2.7.2 Spectroscopic changes upon photo-irradiation.

Spectroscopic and dialysis experiments on $[Ru(tap)_2(bpy)]^{2+}$ indicated that visible irradiation is capable of sensitising the formation of permanent photoadducts with DNA, while electrochemical and emission quenching studies against the free nucleotide bases suggest that a PCET process occurs with guanine.[42] Indeed, a permanent adduct was isolated and its structure elucidated as one of two isomers, with the formation of a new covalent bond between the C-2 or C-7 of one of the tap ligands to the N2 exocyclic amine of guanine.[33,48] Under photo-irradiation, changes to the absorbance spectrum of the metal complex were observed with extensive hyperchromicity evident with increasing irradiation time,[42] with concomitant quenching of the emission intensity of the complex under the same conditions.[53]

Herein, Ru-tap-NLS was subjected to irradiation in the presence of ctDNA (r = 20, PBS, Xe-Arc, 355 nm cut-off filter, 500 W source) and the spectroscopic changes were monitored over time. Figure 5.19a illustrates that clear changes were observed in the absorbance spectrum over irradiation times of up to 3 h. Hyperchromicity and broadening of the MLCT band were apparent but the most pronounced changes occurred at *ca*. 350 nm, while there was additional growth of a new absorption at *ca*. 520 nm. These changes are characteristic of the formation of photo-adducts and were accompanied by successive quenching of the luminescence with increasing exposure to visible irradiation (Figure 5.19b).

There were corresponding changes in luminescence lifetime as shown in Table 5.8, for example, the long component apparent prior to irradiation disappeared and the decay kinetics became biexponential with τ_{long} = 544 ± 6 ns (A = 53 %) and τ_{short} = 75 ± 5 ns (A = 47 %). The origin of this change is unclear and has not been investigated by others who reported on

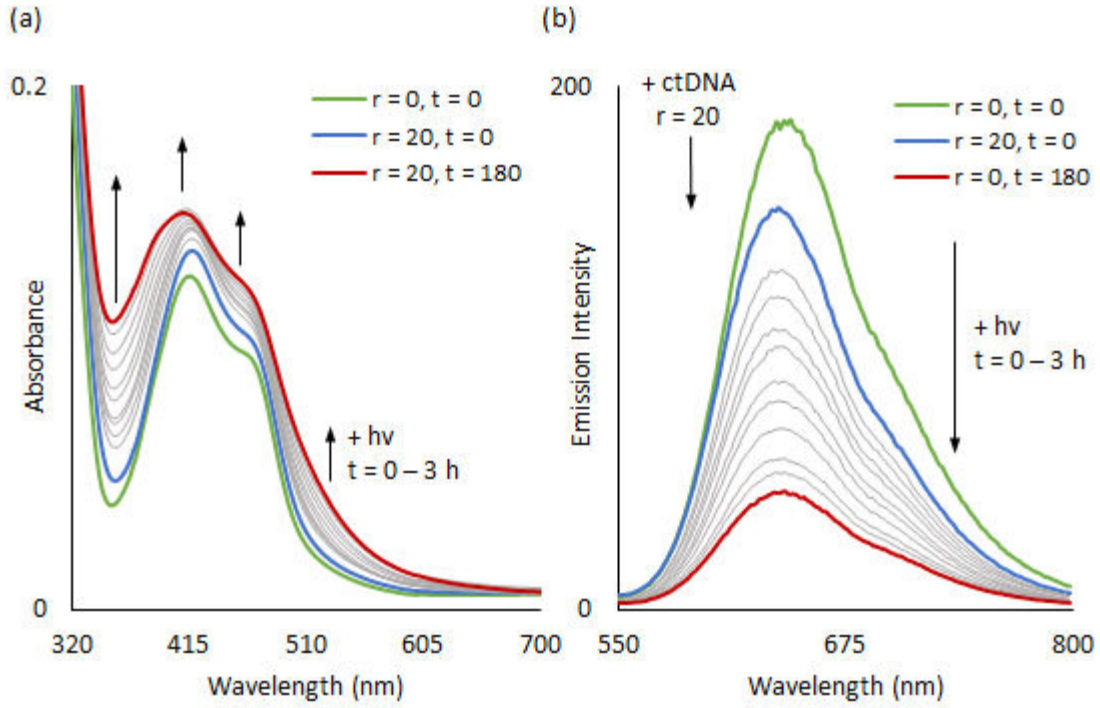

Figure 5.19: Changes to the absorbance (a) and emission (b) spectra of Ru-tap-NLS under irradiation up to 3 h (red), relative to the free probe (green) and in the presence of ctDNA prior to irradiation (r = 20, blue). Conditions: Xe-arc, 500 W source, < 355 nm cut-off filter.

the irradiation of related Ru-tap complexes. Herein, the shorter-lived component is likely due to the formation of photoadducts which places the Ru-tap luminophore in intimate contact with guanine leading to extensive quenching. The longer component may be due to Ru-tap emissive centres which are not strongly associated with DNA considering the similarity of this lifetime with that of Ru-tap-ester in the absence of DNA (τ = 515 ± 1 ns). However, it must be noted that the magnitude of this lifetime is also similar to the quenching observed in the presence of GMP (τ = 483 ns). The disappearance of the longer lifetime of Ru-tap-NLS with DNA before irradiation (i.e. τ = 1294 ± 66 ns) adds additional complexity. Perhaps, adduct formation distorts DNA and reduces protection at A-rich sites. Alternatively, the disappearance of the longer-lived component could signify re-orientation of the Ru-tap complexes to guanine sites with adduct formation. In any case, the change in photophysical behaviour of Ru-tap-NLS in the presence of DNA upon irradiation is strong evidence of the formation of photoproducts.

As established from the spectroscopic titration data reported above, DNA binding of Ru-tap-NLS is driven by the cationic peptide with the Ru-tap moiety less strongly associated as indicated by the comparable insensitivity of the photophysics of Ru-tap-ester in the presence of ctDNA (e.g. Figures 5.14, 5.15). Hence, although Ru-tap-NLS is strongly associated via the peptide, the Ru-tap moiety may be afforded the molecular flexibility to re-orientate during irradiation to achieve a suitable geometry that yields photoadducts with guanine leading to the observed changes in the luminescence lifetime. Indeed, as shown in Figure 5.20, under irradiation the luminescence of Ru-tap-ester also became successively quenched which

Table 5.8: Luminescence lifetime data for Ru-tap-NLS and Ru-tap-ester to indicate changes in the presence of DNA and GMP and post photo-irradiation.

Compound	**τ / free**	**τ / ctDNA**	**τ / GMP**	**τ / ctDNA 3h Irradiation**
Ru-tap-Ester	515 ± 1	535 ± 1	402 ± 2	-
Ru-tap-NLS	605 ± 1	1294 ± 66 (17 %) 482 ± 19 (54 %) 51 ± 5 (29 %)	483 ± 1	544 ± 6 (53 %) 75 ± 5 (47 %)

Notes: Errors included as ± SD (n = 3). Percentage relative amplitudes are given in parentheses.

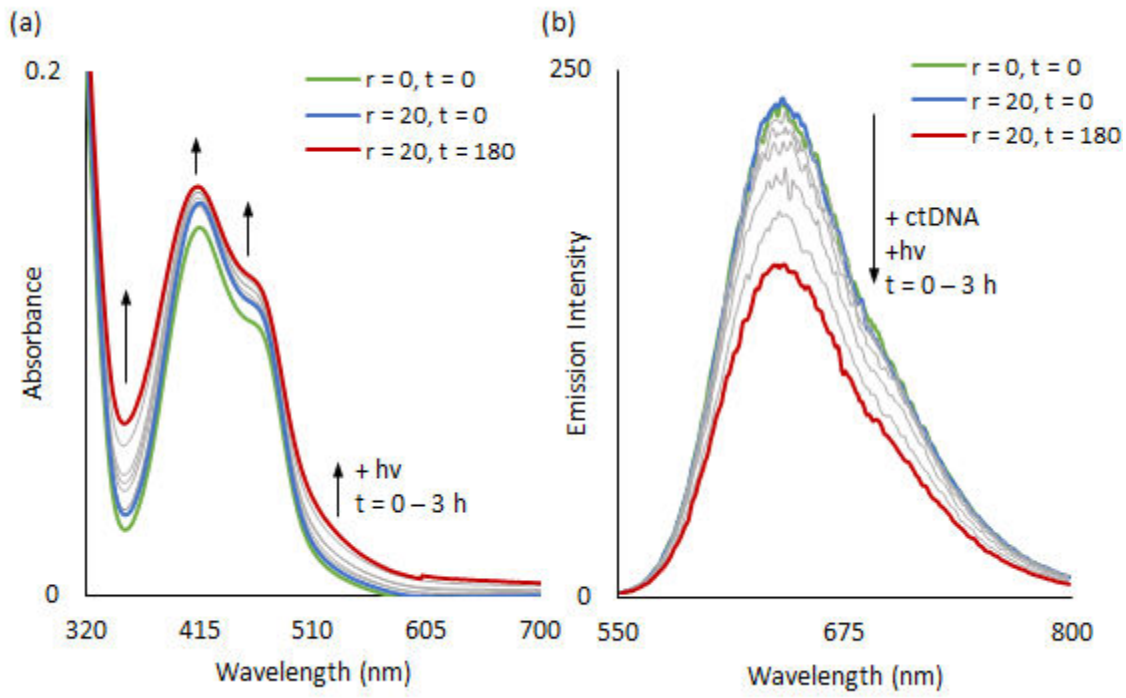

Figure 5.20: Changes to the absorbance (a) and emission (b) spectra of Ru-tap-ester under irradiation up to 3 h (red), relative to the free probe (green) and in the presence of ctDNA prior to irradiation (r = 20, blue). Conditions: Xe-arc, 500 W source, < 355 nm cut-off filter.

---

indicates that although the complex itself does not interact strongly with DNA in the dark, continuous irradiation generates a reactive Ru-tap species that can diffuse and yield adducts with guanine over time. The rate of quenching was slower for the parent complex than observed for Ru-tap-NLS, but this can be rationalised by the stronger affinity of Ru-tap-NLS which places its Ru-tap centre in closer proximity to DNA with higher probability of PCET processes occurring with guanine.

Ru-tap-NLS was also photo-irradiated in the absence of ctDNA and this led to slight changes in the absorbance and emission spectra consistent with moderate photo-dechelation (Figure 5.21). The quantum yield of dechelation is likely enhanced using PBS, a solvent containing ions suited to photo-anation, but in any case, the changes observed for Ru-tap-NLS are comparable to that reported for $[Ru(tap)_2(bpy)]^{2+}$ and are minimal in comparison to the changes observed in the presence of ctDNA. This relative photostability is favourable for the intended cellular application of the probe, given therapeutic activity of Ru-tap-NLS against

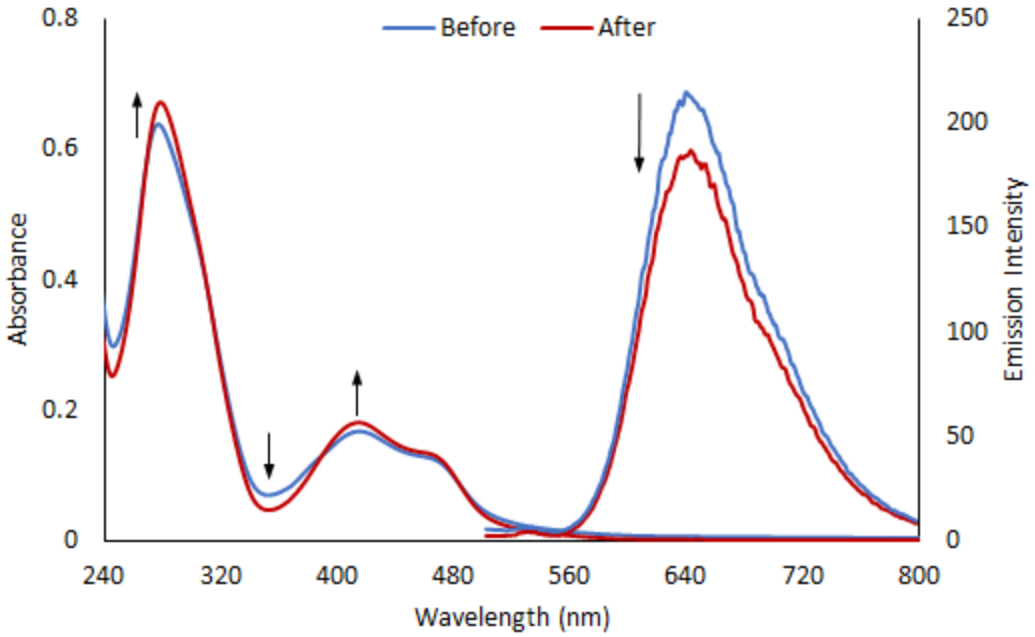

Figure 5.21: Absorbance and emission spectra of Ru-tap-NLS (10 μM, PBS) before and after exposure to irradiation for 3 h as indicated. Conditions: Xe-arc, 500 W source, < 355 nm cut-off filter.

DNA would be driven by photo-oxidative processes and not due to photo-dechelation products such as toxic Ru-aquo or free ligand species. It must also be noted that $[Ru(tap)_3]^{2+}$, a complex with a relative high quantum yield of dechelation, does not undergo photo-decomposition in the presence of guanine. It follows that if precision targeting can be achieved in cellular application, the unique photo-reactivity of Ru-tap towards DNA can be realised exclusively.

The spectroscopic changes in the presence of ctDNA were also followed using circular dichroism (CD). Figure 5.22 shows a representative CD spectrum for ctDNA recorded in PBS buffer and indicates characteristic B-form bisignate curvature. Addition of Ru-tap-NLS (r = [Ru]/[DNA]bp = 0.2) caused a modest but significant distortion of the positive and negative bands signifying an impact on base stacking and helicity. Surprisingly, there appeared to be little change to the CD spectrum upon photo-irradiation which suggests that photo-adduct formation does not significantly impact DNA secondary structure. Rather, the initial change could be attributed to a DNA condensation effect upon association of the

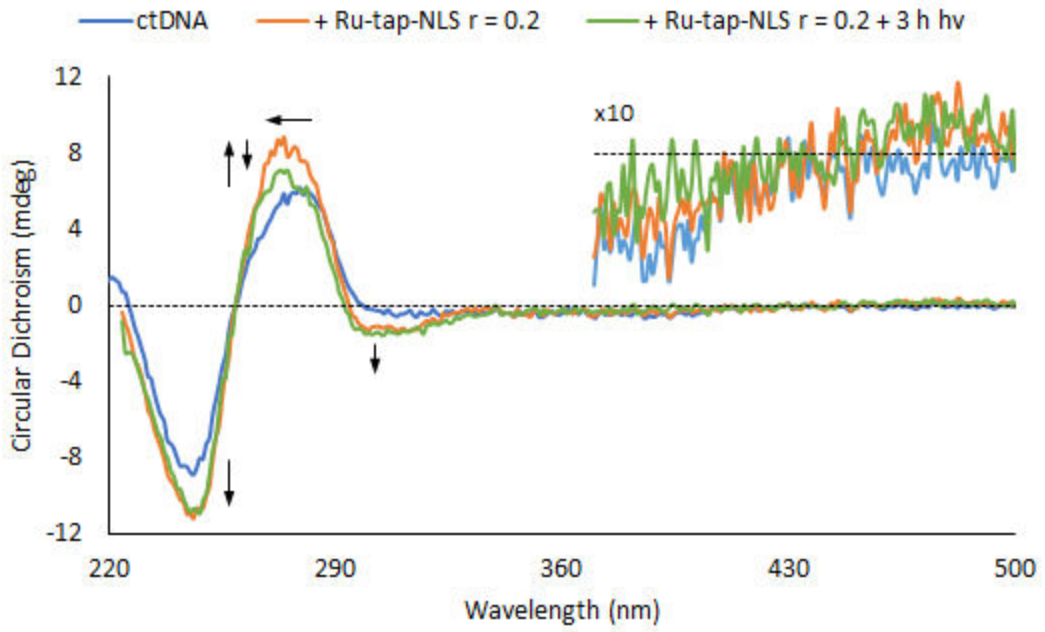

Figure 5.22: Circular dichroism spectra of ctDNA in PBS (blue) and in the presence of Ru-tap-NLS (r = [Ru]/[DNA]bp = 0.2), before (orange) and after (green) irradiation for 3 h. Inset: magnified visible region to indicate minimal spectral change.

---

cationic peptide. A weak induced CD band was also evident around 300 nm and this feature was not impacted by photo-irradiation.

5.2.7.3 Luminescence lifetime at 37 °C

The impact of temperature on the luminescence lifetime of Ru-tap-NLS under cellular imaging conditions was assessed in the presence and absence of ctDNA (r = 20) at 37 °C (Table 5.9). In the absence of DNA, the lifetime was observed to decrease significantly at the increased temperature from τ = 605 ± 1 ns at 20 °C to τ = 505 ± 12 at 37 °C. Kirsch De-Mesmaeker *et al*. reported that $[Ru(tap)_2(bpy)]^{2+}$ responds similarly to $[Ru(bpy)_3]^{2+}$ and derivatives with increasing temperature.[49] Thus, the decrease in emission may be attributed to thermally induced access to the non-radiative ^{3}MC state. To a lesser extent, increased flexibility of the pendant peptide at higher temperatures may decrease its protecting effect from quenching by O_2 at the Ru-tap emissive centre.

Table 5.9: Luminescence lifetime of Ru-tap-NLS at 20 °C and 37 °C in aerated PBS.

Temperature (°C)	τ / free	τ / ctDNA
20	605 ± 1	1294 ± 66 (17 %) 482 ± 19 (54 %) 51 ± 5 (29 %)
37	505 ± 12	1181 ± 31 (7 %) 468 ± 13 (71 %) 50 ± 4 (22 %)

Notes: [ctDNA] r = 20. Errors included as ± SD (n = 3). Percentage relative amplitudes of decay components are given in parentheses.

Similarly, in the presence of DNA, lifetime decreases may be attributed to higher rates of thermal activation to the ^{3}MC state. However, binding may also impact the ^{3}MLCT-^{3}MC conversion at higher temperatures as described by Lecomte *et al*. who studied the luminescence lifetime of *tris*-polyazaromatic Ru(II) complexes.[97] A decrease in the crossover rate to the ^{3}MC state was observed in the presence of DNA compared to its absence because of stabilisation of the ^{3}MLCT state upon binding and a destabilisation of the ^{3}MC state which is sterically less favoured due to Ru-N bond elongation that is constrained when the complex is DNA-bound. This may rationalise the lower lifetime decrease observed for the longest-lived component of the lifetime of Ru-tap-NLS in the presence of DNA with increasing temperature (Table 5.9). This component was attributed to binding in A-rich regions of DNA and indicated a decrease in its lifetime from about 1294 ns to τ_{long} = 1181 ± 31 ns, which represents only an 9 % decrease in τ compared to 17 % in the absence of DNA, perhaps due to less favoured crossover to the ^{3}MC state as described by Lecomte *et al*.[97]

In the presence of DNA, the shortest-lived component of Ru-tap-NLS, attributed to PCET with guanine, remained the same at τ_{short} = 50 ± 4 ns. Similarly, minor changes were also observed for the intermediate lifetime component, indicating that this component arises from guanine quenching like that observed in the presence of GMP (τ = 483 ns). Interestingly, large changes in the relative amplitudes of all lifetime components were observed towards an increase in the population of the intermediate component (54 – 71 %) suggesting that temperature strongly influences the binding modes of Ru-tap-NLS. Further detailed

temperature dependent studies are necessary to elucidate the exact origin of each lifetime component.

5.2.7.4 Impact of DNA binding and photoirradiation on resonance Raman (rRaman) spectra

Figure 5.23 shows the rRaman spectra (473 nm) collected for Ru-tap-NLS in PBS solution in the absence and presence of ctDNA (r = 10), before and after irradiation for 3 hours. Peaks originating from tap vibrational modes dominate the spectrum of Ru-tap-NLS in the absence of DNA, assigned by comparison to the bands reported for $[Ru(bpy)_3]^{2+}$ and $[Ru(tap)_3]^{2+}$.[98,99] In the presence of ctDNA (r = 10), significant decreases in the relative intensities of the tap bands were observed upon normalisation to the bpy mode at 1031 cm^{-1}, most notably at 1278 cm^{-1}, 1456 cm^{-1} and 1539 cm^{-1}. Interestingly, a clear marker band for DNA binding was identified as the tap peak at 1502 cm^{-1} which was present in spectrum of Ru-tap-NLS in the

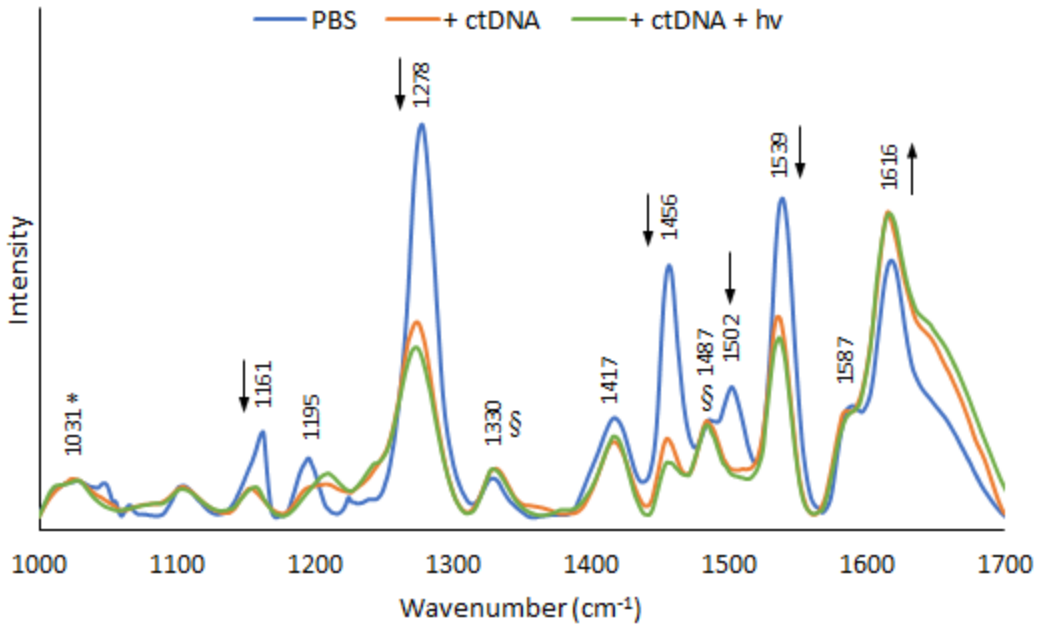

Figure 5.23: rRaman spectra (473 nm) of Ru-tap-NLS in buffer (blue) and in the presence of ctDNA (r = 10) before (orange) and after irradiation for 3 h (green). Spectra were normalised to the bpy mode at 1031 cm^{-1} (*). Peaks assigned to the bpyArCOOR ligand are marked (§) and the inserted arrows indicate the direction of intensity change upon DNA binding.

absence of DNA but disappears upon binding. Peaks at 1031 cm^{-1}, 1330 cm^{-1}, 1417 cm^{-1}, 1487 cm^{-1} and 1587 cm^{-1} did not undergo changes upon DNA binding and are likely attributed to the bpyArCOOR ligand.

The evolution of the ground state rRaman spectrum of Ru-tap complexes in the presence of DNA has not been previously reported, but like in the case of the Ru-dppz complexes studied in Chapter 4, may be rationalised in terms of changes in resonance due to absorbance hypochromicity and bathochromic shifting of the underlying tap component which sits at the red edge of the MLCT band. Less significant changes to the rRaman spectrum were observed following irradiation for 3 h when photo-adducts should have formed; only minor intensity decreases in tap bands were apparent and a slight shifting of the 1195 cm^{-1} peak. This was surprising considering the clear distortion of the MLCT absorbance band (Figure 5.19) with increasing irradiation time, but can be attributed to the photo-adduct being less resonant than the non-adduct at this wavelength of excitation (473 nm).

5.2.8 Photoactivated Plasmid Cleavage.

To investigate the ability of Ru-tap-NLS to damage DNA *in vitro*, a photo-induced plasmid cleavage study was performed using a commercial supercoiled plasmid (pUC19). Figure 5.24 shows agarose electrophoresis gels that indicate the changes in the plasmid topology over time under irradiation at 488 nm (90 mW) in the presence of Ru-tap-NLS (r = [DNA]bp/Ru = 0.1). In the absence of Ru-tap-NLS (lane 1), the plasmid retained its supercoiled structure (Form I) indicating no damage under irradiation at this power, and similarly Form I persisted in the presence of Ru-tap-NLS without irradiation (lane 2). However, as lanes 3 – 6 indicate, irradiation of pUC19 with Ru-tap-NLS induced DNA damage and led to the production of nicked open-circular plasmids (Form II). Notably, DNA damage was evident after just 30 s and the relative intensity of Form II over Form I increases over time.

Importantly, cleavage efficiency using Ru-tap-NLS was not impacted by the presence singlet oxygen since similar cleavage was observed in the presence and absence of sodium azide which is a singlet oxygen scavenger (Figure 5.24 and Appendix C). $[Ru(bpy)_3]^{2+}$, which is an efficient $^1O_2$ sensitiser, was also tested under the same conditions as a control and did not indicate strand cleavage (see Appendix C). Hence, DNA damage due to Ru-tap-NLS is likely

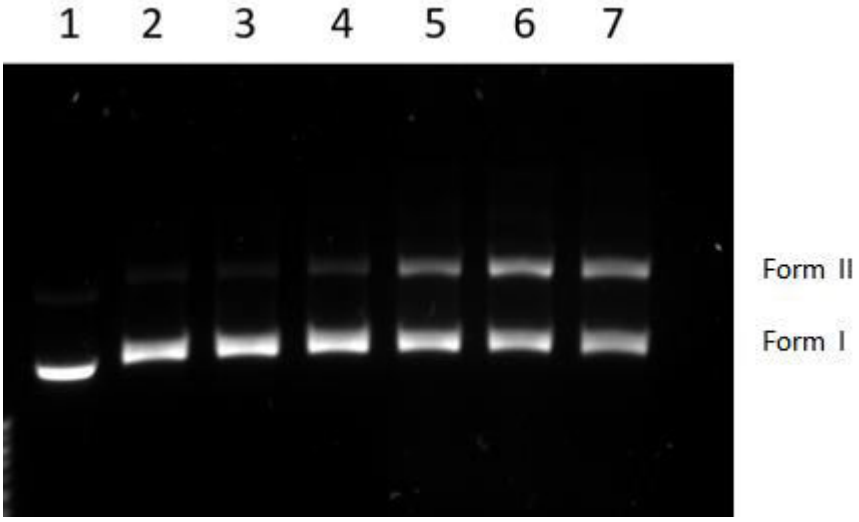

Figure 5.24: Agarose gel electrophoresis of supercoiled (400 ng) pUC19 plasmid DNA exposed to Ru-tap-NLS in a 1:10 ratio, and irradiated at 458 nm (280 mW) in the presence of NaN_3 (5 %) over 30 minutes. The reactions were carried out in a buffer solution made up of 25 mM NaCl and 80 mM Hepes. Lane 1: pUC19 plasmid control. Lane 2: pUC19 + Ru-tap-NLS no irradiation. Lanes 3 – 7: pUC19 + Ru-tap-NLS under irradiation for set times as follows; Lane 3: 30 seconds. Lane 4: 2 minutes. Lane 5: 10 minutes. Lane 6: 20 minutes. Lane 7: 30 minutes Data courtesy of Dr. Aisling Byrne (DCU).

---

occurring due to direct guanine oxidation which leads to single-strand cleavage at one or more sites. Guanine oxidation has been previously observed directly using TRIR in DNA-$[Ru(tap)_2(dppz)]^{2+}$ crystals and early studies by Kelly *et al*. demonstrated photosensitised plasmid cleavage to Form II using $[Ru(tap)_3]^{2+}$.[52,55] The ability of Ru-tap-NLS to rapidly induce plasmid DNA damage under irradiation is promising for photo-induced destruction of DNA in live cells and the singlet oxygen independence of this process may have important future implications for DNA-targeted photodynamic therapy of hypoxic tissues.

5.2.9 Cellular Studies

5.2.9.1 Uptake and Localisation of Ru-tap-NLS.

Cellular uptake of Ru-tap-NLS (100 μM, PBS) was assessed in live HeLa cells using confocal imaging as shown in Figure 5.25. After incubation in the dark for 3 h, Ru-tap-NLS

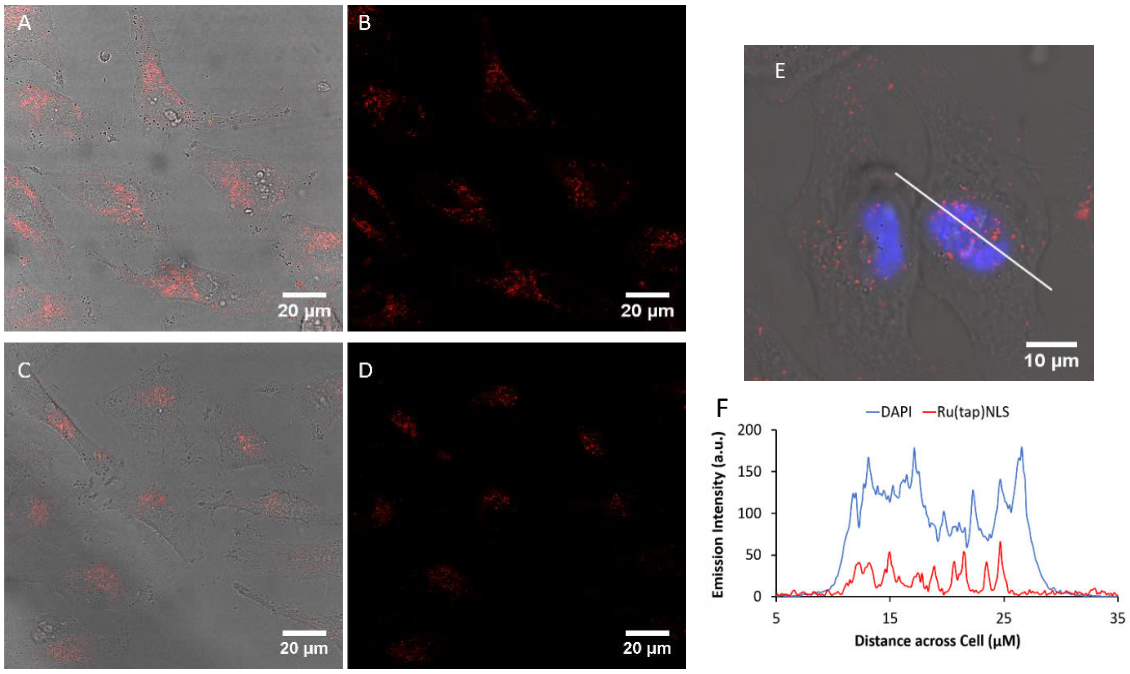

Figure 5.25: Confocal uptake of Ru-tap-NLS by live HeLa cells after 3 h (A and B), and 5 h (C and D). Co-localisation of Ru-tap-NLS in the nucleus was confirmed using DAPI (E). HeLa cells were incubated for 5 h in the absence of light, and DAPI was added 20 minutes prior to imaging. Ru-tap-NLS (100 µM) in red, DAPI (100 nM) in blue, and their co-localisation in pink. The crosshair trace across the cell is represented in the corresponding graph (F), demonstrating co-localisation in the nucleus, analysed using ImageJ. DAPI was excited at 405 nm and emission was collected between 450 – 500 nm. Data courtesy of Dr. Aisling Byrne (DCU).

---

was found distributed throughout the cytoplasm and appeared as very bright spots which suggests localised concentration of the probe within the cell (Figure 5.25, A and B). Ru-tap-NLS demonstrated temperature dependent uptake and did not cross the cellular membrane at 4 °C (Appendix C) which indicated that uptake at 37 °C occurs by an energy dependant mechanism such as endocytosis. Hence, the punctate pattern observed upon uptake after 3 h (Figure 5.25, A and B) may be correspond to endosomal encapsulation of the probe. The parent complex, Ru-tap-ester, does not enter the cell under the same conditions which indicates the role of the NLS peptide in effecting uptake.

Nuclear uptake of Ru-tap-NLS was evident after 5 h where the probe was observed selectively emitting from the nucleus (Figure 5.25, C and D). After 6 h the emission

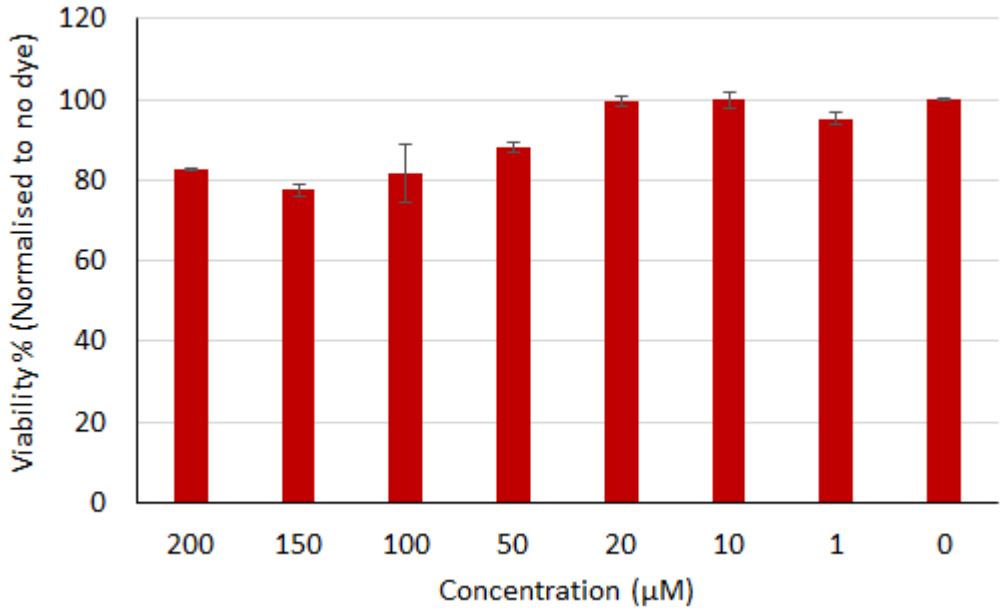

Figure 5.26: Cell viability of HeLa cells after 24 h exposure to varying concentrations of Ru-tap-NLS in the absence of light using the Alamar Blue assay. Viability is measured as a percentage of control cells not exposed to Ru-tap-NLS under the same conditions (n=3). Data courtesy of Dr. Aisling Byrne (DCU).

---

diminished and was then completely extinguished suggesting interaction of Ru-tap-NLS with nuclear DNA leading to luminescence quenching. Nuclear localisation of the probe at 5 h was confirmed by co-localisation studies with DAPI (a nuclear stain) where notably, no emission was observed across the cell outside of the regions stained by DAPI ((Figure 5.25, E and F). The switching-off of the luminescence after 6 h is strong evidence of PCET quenching due to the interaction of Ru-tap-NLS with chromosomal DNA.

5.2.9.2 Cytotoxicity and Photocytotoxicity of Ru-tap-NLS

Dark Cytotoxicity

Ru-tap-NLS exhibited only modest cytotoxicity over 24 h in the dark with about 80 % of cells viable up to 200 µM as shown in Figure 5.26. This is important in the context of photodynamic therapy; DNA damage and consequent cellular destruction can be activated with spatial and temporal control using Ru-tap-NLS.

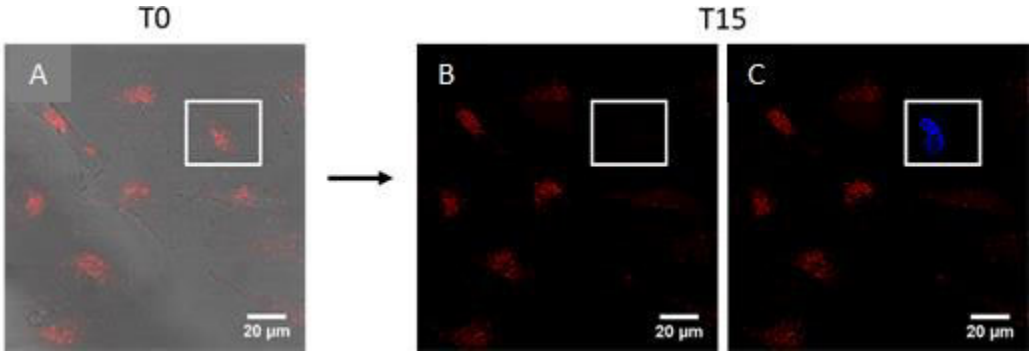

Figure 5.27: Confocal imaging of nuclear localised Ru-tap-NLS in live HeLa cells (A, false colour). A randomly selected cell (white box) was subjected to continuous irradiation for 15 minutes which was found to switch off its emission (B, 470 nm, 1 µW). Cellular death of the exposed cell was confirmed by the entry of DRAQ-7 (blue staining) while the unexposed cells remained viable (C). Data courtesy of Dr. Aisling Byrne (DCU).

Photo-cytotoxicity

The phototoxicity of Ru-tap-NLS was examined by continuously irradiating a single live HeLa containing nuclear localised probe (Figure 5.27, 470 nm, 1 µW). Within the irradiated cell, emission switched-off after 15 minutes, while the surrounding cells remained luminescent. Concomitantly, DRAQ-7 (a dead cell stain) was found to enter the irradiated cell indicating cellular death whereas the surrounding cells remained viable. Importantly, in the absence of Ru-tap-NLS, the cells remain viable under irradiation. Considering the plasmid cleavage study reported above and given that Ru-tap complexes exhibit poor singlet oxygen quantum yields compared to Ru-dppz complexes (as studied in Chapter 4),[58] the rapid cellular destruction observed here likely indicates efficient DNA damage via oxygen independent PCET between Ru-tap-NLS and guanine that leads to detrimental cellular damage. This may have important implications for hypoxic therapies and furthermore, represents a powerful method to selectively induce photodynamic destruction of live cells with spatiotemporal control.

5.3 Conclusions

The first successful application of Ru-tap photo-reactivity towards photo-induced DNA damage in live cells was achieved using NLS-peptide precision targeting of $[Ru(tap)_2(bpyArCOOR)]^{2+}$ to genetic material in the nucleus of HeLa cells. In the dark, Ru-tap-NLS is relatively non-toxic but once localised to DNA, photo-induced cellular destruction can be induced with spatiotemporal control by photo-sensitising guanine oxidation via PET with the Ru-tap complex. This mechanism is likely independent of singlet oxygen sensitisation considering that pUC19 plasmid cleavage by Ru-tap-NLS was not impacted by the presence of an $^1O_2$ scavenger.

Towards the design of an NLS directed Ru-tap probe, two novel conjugatable series of Ru-*bis*-tap complexes were synthesised and characterised; $[Ru(tap)_2(bpyArCOOR)]^{2+}$ and $[Ru(tap)_2(pic\text{-}COOR)]^{2+}$. The latter of these exhibited pH dependent photophysics and was not pursued further in this work but may have future applications in imaging and sensing. Instead, Ru-tap-NLS was obtained pure and in quantitative yield via NLS conjugation to $[Ru(tap)_2(bpyArCOOR)]^{2+}$ and was unambiguously characterised by NMR and HRMS. Ru-tap-NLS and its parent complex, Ru-tap-ester, exhibited photophysics comparable to other reported Ru-*bis*-tap complexes with broad blue-green MLCT absorbance and a relatively oxygen-insensitive luminescence in water but enhanced oxygen sensitivity in acetonitrile. As expected, the emission was quenched by GMP but not AMP which is characteristic of selective PET with guanine as reported previously for Ru-*bis*-tap complexes.

Surprisingly, it was found that the aryl-ester substituent of Ru-tap-ester impedes DNA binding given that this complex exhibits photophysics insensitive to the presence of DNA. Conversely, absorbance hypochromism and emission quenching was observed for Ru-tap-NLS which was shown to bind with high affinity ($K_{app} \approx 10^7$) via electrostatic association of the cationic peptide with the anionic backbone of DNA, suggesting that *in cellulo* application of the probe requires the conjugated NLS not only for targeting but also to drive DNA interactions.

The luminescence lifetime of Ru-tap-NLS in the presence of DNA was complex and conformed to a tri-exponential excited state decay. Similar behaviour has been observed by

others but has not been conclusively addressed. Herein, the components were attributed to binding of Ru-tap-NLS at A-rich or G-rich regions which offer different levels of protection or access to G-quenching of the luminophore. The lifetime was affected by an increase in temperature, but not to the same extent observed in the absence of DNA, which supports quenching by G but also suggests that binding may impact the ^{3}MLCT-^{3}MC crossover. Future work should explore transient absorption and the interaction of Ru-tap-NLS with [poly(dA-dT)]$_2$ and [poly(dC-dG)]$_2$ at different temperatures to investigate this further.

In accordance with previously published reports on Ru-*bis*-tap complexes, photo-irradiation of Ru-tap-ester and Ru-tap-NLS with intense white light yielded photo-products as judged from significant changes to the absorbance and emission spectra of the probes. The rate of photo-reaction was faster for Ru-tap-NLS than Ru-tap-ester, likely due to the high affinity of the conjugated NLS which places Ru-tap-NLS in closer proximity to guanine. The irradiation flux required for the formation of adducts with Ru-tap-NLS herein suggests that adduct formation does not occur to a significant degree in cells and instead, photo-induced destruction likely proceeds via guanine oxidation leading to strand breaks.

Finally, significant changes to the rRaman spectrum of Ru-tap-NLS were observed upon DNA binding for tap associated modes. Surprisingly, less dramatic changes to the rRaman spectrum were observed upon photo-irradiation, despite clear transformation of the absorbance and emission spectra that suggested the formation of photoproducts. This is likely due to the adduct moving out of resonance relative to the non-adduct and future work should investigate the impact of binding on the rRaman spectra at different wavelengths.

5.4 Experimental

5.4.1 General information

All materials, instrumentation and procedures used for synthesis, characterisation and photophysical experiments were as described in Chapter 2 unless otherwise indicated. The synthesis of $[Ru(DMSO)_4Cl_2]$ and bpyArCOOR is described in Chapter 3. Typically, Ru(II) reactions were performed under nitrogen and in the absence of light. All cell work and electrophoresis was performed by Dr. Aisling Byrne (DCU). The synthesis and characterisation of tap and precursors has been reported previously elsewhere.[40,41,78]

5.4.2 Synthesis

2-(4-carboxyphenyl)imidazo[4,5-f]-[1,10]phenanthroline (pic-COOH)

The synthesis and characterisation of this compound has been reported previously.[81] Phendione (420 mg; 2 mmol), 4-carboxybenzaldehyde (360 mg; 2.4 mmol) and ammonium acetate (3.08 g; 40 mmol) were refluxed in 50 mL glacial acetic acid at 160 °C for 3 hours. The solution was cooled to room temperature and the addition of water aided precipitation of a bright yellow solid which was filtered, washed with cold water and acetone, and dried at the vacuum. Yield = 540 mg (79 %). ^{1}H NMR (400 MHz, DMSO-d_6): δ (ppm) 13.95 (s, 1H), 12.71 (s broad, 1H), 9.04 (dd, 2H), 8.93 (dd, 2H), 8.39 (d, 2H), 8.17 (d, 2H), 7.84 (d, 2H). ^{13}C NMR (100 MHz, DMSO-d_6): 167.01, 149.48, 148.13, 143.81, 133.73, 131.40, 130.13, 129.77, 126.21, 123.46, 114.37.

2-(4-methoxycarbonylphenyl)imidazo[4,5-f]-[1,10]phenanthroline (pic-COOMe)

Phendione (300 mg, 1eq) and 4-methoxycarbonylbenzaldehyde (300 mg, 1.3 eq) were heated to 100 °C in AcOH (7 mL) and stirred for 30 minutes. Solid ammonium acetate (2220 mg, 20 eq) was then added and the reaction was left to stir for 3 hours. The orange solution was then cooled to room temperature and 25 mL water was added. The yellow solids were filtered and washed thoroughly with water, acetone and diethyl ether to yield a cream coloured solid. Yield = 456 mg (90 %). ^{1}H NMR (400 MHz, DMSO-d_6): 9.00 (dd, 2H); 8.89 (dd, 2H); 8.38 (d, 2H); 8.09 (d, 2H); 7.79 (dd, 2H); 3.87 (s, 3H). ^{13}C NMR (100 MHz, DMSO-d_6): 165.88, 149.97, 147.77, 143.72, 134.80, 132.03, 129.82, 129.73, 129.56, 126.21, 123.30, 121.86, 52.27.

6-nitroquinoxaline (nitroquin)

4-nitro-o-phenylenediamine (4000 mg) was suspended in 100 mL of ethanol and heated to reflux. Glyoxal (aq, 40%) (7 mL) was added and heating at reflux continued for 3 hours. After cooling the reaction to ambient, the mixture was cooled further on an ice bath to provide the product as yellow crystals which were filtered, washed with cold ethanol and dried. Yield = 3440 mg (75 %). ^{1}H NMR (400 MHz, DMSO-d_6): 9.17 (s, 2H); 8.91 (d, 1 H); 8.57 (dd, 1H); 8.35 (d, 1 H). ^{13}C NMR (100MHz, DMSO-d_6): 148.87, 148.14, 147.59, 144.67, 141.01, 131.27, 125.27, 123.55.

5-amino-6-nitroquinoxaline (aminonitroquin)

Nitroquin (2000 mg) was suspended in 100 mL of methanol and heated to reflux. In a separate vessel placed in an ice bath, sodium metal (860 mg) was added in portions to a solution of hydroxylamine hydrochloride (1200 mg) in 70 mL methanol. After the addition was completed, a sodium chloride precipitate that formed was filtered off, and the methanolic solution was then added to the refluxing Nitroquin solution. After 2 hours at reflux the reaction mixture was cooled to room temperature and the solvent volume reduced to *ca.* 50 mL by rotary evaporation. The crude product that precipitated was filtered. Recrystallization from 3/1 acetic acid/water affords the product as a yellow powder. Yield = 1103 mg (51 %). ^{1}H NMR (400 MHz, DMSO-d_6): 9.09 (d, 1H); 8.93 (d, 1 H); 8.52 (s, br, 2H, N*H*); 8.28 (d, 1 H). ^{13}C NMR (100 MHz, DMSO-d_6): 148.81, 145.78, 145.05, 143.18, 134.11, 126.05, 126.01, 114.30.

5,6-diaminoquinoxaline (diaminoquin)

Aminonitroquin (1780 mg) was heated to reflux in 90 mL ethanol with 10 %wt. Pd/C catalyst (260 mg). After 1 hour, hydrazine hydrate (9.5 mL) was added and the reaction was heated at reflux for a further 2 hours. The reaction mixture was then filtered hot through a pad of celite, which was washed with 40 mL of dichloromethane. The filtrate was reduced to a sticky oil *in vacuo*, then taken up in chloroform and treated with cold hexane to precipitate the product as a burnt orange solid. Yield = 1240 mg (83 %) ^{1}H NMR (400 MHz, DMSO-d_6): 8.54 (d, 2 H); 7.23 (q, 2 H); 5.24 (s, br, 4H, N*H*). ^{13}C NMR (100 MHz, DMSO-d_6): 141.91, 140.12, 136.94, 133.04, 132.42, 126.07, 121.82, 116.35.

1,4,5,8- tetraazaphenanthrene (tap)

Diaminoquin (1050 mg) was dissolved in 15 mL ethanol containing 2 mL glyoxal solution (40% wt.). The mixture was headed to reflux for 6 hours, cooled to room temperature and reduced to dryness under diminished pressure. 50 mL of brine and 10 mL of 25 % w/v sodium hydroxide were added and the suspension that formed was extracted four times with 70 mL chloroform. The combined

organic phases were dried over anhydrous magnesium sulphate and evaporated down to a sticky oil *in vacuo*. Addition of cold hexane with stirring provides crude tap as a gold solid. Recrystallization from IPA/Hexane affords pure tap as a golden yellow solid. Yield = 1060 mg (87 %). ^{1}H NMR (400 MHz, $CDCl_3$): 9.14 (d, 2H); 9.08 (d, 2H); 8.33 (s, 2H). ^{13}C NMR (100 MHz, $CDCl_3$): 146.48, 145.27, 144.31, 140.97, 131.91.

$Ru(tap)_2Cl_2$

Tap (376 mg; 2eq), LiCl (265 mg; 6eq) and ascorbic acid (18 mg; 0.1eq) were stirred in ethylene glycol (10 mL) until full dissolution. $Ru(DMSO)_4Cl_2$ (500 mg; 1eq) was then added in full and stirring continued for a further 15 minutes. The black mixture was then cooled to room temperature and treated with 20 mL of water. The mixture was stirred for 10 minutes before the precipitate was filtered, washed thoroughly with water, acetone and diethyl ether. After drying in the vacuum, a purple solid was obtained. Yield = 418 mg (78 %). ^{1}H NMR (400 MHz, TFA-d): 10.52 (d, 2H); 9.49 (d, 2H); 8.80 (d, 2H); 8.71 (d, 2H); 8.65 (d, 2H); 8.44 (s, 2H). ^{1}H NMR (400 MHz, DMSO-d_6): 10.18 (s, 2 H); 9.48 (s, 2 H); 8.62 (s, 4 H); 8.49 (d, 2 H); 8.34 (s, 2 H).

General procedure for $[Ru(tap)_2(L)](PF_6)_2$

In a typical synthesis, $Ru(tap)_2Cl_2$ (100 mg, 1 eq.) and silver triflate, AgOTf (96 mg, 2 eq.) were heated to reflux in deionised water (3 mL) for 3 hours. The mixture was then cooled on ice and treated with 20 mL of acetone. The activated Ru-aquo complex was then filtered from insoluble AgCl and residual Ru-dichloride by passing the red mixture through a narrow bed of celite. The filtrate was then reduced to dryness *in vacuo* before the residue was taken up in a 4/1 ethylene glycol/water mixture (15 mL) to which the ligand (1.1 eq.) was then added in full. The mixture was heated at reflux for 8 hours and upon completion of the reaction, the mixture was cooled to room temperature and treated with saturated NH_4PF_6 solution until full precipitation of the crude *tris*-chelated complexes had occurred. The solids were filtered, washed with water and dried to afford the crude product which was then dissolved in acetone and filtered through celite. The filtrate was concentrated and added dropwise to stirring diethyl ether which precipitated the purified complexes which were filtered and dried. Further purification by flash chromatography on short silica columns was performed using 90/10/1 MeCN/H_2O/KNO_3 (20 % aq.) as eluent initially followed by 70/30 MeCN/0.1 M TsOH to elute the product. Where necessary, the PF_6^- form could be readily converted to the chloride form by precipitation from acetone using tetrabutylammonium chloride.

$[Ru(tap)_2(bpyArCOOEt)](PF_6)_2$

Yield = Orange Solid; 158 mg, 80 %. ^{1}H NMR (400 MHz, CD_3CN): 9.11 (t, 2 H); 8.91 (d, 2 H); 8.82 (d, 1 H); 8.75 (d, 1 H); 8.61 (qd, 4 H); 8.39 (d, 1 H); 8.31 (d, 1 H); 8.18 (m, 3 H); 8.13 (t, 2 H); 7.97 (d, 2 H); 7.79 (t, 2 H); 7.63 (t, 2 H); 7.40 (t, 1 H); 4.38 (q, 2 H), 1.38 (t, 3 H). ^{1}H NMR (600 MHz, CD_3OD/D_2O, Cl^- form): 9.21 (s, 2 H); 9.11 (d, 1 H, J = 1.8 Hz); 9.02 (d, 1 H, J = 7.2 Hz); 9.01 (m, 2 H, J = 1.8 Hz); 8.68 (q, 4 H, J = 9.6 Hz); 8.58 (d, 1 H, J = 3 Hz); 8.47 (d, 1 H, J = 3 Hz); 8.35 (t, 2 H, J = 3 Hz); 8.23 (t, 1 H, J = 7.2 Hz); 8.20 (d, 2 H, J = 8.4 Hz); 8.06 (d, 2 H, J = 8.4 Hz); 7.93 (m, 2 H, J = 6 Hz); 7.81 (d, 1 H, J = 2.4 Hz); 7.52 (t, 1 H, J = 7.2 Hz); 4.41 (q, 2 H, J = 7.2 Hz); 1.41 (t, 3 H, J = 7.2 Hz). ^{13}C NMR (100 MHz, CD_3CN): 166.41, 158.00, 157.40, 154.16, 154.03, 150.74, 150.45, 150.38, 149.72, 149.66, 149.31, 146.48, 146.45, 146.36, 143.22, 143.19, 142.83, 140.45, 140.13, 133.76, 133.70, 133.24, 131.05, 128.89, 128.72, 126.12, 125.67, 123.26, 62.18, 14.43. Anal. Calculated (Found) for $C_{39}H_{28}F_{12}N_{10}O_2P_2Ru.H_2O$: C 43.46 (43.69), H 2.81 (2.37), N 13.00 (12.51). HRMS (ESI-TOF) *m/z*: Calculated for $C_{39}H_{28}N_{10}O_2F_6PRu$ $[M^{2+} + PF_6^-]^+$: 915.1082; Found: 915.1121.

$[Ru(tap)_2(bpyArCOOH)](PF_6)_2$

Yield = Orange solid; 110 mg, 57 %. ^{1}H NMR (400 MHz, CD_3CN): 9.11 (t, 2 H, J = 2.8 Hz); 8.91 (d, 2 H, J = 2.8 Hz); 8.83 (d, 1 H, J = 2 Hz); 8.76 (d, 1 H, J = 6.4 Hz); 8.61 (qd, 4 H); 8.38 (d, 1 H, J = 2.8 Hz); 8.31 (d, 1 H, J = 2.8 Hz); 8.18 (d, 3 H, J = 8.4 Hz); 8.13 (t, 2 H, J = 2.8 Hz); 7.96 (d, 2 H, J = 8.4 Hz); 7.78 (t, 2 H, J = 6.4 Hz); 7.63 (dd, 1 H, J = 6.4 Hz); 7.40 (td, 1 H, J = 6.4 Hz). ^{13}C NMR (100 MHz, CD_3CN): 157.99, 157.40, 154.16, 154.02, 150.74, 150.44, 150.38, 149.73, 149.67, 149.32, 146.47, 146.44, 146.35, 143.21, 143.19, 142.86, 142.82, 140.60, 140.13, 133.75, 133.70, 132.79, 131.42, 128.89, 128.71, 126.15, 125.69, 123.28. HRMS (ESI-TOF) *m/z*: Calculated for $C_{37}H_{24}N_{10}O_2F_6PRu$ $[M^{2+} + PF_6^-]^+$: 887.0769; Found: 887.0806.

$[Ru(tap)_2(pic\text{-}COOH)](PF_6)_2$

Yield = Orange solid; 153 mg, 76 %. ^{1}H NMR (400 MHz, CD_3CN): 12.53 (s, 1 H); 9.06 (d, 2H, J = 4.4 Hz); 8.96 (dd, 4 H, J = 2.8 Hz); 8.61 (s, 4 H); 8.26 (m, 4 H, J = 2.8, 8 Hz); 8.23 (d, 2 H, J = 2.8 Hz); 8.07 (dd, 2 H, J = 1.2, 5.2 Hz); 8.02 (d, 2 H, J = 8 Hz); 7.75 (dd, 2 H, J = 5.2 Hz). ^{13}C NMR (100 MHz, CD_3CN): 167.00, 152.78, 152.71, 150.39, 150.27, 149.95, 149.50, 146.37, 146.31, 146.18, 143.24, 143.10, 133.96, 133.71, 133.62, 132.92, 132.13, 131.13, 127.42, 127.15. HRMS (ESI-TOF) *m/z*: Calculated for $C_{40}H_{23}N_{12}O_2Ru$ $[M^{2+} - H^+]^+$: 805.1110; Found: 805.1080.

$[Ru(tap)_2(pic\text{-}COOMe)](PF_6)_2$

Yield = Orange solid; 178 mg, 86 %. ^{1}H NMR (400 MHz, Acetone-d_6): 9.19 (d, 2 H, J = 8.4 Hz); 9.06 (dd, 4 H, J = 2.8 Hz); 8.79 (d, 2 H, J = 2.8 Hz); 8.69 (d, 2H, J = 2.8 Hz); 8.67 (s, 4 H); 8.52 (dd, 2 H, J = 1.2, 5.2 Hz); 8.43 (d, 2 H, J = 8.4 Hz); 8.18 (t, 2 H, J = 8.4 Hz); 7.87 (dd, 2 H, J = 8.4, 1.2 Hz); 3.90 (s, 3 H). ^{13}C NMR (100 MHz, CD_3CN): 166.90, 153.08, 152.68, 150.38, 150.29, 149.97, 149.55, 146.42, 146.36, 146.21, 143.28, 143.16, 134.20, 133.75, 133.66, 132.95, 132.41, 130.95, 127.58, 127.11, 52.88. HRMS (ESI-TOF) *m/z*: Calculated for $C_{41}H_{25}N_{12}O_2Ru$ $[M^{2+} - H^+]^+$: 819.1267; Found: 819.1304.

$[Ru(tap)_2(bpyArCONH\text{-}Ahx\text{-}VQRKRQKLMP\text{-}CONH_2)]^{6+}$ (Ru-tap-NLS)

The Ru-tap peptide conjugate was synthesised using a PyBOP/DIPEA/DMF coupling system as described in Chapter 3. Typically, $[Ru(tap)_2(bpyArCOOH)](PF_6)_2$ (10 mg, 1 eq.), PyBOP (2 eq.) and DIPEA (20 μL) were dissolved in DMF (700 μL). The peptide (2 eq.) was added and stirring continued for at least 16 hours at room temperature in the dark. The reaction was then added dropwise to a saturated stirring solution of tetrabutylammonium chloride in acetone to precipitate the crude conjugate as the Cl^- salt. The isolated bright orange solids were washed well with acetone, diethyl ether and dried. Where further purification was required, the conjugate was subjected to preparative TLC on C18-silica using 0.1 % TFA in acetonitrile/water to resolve any impurities, followed by cleavage from the solid phase in the same eluent and re-precipitation as the chloride salt. Yield: Red solid. ^{1}H NMR (600 MHz, 99/1 CD_3OD/D_2O); 9.13 – 9.21 (m, 2 H); 9.07 (br s, 1 H); 9.00 (br m, 3 H); 8.56 – 8.71 (m, 4 H); 8.47 (br s, 1 H); 8.33 – 8.39 (m, 2 H); 8.24 (br m, 1 H); 7.98 – 8.05 (m, 3 H); 7.89 – 7.97 (m, 3 H); 7.87 (d, 1 H); 7.79 (br m, 1 H); 7.50 (br m, 1 H); 3.87 – 4.46 (m, 10 H, Alpha-H Peptide); 3.59 – 3.83 (br m, 3 H); 3.23 (m, 10 H); 2.92 (br m, 4 H); 2.51 – 2.72 (br m, 3 H); 2.26 – 2.46 (2x br s, 8 H); 2.20 (m, 1 H); 1.78 – 2.04 (br m, 14 H); 1.67 (br m, 17 H); 1.52 (m, 4 H); 1.42 (m, 6 H); 1.29 (br d, 3 H); 0.76 – 1.05 (br m, 17 H). HR-MS (Cl^- form; Q-Exactive, Ion-Trap MS^+, CH_3OH/TFA); Calculated for $C_{98}H_{140}N_{32}O_{14}RuS$ $[M]^{6+}$ 353.9999, Found 353.7231; $[M]^{3+}$ Calculated 706.9925, Found 706.4377. HPLC (C18, 0.1 % TFA in H_2O/CH_3CN gradient); Retention time = 11.2 minutes (no parent peak at 14.1 min).

5.5 References

(1) Sherman, S. E.; Lippard, S. J. *Chem. Rev.* **1987**, *87* (5), 1153.
(2) Sigman, D. S.; Landgraf, R.; Perrin, D. M.; Pearson, L. *Met. Ions Biol. Syst.* **1996**, *33*, 485.
(3) Zenkova, M. A. *Artificial Nucleases*; Springer Science & Business Media, 2012.
(4) Knoll, J. D.; Turro, C. *Coord. Chem. Rev.* **2015**, *282–283*, 110.
(5) Monro, S.; Scott, J.; Chouai, A.; Lincoln, R.; Zong, R.; Thummel, R. P.; McFarland, S. A. *Inorg. Chem.* **2010**, *49* (6), 2889.
(6) Lincoln, R.; Kohler, L.; Monro, S.; Yin, H.; Stephenson, M.; Zong, R.; Chouai, A.; Dorsey, C.; Hennigar, R.; Thummel, R. P.; McFarland, S. A. *J. Am. Chem. Soc.* **2013**, *135* (45), 17161.
(7) Baldea, I.; Filip, A. G. *J. Physiol. Pharmacol. Off. J. Pol. Physiol. Soc.* **2012**, *63* (2), 109.
(8) Bertout, J. A.; Patel, S. A.; Simon, M. C. *Nat. Rev. Cancer* **2008**, *8* (12), 967.
(9) Wilson, W. R.; Hay, M. P. *Nat. Rev. Cancer* **2011**, *11* (6), 393.
(10) Eales, K. L.; Hollinshead, K. E. R.; Tennant, D. A. *Oncogenesis* **2016**, *5* (1), e190.
(11) Howerton, B. S.; Heidary, D. K.; Glazer, E. C. *J. Am. Chem. Soc.* **2012**, *134* (20), 8324.
(12) Wachter, E.; Howerton, B. S.; Hall, E. C.; Parkin, S.; Glazer, E. C. *Chem. Commun.* **2013**, *50* (3), 311.
(13) Wachter, E.; Moyá, D.; Parkin, S.; Glazer, E. C. *Chem. – Eur. J.* **2016**, *22* (2), 550.
(14) Wachter, E.; Heidary, D. K.; Howerton, B. S.; Parkin, S.; Glazer, E. C. *Chem. Commun.* **2012**, *48* (77), 9649.
(15) Cuello-Garibo, J.-A.; Pérez-Gallent, E.; van der Boon, L.; Siegler, M. A.; Bonnet, S. *Inorg. Chem.* **2017**, *56* (9), 4818.
(16) Cuello-Garibo, J.-A.; Meijer, M. S.; Bonnet, S. *Chem. Commun.* **2017**, *53* (50), 6768.
(17) Sun, W.; Li, S.; Häupler, B.; Liu, J.; Jin, S.; Steffen, W.; Schubert, U. S.; Butt, H.-J.; Liang, X.-J.; Wu, S. *Adv. Mater.* **2017**, *29* (6), n/a.
(18) Wyland, K. R.; Hoffman, E. E.; Jain, A. *Inorganica Chim. Acta* **2017**, *454*, 62.
(19) Albani, B. A.; Peña, B.; Leed, N. A.; de Paula, N. A. B. G.; Pavani, C.; Baptista, M. S.; Dunbar, K. R.; Turro, C. *J. Am. Chem. Soc.* **2014**, *136* (49), 17095.
(20) Zamora, A.; Denning, C. A.; Heidary, D. K.; Wachter, E.; Nease, L. A.; Ruiz, J.; Glazer, E. C. *Dalton Trans.* **2017**, *46* (7), 2165.
(21) Knoll, J. D.; Albani, B. A.; Turro, C. *Acc. Chem. Res.* **2015**, *48* (8), 2280.
(22) White, J. K.; Schmehl, R. H.; Turro, C. *Inorganica Chim. Acta* **2017**, *454*, 7.
(23) Karaoun, N.; Renfrew, A. K. *Chem. Commun.* **2015**, *51* (74), 14038.
(24) Siewert, B.; van Rixel, V. H. S.; van Rooden, E. J.; Hopkins, S. L.; Moester, M. J. B.; Ariese, F.; Siegler, M. A.; Bonnet, S. *Chem. – Eur. J.* **2016**, *22* (31), 10960.
(25) Rixel, V. H. S. van; Siewert, B.; Hopkins, S. L.; Askes, S. H. C.; Busemann, A.; Siegler, M. A.; Bonnet, S. *Chem. Sci.* **2016**, *7* (8), 4922.
(26) Knoll, J. D.; Albani, B. A.; Turro, C. *Chem. Commun.* **2015**, *51* (42), 8777.
(27) Frasconi, M.; Liu, Z.; Lei, J.; Wu, Y.; Strekalova, E.; Malin, D.; Ambrogio, M. W.; Chen, X.; Botros, Y. Y.; Cryns, V. L.; Sauvage, J.-P.; Stoddart, J. F. *J. Am. Chem. Soc.* **2013**, *135* (31), 11603.
(28) Melvin, T.; Cunniffe, S. M.; O'Neill, P.; Parker, A. W.; Roldan-Arjona, T. *Nucleic Acids Res.* **1998**, *26* (21), 4935.
(29) Sun, Y.; Joyce, L. E.; Dickson, N. M.; Turro, C. *Chem. Commun.* **2010**, *46* (14), 2426.
(30) Saeed, H. K.; Jarman, P. J.; Archer, S.; Sreedharan, S.; Saeed, I. Q.; Mckenzie, L. K.; Weinstein, J. A.; Buurma, N. J.; Smythe, C. G. W.; Thomas, J. A. *Angew. Chem. Int. Ed.* n/a.
(31) Moucheron, C.; Kirsch-De Mesmaeker, A.; Kelly, J. M. *J. Photochem. Photobiol. B* **1997**, *40* (2), 91.

(32) Marcélis, L.; Ghesquière, J.; Garnir, K.; Kirsch-De Mesmaeker, A.; Moucheron, C. *Coord. Chem. Rev.* **2012**, *256* (15–16), 1569.
(33) Jacquet, L.; Davies, R. J. H.; Kirsch-De Mesmaeker, A.; Kelly, J. M. *J. Am. Chem. Soc.* **1997**, *119* (49), 11763.
(34) Blasius, R.; Nierengarten, H.; Luhmer, M.; Constant, J.-F.; Defrancq, E.; Dumy, P.; van Dorsselaer, A.; Moucheron, C.; Kirsch-DeMesmaeker, A. *Chem. – Eur. J.* **2005**, *11* (5), 1507.
(35) Boddu, V. M.; Viswanath, D. S.; Ghosh, T. K.; Damavarapu, R. *J. Hazard. Mater.* **2010**, *181* (1–3), 1.
(36) Silva, G. da; Mattos, E. da C. *J. Aerosp. Technol. Manag.* **2011**, *3* (1), 65.
(37) Rogers, D. Z. *J. Org. Chem.* **1986**, *51* (20), 3904.
(38) Sahai, R.; Rillema, D. P.; Shaver, R.; Van Wallendael, S.; Jackman, D. C.; Boldaji, M. *Inorg. Chem.* **1989**, *28* (6), 1022.
(39) Moucheron, C.; Kirsch-De Mesmaeker, A.; Dupont-Gervais, A.; Leize, E.; Van Dorsselaer, A. *J. Am. Chem. Soc.* **1996**, *118* (50), 12834.
(40) Elmes, R. B. P.; Erby, M.; Cloonan, S. M.; Quinn, S. J.; Williams, D. C.; Gunnlaugsson, T. *Chem. Commun.* **2010**, *47* (2), 686.
(41) Nasielski-Hinkens, R.; Benedek-Vamos, M. *J. Chem. Soc. [Perkin 1]* **1975**, No. 13, 1229.
(42) Lecomte, J.-P.; Kirsch-De Mesmaeker, A.; Feeney, M. M.; Kelly, J. M. *Inorg. Chem.* **1995**, *34* (26), 6481.
(43) Ortmans, I.; Elias, B.; Kelly, J. M.; Moucheron, C.; Kirsch-DeMesmaeker, A. *Dalton Trans.* **2004**, No. 4, 668.
(44) Lecomte, J.-P.; Mesmaeker, A. K.-D.; Kelly, J. M.; Tossi, A. B.; Görner, H. *Photochem. Photobiol.* **1992**, *55* (5), 681.
(45) Elias, B.; Creely, C.; Doorley, G. W.; Feeney, M. M.; Moucheron, C.; Kirsch-DeMesmaeker, A.; Dyer, J.; Grills, D. C.; George, M. W.; Matousek, P.; Parker, A. W.; Towrie, M.; Kelly, J. M. *Chem. – Eur. J.* **2008**, *14* (1), 369.
(46) Feeney, M. M.; Kelly, J. M.; Tossi, A. B.; Mesmaeker, A. K.; Lecomte, J.-P. *J. Photochem. Photobiol. B* **1994**, *23* (1), 69.
(47) Elias, B.; Kirsch-De Mesmaeker, A. *Coord. Chem. Rev.* **2006**, *250* (13–14), 1627.
(48) Perrier, S.; Mugeniwabagara, E.; Kirsch-De Mesmaeker, A.; Hore, P. J.; Luhmer, M. *J. Am. Chem. Soc.* **2009**, *131* (34), 12458.
(49) Masschelein, A.; Jacquet, L.; Kirsch-De Mesmaeker, A.; Nasielski, J. *Inorg. Chem.* **1990**, *29* (4), 855.
(50) Content, S.; Mesmaeker, A. K.-D. *J. Chem. Soc. Faraday Trans.* **1997**, *93* (6), 1089.
(51) Satyanarayana, S.; Dabrowiak, J. C.; Chaires, J. B. *Biochemistry (Mosc.)* **1993**, *32* (10), 2573.
(52) Hall, J. P.; Poynton, F. E.; Keane, P. M.; Gurung, S. P.; Brazier, J. A.; Cardin, D. J.; Winter, G.; Gunnlaugsson, T.; Sazanovich, I. V.; Towrie, M.; Cardin, C. J.; Kelly, J. M.; Quinn, S. J. *Nat. Chem.* **2015**, *7* (12), 961.
(53) Le Gac, S.; Foucart, M.; Gerbaux, P.; Defrancq, E.; Moucheron, C.; Kirsch - De Mesmaeker, A. *Dalton Trans.* **2010**, *39* (40), 9672.
(54) Ghizdavu, L.; Pierard, F.; Rickling, S.; Aury, S.; Surin, M.; Beljonne, D.; Lazzaroni, R.; Murat, P.; Defrancq, E.; Moucheron, C.; Kirsch-De Mesmaeker, A. *Inorg. Chem.* **2009**, *48* (23), 10988.
(55) Kelly, J. M.; McConnell, D. J.; OhUigin, C.; Tossi, A. B.; Mesmaeker, A. K.-D.; Masschelein, A.; Nasielski, J. *J. Chem. Soc. Chem. Commun.* **1987**, No. 24, 1821.
(56) Uji-i, H.; Foubert, P.; De Schryver, F. C.; De Feyter, S.; Gicquel, E.; Etoc, A.; Moucheron, C.; Kirsch-De Mesmaeker, A. *Chem. – Eur. J.* **2006**, *12* (3), 758.
(57) Pauly, M.; Kayser, I.; Schmitz, M.; Dicato, M.; Guerzo, A. D.; Kolber, I.; Moucheron, C.; Mesmaeker, A. K.-D. *Chem. Commun.* **2002**, No. 10, 1086.

(58) Marcélis, L.; Kajouj, S.; Ghesquière, J.; Fettweis, G.; Coupienne, I.; Lartia, R.; Surin, M.; Defrancq, E.; Piette, J.; Moucheron, C.; Kirsch-De Mesmaeker, A. *Eur. J. Inorg. Chem.* **2016**, *2016* (18), 2902.
(59) García-Fresnadillo, D.; Boutonnet, N.; Schumm, S.; Moucheron, C.; Kirsch-De Mesmaeker, A.; Defrancq, E.; Constant, J. F.; Lhomme, J. *Biophys. J.* **2002**, *82* (2), 978.
(60) Le Gac, S.; Surin, M.; Defrancq, E.; Moucheron, C.; Kirsch-De Mesmaeker, A. *Eur. J. Inorg. Chem.* **2013**, *2013* (2), 208.
(61) Le Gac, S.; Rickling, S.; Gerbaux, P.; Defrancq, E.; Moucheron, C.; Kirsch-De Mesmaeker, A. *Angew. Chem.* **2009**, *121* (6), 1142.
(62) Ghesquière, J.; Gauthier, N.; De Winter, J.; Gerbaux, P.; Moucheron, C.; Defrancq, E.; Kirsch-De Mesmaeker, A. *Chem. – Eur. J.* **2012**, *18* (1), 355.
(63) Marcélis, L.; Surin, M.; Lartia, R.; Moucheron, C.; Defrancq, E.; Kirsch-De Mesmaeker, A. *Eur. J. Inorg. Chem.* **2014**, *2014* (19), 3016.
(64) Marcélis, L.; Van Overstraeten-Schlögel, N.; Lambermont, J.; Bontems, S.; Spinelli, N.; Defrancq, E.; Moucheron, C.; Kirsch-De Mesmaeker, A.; Raes, M. *ChemPlusChem* **2014**, *79* (11), 1597.
(65) Reschner, A.; Bontems, S.; Le Gac, S.; Lambermont, J.; Marcélis, L.; Defrancq, E.; Hubert, P.; Moucheron, C.; Kirsch-De Mesmaeker, A.; Raes, M.; Piette, J.; Delvenne, P. *Gene Ther.* **2013**, *20* (4), 435.
(66) Poulsen, B. C.; Estalayo-Adrián, S.; Blasco, S.; Bright, S. A.; Kelly, J. M.; Williams, D. C.; Gunnlaugsson, T. *Dalton Trans.* **2016**, *45* (45), 18208.
(67) Cloonan, S. M.; Elmes, R. B. P.; Erby, M.; Bright, S. A.; Poynton, F. E.; Nolan, D. E.; Quinn, S. J.; Gunnlaugsson, T.; Williams, D. C. *J. Med. Chem.* **2015**, *58* (11), 4494.
(68) Elmes, R. B. P.; Orange, K. N.; Cloonan, S. M.; Williams, D. C.; Gunnlaugsson, T. *J. Am. Chem. Soc.* **2011**, *133* (40), 15862.
(69) Byrne, A.; Burke, C. S.; Keyes, T. E. *Chem. Sci.* **2016**, *7* (10), 6551.
(70) Blackmore, L.; Moriarty, R.; Dolan, C.; Adamson, K.; Forster, R. J.; Devocelle, M.; Keyes, T. E. *Chem. Commun.* **2013**, *49* (26), 2658.
(71) Dolan, C.; Moriarty, R. D.; Lestini, E.; Devocelle, M.; Forster, R. J.; Keyes, T. E. *J. Inorg. Biochem.* **2013**, *119*, 65.
(72) Adamson, K.; Dolan, C.; Moran, N.; Forster, R. J.; Keyes, T. E. *Bioconjug. Chem.* **2014**, *25* (5), 928.
(73) Neugebauer, U.; Pellegrin, Y.; Devocelle, M.; Forster, R. J.; Signac, W.; Moran, N.; Keyes, T. E. *Chem. Commun.* **2008**, No. 42, 5307.
(74) Cosgrave, L.; Devocelle, M.; Forster, R. J.; Keyes, T. E. *Chem. Commun.* **2010**, *46* (1), 103.
(75) Byrne, A.; Dolan, C.; Moriarty, R. D.; Martin, A.; Neugebauer, U.; Forster, R. J.; Davies, A.; Volkov, Y.; Keyes, T. E. *Dalton Trans.* **2015**, *44* (32), 14323.
(76) Pellegrin, Y.; Forster, R. J.; Keyes, T. E. *Inorganica Chim. Acta* **2009**, *362* (6), 1715.
(77) Case, F. H.; Brennan, J. A. *J. Am. Chem. Soc.* **1959**, *81* (23), 6297.
(78) Nasielski-Hinkens, R.; Benedek-Vamos, M.; Maetens, D. *J. Heterocycl. Chem.* **1980**, *17* (5), 873.
(79) Villien, M.; Deroo, S.; Gicquel, E.; Defrancq, E.; Moucheron, C.; Kirsch-De Mesmaeker, A.; Dumy, P. *Tetrahedron* **2007**, *63* (46), 11299.
(80) Steck, E. A.; Day, A. R. *J. Am. Chem. Soc.* **1943**, *65* (3), 452.
(81) Dolan, C. The synthesis and characterisation of inorganic and organic luminophores suitable for biomolecule conjugation. PhD Thesis, Dublin City University. School of Chemical Sciences, 2012.
(82) Kirsch-De Mesmaeker, A.; Jacquet, L.; Nasielski, J. *Inorg. Chem.* **1988**, *27* (24), 4451.
(83) Sullivan, B. P.; Salmon, D. J.; Meyer, T. J. *Inorg. Chem.* **1978**, *17* (12), 3334.
(84) Burke, C. S.; Keyes, T. E. *RSC Adv.* **2016**, *6* (47), 40869.
(85) Mugeniwabagara, E.; Fusaro, L.; Luhmer, M. *Magn. Reson. Chem.* **2013**, *51* (5), 308.

(86) Xie, X.; Mulcahy, S. P.; Meggers, E. *Inorg. Chem.* **2009**, *48* (3), 1053.
(87) Mattiuzzi, A.; Jabin, I.; Moucheron, C.; Mesmaeker, A. K.-D. *Dalton Trans.* **2011**, *40* (28), 7395.
(88) Suzuki, K.; Kobayashi, A.; Kaneko, S.; Takehira, K.; Yoshihara, T.; Ishida, H.; Shiina, Y.; Oishi, S.; Tobita, S. *Phys. Chem. Chem. Phys.* **2009**, *11* (42), 9850.
(89) Rebarz, M.; Marcélis, L.; Menand, M.; Cornut, D.; Moucheron, C.; Jabin, I.; Kirsch-De Mesmaeker, A. *Inorg. Chem.* **2014**, *53* (5), 2635.
(90) Gicquel, E.; Boisdenghien, A.; Defrancq, E.; Moucheron, C.; Mesmaeker, A. K.-D. *Chem. Commun.* **2004**, No. 23, 2764.
(91) Gauthier, N.; De Winter, J.; Gerbaux, P.; Moucheron, C.; Luhmer, M.; Kirsch-De Mesmaeker, A. *Inorg. Chem.* **2010**, *49* (15), 6796.
(92) Rebarz, M.; Ghesquière, J.; Boisdenghien, A.; Defrancq, E.; Moucheron, C.; Kirsch-De Mesmaeker, A. *Inorg. Chem.* **2010**, *49* (23), 10867.
(93) Majorek, K. A.; Porebski, P. J.; Dayal, A.; Zimmerman, M. D.; Jablonska, K.; Stewart, A. J.; Chruszcz, M.; Minor, W. *Mol. Immunol.* **2012**, *52* (3–4), 174.
(94) Wragg, A.; Gill, M. R.; McKenzie, L.; Glover, C.; Mowll, R.; Weinstein, J. A.; Su, X.; Smythe, C.; Thomas, J. A. *Chem. – Eur. J.* **2015**, *21*, 11865.
(95) Spahr, P. F.; Edsall, J. T. *J. Biol. Chem.* **1964**, *239* (3), 850.
(96) Moriyama, Y.; Ohta, D.; Hachiya, K.; Mitsui, Y.; Takeda, K. *J. Protein Chem.* **1996**, *15* (3), 265.
(97) Lecomte, J.-P.; Kirsch-De Mesmaeker, A.; Orellana, G. *J. Phys. Chem.* **1994**, *98* (20), 5382.
(98) Marcélis, L.; Rebarz, M.; Lemaur, V.; Fron, E.; De Winter, J.; Moucheron, C.; Gerbaux, P.; Beljonne, D.; Sliwa, M.; Kirsch-De Mesmaeker, A. *J. Phys. Chem. B* **2015**, *119* (12), 4488.
(99) Basu, A.; Gafney, H. D.; Strekas, T. C. *Inorg. Chem.* **1982**, *21* (6), 2231.

Chapter 6

Ru(II) luminophores: additional applications in biological imaging and sensing

Notes

All cell work reported in this chapter was performed by Dr. Aisling Byrne (DCU). All electrochemistry was carried out by Dr. Kerileng Molapo (DCU).

6.1 Introduction

The chapter explores additional biological imaging and sensing applications of selected Ru(II) luminophores synthesised under the work of Chapter 3 of this thesis. The three areas under investigation are; (i) DNA binding induced electrochemiluminscence (ECL) of Ru-dppz complexes, (ii) an exploration of the candidacy of metal complex luminophores for high resolution STED imaging, and (iii) the application of peptide-directed Ru-dppz complexes for light-switch imaging of amyloid-β (Aβ) fibrillisation in live cells.

6.1.1 DNA binding induced electrochemiluminescence at monolayers of a Ru(II) molecular light switch

Electrochemiluminescence (ECL) detection is a powerful modality to probe redox active analytes. ECL does not require an excitation light source which eliminates the optical background and thus leads to enhanced sensitivity and selectivity over a wide linear dynamic range.[1] Metal complex luminophores have previously been exploited for ECL DNA detection, most notably using Ru(II) and Os(II) complexes as pioneered by the Bard group.[2,3] Typically, electro-generation of an oxidised metal complex instigates DNA base oxidations, usually at guanine and adenine, and yields a metal complex in its excited state from which luminescence may occur.

Recently, Xu *et al*. explored the ECL response of $[Ru(bpy)_2(dppz)]^{2+}$ in the presence of oxalate as a co-reactant and found negligible ECL in aqueous media but significant ECL 'switch-on' in the presence of DNA.[4] The light-switch effect of $[Ru(bpy)_2(dppz)]^{2+}$ following optical excitation has been investigated in detail by several groups[5–7] and forms the basis of Chapter 4 of this thesis towards live cell DNA imaging. In brief, the origin of the effect can be attributed to different Ru-dppz based excited states which persist in aqueous and non-aqueous media; a bright and dark state localised on the phen and phenazine moieties respectively, the accessibility of which is mediated by hydrogen bonding to the phenazine nitrogens.[7]

To date, most metal complex ECL detections of DNA have been performed in solution, but immobilisation of the ECL probe at a surface offers previously underexploited advantages.

For example; the benefit of improved process cycling, a reduction in ECL reagent consumption, and an enhancement of the ECL response due to surface confinement that prevents analyte and probe diffusion out of the detection zone. An objective of the present work was therefore to combine the light-switch properties of Ru-dppz complexes with the advantages of surface confinement at a monolayer for the capture and report sensing of DNA using ECL.

6.1.2 Candidacy of precision-targeted ruthenium(II) luminophores for cell imaging by stimulated emission depletion (STED) microscopy

The development of super-resolution microscopies that break the light diffraction limit has provided exciting new opportunities to study cellular structure and function at the nanoscale.[8] STED is one of the best known of these techniques and operates by stimulating a de-excitation of the luminophore in a doughnut-shaped depletion zone around the focal region (Figure 6.1).[9,10] The resolution achieved by the STED process is inherently linked to the photophysics of the luminophore and a good STED probe must fulfil several critical criteria.[11,12] Since STED efficiency is related to laser power, the probe must exhibit excellent photostability and sufficient cross-section of its emission band with the depletion laser. It follows that the probe should possess sufficiently Stokes-shifted emission to enable maximum overlap with the depletion laser without sensitising a photoactive or long-lived dark state. The STED pulse must interact with the probe in its excited state and the pulse width must be narrower than the excited state lifetime of the fluorophore. This implies longer-lived luminophores are better suited to the technique which also facilitates time-gating experiments to improve sensitivity.

As discussed in Chapter 1, to date, organic probes have been used exclusively for STED despite their inability to fully meet the key criteria of an ideal STED probe with typically narrow Stokes-shifts, short-lived excited states and susceptibility to photodegradation. Luminescent metal complexes such as those of Ru(II) offer untapped potential as they possess characteristically long lifetimes, strongly Stokes-shifted emission and good photostability. All suitable imaging probes must localise precisely to their target, and as established in previous chapters of this thesis, peptide conjugation is a highly effective

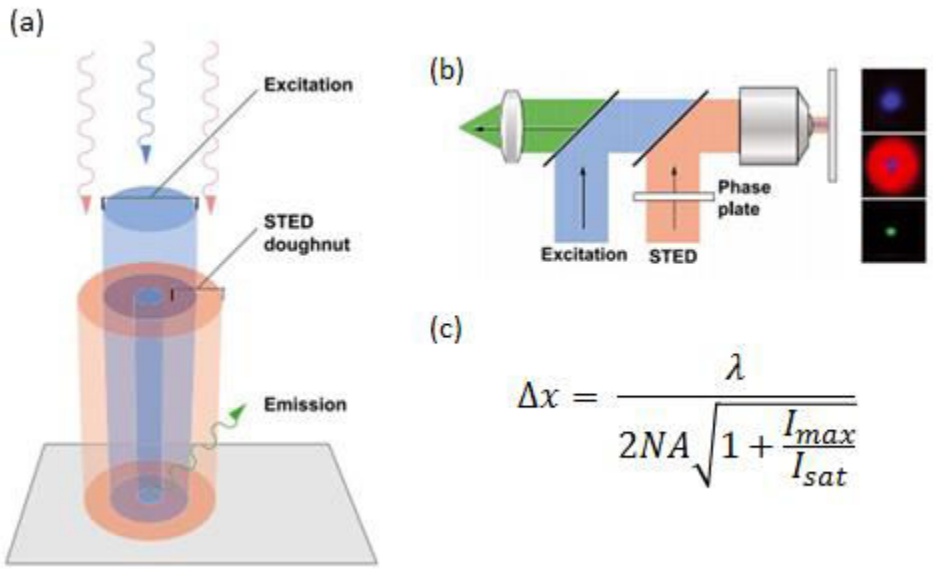

Figure 6.1: Principle of STED. (a) The STED laser (red) depletes a doughnut shaped region around the luminophore excited initially by the excitation laser (blue). The resolution of the consequent emission is enhanced as shown in (b). Image adapted from Blom and Brismar.[13] (c) The lateral resolution in STED (Δx) depends on λ (the emission wavelength), the numerical aperture (NA), the peak intensity at the STED depletion zone (I_{max}), and the STED laser intensity that yields 50% depletion of the probe emission intensity (I_{sat}).

---

method to precision target Ru(II) complexes to select organelles. In Chapter 4, Ru-NLS was shown to illuminate chromosomal DNA with remarkable clarity under STED imaging. In this chapter, the candidacy of peptide-directed Ru(II) luminophores to act as efficient STED probes was further investigated using different probes targeted to different cellular locales such as the actin and endoplasmic reticulum.

6.1.3 Towards targeted imaging of Amyloid-beta aggregation in live cells using light-switching Ru(II) peptide conjugates

The β-amyloid peptide (Aβ) typically comprises 39–43 amino acids and can spontaneously self-aggregate into fibrils, aggregates and plaque deposits which have been linked to neurodegenerative disorders such as Alzheimer's disease.[14] Development of novel methods of detection, destruction and prevention of these formations has been an area of intense

interest in recent years. $[Ru(bpy)_2(dppz)]^{2+}$ demonstrates light-switch activity selectively against fibrillar forms of Aβ with negligible luminescence observed in the presence of monomers.[15,16] A critical issue towards realising the diagnostic potential of $[Ru(bpy)_2(dppz)]^{2+}$ is selectivity for Aβ in the presence of other biological substrates. For example, Ru(II)-dppz complexes were demonstrated in Chapter 4 of this thesis to act as molecular light-switches for DNA. Additionally, similar Ru(II)-phenazine complexes have been reported to bind other biomacromolecules such as RNA[17], proteins[15,18] and cellular membranes[19–21]. Peptide conjugation is a useful method to implement a targeting element in the probe. Research involving Aβ binding has focussed on derivatives of lipophilic motifs of the amyloid sequence that mediate aggregation, such as ^{16}KLVFF[20], but this can lead to self-aggregation and poor specificity of the probe.[22–25] However, a recent report by Aoraha *et al*. described a synthetic peptide that does not self-aggregate and does not bind monomers.[26] Their sequence, KLVFWAK, was exploited in the present work to produce a Ru(II)-dppz conjugate designed to target fibrillar or higher order toxic structures of Aβ. Furthermore, it is anticipated that the probe will be suited to high resolution STED imaging of Aβ deposits in live cells.

6.2 Results and discussion

6.2.1 ECL as a probe of DNA binding by Ru-dppz complexes

6.2.1.1 Photophysical and electrochemical characterisation of the probe

$[Ru(bpyArCOOH)_2(dppz)]^{2+}$ was selected as a suitable ECL probe for DNA due to its Ru-dppz light-switch properties and the presence of two pendant carboxylic acid groups that facilitate its surface binding to electrodes (Figure 6.2). The synthesis of this complex is described in Chapter 3 of this thesis and the complex was used in the ECL study as a mixture of its geometric isomers.

The photophysics of $[Ru(bpyArCOOH)_2(dppz)]^{2+}$ closely mimic that observed for the archetype complex, $[Ru(bpy)_2(dppz)]^{2+}$, and its monofunctionalised analogue, $[Ru(dppz)(bpy)(bpyArCOOH)]^{2+}$, which are studied in greater detail in Chapter 4. Briefly, $[Ru(bpyArCOOH)_2(dppz)]^{2+}$ exhibits the expected bpy and dppz based absorptions in the

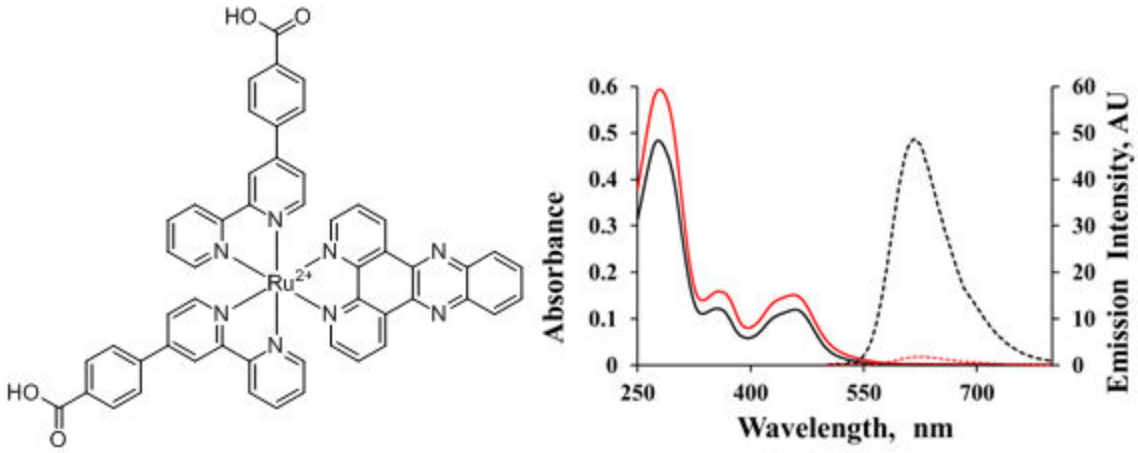

Figure 6.2: Left: Structure of $[Ru(bpyArCOOH)_2(dppz)]^{2+}$. Right: Absorbance (solid lines) and emission spectra (dashed lines) of $[Ru(bpyArCOOH)_2(dppz)]^{2+}$ in water (red) and acetonitrile (black).

UV region at *ca*. 280 and 360 nm respectively, and a broad MLCT band in the visible region centred at 466 nm (as shown in Figure 6.2). The complex is emissive in acetonitrile (λ_{em} = 610 nm) but switches off almost completely in water.

The solvent dependant electrochemistry of $[Ru(bpyArCOOH)_2(dppz)]^{2+}$ in contact with acetonitrile and PBS was investigated after its adsorption as a monolayer on ITO. In acetonitrile, a single reversible oxidation was observed at a formal potential of 1.307 V and was attributed to the $Ru^{+2/+3}$ couple. In PBS, two oxidations at 0.82 V and 1.22 V were observed, the former of which dominated the response at fast scan rates, was quasi-reversible and was likely due to the $Ru^{+2/+3}$ couple. Voltammetry confirmed the surface confinement of $[Ru(bpyArCOOH)_2(dppz)]^{2+}$ and the stability of the monolayer.

6.2.1.2 Impact of DNA-binding on the electrochemistry and resonance Raman spectrum of $[Ru(bpyArCOOH)_2(dppz)]^{2+}$

Voltammetry before and after the $[Ru(bpyArCOOH)_2(dppz)]^{2+}$ monolayer was exposed to 100 µM stDNA for 3 h indicated strikingly different responses (Figure 6.3, stDNA = DNA from salmon testes, PBS). Relative to free PBS solution, there was a decrease in peak current and significant anodic shifts of the oxidative peak potentials after DNA incubation from 0.82 V to 1.00 V and 1.22 V to 1.35 V respectively. There was also an increase in non-Faradaic

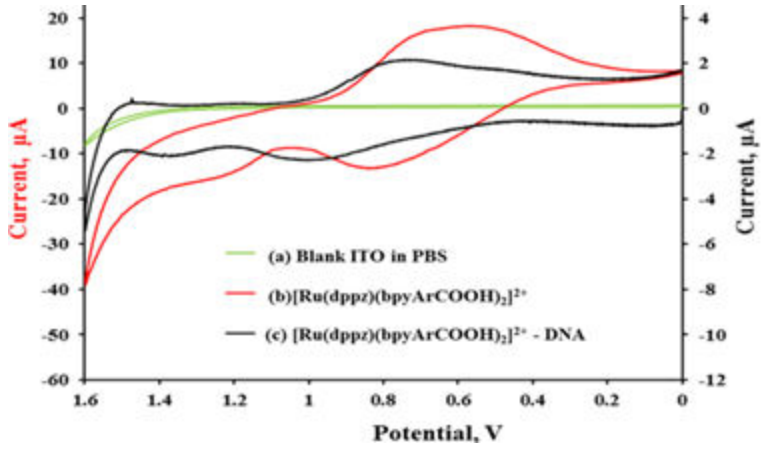

Figure 6.3: Cyclic voltammetry of blank ITO and the $[Ru(bpyArCOOH)_2(dppz)]^{2+}$ monolayer in the presence and absence of DNA as indicated. Data courtesy of Dr. Kerileng Molapo (DCU).

---

current which contributed to increased background, probably due to increased impedance upon DNA binding across the surface. The anodic shifts may be attributed to decreased electron density at the redox centre because of the formation of this DNA film which reduces ion transport. However, it was notable that the shift was towards potentials observed in acetonitrile which may speculatively indicate DNA intercalation of Ru-dppz.

DNA binding at the $[Ru(bpyArCOOH)_2(dppz)]^{2+}$ monolayer was further assessed using resonance Raman (rRaman, 488 nm) which showed modest shifting (3 – 5 cm^{-1}) of certain dppz peaks in the spectrum of the DNA-exposed Ru(II) monolayer relative to the free complex whereas the bpy modes remained relatively unperturbed. The spectrum of $[Ru(bpyArCOOH)_2(dppz)]^{2+}$ in the absence of DNA indicated bpy and dppz modes but was unsurprisingly dominated by Ru-dppz MLCT signals due to stronger resonance with the 488 nm laser at the red-edge of the MLCT absorbance band.[27] Hence, in the presence of DNA, changes in the relative intensity of the dppz peaks compared to the free complex are consistent with shifting of the underlying dppz component of the MLCT band upon DNA intercalation which impacts resonance. This data has been previously reported in full elsewhere.[28]

6.2.1.3 ECL response of $[Ru(bpyArCOOH)_2(dppz)]^{2+}$ upon DNA binding

To study the ECL response of $[Ru(bpyArCOOH)_2(dppz)]^{2+}$ in the presence of DNA, oxalate was installed as a co-reactant to reduce the electrogenerated DNA-bound oxidised Ru(III) species with concomitant generation of the luminescent Ru(II) complex in the excited state. In the absence of DNA, ECL efficiency (ϕ_{ECL}) was poor, calculated at 1.8 %, but upon incubation with DNA, ϕ_{ECL} significantly increased to 20 % and the switch-onset potential was shifted to – 1.3 V (vs -1.2 V in PBS). These observations mirror that observed in the voltammetry and rRaman data and were consistent with DNA intercalation.

The ECL specificity for DNA reflects solution studies on Ru-dppz compounds closely related to $[Ru(bpy)_2(dppz)]^{2+}$ (such as those studied in Chapter 4 herein). In the presence of BSA, which has been shown to non-specifically interact with metal complexes in solution,[18,29] ϕ_{ECL} was determined at just 2.3 % - a value comparable to that observed in free buffer solution. The ECL switch-on versus DNA indicated good linearity up to 80 μM whereupon a plateau was observed due to binding site saturation as limited by the surface coverage of $[Ru(bpyArCOOH)_2(dppz)]^{2+}$ at the electrode. The limit of detection was determined at 5 μM stDNA and a pseudo binding constant was determined at $K_b \approx 10^4\ M^{-1}$, reduced relative to solution studies ($K_b \approx 10^6$)[30] most likely due to ideal binding inaccessibility at the monolayer. The ECL response was demonstrated to be virtually independent of DNA base composition by comparison of ϕ_{ECL} versus [poly(G).poly(C)] and [poly(A).poly(T)] DNA (Figure 6.4).

This study clearly indicates the diagnostic value of ECL towards DNA detection using Ru-dppz light-switch complexes. The ECL efficiency was shown to markedly increase upon DNA binding by intercalation as confirmed from voltammetry and rRaman experiments. This technique has exciting potential for future efforts in developing structure specific light-switch ECL to compliment the continual expansion of optical DNA sensors based on metal complexes.

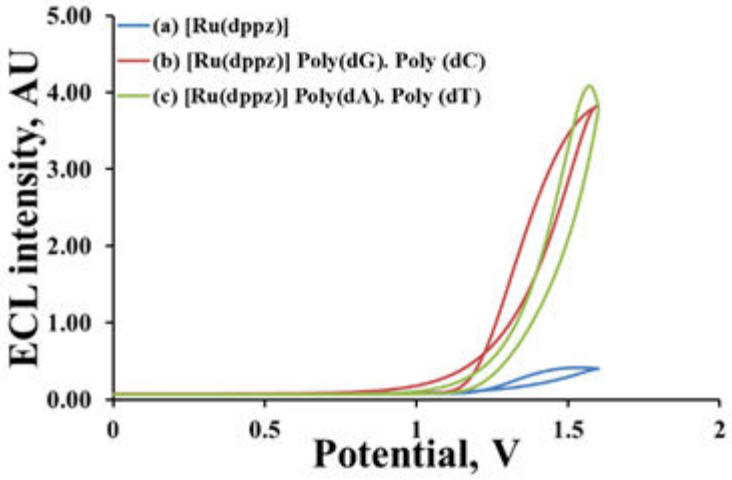

Figure 6.4: ECL response of $[Ru(bpyArCOOH)_2(dppz)]^{2+}$ ([Ru(dppz)]) in the absence (blue trace) and presence of DNA as indicated. Data courtesy of Dr. Kerileng Molapo (DCU).

6.2.2 High resolution STED imaging of cells using ruthenium(II) luminophores.

6.2.2.1 Suitable Ru(II) probes for STED imaging

In Chapter 4, a nuclear-targeted Ru-dppz complex was shown to be capable of imaging DNA with superior resolution under STED than by conventional confocal microscopy. The light-switch luminescence of this complex rendered it non-emissive unless the dppz ligand was sufficiently protected from quenching by water, for example, by binding within membranes or DNA. To further probe the candidacy of Ru(II) complexes as effective STED probes, a water emissive complex was exploited for peptide conjugation towards targeted cellular application, namely; $[Ru(bpy)_2(phenArCOOH)]^{2+}$. $[Ru(bpy)_2(phenArCOOH)]^{2+}$ was conjugated to; the Penetratin sequence to provide Ru-phen-ER, and octa-arginine (RRRRRRRR, R8) to yield Ru-phen-R8. The Penetratin sequence, RQIKIWFQNRRMKWKK (hereafter, ER), corresponds to the third helix of the DNA binding homeodomain of Antennapedia and was exploited here for targeting the endoplasmic reticulum.[31] The synthesis and characterisation of $[Ru(bpy)_2(phenArCOOH)]^{2+}$, Ru-phen-ER and Ru-phen-R8 is reported in Chapter 3 of this thesis.

6.2.2.2 Uptake, localisation and STED imaging of Ru-phen-ER and Ru-phen-R8

Confocal imaging revealed that both Ru-phen-ER and Ru-phen-R8 rapidly entered HeLa cells and were seen distributed throughout the cytoplasm after 2 hours. Co-staining with Ru-phen-R8 and AlexaFluor 532 caused the Ru(II) probe to enter the actin which permitted a comparison of STED efficiency using a 660 nm depletion line following independent excitation (Figure 6.5). Since the organic probe exhibits a narrow Stokes shift, the depletion wavelength was required to sit at the red-edge of its emission band. In contrast, due to its large Stokes shift, the depletion line strongly overlaps with the emission of the Ru(II) probe, increasing the efficiency of stimulated depletion which should enhance resolution. As expected, this led to superior image quality of actin filaments using the Ru(II) probe which demonstrated better STED efficiency, recording a reduction in the full width half maximum value (FWHM) of 60 % versus confocal in comparison to AlexaFluor in which the FWHM is reduced by 10 %.

In HeLa cells, Ru-phen-ER selectively localised to the endoplasmic reticulum after 4 hours as confirmed by co-localisation against ER Tracker Blue. Remarkably, using STED microscopy, the luminescence intensity in the lateral direction on probing Ru-phen-ER revealed the tubular structure of the smooth ER which was not resolved using confocal imaging (Figure 6.6). The longer-lived nature of Ru(II) luminophores also permits time gating experiments to reduce background effects and the point spread function of the confocal volume which further improves resolution. In a comparative experiment, the FWHM value of AlexaFluor 532 decreased slightly using time-gating whereas enhanced resolution was achieved for Ru-phen-ER. Importantly, the photostability of both probes are comparable but the performance of the Ru(II) probe is impressive in this context considering the much greater overlap of its emission with the depletion line.

Cells treated with Ru-phen-ER at imaging concentration indicated little toxicity (> 97 % viable) over 24 hours. However, Ru-phen-R8 exhibited potent cytotoxicity (0 % viability) which can be attributed to non-specific localisation and further highlights the precision targeting of the ER probe which remains confined at the organelle with minimal toxic activity. In summary, Ru(II) luminophores were shown to be well-suited to STED microscopy with comparable and, in some cases superior, performance to commercial dyes.

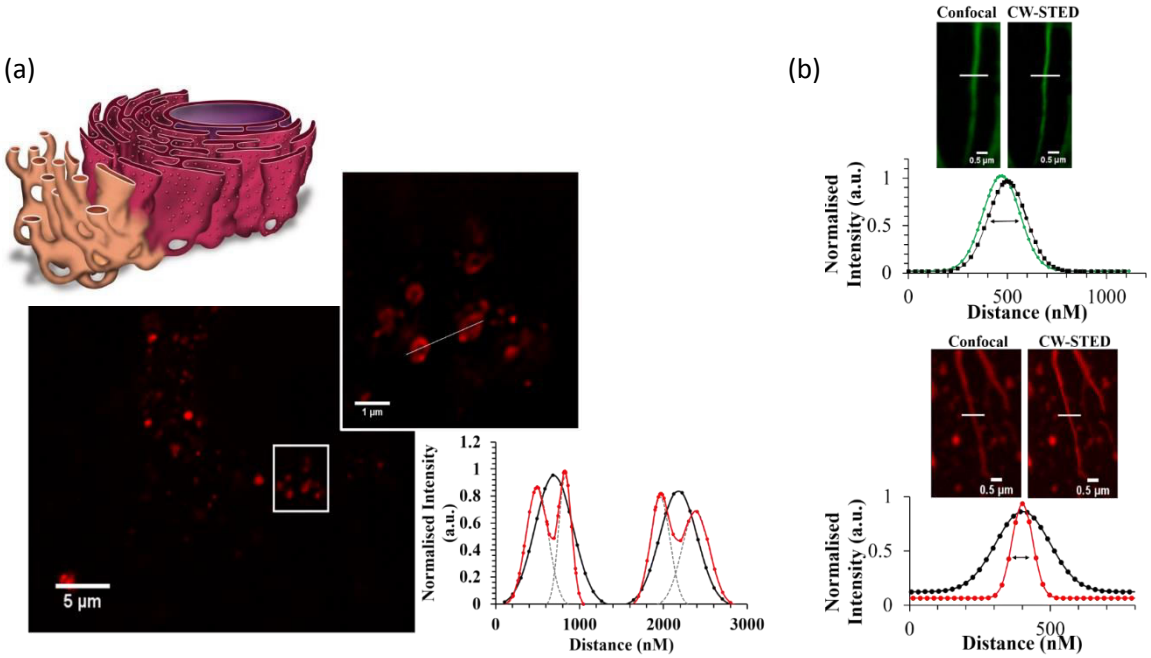

Figure 6.5: (a) Ru-phen-ER under STED imaging reveals the tubular nature of the smooth ER as indicated by the cross-sectional traces (bottom right). Confocal imaging (black trace) resolves spheroidal structure, whereas STED imaging leads to higher resolution of the ER tubular structure (red trace). Image credit for ER structure: emaze.com (b) Imaging actin structure reveals that Ru-R8 (bottom, red) achieves a greater improvement in resolution (FWHM) in comparison to AlexaFluor 532 (top, green) upon moving from confocal (black traces) to STED. Cellular images courtesy of Dr. Aisling Byrne, DCU.

In combination with directing peptides, these conjugates represent a valuable new class of precision targeted tools for super-resolution cellular imaging.

6.2.3 Synthesis and characterisation of a light-switch Ru(II) peptide conjugate as a potential probe for Amyloid-beta aggregation.

6.2.3.1 Synthesis and structural characterisation

The synthesis of $[Ru(dppz)(bpy)(bpyArCOOH)]^{2+}$ was described in Chapter 3 and was exploited here as a conjugatable Ru-dppz complex for light-switch sensing of Aβ deposits. Peptide coupling with $[Ru(dppz)(bpy)(bpyArCOOH)]^{2+}$ (used as its isomer mixture) was performed as described in Chapter 3 to yield [Ru(dppz)(bpy)(bpyArCONH-ahx-

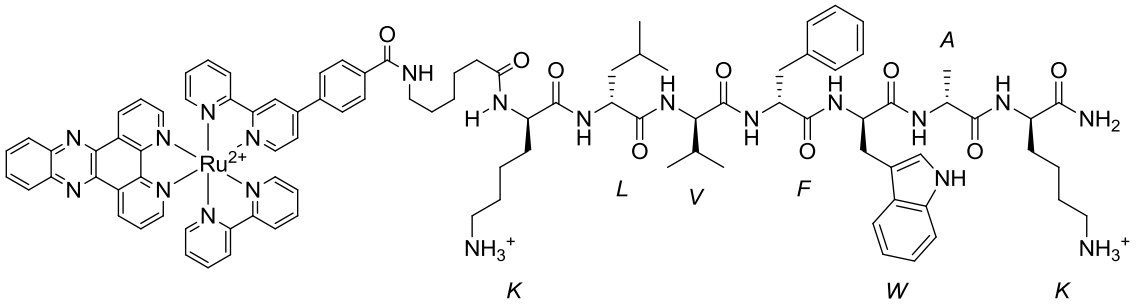

Figure 6.6: Chemical structure of Ru-Amy.

KLVFWAK]$^{4+}$ (hereafter Ru-Amy, structure shown in Figure 6.6). Successful mono-conjugation was evident from the ^{1}H NMR spectrum (Figure 6.7), simplified by the addition of D_2O to promote deuterium exchange with acidic protons in the peptide. The spectrum exhibited the expected peaks attributable to the Ru-dppz complex and additional signals in the aromatic region integrating to 10 H in total were assigned to the Phe and Trp residues of the peptide. Aliphatic peptide signals were observed upfield, including a cluster of alpha-H peaks at *ca*. δ 3.8 – 4.5 ppm, integrating as expected to 7 H. HR-MS analysis indicated excessive fragmentation, tentatively attributable primarily to different Lys breakdowns, but two clear signals assignable to a Ru-Amy molecular ion less 1 H were found at *m/z* = 638.2635 and 956.8931 corresponding to $[(M\text{-}H)^{+4} + TFA^{-}]^{3+}$ and $[(M\text{-}H)^{+4} + TFA^{-} - H^{+}]^{2+}$ respectively. No signals assignable to a parent structure were observed in the MS data. HPLC of the conjugate, analysed on diphenyl reverse phase with CH_3CN/H_2O (0.1 % TFA) gradient elution, indicated purity of Ru-Amy which eluted as a broad peak with a maximum at 15.8 minutes. No significant peak was observed corresponding to parent Ru-COOH peak which elutes at 17.3 minutes. Combined, this analysis suggests successful synthesis of Ru-Amy which was obtained at a high degree of purity.

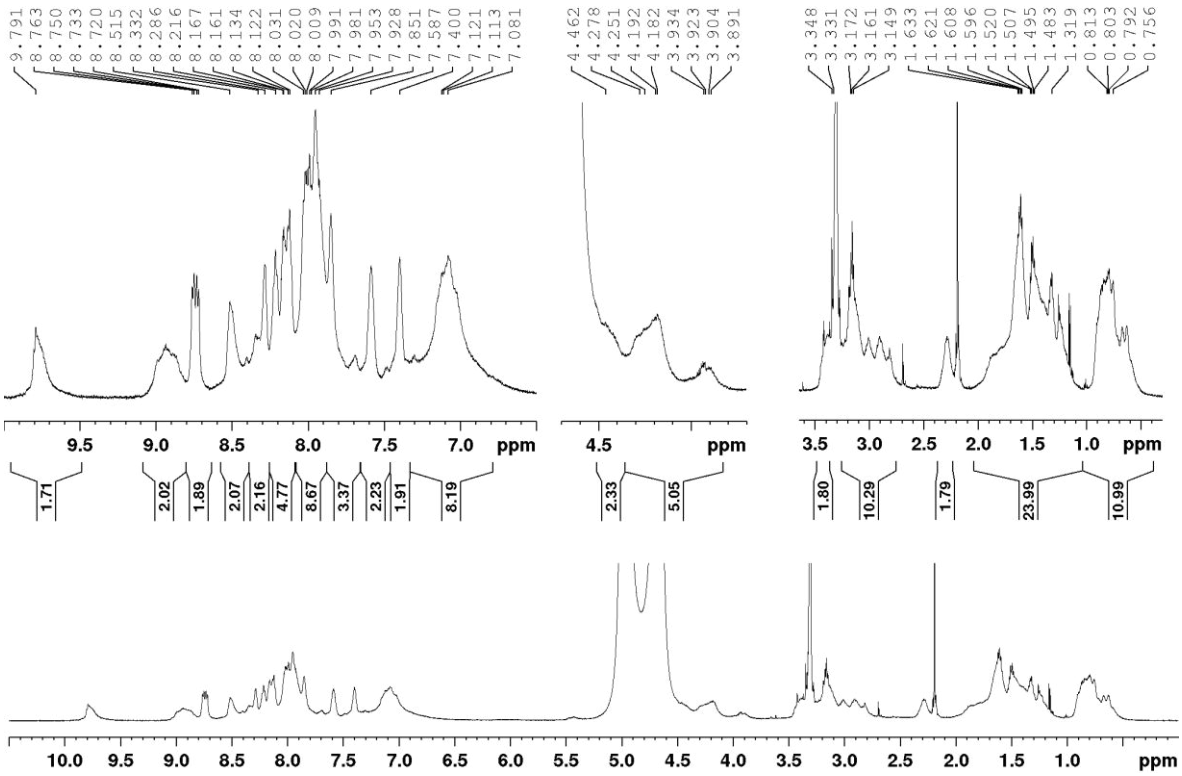

Figure 6.7: ^{1}H NMR (600 MHz) spectrum of Ru-Amy recorded in CD_3OD/D_2O.

6.2.3.2 Photophysical characterisation of Ru-Amy

The absorbance spectra of Ru-Amy, as shown in Figure 6.8, indicated the expected bands as observed for the parent complex; $[Ru(dppz)(bpy)(bpyArCOOEt)]^{2+}$ (Ru-ester, Chapter 4). Ligand-centred transitions attributable to bpy and dppz were observed in the UV region, while a broad MLCT band was evident in the visible region with a maximum centred at about 450 nm. Typical of Ru-dppz complexes, Ru-Amy was found to be emissive in acetonitrile (λ = 620 nm) but was almost completely extinguished in water. A summary of photophysical data for Ru-Amy and Ru-ester is provided in Table 6.1.

In Chapter 4 of this thesis, the luminescence lifetimes of the studied Ru-dppz peptide conjugates were biexponential in aerated media but mono-exponential upon nitrogen purge. This indicated that the longer-lived component in that case was due to a protecting effect of the pendant peptide from quenching by O_2. Conversely, as shown in Table 6.1, the luminescence lifetime of Ru-Amy in both aerated and deaerated acetonitrile was identical

Table 6.1: Summary of photophysical data for Ru-Amy and Ru-ester.

	Solvent[a]	**λ_{abs} (ε)**[b] nm (x10^3 M^{-1} cm^{-1})	**λ_{em}** nm	**τ_{lum}**[c] ns	
				Aerated	Deaerated
Ru-Amy	MeCN	287 (134.2), 359 (32.9), 452(29.4)	620	292 ± 17 (74 %)	315 ± 6 (72 %)
		283 (82.6), 360 (19.2), 447 (17.6).		102 ± 5 (26 %)	111 ± 1 (28 %)
	H_2O	283 (55.3), 356 (18.6), 452 (16.0).			
	PBS				
Ru-ester	MeCN	282 (112.6), 355 (29.0), 454(28.1)	617	239 ± 1	372 ± 17
	H_2O	281 (86.1), 359 (20.3), 452 (18.5).			
	PBS	282 (57.9), 363 (18.4), 455 (18.3).			

Notes: a) PBS pH 7.4 b) Averaged from triplicate analyses c) 450 nm excitation, data fit to tailfit criteria; $0.9 < \chi^2 < 1.1$. De-aeration by N_2 purge for 15 minutes. Averaged data is shown ±S.D. For bi-exponential fitting, % relative amplitude values are provided in parentheses.

and conformed to dual-exponential decay kinetics. The long component ($\tau \approx 300$ ns, $\alpha \approx 73$ %) of the decay was moderately longer-lived than Ru-ester which indicates that the peptide impacts the local environment of the Ru-dppz luminophore of Ru-Amy.

The shorter-lived component of the lifetime of Ru-Amy was significantly quenched, for example in aerated acetonitrile; at 102 ns on average ($\alpha = 26$ %). Ru-dppz complexes can be quenched because of hydrogen bonding to the phenazine nitrogens of the coordinated dppz ligand. The peptide of Ru-Amy contains two Lys residues that may operate as H-bond donors but this is unlikely to cause the observed quenching considering that other Ru-dppz conjugates, such as Ru-NLS and Ru-MPP (Chapter 4), also contain Lys and do not exhibit similar quenching. Hence, the short-lived component likely originates from quenching due to the Trp residue which has not been previously encountered in this thesis. Hammarström and coworkers previously investigated PCET between $[Ru(bpy)_3]^{2+}$ and Trp where water has acted as a proton acceptor.[32] Herein, the observed Ru-Amy quenching may originate from a similar PCET mechanism with Trp, perhaps facilitated by proximal proton-accepting amino acids of the peptide. Furthermore, the planarity of the interacting moieties may lead to π-stacking of Trp and Ru-dppz that encourages their photochemistry.

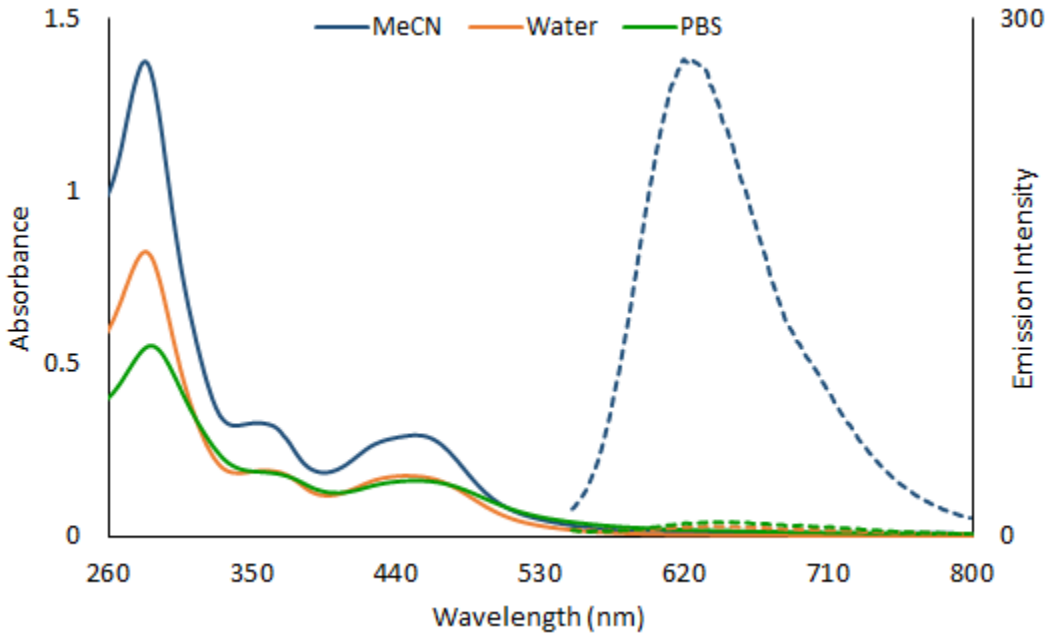

Figure 6.8: Absorbance (solid) and emission (dashed) spectra of Ru-Amy (10 μM) in different solvents as indicated.

6.2.3.3 Future work: Towards a light-switch probe for Aβ aggregates in live cells

Ru-Amy exhibits the light-switch properties typical of Ru-dppz complexes and is suited to Aβ sensing. Future work will investigate the switching-on of Ru-Amy in different structural forms of Aβ. Ideally, the probe will exhibit light-switching selectivity for fibrils and aggregates which have been linked to Aβ toxicity. It will also be interesting to assess the luminescence lifetime response to different Aβ structures towards FLIM based diagnostics in cells. Photophysical responses to Aβ should be compared to Thioflavin T (a commercial amyloid stain) and $[Ru(bpy)_2(dppz)]^{2+}$ (to determine the impact of the directing peptide). Finally, cellular application of Ru-Amy will be investigated. Uptake and cytotoxicity of Ru-Amy will be assessed in the presence and absence of Aβ plaques. In the presence of Aβ assemblies, targeting selectivity of Ru-Amy will be determined and if successful, the probe may be suited to high resolution imaging of Aβ structures in live cells using STED microscopy.

6.3 Conclusions

This chapter describes additional applications of Ru(II) luminophores for biological imaging and sensing. Carboxy-functionalised Ru-dppz complexes were shown to be suited to surface immobilisation at an electrode for ECL detection of DNA. Incubation of the Ru-dppz monolayer in the presence of DNA led to decreases in peak current and significant anodic shifts of the oxidative peak potentials. This shifting was attributed to capture of a DNA film at the electrode surface and may also be speculative evidence for DNA intercalation of the immobilised probe. A clear indicator of DNA capture was indicated by the switch-on of ECL with efficiency 10-fold greater in DNA than background levels. The ECL response was linear up to DNA saturation at about 80 μM with a limit of detection estimated at 5 μM. As expected, the ECL response was relatively insensitive to DNA sequence. This study highlighted the power of ECL for DNA detection using a molecular light-switch complex and provides a compliment to the extensive optical studies on the DNA interactions of Ru-dppz compounds reported in the literature.

The candidacy of Ru(II) luminophores as effective probes for STED microscopy was further highlighted. A Ru(II)-Penetratin conjugate was precision targeted to the endoplasmic reticulum of HeLa cells where superior tubular resolution of the smooth ER was apparent under STED in comparison to conventional confocal imaging. The long-lived luminescence lifetime of the Ru(II) probe permitted time-gating STED experiments which led to further improvements in resolution as judged by a decrease in FWHM. Co-staining a Ru-R8 conjugate with AlexaFluor led to accumulation at the actin permitting a direct comparison of the STED efficiency of both dyes. In this instance, the Ru(II) dye exhibited a 60 % decrease in FWHM relative to confocal in comparison to the organic probe which experienced only a 10 % enhancement. The greater STED efficiency arises from the strong Stokes shift of the metal complex luminophore which permitted greater overlap of the depletion laser with its emission maximum. Notably, even with a greater emission cross-section, the photostability of the Ru(II) probe was equal to that of the organic dye. This study, along with data presented in Chapter 4 herein, represented the first example of the application of metal complexes to STED imaging of cells and clearly supports their candidacy for further super-resolution applications to study cellular structure at the nanoscale.

Finally, the synthesis of a peptide modified Ru-dppz complex designed to specifically target toxic higher order structures of Aβ was described. The conjugate was obtained quantitatively in high purity using the protocol developed in Chapter 3 of this thesis and was fully characterised by NMR and HRMS. Preliminary photophysical experiments indicate that the conjugate exhibits photophysical properties typical of Ru-dppz complexes. However, the presence of Trp in the peptide sequence leads to oxygen independent quenching of the luminescence lifetime in acetonitrile. Future studies will investigate the ability of the probe to distinguish higher order amyloid selectively with a luminescent response upon binding. If successful, cellular application of the conjugate will be examined, possibly in high resolution using STED microscopy.

6.4 Experimental

6.4.1 General Information

All electrochemical studies were performed by Dr. Kerileng Molapo (DCU) and methods and results related to these experiments have been reported in full elsewhere.[28] Similarly, all cell work was performed by Dr. Aisling Byrne (DCU) and full methods and additional data were reported previously elsewhere.[33,34] All other experimental work was performed using materials and methods as described in Chapter 2 of this thesis.

6.4.2 Synthesis

$[Ru(dppz)(bpy)(bpyAr\text{-}CONH\text{-}Ahx\text{-}KLVFWAK\text{-}CONH_2)]^{4+}$; Ru-Amy

Yield: Red solid. ^{1}H NMR (600 MHz, 99/1 CD_3OD/D_2O); 9.78 (br s, 2 H); 8.82 – 9.04 (m, 2 H); 8.76 (dd, 2 H); 8.40 – 8.57 (m, 2 H); 8.26 – 8.39 (m, 2 H); 8.09 – 8.25 (m, 5 H); 7.89 – 8.08 (m, 9 H); 7.66 – 7.88 (m, 3 H); 7.46 – 7.65 (m, 2 H); 7.40 (br s, 2 H, Trp-*H*); 6.79 – 7.33 (br s, 8 H, Phe and Trp-*H*); 4.45 (br m, 2 H, alpha-*H* Trp and Phe); 3.82 – 4.36 (m, 5 H, alpha-*H* peptide); 3.42 (m, 2 H); 2.75 – 3.25 (m, 10 H); 2.28 (br s, 2 H); 1.05 – 2.04 (m, 24 H); 0.39 – 1.04 (m, 11 H, Val and Leu-C*H*$_3$). HR-MS (Q-Orbitrap MS^+, MeOH/TFA); Calculated for $C_{99}H_{111}F_3N_{20}O_{11}Ru$ $[(M\text{-}H)^{+4} + TFA^-]^{3+}$: 638.2573, Found 638.2635; Calculated for $C_{99}H_{111}F_3N_{20}O_{11}Ru$ $[(M\text{-}H)^{+4} + TFA^- - H^+]^{2+}$: 956.8824, Found 956.8931. HPLC (RP-diphenyl, 0.1 % TFA in H_2O/CH_3CN gradient); Retention time = 14 – 18 minutes (maximum at 15.8 minutes, no parent peak at 17.3 min).

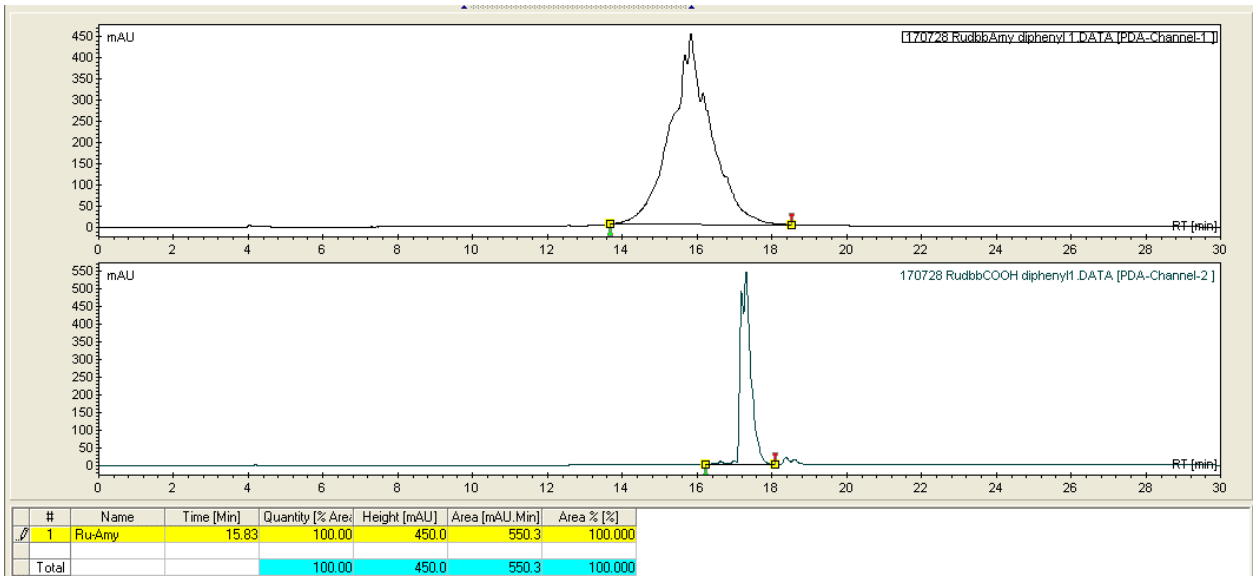

#	Name	Time [Min]	Quantity [% Area]	Height [mAU]	Area [mAU.Min]	Area % [%]
1	Ru-Amy	15.83	100.00	450.0	550.3	100.000
Total			100.00	450.0	550.3	100.000

Figure 6.9: HPLC chromatogram of Ru-Amy and parent complex run under HPLC general method 2.

6.5 References

(1) Forster, R. J.; Bertoncello, P.; Keyes, T. E. *Annu. Rev. Anal. Chem.* **2009**, *2* (1), 359.
(2) Carter, M. T.; Bard, A. J. *Bioconjug. Chem.* **1990**, *1* (4), 257.
(3) Rodriguez, M.; Bard, A. J. *Anal. Chem.* **1990**, *62* (24), 2658.
(4) Hu, L.; Bian, Z.; Li, H.; Han, S.; Yuan, Y.; Gao, L.; Xu, G. *Anal. Chem.* **2009**, *81* (23), 9807.
(5) Brennaman, M. K.; Meyer, T. J.; Papanikolas, J. M. *J. Phys. Chem. A* **2004**, *108* (45), 9938.
(6) Chen, W.; Turro, C.; Friedman, L. A.; Barton, J. K.; Turro, N. J. *J. Phys. Chem. B* **1997**, *101* (35), 6995.
(7) Poynton, F. E.; Hall, J. P.; Keane, P. M.; Schwarz, C.; Sazanovich, I. V.; Towrie, M.; Gunnlaugsson, T.; Cardin, C. J.; Cardin, D. J.; Quinn, S. J.; Long, C.; Kelly, J. M. *Chem. Sci.* **2016**, *7* (5), 3075.
(8) Hell, S. W. *Science* **2007**, *316* (5828), 1153.
(9) Hell, S. W.; Wichmann, J. *Opt. Lett.* **1994**, *19* (11), 780.
(10) Klar, T. A.; Hell, S. W. *Opt. Lett.* **1999**, *24* (14), 954.
(11) Fernández-Suárez, M.; Ting, A. Y. *Nat. Rev. Mol. Cell Biol.* **2008**, *9* (12), 929.
(12) Hotta, J.; Fron, E.; Dedecker, P.; Janssen, K. P. F.; Li, C.; Müllen, K.; Harke, B.; Bückers, J.; Hell, S. W.; Hofkens, J. *J. Am. Chem. Soc.* **2010**, *132* (14), 5021.
(13) Blom, H.; Brismar, H. *J. Intern. Med.* **2014**, *276* (6), 560.
(14) Lee, S. J. C.; Nam, E.; Lee, H. J.; Savelieff, M. G.; Lim, M. H. *Chem. Soc. Rev.* **2017**, *46* (2), 310.
(15) Cook, N. P.; Torres, V.; Jain, D.; Martí, A. A. *J. Am. Chem. Soc.* **2011**, *133* (29), 11121.
(16) Cook, N. P.; Ozbil, M.; Katsampes, C.; Prabhakar, R.; Martí, A. A. *J. Am. Chem. Soc.* **2013**, *135* (29), 10810.
(17) McConnell, A. J.; Song, H.; Barton, J. K. *Inorg. Chem.* **2013**, *52* (17).
(18) Wragg, A.; Gill, M. R.; McKenzie, L.; Glover, C.; Mowll, R.; Weinstein, J. A.; Su, X.; Smythe, C.; Thomas, J. A. *Chem. – Eur. J.* **2015**, *21*, 11865.
(19) Svensson, F. R.; Li, M.; Nordén, B.; Lincoln, P. *J. Phys. Chem. B* **2008**, *112* (35), 10969.

(20) Svensson, F. R.; Matson, M.; Li, M.; Lincoln, P. *Biophys. Chem.* **2010**, *149* (3), 102.
(21) Cosgrave, L.; Devocelle, M.; Forster, R. J.; Keyes, T. E. *Chem. Commun.* **2010**, *46* (1), 103.
(22) Tjernberg, L. O.; Näslund, J.; Lindqvist, F.; Johansson, J.; Karlström, A. R.; Thyberg, J.; Terenius, L.; Nordstedt, C. *J. Biol. Chem.* **1996**, *271* (15), 8545.
(23) Lowe, T. L.; Strzelec, A.; Kiessling, L. L.; Murphy, R. M. *Biochemistry (Mosc.)* **2001**, *40* (26), 7882.
(24) Castelletto, V.; Cheng, G.; Hamley, I. W. *Chem. Commun.* **2011**, *47* (46), 12470.
(25) Truex, N. L.; Wang, Y.; Nowick, J. S. *J. Am. Chem. Soc.* **2016**.
(26) Aoraha, E.; Candreva, J.; Kim, J. R. *Mol. Biosyst.* **2015**, *11* (8), 2281.
(27) Coates, C. G.; Jacquet, L.; McGarvey, J. J.; Bell, S. E. J.; Al-Obaidi, A. H. R.; Kelly, J. M. *J. Am. Chem. Soc.* **1997**, *119* (30), 7130.
(28) Molapo, K. M. Electrochemiluminescence: from biomolecules to whole cells. PhD Thesis, Dublin City University. School of Chemical Sciences, 2016.
(29) Adamson, K.; Dolan, C.; Moran, N.; Forster, R. J.; Keyes, T. E. *Bioconjug. Chem.* **2014**, *25* (5), 928.
(30) Friedman, A. E.; Chambron, J. C.; Sauvage, J. P.; Turro, N. J.; Barton, J. K. *J. Am. Chem. Soc.* **1990**, *112* (12), 4960.
(31) Derossi, D.; Joliot, A. H.; Chassaing, G.; Prochiantz, A. *J. Biol. Chem.* **1994**, *269* (14), 10444.
(32) Zhang, M.-T.; Hammarström, L. *J. Am. Chem. Soc.* **2011**, *133* (23), 8806.
(33) Byrne, A. The application of Ru(II) polypyridyl complexes to cellular imaging and sensing. PhD Thesis, Dublin City University, 2016.
(34) Byrne, A.; Burke, C. S.; Keyes, T. E. *Chem. Sci.* **2016**, *7* (10), 6551.

Chapter 7

Conclusions and future work

7.1 Conclusions

This work of this thesis explores the candidacy of precision-targeted Ru(II) luminophores for live cellular imaging. A primary objective at the outset of the work was the selective targeting of DNA in the mitochondria and nucleus of live cells using Ru(II) complexes whose interactions with DNA had been demonstrated *ex-cellulo* but had yet to be exploited *in-cellulo*. Chapter 4 presented the successful application of a Ru-dppz derivative targeted to sites of genetic material using NLS and MPP signal peptides. Chromosomal DNA was illuminated with excellent contrast using the light-switch complex and STED imaging permitted the tracking of mitosis in high resolution. The Ru-dppz MPP conjugate appeared to accumulate within the mitochondria with bright punctate staining providing strong evidence for binding to mtDNA by a Ru-dppz complex for the first time. In Chapter 5, a Ru-tap complex was shown to successfully penetrate the nucleus where it preconcentrated and bound to nuclear DNA with concomitant quenching of its luminescence. This demonstration was the first example of selectively targeting a Ru-tap complex to nuclear DNA in live cells. Importantly, in both the Ru-dppz and Ru-tap cases, the use of the probes did not impact cellular viability under imaging conditions for several hours.

A secondary objective of this work was to explore the phototoxicity of the Ru(II) complexes once they had been precision targeted to cellular DNA. In particular, a key aim was to explore the photo-reactivity of a Ru-tap conjugate due its oxygen independent photochemistry with guanine. Indeed, as shown in Chapter 5, the nuclear localised Ru-tap conjugate was found to photo-induce efficient cellular destruction under illumination, probably by direct guanine oxidation via a PET mechanism that leads to DNA damage and subsequent cellular death. The work in Chapter 4 showed that the Ru-dppz complex was also capable of photo-induced toxicity under irradiation once localised at the mitochondria. In this case, DNA damage and cellular apoptosis was likely mediated by the localised generation of toxic singlet oxygen. In both cases, photo-toxicity could be induced with spatiotemporal control and represents a powerful avenue towards controlled therapy for medicinal use or for the study of the dynamics of cellular destruction.

Before cellular application, the parent complexes and conjugates presented in Chapters 4 and 5 were fully characterised photophysically in the presence and absence of DNA. As reported

in Chapter 4, the Ru-dppz derivatives demonstrate light-switch luminescence, switching-on upon binding DNA with a luminescence lifetime that was biexponential, attributed to binding in a canted or perpendicular geometry. Unsurprisingly, an analysis of the resolved geometrical isomers of $[Ru(dppz)(bpy)(bpyArCOOH)]^{2+}$ indicated that the orientation of the aryl-R substituent impacted DNA affinity and the relative proportion of binding geometries. However, due to electrostatic binding, peptide conjugation enhances the binding affinity by an order of magnitude (from $K_b = 10^6$ to 10^7 M^{-1}). A similar phenomenon was observed for the Ru-tap-NLS conjugate reported in Chapter 5. The parent complex, $[Ru(tap)_2(bpyArCOOEt)]^{2+}$, was found to be impeded from binding DNA due to aryl-ester substituent but peptide conjugation led to DNA binding with high affinity. The Ru-tap complexes exhibited typical optical properties of polyazaaromatic complexes, bearing an excited state sufficiently positive to undergo PCET with guanine residues of DNA leading to the formation of photoproducts.

An important point to stress regarding the Ru-dppz conjugates tested in Chapter 4 is that their geometric and optical isomerism leads to the presence of four isomers in the parent complexes and peptide conjugates. The differences between these isomers likely impacts DNA binding based on data from Chapter 4 which makes their analysis difficult when tested as a mixture. In future work, it may be advisable to attempt to resolve the isomers (using chromatography or otherwise) or to transition to more symmetrical complexes to reduce complexity.

The Ru-tap and Ru-dppz complexes reported herein merit further investigation towards biological sensing applications. Indeed, as reported in Chapter 5, a pic-R derivative of the Ru-tap series was shown to exhibit pH dependent photophysics which may have potential for translation to cellular sensing. Chapter 6 describes two other applications of Ru-dppz complexes. Firstly, carboxy functionalised derivatives of Ru-dppz were shown to assemble into monolayers on electrodes to enable the capture and sensing of DNA by ECL. The ECL efficiency was greatly enhanced in the presence of nucleotides but diminished in its absence and thus this technique compliments solution based spectroscopic studies on DNA binding of metal complexes. Secondly, a peptide modified Ru-dppz conjugate was synthesised towards the targeting of higher order toxic aggregates of amyloid beta. Preliminary

photophysical data indicated light-switch sensitivity was maintained upon conjugation which holds promise for future cellular applications of the probe.

A key outcome of this work was a demonstration of the suitability of Ru(II) luminophores for high resolution STED microscopy. As microscopy evolves further, it is important to develop photoprobes designed to withstand the high demands placed on the luminophore to effectively exploit these advancements. Currently, commercial STED probes are exclusively organic dyes but Ru(II) luminophores exhibit excellent photophysical properties ideally suited to STED. These include an excellent photostability to cope with the high power of the STED laser which can sit at the emission maximum because of the strong Stokes shift of the luminophore, thereby improving the depletion efficiency which enhances resolution. In Chapter 4, STED was used in tandem with a nuclear targeted Ru-dppz light-switch probe to illuminate chromosomal DNA with outstanding clarity which permitted the tracking of various stages of cellular mitosis. In Chapter 6, the applicability of Ru(II) probes to STED imaging was further examined using a Ru(II) complex targeted to the endoplasmic reticulum or the actin. Superior image quality under STED versus confocal imaging was clearly evident by the resolution of the tubular structure of the smooth ER and an 80 % enhancement in the FWHM for the Ru(II) probe which was not apparent in a commercially available organic dye.

This work provides compelling evidence for signal peptide vectorisation as a powerful strategy towards achieving efficient uptake and precise subcellular localisation of Ru(II) complexes. In this instance, peptide targeting was exploited to selectively deliver molecular light-switch complexes to genetic material in the nucleus and mitochondria in live cells for the first time; permitting remarkable contrast imaging as reported for Ru-dppz derivatives in Chapter 4, or DNA-targeted photodamage by Ru-tap complexes as described in Chapter 5. Peptide modification was also demonstrated to be versatile, and built upon previous work within our group, by successfully transporting different Ru(II) complex cargo to the same cellular target. Currently, no other uptake and localisation strategy is capable of such robust precision targeting.

The future adoption of Ru(II) luminophores relies on their preparation in high yield and purity. Hence, as described in Chapter 3, a crucial outcome of the present work was the

development of efficient synthesis routes to conjugatable derivatives of Ru(II) complexes suited to cellular imaging. Highly asymmetrical *tris*-heteroleptic complexes of Ru(II) were obtained by a novel synthesis which provided complexes of this type in the highest yield reported to date (> 82 %). The success of this route can be attributed to a key Ru-oxalate intermediate which permitted quantitative stepwise addition of bidentate polypyridyl ligands to the Ru(II) coordination sphere. Satisfyingly, the use of an oxalate intermediate was found to extend to *bis*-heteroleptic complexes which permitted the synthesis of highly lipophilic Ru(II) complexes in yields exceeding that commonly reported by classical syntheses. The efficient protocol to *tris*-heteroleptic complexes provided a di-conjugatable Ru(II) parent complex which was shown to be capable of asymmetric functionalisation with PEG and peptide conjugations by a couple – cleave – couple protocol. It was found that peptide coupling is quite inefficient but can be driven to completion using a two-fold excess of peptide under PyBOP coupling conditions. These synthetic advancements enabled the efficient preparation of the novel complexes and conjugates reported throughout this thesis and will undoubtedly contribute to expanding the library of Ru(II) cellular probes by our group and others.

Perhaps driven by stigma and the excellent examples of dark reacting metallodrugs, there has been a hesitance in the research community in adopting metal complex luminophores for cellular application. It is hoped that the advancements described in this work will contribute to a field which continues to gather momentum in breaking down these preconceptions.

7.2 Future Work

This thesis underscores the candidacy of Ru(II) luminophores for the targeted cellular imaging and photo-destruction of DNA. The successes described here open new avenues to develop this work further in several key directions. For example, e*x-cellulo*, there has been a wealth of research reported concerning the interaction of Ru(II) complexes with DNA; from targeting special structures like the G-quadruplex or mismatches to developing potent phototoxic probes towards DNA destruction. These complexes could now be investigated in live cells using the peptide targeting strategy that was effective herein in delivering derivatives of $[Ru(bpy)_2(dppz)]^{2+}$ and $[Ru(tap)_2(bpy)]^{2+}$ to nuclear and mitochondrial DNA.

On the other hand, binding data for the peptide conjugates studied in this work suggests that the conjugated peptide drives binding affinity with DNA. This could destroy any selectivity built into the parent Ru(II) complex so there is a need to develop a targeting strategy that does not impact the binding selectivity of the probe with DNA. As discussed in Chapter 1, there is a dearth of reports that can reproducibly transport different metal complexes to the same cellular target and none which are as efficient as signal peptide targeting. Therefore, a possible solution which exploits peptide targeting but does not impact DNA binding may be to introduce a cleavable linker between the peptide and probe. Critically, the release of the probe from the targeting peptide must be controlled to prevent off-target effects, perhaps using specific enzymatic cleavage or photolysis.

The development of efficient routes to *tris*-heteroleptic complexes of Ru(II) in Chapter 3 now permits the synthesis of highly asymmetric constructs which can be tuned photophysically or designed with various steric factors to guide selective bio-interactions. There are few reports in the literature which utilise such highly asymmetric complexes and hence, there is an opportunity in future work to expand the catalogue of Ru(II) compounds using these novel synthesis routes to produce new compounds that may find application across a number of research domains. Another point mentioned in Chapter 3 was the inefficient amide coupling protocol which, although quantitative in terms of Ru-COOH, led to at least a 50 % loss of peptide in every reaction. Future work should attempt to improve peptide economy by transitioning to alternative coupling methods such as click chemistry.

This work demonstrated the ability of Ru-dppz complexes to act as both an imaging and phototoxic reagent by attenuation of the incident photoirradiation intensity. Although difficult, future work should investigate two-colour combi-probes which are capable of independent activation for imaging or phototoxic effects. Additionally, there is an opportunity to evolve towards theranosis by implementing a diagnostic element in the probe design to report on the effects of phototoxicity and to monitor the toxic dose. Combining several elements with a targeting strategy would be difficult within a molecular scaffold which may indicate that encapsulation and particle delivery is an avenue that should be investigated in future work.

Appendix A

Supplementary information – Chapter 3

A.1 Structural characterisation data

A.1.1 Ligands

A.1.1.1 dppz and aphen

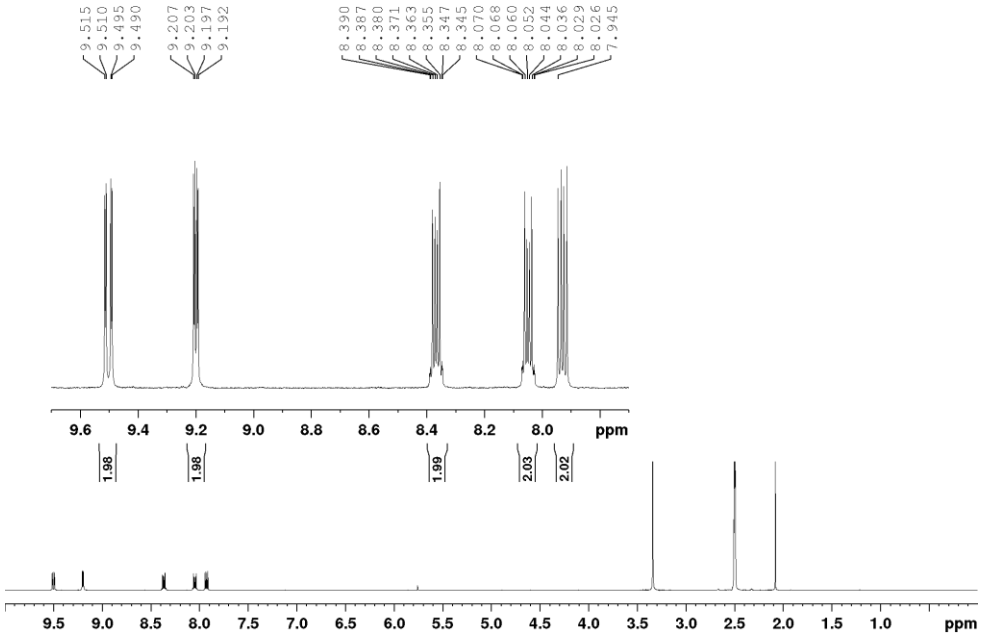

Figure A.1: ^{1}H NMR (400 MHz, DMSO-d_6) spectrum of dppz. Peak at 2.09 ppm is residual acetone.

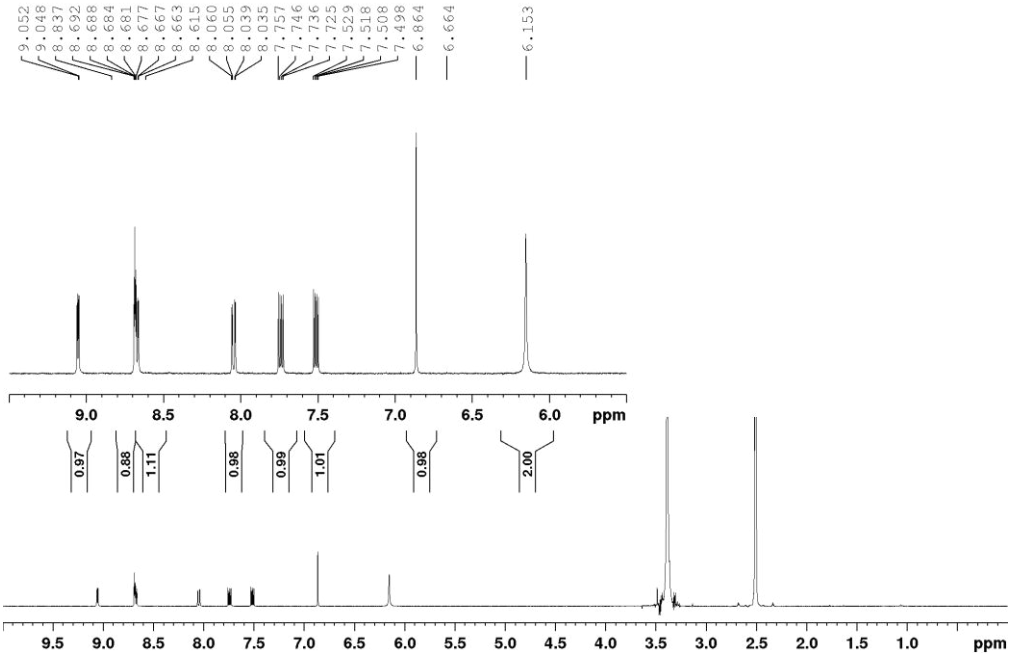

Figure A.2: ^{1}H NMR (400 MHz, DMSO-d_6) spectrum of aphen.

A.1.1.2 4-bpyArCOOR and precursors

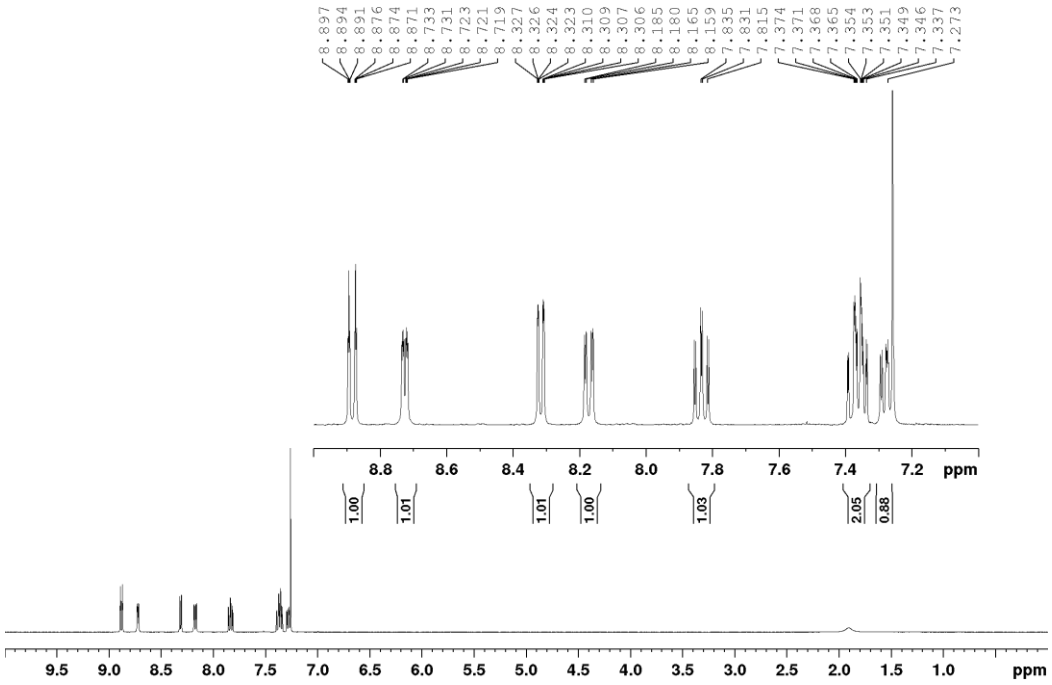

Figure A.3: ^{1}H NMR (400 MHz, CD_3Cl) spectrum of bpy-N-oxide.

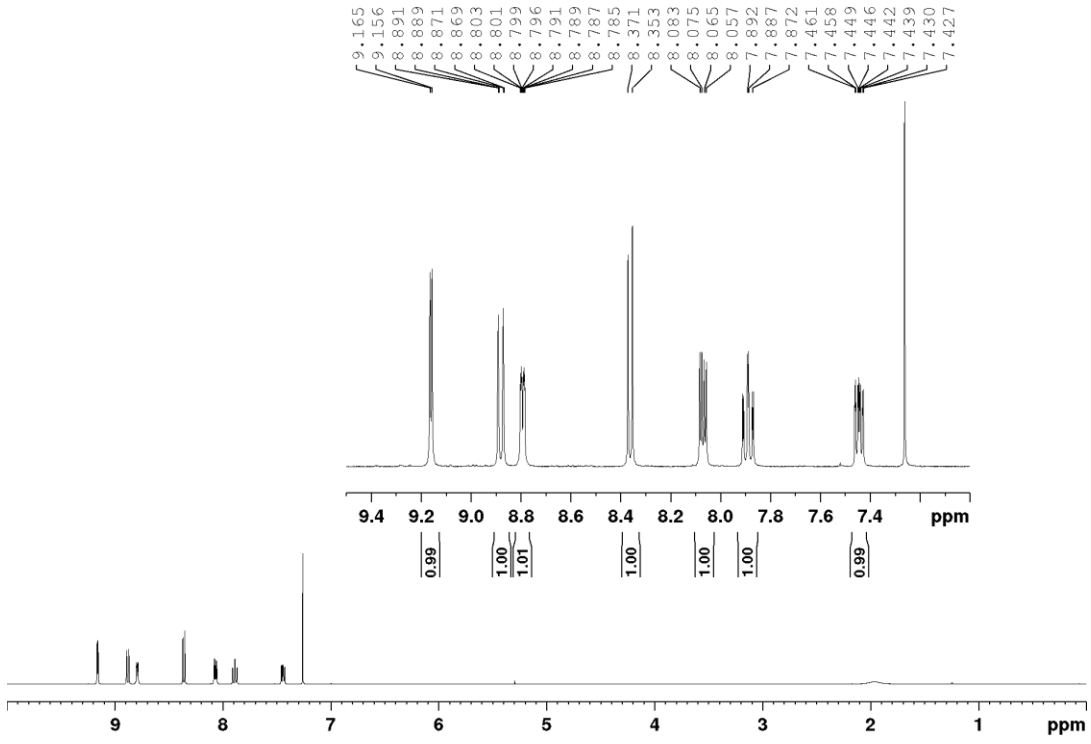

Figure A.4: ^{1}H NMR (400 MHz, CD_3Cl) spectrum of nitro-bpy-N-oxide.

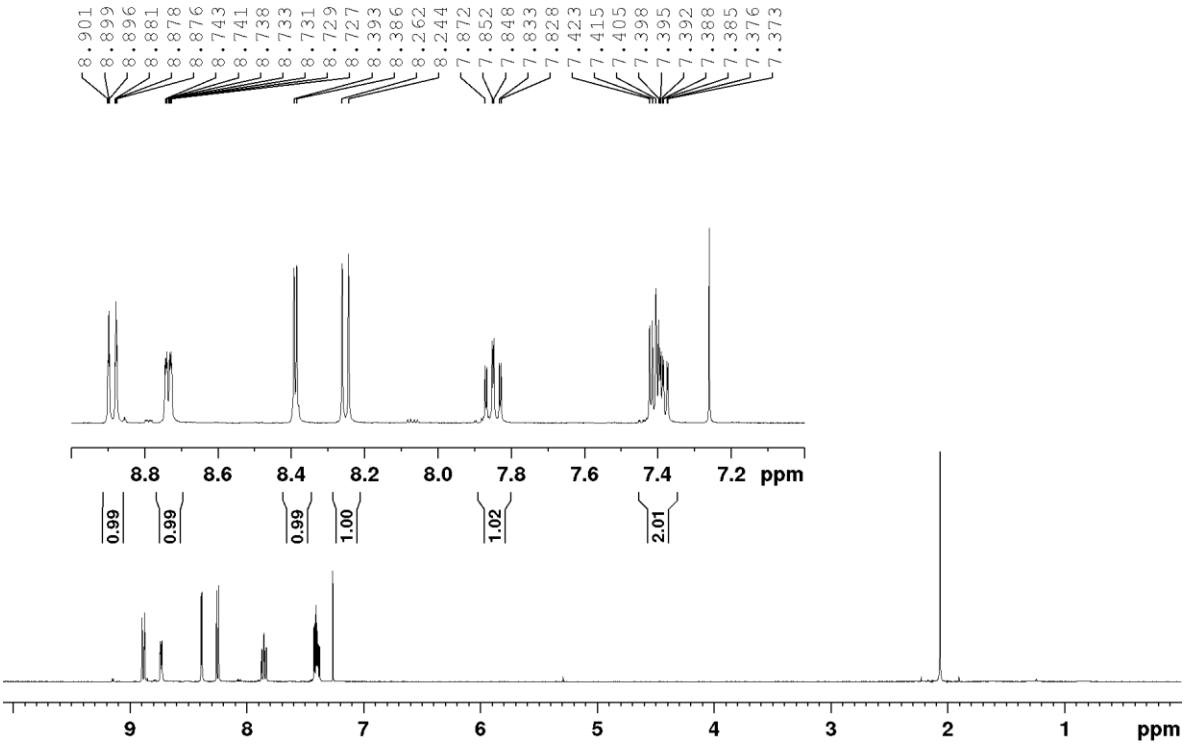

Figure A.5: ^{1}H NMR (400 MHz, CD_3Cl) spectrum of bromo-bpy-N-oxide.

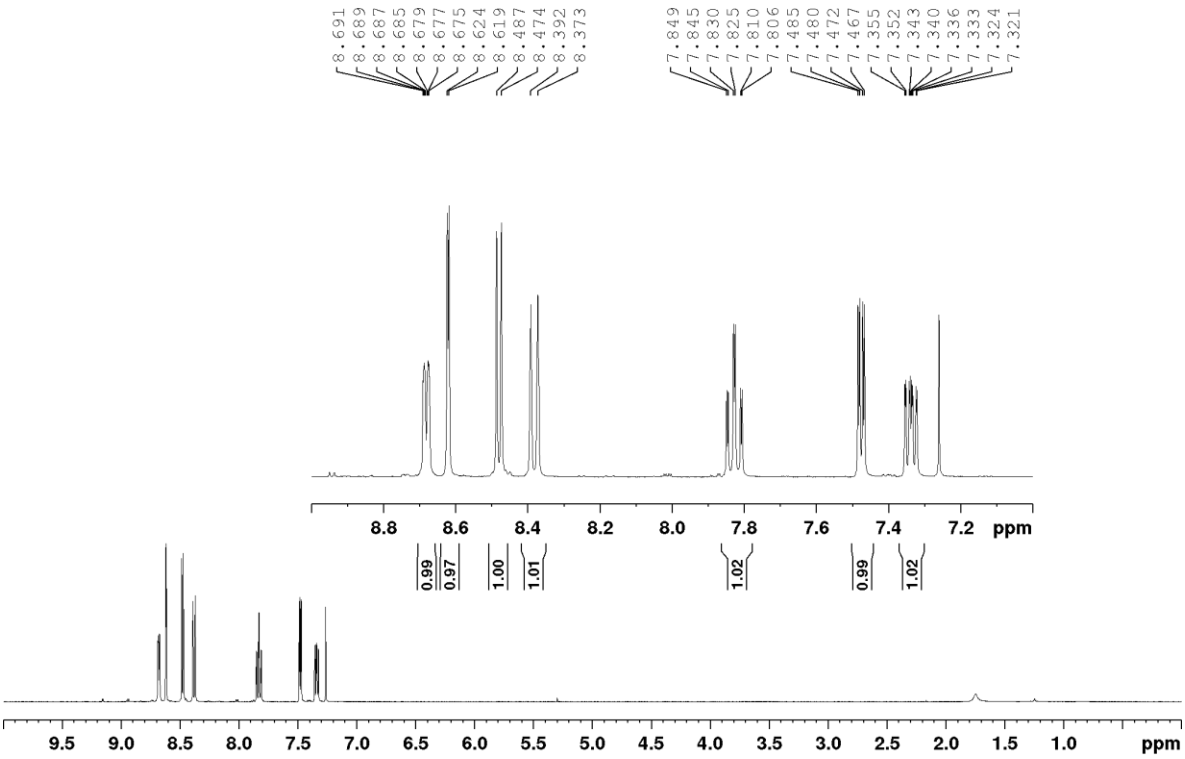

Figure A.6: ^{1}H NMR (400 MHz, CD_3Cl) spectrum of 4-Brbpy.

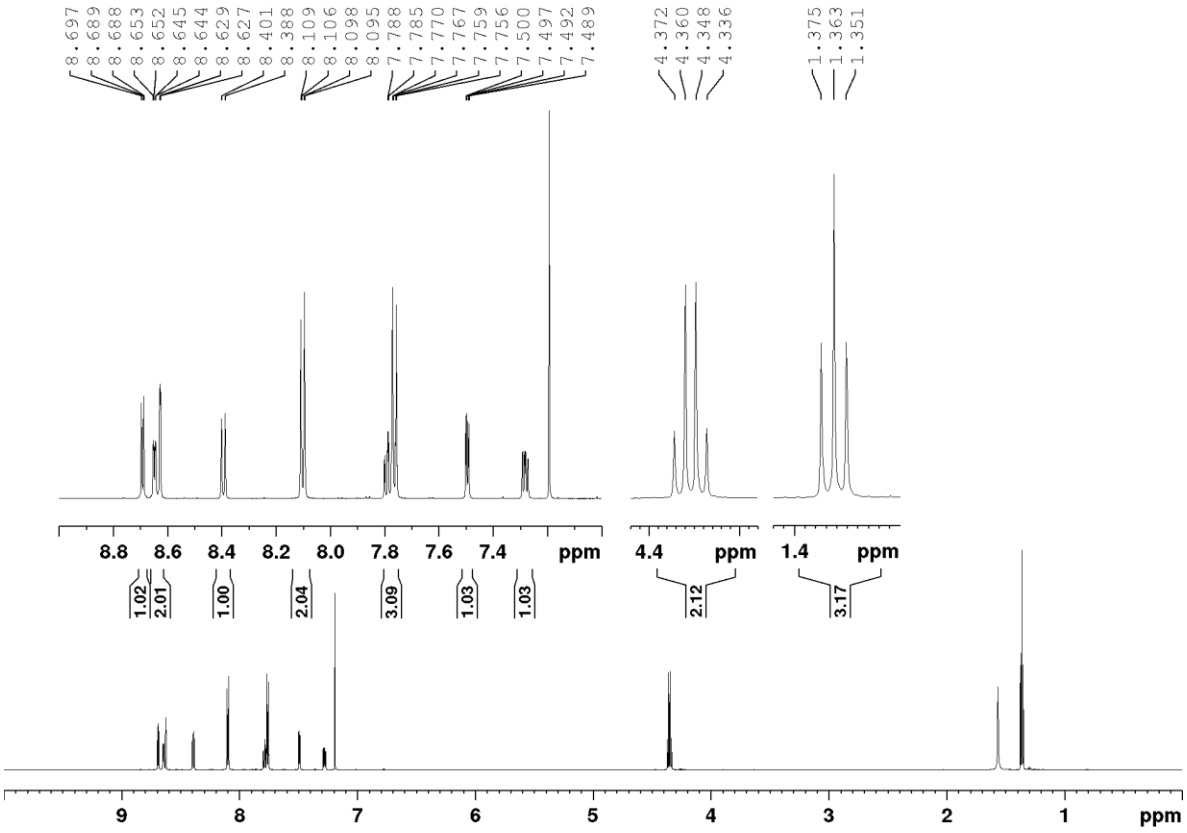

Figure A.7: ^{1}H NMR (600 MHz, CD_3Cl) spectrum of 4-bpyArCOOEt.

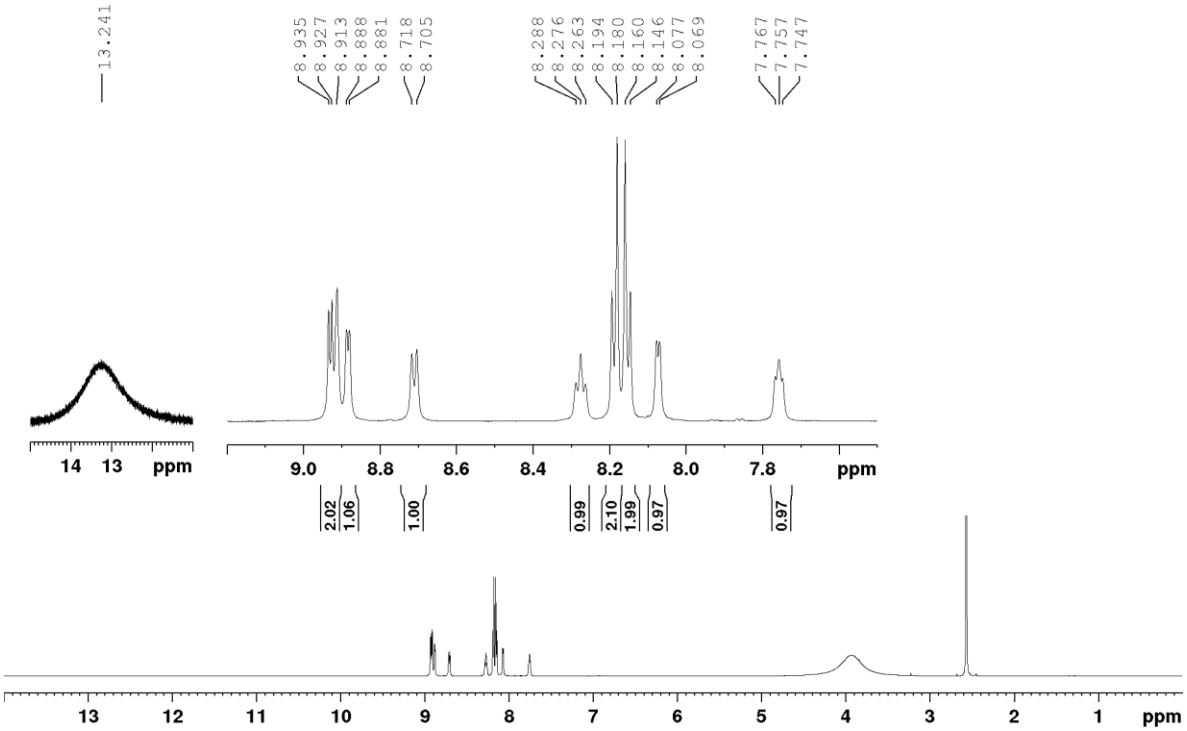

Figure A.8: ^{1}H NMR (600 MHz, DMSO-d6) spectrum of 4-bpyArCOOH.

Single Mass Analysis
Tolerance = 100.0 PPM / DBE: min = -1.5, max = 1000.0
Isotope cluster parameters: Separation = 1.0 Abundance = 1.0%

Monoisotopic Mass, Odd and Even Electron Ions
1 formula(e) evaluated with 1 results within limits (all results (up to 1000) for each mass)

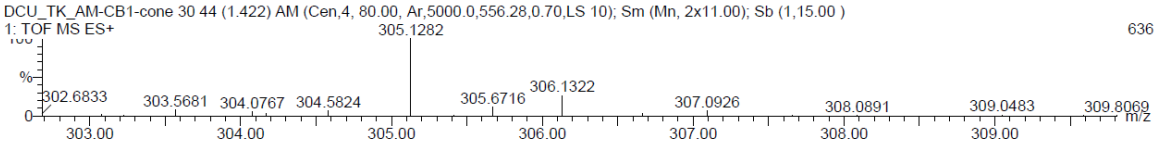

Minimum:				-1.5		
Maximum:		200.0	100.0	1000.0		
Mass	Calc. Mass	mDa	PPM	DBE	Score	Formula
305.1282	305.1290	-0.8	-2.6	12.5	1	C19 H17 N2 O2

Figure A.9: Single mass analysis HR-MS (ESI-qTOF, MS+) spectrum of 4-bpyArCOOEt.

Single Mass Analysis
Tolerance = 50.0 PPM / DBE: min = -1.5, max = 1000.0
Isotope cluster parameters: Separation = 1.0 Abundance = 1.0%

Monoisotopic Mass, Odd and Even Electron Ions
2 formula(e) evaluated with 1 results within limits (all results (up to 1000) for each mass)

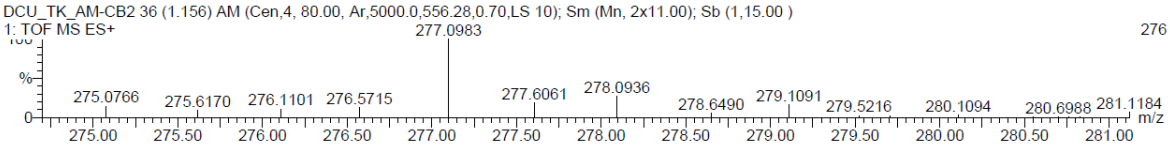

Minimum:				-1.5		
Maximum:		200.0	50.0	1000.0		
Mass	Calc. Mass	mDa	PPM	DBE	Score	Formula
277.0983	277.0977	0.6	2.2	12.5	1	C17 H13 N2 O2

Figure A.10: Single mass analysis HR-MS (ESI-qTOF, MS+) spectrum of 4-bpyArCOOH.

A.1.1.3 5-bpyArCOOR and precursors

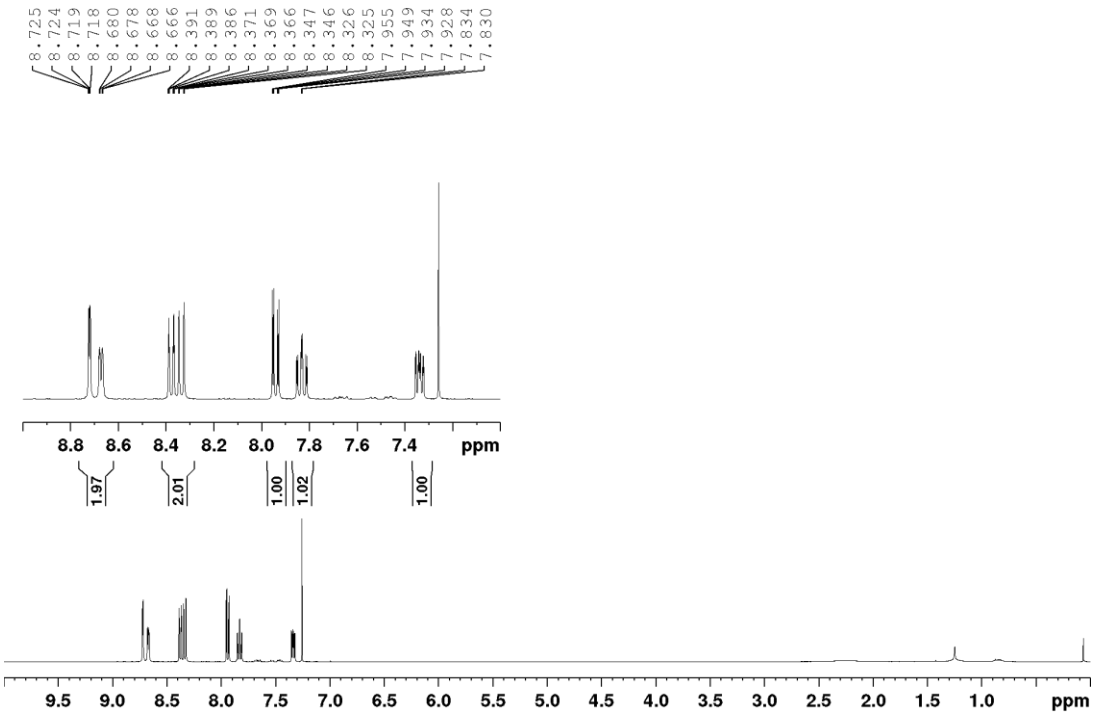

Figure A.11: ^{1}H NMR (400 MHz, $CDCl_3$) spectrum of 5-Brbpy.

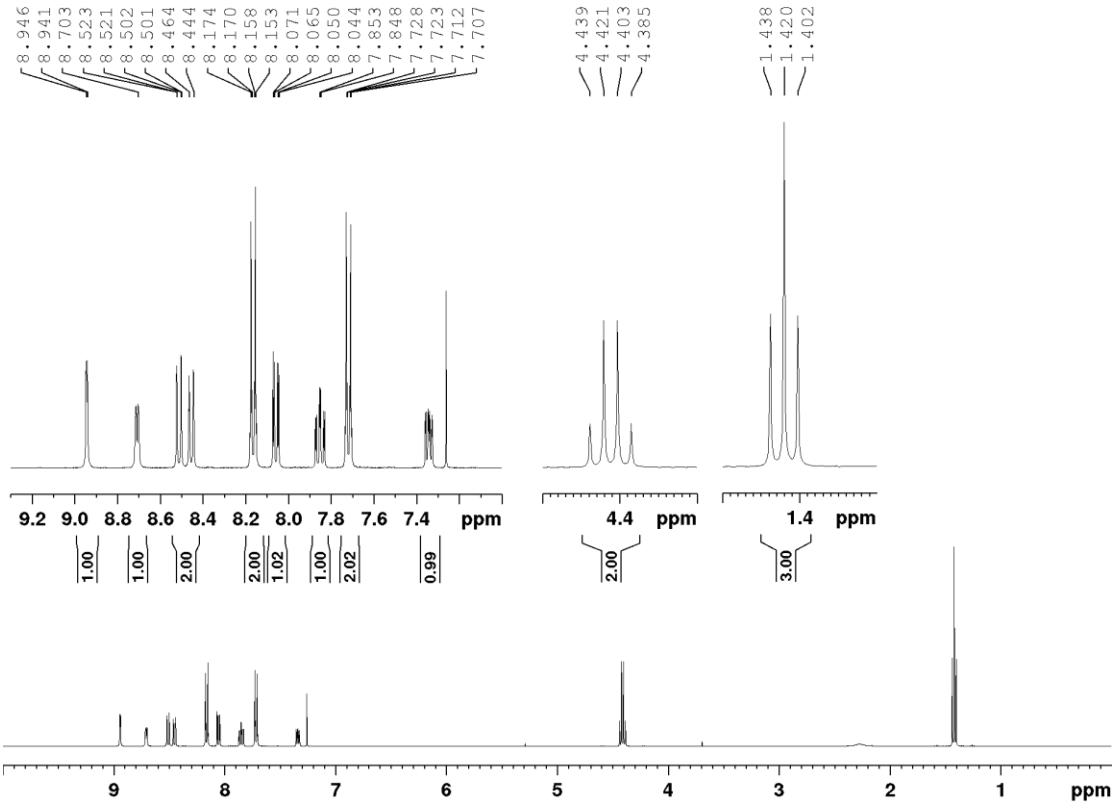

Figure A.12: ^{1}H NMR (400 MHz, $CDCl_3$) spectrum of 5-bpyArCOOEt.

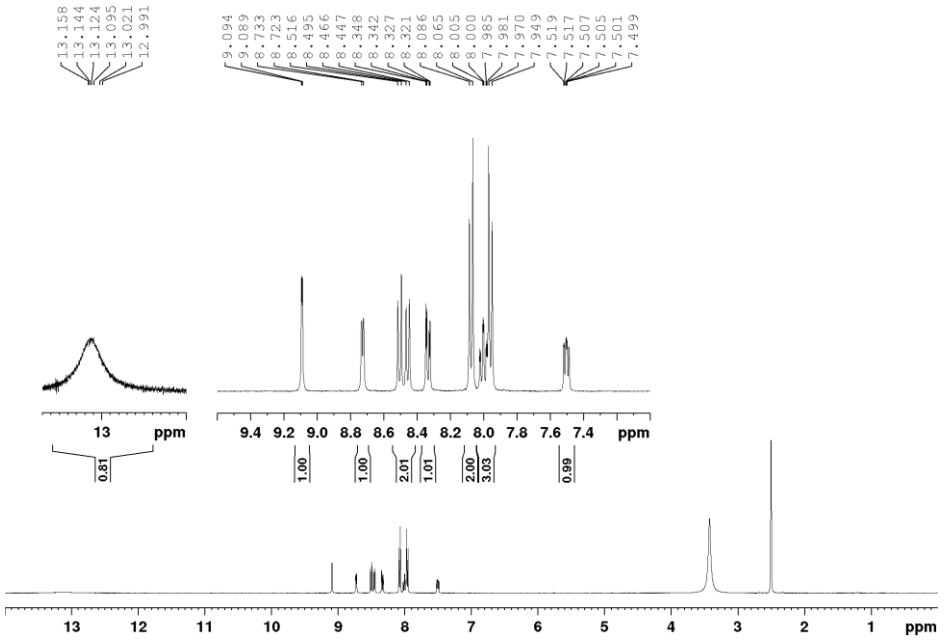

Figure A.13: ^{1}H NMR (400 MHz, DMSO-d_6) spectrum of 5-bpyArCOOH.

Single Mass Analysis
Tolerance = 5.0 PPM / DBE: min = -1.5, max = 1000.0
Isotope cluster parameters: Separation = 1.0 Abundance = 1.0%

Monoisotopic Mass, Odd and Even Electron Ions
38 formula(e) evaluated with 1 results within limits (all results (up to 1000) for each mass)

DCU_TK-CB2 20 (0.648) AM (Cen,4, 80.00, Ar,5000.0,556.28,0.70,LS 10); Sm (Mn, 2x4.00); Sb (1,15.00)
1: TOF MS ES+ 277.0974 623

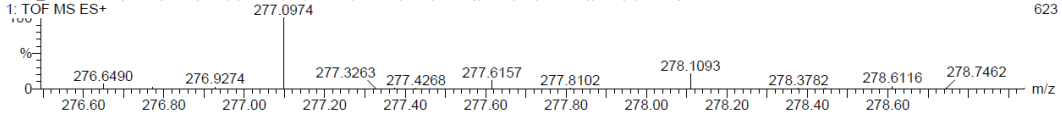

Minimum:				-1.5		
Maximum:		200.0	5.0	1000.0		
Mass	Calc. Mass	mDa	PPM	DBE	Score	Formula
277.0974	277.0977	-0.3	-1.1	12.5	1	C17 H13 N2 O2

Figure A.14: Single mass analysis HR-MS (ESI-qTOF, MS+) spectrum of 5-bpyArCOOEt.

Single Mass Analysis
Tolerance = 5.0 PPM / DBE: min = -1.5, max = 1000.0
Isotope cluster parameters: Separation = 1.0 Abundance = 1.0%

Monoisotopic Mass, Odd and Even Electron Ions
41 formula(e) evaluated with 1 results within limits (all results (up to 1000) for each mass)

DCU_TK-CB1 26 (0.841) AM (Cen,4, 80.00, Ar,5000.0,556.28,0.70,LS 10); Sm (Mn, 2x7.00); Sb (1,15.00); Cm (23:26)
1: TOF MS ES+ 305.1292 1.53e4

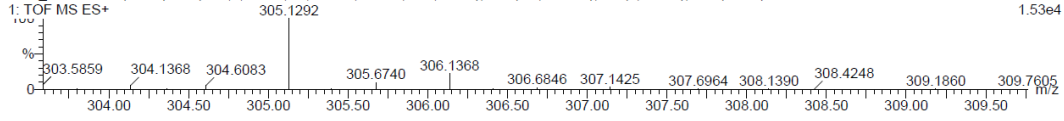

Minimum:				-1.5		
Maximum:		200.0	5.0	1000.0		
Mass	Calc. Mass	mDa	PPM	DBE	Score	Formula
305.1292	305.1290	0.2	0.6	12.5	1	C19 H17 N2 O2

Figure A.15: Single mass analysis HR-MS (ESI-qTOF, MS+) spectrum of 5-bpyArCOOH.

A.1.2 Complexes

A.1.2.1 Ru-DMSO and Ru-oxalate complexes.

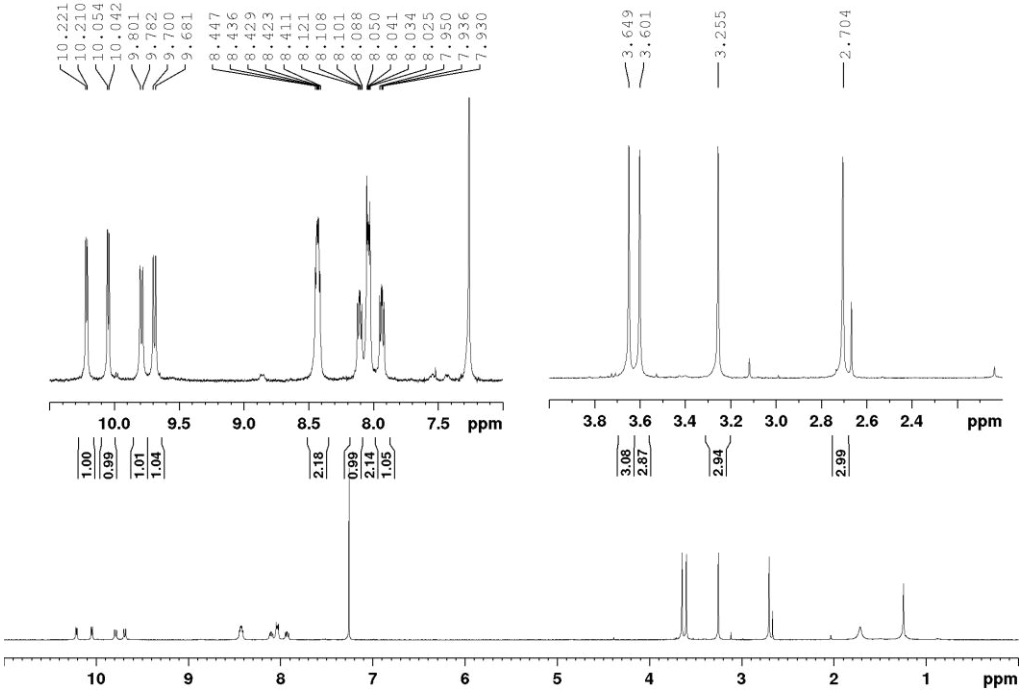

Figure A.16: ^{1}H NMR (400 MHz, $CDCl_3$) spectrum of [Ru(dppz)$(DMSO)_2Cl_2$]. Residual solvent peaks attributable to diethyl ether and water.

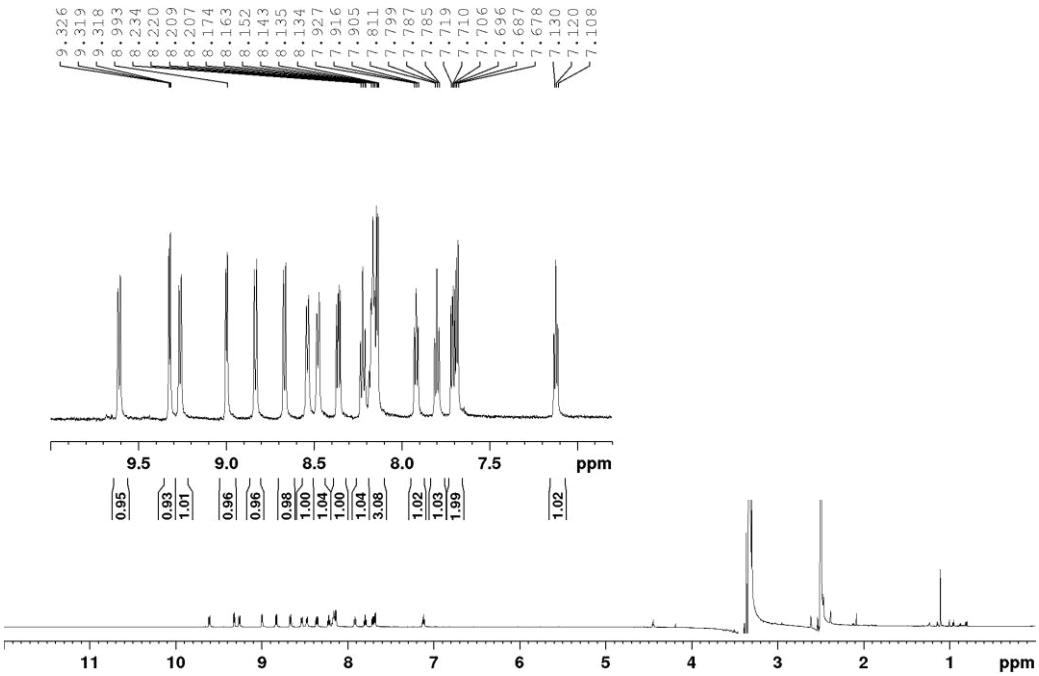

Figure A.17: ^{1}H NMR (600 MHz, DMSO-d_6) spectrum of [Ru(dppz)(bpy)(ox)].

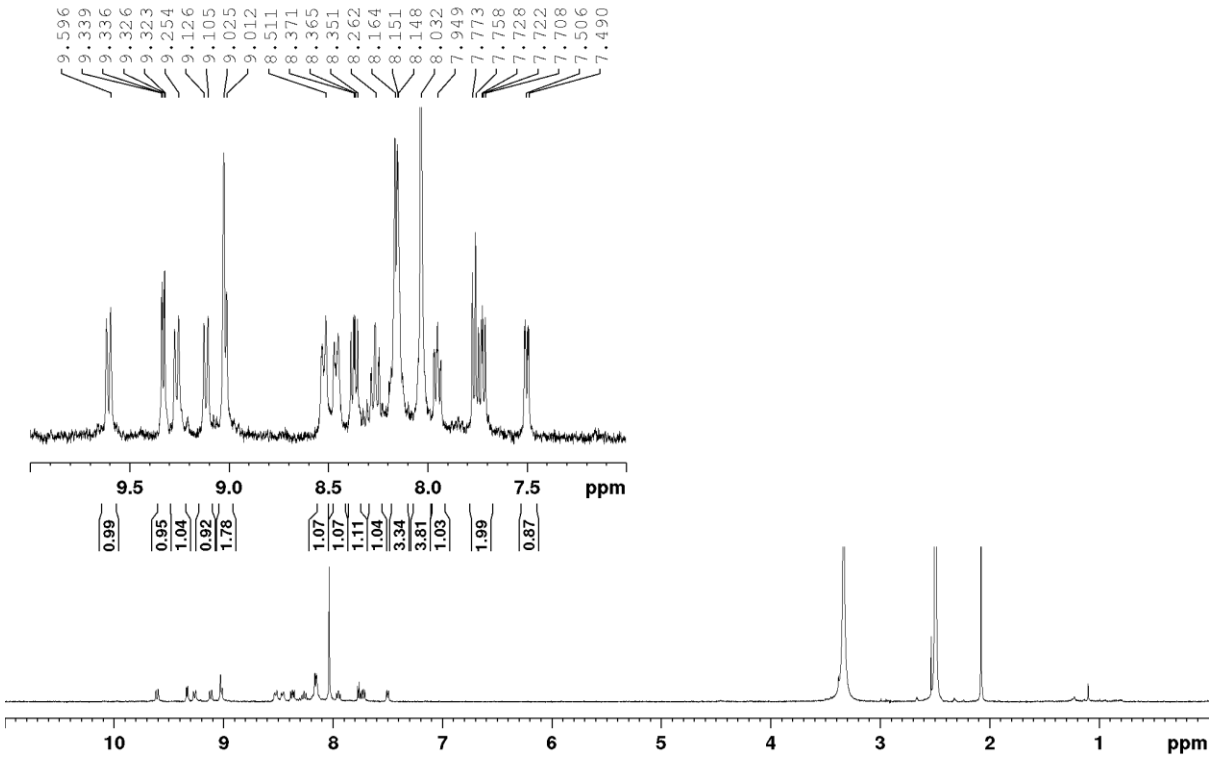

Figure A.18: ^{1}H NMR (400 MHz, DMSO-d_6) spectrum of [Ru(dppz)(bpyArCOOH)(ox)].

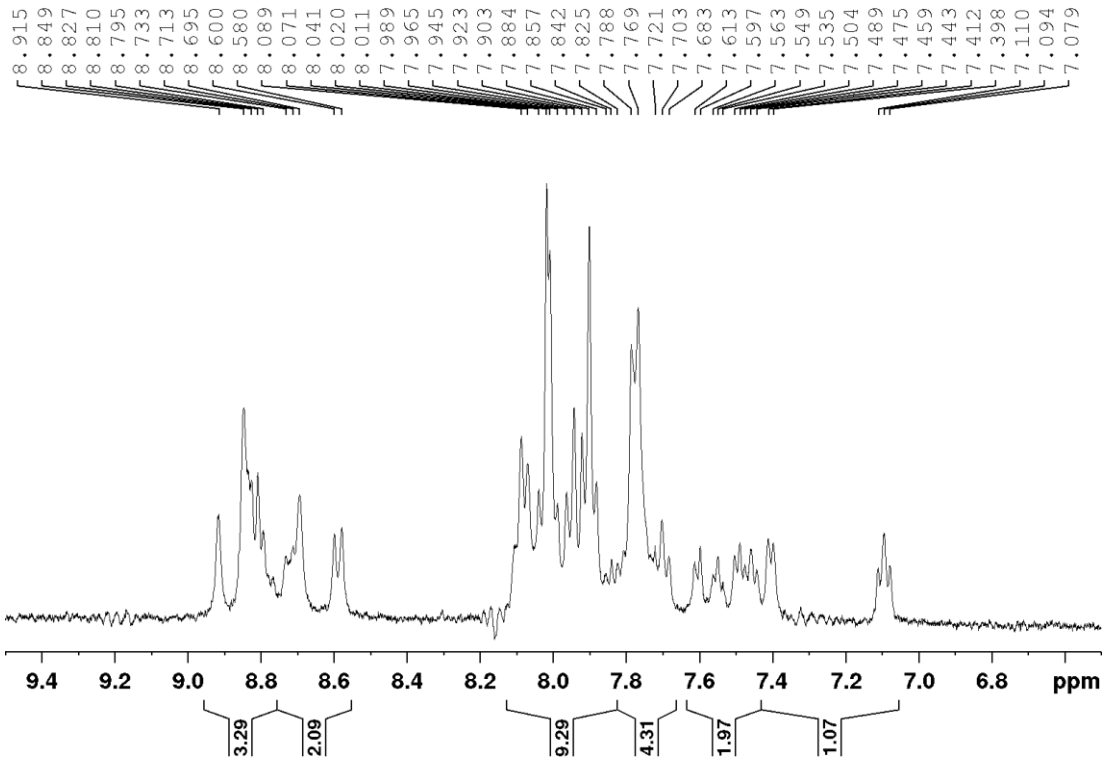

Figure A.19: ^{1}H NMR (400 MHz, DMSO-d_6/D2O/NaOD) spectrum of [Ru(bpyArCOOH)$_2$(ox)].

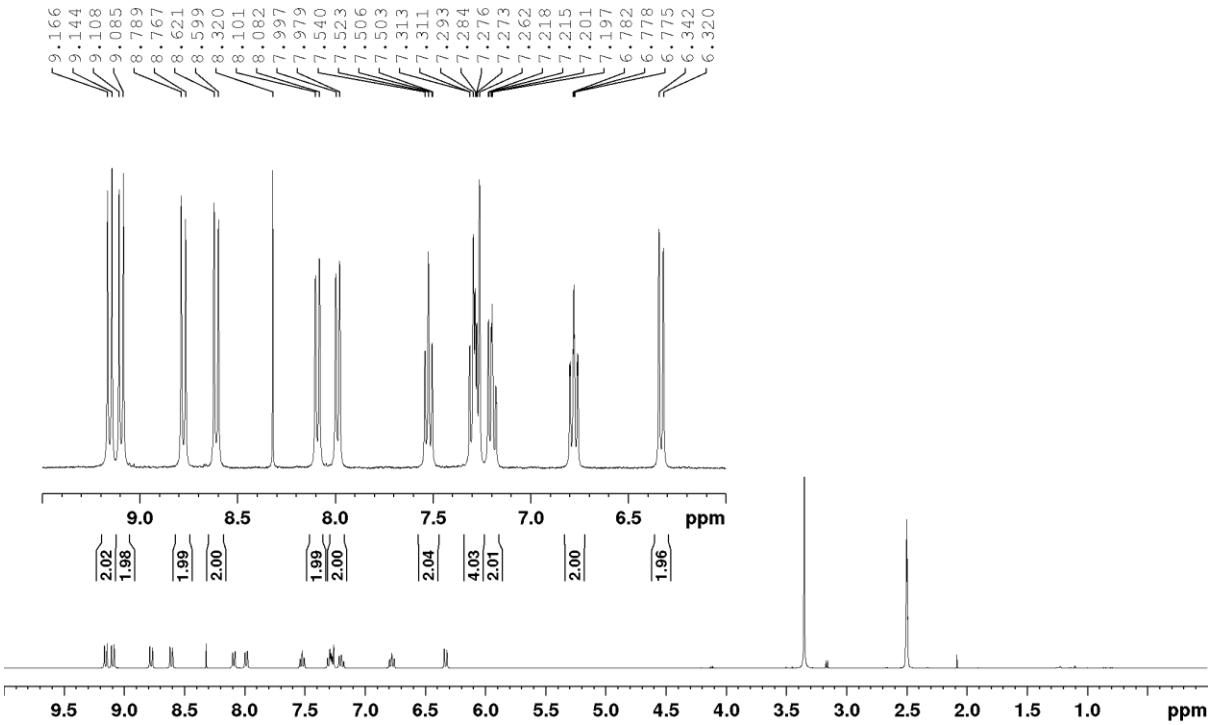

Figure A.20: ^{1}H NMR (400 MHz, DMSO-d_6) spectrum of [Ru(biq)$_2$(ox)]. Residual chloroform peak at 8.32 ppm.

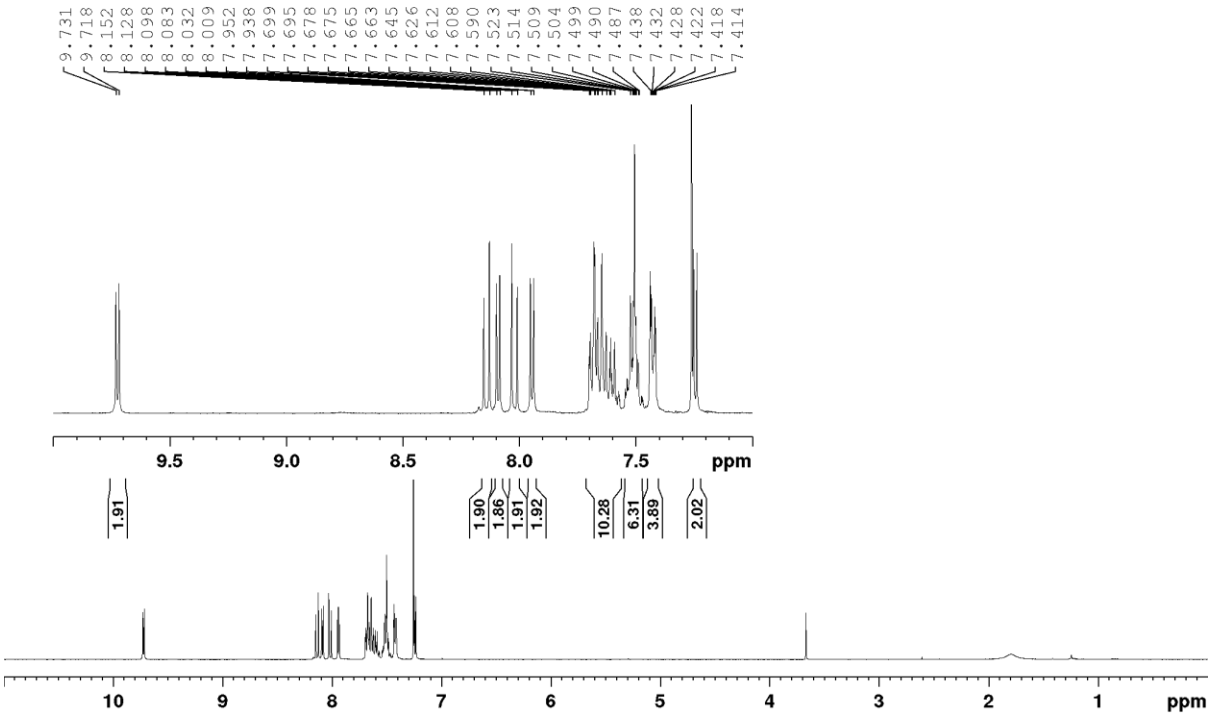

Figure A.21: ^{1}H NMR (400 MHz, $CDCl_3$) spectrum of [Ru(dpp)$_2$(ox)].

A.1.2.2 bis- and tris-heteroleptic Ru(II) polypyridyl complexes.

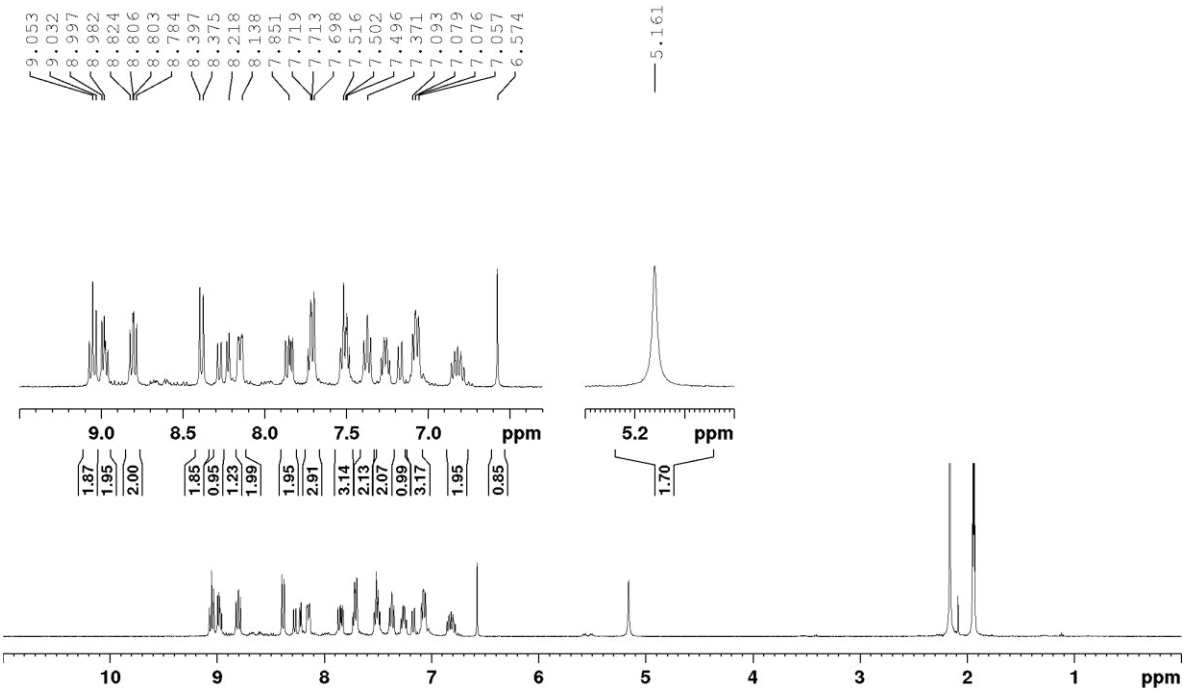

Figure A.22: ^{1}H NMR (400 MHz, CD_3CN) spectrum of $[Ru(biq)_2(aphen)](PF_6)_2$.

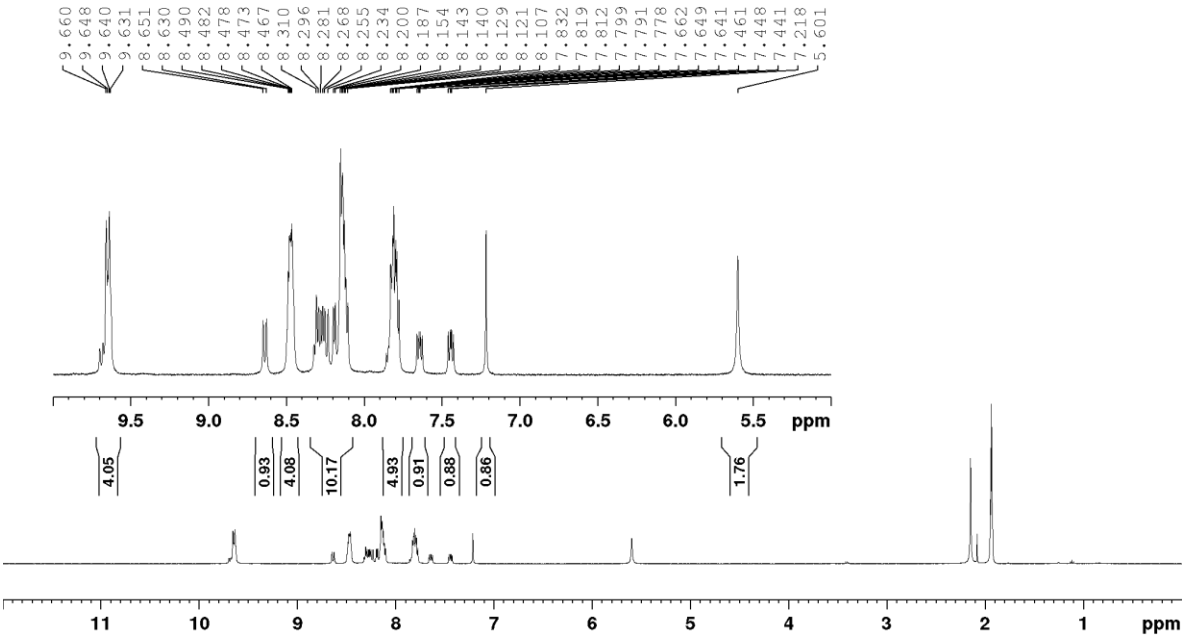

Figure A.23: ^{1}H NMR (400 MHz, CD_3CN) spectrum of $[Ru(dppz)_2(aphen)](PF_6)_2$.

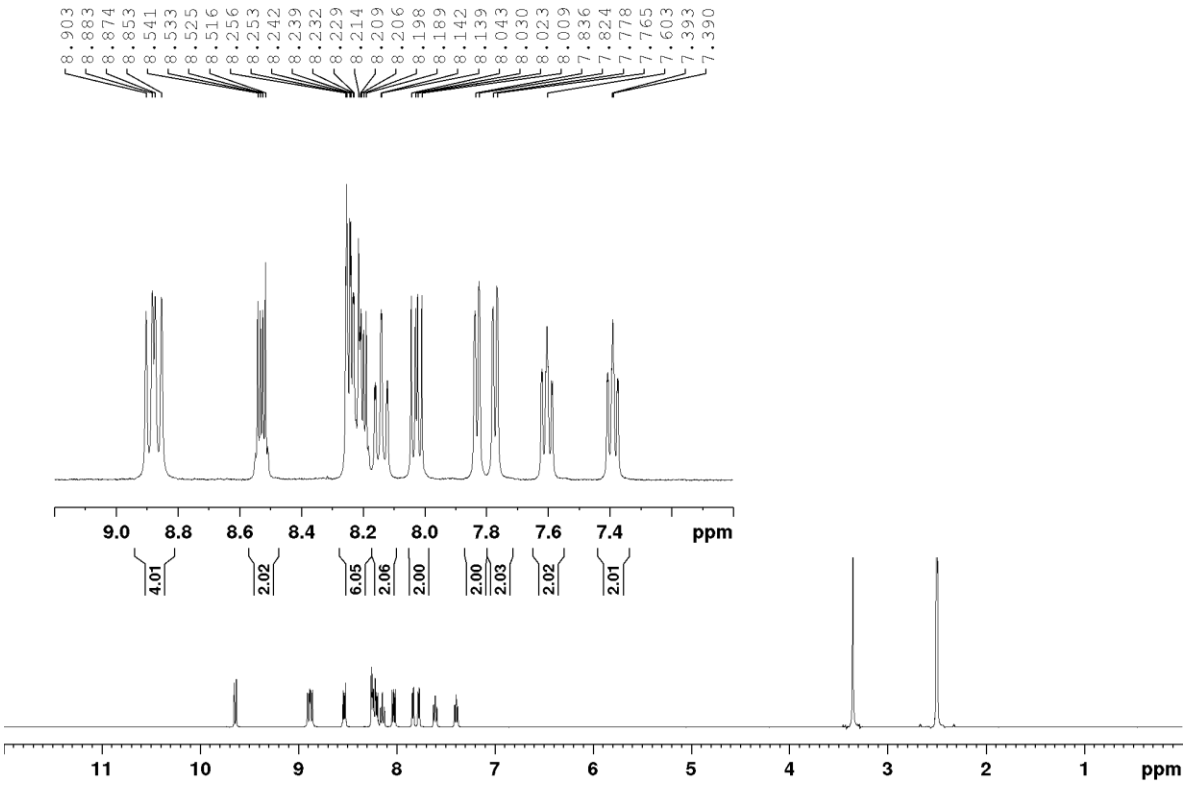

Figure A.24: ^{1}H NMR (400 MHz, DMSO-d_6) spectrum of $[Ru(bpy)_2(dppz)](PF_6)_2$.

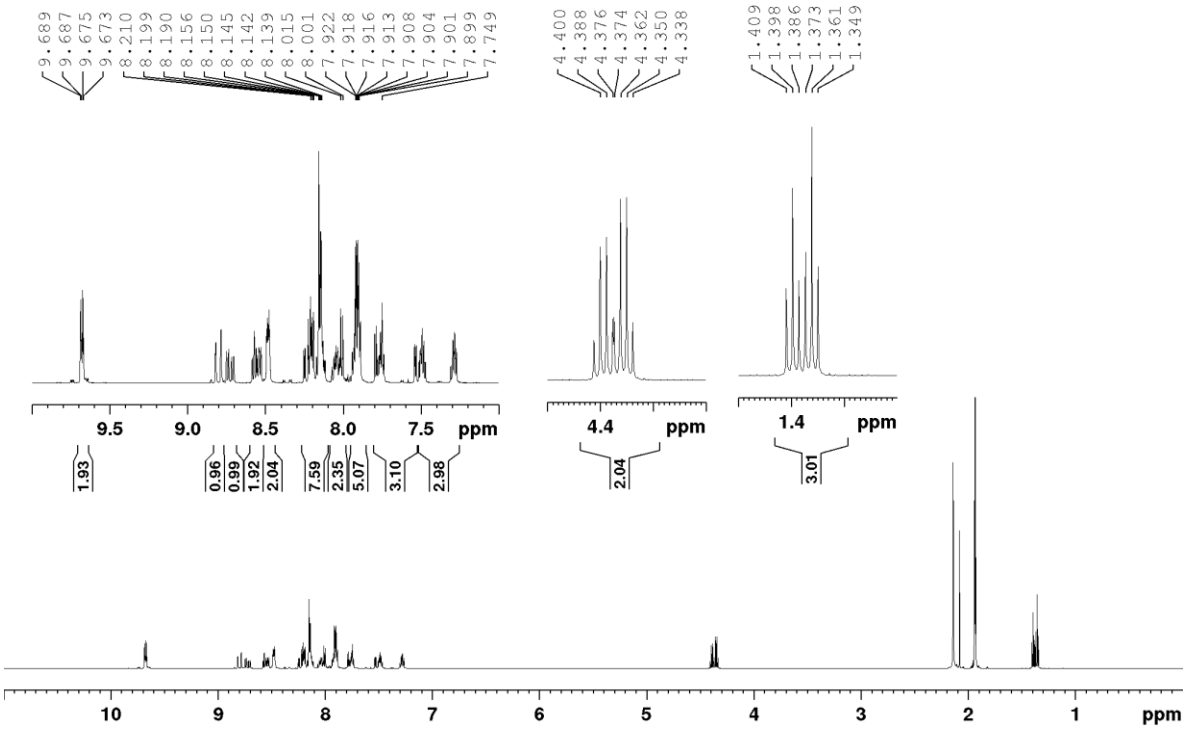

Figure A.25: ^{1}H NMR (600 MHz, CD_3CN) spectrum of $[Ru(dppz)(bpy)(bpyArCOOEt)](PF_6)_2$.

Single Mass Analysis
Tolerance = 5.0 PPM / DBE: min = -1.5, max = 1000.0
Isotope cluster parameters: Separation = 1.0 Abundance = 1.0%

Monoisotopic Mass, Odd and Even Electron Ions
392 formula(e) evaluated with 1 results within limits (all results (up to 1000) for each mass)

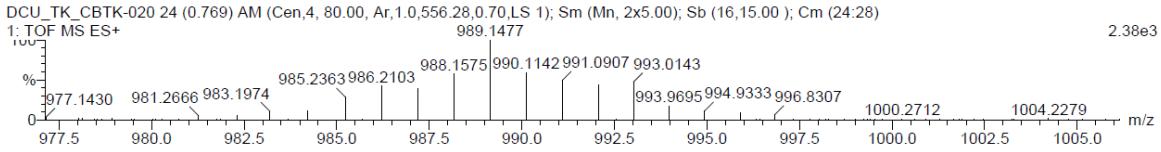

Minimum:				-1.5		
Maximum:		200.0	5.0	1000.0		
Mass	Calc. Mass	mDa	PPM	DBE	Score	Formula
989.1477	989.1490	-1.3	-1.3	32.5	1	C47 H34 N8 O2 Ru F6 P

Figure A.26: Single mass analysis HR-MS (ESI-qTOF, MS+) spectrum of [Ru(dppz)(bpy)(bpyArCOOEt)]$(PF_6)_2$.

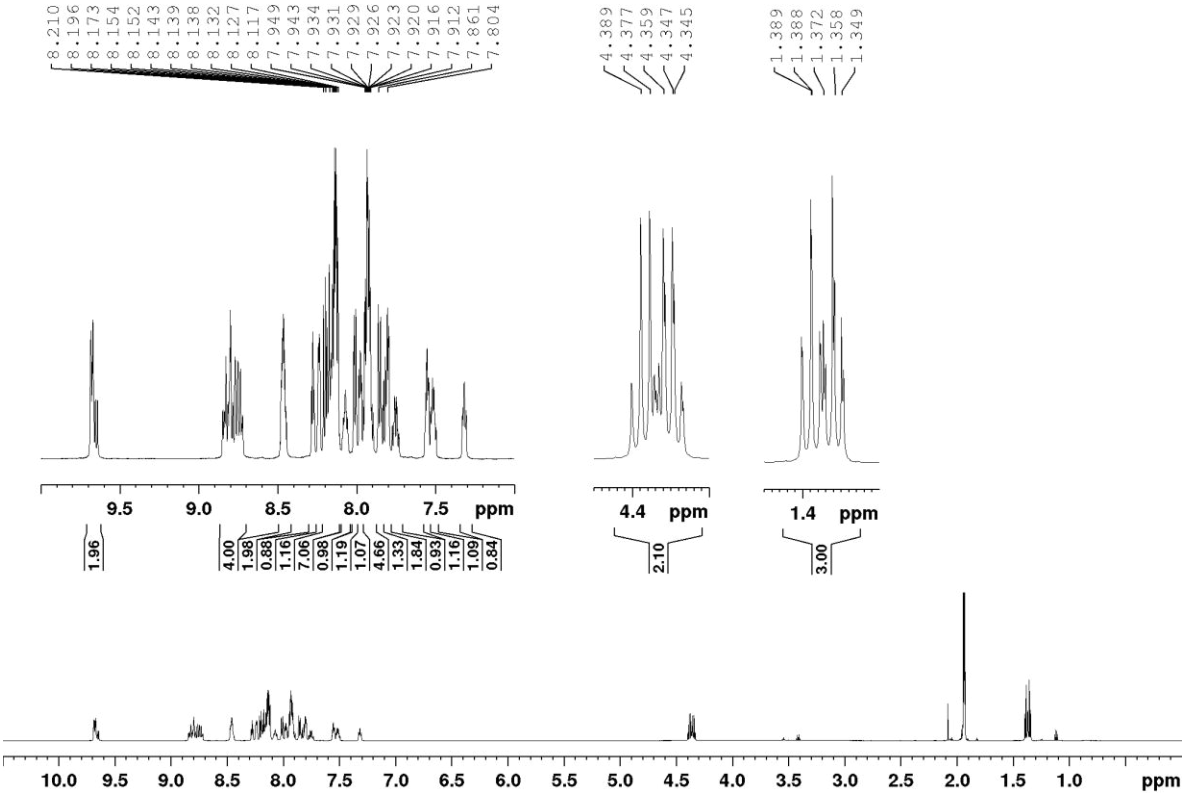

Figure A.27: ^{1}H NMR (600 MHz, CD_3CN) spectrum of [Ru(dppz)(bpyArCOOH)(bpyArCOOEt)] $(PF_6)_2$.

Single Mass Analysis
Tolerance = 6.0 PPM / DBE: min = -1.5, max = 1000.0
Isotope cluster parameters: Separation = 1.0 Abundance = 1.0%

Monoisotopic Mass, Odd and Even Electron Ions
459 formula(e) evaluated with 1 results within limits (all results (up to 1000) for each mass)

DCU_TK_CBTK-031 r 9 (0.285) AM (Cen,4, 80.00, Ar,1.0,556.28,0.70,LS 1); Sm (Mn, 2x2.00); Sb (16,15.00); Cm (9:16)
1: TOF MS ES+ 9.27e3

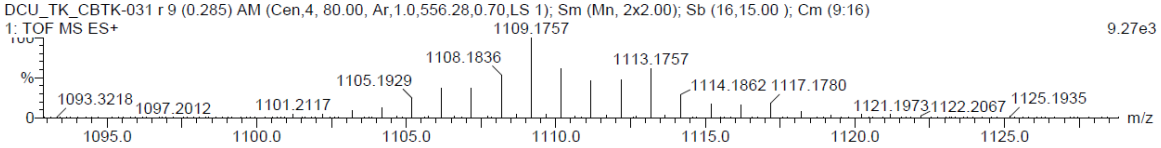

Minimum:				-1.5		
Maximum:		200.0	6.0	1000.0		
Mass	Calc. Mass	mDa	PPM	DBE	Score	Formula
1109.1757	1109.1701	5.6	5.0	37.5	1	C54 H38 N8 O4 F6 P Ru

Figure A.28: Single mass analysis HR-MS (ESI-qTOF, MS+) spectrum of [Ru(dppz)(bpyArCOOH)(bpyArCOOEt)]$(PF_6)_2$

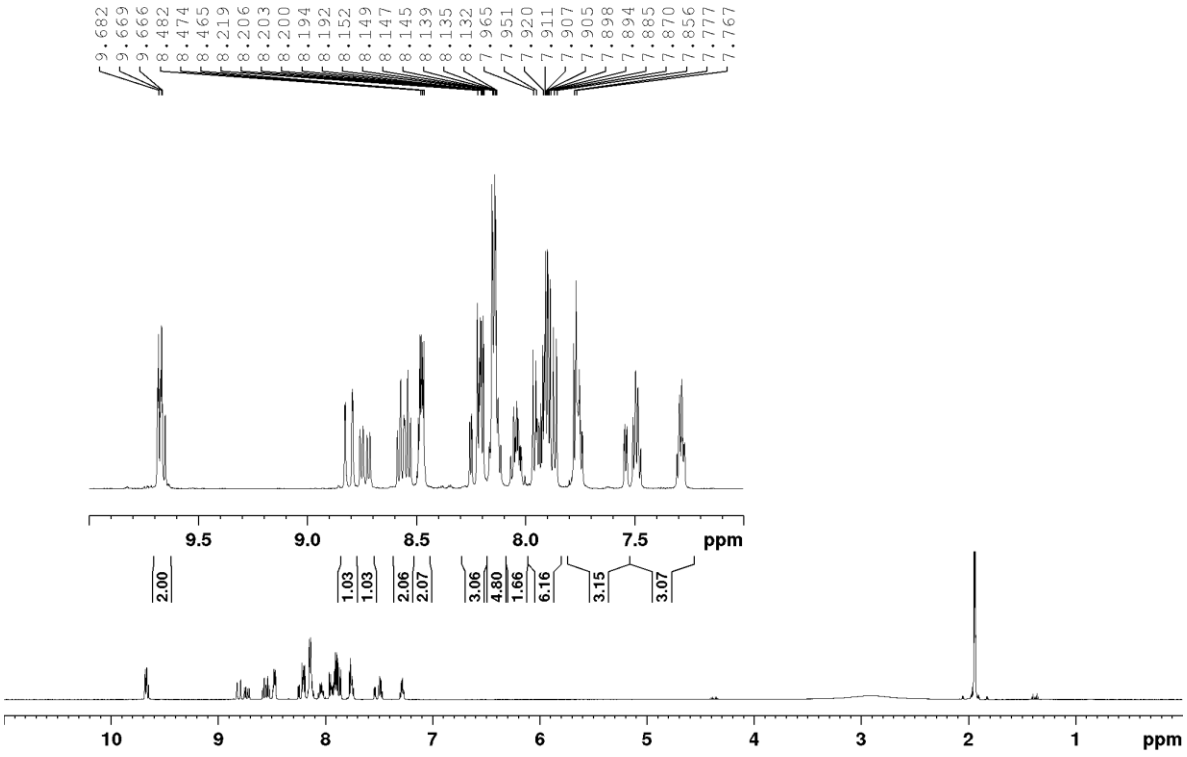

Figure A.29: ^{1}H NMR (600 MHz, CD_3CN) spectrum of [Ru(dppz)(bpy)(bpyArCOOH)]$(PF_6)_2$.

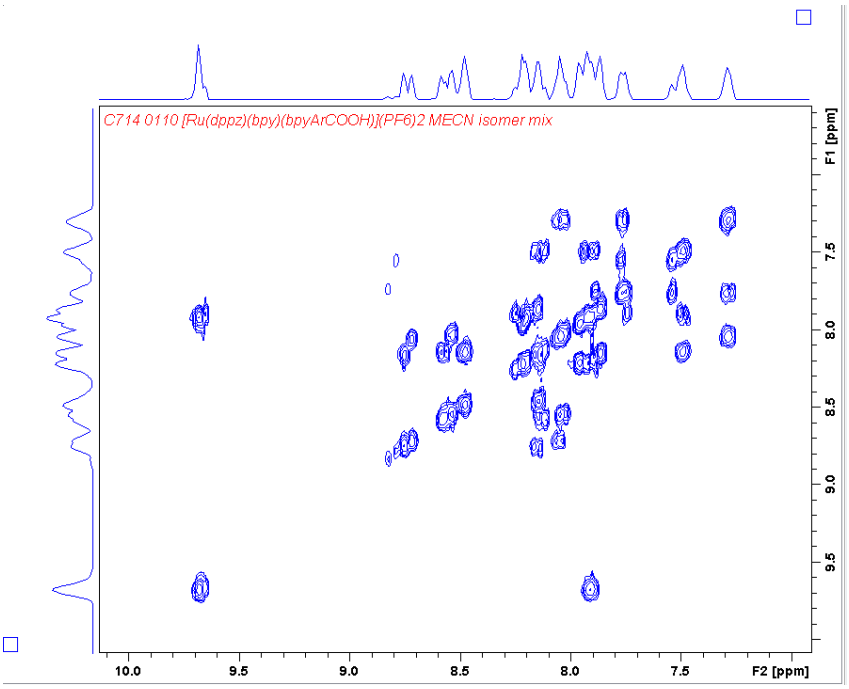

Figure A.30: COSY NMR (600 MHz, CD_3CN) spectrum of $[Ru(dppz)(bpy)(bpyArCOOH)](PF_6)_2$.

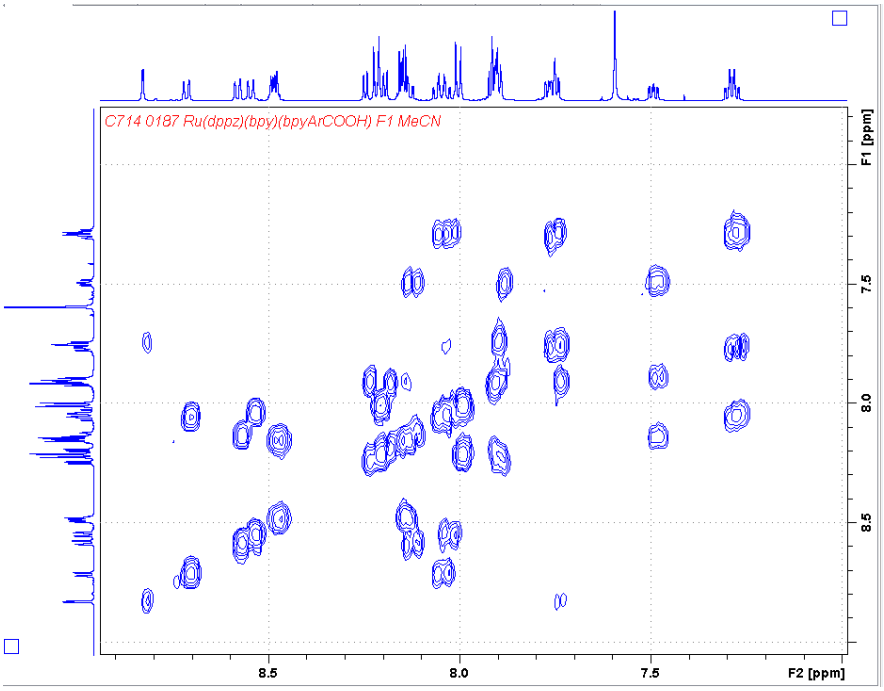

Figure A.31: COSY NMR (600 MHz, CD_3CN) spectrum of the t-dppz isomer of $[Ru(dppz)(bpy)(bpyArCOOH)](PF_6)_2$.

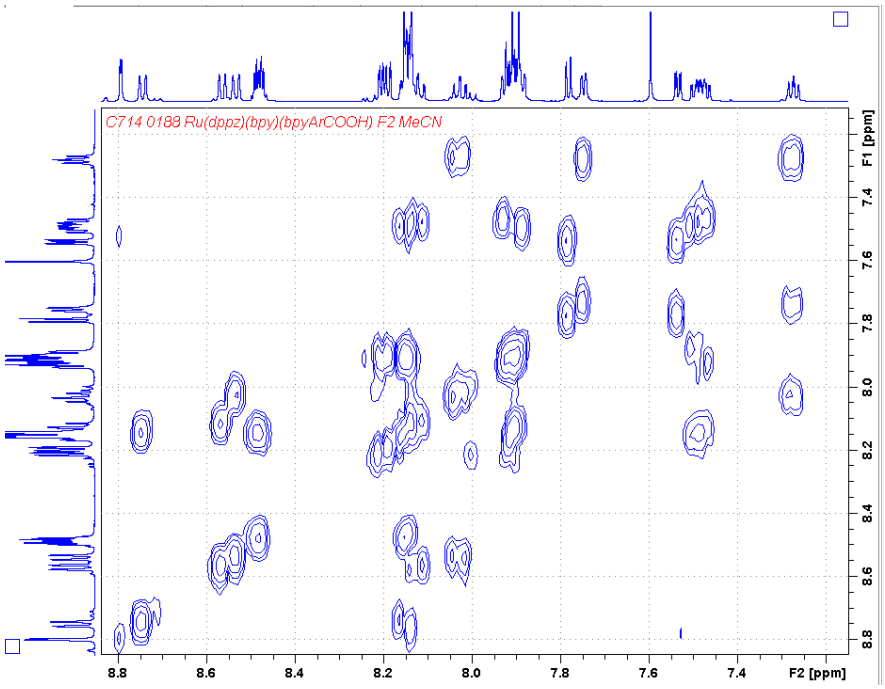

Figure A.32: COSY NMR (600 MHz, CD_3CN) spectrum of the t-bpy isomer of $[Ru(dppz)(bpy)(bpyArCOOH)](PF_6)_2$.

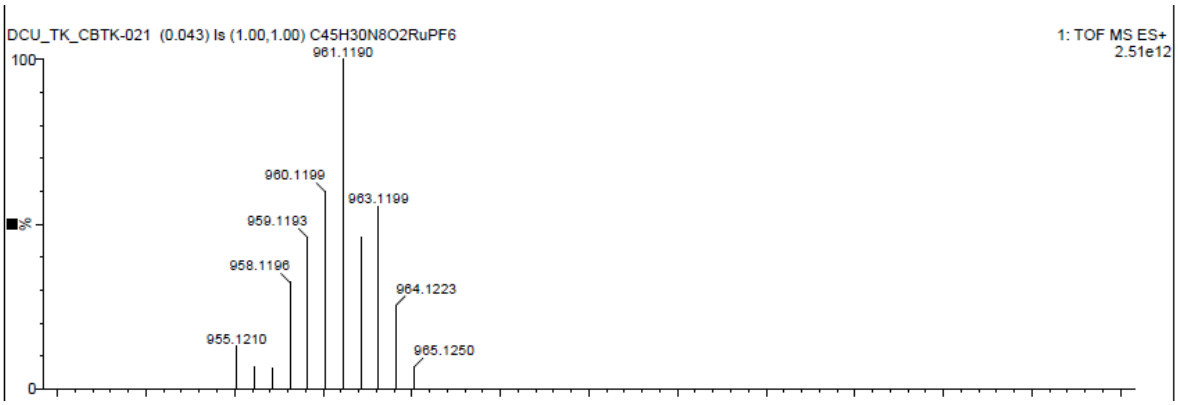

Figure A.33: HR-MS (ESI-qTOF, MS+) spectrum of $[Ru(dppz)(bpy)(bpyArCOOH)](PF_6)_2$.

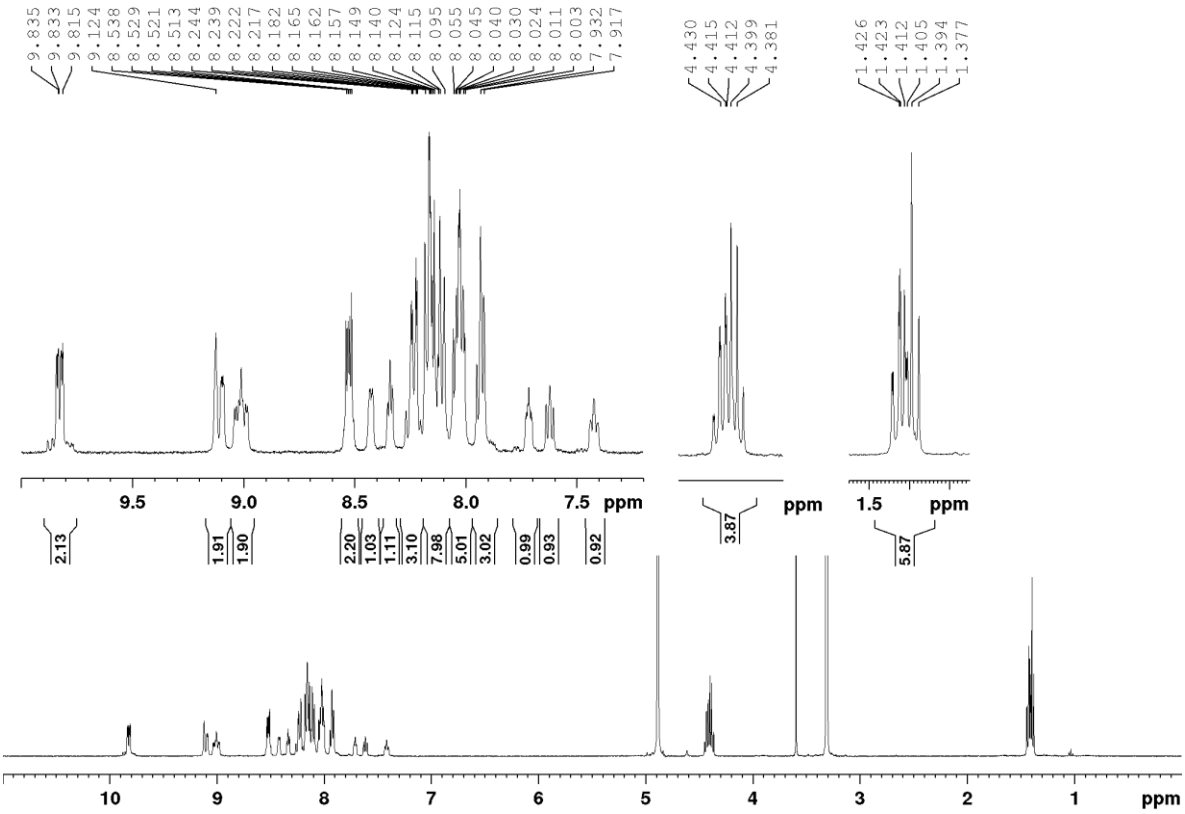

Figure A.34: ^{1}H NMR (600 MHz, CD_3OD/D_2O) spectrum of $[Ru(bpyArCOOEt)_2(dppz)]Cl_2$.

Single Mass Analysis
Tolerance = 5.0 PPM / DBE: min = -1.5, max = 1000.0
Isotope cluster parameters: Separation = 1.0 Abundance = 1.0%

Monoisotopic Mass, Odd and Even Electron Ions
149 formula(e) evaluated with 1 results within limits (all results (up to 1000) for each mass)

DCU_TK-CB3 25 (0.817) AM (Cen,4, 80.00, Ar,5000.0,556.28,0.70,LS 10); Sm (Mn, 2x4.00); Sb (1,15.00); Cm (13:26-(1:15+58:75))
1: TOF MS ES+

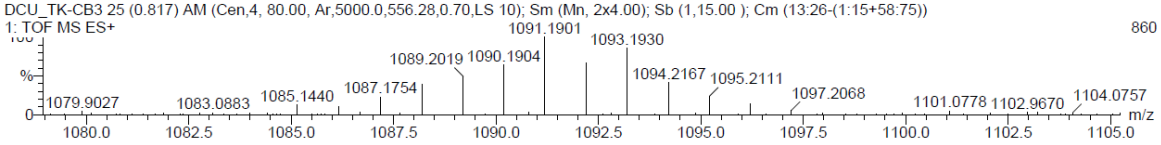

Minimum:				-1.5		
Maximum:		200.0	5.0	1000.0		
Mass	Calc. Mass	mDa	PPM	DBE	Score	Formula
1091.1901	1091.1858	4.3	4.0	39.5	1	C56 H42 N8 O8 Cl Ru

Figure A.35: Single mass analysis HR-MS (ESI-qTOF, MS+) spectrum of $[Ru(bpyArCOOEt)_2(dppz)](ClO_4)_2$.

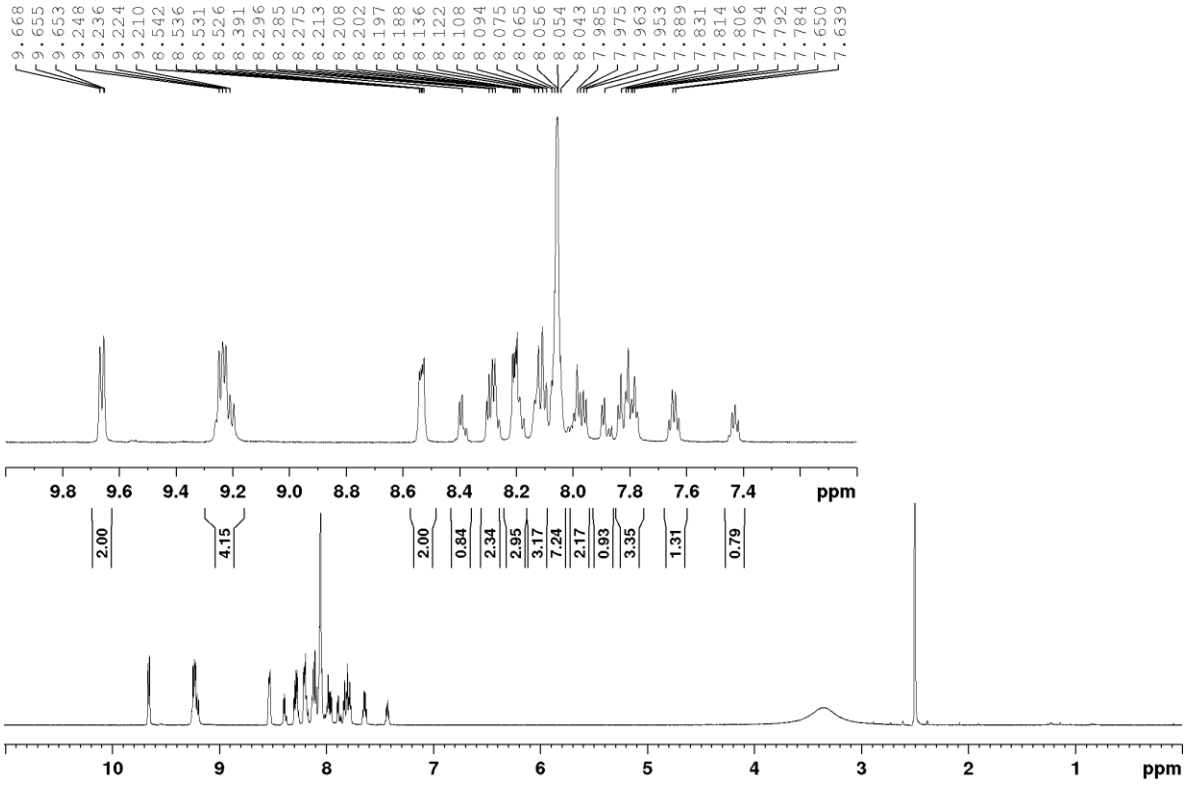

Figure A.36: ^{1}H NMR (600 MHz, DMSO-d_6) of $[Ru(dppz)(bpyArCOOH)_2]^{2+}$ (resolved major isomer).

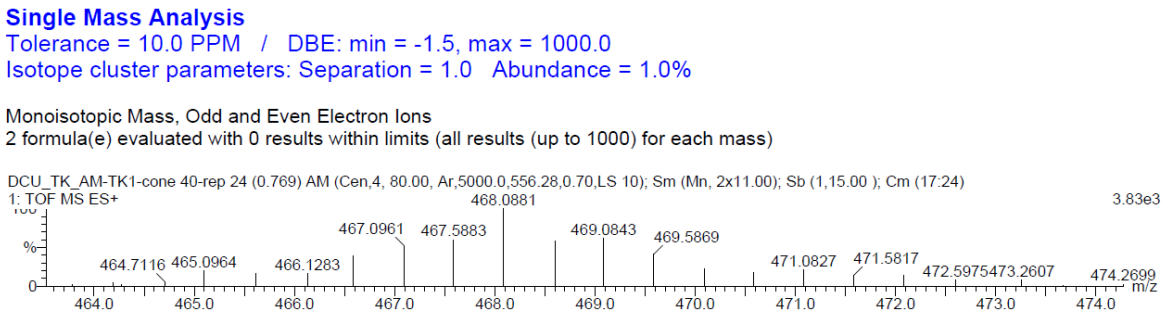

Figure A.37: Single mass analysis HR-MS (ESI-qTOF, MS+) spectrum of $[Ru(bpyArCOOH)_2(dppz)]^{2+}$ to show the $[M]^{2+}$ region.

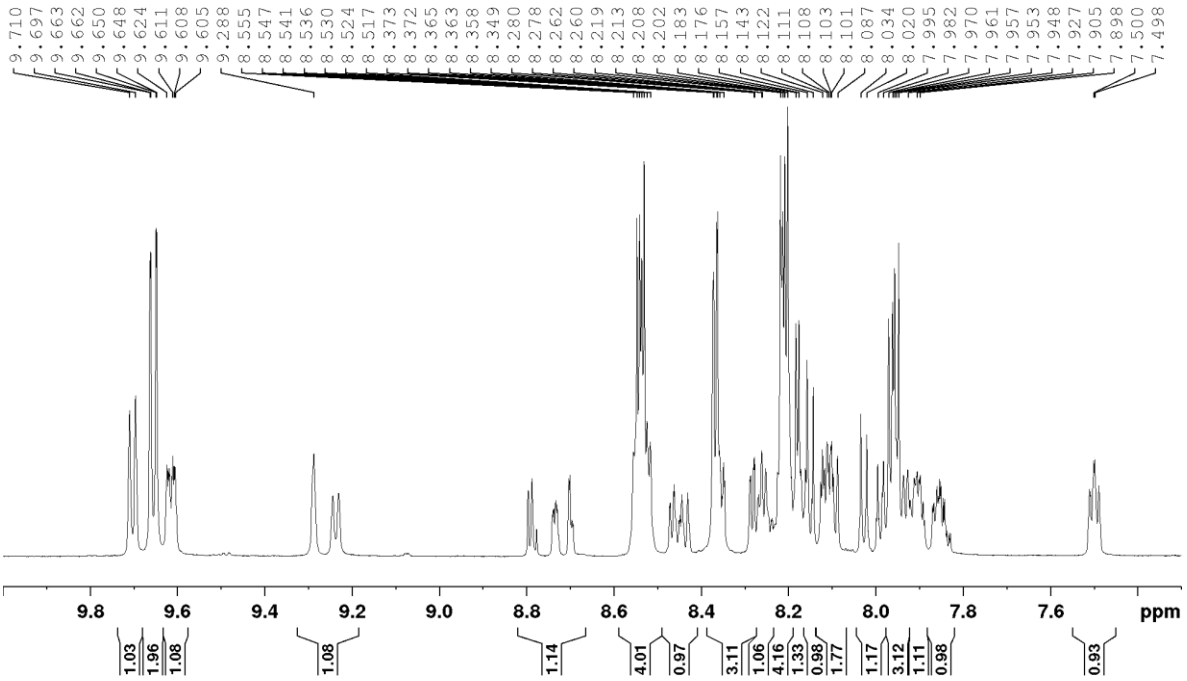

Figure A.38: ^{1}H NMR (600 MHz, CD_3CN) spectrum of $[Ru(dppz)_2(bpyArCOOH)](PF_6)_2$.

A.1.3 Conjugates

A.1.3.1 Ru(II) single peptide conjugates

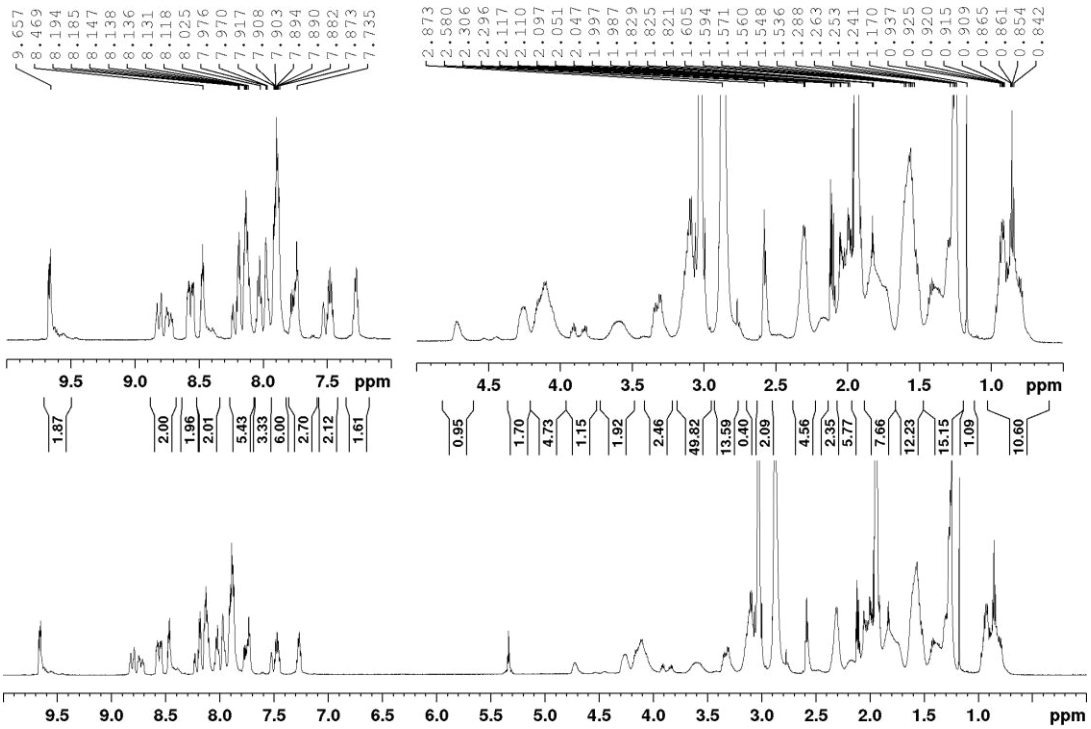

Figure A.39: ^{1}H NMR (600 MHz, CD_3CN/D_2O) spectrum of Ru-NLS..

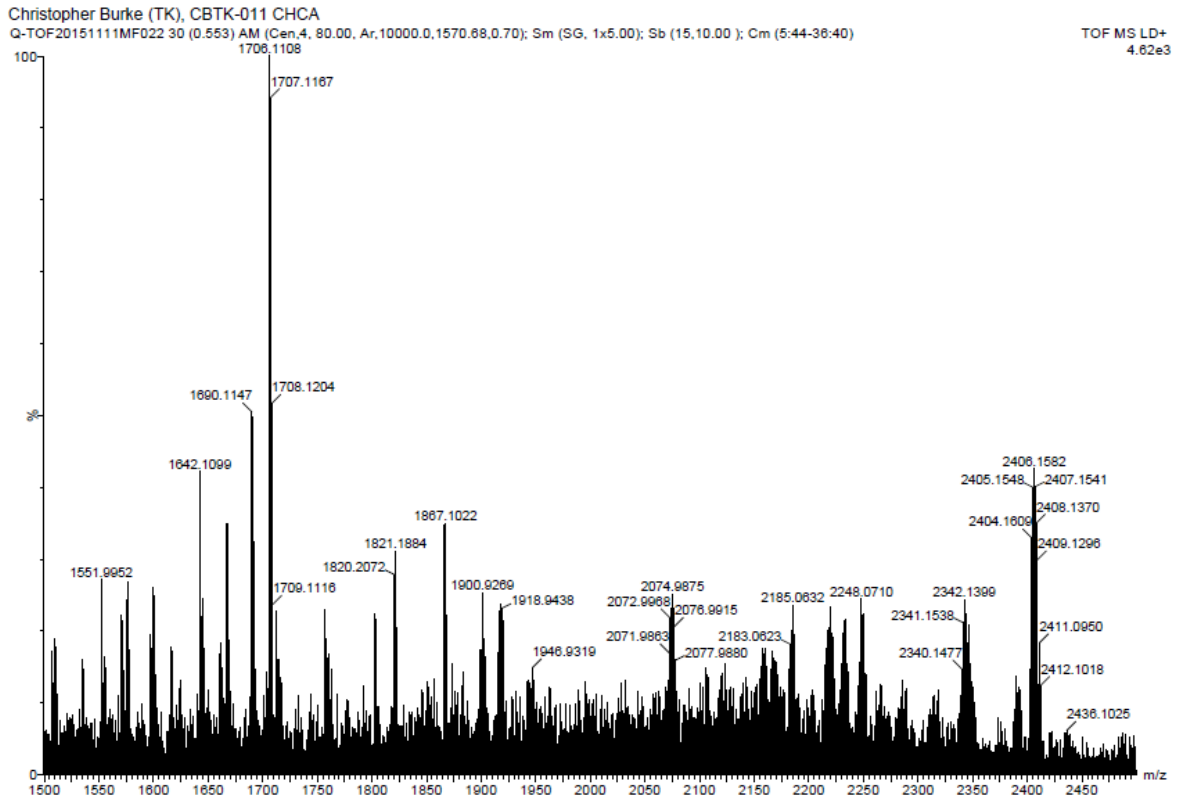

Figure A.40: HR-MS (ESI-qTOF, MS+) spectrum of Ru-NLS.

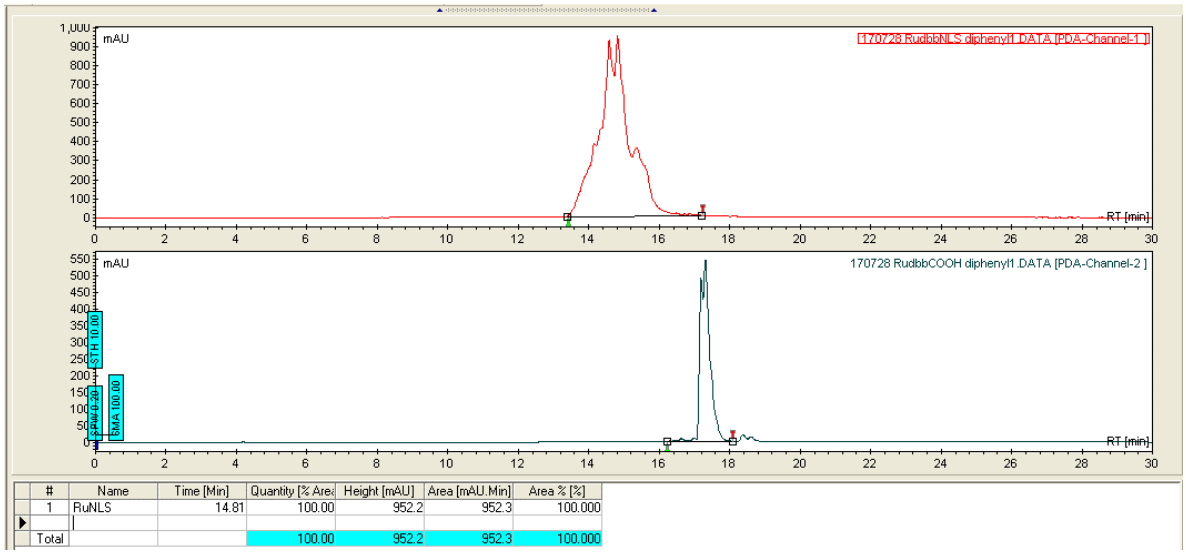

Figure A.41: HPLC chromatograms for Ru-NLS (top trace) and parent complex (bottom trace) run under HPLC General Method 2 (Chapter 2).

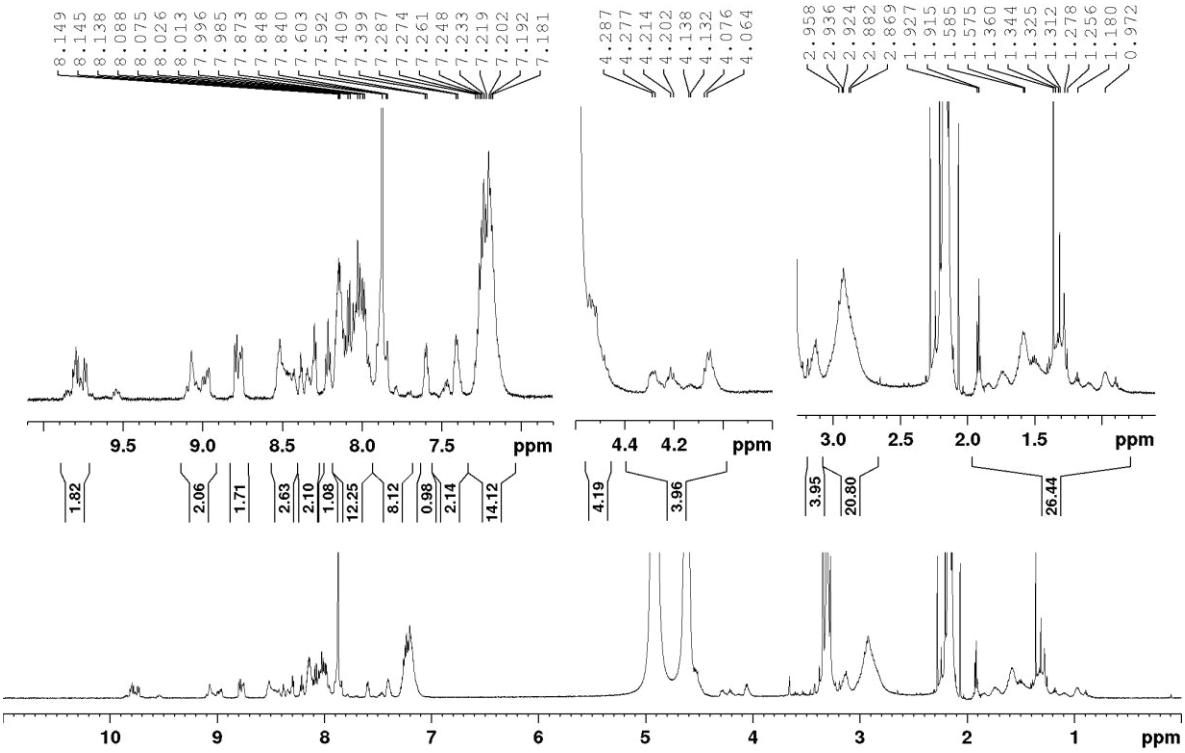

Figure A.42: ^{1}H NMR (600 MHz, CD_3OD/D_2O) spectrum of Ru-MPP..

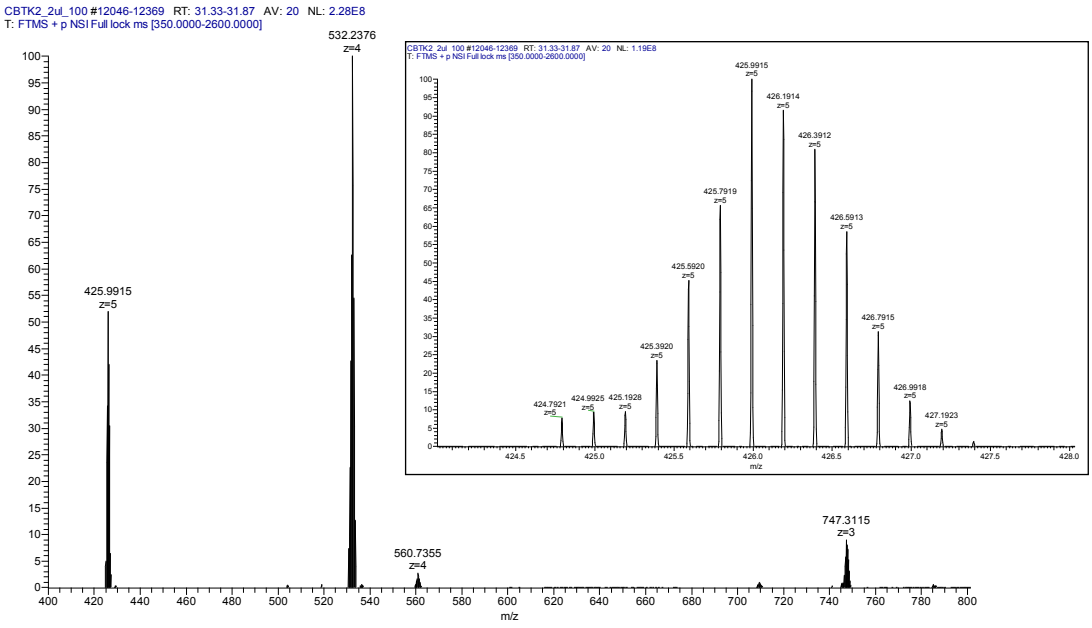

Figure A.43: HR-MS (ESI-qTOF, MS+) spectrum of Ru-MPP with inset to indicate $[M]^{5+}$ region.

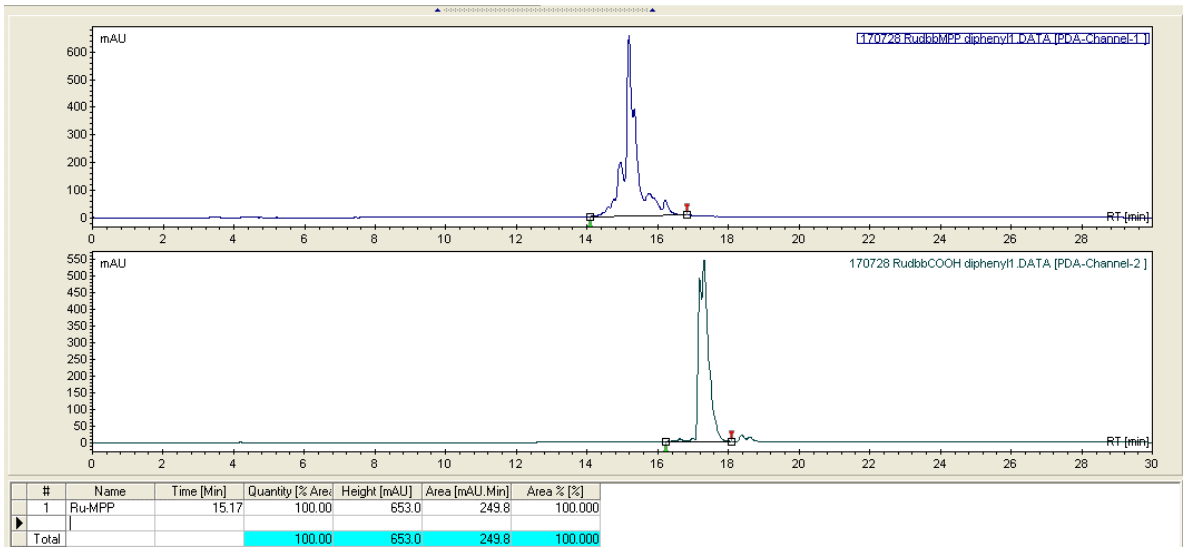

#	Name	Time [Min]	Quantity [% Area]	Height [mAU]	Area [mAU.Min]	Area % [%]
1	Ru-MPP	15.17	100.00	653.0	249.8	100.000
Total			100.00	653.0	249.8	100.000

Figure A.44: HPLC chromatograms for Ru-MPP (top trace) and parent complex (bottom trace) run under HPLC General Method 2 (Chapter 2).

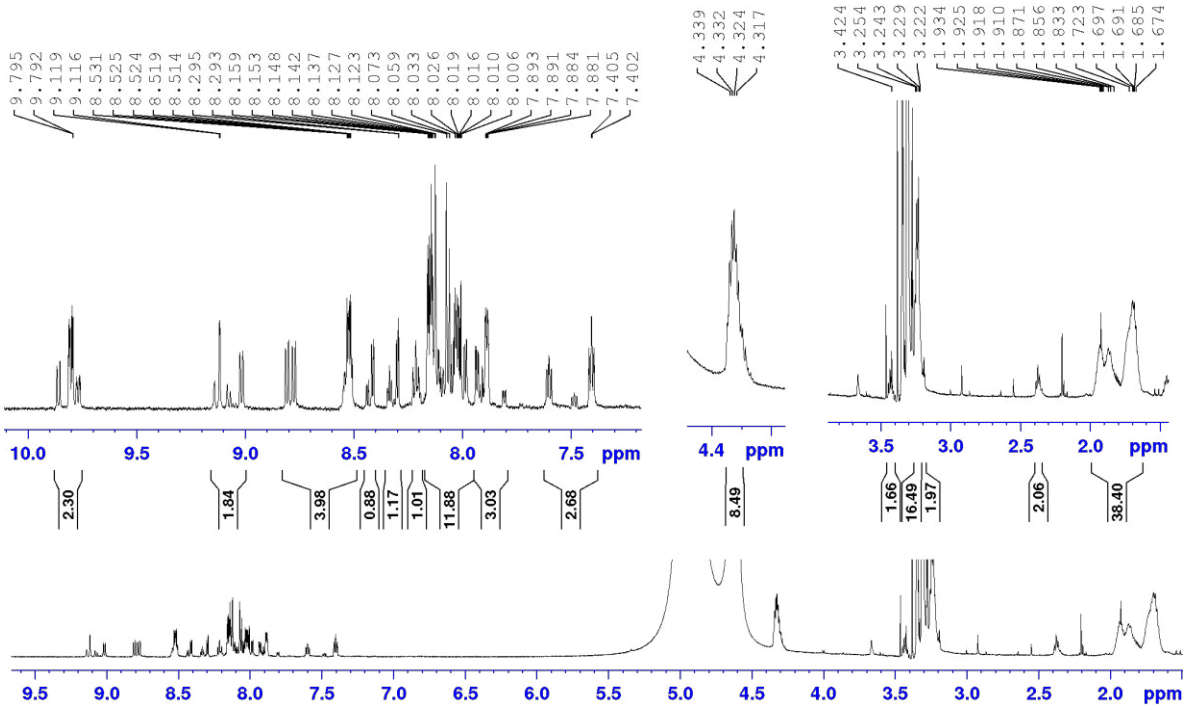

Figure A.45: ^{1}H NMR (600 MHz, CD_3OD/D_2O) spectrum of Ru-R8.

Single Mass Analysis
Tolerance = 100.0 PPM / DBE: min = -1.5, max = 500.0
Element prediction: Off
Number of isotope peaks used for i-FIT = 3

Monoisotopic Mass, Odd and Even Electron Ions
910 formula(e) evaluated with 1 results within limits (all results (up to 1000) for each mass)
Elements Used:
C: 0-99 H: 0-138 N: 0-42 O: 0-10 Ru: 0-1

Christopher Burke (TK). CBTK-010 4.26e+002
Q-TOF20151112MF003 52 (1.264) AM (Cen,4, 80.00, Ar,10000.0,1570.68,0.70); Sm (SG, 1x5.00); Sb (15,10.00); Sm (SG, 3x3.00); Sb (15,30.00); Cm (49:86

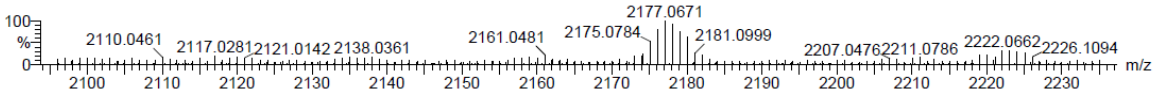

Minimum:				-1.5			
Maximum:		5.0	100.0	500.0			
Mass	Calc. Mass	mDa	PPM	DBE	i-FIT	i-FIT (Norm)	Formula
2177.0671	2177.0625	4.6	2.1	52.0	51.6	0.0	C99 H138 N42 O10 Ru

Figure A.46: Single mass analysis and HR-MS (ESI-qTOF, MS+) spectrum of Ru-R8.

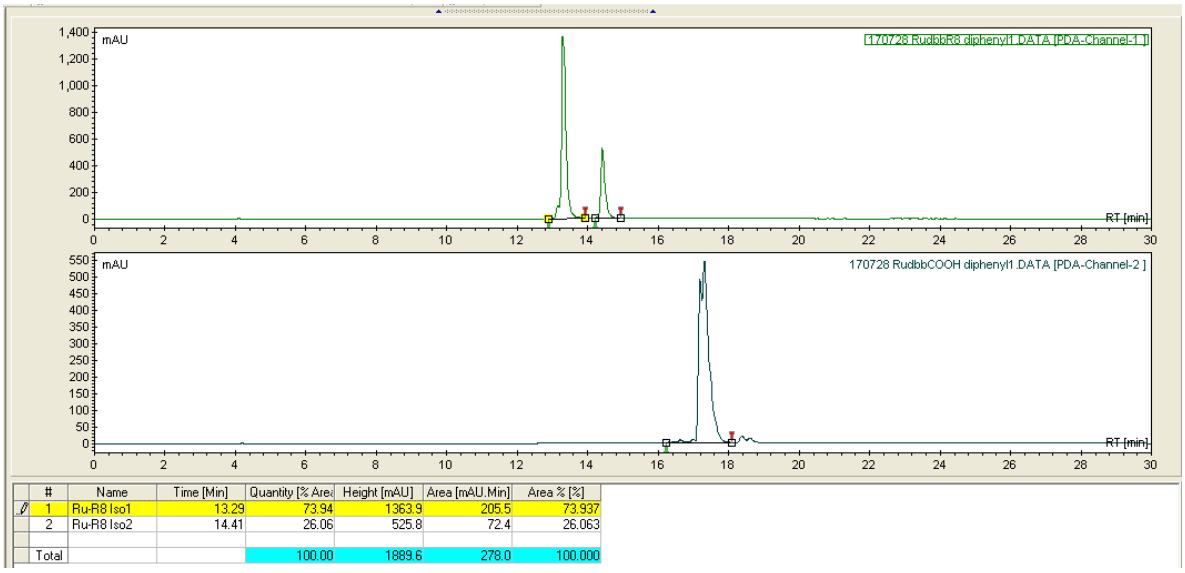

#	Name	Time [Min]	Quantity [% Area]	Height [mAU]	Area [mAU.Min]	Area % [%]
1	Ru-R8 Iso1	13.29	73.94	1363.9	205.5	73.937
2	Ru-R8 Iso2	14.41	26.06	525.8	72.4	26.063
Total			100.00	1889.6	278.0	100.000

Figure A.47: HPLC chromatograms for Ru-R8 (top trace) and parent complex (bottom trace) run under HPLC General Method 2 (Chapter 2).

A.1.3.2 Ru(II) di-conjugates and precursors

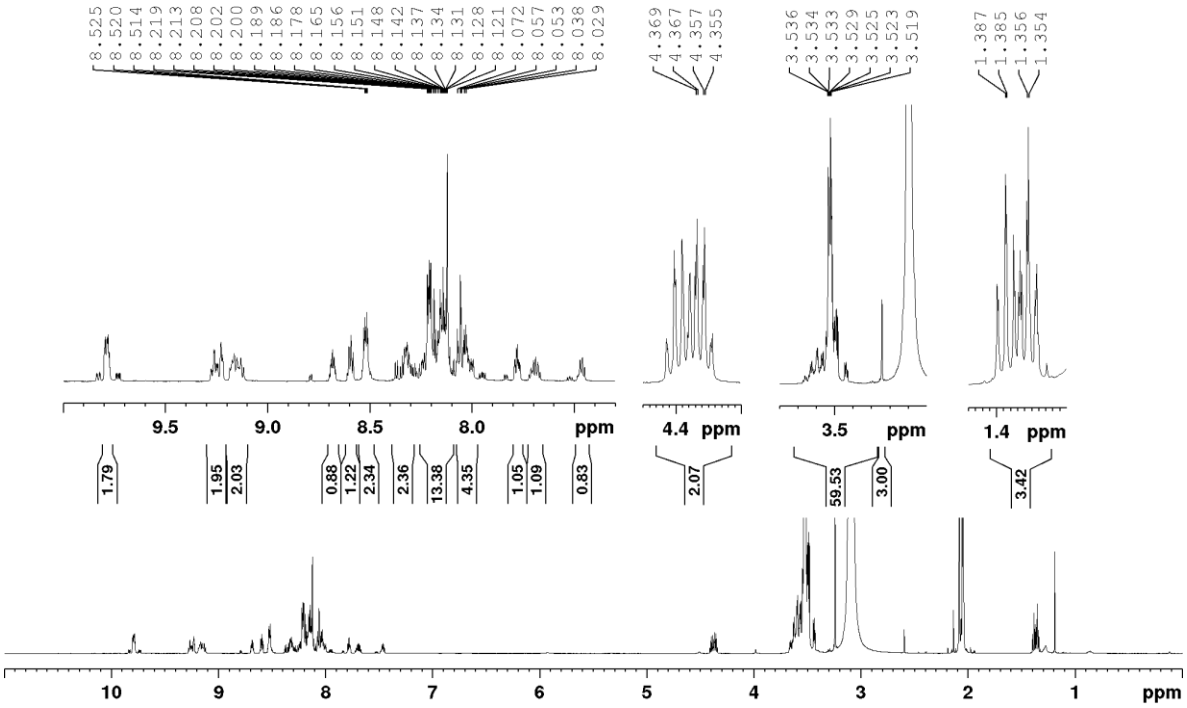

Figure A.48: ^{1}H NMR (600 MHz, Acetone-d_6) spectrum of [Ru(dppz)(bpyAr-PEG)(bpyArCOOEt)]$(PF_6)_2$.

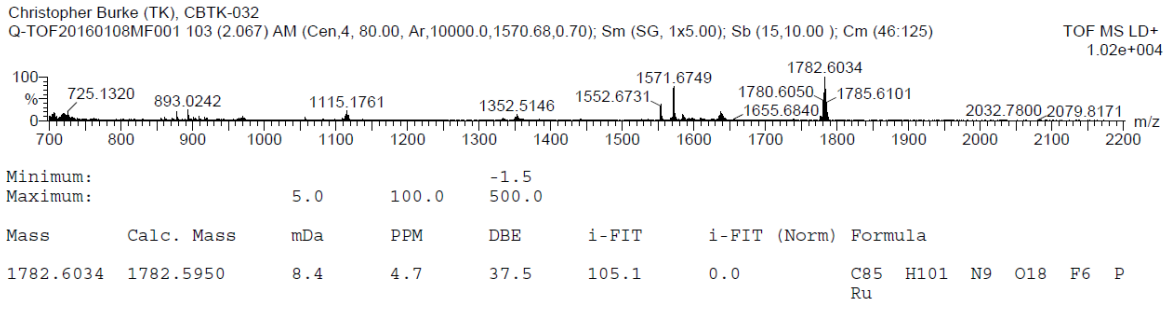

Minimum:				-1.5			
Maximum:		5.0	100.0	500.0			
Mass	Calc. Mass	mDa	PPM	DBE	i-FIT	i-FIT (Norm)	Formula
1782.6034	1782.5950	8.4	4.7	37.5	105.1	0.0	C85 H101 N9 O18 F6 P Ru

Figure A.49: Single mass analysis and HR-MS (ESI-qTOF, MS+) spectrum of [Ru(dppz)(bpyAr-PEG)(bpyArCOOEt)]$(PF_6)_2$.

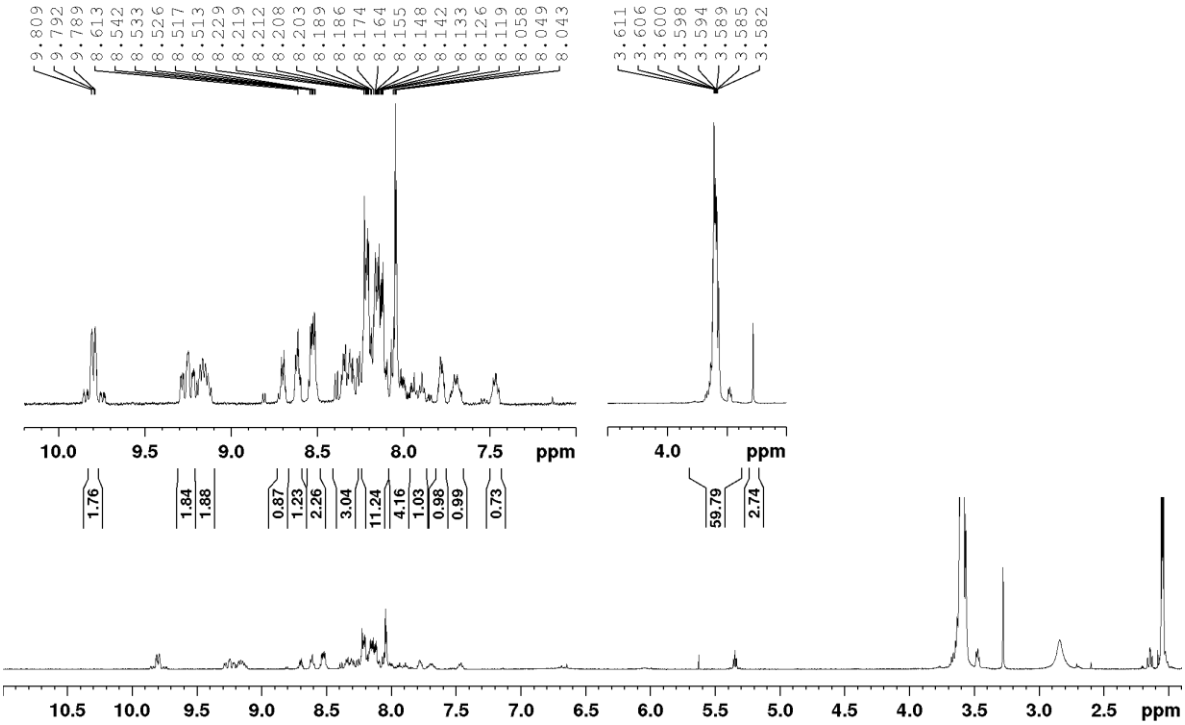

Figure A.50: ^{1}H NMR (600 MHz, Acetone-d_6) spectrum of [Ru(dppz)(bpyAr-PEG)(bpyArCOOH)]$(PF_6)_2$.

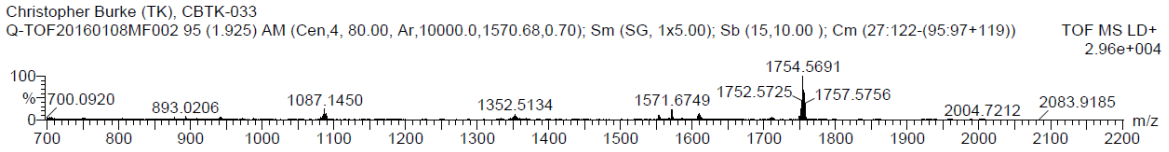

Minimum:				-1.5			
Maximum:		5.0	100.0	500.0			
Mass	Calc. Mass	mDa	PPM	DBE	i-FIT	i-FIT (Norm)	Formula
1754.5691	1754.5637	5.4	3.1	37.5	122.0	0.0	C83 H97 N9 O18 F6 P Ru

Figure A.51: Single mass analysis and HR-MS (ESI-qTOF, MS+) spectrum of [Ru(dppz)(bpyAr-PEG)(bpyArCOOH)]$(PF_6)_2$.

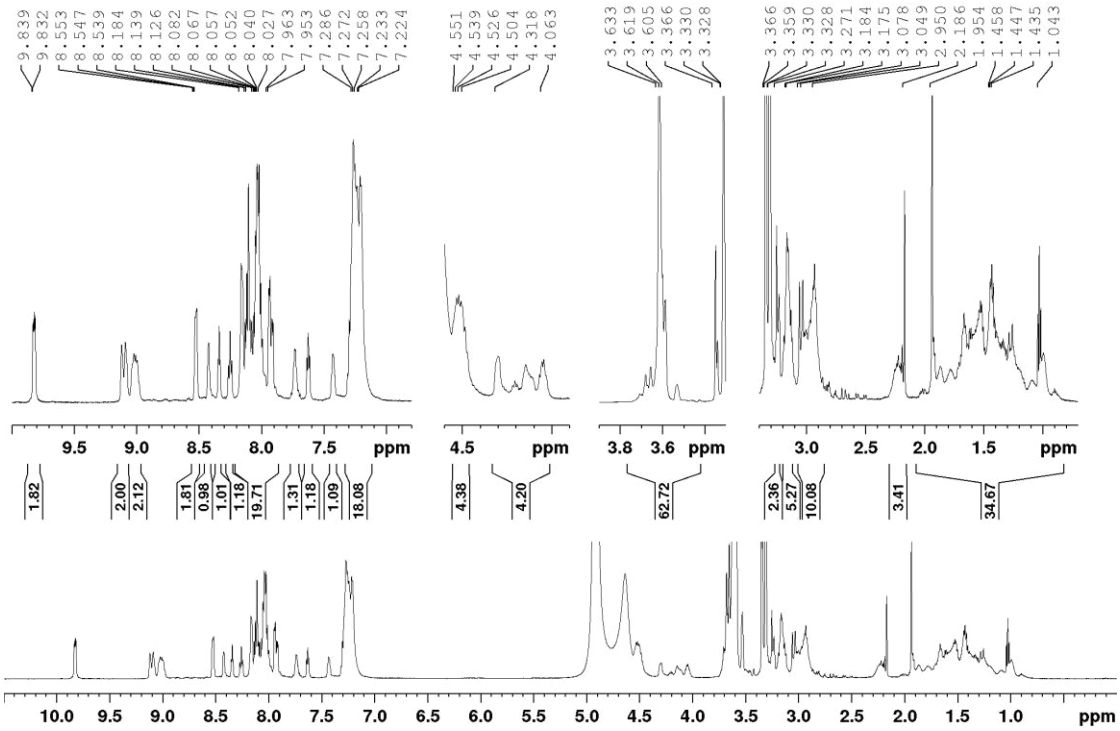

Figure A.52: ^{1}H NMR (600 MHz, CD_3OD/D_2O) spectrum of [Ru(dppz)(bpyAr-PEG)(bpyAr-MPP)]$^{5+}$.

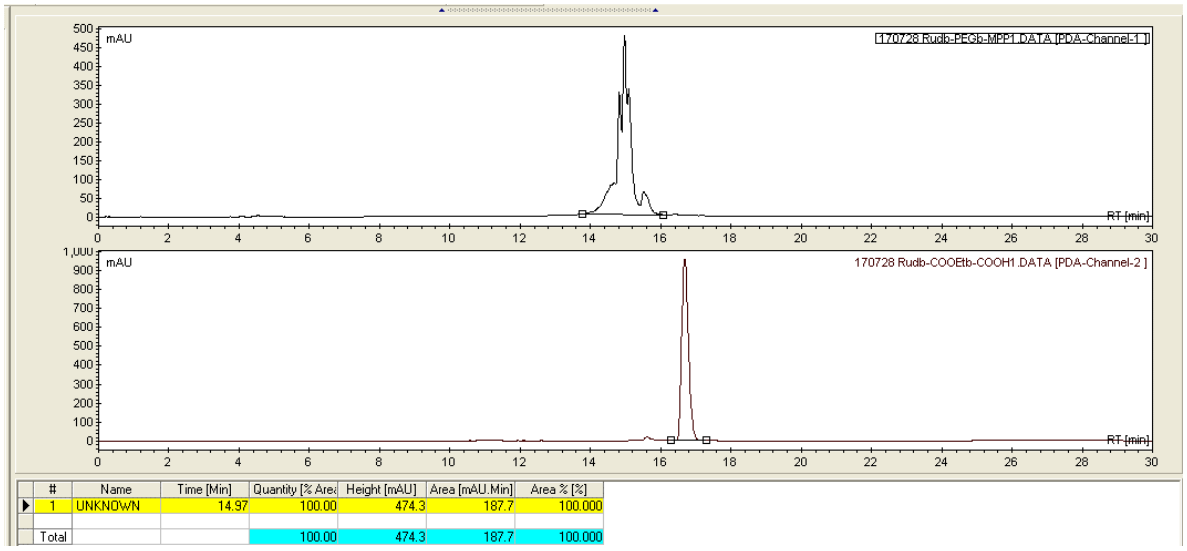

#	Name	Time [Min]	Quantity [% Area]	Height [mAU]	Area [mAU.Min]	Area % [%]
1	UNKNOWN	14.97	100.00	474.3	187.7	100.000
Total			100.00	474.3	187.7	100.000

Figure A.53: HPLC chromatograms for [Ru(dppz)(bpyAr-PEG)(bpyAr-MPP)]$^{5+}$. (top trace) and parent complex (bottom trace) run under HPLC General Method 2 (Chapter 2).

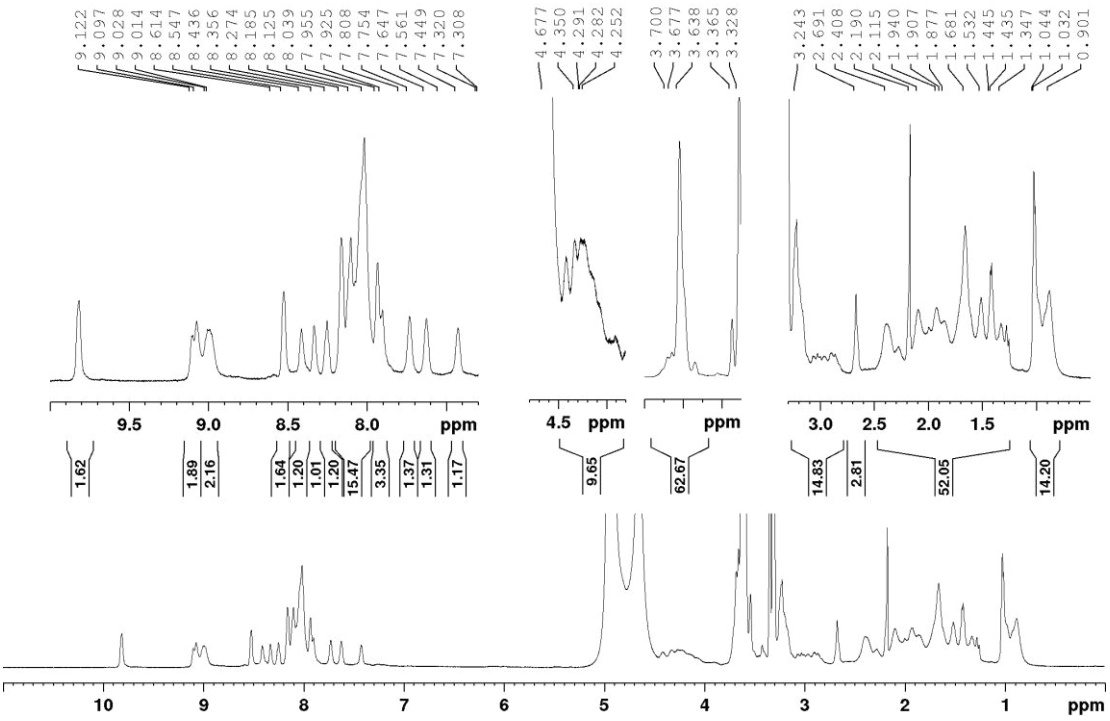

Figure A.54: ^{1}H NMR (600 MHz, CD_3OD/D_2O) spectrum of [Ru(dppz)(bpyAr-PEG)(bpyAr-NLS)]$^{10+}$.

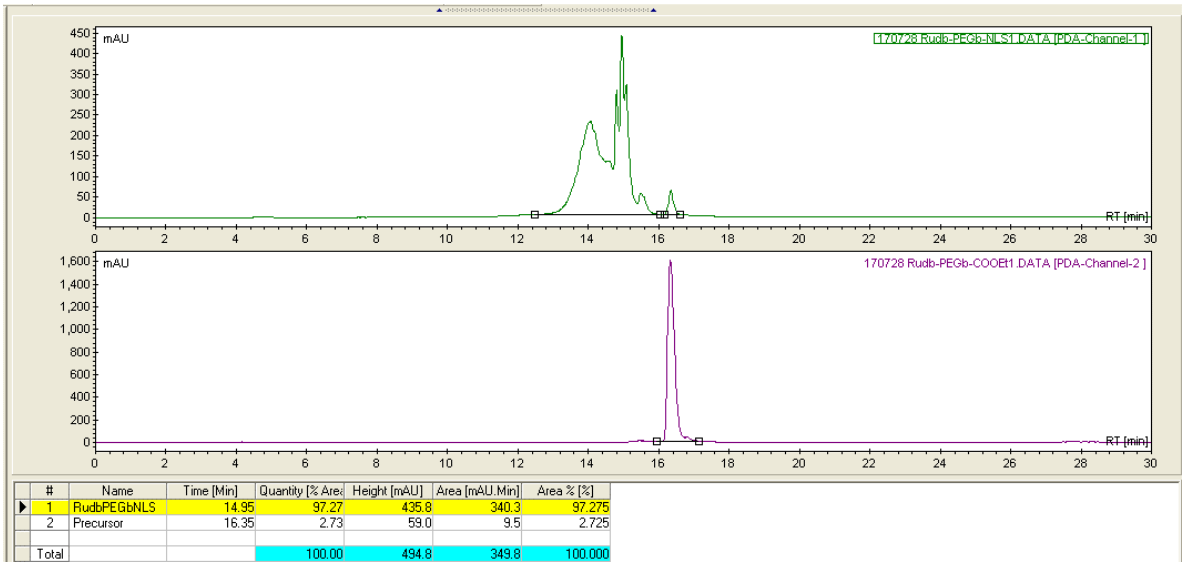

#	Name	Time [Min]	Quantity [% Area]	Height [mAU]	Area [mAU.Min]	Area % [%]
1	RudbPEGbNLS	14.95	97.27	435.8	340.3	97.275
2	Precursor	16.35	2.73	59.0	9.5	2.725
Total			100.00	494.8	349.8	100.000

Figure A.55: HPLC chromatograms for [Ru(dppz)(bpyAr-PEG)(bpyAr-NLS)]$^{5+}$. (top trace) and precursor PEG complex (bottom trace) run under HPLC General Method 2 (Chapter 2).

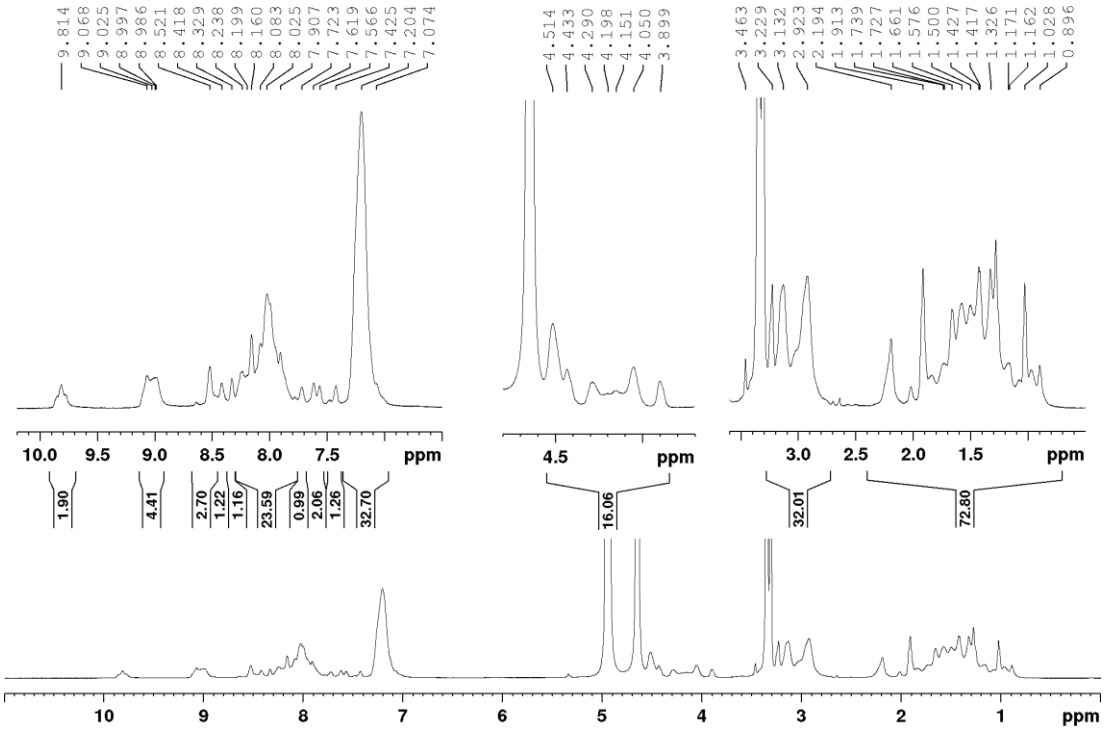

Figure A.56: ^{1}H NMR (600 MHz, CD_3OD/D_2O) spectrum of $[Ru(dppz)(bpyAr\text{-}MPP)_2]^{8+}$.

Appendix B

Supplementary Information – Chapter 4

B.1 Additional photophysical data

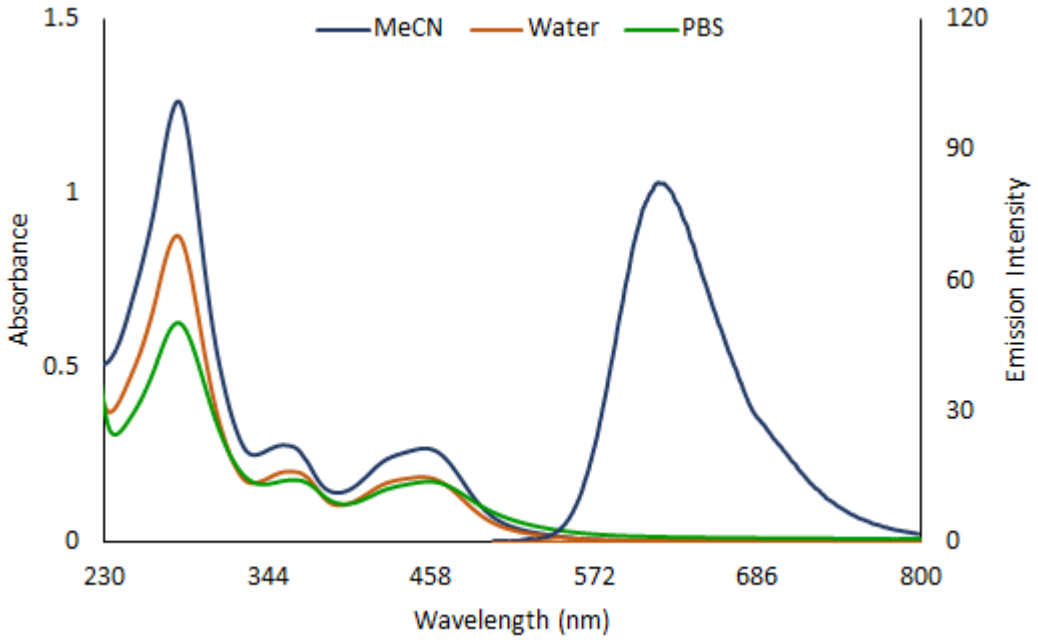

Figure B.1: Absorbance and emission spectra of Ru-ester measured at 10 µM in acetonitrile, water, and PBS pH 7.4 as indicated. Emission slits were set to 10 nm and excitations were performed at λ_{max} (vis).

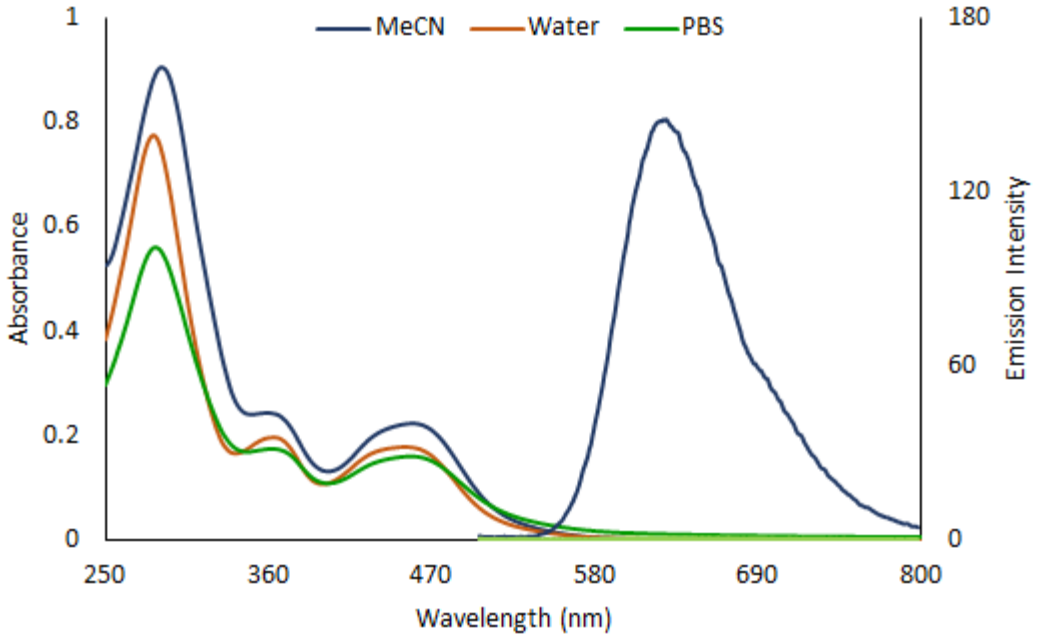

Figure B.2: Absorbance and emission spectra of Ru-MPP measured at 10 µM in acetonitrile, water, and PBS pH 7.4 as indicated. Emission slits were set to 10 nm and excitations were performed at λ_{max} (vis).

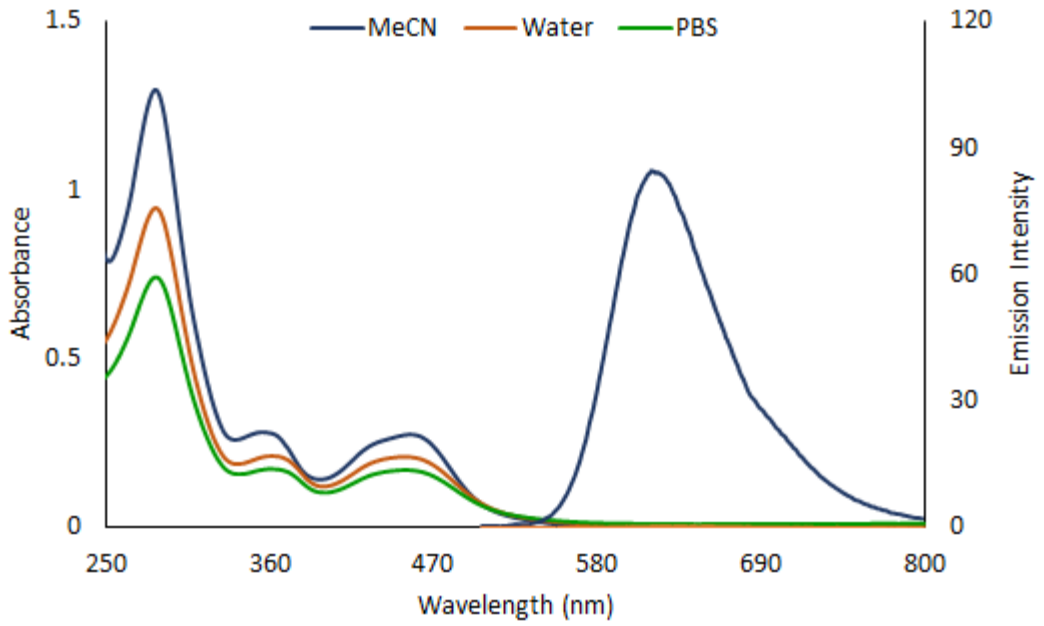

Figure B.3: Absorbance and emission spectra of Ru-NLS measured at 10 µM in acetonitrile, water, and PBS pH 7.4 as indicated. Emission slits were set to 10 nm and excitations were performed at λ_{max} (vis).

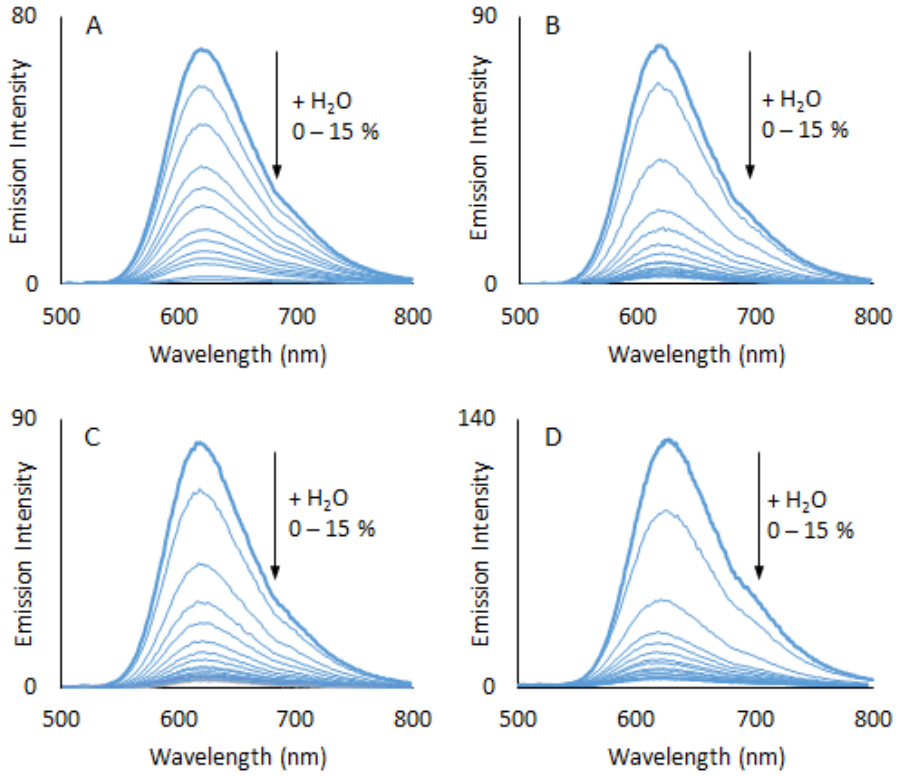

Figure B.4: Switching off the emission of Ru-dppz complexes in acetonitrile with increasing water ratio. (a) Ru-acid. (b) Ru-ester. (c) Ru-NLS. (d) Ru-MPP.

B.2 Additional binding data

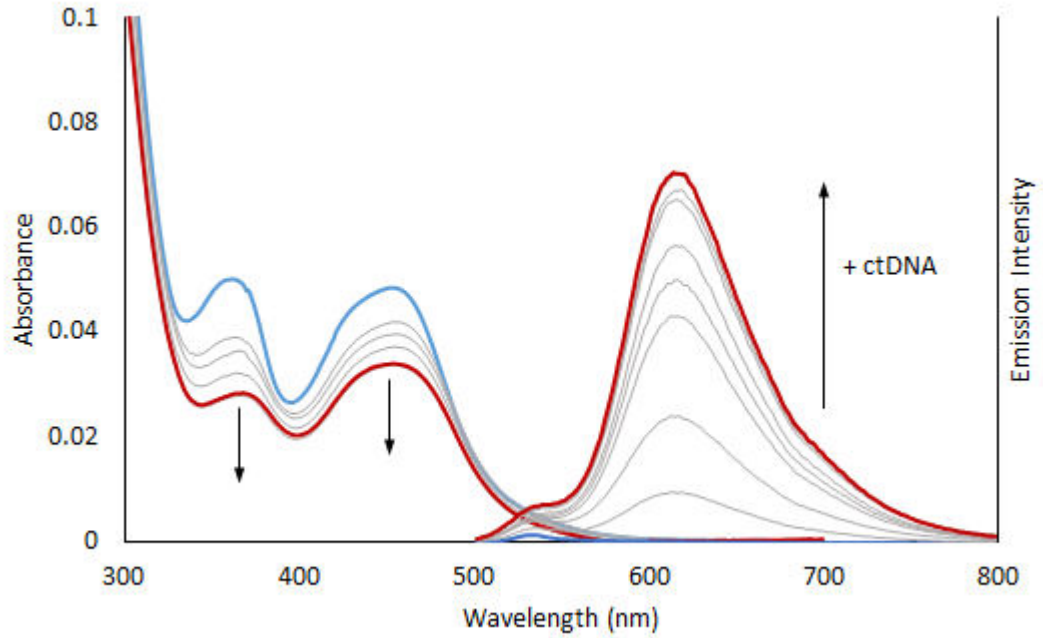

Figure B.5: Changes to absorbance and emission spectra of Ru-ester in PBS upon addition of ctDNA from r = 0 (blue trace) up to saturation (red trace).

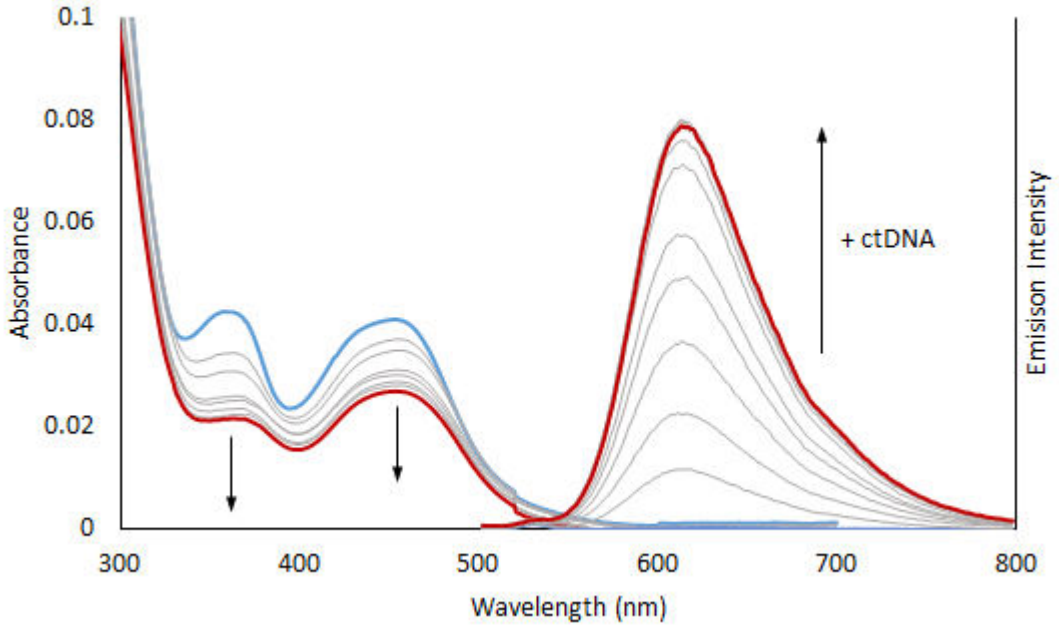

Figure B.6: Changes to absorbance and emission spectra of Ru-NLS in PBS upon addition of ctDNA from r = 0 (blue trace) up to saturation (red trace).

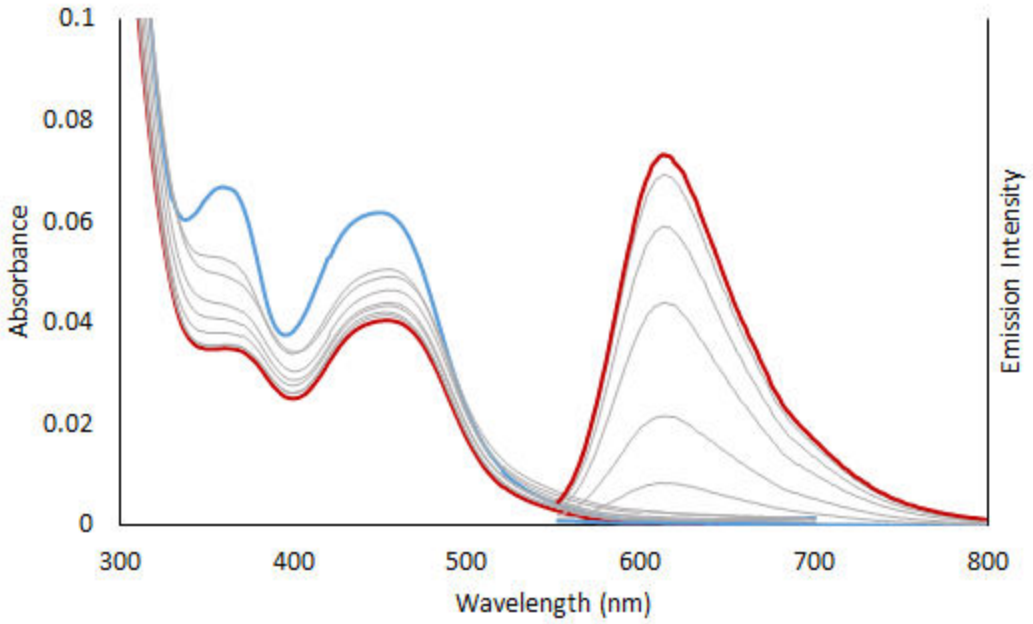

Figure B.7: Changes to absorbance and emission spectra of Ru-MPP in PBS upon addition of ctDNA from r = 0 (blue trace) up to saturation (red trace).

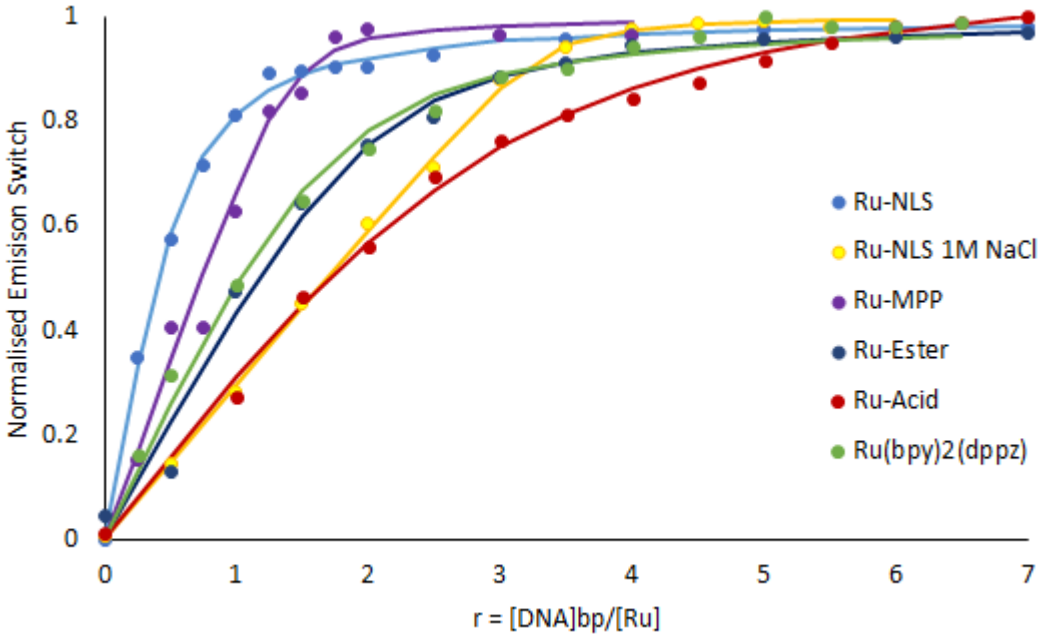

Figure B.8: Representative DNA binding curves for the Ru-dppz complexes as indicated.

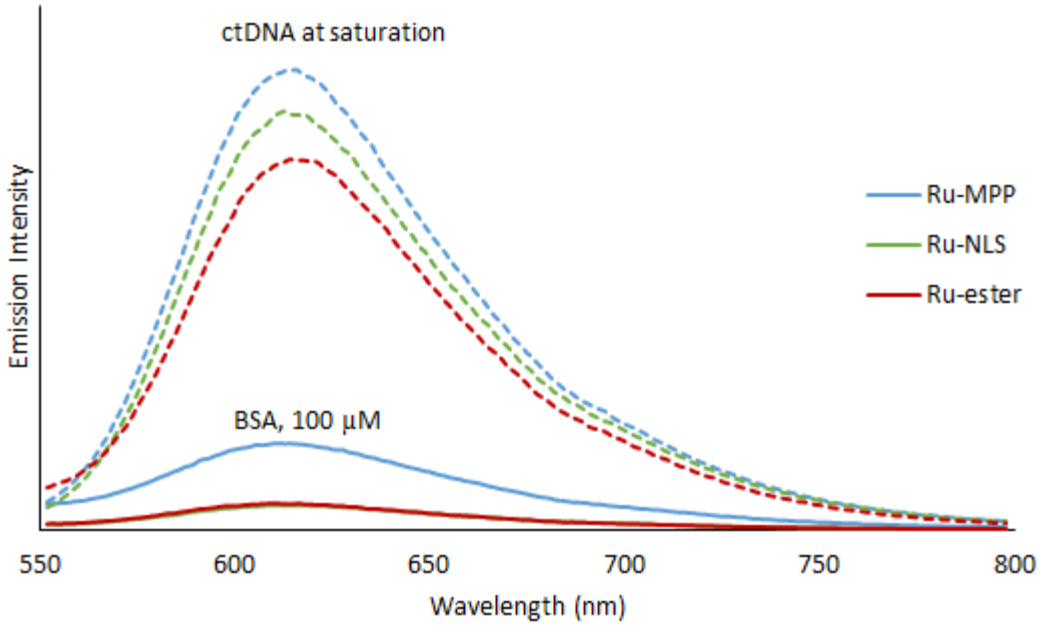

Figure B.9: Relative emission for the Ru-dppz complexes in ctDNA at saturation or BSA as indicated. Emission/Excitation slits set to 10 nm in all cases, [Ru] = 5 µM (PBS).

B.3 Additional rRaman data

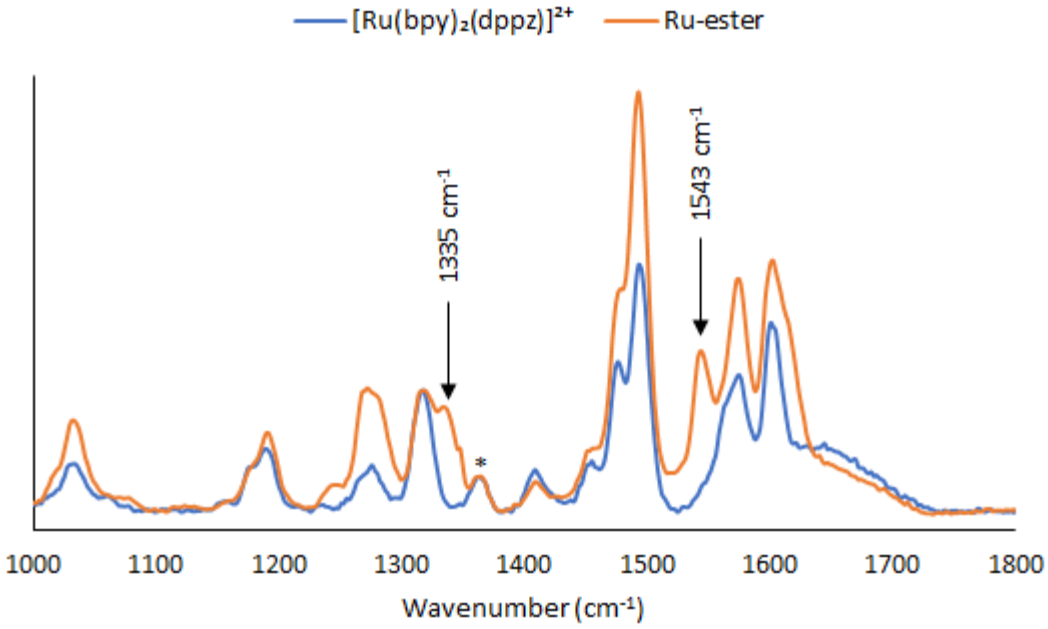

Figure B.10: rRaman spectra of $[Ru(bpy)_2(dppz)]^{2+}$ and Ru-ester (100 µM PBS, 473 nm). Data is normalised to the peak at 1362 cm^{-1} (*). New peaks attributed to -Ar-COOEt functionalisation are indicated by the arrows.

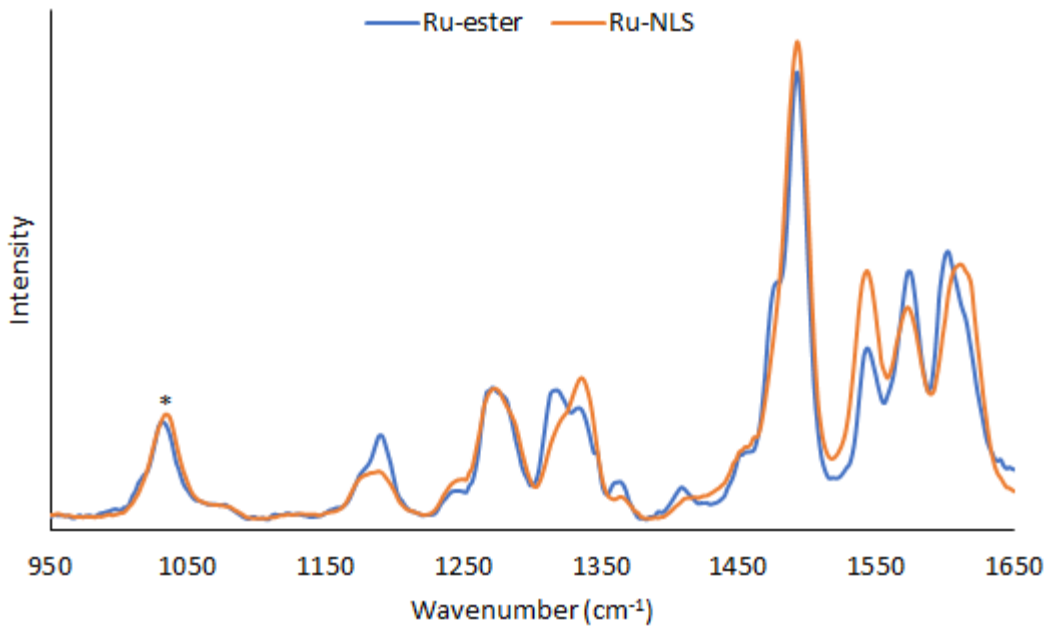

Figure B.11: rRaman spectra of Ru-ester and Ru-NLS as indicated in PBS buffer in the absence of DNA. Spectra are normalised to the peak at 1031 cm^{-1} (*).

B.3 Additional cellular imaging data

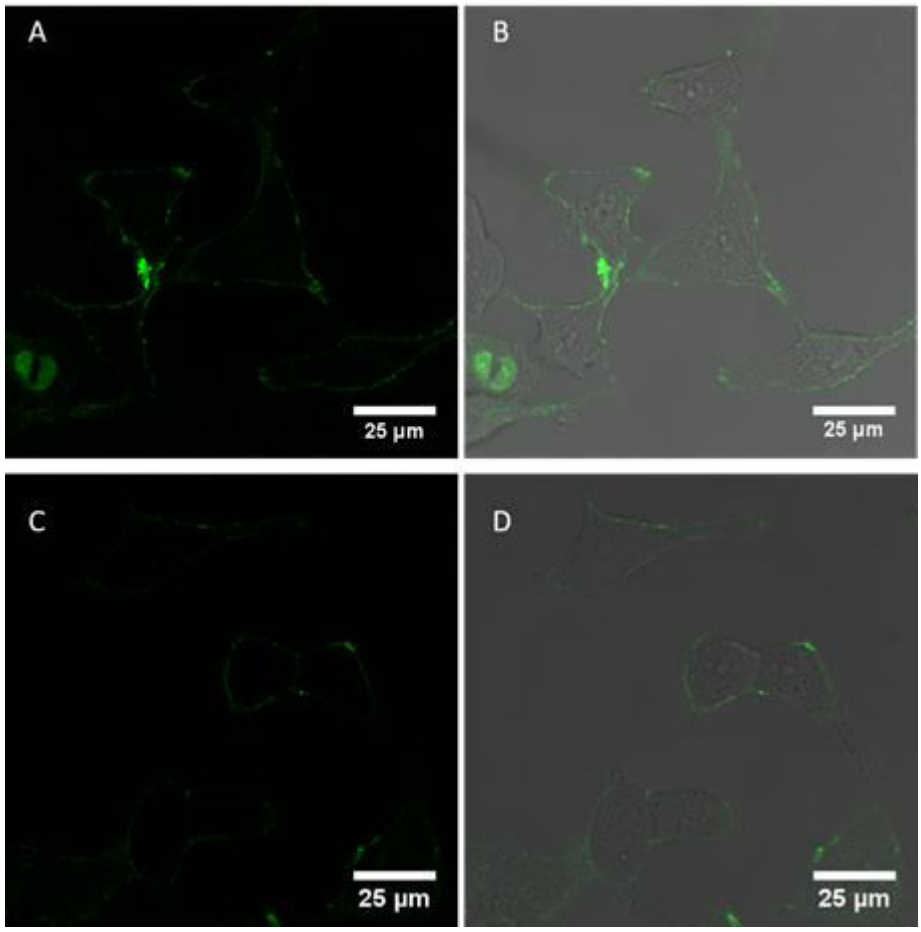

Figure B.12: Confocal imaging of HeLa cells incubated with Ru-MPP 10 µM (A and B), and Ru-NLS 40 µM (C and D) at 4 °C for 2 h in cell media, showing the compounds bound to the cell membrane (A and C), and the backscatter images (B and D). Data courtesy of Dr. Aisling Byrne.

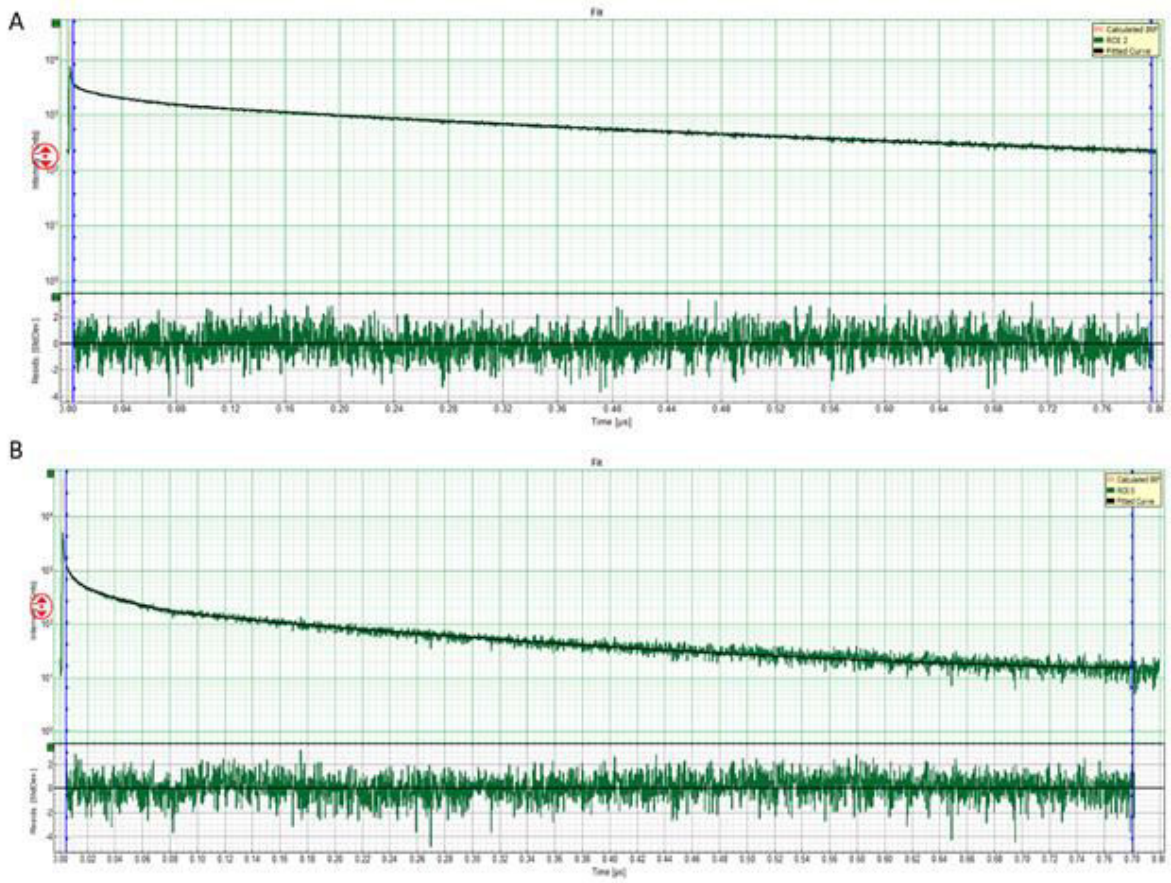

Figure B.13: Representative FLIM decays of Ru-NLS (A) and Ru-MPP (B) in live HeLa cells at 37°C when fit to 2 exponential components. Data courtesy of Dr. Aisling Byrne.

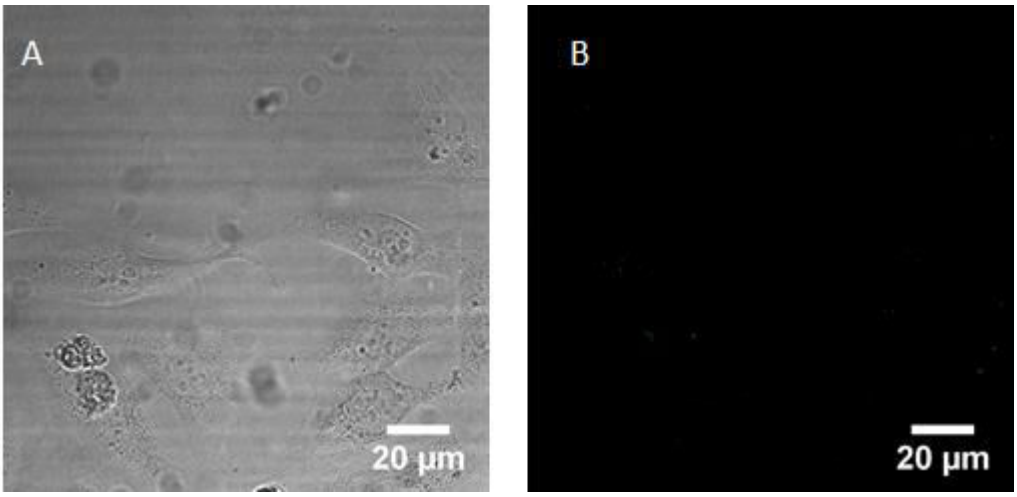

Figure B.14: Confocal imaging of HeLa cells incubated with Ru-ester parent complex (70 µM) for 6 h at 37 °C in the absence of light. Cells were washed with PBS prior to imaging. (A) shows the overlay of the Ru and white light channels, and (B) shows the Ru channel only. Ex 470, Em 565 – 700 nm. Data courtesy of Dr. Aisling Byrne.

Appendix C

Supplementary information – Chapter 5

C.1 Structural characterisation data

C.1.1 Ligands

C.1.1.1 pic-COOR

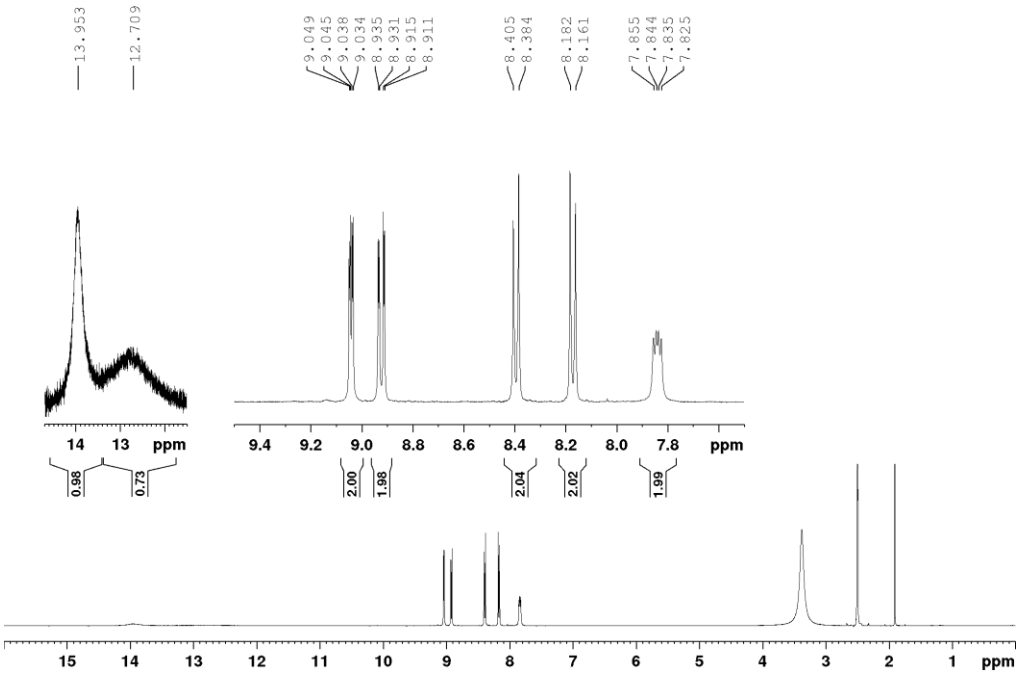

Figure C.1: ^{1}H NMR (400 MHz, DMSO-d_6) spectrum of pic-COOH. Peak at 1.91 ppm is residual acetic acid.

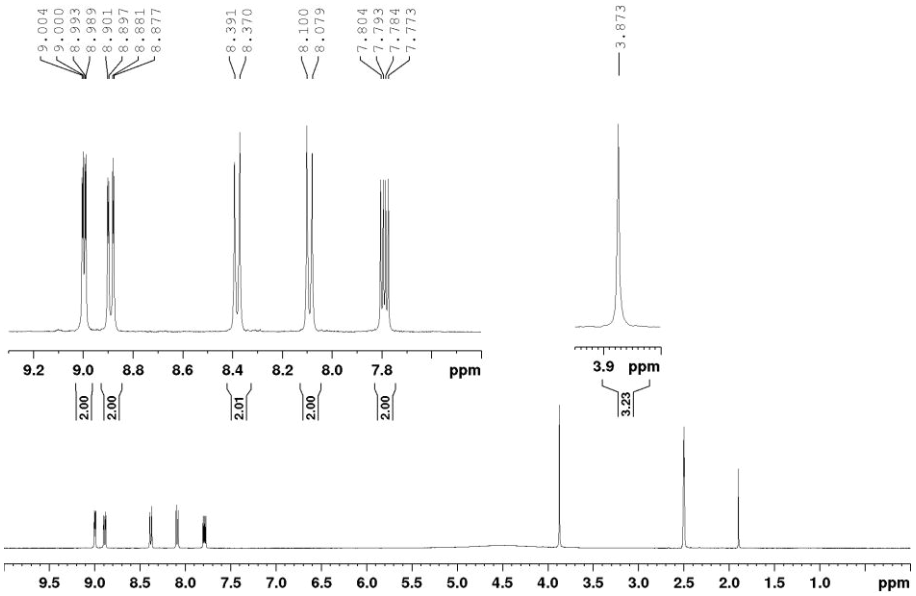

Figure C.2: ^{1}H NMR (400 MHz, DMSO-d_6) spectrum of pic-COOMe. . Peak at 1.91 ppm is residual acetic acid.

C.1.1.2 tap and precursors

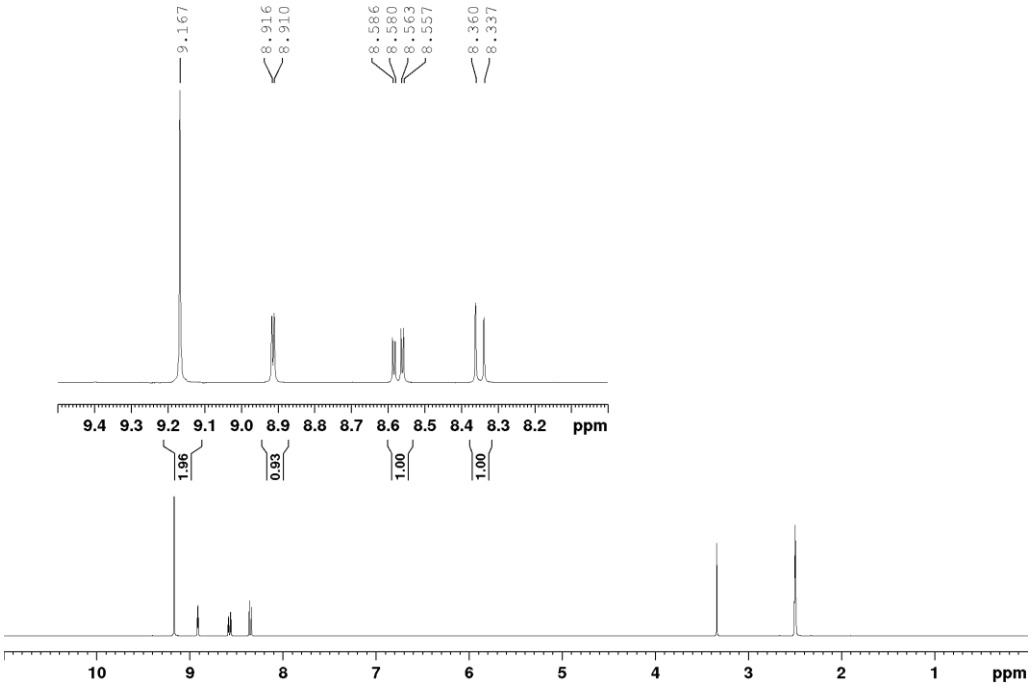

Figure C.3: ^{1}H NMR (400 MHz, DMSO-d_6) spectrum of nitroquin.

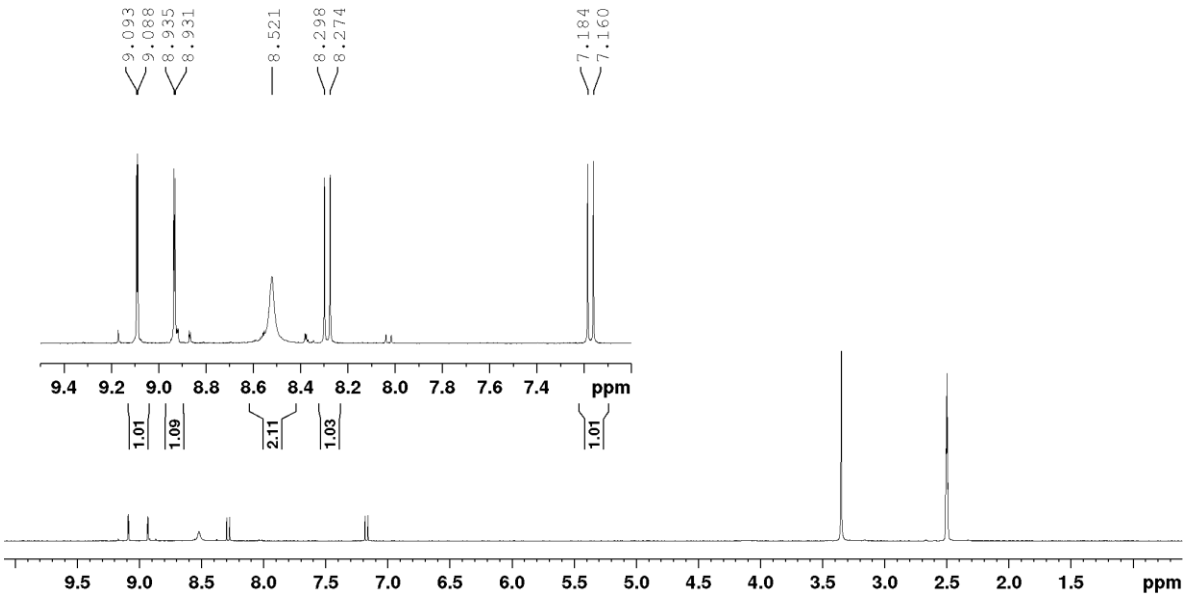

Figure C.4: ^{1}H NMR (400 MHz, DMSO-d_6) spectrum of nitroaminoquin.

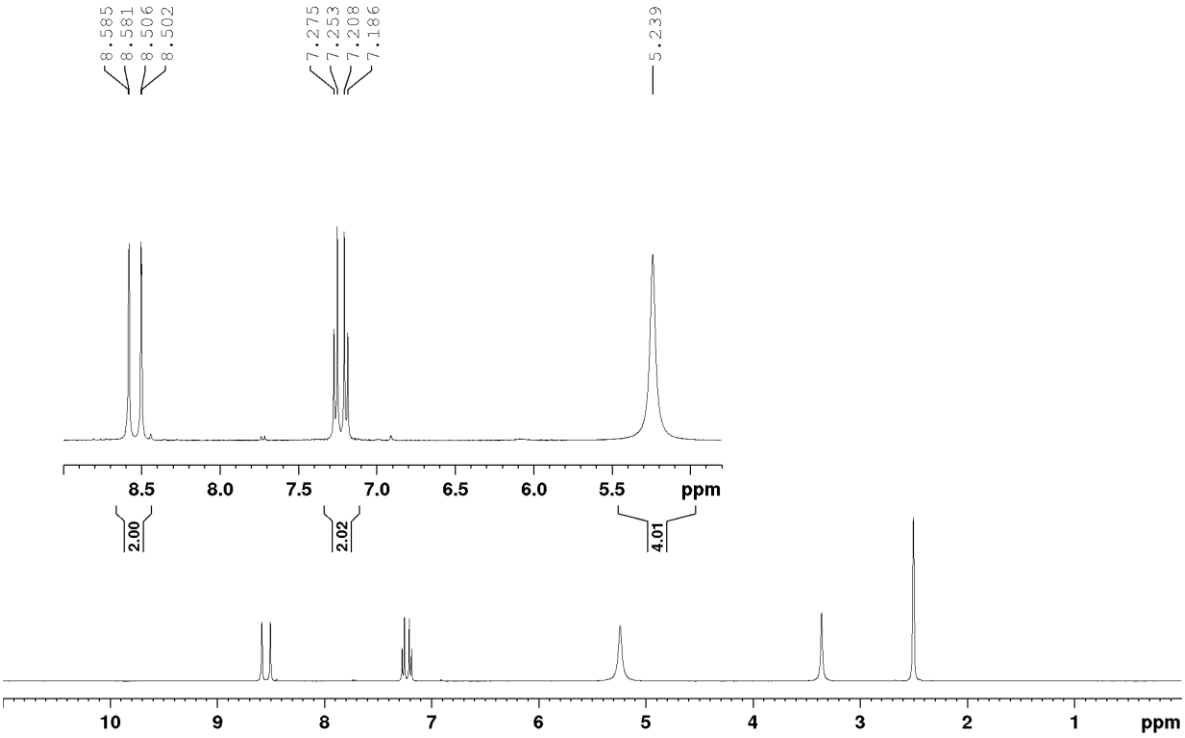

Figure C.5: ^{1}H NMR (400 MHz, DMSO-d_6) spectrum of diaminoquin.

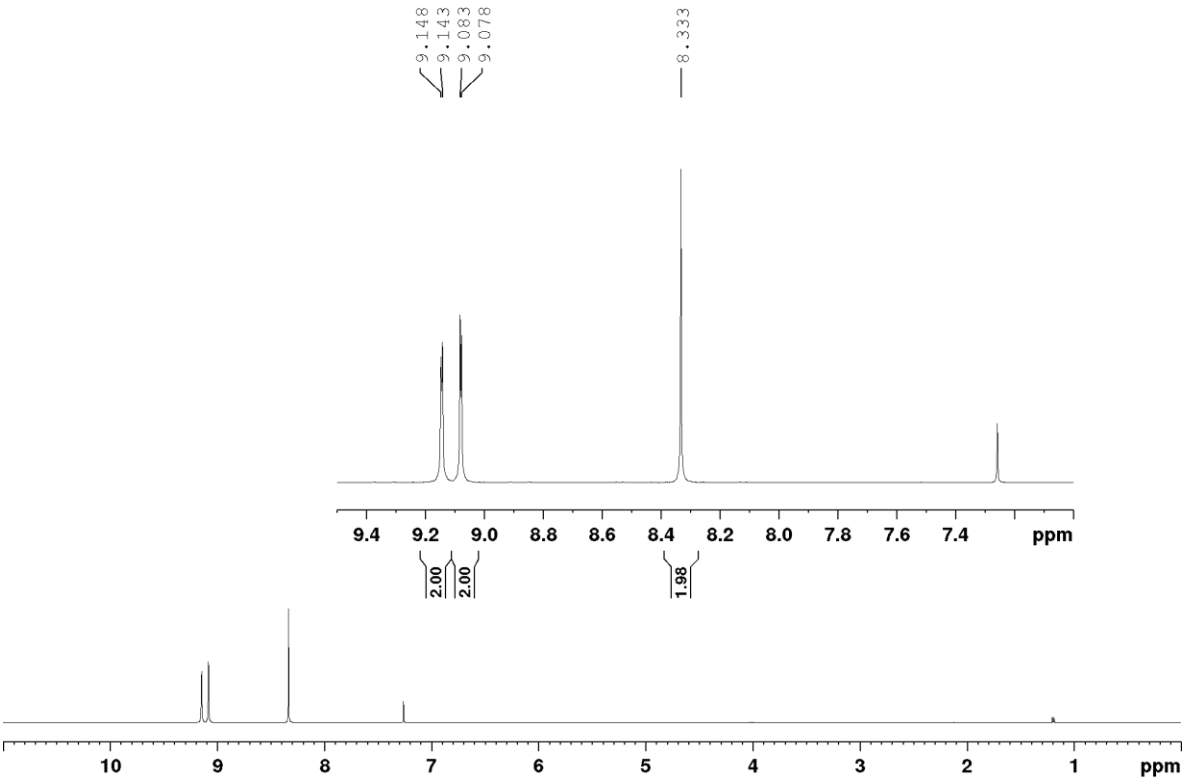

Figure C.6: ^{1}H NMR (400 MHz, $CDCl_3$) spectrum of tap.

C.1.2 Complexes

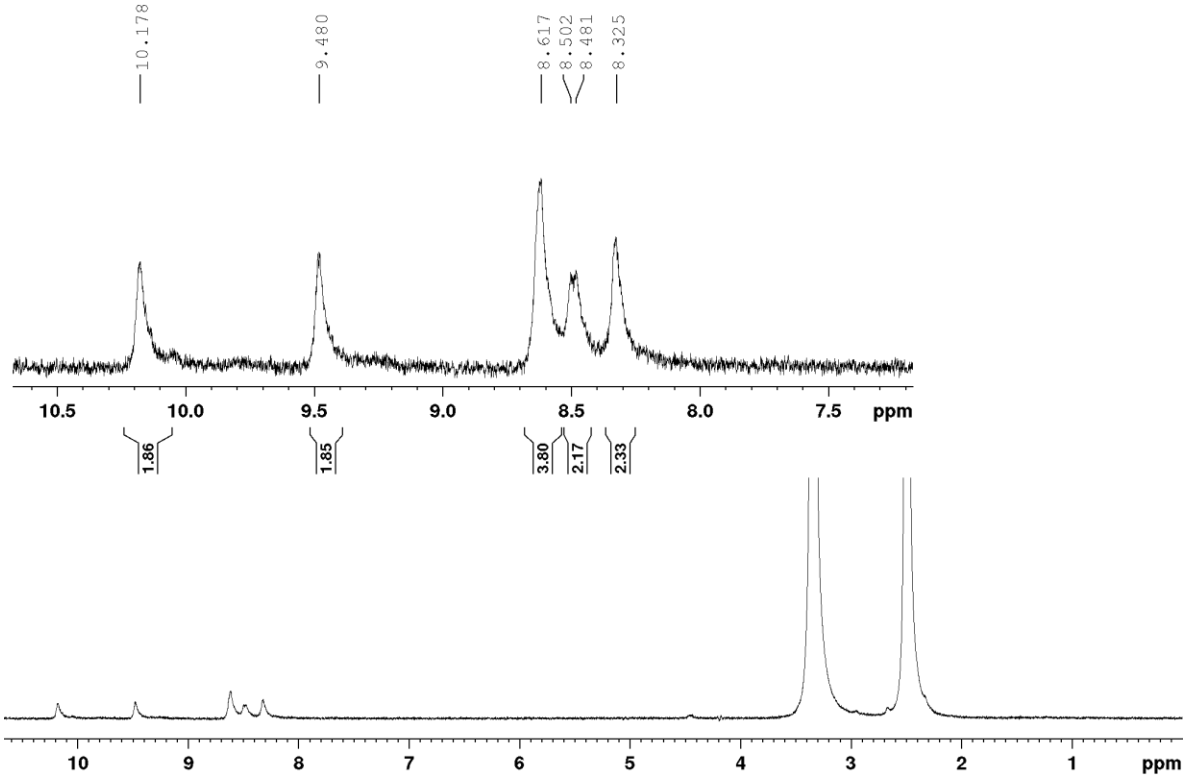

Figure C.7: ^{1}H NMR (400 MHz, DMSO-d_6) spectrum of $[Ru(tap)_2Cl_2]$.

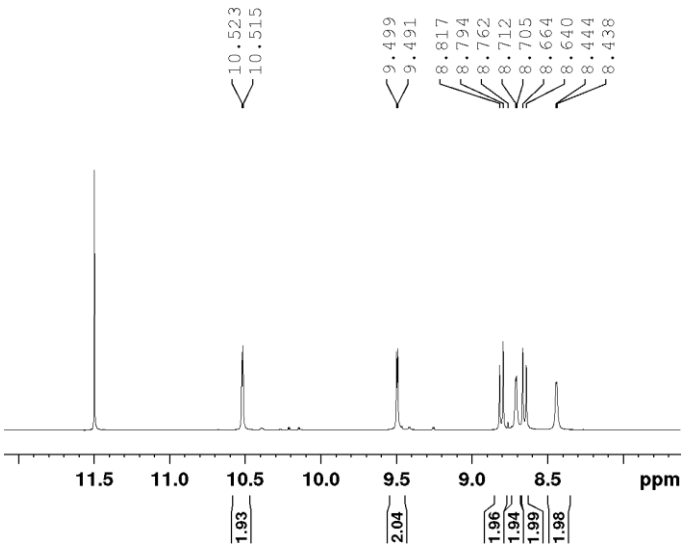

Figure C.8: ^{1}H NMR (400 MHz, TFA-d) spectrum of $[Ru(tap)_2Cl_2]$.

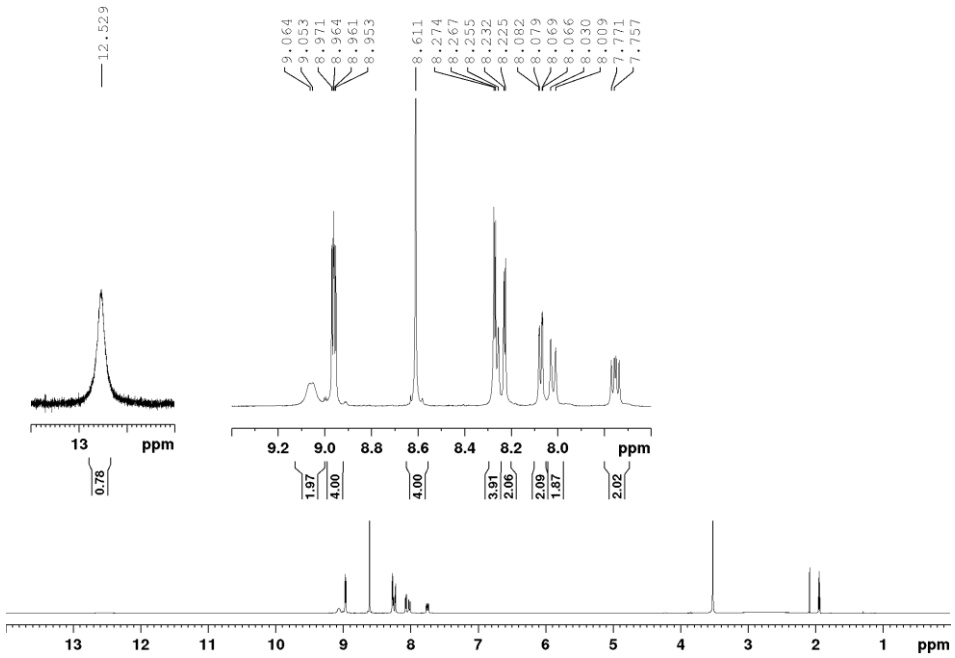

Figure C.9: ^{1}H NMR (400 MHz, CD_3CN) spectrum of $[Ru(tap)_2(pic\text{-}COOH)](PF_6)_2$. Residual acetone and ethylene glycol peaks at 2.08 and 3.51 ppm respectively.

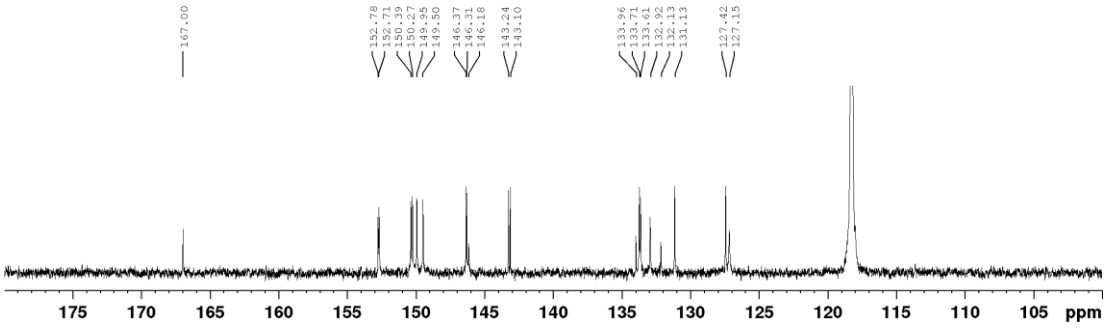

Figure C.10: ^{13}C NMR (100 MHz, CD_3CN) spectrum of $[Ru(tap)_2(pic\text{-}COOH)](PF_6)_2$.

Single Mass Analysis
Tolerance = 5.0 PPM / DBE: min = -1.5, max = 1000.0
Isotope cluster parameters: Separation = 1.0 Abundance = 1.0%

Monoisotopic Mass, Odd and Even Electron Ions
103 formula(e) evaluated with 1 results within limits (all results (up to 1000) for each mass)

DCU_TK_CBTK-002 12 (0.382) AM (Cen,4, 80.00, Ar,1.0,556.28,0.70,LS 1); Sm (Mn, 2x5.00); Sb (16,15.00); Sb (16,15.00); Cm (12:23)
1: TOF MS ES+ 7.74e3

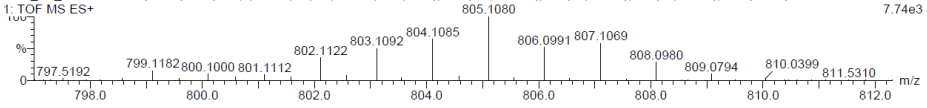

Minimum:				-1.5		
Maximum:		200.0	5.0	1000.0		
Mass	Calc. Mass	mDa	PPM	DBE	Score	Formula
805.1080	805.1110	-3.0	-3.8	35.5	1	C40 H23 N12 O2 Ru

Figure C.11: Single mass analysis HR-MS (ESI-qTOF, MS+) spectrum of $[Ru(tap)_2(pic\text{-}COOH)](PF_6)_2$.

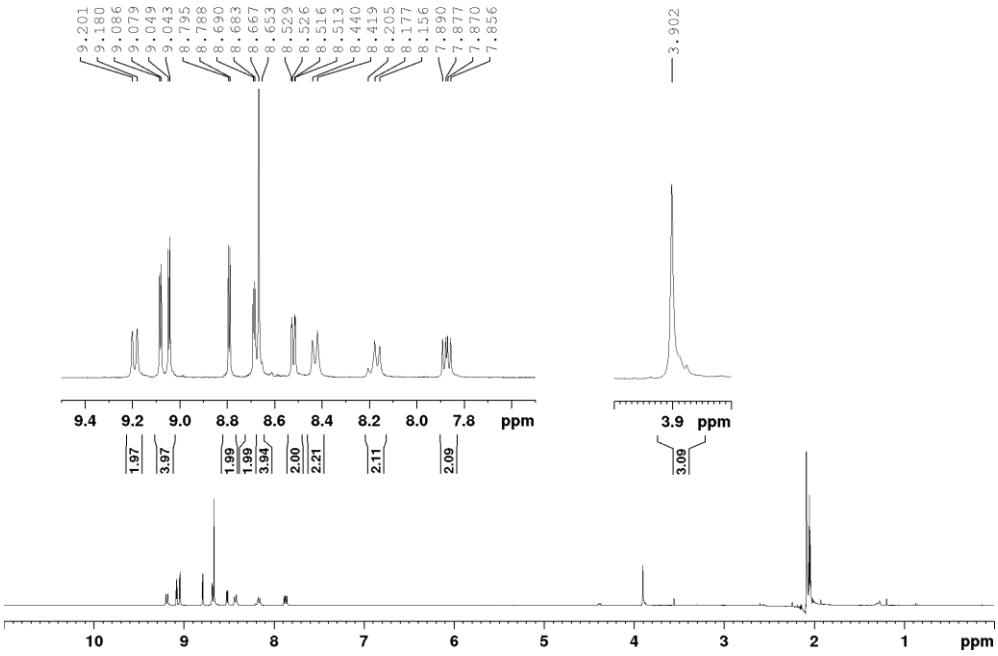

Figure C.12: ^{1}H NMR (400 MHz, acetone-d_6) spectrum of $[Ru(tap)_2(pic\text{-}COOMe)](PF_6)_2$.

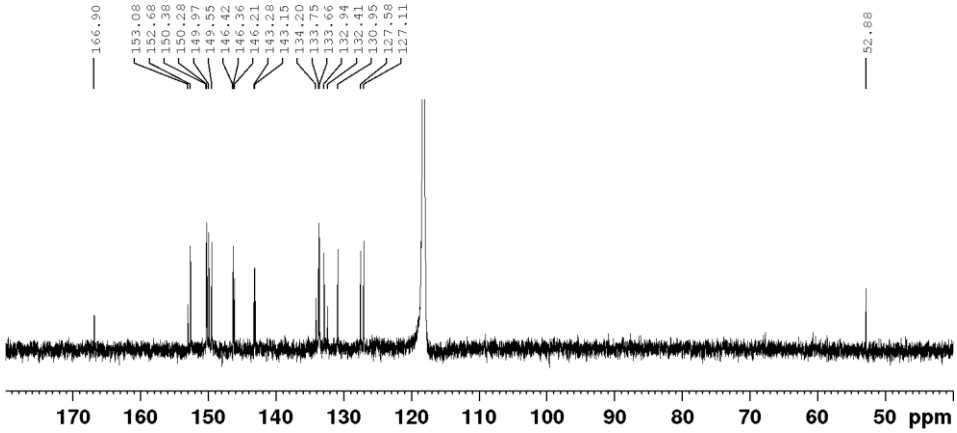

Figure C.13: ^{13}C NMR (100 MHz, CD_3CN) spectrum of $[Ru(tap)_2(pic\text{-}COOMe)](PF_6)_2$.

Single Mass Analysis
Tolerance = 5.0 PPM / DBE: min = -1.5, max = 1000.0
Isotope cluster parameters: Separation = 1.0 Abundance = 1.0%

Monoisotopic Mass, Odd and Even Electron Ions
85 formula(e) evaluated with 1 results within limits (all results (up to 1000) for each mass)

DCU_TK_CBTK-001 9 (0.285) AM (Cen,4, 80.00, Ar,1.0,556.28,0.70,LS 1); Sm (Mn, 2x7.00); Sb (16,15.00); Sb (16,15.00); Cm (3:10)
1: TOF MS ES+

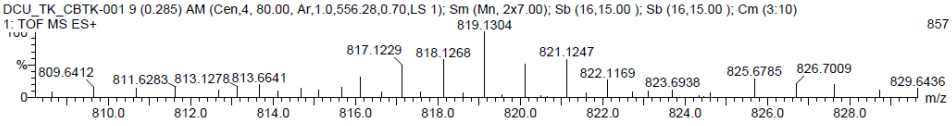

Minimum:				-1.5		
Maximum:		200.0	5.0	1000.0		
Mass	Calc. Mass	mDa	PPM	DBE	Score	Formula
819.1304	819.1267	3.7	4.5	35.5	1	C41 H25 N12 O2 Ru

Figure C.14: Single mass analysis HR-MS (ESI-qTOF, MS+) spectrum of $[Ru(tap)_2(pic\text{-}COOMe)](PF_6)_2$.

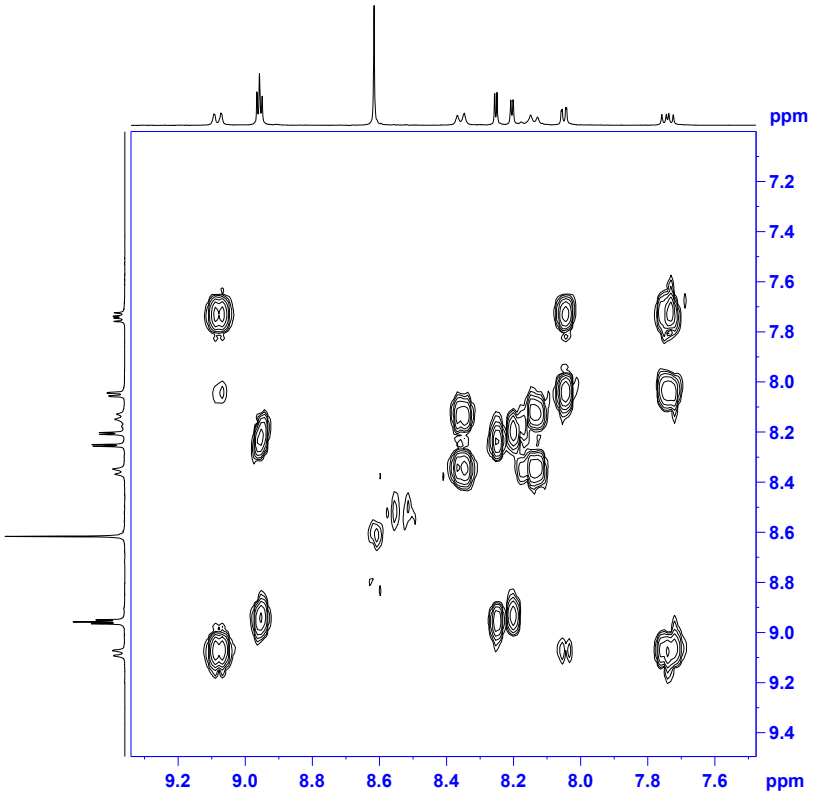

Figure C.15: COSY NMR (CD_3CN) spectrum of $[Ru(tap)_2(pic\text{-}COOMe)](PF_6)_2$ to show aromatic region only.

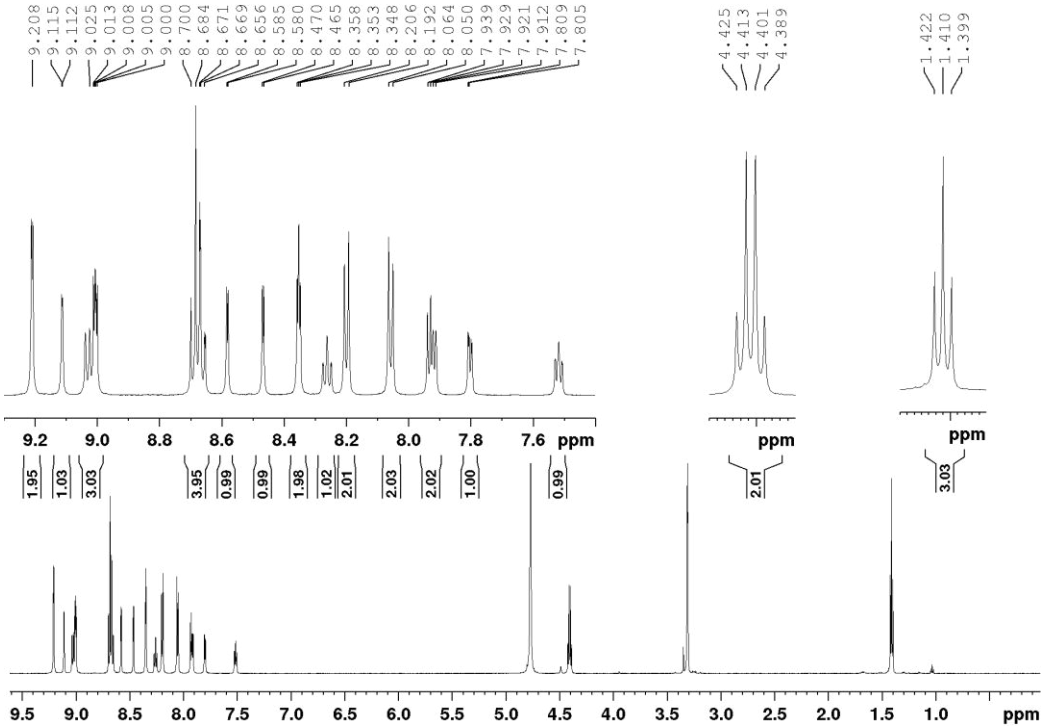

Figure C.16: ^1H NMR (600 MHz) spectrum of $[Ru(tap)_2(bpyArCOOEt)]Cl_2$ in CD_3OD/D_2O. Inset: Aromatic region and close up of ester peaks.

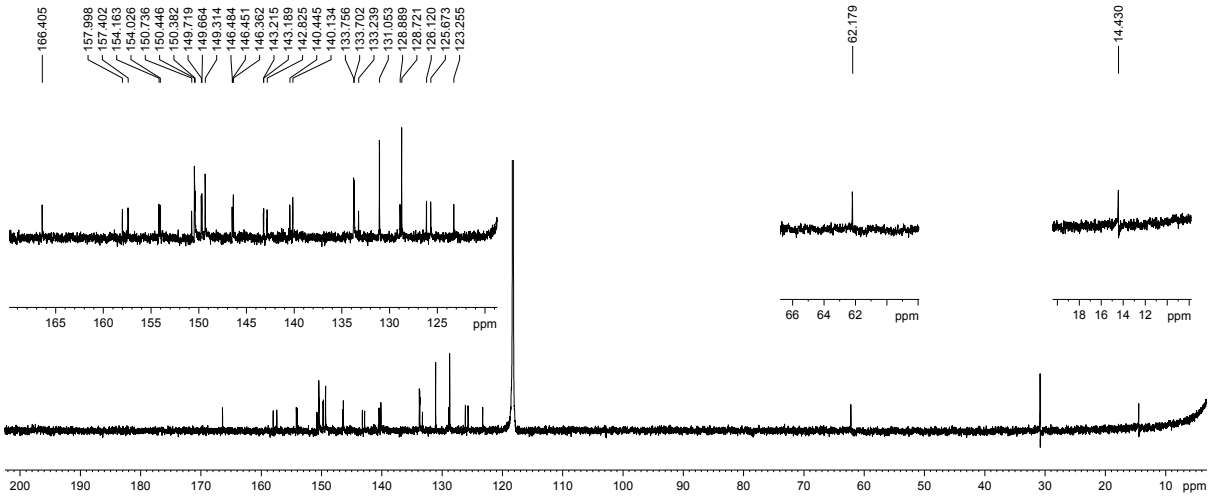

Figure C.17: ^{13}C NMR (100 MHz) spectrum of $[Ru(tap)_2(bpyArCOOEt)](PF_6)_2$ in CD_3CN. Inset: regions of interest.

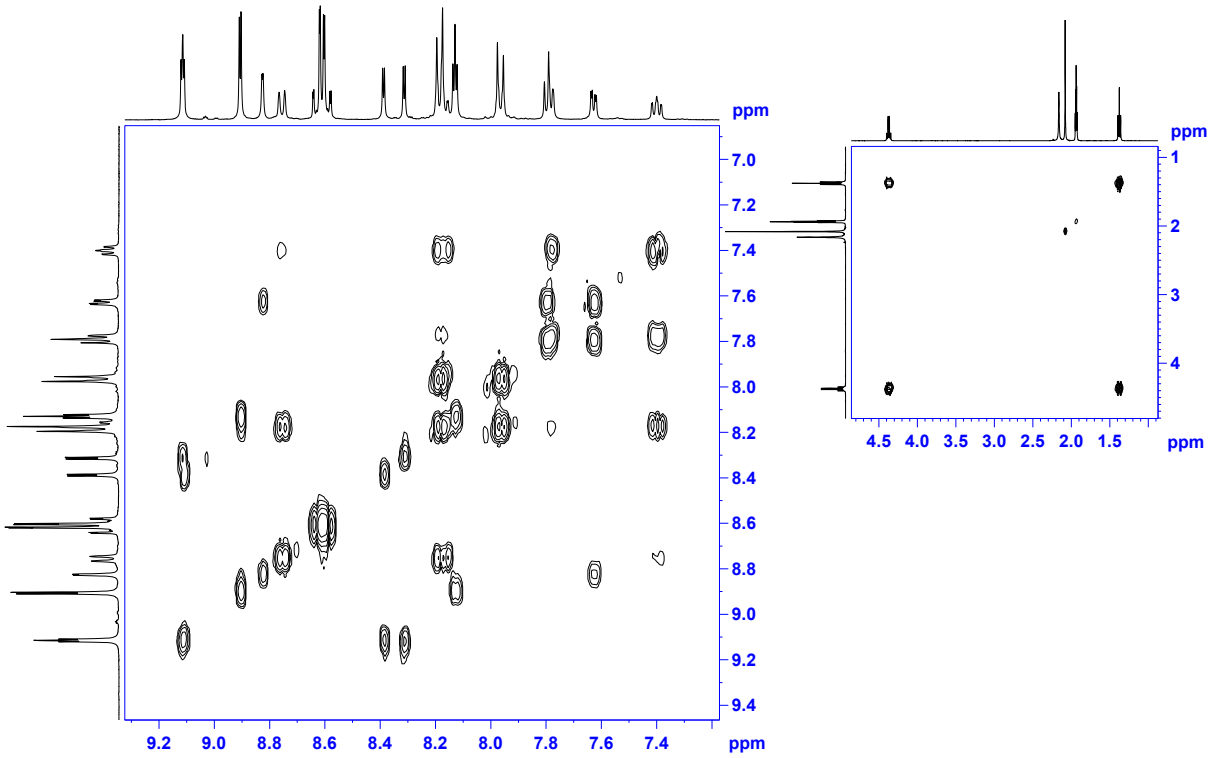

Figure C.18: COSY NMR spectrum of $[Ru(tap)_2(bpyArCOOEt)](PF_6)_2$ in CD_3CN to show aromatic (major) and aliphatic (minor) regions.

Single Mass Analysis
Tolerance = 5.0 PPM / DBE: min = -1.5, max = 1000.0
Isotope cluster parameters: Separation = 1.0 Abundance = 1.0%

Monoisotopic Mass, Odd and Even Electron Ions
276 formula(e) evaluated with 1 results within limits (all results (up to 1000) for each mass)

DCU_TK_CBTK-003 13 (0.430) AM (Cen,4, 80.00, Ar,1.0,556.28,0.70,LS 1); Sm (Mn, 2x5.00); Sb (16,15.00); Sb (16,15.00); Cm (13:32)
1: TOF MS ES+ 7.76e3

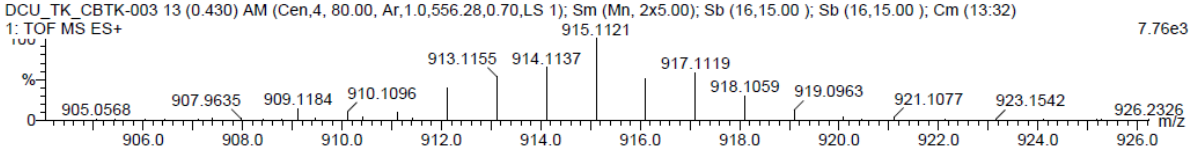

Minimum:				-1.5		
Maximum:		200.0	5.0	1000.0		
Mass	Calc. Mass	mDa	PPM	DBE	Score	Formula
915.1121	915.1082	3.9	4.3	28.5	1	C39 H28 N10 O2 F6 P Ru

Figure C.19: Single mass analysis HRMS spectrum of $[Ru(tap)_2(bpyArCOOEt)](PF_6)_2$ (ESI(+)-qTOF) to indicate $[M^{2+} + PF_6^-]^+$.

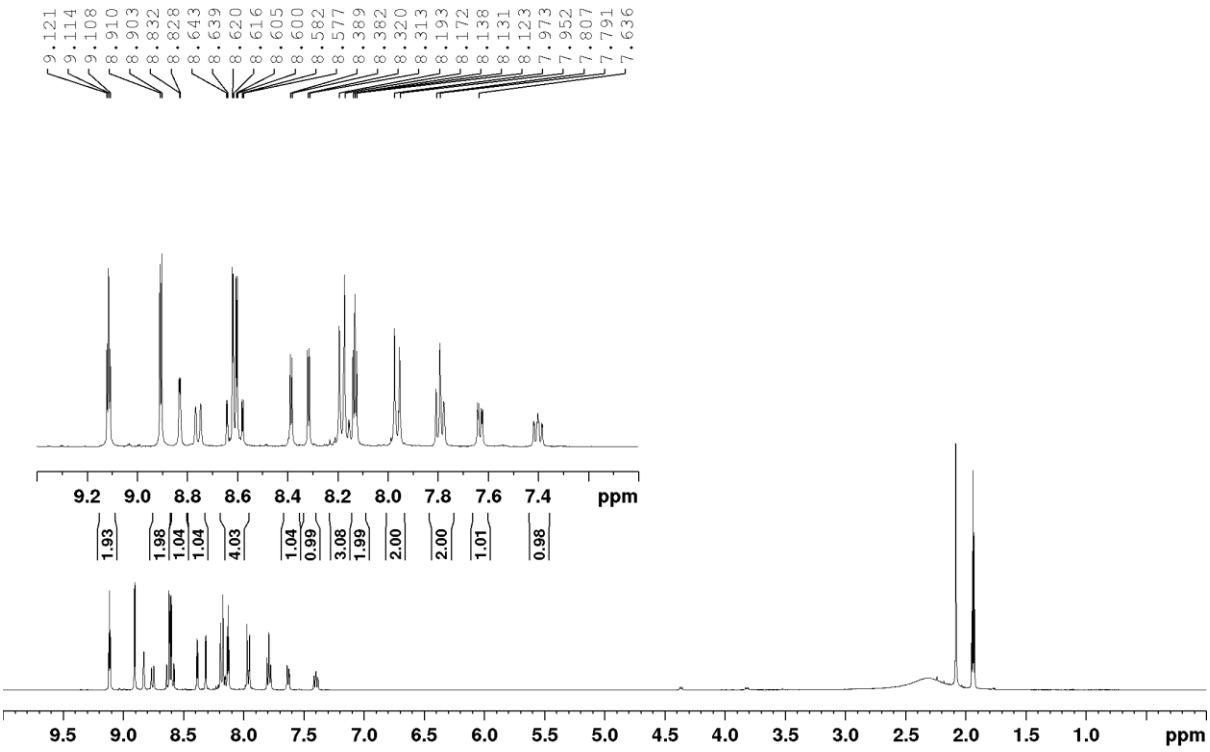

Figure C.20: ^1H NMR (400 MHz) spectrum of $[Ru(tap)_2(bpyArCOOH)](PF_6)_2$ in CD_3CN. Inset: aromatic region.

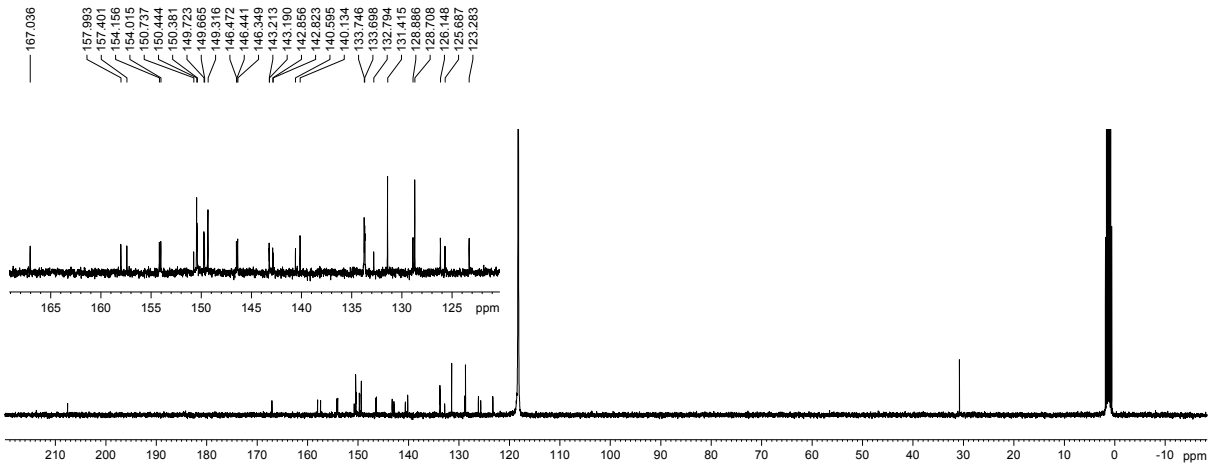

Figure C.21: ^{13}C NMR (100 MHz) spectrum of $[Ru(tap)_2(bpyArCOOH)](PF_6)_2$ in CD_3CN. Inset: aromatic region.

Single Mass Analysis
Tolerance = 5.0 PPM / DBE: min = -1.5, max = 1000.0
Isotope cluster parameters: Separation = 1.0 Abundance = 1.0%

Monoisotopic Mass, Odd and Even Electron Ions
192 formula(e) evaluated with 1 results within limits (all results (up to 1000) for each mass)

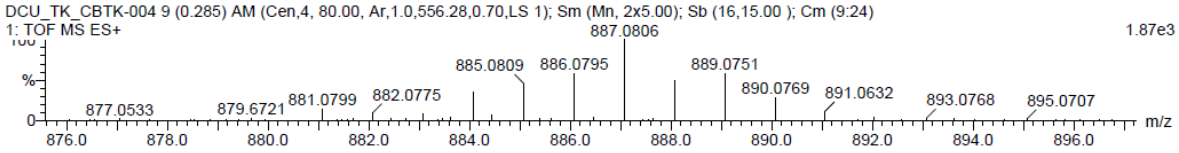

Minimum:				-1.5		
Maximum:		200.0	5.0	1000.0		
Mass	Calc. Mass	mDa	PPM	DBE	Score	Formula
887.0806	887.0769	3.7	4.2	28.5	1	C37 H24 N10 O2 F6 P Ru

Figure C.22: Single mass analysis HRMS spectrum of $[Ru(tap)_2(bpyArCOOH)](PF_6)_2$ (ESI(+)-qTOF) to indicate $[M^{2+} + PF_6^-]^+$.

C.1.3 Conjugates

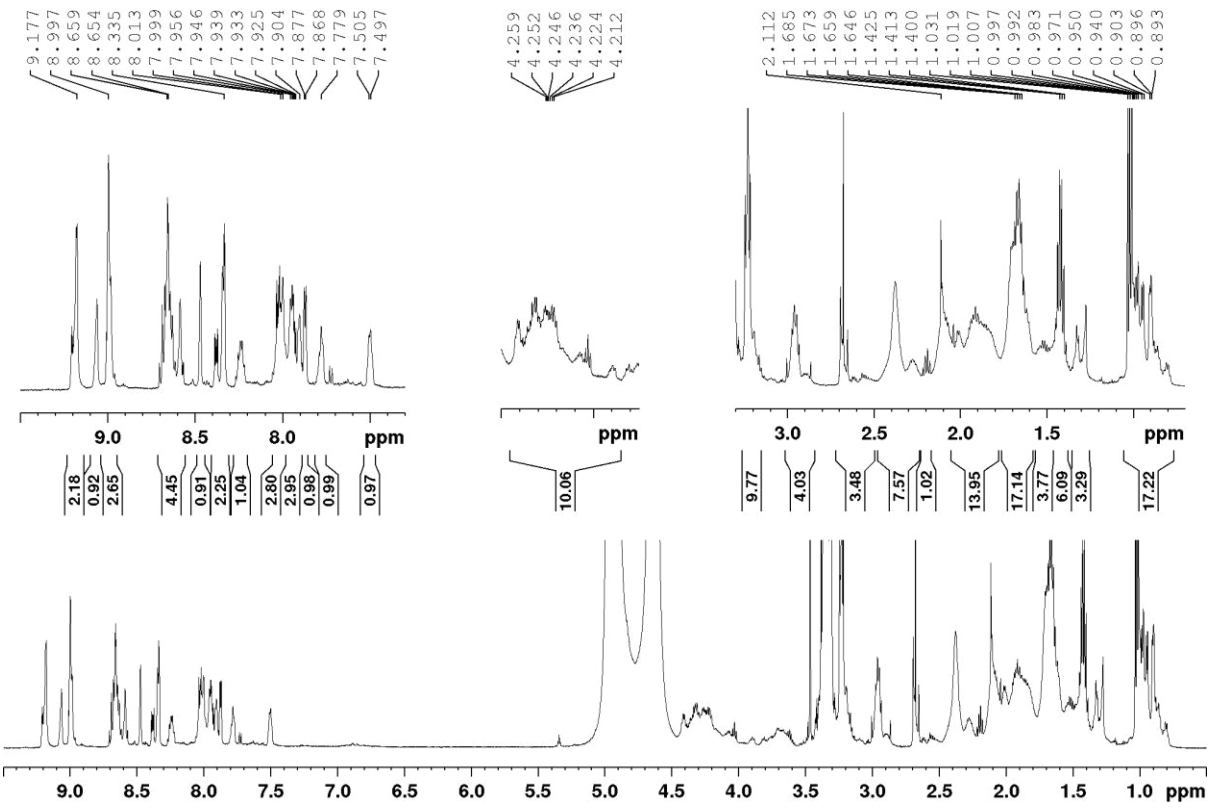

Figure C.24: ^{1}H NMR (600 MHz) spectrum of Ru-tap-NLS in CD_3OD/D_2O. Insets to show key regions. Signal at 2.12 ppm is attributed to residual acetone.

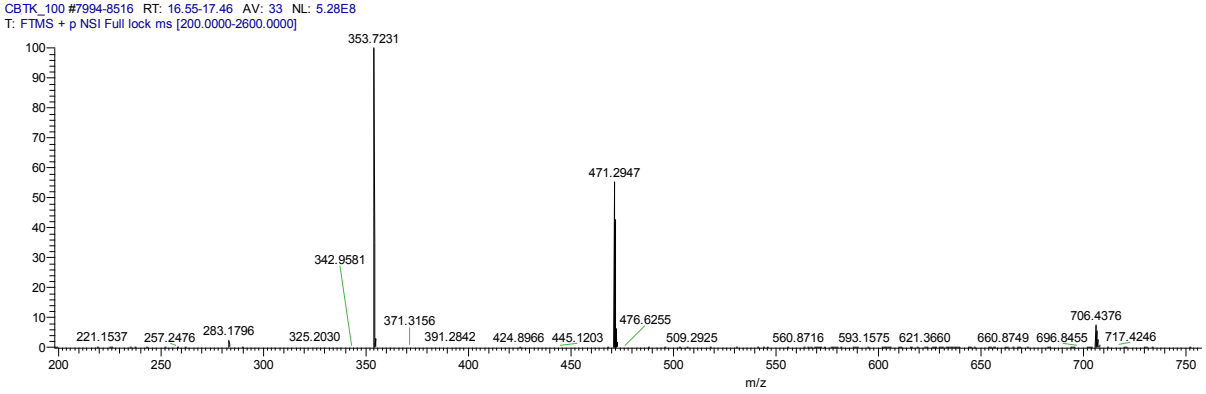

Figure C.25: HRMS Spectrum (Q-Exactive, MS+) of Ru-tap-NLS.

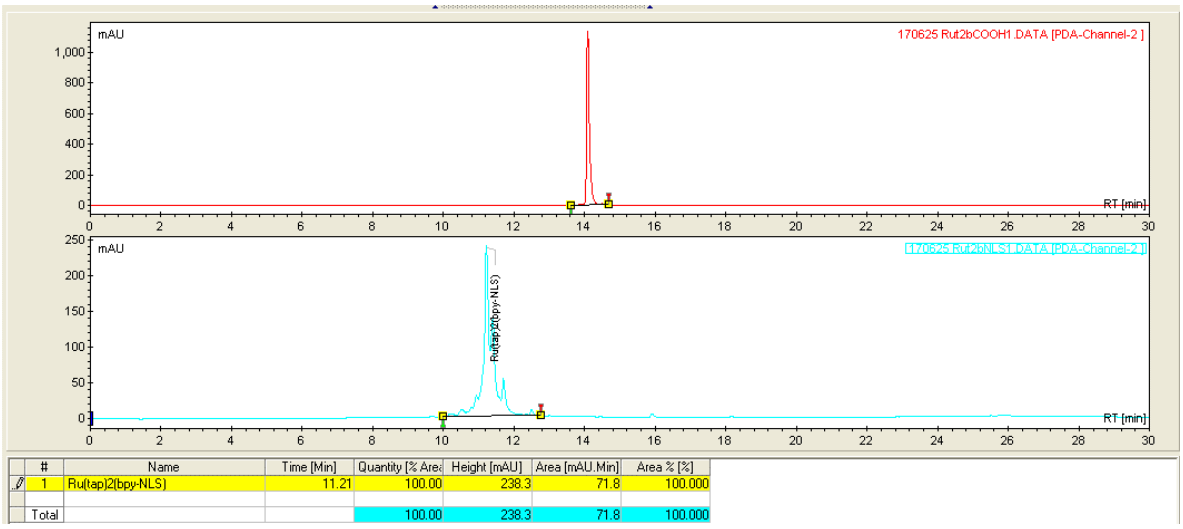

#	Name	Time [Min]	Quantity [% Area]	Height [mAU]	Area [mAU.Min]	Area % [%]
1	Ru(tap)2(bpy-NLS)	11.21	100.00	238.3	71.8	100.000
Total			100.00	238.3	71.8	100.000

Figure C.26: HPLC Chromatograms (RP-C18, CH_3CN/H_2O (0.1 % TFA) gradient, 450 nm) to indicate purity of the conjugate (blue trace, bottom) relative to the parent complex (red trace, top).

C.2 Additional binding data

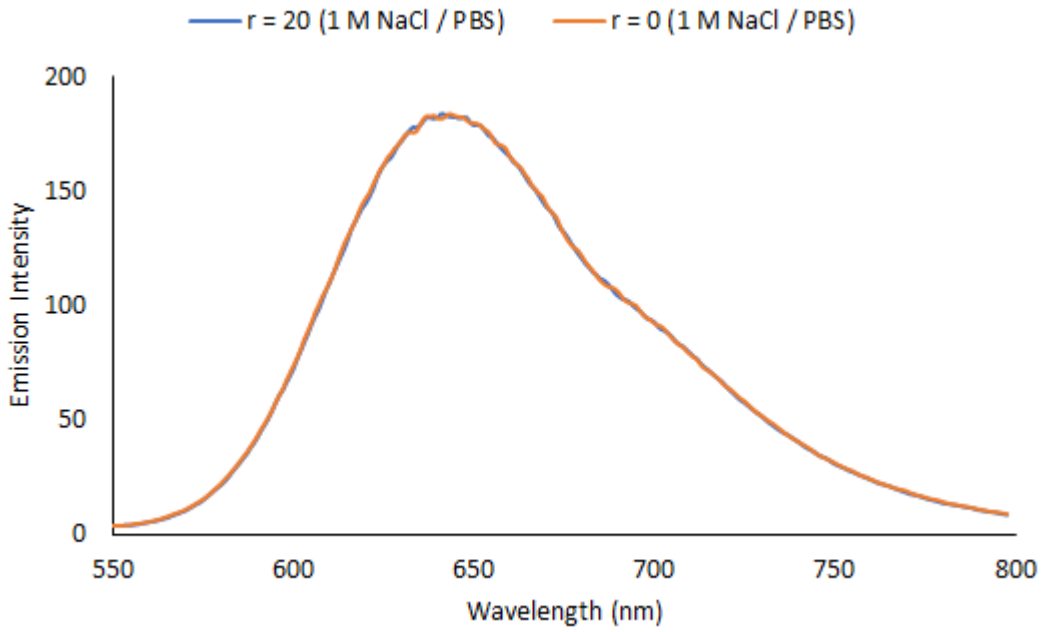

Figure C.27: Emission spectrum of Ru-tap-NLS in the presence (blue) and absence (orange) of ctDNA at high ionic strength.

C.3 Additional electrophoresis and cellular imaging data

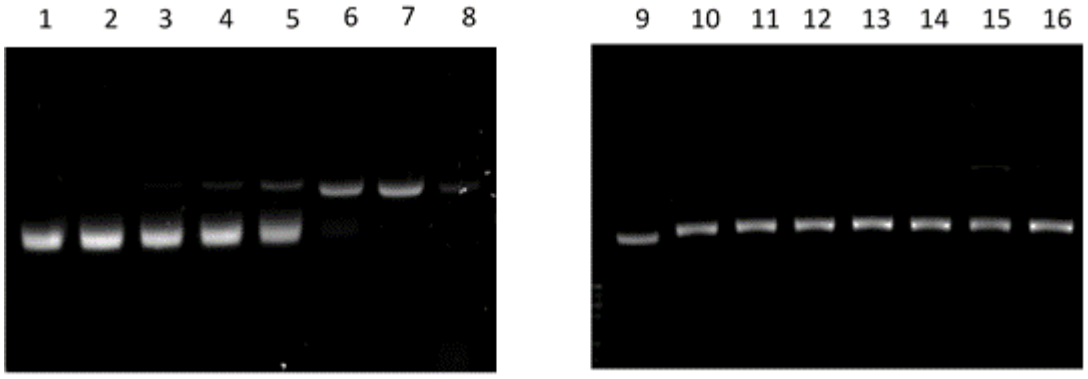

Figure C.28: Gel electrophoresis of $[Ru(bpy)_3]^{2+}$ and pUC19 plasmid DNA (400 ng) in the absence (1-8) and presence (9-16) of the singlet oxygen scavenger sodium azide (5 %). Lane 1 & 9 pUC19 only. Lane 2 & 10 pUC19 + Ru No irradiation. Lane 3 & 11 30 seconds. Lane 4 & 12 1 min. Lane 5 & 13 2 min. Lane 6 & 14 5 min. Lane 7 & 15 10 min. Lane 8 & 16 20 min. Samples were irradiated using a 458 nm argon ion laser (280 mW), and separated on a 1.2 % agarose gel. Data courtesy of Dr. Aisling Byrne (DCU).

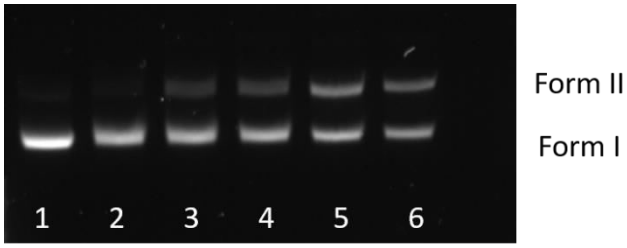

Figure C.29: Agarose gel electrophoresis of supercoiled (400 ng) pUC19 plasmid DNA exposed to Ru-tap-NLS in a 1:10 ratio, and irradiated at 488 nm over 30 minutes. The reactions were carried out in a buffer solution made up of 25 mM NaCl and 80 mM Hepes. Lane 1: pUC19 plasmid control. Lane 2: pUC19 + Ru-tap-NLS no irradiation. Lane 3: 30 seconds. Lane 4: 2 minutes. Lane 5: 10 minutes. Lane 6: 30 minutes. Data courtesy of Dr. Aisling Byrne (DCU).

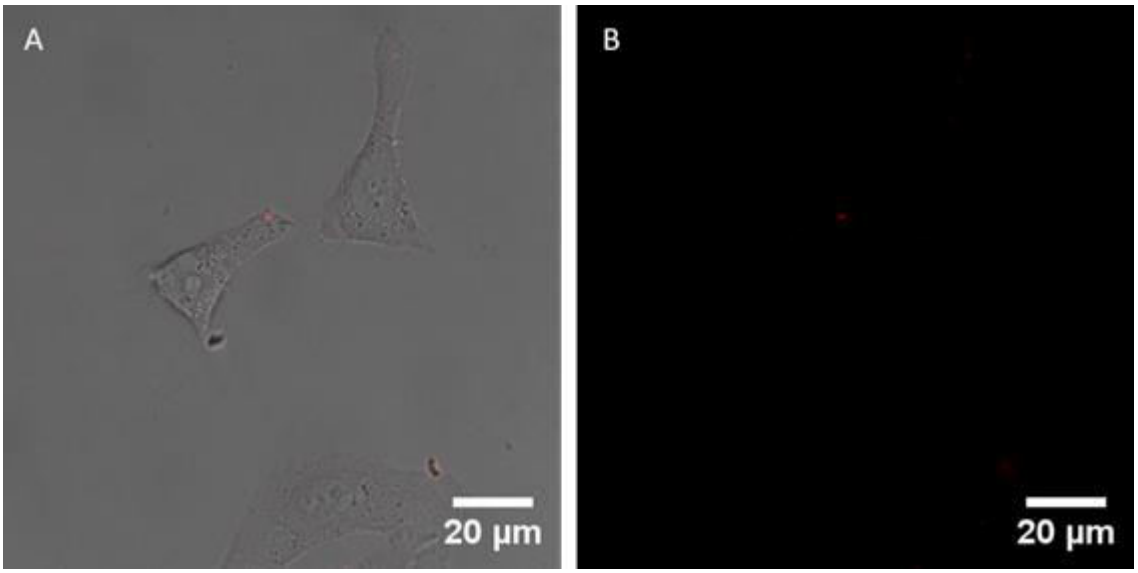

Figure C.30: Live confocal imaging of HeLa cells incubated with Ru-tap-NLS (100 µM) at 4 °C for 5 h in the absence of light. The overlay of the transmission and Ru-tap-NLS channels (A) and the Ru-tap-NLS channel only (B). Ex 470 nm, Em 565- 700 nm. Data courtesy of Dr. Aisling Byrne (DCU).

Thesis Outputs: Publications and Conferences

Elements of the work of this thesis has been disseminated elsewhere as follows:

Publications

1. Martin, A., Byrne, A., Burke, C. S., Forster, R. J. and Keyes, T. E. (2014). Peptide-Bridged Dinuclear Ru(II) Complex for Mitochondrial Targeted Monitoring of Dynamic Changes to Oxygen Concentration and ROS Generation in Live Mammalian Cells. *J. Am. Chem. Soc.* 136**,** 15300–15309.
2. Burke, C. S., Byrne, A. and Keyes, T. E. Transition Metal Luminophores for Cell Imaging. in *Advances in Imaging and Sensing*, 227–254 (CRC Press, 2016).
3. Burke, C. S. and Keyes, T. E. (2016) An efficient route to asymmetrically diconjugated tris(heteroleptic) complexes of Ru(II). *RSC Adv*. 6, 40869–40877.
4. Byrne, A., Burke, C. S. and Keyes, T.E. (2016). Precision targeted ruthenium(II) luminophores; highly effective probes for cell imaging by stimulated emission depletion (STED) microscopy. *Chem. Sci*. 7, 6551–6562.
5. Dolan, C., Burke, C. S., Byrne, A. and Keyes, T. E. Chapter Two - Cellular Uptake and Sensing Capability of Transition Metal Peptide Conjugates. in *Inorganic and Organometallic Transition Metal Complexes with Biological Molecules and Living Cells* (ed. Lo, K. K.-W.) 55–89 (Academic Press, 2017).
6. Byrne, A., Jacobs, J., Burke, C.S., Martin, A., Heise, A., and Keyes, T.E. (2017). Rational design of polymeric core shell ratiometric oxygen-sensing nanostructures. *Analyst,* 142, 3400–3406.
7. Molapo, K. M., Burke, C. S., Forster, R. J., Iwuoha, E. I. and Keyes, T. E. (2017). DNA binding induced electrochemiluminescence at monolayers of a Ru(II) molecular light switch. *Submitted*.
8. Burke, C. S., Byrne, A. and Keyes, T. E. (2017). Precision targeting nuclear and mitochondrial DNA in live cells using peptide-directed light-switch Ru(II) complexes. *Manuscript in preparation*.
9. Burke, C. S., Byrne, A. and Keyes, T. E. (2017). A nuclear-targeted Ru(II) tetraazaphenathrene peptide conjugate for photo-induced DNA destruction in live cells. *Manuscript in preparation*.

Conference Posters and Presentations

July 2017 – Applications of Photoactive Coordination Chemistry (APCC 2017). *University of St. Andrews, St. Andrews, Fife, Scotland.*
Oral Presentation: Peptide Modified Ru(II) Complexes: Precision Tools for Targeting Nucleic Acids in Live Cells. Christopher S. Burke, Aisling Byrne and Tia. E. Keyes.

November 2016 - Irish Institute for Metal Based Drugs, IIMBD 7. *Dublin Institute of Technology (DIT), Grangegorman, Dublin 7.*
Poster and Flash Presentation: Peptide-directed Ru(II)-dppz Complexes as Light-switching DNA Probes for High-Resolution Cellular Imaging. Christopher S. Burke, Aisling Byrne and Tia. E. Keyes.

September 2016 - Gesellschaft Deutscher Chemiker (GDCh) 25. Lecture Conference on Photochemistry. *Döbereiner-Hörsaal, Friedrich-Schiller- Universität, Jena, Thuringia, Germany*.
Poster and Flash Presentation: Peptide-directed Ru(II)-dppz Complexes as Light-switching DNA Probes for High-Resolution Cellular Imaging. Christopher S. Burke, Aisling Byrne and Tia. E. Keyes.

June 2014 - Gordon Research Conference: Metals in Medicine. *Proctor Academy, Andover, NH, USA.*
Poster and Flash Presentation: Novel Ru-BODIPY O_2 Probe for Live Cellular Imaging. Christopher S. Burke, Aaron Martin, Aisling Byrne, Conor Long, Robert J. Forster and Tia. E. Keyes.

Structured PhD Graduate Training Elements

Under the requirements of a structured PhD programme, I have successfully completed 30 ECTS credits of Graduate Training Elements (GTEs) as follows;

GS607FS	Practical Chemistry Demonstrating	10 credits
BDI503	Advances in Diagnostics and Nanobiotechnology	7.5 credits
BE525	Introduction to Animal Cell Culture and Theory	2.5 credits
PS523	Advanced Spectroscopy II	5 credits
GS609CS	Strategies for Getting Published	5 credits